Scalable Control Allocation Methods for the Modular Multilevel Converter

Grégoire Le Goff

THÈSE

En vue de l'obtention du

DOCTORAT DE L'UNIVERSITÉ DE TOULOUSE

Délivré par :

Institut National Polytechnique de Toulouse (Toulouse INP)

Discipline ou spécialité :

Génie Electrique

Présentée et soutenue par :

M. GREGOIRE LE GOFF

le vendredi 25 novembre 2022

Titre :

Méthodes scalables de commande par allocation pour le convertisseur modulaire multiniveaux : de la modélisation à l'implémentation temps réel

---

Ecole doctorale :

Génie Electrique, Electronique, Télécommunications (GEETS)

Unité de recherche :

Laboratoire Plasma et Conversion d'Energie (LAPLACE)

Directeur(s) de Thèse :

M. MAURICE FADEL

Rapporteurs :

M. MAURO CARPITA, HAUTE ECOLE D'INGENIERIE ET DE GESTION
M. XAVIER GUILLAUD, ECOLE CENTRALE DE LILLE

Membre(s) du jury :

M. LUCA ZACCARIAN, LAAS TOULOUSE, Président
M. ABDELKRIM BENCHAIB, SUPERGRID INSTITUTE, Membre
M. MARC BODSON, UNIVERSITY OF UTAH SALT LAKE CITY, Membre
M. MAURICE FADEL, TOULOUSE INP, Membre
MME ANTONETA IULIANA BRATCU, INP GRENOBLE, Membre
M. PHILIPPE LADOUX, TOULOUSE INP, Membre

Dedication

For Science, Perenniality and Biodiversity

Pour la Science, la Pérennité et la Biodiversité

In memory of James Clerk Maxwell.

In 1865, James Clerk Maxwell published a part of his work on electricity and magnetism [Max65], it unified the knowledge on electromagnetism while proposing new contributions such as the doctrine according to which the magnetic field would not only be related to the current of conduction but also to the time-variation of the electric displacement field.

In 1868, he proposed an approach to analyze the dynamics of a system, Watt's governor, by considering it as a linear system, and describing early attempts to design its control by a feedback system [Max68]. These works made him a pioneer of modern automatic control.

From this oustanding work, James Clerk Maxwell can be considered both as one of the founders of modern electromagnetism and automatic control. Disciplines that led to the fields of electrical, electronic, computer and control engineering. The disciplinary field, to which the works proposed here belong, is in line with the legacy of James Clerk Maxwell.

To the one who gave me all her daily support to make this project a success, Marion

Citation

"They did not know it was impossible, so they did it."
"Ils ne savaient pas que c'était impossible, alors ils l'ont fait."
Samuel Langhorne Clemens, known as Mark Twain (1835-1910)

Citation

Acknowledgments

Although this manuscript is written in English, I must thank the people who helped and supported me during these three years of thesis. Those people are almost all French-speaking, which is why the major part of the acknowledgments are in French.

Pour choisir où aller, il faut connaître d'où nous venons. Cultiver ses racines pour déployer ses ailes.

Le chemin qui m'a mené à l'aboutissement que représente cette thèse est un chemin que je suis de longue date. En 2011 j'ai choisi les Sciences de l'Ingénieur comme enseignement d'exploration en seconde et c'est à ce moment que ma vocation pour les sciences et techniques est née. En fin d'année scolaire, j'annonçais à ma professeure principale ma volonté de devenir physicien nucléaire. L'année suivante, je remplaçais les Sciences de la Vie et de la Terre par les Sciences de l'Ingénieur pour aller jusqu'au baccalauréat. J'ai découvert le Génie Electrique et l'Automatique à cette période, disciplines que j'ai très rapidement appréciées pour le fait qu'elles sont à l'interface entre théorique et pratique. Et c'est tout particulièrement cette cohésion entre théorie et pratique qui m'anime: comment, à partir de modèles mathématiques abstraits, il est possible de décrire, comprendre et agir sur la nature physique du monde. En sortant du Lycée mon projet avait légèrement évolué pour le souhait de devenir ingénieur en mécatronique.

Je voudrais donc ici en profiter pour remercier mes professeurs de Lycée avec qui j'ai gardé contact tout au long de mon parcours. Carole Pliquet et Anne-Laure Roncoroni pour l'enseignement des Mathématiques; Mélanie Boudier pour l'enseignement des Sciences Physiques et Thierry Le Parc pour celui des Sciences de l'Ingénieur. Ils ont su éveiller ma curiosité et m'accompagner dans le développement de mes savoirs en sciences avec un enseignement de qualité. Grâce à eux j'ai pu prendre confiance en moi en sciences.

Je suis ensuite arrivé en classes prépa où je me suis d'abord heurté à l'abstraction Mathématique avec François Maltey aux méthodes pédagogiques décalées et avec lequel j'ai découvert la résolution des équations différentielles et les espaces vectoriels. Je n'aurais jamais anticipé, à ce moment-là, que j'aurai eu à replonger dans les espaces vectoriels et la diagonalisation de matrices pour ma thèse. Bien que les premiers mois en prépa aient été difficiles psychologiquement, j'en garde un très bon souvenir car j'ai pu me plonger pleinement dans les sciences et aborder une diversité passionnante de disciplines. J'ai pu y forger mes méthodes personnelles de capitalisation de savoirs tout en m'épanouissant dans l'acquisition de ces savoirs et des outils pour modéliser et comprendre le monde.

Je voudrais donc ici remercier mes enseignants de prépa pour m'avoir permis de développer rapidement et efficacement mes savoirs en sciences tout en cultivant mon goût pour ces dernières. François Maltey et Mr. Calvez pour l'enseignement des Mathématiques, Marine Le Roux et Yvon Le Gall pour l'enseignement des Sciences Physiques, Gwenaël Trégo et Claude Lossec pour l'enseignement des Sciences de l'Ingénieur.

J'ai découvert l'existence du parcours mécatronique à l'ENSEEIHT en deuxième année de prépa, en accord avec mes souhaits de fin de lycée qui n'avaient pas changés (ingénieur en mécatron-

ique), j'ai donc placé l'ENSEEIHT en haut de mes vœux pour les concours. Mes résultats aux concours m'ont permis d'intégrer l'ENSEEIHT dans le département GEA (aujourd'hui 3EA) et ce sont alors trois années de plein épanouissement scientifique et technique dans les disciplines du Génie Electrique et de l'Automatique qui se sont ouvertes à moi. Grâce à cette formation d'ingénieur j'ai pu acquérir les connaissances, méthodes et savoir-faire que je chérissais déjà en fin de Lycée. Tout au long de mon parcours de spécialisation à l'ENSEEIHT, les choix d'options n'ont pas toujours été les plus simples. En définitive j'ai choisi le parcours de Conception Mécatronique des Actionneurs Electromécaniques tout en gardant une appétence forte à la fois pour l'Electronique de Puissance et l'Automatique. L'interaction entre les différentes spécialités et leurs imbrications croisées m'ont conduit à conserver et développer ma culture transversale du domaine plutôt que de ne choisir qu'une spécialité. En sortant de l'ENSEEIHT je dispose alors d'une double casquette Génie Electrique et Automatique avec une spécialisation en conception des actionneurs électromécaniques tout de même.

Je voudrais donc ici remercier les professeurs et enseignant-chercheurs de l'ENSEEIHT qui m'ont dispensé un enseignement de qualité et m'ont permis de devenir ingénieur dans mes disciplines de prédilection. Par ordre de rencontre dans mon parcours à l'ENSEEIHT je remercie donc: Nicolas Roux pour une pédagogie animée qui donne envie d'apprendre, Bruno Sareni pour ses cours clairs et efficaces, Frédéric Messine pour son fameux *"Y'a pas de souci particulier !"* et le goût que j'ai développé pour l'optimisation, François Pigache pour son accompagnement et son aide depuis mon arrivée à Toulouse, pour le plaisir que j'ai eu à collaborer avec lui sur l'amélioration des enseignements en Electromagnétisme et en Modélisation des Machines Electriques, Carole Henaux pour m'avoir convaincu de choisir la spécialité Mécatronique, Philippe Ladoux pour ses Réseaux Haute-Tension et sa *"moulinette à calculs"*, Hubert Piquet pour son *focus* sur les Cellules de Commutations, Stéphane Caux pour son aide précieuse en Automatique, Pascal Maussion pour ses œuvres d'art sous forme de schéma-blocs au tableau, Bruno Dagues pour son *"vous êtes le bienvenu"*, Guillaume Gateau pour la première Commande Numérique de Moteur Electrique que j'ai réalisée dans ma vie, Antoine Picot pour le goût que j'ai développé pour la Programmation, Jérémi Régnier pour son aide tout au long de mon PFE, Clément Nadal pour la rigueur, la propreté et la beauté de ses cours qui m'ont fait aimé les Machines Electriques encore plus que je ne pensais en être capable, Jean-Charles Fabre pour m'avoir permis de comprendre à quel point la Programmation Orientée Objet est une approche puissante, Maurice Fadel - avant d'être mon directeur de thèse - pour la découverte de la Modélisation, l'Analyse et la Commande des Systèmes dans l'Espace d'Etat, un outil qui a changé ma façon d'aborder l'Automatique, Maria David pour la MADA et son amour pour la transmission du savoir, Sandra Ngueveu pour sa pédagogie en TD qui révèle la vraie nature des étudiants, Germain Garcia pour m'avoir fait découvrir et aimer la Commande des Systèmes Multivariables, et Yvan Lefèvre pour la **Science**, pour la beauté même du Savoir.

J'arrive alors à mon diplôme d'ingénieur avec les compétences que je souhaitais développer en sortie de Lycée, mais j'ai envie de continuer à approfondir ses compétences, de développer une expertise. Je m'oriente alors vers une thèse avec la volonté de conserver ma double casquette Génie Electrique et Automatique. Parmi les sujets identifiés, le sujet qui traite de la Commande des convertisseurs par optimisation en ligne m'attire tout particulièrement. Depuis quelques temps déjà j'utilise des méthodes d'optimisation pour la conception des actionneurs électromécaniques, et je réalise habituellement des lois de commande avec des gains fixes qui sont prédéterminés avec différentes méthodes. L'idée de concevoir une loi de commande qui optimise en temps réel le fonctionnement du système électrique éveille en moi un fort intérêt.

Je choisi alors de faire ma thèse sur ce sujet de l'Automatique en l'Electronique de Puissance que me propose Maurice Fadel dont le document présent en est le manuscrit.

En commençant la thèse je voyais cela uniquement comme une spécialisation, une opportunité de développer une expertise, d'approfondir un sujet. Mais en réalité la thèse est bien plus que cela et grâce à l'accompagnement de Maurice Fadel et Marc Bodson, j'ai pu en tirer le bénéfice maximum. La thèse est un dispositif de développement personnel tant sur l'expertise thématique dans un domaine que sur des compétences transversales, mais aussi une opportunité de développement mental et philosophique.

On y apprend d'abord à se remettre en question alors que l'on pense avoir pleinement compris quantités de savoirs une fois le diplôme d'ingénieur en poche. On y apprend à questionner nos propres certitudes en sciences et on devient plus humble vis-à-vis de ce que représente le savoir. Et, par extension, on en vient à questionner le monde qui nous entoure, le sens même de la recherche. Cela nous permet de comprendre la différence entre la science et la recherche et comment elles interagissent.

Si je devais résumer le métier de chercheur, je dirais que ce dernier explore des nouvelles idées pour résoudre des problématiques établies ou pour apporter des réponses à des questions identifiées en s'appuyant sur ce que ses prédécesseurs et pairs ont découvert.

Par-delà la thématique scientifique sur laquelle j'ai travaillé, je voudrais donc chaleureusement remercier Maurice et Marc pour m'avoir accompagné tout au long de ma thèse et d'avoir installé le cadre pour me permettre de me développer personnellement et acquérir ces différentes compétences. Maurice est un super coach qui m'a guidé vers les bonnes décisions et les bons choix en me laissant toujours l'espace nécessaire pour développer mon autonomie et explorer mes propres idées, aussi originales soient-elles que l'étude des systèmes polyphasés jusqu'à 101 phases ! Marc m'a accueilli dans son laboratoire à l'University of Utah à Salt Lake City aux États-Unis. Cette expérience m'a permis de diversifier mes recherches en abordant des thématiques avec une coloration plus forte en Automatique. J'ai vraiment apprécié passer quelques mois là-bas pour découvrir un autre environnement de recherche internationale et d'autres approches du métier de chercheur. Bien que mes interactions avec Marc aient été plus réduites que celles avec Maurice, dû à l'éloignement géographique, Marc a toujours eu cette capacité de clairvoyance vis à vis des travaux que j'ai menés. Par conséquent, Marc a toujours été de bon conseil en apportant un regard neuf et une vision complémentaire à celles que nous partagions avec Maurice. Un grand Merci à tous les deux pour cela ! Je ne saurais mesurer combien l'expérience cumulée des deux carrières de chercheurs que sont les vôtres m'ont conduit à la belle réussite de ce projet.

Je souhaite aussi remercier Jean-Marc Blaquière ainsi que Olivier Durrieu de Madron pour l'aide indispensable qu'ils m'ont apportée pour mettre en place le dispositif expérimental, en particulier Jean-Marc Blaquière qui a fait la conception du MMC et qui en connaissait donc les moindres détails et les points auxquels il fallait être particulièrement vigilant. Merci encore pour le temps qu'il m'a accordé. Merci aussi à Jacques Benaioun pour l'aide informatique apportée tout au long du projet et pour les multiples soucis informatiques auxquels il a pu remédier avec une très grande efficacité. Je le remercie aussi pour avoir rendu possible l'utilisation facilité de la plateforme OPAL-RT pour l'ensemble des essais Hardware-In-the-Loop.

Je voudrais ici aussi remercier sincèrement et humblement mon jury de soutenance, un jury de grande qualité composé de chercheurs d'expérience couvrant à la fois les domaines du Génie Electrique et de l'Automatique, qui a évalué mes travaux dans leur ensemble pour conclure à la délivrance du grade de Docteur. Merci à Xavier Guillaud et à Mauro Carpita d'avoir accepté d'être les rapporteurs de mes travaux. Merci pour l'énergie et le temps que vous avez investi dans la relecture de mon manuscrit, merci pour votre retour critique et les suggestions qui en découlent pour la suite des travaux sur ce sujet. Un certain nombre de points ont été abordés qui mettent en avant le potentiel des méthodes développées et soulignent les développements à

réaliser pour élever le niveau de maturité technologique de certains aspect des travaux. Merci à Xavier Guillaud pour les riches et longues discussions que nous avons eues qui m'ont permis d'identifier les leviers sur lesquels agir pour continuer à mieux affirmer le bénéfice des méthodes d'allocation.

Merci au président de mon jury de soutenance, Luca Zaccarian, d'avoir évoqué des pistes très pertinentes pour améliorer les performances de la commande par allocation mise en place, elles donnent envie de continuer à explorer le sujet ! Merci aux examinateurs, Abdelkrim Benchaib, Antoneta Iuliana Bratcu et Philippe Ladoux pour leur évaluation de mon travail et leurs précieux retours dont je tiens compte actuellement pour esquisser la suite de mon projet professionnel.

La réalisation de cet aboutissement que représente la thèse n'est pas possible sans un soutien humain et moral, en particulier dans les périodes de doutes qui sont intenses et nombreuses. Je voudrais donc prendre ici le temps de remercier ma famille et mes amis pour leur aide qu'ils m'ont apportée, consciemment ou inconsciemment, dans cette épreuve.

Je souhaite remercier mon père, Pierre, qui a eu une influence décisive sur mon parcours professionnel en choisissant de me parler anglais au quotidien depuis ma naissance. C'est une compétence pour laquelle je ne saurais mesurer la chance que j'ai de la posséder, et je ne saurais mesurer à quel point elle m'a facilité la vie tout au long de la thèse et pas seulement. Je remercie ma mère, Isabelle, pour l'espace de liberté qu'elle a créé tout au long de mon parcours scolaire, me permettant de pleinement me développer et d'apprendre à mieux connaître mes appétences disciplinaires. Ce qui m'a conduit à comprendre assez tôt ce qui m'amine désormais.

Je tiens aussi à remercier mes grand-parents paternels Odile et Jean, ma tante Françoise, et ma belle-mère Yveline qui m'ont apporté énormément de soutien au quotidien tout au long de mon parcours pour forger et consolider mes acquis. Mes grand-parents maternels Denise et Yves, ma tante et mon oncle, Fabienne et Peter, qui m'ont inspiré très tôt déjà et m'ont permis de voir le monde différemment, de voir sa vraie nature et comment l'aborder avec résilience. Comme des avant-gardistes de l'ère qui nous vient. Ma famille m'a enseigné le goût de l'effort, nécessaire à toute réussite.

Merci à mon beau-père Thomas et à la famille Pelletier pour le soutien qu'ils m'ont apporté depuis que je les ai rencontrés.

Je remercie mon frère, Raphaël, et mes sœurs, Camille et Clémence, pour m'avoir permis de m'évader de mes travaux en me surprenant avec leur curiosité. Et je vais faire de mon mieux pour les accompagner dans leur développement personnel et leur permettre d'appréhender avec lucidité la réalité, aussi brutale et inexorable soit-elle, de la société qui va être la nôtre à l'avenir.

I would also like to thank my godfather Dennis, and Jim, for helping me develop my English language skills and opening me up to the world. I am grateful to have seen them again in the US during my stay for the PhD and I thank them for the great time we had together, the exchanges we had on a wide variety of cultural topics. These exchanges contributed to my current reflections on the meaning of research and its associated role in our contemporary society.

Je remercie désormais mes amis qui sont arrivées à différents moments de mon aventure mais qui ont tous contribués, de près ou de loin, à cet accomplissement. Par ordre chronologique d'arrivée dans mon aventure :

Merci Patrick, Jenny, Eloïse, *Elo*, et Roma pour m'avoir accueilli à Toulouse et m'avoir accompagné durant certains des moments les plus chaotiques de ce chemin. Merci *Elo* pour ce brin de

folie, ne change pas !

Merci Lucie, *Lulu*, pour tout ton soutien depuis si longtemps, et depuis le début de mon parcours au Lycée. Merci pour tes conseils, ton aide et ta bienveillance dans les moments les plus critiques.

Merci Julie, *Josette*, pour ces super moments que nous partageons depuis notre arrivée à Toulouse, du BAC aux nuits blanches, des rapports de BE aux soirées séries, des déménagements aux pitreries, et surtout, aux pitreries !

Merci Rémy pour avoir été là quand il a fallu gravir des montagnes ensemble face à l'adversité et au manque de temps en vue de l'obtention de notre diplôme en rédaction de rapport *nicht von pappe*.

Merci Jordan pour nos partages de concepts sur pleins de sujets que nous avons, continuons comme ça !

Merci Adrien de me permettre de réaliser qu'il existe d'autres personnes pleinement conscientes de la rigidité du mur qui nous fait face. Cela me donne des raisons de croire qu'il y a encore des possibilités d'arriver à rendre le choc plus doux.

Merci Alice pour les moments que nous partageons depuis le WEI, et surtout, merci de m'aider à défendre les intérêts de la Bretagne et de sa culture en Occitanie avec ferveur !

Merci Chloé, *Cloclo les jonctions PN*, pour ces échanges prolifiques que nous avons sur le monde, la société et les sciences. Et surtout, merci pour tes idées novatrices qui vont révolutionner les convertisseurs statiques !

Merci à la *French Avenue* de Salt Lake City, Clara, Roman, Marjorie, Aurélien, Jules, Alexandre pour ce superbe dépaysement culturel, surtout avec des crêpes et une Croziflette au reblochon français à mon arrivée aux US. Remerciements spéciaux à Clara et Roman pour ce superbe road trip au Grand Canyon et à Monument Valley. Je ne serais jamais arrivé à fournir un manuscrit de cette qualité dans les temps sans ton template LaTeX Roman, merci encore ! Et merci à toi Clara, pour la découverte des folies américaines, de leurs boissons autour d'une masse ou deux et des beaux moments partagés. Quelle chance nous avons eu de t'avoir avec nous à la soutenance, merci encore !

It is also considered critical to thank the US Rangers of the Grand Canyon National Park for their effort in giving us the tremendous opportunity to take pictures of the Grand Canyon at sunset.

Merci aux membres du superbe bureau 417, Quentin, Youssef et Pawel pour votre soutien quotidien tout au long du voyage de la barque que nous avons partagée. Merci Quentin pour *Fertiligène* et ses moments de libération avec *One More Time*. Merci Pawel pour m'avoir fait sursauté un nombre incalculable de fois, *j'ai bien mangé !* Merci Youssef pour avoir rendu notre vie de doctorant bien plus agréable et d'avoir révolutionné le concept même de doctorat avec le Soleil que tu continues de nous apporter au quotidien. Bon vent les gars et surtout, bon courage pour la fin, n'oubliez pas qu'il y a une lueur qui vous attend là, au bout du tunnel ! *Pour la Science, la Pérennité et la Biodiversité !*

Un grand merci aussi aux autres doctorants, que j'ai moins cotoyés mais qui sont restés fidèles au poste dans la tourmente, d'avoir rendu ce chemin moins cahoteux, Mathieu, Davin, Andréa, Ryan, Hugo, Lucien, Noé, Abdul, Corentin, Paul, Maxime P., André et Maxime B.

Finalement, je voudrais accorder ces derniers mots à Marion qui m'a accompagné et épaulé chaque jour depuis le début de cette aventure et même avant. Tout au long de ce projet Marion a été comme ce roc au milieu de la tempête qui ne vacille pas et sur lequel j'ai toujours pu compter au quotidien, comme ce havre de paix qui permet de se ressourcer, de prendre du recul sur l'épreuve pour ensuite y retourner toujours plus fort et déterminé à atteindre l'accomplissement. En tout cas, sache que j'ai pleinement confiance en tes capacités de mener avec succès ton projet actuel jusqu'à son aboutissement, tu fais preuve d'une persévérance, d'une intégrité et d'une curiosité rare. Je chéris ces moments que nous passons à échanger sur nos projets de recherche en essayant toujours de pousser plus loin et de trouver des solutions aux problématiques que l'on rencontre en faisant du brainstorming ensemble. J'ai trouvé en toi, Marion, quelqu'un qui me ressemble beaucoup, qui me comprend et qui partage non seulement un nombre important de valeurs et d'activités avec moi mais aussi le même langage. Tu ne sais sans doute pas à quel point tu as été précieuse à l'aboutissement de ce projet et je ne saurais trouver les mots adéquats pour le décrire, alors **Merci**, tout simplement !

A toutes les personnes concernées, pour les moments passés ensemble que j'ai dû sacrifier en vue de l'accomplissement de ce projet, je vous demande Pardon !

A tous ceux que j'ai involontairement oubliés dans cette longue liste et qui ont contribués de près ou de loin à ce projet, un grand Merci à vous !

Abstract

In the context of a rise in the use of static power converters, the beneficial features of Multilevel Modular Converters (MMCs) have led to their popularization. However, as the number of voltage levels and the number of phases increases, these converters have an increasing number of degrees of freedom to handle. Thus, MMCs represent a challenge for control because the number of control variables is higher than the constraints to be satisfied, making them overactuated systems and opening the way to optimization. Having first appeared in the 1980s in aeronautics to take advantage of the multiplicity of aerodynamic and redundant surfaces that an aircraft presents in order to control its trajectory (flaps, ailerons, control surfaces...), the control allocation methods have proven their worth and were progressively applied in different technologic fields. At the same time, control allocation has been the topic of research works leading to the integration of optimization algorithms in these control methods.

The thesis concerns the development and implementation of real-time control allocation methods, with a focus on online optimization, for an MMC-based power conversion system.

The first part of the thesis focuses on the control-oriented modelling of the MMC converter for the application of allocation methods. This step involves the development of different control models with different levels of detail and complexity. A strong result of this first part is a control model whose complexity is no longer impacted by the number of phases of the considered electrical system.

The second part of the work concerns the development of a new allocation method for MMCs that takes advantage of the beneficial features of state-of-the-art methods. This approach leads to the programming of a new allocation algorithm with dynamic and static characteristics that can be easily adjusted and adapted. Its integration with existing methods is readily and seamlessly achieved.

The third part of the work combines the two previous steps. First in simulation, the control allocation method of the converter is programmed and then tested and validated. For control, different architectures are designed and compared in order to evaluate their ability to achieve the performance required for the proper operation of the system. An analysis of the different control algorithms is then carried out. The main result of this part is the design of a new allocation algorithm allowing one to control the voltages across the capacitors as well as all the currents in each branch of the converter, achieving this result independently of the number of phases. The fourth step is about the experimental validation of the developed methods. To do so, the MMC converter available at the LAPLACE laboratory is used as well as a set of rapid prototyping tools (OPAL-RT) allowing to test and develop the algorithms in a safe and efficient way using a Hardware-In-the-Loop (HIL) technique.

The fifth part of the work concerns the extension of the control algorithms outside the nominal operating zone of the converter. An approach is considered highlighting the capabilities of the allocation methods to reconfigure the operation of the MMC when a fault appears in one of the sub-modules. The results obtained in simulations show an improvement of the resilience of the converter, i.e., a continuity of operation in the presence of faults that justifies a future

continuation of the work in that direction.

The proposed contributions then conclude with perspectives for future exploration and investigation on the topic of allocation methods in electrical engineering.

Résumé

Dans le cadre de la montée en puissance des convertisseurs statiques, les différents avantages qu'il y a à utiliser les Convertisseurs Modulaires Multiniveaux (MMC) ont mené à leur popularisation. Cependant, à mesure que le nombre de niveaux de tension et le nombre de phase augmentent, ces convertisseurs présentent un nombre de plus en plus important de degrés de liberté pour en effectuer la commande. Ainsi les MMC représentent un défi pour la commande car le nombre de variables de commande est alors supérieur aux contraintes à satisfaire, faisant d'eux des systèmes redondants ou encore sous-déterminés ce qui ouvre la voie de l'optimisation. D'abord apparues dans les années 1980 dans l'aéronautique pour tirer profit de la multiplicité des surfaces aérodynamiques et des redondances associées que présente un avion afin d'en contrôler sa trajectoire (volets, ailerons, gouvernes...), les méthodes de commande par allocation ont fait leurs preuves en étant progressivement appliquées dans différents domaines technologiques. En parallèle ces algorithmes ont fait l'objet de travaux pour améliorer les performances obtenues et notamment s'adapter aux systèmes commandés.

Le sujet de la thèse concerne donc le développement et l'implémentation en temps réel de méthodes de commande par allocation, avec un souci d'optimisation en ligne, pour un système de conversion d'énergie à base de MMC.

La première partie de la thèse portent sur la modélisation du convertisseur MMC en vue de sa commande à partir de méthodes d'allocation. Ce qui implique le développement de différents modèles de commande avec différents niveaux de détails et de complexité. Un résultat fort issu de cette première partie est un modèle de commande dont la complexité n'est plus influencée par le nombre de phases du système électrique considéré.

La deuxième étape des travaux concerne le développement d'une nouvelle méthode d'allocation qui met à profit les avantages des méthodes présentes dans l'état de l'art pour en concevoir une nouvelle plus adaptée. Ainsi cette démarche a conduit à la programmation d'un nouvel algorithme d'allocation présentant des caractéristiques dynamiques et statiques réglables et adaptables simplement, son intégration aux méthodes déjà existantes est aisée et presque immédiat.

La troisième étape des travaux combine les travaux précédents. Tout d'abord en simulation, la méthode de commande par allocation du convertisseur est programmée puis testée pour finalement être validée. Pour la commande différentes architectures sont conçues permettant de réaliser des comparatifs afin d'évaluer leur capacité à atteindre les performances requises pour le bon fonctionnement du système. Il en découle une analyse des différents algorithmes de commande proposés. Le résultat principal de cette partie est la conception d'un nouvel algorithme d'allocation permettant de contrôler les tensions aux bornes des condensateurs ainsi que les tous les courants du convertisseur dans chacune des branches et ce indépendamment du nombre de phases.

La quatrième étape porte sur la validation expérimentale des méthodes développées. Pour se faire, le convertisseur MMC disponible au laboratoire LAPLACE est utilisé ainsi qu'un ensemble d'outils de prototypage rapide (OPAL-RT) permettant de tester et mettre au point les algorithmes de façon sûre et efficace.

La cinquième partie des travaux concerne l'extension, hors de la zone de fonctionnement nominale du convertisseur, des algorithmes de commande développés. En effet une ouverture est proposée mettant en exergue les capacités des méthodes d'allocation à reconfigurer le fonctionnement du MMC lorsqu'un défaut apparait dans l'un des sous-modules. Les résultats obtenus en simulation montrent une amélioration de la disponibilité du convertisseur, c'est-à-dire une continuité de fonctionnement en présence de défauts ce qui justifie l'intérêt de poursuivre les travaux dans cette direction.

Les contributions proposées se concluent alors avec des perspectives d'exploration et d'investigations futures sur le sujet des méthodes d'allocation en génie électrique.

Contents

List of Figures

List of Tables

List of Notations

A | B | C | D | E | F | G | H | I | J | K | L | M | N | O | P | Q | R | S | T | U | V | W | X | Y | Z

A

the general notations

The general notation framework is shown on Figure 2. 10

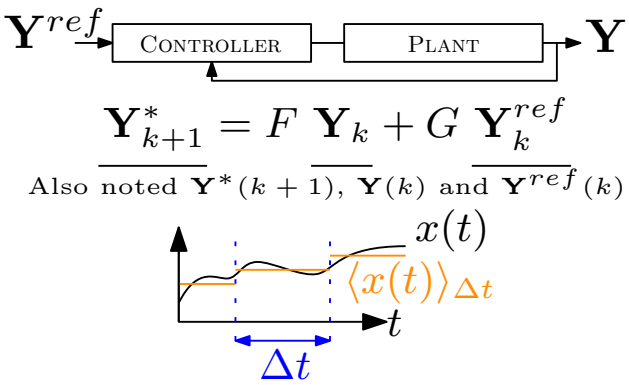

Figure 1: General notation framework of the document on an example of closed-loop system.

A — The general notation for a matrix or a scalar is with normal writing. It can be noted A in general. . . . . xxix, 10

$\mathbf{Y}$ — The general notation of a vector uses a **bold** type. It can be noted $\mathbf{Y}$ in general, and $\mathbf{Y}_k$ or $\mathbf{Y}(k)$ in discrete time-domain. . . . . xxix, 10

$\mathbf{Y}^{ref}$ — The general notation for a reference signal is with the superscript ^{ref}. It can be noted $\mathbf{Y}^{ref}$ in general, and $\mathbf{Y}^{ref}_k$ or $\mathbf{Y}^{ref}(k)$ in discrete time-domain. xxix, 10

$\mathbf{Y}^*$ — The general notation for a desired dynamic behavior in a reference model is with the superscript *. It can be noted $\mathbf{Y}^*$ in general, and $\mathbf{Y}^*_k$ or $\mathbf{Y}^*(k)$ in discrete time-domain. . . . . xxix, 10

$\langle x(t) \rangle_{\Delta t}$ — For the signal $x(t)$, $\langle x(t) \rangle_{\Delta t}$ is the general notation for its average on the time window Δt.

$$\langle x(t) \rangle_{\Delta t} \triangleq \frac{1}{\Delta t} \int_t^{t+\Delta t} x(\tau)\, d\tau$$

. xxix

A — The continuous time state matrix in a state-space model. $A \in \mathbb{R}^{n_x \times n_x}$ . . xxix, 144

$\mathbf{a}$ — The reached action vector when $\mathbf{U}$ is applied to the system. $\mathbf{a} \in \mathbb{R}^{n_a}$ xxix, 38, 40, 144, 145

$\mathbf{a_d}$ — The desired action vector in the control allocation problem. $\mathbf{a_d} \in \mathbb{R}^{n_a}$ . . . . . xxix, xxxi, xl, 34, 37–41, 46, 62, 145–152, 154, 155, 158, 162, 165, 166, 169, 179, 213, 241, I

$\mathbf{a_{d_{MMC}}}$ Desired action vector of the global high-level-low-level control allocation,

$$\mathbf{a_{d_{MMC}}} \triangleq \mathbf{Y^*_{MMC}} - C_{MMC}\left(F_{MMC}\mathbf{X_{MMC}} + H_{MMC}\mathbf{E_{MMC}}\right) \in \mathbb{R}^{2m(N+1)}$$

. xxx

$\hat{\mathbf{a}}_\mathbf{d}$ The complete action vector in the general form of control allocation. $\hat{\mathbf{a}}_\mathbf{d} \in \mathbb{R}^{n_a+n_{ap}}$ . . . . . xxx, xl, 147, 170

$\hat{\mathbf{a}}_{\mathbf{d_{MMC}}}$ Desired action vector of the global high-level-low-level control allocation,

$$\hat{\mathbf{a}}_{\mathbf{d_{MMC}}} \triangleq \mathbf{w}^{\frac{1}{l}} \circ \mathbf{a_{d_{MMC}}} \in \mathbb{R}^{2m(N+1)}$$

. . . . . xxx, xl, 192

$\hat{\mathbf{a}}_{\mathbf{dHL}}$ Entire desired action vector for the high-level control allocation from the entire set of currents in the natural reference frame,

$$\hat{\mathbf{a}}_{\mathbf{dHL}} \triangleq \mathbf{w_I}^{\frac{1}{l}} \circ \mathbf{a_{dHL}}$$

where the operation $\cdot^{\frac{1}{l}}$ is applied to term by term to the weighting vector . . . xxx, xl, 186

$\hat{\mathbf{a}}_{\mathbf{dHL}}^{\mathbf{dq}012}$ Entire desired action vector for the high-level control allocation from the entire set of currents in the Park 12 reference frame,

$$\hat{\mathbf{a}}_{\mathbf{dHL}}^{\mathbf{dq}012} \triangleq \mathbf{w_I}^{\frac{1}{l}} \circ \mathbf{a}_{\mathbf{dHL}}^{\mathbf{dq}012}$$

. . . . . xxx, 188, 189, 229, 230

$\mathbf{a_{dHL}}$ Desired action vector for the high-level control allocation from the entire set of currents in the natural reference frame,

$$\mathbf{a_{dHL}}(k) \triangleq \mathbf{Y^*_{HL}}(k+1) - \tilde{C}_{HL}\tilde{F}_{HL}\tilde{\mathbf{X}}_{\mathbf{HL}}(k) - \tilde{C}_{HL}\tilde{H}_{HL}\tilde{\mathbf{E}}_{\mathbf{HL}}(k)$$

. xxx

$\mathbf{a}_{\mathbf{dHL}}^{\mathbf{dq}012}$ Desired action vector for the high-level control allocation from the entire set of currents in the Park 12 reference frame,

$$\mathbf{a}_{\mathbf{dHL}}^{\mathbf{dq}012}(k) \triangleq \mathbf{Y}_{\mathbf{HL}}^{\mathbf{dq}012*}(k+1) - C_{HL}^{dq012}F_{HL}^{dq012}\mathbf{X}_{\mathbf{HL}}^{\mathbf{dq}012}(k) - C_{HL}^{dq012}H_{HL}^{dq012}\mathbf{E}_{\mathbf{HL}}^{\mathbf{dq}012}(k)$$

. . . . . xxx, xxxi, xl, xli, 229, 230

$\hat{\mathbf{a}}_{\mathbf{dLL}}$ Entire desired action vector for the low-level control allocation from the entire MMC,

$$\hat{\mathbf{a}}_{\mathbf{dLL}} \triangleq \begin{bmatrix} \mathbf{a_{dLL}}(k) \\ w_{v_C}{}^{\frac{1}{l}}\mathbf{a_{pLL}}(k) \end{bmatrix}$$

. . . . . xxx, xli, 182

$\hat{\mathbf{a}}_{\mathbf{dLL}}^{\mathbf{xy}}$ Complete desired action vector for the low-level control allocation from the arm $\#xy$,

$$\hat{\mathbf{a}}_{\mathbf{dLL}}^{\mathbf{xy}}(k) \triangleq \begin{bmatrix} \mathbf{a}_{\mathbf{dLL}}^{\mathbf{xy}}(k) \\ w_{v_C}{}^{\frac{1}{l}}\mathbf{a}_{\mathbf{pLL}}^{\mathbf{xy}}(k) \end{bmatrix} = \begin{bmatrix} v_{xy}^{ref}(k) \\ w_{v_C}{}^{\frac{1}{l}}\left(\mathbf{v}_{\mathbf{C_{xy}}}^{ref}(k) - \mathbf{v_{C_{xy}}}(k)\right) \end{bmatrix} - \begin{bmatrix} \sigma(x)\mathbf{T_{xy}}{}^T\mathbf{X}_{\mathbf{LL}}^{\mathbf{xy}}(k) + \sigma(x)i_{xy}^*(k)\mathbf{Z_{xy}} \\ w_{v_C}{}^{\frac{1}{l}}\frac{T_c}{C}i_{xy}^*(k)\mathbf{T_{xy}} \end{bmatrix}$$

. . . . . xxx, xli, 181, 201, 214

$\mathbf{a}_\mathbf{d}^\mathbf{I}$ The integral component of the control allocation with integral compensator action vector. $\mathbf{a}_\mathbf{d}^\mathbf{I} \in \mathbb{R}^{n_a}$ . . . . . xxx, xxxi, 155, 157, 158, 166, 169

$\mathbf{a}_{\mathbf{d_I HL}}^{\mathbf{dq012}}$ Integral compensator desired action vector for the high-level control allocation with integral compensator from the entire set of currents in the Park 12 reference frame,

$$\mathbf{a}_{\mathbf{d_I HL}}^{\mathbf{dq012}} \triangleq \left(\mathbb{I}_{2m'} - Z_{HL,M}^{dq012}\right)\left[(z-1)^{-1}\left(\mathbb{I}_{2m'} - F_{HL,M}^{dq012}\right)\left(\mathbf{Y}_{\mathbf{HL}}^{\mathbf{dq012}^{ref}} - \mathbf{Y}_{\mathbf{HL}}^{\mathbf{dq012}}\right) - \mathbf{Y}_{\mathbf{HL}}^{\mathbf{dq012}}\right]$$

. . . . . xxxi, 230

$\mathbf{a}_{\mathbf{dLL}}$ Desired action vector for the low-level control allocation from the entire MMC,

$$\mathbf{a}_{\mathbf{dLL}} \triangleq \begin{bmatrix} \mathbf{a}_{\mathbf{d_{LL}}}^{\mathbf{py}_1} \\ \vdots \\ \mathbf{a}_{\mathbf{d_{LL}}}^{\mathbf{xy}} \\ \vdots \\ \mathbf{a}_{\mathbf{d_{LL}}}^{\mathbf{py_m}} \\ \mathbf{a}_{\mathbf{d_{LL}}}^{\mathbf{ny}_1} \\ \dots \\ \mathbf{a}_{\mathbf{d_{LL}}}^{\mathbf{ny_m}} \end{bmatrix}$$

. . . . . xxx, xxxi, 182

$\mathbf{a}_{\mathbf{d_{LL}}}^{\mathbf{xy}}$ Desired action vector for the low-level control allocation from the arm $\#xy$,

$$\mathbf{a}_{\mathbf{d_{LL}}}^{\mathbf{xy}}(k) \triangleq v_{xy}^{ref}(k) - \sigma(x)\mathbf{T_{xy}}^{T}\mathbf{X}_{\mathbf{LL}}^{\mathbf{xy}}(k)$$

. . . . . xxx, xxxi, xlii, 181

$\mathbf{a}_{\mathbf{d_{PE}}}$ Desired action vector for the power-energy control allocation. This vector represents the targeted MMC power balance in closed-loop,

$$\mathbf{a}_{\mathbf{d_{PE}}}(k) \triangleq \mathbf{Y}_{\mathbf{PE}}^{*}(k+1) - C_{PE}X_{PE}(k) - T_c C_{PE}\mathbf{E_{PE}}(k)$$

. . . . . xxxi, xxxviii, lxii, 194

$\tilde{\mathbf{a}}_{\mathbf{d}}$ The desired action vector of the control allocation with integral compensator. $\tilde{\mathbf{a}}_{\mathbf{d}} \in \mathbb{R}^{n_a}$,

$$\tilde{\mathbf{a}}_{\mathbf{d}} = \mathbf{a}_{\mathbf{d}} + \mathbf{a}_{\mathbf{d}}^{\mathbf{I}}$$

. . . . . xxxi, 155, 158, 166, 169, 170

$\tilde{\mathbf{a}}_{\mathbf{d_{HL}}}^{\mathbf{dq012}}$ The new desired action vector taking into account the integral action for the high-level control allocation with integral compensator from the entire set of currents in the Park 12 reference frame,

$$\tilde{\mathbf{a}}_{\mathbf{d_{HL}}}^{\mathbf{dq012}}(k) \triangleq \mathbf{a}_{\mathbf{d_{HL}}}^{\mathbf{dq012}}(k) + \tilde{\mathbf{a}}_{\mathbf{d_{HL}}}^{\mathbf{dq012}}(k)$$

. . . . . xxxi, 230

A_{HL} Continuous time dynamic matrix for the high-level SSM,

$$A_{HL} \triangleq \begin{bmatrix} -\frac{R_m^{eq}}{L_m^{eq}} & & & \\ & -\frac{R_s^{eq}}{L_s^{eq}} & & \\ & & -\frac{R_c^{eq}}{L_c^{eq}}\mathbb{I}_m & \\ & & & -\frac{R_o^{eq}}{L_o^{eq}}\mathbb{I}_m \end{bmatrix} \in \mathcal{M}_{2m+2}(\mathbb{R})$$

. . . . . xxxi, xxxii, 84–86

A_{HL}^{dq0} Continuous time dynamic matrix for the high-level SSM in the Park reference frame,

$$A_{HL}^{dq0} \triangleq \begin{bmatrix} -\frac{R_m^{eq}}{L_m^{eq}} & & & & & \\ & -\frac{R_s^{eq}}{L_s^{eq}} & & & & \\ & & -\frac{R_c^{eq}}{L_c^{eq}} & n\omega & & \\ & & -n\omega & -\frac{R_c^{eq}}{L_c^{eq}} & & \\ & & & & -\frac{R_o^{eq}}{L_o^{eq}} & \omega \\ & & & & -\omega & -\frac{R_o^{eq}}{L_o^{eq}} \end{bmatrix} \in \mathcal{M}_6(\mathbb{R})$$

. . . . . xxxii, xliii, xlvi, xlvii, 95

A_{HL}^{dq012} Continuous time dynamic matrix for the high-level SSM in the Park 12 reference frame,

$$A_{HL}^{dq012} \triangleq \begin{bmatrix} -\frac{R_m^{eq}}{L_m^{eq}} & & & & & & & & & \\ & -\frac{R_s^{eq}}{L_s^{eq}} & & & & & & & & \\ & & -\frac{R_c^{eq}}{L_c^{eq}} & \omega & & & & & & \\ & & -\omega & -\frac{R_c^{eq}}{L_c^{eq}} & & & & & & \\ & & & & -\frac{R_c^{eq}}{L_c^{eq}} & 2\omega & & & & \\ & & & & -2\omega & -\frac{R_c^{eq}}{L_c^{eq}} & & & & \\ & & & & & & -\frac{R_o^{eq}}{L_o^{eq}} & \omega & & \\ & & & & & & -\omega & -\frac{R_o^{eq}}{L_o^{eq}} & & \\ & & & & & & & & -\frac{R_o^{eq}}{L_o^{eq}} & 2\omega \\ & & & & & & & & -2\omega & -\frac{R_o^{eq}}{L_o^{eq}} \end{bmatrix} \in \mathcal{M}_{2m'}(\mathbb{R})$$

. . . . . xxxii, xliii, xlvi, xlvii, 109, 110

$\tilde{A}_{HL}$ Minimal state-space realization continuous time dynamic matrix for the high-level SSM,

$$\tilde{A}_{HL} \triangleq C_{HL} A_{HL} {C_{HL}}^T \in \mathcal{M}_{2m}(\mathbb{R})$$

. . . . . xxxii, xliii, xlvi, xlvii, 86

A_{LL}^{xy} Continuous time dynamic matrix for the low-level SSM from the arm $\#xy$,

$$A_{LL}^{xy} \triangleq \mathbb{O}_{N,N}$$

. . . . . xxxii, 66

α_C^{max} Maximum overvoltage ratio across the capacitors of the submodules,

$$\alpha_C^{max} \triangleq \frac{v_C^{max}}{v_C^{nom}} - 1$$

. . . . . xxxii, lix, lxix, 240, 241

$\mathbf{a_p}$ The preferred action vector. $\mathbf{a_p} \in \mathbb{R}^{n_{a_p}}$ . . . . . xxxii, 147, 170

A_{PE} Continuous time dynamic matrix for the power-energy SSM,

$$A_{PE} \triangleq 0$$

. . . . . xxxii, 113

$\mathbf{a_{pLL}}$ Preference desired action vector for the low-level control allocation from the entire MMC,

$$\mathbf{a_{pLL}} \triangleq \begin{bmatrix} \mathbf{a}_{\mathbf{pLL}}^{\mathbf{py}_1} \\ \vdots \\ \mathbf{a}_{\mathbf{pLL}}^{\mathbf{xy}} \\ \vdots \\ \mathbf{a}_{\mathbf{pLL}}^{\mathbf{py}_m} \\ \mathbf{a}_{\mathbf{pLL}}^{\mathbf{ny}_1} \\ \vdots \\ \mathbf{a}_{\mathbf{pLL}}^{\mathbf{ny}_m} \end{bmatrix}$$

. . . . . xxx, xxxiii, 182

$\mathbf{a}_{\mathbf{pLL}}^{\mathbf{xy}}$ Preference desired action vector for the low-level control allocation from the arm $\#xy$,

$$\mathbf{a}_{\mathbf{pLL}}^{\mathbf{xy}}(k) \triangleq \mathbf{v}_{\mathbf{C_{xy}}}^{ref}(k) - \mathbf{v}_{\mathbf{C_{xy}}}(k) - \frac{T_c}{C} i_{xy}^{*}(k)\mathbf{T_{xy}}$$

. . . . . xxx, xxxiii, xlii, 181, 213

$\mathcal{A}$ The linear constraint matrix in the LP, and in the QP. 149, 150, 181–183, 186, 188, 192, 193

B

B The continuous time input matrix in a state-space model. $B \in \mathbb{R}^{n_x \times n_u}$ xxxiii, 144, 145, 148, 165

b The continuous time input function in a state-space model. $b : \mathbb{R}^{n_u} \mapsto \mathbb{R}^{n_x}$ . . xxxiii, 144, 145, 148

$\mathcal{B}^c$ Static virtual basis in the m-phase case,

$$\mathcal{B}^c \triangleq \{\mathbf{x}_1^{\mathbf{c}}, \mathbf{x}_2^{\mathbf{c}}, \ldots, \mathbf{x}_{\mathbf{k}}^{\mathbf{c}}, \ldots, \mathbf{x}_{\mathbf{m}}^{\mathbf{c}}\}$$

. . . . . xxxiii, xxxvii, xxxviii, lxxvi, 98–103, 105

$\mathcal{B}_p^c$ Static virtual othogonal basis of the subspace E_p^c. For more details see equations (3.114) and (3.115) 98, 99

B_Δ^m Continuous time control submatrix "Δ" for the high-level SSM,

$$B_\Delta^m \triangleq -\frac{1}{2} N_\Delta(m) \in \mathcal{M}_m(\mathbb{R})$$

. . . . . xxxiii, xxxiv, 91, 93, 108, 109

$B_\Delta^{\alpha\beta 0}$ Continuous time control submatrix "Δ" for the high-level SSM in the $\{\alpha, \beta, 0\}$ reference frame,

$$B_\Delta^{\alpha\beta 0} \triangleq [C_K] B_\Delta^m [C_K]^+ \in \mathcal{M}_3(\mathbb{R})$$

. . . . . xxxiii, 91

B_Δ^{dq0} Continuous time control submatrix "Δ" for the high-level SSM in the $\{d, q, 0\}$ reference frame,

$$B_\Delta^{dq0} \triangleq [P(-\theta)][C_K] B_\Delta^m [C_K]^+ [P(\theta)] = \begin{bmatrix} -\frac{1}{2} & 0 & 0 \\ 0 & -\frac{1}{2} & 0 \\ 0 & 0 & 0 \end{bmatrix} \in \mathcal{M}_3(\mathbb{R})$$

. . . . . xxxiii, xxxiv, 93, 94

B_{Δ}^{dq012} Continuous time control submatrix "Δ" for the high-level SSM in the $\{d_1, q_1, d_2, q_2, 0\}$ reference frame,

$$B_{\Delta}^{dq012} \triangleq [P(-\theta)_{12}^{m}]\left[C_{K_{12}}^{m}\right]B_{\Delta}^{m}\left[C_{K_{12}}^{m}\right]^{+}[P(\theta)_{12}^{m}] = \begin{bmatrix} -\frac{1}{2} & 0 & 0 & 0 & 0 \\ 0 & -\frac{1}{2} & 0 & 0 & 0 \\ 0 & 0 & -\frac{1}{2} & 0 & 0 \\ 0 & 0 & 0 & -\frac{1}{2} & 0 \\ 0 & 0 & 0 & 0 & 0 \end{bmatrix} \in \mathcal{M}_{5,m'}(\mathbb{R})$$

. . . . . xxxiv, 108

$B_{\Delta}^{dq0_n}$ Continuous time control submatrix "Δ" for the high-level SSM in the $\{d, q, 0\}$ reference frame at n times the $\mathbf{I_o}$ fondamental frequency,

$$B_{\Delta}^{dq0_n} \triangleq [P(-n\theta)][C_K]B_{\Delta}^{m}[C_K]^{+}[P(n\theta)] \in \mathcal{M}_3(\mathbb{R})$$

. . . . . xxxiv, 92, 93

$\tilde{B}_{\Delta}^{dq0}$ Reduced continuous time control submatrix "Δ" for the high-level SSM in the $\{d, q, 0\}$ reference frame,

$$\tilde{B}_{\Delta}^{dq0} \triangleq \begin{bmatrix} 1 & 0 & 0 \\ 0 & 1 & 0 \end{bmatrix} B_{\Delta}^{dq0} = \begin{bmatrix} -\frac{1}{2} & 0 & 0 \\ 0 & -\frac{1}{2} & 0 \end{bmatrix} \in \mathcal{M}_{2,3}(\mathbb{R})$$

. . . . . xxxiv, xli, 94, 95

$\tilde{B}_{\Delta}^{dq012}$ Reduced continuous time control submatrix "Δ" for the high-level SSM in the $\{d_1, q_1, d_2, q_2, 0\}$ reference frame,

$$\tilde{B}_{\Delta}^{dq012} \triangleq \begin{bmatrix} \mathbb{I}_4 & \mathbb{O}_{4,1} \end{bmatrix} B_{\Delta}^{dq012} = \begin{bmatrix} -\frac{1}{2} & 0 & 0 & 0 & 0 \\ 0 & -\frac{1}{2} & 0 & 0 & 0 \\ 0 & 0 & -\frac{1}{2} & 0 & 0 \\ 0 & 0 & 0 & -\frac{1}{2} & 0 \end{bmatrix} \in \mathcal{M}_{4,m'}(\mathbb{R})$$

. . . . . xxxiv, xli, 108–110

B_{HL} Continuous time control matrix for the high-level SSM,

$$B_{HL} \triangleq -\frac{1}{2}\begin{bmatrix} \frac{N_{\Sigma}(m)}{L_m^{eq}} & \frac{N_{\Sigma}(m)}{L_m^{eq}} \\ \frac{N_{\Sigma}(m)}{L_s^{eq}} & -\frac{N_{\Sigma}(m)}{L_s^{eq}} \\ \frac{N_{\Delta}(m)}{L_c^{eq}} & -\frac{N_{\Delta}(m)}{L_c^{eq}} \\ \frac{N_{\Delta}(m)}{L_o^{eq}} & \frac{N_{\Delta}(m)}{L_o^{eq}} \end{bmatrix} \in \mathcal{M}_{2m+2,2m}(\mathbb{R})$$

. . . . . xxxiv, xxxv, 84–86

B_{HL}^{dq0} Continuous time control matrix for the high-level SSM in the Park reference frame,

$$B_{HL}^{dq0} \triangleq \begin{bmatrix} B_{\Sigma}^{dq0}/L_m^{eq} & B_{\Sigma}^{dq0}/L_m^{eq} \\ B_{\Sigma}^{dq0}/L_s^{eq} & -B_{\Sigma}^{dq0}/L_s^{eq} \\ \tilde{B}_{\Delta}^{dq0}P((1-n)\theta)/L_c^{eq} & -\tilde{B}_{\Delta}^{dq0}P((1-n)\theta)/L_c^{eq} \\ \tilde{B}_{\Delta}^{dq0}/L_o^{eq} & \tilde{B}_{\Delta}^{dq0}/L_o^{eq} \end{bmatrix} \in \mathcal{M}_6(\mathbb{R})$$

. . . . . xxxiv, xlvi, 95

B_{HL}^{dq012} Continuous time control matrix for the high-level SSM in the Park 12 reference frame,

$$B_{HL}^{dq012} \triangleq \begin{bmatrix} B_{\Sigma}^{dq012}/L_m^{eq} & B_{\Sigma}^{dq012}/L_m^{eq} \\ B_{\Sigma}^{dq012}/L_s^{eq} & -B_{\Sigma}^{dq012}/L_s^{eq} \\ \tilde{B}_{\Delta}^{dq012}/L_c^{eq} & -\tilde{B}_{\Delta}^{dq012}/L_c^{eq} \\ \tilde{B}_{\Delta}^{dq012}/L_o^{eq} & \tilde{B}_{\Delta}^{dq012}/L_o^{eq} \end{bmatrix} \in \mathcal{M}_{2m'}(\mathbb{R})$$

. . . . . xxxiv, xlvi, 109, 110

$\tilde{B}_{HL}$ Minimal state-space realization continuous time control matrix for the high-level SSM,

$$\tilde{B}_{HL} \triangleq C_{HL} B_{HL} \in \mathcal{M}_{2m}(\mathbb{R})$$

. . . . . xxxv, xlvi, 86

B_{LL}^{xy} Continuous time control matrix for the low-level SSM from the arm $\#xy$,

$$B_{LL}^{xy} \triangleq \frac{i_{xy}^*}{C} L_{xy}$$

. . . . . xxxv, 66

$\mathcal{B}^m$ Natural basis in the m-phase case,

$$\mathcal{B}^m \triangleq \{\mathbf{x_1^m}, \mathbf{x_2^m}, \ldots, \mathbf{x_k^m}, \ldots, \mathbf{x_m^m}\}$$

. . . . . xxii, xxxv, xxxvii, xxxviii, xliv, xlv, lv, lxxvii, 97–102, 133

B_{PE} Continuous time control matrix for the power-energy SSM,

$$B_{PE} \triangleq m\,(v_p - v_n)$$

. . . . . xxxv, lviii, 113, 193, 194

B'_{PE} Continuous time nonlinear control matrix for the power-energy SSM,

$$B'_{PE} \triangleq -2m^2 R_s \in \mathbb{R}$$

. . . . . xxxv, lviii, 113, 193, 194

b The linear constraint vector in the LP, and in the QP 149, 150

B_{Σ}^{m} Continuous time control submatrix "Σ" for the high-level SSM,

$$B_{\Sigma}^{m} \triangleq -\frac{1}{2} N_{\Sigma}(m) \in \mathcal{M}_{1,m}(\mathbb{R})$$

. . . . . xxxv, 107

B_{Σ}^{dq0} Continuous time control submatrix "Σ" for the high-level SSM in the $\{d, q, 0\}$ reference frame,

$$B_{\Sigma}^{dq0} \triangleq \begin{bmatrix} 0 & 0 & 1 \end{bmatrix} B_{\Sigma}^{m} [C_K]^{+} [P(\theta)] = \frac{k_0}{mK} \begin{bmatrix} 0 & 0 & -\frac{1}{2} \end{bmatrix} \in \mathcal{M}_{1,3}(\mathbb{R})$$

. . . . . xxxiv, xxxv, 90, 91, 95

B_{Σ}^{dq012} Continuous time control submatrix "Σ" for the high-level SSM in the $\{d_1, q_1, d_2, q_2, 0\}$ reference frame,

$$B_{\Sigma}^{dq012} \triangleq \begin{bmatrix} 0 & 0 & 0 & 0 & 1 \end{bmatrix} B_{\Sigma}^{m} \left[C_{K_{12}}^{m}\right]^{+} [P(\theta)_{12}^{m}] = \frac{k_0}{mK} \begin{bmatrix} 0 & 0 & 0 & 0 & -\frac{1}{2} \end{bmatrix} \in \mathcal{M}_{1,5}(\mathbb{R})$$

. . . . . xxxiv, xxxv, 107, 108, 110

C

C Capacity of the submodules' capacitors xxx, xxxiii, xxxv, xxxviii, xlii, lviii, 13, 20, 21, 55, 56, 58, 59, 62, 64–66, 68, 180, 181, 196, 206, 213, 218

$LLCAP_{xy}$ The low-level control allocation problem of an arm $\#xy$ represents the low-level control objective of a single arm of the MMC. It is defined by (5.8). . . . . xxxvi, 181, 236

$LLCAOP_{xy}$ The low-level control allocation optimization problem of an arm $\#xy$ represents the $LLCAP_{xy}$ formulated as an optimization problem to be solved in real time. It is defined by (5.9). 181, 182, 201, 216

$LLCAP$ The low-level control allocation problem of the entire MMC represents the low-level control objective of the MMC. It is defined by (5.10). . . . . xxxvi, 182

$LLCAOP$ The low-level control allocation optimization problem of the entire MMC represents the $LLCAP$ formulated as an optimization problem to be solved in real time. It is defined by (5.11). 182, 192, 193

$HLCAP_{m-ph}$ The high-level control allocation problem m-ph represents the high-level control objective of the MMC in the stationary reference frame. It is defined by (5.17). . . . . xxxvi, 186

$HLCAOP_{m-ph}$ The high-level control allocation optimization problem m-ph represents the $HLCAP_{m-ph}$ formulated as an optimization problem to be solved in real time. It is defined by (5.18). 186, 197, 205

C_{MMC} Output matrix of the global high-level-low-level state-space model describing the dynamic behavior of the voltages and currents of the entire MMC,

$$C_{MMC} \triangleq \mathbb{I}_{2m(N+1)}$$

. . . . . xxx, xxxvi, lvii, 192

$HLCAP_{Park\ 12}$ The high-level control allocation problem Park12 represents the high-level control objective of the MMC in the Park 12 synchronously rotating reference frame. It is defined by (5.29). . . . . xxxvi, 188, 229, 230

$HLCAOP_{Park\ 12}$ The high-level control allocation optimization problem Park12 represents the $HLCAP_{Park\ 12}$ formulated as an optimization problem to be solved in real time. It is defined by (5.30). 188, 197

$HLLLCAP$ The high-level-low-level control allocation problem represents both the high-level control and the low-level control objectives of the MMC simultaneously embedded in a single control allocation problem. It is defined by (5.37). xxxvi, 192

$MMCCAOP$ The modular multilevel converter control allocation optimization problem represents the $HLLLCAP$ formulated as an optimization problem to be solved in real time. It is defined by (5.38). 192, 193, 197

$PECAP$ The power-energy control allocation problem represents both the power-energy control objectives of the MMC. It is defined by (??). 194, 197

C_{HL} Continuous time output matrix for the high-level SSM,

$$C_{HL} \triangleq \begin{bmatrix} 1 & & & & & & \\ & 1 & & & & & \\ & & \mathbb{I}_{m-1} & \mathbb{O}_{m-1,1} & & & \\ & & & & \mathbb{I}_{m-1} & \mathbb{O}_{m-1,1} \end{bmatrix} \in \mathcal{M}_{2m,2m+2}(\mathbb{R})$$

. . . . . xxxii, xxxv–xxxvii, xlii, lxxvi, 84–86

C_{HL}^{dq0} Continuous time output matrix for the high-level SSM in the Park reference frame,

$$C_{HL}^{dq0} \triangleq \begin{bmatrix} 1 & & & \\ & 1 & & \\ & & \mathbb{I}_2 & \\ & & & \mathbb{I}_2 \end{bmatrix} \in \mathcal{M}_6(\mathbb{R})$$

. . . . . xxxvi, 95

C_{HL}^{dq012} Continuous time output matrix for the high-level SSM in the PARK 12 reference frame,

$$C_{HL}^{dq012} \triangleq \begin{bmatrix} 1 & & & & \\ & 1 & & & \\ & & \mathbb{I}_{m'-1} & & \\ & & & \mathbb{I}_{m'-1} \end{bmatrix} \in \mathcal{M}_{2m'}(\mathbb{R})$$

. . . . . xxx, xxxvii, lvii, 109, 110, 187

$\tilde{C}_{HL}$ Minimal state-space realization continuous time output matrix for the high-level SSM,

$$\tilde{C}_{HL} \triangleq C_{HL} {C_{HL}}^T = \mathbb{I}_{2m} \in \mathcal{M}_{2m}(\mathbb{R})$$

. . . . . xxx, xxxvii, lvii, 86, 185

$\mathbf{c_i}$ Eigenvector of the linear map λ,

$$\mathbf{c_i} = \frac{K}{\sqrt{2}} \begin{bmatrix} 1 \\ e^{j\theta_m(i-1)} \\ e^{j\theta_m(i-1)2} \\ e^{j\theta_m(i-1)3} \\ \vdots \\ e^{j\theta_m(i-1)(m-2)} \\ e^{j\theta_m(i-1)(m-1)} \end{bmatrix}$$

. . . . . xxvi, xxxvii, 98–100, 102–105

$[C_K]$ Transformation matrix from the natural reference frame $\{1, 2, \ldots, m\}$ to the $\{\alpha, \beta, 0\}$ reference frame,

$$[C_K] \triangleq K \begin{bmatrix} 1 & \cos(\theta_m) & \cos(2\theta_m) & \ldots & \cos((m-1)\theta_m) \\ 0 & \sin(\theta_m) & \sin(2\theta_m) & \ldots & \sin((m-1)\theta_m) \\ 1/k_0 & 1/k_0 & 1/k_0 & \ldots & 1/k_0 \end{bmatrix} \in \mathcal{M}_{3,m}(\mathbb{R})$$

. . . . . xxxiii, xxxiv, xxxvii, xli, xliv, xlviii, li, lxxi–lxxiv, 89–95

$[C_K]^+$ Pseudo-inverse matrix of $[C_K]$. Transformation matrix from the $\{\alpha, \beta, 0\}$ reference frame to the natural reference frame $\{1, 2, \ldots, m\}$,

$$[C_K]^+ \triangleq \frac{2}{K^2 m} [C_K]^T \in \mathcal{M}_{m,3}(\mathbb{R})$$

. . . . . xxxiii–xxxv, xxxvii, 90, 91, 93, 133

$[C_K^m]$ Generalized CONCORDIA and CLARKE transformation matrix from the natural basis $\mathcal{B}^m$ to the $\mathcal{B}^c$ static basis, see equations (3.119) and (3.120) for the definition of $[C_K^m]$ . . . . . xxxvii, xxxviii, 98, 101, 102, 104

$\left[C_{K_{12}}^m\right]$ Transformation matrix from the natural reference frame $\{1, 2, \ldots, m\}$ to the $\{\alpha_1, \beta_1, \alpha_2, \beta_2, 0\}$ reference frame. In the case where $m \geq 5$ this matrix is defined by equation (3.130). For the definition of $\left[C_{K_{12}}^m\right]$ in the cases where $m \leq 5$, see Section 3.E.2.2 xxxiv, xxxvii, xli, xliv, xlviii, li, lxii, lxxi–lxxiv, 105, 107–110

$\left[C_{K_{12}}^m\right]^+$ Pseudo-inverse matrix of $\left[C_{K_{12}}^m\right]$. Transformation matrix from the $\{\alpha_1, \beta_1, \alpha_2, \beta_2, 0\}$ reference frame to the natural reference frame $\{1, 2, \ldots, m\}$,

$$\left[C_{K_{12}}^m\right]^+ \triangleq \frac{2}{K^2 m} \left[C_{K_{12}}^m\right]^T \in \mathcal{M}_{m,m'}(\mathbb{R})$$

. . . . . xxxiv, xxxv, xxxvii, 105, 108, 133

$[C_K^m]^{-1}$ Inverse matrix of $[C_K^m]$. Transformation matrix from the $\mathcal{B}^c$ static basis to the natural reference frame $\mathcal{B}^m$,

$$[C_K^m]^{-1} \triangleq \frac{2}{K^2 m}[C_K^m]^T \in \mathcal{M}_m(\mathbb{R})$$

. . . . . xxxviii, 102

C_{LL} Low-level state-space output matrix of the dynamic behavior of the arms of the entire MMC,

$$C_{LL} \triangleq \begin{bmatrix} \mathbf{T_{py_1}}^T & & & & & \\ & \ddots & & & & \\ & & \mathbf{T_{py_m}}^T & & & \\ & & & -\mathbf{T_{ny_1}}^T & & \\ & & & & \ddots & \\ & & & & & -\mathbf{T_{ny_m}}^T \end{bmatrix} \in \mathbb{R}^{2m \times 2mN}$$

. . . . . xxxviii, xliii

C_{PE} Continuous time output matrix for the power-energy SSM,

$$C_{PE} \triangleq 1$$

. . . . . xxxi, xxxviii, lviii, 113, 193, 194

$\mathbf{c}$ The weighting matrix in the LP, and in the QP cost functions for the linear term 149, 150

C The output matrix in a state-space model. $C \in \mathbb{R}^{n_y \times n_x}$ 144, 145, 151, 152, 155, 158, 165

D

d_n Factor defining the AC component of v_{ny} for the steady-state analysis of section 3.H.1, see equation (3.166) for more details. . . . . xxii, 116, 117, 120, 121, 128

d_p Factor defining the AC component of v_{py} for the steady-state analysis of section 3.H.1, see equation (3.166) for more details. . . . . xxii, 116, 117, 120, 121, 128

$\mathbf{D^e}$ Vector containing the entire set of duty cycles from the submodules of the entire MMC,

$$\mathbf{D^e} \triangleq \begin{bmatrix} \mathbf{D^e_{py_1}} \\ \vdots \\ \mathbf{D^e_{xy}} \\ \vdots \\ \mathbf{D^e_{py_m}} \\ \mathbf{D^e_{ny_1}} \\ \vdots \\ \mathbf{D^e_{ny_m}} \end{bmatrix}$$

. . . . . xxxviii, xxxix, lxviii, 182, 192, 197

Δ_{PE} The discriminant related to the polynomial P representing the power-energy allocation equation,

$$\Delta_{PE} \triangleq {M_{PE}}^2 + 4M'_{PE}\mathbf{a_{dPE}}$$

. . . . . xxxviii, 194

$\mathbf{D}^{\mathbf{e}^{\max}}$ Upper boundary of the switching cell duty cycles vector $\mathbf{D}^{\mathbf{e}}$ 182, 192

$\mathbf{D}^{\mathbf{e}^{\min}}$ Lower boundary of the switching cell duty cycles vector $\mathbf{D}^{\mathbf{e}}$ 182, 192

$\mathbf{D}^{\mathbf{es}}_{\mathbf{xy}}$ Vector containing the entire set of duty cycles from the submodules of the arm $\#xy$ and is therefore considered as a control vector for the low-level part of the system. It contains all the D_{xyj}s as well as the D'_{xyj}s of this arm. In this vector the D_{xyj}s and D'_{xyj}s are organized in a different way than in $\mathbf{D}^{\mathbf{e}}_{\mathbf{xy}}$,

$$\mathbf{D}^{\mathbf{es}}_{\mathbf{xy}} \triangleq \langle \mathbf{S}^{\mathbf{es}}_{\mathbf{xy}} \rangle_{T_c}$$

. xxxix

$\mathbf{D}^{\mathbf{e}}_{\mathbf{xy}}$ Vector containing the entire set of duty cycles from the submodules of the arm $\#xy$ and is therefore considered as a control vector for the low-level part of the system. It contains all the D_{xyj}s as well as the D'_{xyj}s of this arm. In this vector the D_{xyj}s and D'_{xyj}s are organized in a different way than in $\mathbf{D}^{\mathbf{es}}_{\mathbf{xy}}$,

$$\mathbf{D}^{\mathbf{e}}_{\mathbf{xy}} \triangleq \langle \mathbf{S}^{\mathbf{e}}_{\mathbf{xy}} \rangle_{T_c}$$

. . . . . xxxviii, xxxix, lxviii, 66, 180, 181, 201

$\mathbf{D}^{\mathbf{e}^{\max}}_{\mathbf{xy}}$ Upper boundary of the switching cell duty cycles vector $\mathbf{D}^{\mathbf{e}}_{\mathbf{xy}}$ . . . 180, 181, 201

$\mathbf{D}^{\mathbf{e}^{\min}}_{\mathbf{xy}}$ Lower boundary of the switching cell duty cycles vector $\mathbf{D}^{\mathbf{e}}_{\mathbf{xy}}$ . . 180, 181, 201

D_{HL} Continuous time feedthrough matrix for the high-level SSM,

$$D_{HL} \triangleq \mathbb{O}_{2m,2m} \in \mathcal{M}_{2m}(\mathbb{R})$$

. . . . . xxxix, 84–86

$\tilde{D}_{HL}$ Minimal state-space realization continuous time feedthrough matrix for the high-level SSM,

$$\tilde{D}_{HL} \triangleq D_{HL} \in \mathcal{M}_{2m}(\mathbb{R})$$

. . . . . xxxix, 86

D_{LL} Low-level state-space feedthrough matrix of the dynamic behavior of the arms of the entire MMC,

$$D_{LL} \triangleq M_{LL} \in \mathbb{R}^{2m \times 4mN}$$

. . . . . xxxix, xlv

D_{PE} Continuous time feedthrough matrix for the power-energy SSM,

$$D_{PE} \triangleq 0$$

. . . . . xxxix, 113

$\delta\mathbf{U}$ The input matched disturbance vector. $\delta\mathbf{U} \in \mathbb{R}^{n_u}$ . . xxxix, lxvii, 151, 152, 155, 156, 158, 159

D_{xyj} Duty cycle of the first cell from the SM $\#xyj$. This duty cycle drives the two transistors of the first cell from the SM in opposition,

$$D_{xyj} \triangleq \langle S_{xyj} \rangle_{T_c}$$

. . . . . xxxix, lxviii, 21, 29, 242

D'_{xyj} Duty cycle of the second cell from the SM $\#xyj$. This duty cycle drives the two transistors of the second cell from the SM in opposition,

$$D'_{xyj} \triangleq \langle S'_{xyj} \rangle_{T_c}$$

. . . . . xxxix, lxviii, 21, 242

E

$\mathbf{E}$ The additive nonlinearity vector in a state-space model. $\mathbf{E} \in \mathbb{R}^{n_x}$ xl, 144, 145, 151, 152, 155, 158, 165, 169, 170

$\mathbf{e}$ The deviation error to the verification of the allocation equation,

$$\mathbf{e} = \mathcal{M}(\mathbf{U}) - \mathbf{a_d} = \begin{bmatrix} e_1 \\ \vdots \\ e_i \\ \vdots \\ e_{n_a} \end{bmatrix}$$

The upper boundary on $\mathbf{e}$ is noted $\mathbf{e}_{max}$ xl, liv, 40, 41, 146–150, 166, 211–214, I

E_p^c Subspace E_p^c associated with a single eigenvalue Λ_i from λ . . xxxiii, xl, 98, 99

$\mathbf{E_{MMC}}$ Additive nonlinearity vector of the global high-level-low-level state-space model describing the dynamic behavior of the voltages and currents of the entire MMC,

$$\mathbf{E_{MMC}} \triangleq \begin{bmatrix} \mathbf{E_{LL}} \\ \frac{1}{T_c}\tilde{H}_{HL}\tilde{\mathbf{E}}_{\mathbf{HL}} \end{bmatrix} \in \mathbb{R}^{2m(N+1)}$$

. . . . . xxx, xl, 192

ε_g The extremum gap of a given vector $\mathbf{x}$ is defined according to:

$$\varepsilon_g(\mathbf{x}) = |max(\mathbf{x}) - min(\mathbf{x})|$$

Figure 5.20 shows an example of the extremum gap of a vector . . . xl, 207–209

$\hat{\mathbf{e}}$ The deviation error to the verification of the general allocation equation,

$$\hat{\mathbf{e}} = \hat{\mathcal{M}}(\mathbf{U}) - \hat{\mathbf{a}}_\mathbf{d}$$

. . . . . xl, 147

$\hat{\mathbf{e}}_{\mathbf{MMC}}$ The entire deviation error to the verification of the high-level-low-level control allocation from the entire MMC,

$$\hat{\mathbf{e}}_{\mathbf{MMC}} = \hat{M}_{MMC}\mathbf{U_{LL}} - \hat{\mathbf{a}}_{\mathbf{d_{MMC}}}$$

and $\hat{\mathbf{e}}^{\mathbf{max}}_{\mathbf{MMC}}$ is its upper boundary . . . . . xl, liv, 192

$\hat{\mathbf{e}}_{\mathbf{HL}}$ The entire deviation error to the verification of the high-level control allocation from the entire set of currents in the natural reference frame,

$$\hat{\mathbf{e}}_{\mathbf{HL}} = \hat{M}_{HL}\mathbf{U_{HL}} - \hat{\mathbf{a}}_{\mathbf{dHL}}$$

and $\hat{\mathbf{e}}^{\mathbf{max}}_{\mathbf{HL}}$ is its upper boundary . . . . . xl, liv, 186

$\hat{\mathbf{e}}^{\mathbf{dq}012}_{\mathbf{HL}}$ The entire deviation error to the verification of the high-level allocation equation in the Park 12 reference frame,

$$\hat{\mathbf{e}}^{\mathbf{dq}012}_{\mathbf{HL}} = \mathbf{w_I}^{\frac{1}{l}}\, M^{dq012}_{HL}\mathbf{U}^{\mathbf{dq}012}_{\mathbf{HL}} - \mathbf{w_I}^{\frac{1}{l}}\, \mathbf{a}^{\mathbf{dq}012}_{\mathbf{dHL}} \in \mathbb{R}^{2m'}$$

. . . . . xl, liv, 188

$\mathbf{E_{HL}}$ Additive nonlinearity vector for the high-level SSM,

$$\mathbf{E_{HL}} \triangleq \begin{bmatrix} N_\Sigma(2)/L_m^{eq} \\ [1\ \ 0] \cdot N_\Delta(2)/L_s^{eq} \\ 0 \\ 0 \end{bmatrix} \mathbf{V_x} + \begin{bmatrix} -N_\Sigma(m)/L_m^{eq} \\ 0 \\ 0 \\ -N_\Delta(m)/L_o^{eq} \end{bmatrix} \mathbf{V_y} + \begin{bmatrix} -N_\Sigma(1)/L_m^{eq} \\ 0 \\ 0 \\ 0 \end{bmatrix} V_{n_{AD}} \in \mathbb{R}^{2m+2}$$

. . . . . xli, xlii, 84–86

$\mathbf{E_{HL}^{dq0}}$ Additive nonlinearity vector for the high-level SSM in the Park reference frame,

$$\mathbf{E_{HL}^{dq0}} \triangleq \begin{bmatrix} N_\Sigma(2)/L_m^{eq} \\ [1\ \ 0] \cdot N_\Delta(2)/L_s^{eq} \\ \mathbb{O}_{2,2} \\ \mathbb{O}_{2,2} \end{bmatrix} \mathbf{V_x} + \begin{bmatrix} -N_\Sigma(m)/L_m^{eq} \\ \mathbb{O}_{1,m} \\ \mathbb{O}_{2,m} \\ 2\tilde{B}_\Delta^{dq0}[P(-\theta)][C_K]/L_o^{eq} \end{bmatrix} \mathbf{V_y} + \begin{bmatrix} -N_\Sigma(1)/L_m^{eq} \\ \mathbb{O}_{1,1} \\ \mathbb{O}_{2,1} \\ \mathbb{O}_{2,1} \end{bmatrix} V_{n_{AD}} \in \mathbb{R}^6$$

. . . . . xli, 95

$\mathbf{E_{HL}^{dq012}}$ Additive nonlinearity vector for the high-level SSM in the Park 12 reference frame,

$$\mathbf{E_{HL}^{dq012}} \triangleq \begin{bmatrix} N_\Sigma(2)/L_m^{eq} \\ [1\ \ 0] \cdot N_\Delta(2)/L_s^{eq} \\ \mathbb{O}_{m'-1,2} \\ \mathbb{O}_{m'-1,2} \end{bmatrix} \mathbf{V_x} + \begin{bmatrix} -N_\Sigma(m)/L_m^{eq} \\ \mathbb{O}_{1,m} \\ \mathbb{O}_{m'-1,m} \\ 2\tilde{B}_\Delta^{dq012}[P(-\theta)_{12}^m][C_{K_{12}}^m]/L_o^{eq} \end{bmatrix} \mathbf{V_y} + \begin{bmatrix} -N_\Sigma(1)/L_m^{eq} \\ \mathbb{O}_{1,1} \\ \mathbb{O}_{m'-1,1} \\ \mathbb{O}_{m'-1,1} \end{bmatrix} V_{n_{AD}} \in \mathbb{R}^{2m'}$$

. . . . . xxx, xli, 109, 110, 187, 188

$\mathbf{e_{HL}^{dq012}}$ The deviation error to the verification of the high-level allocation equation in the Park 12 reference frame,

$$\mathbf{e_{HL}^{dq012}} = M_{HL}^{dq012}\mathbf{U_{HL}^{dq012}} - \mathbf{a_{dHL}^{dq012}} \in \mathbb{R}^{2m'}$$

The upper boundary on $\mathbf{e_{HL}^{dq012}}$ is noted ToDoBis . . . . . xli, 187

$\mathbf{\hat{e}_{LL}}$ The entire deviation error to the verification of the low-level control allocation from the entire MMC,

$$\mathbf{\hat{e}_{LL}} = \hat{M}_{LL}\mathbf{U_{LL}} - \mathbf{\hat{a}_{dLL}}$$

and $\mathbf{\hat{e}_{LL}^{max}}$ is its upper boundary . . . . . xli, lv, 182

$\mathbf{\hat{e}_{LL}^{xy}}$ The entire deviation error to the verification for the low-level control allocation from the arm $\#xy$,

$$\mathbf{\hat{e}_{LL}^{xy}} = \hat{M}_{LL}^{xy}\mathbf{U_{LL}^{xy}} - \mathbf{\hat{a}_{dLL}^{xy}}$$

and $\hat{\mathbf{e}}_{\mathbf{LL}}^{\mathbf{xy}^{\max}}$ is its upper boundary ..... xli, xlii, lv, 181, 201

$\tilde{\mathbf{E}}_{\mathbf{HL}}$ Minimal state-space realization additive nonlinearity vector for the high-level SSM,

$$\tilde{\mathbf{E}}_{\mathbf{HL}} \triangleq C_{HL}\mathbf{E}_{\mathbf{HL}} \in \mathbb{R}^{2m}$$

..... xxx, xl, xlii, 86, 185, 186

$\mathbf{E}_{\mathbf{LL}}$ Low-level state-space additive nonlinearity vector of the dynamic behavior of the arms of the entire MMC,

$$\mathbf{E}_{\mathbf{LL}} \triangleq \begin{bmatrix} \frac{i^*_{py_1}(k)}{C}\mathbf{T}_{\mathbf{py_1}} \\ \vdots \\ \frac{i^*_{py_m}(k)}{C}\mathbf{T}_{\mathbf{py_m}} \\ \frac{i^*_{ny_1}(k)}{C}\mathbf{T}_{\mathbf{ny_1}} \\ \vdots \\ \frac{i^*_{ny_m}(k)}{C}\mathbf{T}_{\mathbf{ny_m}} \end{bmatrix} \in \mathbb{R}^{2mN}$$

..... xl, xlii

$\mathbf{E}_{\mathbf{LL}}^{\mathbf{xy}}$ Additive nonlinearity vector for the low-level SSM of the submodules from the arm $\#xy$,

$$\mathbf{E}_{\mathbf{LL}}^{\mathbf{xy}} \triangleq \frac{i^*_{xy}}{C}\mathbf{T}_{\mathbf{xy}}$$

..... xlii, 66

$\mathbf{e}_{\mathbf{LL}}^{\mathbf{xy}}$ The deviation error to the verification for the low-level control allocation from the arm $\#xy$,

$$\mathbf{e}_{\mathbf{LL}}^{\mathbf{xy}} = M_{LL}^{xy}\mathbf{U}_{\mathbf{LL}}^{\mathbf{xy}} - \mathbf{a}_{\mathbf{d}}\mathbf{U}_{\mathbf{LL}}^{\mathbf{xy}}$$

and $\mathbf{e}_{\mathbf{LL}}^{\mathbf{xy}^{\max}}$ is its upper boundary ..... xlii, 180

E_{MMC} Total energy contained in the capacitors of the MMC xxii, lxxvii, 13, 112–114, 193, 194

E_{MMC}^{ref} Reference setpoint for the total energy contained in the capacitors of the MMC 194, 196, 197

$\mathbf{E}_{\mathbf{PE}}$ Additive nonlinearity vector for the power-energy SSM,

$$\mathbf{E}_{\mathbf{PE}} \triangleq -P_{\bar{s}} \in \mathbb{R}$$

..... xxxi, xlii, 113, 193, 194

$\mathbf{e}_{\mathbf{pLL}}^{\mathbf{xy}}$ The preference deviation error to the verification for the low-level control allocation from the arm $\#xy$,

$$\mathbf{e}_{\mathbf{pLL}}^{\mathbf{xy}} = M_{pLL}^{xy}\mathbf{U}_{\mathbf{LL}}^{\mathbf{xy}} - \mathbf{a}_{\mathbf{pLL}}^{\mathbf{xy}}\mathbf{U}_{\mathbf{LL}}^{\mathbf{xy}}$$

and $\mathbf{e}_{\mathbf{pLL}}^{\mathbf{xy}^{\max}}$ is its upper boundary ..... xlii, 180, 208, 209

$\varepsilon_{\mathbf{s}}$ The static error. According to the final value theorem the static error is defined:

$$\varepsilon_{\mathbf{s}} = \lim_{z\to 1}(z-1)\left(\mathbf{Y}^{ref}(z) - \mathbf{Y}(z)\right) = \lim_{s\to 0} s\left(\mathbf{Y}^{ref}(s) - \mathbf{Y}(s)\right)$$

..... xlii, 152, 153, 156, 159, 219, 220, 223, 231

$\varepsilon_{\mathbf{v}}$ The vectorial error. This error is defined for the currents $\mathbf{I}_{\mathbf{c}}$ and $\mathbf{I}_{\mathbf{o}}$. It contains all the informations about the error between the reference and the measured

value according to the following equation as an average on the full simulation time considered. For example for $\mathbf{Y}$, this error is defined:

$$\varepsilon_{\mathbf{v}} = \frac{||\mathbf{Y}^{ref} - \mathbf{Y}||_2}{||\mathbf{Y}^{ref}||_2}$$

. . . . . xliii, 219, 220, 223, 231

F

F The discrete time state matrix in a state-space model. $F \in \mathbb{R}^{n_x \times n_x}$. xliii, 144, 145, 151, 152, 155, 158, 165, 168–170

F_{CL} The closed-loop state matrix when using a control allocation with integral compensator architecture. 157

F_{MMC} State matrix of the global high-level-low-level state-space model describing the dynamic behavior of the voltages and currents of the entire MMC,

$$F_{MMC} \triangleq \begin{bmatrix} \mathbb{I}_{2mN} & \mathbb{O}_{2mN,2m} \\ \tilde{G}_{HL} C_{LL} & \tilde{F}_{HL} \end{bmatrix} \in \mathbb{R}^{2m(N+1) \times 2m(N+1)}$$

. . . . . xxx, xliii, 192

$F_{MMC,M}$ The discrete time state matrix of the high-level-low-level reference state-space model,

$$F_{MMC} \triangleq \begin{bmatrix} F_{LL,M} & \mathbb{O}_{2mN,2m} \\ \mathbb{O}_{2mN,2m} & F_{HL,M} \end{bmatrix} \in \mathbb{R}^{2m(N+1) \times 2m(N+1)}$$

. lxxvii

F_{HL}^{dq0} Discrete time dynamic matrix for the high-level SSM in the Park reference frame,

$$F_{HL}^{dq0} \triangleq e^{A_{HL}^{dq0} T_c} \in \mathcal{M}_{2\cdot 3}(\mathbb{R})$$

. . . . . xliii, xlvi, xlvii, 95

F_{HL}^{dq012} Discrete time dynamic matrix for the high-level SSM in the Park 12 reference frame,

$$F_{HL}^{dq012} \triangleq e^{A_{HL}^{dq012} T_c} \in \mathcal{M}_{2m'}(\mathbb{R})$$

. . . . . xxx, xliii, xlvi, xlvii, 110, 187, 188

$F_{HL,M}^{dq012}$ The discrete time state matrix of the high-level reference state-space model of the currents in the Park 12 reference frame. $F_{HL,M}^{dq012} \in \mathbb{R}^{2m' \times 2m'}$ . . xxxi, xliii, lxxviii, 187, 189, 230

$F_{HL,M}$ The discrete time state matrix of the high-level reference state-space model of the currents in the natural reference frame. $F_{HL,M} \in \mathbb{R}^{2m \times 2m}$ . . xliii, lxxviii, 185, 187, 192

$\tilde{F}_{HL}$ Discrete time dynamic matrix for the high-level SSM,

$$\tilde{F}_{HL} \triangleq e^{\tilde{A}_{HL} T_c} \in \mathcal{M}_{2m}(\mathbb{R})$$

. . . . . xxx, xliii, xlvi, xlvii, 86, 185, 186

$\mathbf{\Phi_c}$ Vector containing the m circulating current magnetic flux components:

$$\mathbf{\Phi_c} \triangleq L_c^{eq} \mathbf{I_c}$$

. . . . . xliii, xliv, 91, 93, 108

$\mathbf{\Phi_c^{\alpha\beta 0}}$ Vector containing the circulating current magnetic flux in the $\{\alpha, \beta, 0\}$ reference frame,

$$\mathbf{\Phi_c^{\alpha\beta 0}} \triangleq [C_K]\mathbf{\Phi_c} = [\Phi_c^{\alpha}, \Phi_c^{\beta}, \Phi_c^{0}]^T \in \mathbb{R}^3$$

. . . . . xliv, 91

$\mathbf{\Phi_c^{\alpha\beta 0^{12}}}$ Vector containing the circulating current magnetic flux in the $\{\alpha_1, \beta_1, \alpha_2, \beta_2, 0\}$ reference frame,

$$\mathbf{\Phi_c^{\alpha\beta 0^{12}}} \triangleq \left[C_{K_{12}}^m\right]\mathbf{\Phi_c} = [\Phi_c^{\alpha_1}, \Phi_c^{\beta_1}, \Phi_c^{\alpha_2}, \Phi_c^{\beta_2}, \Phi_c^{0}]^T \in \mathbb{R}^5$$

. xliv

φ_c^{ref} Reference phase of the circulating current from the MMC 197, 216

$\mathbf{\Phi_c^{dq0}}$ Vector containing the circulating current magnetic flux in the $\{d, q, 0\}$ synchronous rotating frame,

$$\mathbf{\Phi_c^{dq0}} \triangleq [P(-\theta)]\mathbf{\Phi_c^{\alpha\beta 0}} = [P(-\theta)][C_K]\mathbf{\Phi_c} = [\Phi_c^{d}, \Phi_c^{q}, \Phi_c^{0}]^T \in \mathbb{R}^3$$

. . . . . xliv, 92, 93

$\mathbf{\Phi_c^{dq012}}$ Vector containing the circulating current magnetic flux in the $\{d_1, q_1, d_2, q_2, 0\}$ synchronous rotating frame,

$$\mathbf{\Phi_c^{dq012}} \triangleq [P(-\theta)_{12}^m]\mathbf{\Phi_c^{\alpha\beta 0^{12}}} = [P(-\theta)_{12}^m]\left[C_{K_{12}}^m\right]\mathbf{\Phi_c} = [\Phi_c^{d_1}, \Phi_c^{q_1}, \Phi_c^{d_2}, \Phi_c^{q_2}, \Phi_c^{0}]^T \in \mathbb{R}^5$$

. . . . . xliv, 108

$\mathbf{\Phi^m}$ Magnetic flux vector in a polyphase circuit of m phases . . . . . lv, 98

$\mathbf{\Phi_o}$ Vector containing the m output current magnetic flux components:

$$\mathbf{\Phi_o} \triangleq L_o^{eq}\mathbf{I_o}$$

. . . . . xliv, xlvii, li, 109

φ_o^{ref} Reference phase of the output current from the MMC 196, 197

φ_P Power factor angle in the AC network 196, 205

φ_v Origin phase of the phase voltage across the AC network . . li, lxix, lxxiv, 116, 117, 119, 121, 196, 206, 218, 243

φ_y Phase of the phase voltage across the AC network,

$$\varphi_{y_j} = \frac{2\pi}{m}(j-1)$$

. . . . . xliv, lxxiv, 116, 119, 120, 128, 196, 197

$f_k(t)$ Components $\#k$ of the vector $\mathbf{f_m}$ which is along $\mathbf{x_k^m}$ in the natural basis $\mathcal{B}^m$. xliv, xlv, 102

$f_k^h(t)$ Harmonic component of rank $\#h$ of $f_k(t)$ . . . . . xlv, 102

$F_{LL,M}$ The discrete time state matrix of the low-level reference state-space model of the capacitors,

$$F_{LL,M} = \begin{bmatrix} F_{LL,M}^{xy} & & & & \\ & \ddots & & & \\ & & F_{LL,M}^{xy} & & \\ & & & \ddots & \\ & & & & F_{LL,M}^{ny_m} \end{bmatrix} \in \mathbb{R}^{2mN\times 2mN}$$

. . . . . xliii, xliv, 192

$F_{LL,M}^{xy}$ The discrete time state matrix of the low-level reference state-space model of the capacitors in the arm $\#xy$. $F_{LL,M}^{xy} \in \mathbb{R}^{N\times N}$ . . . . . xliv, 183

F_M The discrete time state matrix in a reference state-space model. $F_M \in \mathbb{R}^{n_y \times n_y}$ xxiii, xlv, 145, 151–153, 155–162, 165–168, 170, 172

$\mathbf{f_m}$ Electrical signal (current, voltage or magnetic flux) vector containing the vector components in the natural basis $\mathcal{B}^m$,

$$\mathbf{f_m} = \begin{bmatrix} f_1(t) \\ f_2(t) \\ \vdots \\ f_k(t) \\ \vdots \\ f_m(t) \end{bmatrix}$$

. . . . . xliv, xlv, 102

$\mathbf{f_m^h}$ Vector containing only the harmonic components of rank $\#h$ from $\mathbf{f_m}$ in the natural basis $\mathcal{B}^m$,

$$\mathbf{f_m^h} = \begin{bmatrix} f_1^h(t) \\ f_2^h(t) \\ \vdots \\ f_k^h(t) \\ \vdots \\ f_m^h(t) \end{bmatrix}$$

. . . . . xlv, 102, 103

f_o The fondamental frequency (Hz) of the $\mathbf{I_o}$, $\mathbf{V_y}$, $\underline{V_{AC}}$ and $\underline{V_o'}$ signals. $f_s \triangleq 1/T_o$ lx, 187, 206, 218, 243

$F_{PE,M}$ The discrete time state matrix of the power-energy reference state-space model of the energy. $F_{PE,M} \in \mathbb{R}$ . . . . . xlv, lxxix, 193–195

f The additive term in the QP cost function 150

f_s The switching frequency (Hz) of the pulse width modulation. $f_s \triangleq 1/T_s$. xlv, 29

G

G The discrete time input matrix in a state-space model. $G \in \mathbb{R}^{n_x \times n_u}$. xlv, 144, 145, 152, 155, 165, 169, 170

G_{CL} The closed-loop input matrix when using a control allocation with integral compensator architecture. 157

G_{MMC} Input matrix of the global high-level-low-level state-space model describing the dynamic behavior of the voltages and currents of the entire MMC,

$$G_{MMC} \triangleq \begin{bmatrix} G_{LL} \\ \tilde{G}_{HL} D_{LL} \end{bmatrix} \in \mathbb{R}^{2m(N+1) \times 4mN}$$

. . . . . xlv, lvii, 192

$G_{MMC,M}$ The discrete time input matrix of the high-level-low-level reference state-space model,

$$G_{MMC} \triangleq \begin{bmatrix} G_{LL,M} & \mathbb{O}_{2mN,2m} \\ \mathbb{O}_{2mN,2m} & G_{HL,M} \end{bmatrix} \in \mathbb{R}^{2m(N+1) \times 2m(N+1)}$$

. lxxvii

G_{HL}^{dq0} Discrete time control matrix for the high-level SSM in the Park reference frame,

$$G_{HL}^{dq0} \triangleq {A_{HL}^{dq0}}^{-1} \left(F_{HL}^{dq0} - \mathbb{I}_{2m'} \right) B_{HL}^{dq0} \in \mathcal{M}_{2\cdot 3}(\mathbb{R})$$

. . . . . xlvi, 95

G_{HL}^{dq012} Discrete time control matrix for the high-level SSM in the Park 12 reference frame,

$$G_{HL}^{dq012} \triangleq {A_{HL}^{dq012}}^{-1} \left(F_{HL}^{dq012} - \mathbb{I}_{2m'} \right) B_{HL}^{dq012} \in \mathcal{M}_{2m'}(\mathbb{R})$$

. . . . . xlvi, lvii, 110, 187

$G_{HL,M}^{dq012}$ The discrete time input matrix of the high-level reference state-space model of the currents in the Park 12 reference frame. $G_{HL,M}^{dq012} \in \mathbb{R}^{2m' \times 2m'}$ xlvi, lxxviii, 187, 189

$G_{HL,M}$ The discrete time input matrix of the high-level reference state-space model of the currents in the natural reference frame. $G_{HL,M} \in \mathbb{R}^{2m \times 2m}$ . . . . . xlv, xlvi, lxxviii, 185, 187, 192

$\tilde{G}_{HL}$ Discrete time control matrix for the high-level SSM,

$$\tilde{G}_{HL} \triangleq {\tilde{A}_{HL}}^{-1} \left(\tilde{F}_{HL} - \mathbb{I}_{2m} \right) \tilde{B}_{HL} \in \mathcal{M}_{2m}(\mathbb{R})$$

. . . . . xliii, xlv, xlvi, lvii, 86, 185

G_{LL} Low-level state-space input matrix of the dynamic behavior of the arms of the entire MMC,

$$G_{LL} \triangleq M_{pLL} \in \mathbb{R}^{2mN \times 4mN}$$

. . . . . xlv, xlvi

$G_{LL,M}$ The discrete time input matrix of the low-level reference state-space model of the capacitors,

$$G_{LL,M} = \begin{bmatrix} G_{LL,M}^{xy} & & & & \\ & \ddots & & & \\ & & G_{LL,M}^{xy} & & \\ & & & \ddots & G_{LL,M}^{ny_m} \end{bmatrix} \in \mathbb{R}^{2mN \times 2mN}$$

. . . . . xlv, xlvi, 192

$G_{LL,M}^{xy}$ The discrete time input matrix of the low-level reference state-space model of the capacitors in the arm $\#xy$. $G_{LL,M}^{xy} \in \mathbb{R}^{N \times N}$ . . . . . xlvi, 183

G_M The discrete time input matrix in a reference state-space model. $G_M \in \mathbb{R}^{n_y \times n_y}$ xxiii, xlvi, 145, 151–153, 155–162, 165–168, 170, 172

$G_{PE,M}$ The discrete time input matrix of the power-energy reference state-space model of the energy. $G_{PE,M} \in \mathbb{R}$ . . . . . xlvi, lxxix, 193–195

H

H The discrete time input factor matrix in a state-space model. $H \in \mathbb{R}^{n_x \times n_x}$ . . . xlvi, 144, 145, 151, 152, 155, 158, 165, 169, 170

H_{MMC} Additive nonlinearity matrix of the global high-level-low-level state-space model describing the dynamic behavior of the voltages and currents of the entire MMC,

$$H_{MMC} \triangleq T_c$$

. . . . . xxx, xlvi, 192

H_{HL}^{dq0} Discrete time additive nonlinearity matrix for the high-level SSM in the Park reference frame,

$$H_{HL}^{dq0} \triangleq {A_{HL}^{dq0}}^{-1} \left(F_{HL}^{dq0} - \mathbb{I}_{2\cdot 3} \right) \in \mathcal{M}_{2\cdot 3}(\mathbb{R})$$

. . . . . xlvii, 95

H_{HL}^{dq012} Discrete time additive nonlinearity matrix for the high-level SSM in the Park 12 reference frame,

$$H_{HL}^{dq012} \triangleq {A_{HL}^{dq012}}^{-1} \left(F_{HL}^{dq012} - \mathbb{I}_{2m'} \right) \in \mathcal{M}_{2m'}(\mathbb{R})$$

. . . . . xxx, xlvii, 110, 187, 188

$\tilde{H}_{HL}$ Discrete time additive nonlinearity matrix for the high-level SSM,

$$\tilde{H}_{HL} \triangleq {\tilde{A}_{HL}}^{-1} \left(\tilde{F}_{HL} - \mathbb{I}_{2m} \right) \in \mathcal{M}_{2m}(\mathbb{R})$$

. . . . . xxx, xl, xlvii, 86, 185, 186

$\mathcal{H}$ The weighting matrix in the QP cost function for the quadratic term 150

$\mathcal{H}$ The Heaviside step function,

$$\mathcal{H}(t) = \begin{cases} 1, \text{for } t > 0 \\ 0, \text{for } t \leq 0 \end{cases}$$

. . . . . xlvii, 152, 156, 159, 167

I

$\hat{I}_{AC}$ Amplitude of the phase current across the AC network,

$$\hat{I}_{AC} \triangleq 2\hat{I}_o$$

. xlvii

$\underline{I_{AC}}$ Complex phasor describing the phase current across the AC network,

$$\underline{I_{AC}} \triangleq \hat{I}_{AC}\, e^{-j\mathbf{\Phi_o}} = 2\underline{I_o}$$

. . . . . xlvii, lxxii

$\mathbf{I_c}$ Circulating current flowing within the legs of the MMC. Since this current only flows within the converter, DC-side and AC-side grids are not influenced by those currents. The circulating current vector reads:

$$\mathbf{I_c} \triangleq \begin{bmatrix} i_{c_{y_1}} \\ i_{c_{y_2}} \\ \vdots \\ i_{c_{y_j}} \\ \vdots \\ i_{c_{y_m}} \end{bmatrix} = \left[\tilde{\mathbf{I}}_{\mathbf{c}} i_{c_{y_m}} \right]$$

. . xlii, xliii, xlvii, xlviii, lv, lx, lxiv, lxxvi, lxxix, 15, 22, 25, 31, 32, 75–80, 82–85, 87, 88, 91–95, 108, 115, 116, 119, 124, 127, 128, 131, 189, 190, 207, 216, 219, 220, 223, 224, 231

$\tilde{\mathbf{I}}_{\mathbf{c}}$ Circulating current reduced vector:

$$\tilde{\mathbf{I}}_{\mathbf{c}} \triangleq \begin{bmatrix} i_{c_{y_1}} \\ i_{c_{y_2}} \\ \vdots \\ i_{c_{y_j}} \\ \vdots \\ i_{c_{y_{m-1}}} \end{bmatrix}$$

. . . . . xlvii, xlviii, lxxvi, lxxvii, 85, 185, 186, 192

$\mathbf{I}_{\mathbf{c}}^{\alpha\beta 0}$ Circulating current flowing within the legs of the MMC in the $\{\alpha, \beta, 0\}$ reference frame,

$$\mathbf{I}_{\mathbf{c}}^{\alpha\beta 0} \triangleq [C_K]\mathbf{I}_{\mathbf{c}} = [I_c^{\alpha}, I_c^{\beta}, I_c^{0}]^T \in \mathbb{R}^3$$

. . . . . xlviii, 91

$\mathbf{I}_{\mathbf{c}}^{\alpha\beta 0^{12}}$ Vector containing the circulating current flowing within the legs of the MMC in the $\{\alpha_1, \beta_1, \alpha_2, \beta_2, 0\}$ synchronous rotating frame,

$$\mathbf{I}_{\mathbf{c}}^{\alpha\beta 0^{12}} \triangleq \left[C_{K_{12}}^{m}\right]\mathbf{I}_{\mathbf{o}} = [I_c^{\alpha_1}, I_c^{\beta_1}, I_c^{\alpha_2}, I_c^{\beta_2}, I_c^{0}]^T \in \mathbb{R}^5$$

. xlviii

$\hat{I}_c$ Amplitude of the circulating current of the MMC 117

$\hat{I}_c^{max}$ Maximum amplitude of $\mathbf{I}_{\mathbf{c}}$ in steady-state, see section 3.H.1 for more details,

$$\hat{I}_c^{max} \triangleq \frac{1}{Z_c}\frac{q}{2}V_{DC}$$

. . . . . xlviii, 117

$\hat{I}_c^{min}$ Minimum amplitude of $\mathbf{I}_{\mathbf{c}}$ in steady-state, see section 3.H.1 for more details,

$$\hat{I}_c^{min} \triangleq -\frac{1}{Z_c}\frac{q}{2}V_{DC}$$

. . . . . xlviii, 117

$\mathbf{I}_{\mathbf{c}}^{\mathbf{dq}0}$ Circulating current flowing within the legs of the MMC in the $\{d, q, 0\}$ synchronous rotating frame,

$$\mathbf{I}_{\mathbf{c}}^{\mathbf{dq}0} \triangleq [P(-\theta)]\mathbf{I}_{\mathbf{c}}^{\alpha\beta 0} = [P(-\theta)][C_K]\mathbf{I}_{\mathbf{c}} = [I_c^{d}, I_c^{q}, I_c^{0}]^T \in \mathbb{R}^3$$

. . . . . xlviii, xlix, 92, 93

$\mathbf{I}_{\mathbf{c}}^{\mathbf{dq}012}$ Circulating current flowing within the legs of the MMC in the $\{d_1, q_1, d_2, q_2, 0\}$ synchronous rotating frame,

$$\mathbf{I}_{\mathbf{c}}^{\mathbf{dq}012} \triangleq [P(-\theta)_{12}^{m}]\mathbf{I}_{\mathbf{c}}^{\alpha\beta 0^{12}} = [P(-\theta)_{12}^{m}]\left[C_{K_{12}}^{m}\right]\mathbf{I}_{\mathbf{c}} = [I_c^{d_1}, I_c^{q_1}, I_c^{d_2}, I_c^{q_2}, I_c^{0}]^T \in \mathbb{R}^5$$

. . . . . xlviii, 108, 133

$\tilde{\mathbf{I}}_{\mathbf{c}}^{\mathbf{dq}012}$ Reduced circulating current flowing within the legs of the MMC in the $\{d_1, q_1, d_2, q_2, 0\}$ synchronous rotating frame,

$$\tilde{\mathbf{I}}_{\mathbf{c}}^{\mathbf{dq}012} \triangleq \begin{bmatrix} 1 & 0 & 0 & 0 & 0 \\ 0 & 1 & 0 & 0 & 0 \\ 0 & 0 & 1 & 0 & 0 \\ 0 & 0 & 0 & 1 & 0 \end{bmatrix} \mathbf{I}_{\mathbf{c}}^{\mathbf{dq}012} = [I_c^{d_1}, I_c^{q_1}, I_c^{d_2}, I_c^{q_2}]^T \in \mathbb{R}^4$$

$\tilde{\mathbf{I}}_{\mathbf{c}}^{\mathbf{dq0}}$ ..... xlviii, lxxvi, lxxviii, 108, 109, 187
Reduced circulating current flowing within the legs of the MMC in the $\{d, q, 0\}$ synchronous rotating frame,

$$\tilde{\mathbf{I}}_{\mathbf{c}}^{\mathbf{dq0}} \triangleq \begin{bmatrix} 1 & 0 & 0 \\ 0 & 1 & 0 \end{bmatrix} \mathbf{I}_{\mathbf{c}}^{\mathbf{dq0}} = [I_c^d, I_c^q]^T \in \mathbb{R}^2$$

$\tilde{\mathbf{I}}_{\mathbf{c}}^{\mathbf{dq}012\,ref}$ ..... xlix, lxxvi, lxxviii, 94, 95
Circulating current reference in the Park 12 reference frame,

$$\tilde{\mathbf{I}}_{\mathbf{c}}^{\mathbf{dq}012\,ref} \triangleq [I_c^{d_1\,ref}, I_c^{q_1\,ref}, I_c^{d_2\,ref}, I_c^{q_2\,ref}]^T$$

$\mathbf{I}_{\mathbf{c}}^{ref}$ ..... xlix, lxxviii, 197
Circulating current reference,

$$\mathbf{I}_{\mathbf{c}}^{ref} \triangleq \begin{bmatrix} i_{c_{y_1}}^{ref} \\ i_{c_{y_2}}^{ref} \\ \vdots \\ i_{c_{y_j}}^{ref} \\ \vdots \\ i_{c_{y_m}}^{ref} \end{bmatrix}$$

$\hat{I}_c^{ref}$ ..... xlix, 189, 197, 205
Reference amplitude of the circulating current from the MMC .. 197, 205, 216

$\tilde{\mathbf{I}}_{\mathbf{c}}^{ref}$
Circulating current reference reduced vector,

$$\tilde{\mathbf{I}}_{\mathbf{c}}^{ref} \triangleq \begin{bmatrix} i_{c_{y_1}}^{ref} \\ i_{c_{y_2}}^{ref} \\ \vdots \\ i_{c_{y_j}}^{ref} \\ \vdots \\ i_{c_{y_{m-1}}}^{ref} \end{bmatrix}$$

$\mathbf{i}_{\mathbf{C_{xy}}}$ ..... xlix, lxxvii, lxxviii
Vector containing the entire set of capacitor currents of the submodules from the arm $\#xy$,

$$\mathbf{i}_{\mathbf{C_{xy}}} \triangleq [i_{C_{xy1}}, i_{C_{xy2}}, \ldots, i_{C_{xyN}}]^T \in \mathbb{R}^N$$

$i_{C_{xyj}}$ ..... xlix, 64, 65
Current flowing through the capacitors of the SM $\#yj$ among $[\![1; N]\!]$ of the arm $\#x$ among $\{n, p\}$, of the leg $\#y$ among $\{y_1, \ldots, y_m\}$ .. 12, 20, 21, 53–56, 58–60, 62, 64

I_{DC} DC-source current supplying the MMC 113

I_m Common mode current flowing between the DC-side and AC-side neutral points when those are connected ..... l, liv, lvi, lxv, lxxvi, lxxvii, lxxix, 15, 22, 25, 31, 32, 75–81, 84, 85, 87, 90, 91, 107, 113, 115, 119, 124, 127, 137–139, 185–187, 190, 192, 216, 220, 230, 231

$\mathbf{i}^{\mathbf{m}}$
Current vector in a polyphase circuit of m phases. See Figure 3.5 for an example,

$$\mathbf{i}^{\mathbf{m}} = \sum_{k=1}^{m} i_k(t) \cdot \mathbf{x}_{\mathbf{k}}^{\mathbf{m}}$$

. . . . . xlix, lv, 98

$\hat{I}_m$ Amplitude of the common mode current of the MMC,

$$\hat{I}_m = I_m = i_m$$

. . . . . l, 117

$\hat{I}_m^{max}$ Maximum amplitude of I_m in steady-state, see section 3.H.1 for more details,

$$\hat{I}_m^{max} \triangleq \frac{1}{Z_m}\left(\frac{q}{2}V_{DC} - V_{n_{AD}}\right)$$

. . . . . l, 117

$\hat{I}_m^{min}$ Minimum amplitude of I_m in steady-state, see section 3.H.1 for more details,

$$\hat{I}_m^{min} \triangleq \frac{1}{Z_m}\left(-\frac{q}{2}V_{DC} - V_{n_{AD}}\right)$$

. . . . . l, 117

I_m^{dq0} Common mode current flowing between the DC-side and AC-side neutral points in the $\{d, q, 0\}$ reference frame,

$$I_m^{dq0} \triangleq I_m \in \mathbb{R}$$

. . . . . l, lxxvi, lxxviii, 90, 91, 95

I_m^{dq012} Common mode current flowing between the DC-side and AC-side neutral points in the $\{d_1, q_1, d_2, q_2, 0\}$ reference frame,

$$I_m^{dq012} \triangleq I_m \in \mathbb{R}$$

. . . . . l, lxxvi, lxxviii, 107, 109, 187

$I_m^{dq012ref}$ Common mode current reference in the Park 12 reference frame,

$$I_m^{dq012ref} \triangleq I_m^{ref}$$

. . . . . l, lxxviii

I_m^{ref} Common mode current reference . . . . . l, lxxvii, lxxviii, 196, 197, 216

i_n Current flowing from the DC bus negative pole to the MMC . . liii, lxi, 13, 25, 76–83, 112, 113

i_{ny} Current flowing through the arm #n of the leg #y among $\{y_1, \ldots, y_m\}$. liv, 15, 22, 25, 76–83, 190

$\mathbf{I_o}$ Vector containing the m output currents flowing through the AC-side load with I_m. The output current vector reads:

$$\mathbf{I_o} \triangleq \begin{bmatrix} i_{o_{y_1}} \\ i_{o_{y_2}} \\ \vdots \\ i_{o_{y_j}} \\ \vdots \\ i_{o_{y_m}} \end{bmatrix} = \begin{bmatrix} \tilde{\mathbf{I}}_\mathbf{o} i_{o_{y_m}} \end{bmatrix}$$

. . . . . xxxiv, xlii, xliv, xlv, xlviii, l, li, liv, lvi, lx, lxvii, lxxii–lxxiv, lxxvi, lxxix, lxxx, 15, 22, 25, 31, 32, 75–80, 83–85, 87, 88, 91, 92, 94, 95, 109, 115, 119, 124, 126–128, 131, 134, 187, 189, 190, 207, 216, 219, 220, 223, 224, 229, 231, 236, 244

$\tilde{\mathbf{I}}_{\mathbf{o}}$ Output current reduced vector:

$$\tilde{\mathbf{I}}_{\mathbf{o}} \triangleq \begin{bmatrix} i_{o_{y_1}} \\ i_{o_{y_2}} \\ \vdots \\ i_{o_{y_j}} \\ \vdots \\ i_{o_{y_{m-1}}} \end{bmatrix}$$

. . . . . l, li, lxxvi, lxxvii, 85, 185, 186, 192

$\mathbf{I}_{\mathbf{o}}^{\alpha\beta 0}$ Vector containing the output current flowing through the AC-side load in the $\{\alpha, \beta, 0\}$ reference frame,

$$\mathbf{I}_{\mathbf{o}}^{\alpha\beta 0} \triangleq [C_K]\mathbf{I}_{\mathbf{o}} = [I_o^{\alpha}, I_o^{\beta}, I_o^{0}]^T \in \mathbb{R}^3$$

. li

$\mathbf{I}_{\mathbf{o}}^{\alpha\beta 0^{12}}$ Vector containing the output current flowing through the AC-side load in the $\{\alpha_1, \beta_1, \alpha_2, \beta_2, 0\}$ synchronous rotating frame,

$$\mathbf{I}_{\mathbf{o}}^{\alpha\beta 0^{12}} \triangleq \left[C_{K_{12}}^{m}\right]\mathbf{I}_{\mathbf{o}} = [I_o^{\alpha_1}, I_o^{\beta_1}, I_o^{\alpha_2}, I_o^{\beta_2}, I_o^{0}]^T \in \mathbb{R}^5$$

. li

$\hat{I}_o$ Amplitude of the output current from the MMC . . . . . xlvii, li, 117

$\hat{I}_o^{max}$ Maximum amplitude of $\mathbf{I}_{\mathbf{o}}$ in steady-state, see section 3.H.1 for more details,

$$\hat{I}_o^{max} \triangleq \frac{1}{Z_o}\left|\frac{q}{2}V_{DC} - \hat{V}_{AC}\cdot e^{-j\varphi_v}\right|$$

. . . . . li, 117, 205, 216, 217, 242

$\hat{I}_o^{min}$ Minimum amplitude of $\mathbf{I}_{\mathbf{o}}$ in steady-state, see section 3.H.1 for more details,

$$\hat{I}_o^{min} \triangleq \frac{1}{Z_o}\left|-\frac{q}{2}V_{DC} + \hat{V}_{AC}\cdot e^{-j\varphi_v}\right|$$

. . . . . li, 117

$\underline{I_o}$ Complex phasor describing the current $\mathbf{I}_{\mathbf{o}}$ in steady-state when considering a single fondamental component for the analysis of the operating limits,

$$\underline{I_o} \triangleq \hat{I}_o\, e^{-j\mathbf{\Phi_o}}$$

. . . . . xlvii, li, lxxii

$\mathbf{I}_{\mathbf{o}}^{\mathbf{dq}0}$ Vector containing the output current flowing through the AC-side load in the $\{d, q, 0\}$ synchronous rotating frame,

$$\mathbf{I}_{\mathbf{o}}^{\mathbf{dq}0} \triangleq [P(-\theta)]\mathbf{I}_{\mathbf{o}}^{\alpha\beta 0} = [P(-\theta)][C_K]\mathbf{I}_{\mathbf{o}} = [I_o^{d}, I_o^{q}, I_o^{0}]^T \in \mathbb{R}^3$$

. . . . . li, lii

$\mathbf{I}_{\mathbf{o}}^{\mathbf{dq}012}$ Vector containing the output current flowing through the AC-side load in the $\{d_1, q_1, d_2, q_2, 0\}$ synchronous rotating frame,

$$\mathbf{I}_{\mathbf{o}}^{\mathbf{dq}012} \triangleq [P(-\theta)_{12}^{m}]\mathbf{I}_{\mathbf{o}}^{\alpha\beta 0^{12}} = [P(-\theta)_{12}^{m}]\left[C_{K_{12}}^{m}\right]\mathbf{I}_{\mathbf{o}} = [I_o^{d_1}, I_o^{q_1}, I_o^{d_2}, I_o^{q_2}, I_o^{0}]^T \in \mathbb{R}^5$$

. . . . . li, lii, 133

$\tilde{\mathbf{I}}_{\mathbf{o}}^{\mathbf{dq}012}$ Vector containing the reduced output current flowing through the AC-side load in the $\{d_1, q_1, d_2, q_2, 0\}$ synchronous rotating frame,

$$\tilde{\mathbf{I}}_{\mathbf{o}}^{\mathbf{dq}012} \triangleq \begin{bmatrix} 1 & 0 & 0 & 0 & 0 \\ 0 & 1 & 0 & 0 & 0 \\ 0 & 0 & 1 & 0 & 0 \\ 0 & 0 & 0 & 1 & 0 \end{bmatrix} \mathbf{I}_{\mathbf{o}}^{\mathbf{dq}012} = [I_o^{d_1}, I_o^{q_1}, I_o^{d_2}, I_o^{q_2}]^T \in \mathbb{R}^4$$

. . . . . lii, lxxvi, lxxviii, 109, 187

$\tilde{\mathbf{I}}_{\mathbf{o}}^{\mathbf{dq}0}$ Vector containing the reduced output current flowing through the AC-side load in the $\{d, q, 0\}$ synchronous rotating frame,

$$\mathbf{I}_{\mathbf{o}}^{\mathbf{dq}0} \triangleq \begin{bmatrix} 1 & 0 & 0 \\ 0 & 1 & 0 \end{bmatrix} \mathbf{I}_{\mathbf{o}}^{\mathbf{dq}0} = [I_o^d, I_o^q]^T \in \mathbb{R}^2$$

. . . . . lxxvi, lxxviii, 94, 95

$i_{c_{y_j}}$ Circulating current $\#j$ out of m which flows through the legs of the MMC . . xlvii, xlviii, l, li

$\tilde{\mathbf{I}}_{\mathbf{o}}^{\mathbf{dq}012ref}$ Output current reference in the Park 12 reference frame,

$$\tilde{\mathbf{I}}_{\mathbf{o}}^{\mathbf{dq}012ref} \triangleq [I_o^{d_1 ref}, I_o^{q_1 ref}, I_o^{d_2 ref}, I_o^{q_2 ref}]^T$$

. . . . . lii, lxxviii, 196

$\mathbf{I}_{\mathbf{o}}^{ref}$ Output current reference,

$$\mathbf{I}_{\mathbf{o}}^{ref} \triangleq \begin{bmatrix} i_{o_{y_1}}^{ref} \\ i_{o_{y_2}}^{ref} \\ \vdots \\ i_{o_{y_j}}^{ref} \\ \vdots \\ i_{o_{y_m}}^{ref} \end{bmatrix}$$

. . . . . xxiv, lii, 189, 196, 197, 205, 216, 217, 219

$\hat{I}_o^{ref}$ Reference amplitude of the output current from the MMC 196, 205, 217

$\tilde{\mathbf{I}}_{\mathbf{o}}^{ref}$ Output current reference reduced vector,

$$\tilde{\mathbf{I}}_{\mathbf{o}}^{ref} \triangleq \begin{bmatrix} i_{o_{y_1}}^{ref} \\ i_{o_{y_2}}^{ref} \\ \vdots \\ i_{o_{y_j}}^{ref} \\ \vdots \\ i_{o_{y_{m-1}}}^{ref} \end{bmatrix}$$

. . . . . lii, lxxvii, lxxviii

i_p Current flowing from the DC bus positive pole to the MMC . . . liii, lxi, 13, 25, 76–83, 112, 113

i_{py} Current flowing through the arm $\#p$ of the leg $\#y$ among $\{y_1, \ldots, y_m\}$. liv, 15, 22, 25, 76–83, 190

I_s Current proportional to the DC-source current supplying the MMC . xxii, liii, lvi, lxi, lxv, lxix, lxxvi, lxxvii, lxxx, 15, 22, 25, 31, 32, 75–82, 84, 85, 87, 91, 107, 113–115, 119, 124, 127, 185–187, 190, 192–194, 205, 216, 219, 220, 224, 230, 231, 243

$\hat{I}_s$ Amplitude of the common mode current of the MMC,

$$\hat{I}_s = I_s = i_s$$

. . . . . liii, 117

$\hat{I}_s^{max}$ Maximum amplitude of I_s in steady-state, see section 3.H.1 for more details,

$$\hat{I}_s^{max} \triangleq \frac{1}{Z_s}\left(q - \frac{1}{2}\right) V_{DC}$$

. . . . . liii, 117, 194

$\hat{I}_s^{min}$ Minimum amplitude of I_s in steady-state, see section 3.H.1 for more details,

$$\hat{I}_s^{min} \triangleq -\frac{1}{Z_s}\frac{1}{2} V_{DC}$$

. . . . . liii, 117, 194

I_s^{dq0} Current proportional to the DC-source current supplying the MMC in the $\{d, q, 0\}$ reference frame,

$$I_s^{dq0} \triangleq I_s \in \mathbb{R}$$

. . . . . liii, lxxvi, lxxviii, 91, 95

I_s^{dq012} Current proportional to the DC-source current supplying the MMC in the $\{d_1, q_1, d_2, q_2, 0\}$ reference frame,

$$I_s^{dq012} \triangleq I_s \in \mathbb{R}$$

. . . . . liii, lxxvi, lxxviii, 107–109, 187

$I_s^{dq012ref}$ Source current reference in the Park 12 reference frame,

$$I_s^{dq012ref} \triangleq I_s^{ref}$$

. . . . . liii, lxxviii

I_s^{ref} Source current reference . . . . . liii, lxxvii, lxxviii, 193, 196, 197, 216

i_{xy}^* Current flowing through all the Submodules (SMs) of the arm $\#x$ among $\{n, p\}$, of the leg $\#y$ among $\{y_1, \ldots, y_m\}$,

$$i_{xy}^* \triangleq \sigma(x) \cdot i_{xy}$$

. . . . . xxi, xxx, xxxiii, xxxv, xlii, liii, lvi, lviii, lxi–lxiv, lxvi, lxviii, 12, 19–21, 31, 54–59, 62, 64–68, 180, 181, 213

$\mathbf{I_x}$ Vector which compnents are the currents flowing from the DC bus within the Modular Multilevel Converter (MMC) through the positive and the negative pole,

$$\mathbf{I_x} \triangleq \begin{bmatrix} i_p \\ i_n \end{bmatrix}$$

. . . . . liii, lxi, 112, 113

i_x One of the two compnents of the DC bus current components,

$$i_x \triangleq \begin{cases} i_p, \text{ if } x = p \\ i_n, \text{ if } x = n \end{cases}$$

. . . . . liii, 79

$\mathbf{I_{xy}}$ Vector containing all the arm currents i_{xy} of the MMC,

$$\mathbf{I_{xy}} \triangleq \begin{bmatrix} i_{py_1} \\ \vdots \\ i_{py_m} \\ i_{ny_1} \\ \vdots \\ i_{ny_m} \end{bmatrix} \in \mathbb{R}^{2m}$$

. . . . . xxiii, liv, 191, 218, 219

i_{xy} Current flowing through the arm $\#x$ among $\{n, p\}$, of the leg $\#y$ among $\{y_1, \ldots, y_m\}$ . . . . . liii, liv, 12, 13, 15, 22, 32, 76, 79, 80, 205, 207

$\mathbf{I_y}$ Vector which components are the currents flowing from the MMC towards the AC network,

$$\mathbf{I_y} \triangleq \begin{bmatrix} i_{y_1} \\ i_{y_2} \\ \vdots \\ i_y \\ \vdots \\ i_{y_m} \end{bmatrix}$$

. . . . . liv, lx, lxi, 112, 113

i_y $\#y$ phase current across the AC network in load convention,

$$i_y = i_{py} + i_{ny} = 2\left(i_m + i_{o_y}\right)$$

. . . . . liv, lx, lxi, 13, 22, 25, 77, 79, 112

I_z The integral compensator gain of the control allocation with integral compensator architectures. $I_z \in \mathbb{R}^{n_y \times n_y}$ . . . . . liv, 155–162, 166

J

J_l The control allocation optimization problem cost function,

$$J_l = ||\mathbf{e}||_l^l$$

with l the selected norm . . . . . liv, lv, 146–150, 166, 170, 212, 213, I

$J_{l_{MMC}}$ The high-level-low-level control allocation from the entire MMC optimization problem cost function,

$$J_{l_{MMC}} = ||\hat{\mathbf{e}}_{\mathbf{MMC}}||_l^l$$

with l the selected norm . . . . . liv, 192

$J_{l_{HL}}$ The high-level control allocation optimization problem cost function from the entire set of currents in the natural reference frame,

$$J_{l_{HL}} = ||\hat{\mathbf{e}}_{\mathbf{HL}}||_l^l$$

with l the selected norm . . . . . liv, 186

$J_{l_{HL}^{dq012}}$ The high-level control allocation optimization problem cost function from the entire set of currents in the Park 12 reference frame,

$$J_{l_{HL}^{dq012}} = ||\hat{\mathbf{e}}_{\mathbf{HL}}^{\mathbf{dq012}}||_l^l$$

with l the selected norm . . . . . liv, 188

$J_{l_{LL}}$ The low-level control allocation from the entire MMC optimization problem cost function,

$$J_{l_{LL}} = ||\hat{\mathbf{e}}_{\mathbf{LL}}||_l^l$$

with l the selected norm . . . . . lv, 182

$J_{l_{LL}}^{xy}$ The low-level control allocation from the arm $\#xy$ optimization problem cost function,

$$J_{l_{LL}}^{xy} = ||\hat{\mathbf{e}}_{\mathbf{LL}}^{\mathbf{xy}}||_l^l$$

with l the selected norm . . . . . lv, 180, 181, 201

K

K Matrix factor of the Park transform,

$$K \triangleq \begin{cases} \frac{2}{m}, \text{ if Clarke conservation is used} \\ \sqrt{\frac{2}{m}}, \text{ if Concordia conservation is used} \end{cases}$$

. . . . . xxxv, xxxvii, xxxviii, lv, 89, 90, 101, 102, 105–107

k Variable standing for the discrete time current instant. This notation enables to define the current time as:

$$t = k\, T_c$$

. . xxix–xxxi, xxxiii, xlii, lv, lxx, lxxi, lxxvii–lxxix, 67, 68, 86, 95, 110, 113, 144, 145, 151, 152, 155, 157, 158, 165, 169, 170, 180–183, 185–189, 192–194, 196, 197, 211–213, 229, 230

k_0 Homopolar component factor of the Park transform,

$$k_0 \triangleq \sqrt{2}$$

. . . . . xxxv, lv, lxx, lxxi, 89, 90, 105, 107

K_z The proportional gain of some control allocation with integral compensator architectures. $K_z \in \mathbb{R}^{n_y \times n_y}$ . . . . . lv, 158–162, 166

L

L MMC arm inductance . . . . . lv, lvi, 13, 22, 25, 79–83, 121, 206, 218, 243

l The control allocation optimization problem cost function norm, see J_l for more details xxx, xl, liv, lv, lvii, lviii, 146–148, 180–182, 186, 188, 192, 201, 213, 229, 230, I

λ Linear map between magnetic flux and current in a polyphase circuit of m phases,

$$\mathbf{\Phi^m} \triangleq \lambda(\mathbf{i^m})$$

. . . . . xxxvii, xl, lv, 98, 102

Λ_i Eigenvalue of the linear map λ . . . . . xl, 98, 99

L_c^{eq} Equivalent inductance that is seen by the circulating current $\mathbf{I_c}$ when the converter is operating,

$$L_c^{eq} = L$$

. . . . . xxxi, xxxii, xxxiv, xliii, lv, lxxix, 82–85, 91, 93–95, 108, 110

L^m Generalized inductance matrix in the natural basis $\mathcal{B}^m$,

$$L^m \triangleq mat(\lambda, \mathcal{B}^m) \in \mathcal{M}_m(\mathbb{R})$$

L_m^{eq} Equivalent inductance that is seen by the common mode current I_m when the converter is operating,

$$L_m^{eq} = mL_s + L + 2L_o$$

L_o AC network phase line inductance

L_o^{eq} Equivalent inductance that is seen by the output current $\mathbf{I_o}$ when the converter is operating,

$$L_o^{eq} = L + 2L_o$$

L_s DC bus inductance

L_s^{eq} Equivalent inductance that is seen by the source current I_s when the converter is operating,

$$L_s^{eq} = mL_s + L$$

L_{xy} Matrix containing the entire set of l_{xyj}s and l'_{xyj}s of the submodules from the arm $\#xy$,

$$L_{xy} \triangleq \begin{bmatrix} l_{xy1} & l'_{xy1} & & & & & & \\ & & l_{xy2} & l'_{xy2} & & & & \\ & & & & \ddots & \ddots & & \\ & & & & & & l_{xyN} & l'_{xyN} \end{bmatrix} \in \mathcal{M}_{N,2N}(\mathbb{N})$$

l_{xyj} Parameter of the submodule $\#xyj$. This parameter is needed to define the global state S_{xyj}^{FB} of the full-bridge submodule,

$$l_{xyj} = \left[\hat{p}_{xyj}(i^*_{xy}, v_{C_{xyj}})\overline{S^b_{xyj}}\,\overline{S^{b'}_{xyj}} + \left|sign(i^*_{xy})\right|\overline{S^b_{xyj}}S^{b'}_{xyj}\right]\overline{S^f_{xyj}}$$

l'_{xyj} Parameter of the submodule $\#xyj$. This parameter is needed to define the global state S_{xyj}^{FB} of the full-bridge submodule,

$$l'_{xyj} = \left[\tilde{p}_{xyj}(i^*_{xy}, v_{C_{xyj}})\overline{S^b_{xyj}}\,\overline{S^{b'}_{xyj}} - \left|sign(i^*_{xy})\right|S^b_{xyj}\overline{S^{b'}_{xyj}}\right]\overline{S^f_{xyj}}$$

M

M The effectiveness matrix in the control allocation problem. $M \in \mathbb{R}^{n_a \times n_u}$.

m The number of phases in the AC-side polyphase network

m_n Factor defining the DC component of v_{ny} for the steady-state analysis of section 3.H.1, see equation (3.166) for more details.

m_p Factor defining the DC component of v_{py} for the steady-state analysis of section 3.H.1, see equation (3.166) for more details. . . . . xxii, 116, 117, 120, 121, 128

$\mathcal{M}$ The effectiveness function in the control allocation problem. $\mathcal{M} : \mathbb{R}^{n_u} \mapsto \mathbb{R}^{n_a}$ xl, lvii, 34, 62, 144–147, 155, 179, I

$\hat{\mathcal{M}}$ The complete effectiveness function. $\hat{\mathcal{M}} : \mathbb{R}^{n_u} \mapsto \mathbb{R}^{n_a+n_{a_p}}$ . . . . . xl, lvii, 147

$\mathcal{M}_p$ The preference effectiveness function. $\mathcal{M}_p : \mathbb{R}^{n_u} \mapsto \mathbb{R}^{n_{a_p}}$ . . . . . lvii, 147

M_{MMC} Effectivness matrix of the global high-level-low-level control allocation,

$$M_{MMC} \triangleq C_{MMC} G_{MMC} \in \mathbb{R}^{2m(N+1)\times 4mN}$$

. . . . . lvii, 192

$\hat{M}$ The complete effectiveness matrix. $\hat{M} : \mathbb{R}^{n_u \times (n_a+n_{a_p})}$ . . . . . lvii, 170

$\hat{M}_{MMC}$ Effectivness matrix of the global high-level-low-level control allocation,

$$\hat{M}_{MMC} \triangleq \mathbf{w}^{\frac{1}{l}} \circ M_{MMC} \in \mathbb{R}^{2m(N+1)\times 4mN}$$

. . . . . xl, lvii, 192

$\hat{M}_{HL}$ Entire effectivness matrix for the high-level control allocation from the entire set of currents in the natural reference frame,

$$\hat{M}_{HL} \triangleq \mathbf{w_I}^{\frac{1}{l}} \circ \tilde{C}_{HL} \tilde{G}_{HL}$$

where the operation $\cdot^{\frac{1}{l}}$ is applied to term by term to the weighting vector. xl, lvii, 186, 189

$\hat{M}_{HL}^{dq012}$ Entire effectivness matrix for the high-level control allocation from the entire set of currents in the Park 12 reference frame,

$$\hat{M}_{HL}^{dq012} \triangleq \mathbf{w_I}^{\frac{1}{l}} \; M_{HL}^{dq012}$$

. . . . . lvii, 188, 189, 229, 230

M_{HL} Effectivness matrix for the high-level control allocation from the entire set of currents in the natural reference frame,

$$M_{HL} \triangleq \tilde{C}_{HL} \tilde{G}_{HL}$$

. . . . . lvii, 185, 186

M_{HL}^{dq012} Effectivness matrix for the high-level control allocation from the entire set of currents in the Park 12 reference frame,

$$M_{HL}^{dq012} \triangleq C_{HL}^{dq012} G_{HL}^{dq012}$$

. . . . . xl, xli, lvii, 187, 188

$\hat{M}_{LL}$ Entire effectivness matrix for the low-level control allocation from the entire MMC,

$$\hat{M}_{LL} \triangleq \begin{bmatrix} M_{LL} \\ w_{v_C}{}^{\frac{1}{l}} M_{pLL} \end{bmatrix}$$

. . . . . xli, lvii, 182

M_{LL} Effectivness matrix for the low-level control allocation from the entire MMC,

$$M_{LL} \triangleq \begin{bmatrix} M_{LL}^{py_1} & & & & \\ & M_{LL}^{ny_1} & & & \\ & & \ddots & & \\ & & & M_{LL}^{py_m} & \\ & & & & M_{LL}^{ny_m} \end{bmatrix}$$

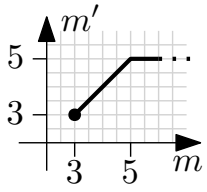

Figure 2: Definition of m' as a function of m.

. . . . . xxxix, lvii, 182

M_{LL}^{xy} Effectivness matrix for the low-level control allocation from the arm $\#xy$,

$$M_{LL}^{xy} \triangleq \left[\sigma(x)\mathbf{X_{LL}^{xy}}^T L_{xy}\right] = \left[\sigma(x)\mathbf{v_{C_{xy}}}^T L_{xy}\right]$$

. . . . . xlii, lviii, 181, 213

$\hat{M}_{LL}^{xy}$ Complete effectivness matrix for the low-level control allocation from the arm $\#xy$,

$$\hat{M}_{LL}^{xy} \triangleq \begin{bmatrix} M_{LL}^{xy} \\ w_{v_C}{}^{\frac{1}{l}}\, M_{pLL}^{xy} \end{bmatrix} = \begin{bmatrix} \sigma(x)\mathbf{X_{LL}^{xy}}^T L_{xy} \\ w_{v_C}{}^{\frac{1}{l}}\, \frac{T_c}{C} i_{xy}^* L_{xy} \end{bmatrix}$$

. . . . . xli, lviii, 181, 201, 213

M_{pLL}^{xy} Preference effectivness matrix for the low-level control allocation from the arm $\#xy$,

$$M_{pLL}^{xy} \triangleq \left[\frac{T_c}{C} i_{xy}^* L_{xy}\right]$$

. . . . . xlii, lviii, 181, 213

m_{ny} The arm $\#ny$ modulation index,

$$m_{ny} \triangleq \frac{v_{ny}}{V_{DC}}$$

. . . . . lviii, 116

M_p The preference effectiveness matrix. $M_p : \mathbb{R}^{n_u \times n_{a_p}}$ . . . . . lviii, 170

m' The size of the vectors in the Park 12 reference frame. m' is defined as a function of m, this relationship is shown on Figure 2.

$$m' = \begin{cases} m, \text{ if } m \leq 5 \\ 5, \text{ if } m \geq 5 \end{cases}$$

. . . xxi–xxiii, xxvi, xxxi, xxxii, xxxiv, xxxvii, xl, xli, xliii, xlvi, xlvii, lviii, lxviii, lxx, lxxi, lxxvi, lxxviii, lxxix, 106, 111, 133, 138, 139, 188, 189, 230

M_{PE} Discrete linear effectivness matrix for the power-energy control allocation,

$$M_{PE} \triangleq T_c C_{PE} B_{PE} = T_c m \left(v_p - v_n\right)$$

. . . . . xxxviii, lviii, lxii, 194

M'_{PE} Discrete nonlinear effectivness matrix for the power-energy control allocation,

$$M'_{PE} \triangleq T_c C_{PE} B'_{PE} = -2T_c m^2 R_s$$

. . . . . xxxviii, lviii, lxii, 194

M_{pLL} Preference matrix for the low-level control allocation from the entire MMC,

$$M_{pLL} \triangleq \begin{bmatrix} M_{pLL}^{py_1} & & & & \\ & M_{pLL}^{ny_1} & & & \\ & & \ddots & & \\ & & & M_{pLL}^{py_m} & \\ & & & & M_{pLL}^{ny_m} \end{bmatrix}$$

m_{py} The arm $\#py$ modulation index,

$$m_{py} \triangleq \frac{v_{py}}{V_{DC}}$$

m_{xy} The arm $\#xy$ modulation index,

$$m_{xy} \triangleq \frac{v_{xy}}{V_{DC}}$$

N

N The number of submodules in an arm of the MMC . . . . . xxii, xxvi, xxx, xxxii, xxxvi, xxxviii–xl, xlii–xlvi, xlix, lvi, lvii, lix, lx, lxii, lxv, lxvii–lxx, lxxii, lxxiii, lxxv–lxxviii, lxxx, 10, 12–14, 18, 20, 21, 28, 29, 61, 62, 64–66, 73–75, 87, 96, 115, 136, 138, 139, 178, 181, 183, 186, 192, 193, 196, 198, 199, 204–209, 213, 216, 218, 235, 240–243

n Letter standing for the negative pole of the DC bus, used to describe the connection of a given to the negative pole of the DC bus . . . . xlix, l, liii, liv, lxvi, lxxi–lxxiii, lxxvi, 12, 13, 196

$N_{\mathfrak{A}}$ The number of *Available* submodules in an arm of the MMC,

$$N_{\mathfrak{A}} = N - N_{\mathfrak{E}}$$

n_{AC} AC network neutral point . . . . . lxxi, 13

n_{DC} DC bus neutral point . . . . . lxxi–lxxiii, 13

$N_{\mathfrak{E}}$ The number of *Excluded* submodules in an arm of the MMC,

$$N_{\mathfrak{E}} = N_{\mathfrak{F}} - N_{\mathfrak{I}}$$

$N_{\mathfrak{F}}$ The number of *Faulty* submodules in an arm of the MMC,

$$N_{\mathfrak{F}} = N - N_{\mathfrak{H}}$$
$$N_{\mathfrak{F}} = N_{\mathfrak{I}} + N_{\mathfrak{E}}$$

$N_{\mathfrak{F}}^{max}$ The maximum number of submodules in an arm of the MMC that can be *Faulty* before to start reducing the operating zone of the converter,

$$N_{\mathfrak{F}}^{max} = \left\lfloor N \frac{\alpha_C^{max}}{1+\alpha_C^{max}} \right\rfloor$$

$N_{\mathfrak{H}}$ The number of *Healthy* submodules in an arm of the MMC,

$$N_{\mathfrak{H}} = N - N_{\mathfrak{F}}$$

$N_{\mathfrak{I}}$ The number of *Included* submodules in an arm of the MMC,

$$N_{\mathfrak{I}} = N_{\mathfrak{F}} - N_{\mathfrak{E}}$$

. . . . . lix, 240, 241

n_{SM} Total number of submodules in the MMC,

$$n_{SM} \triangleq 2Nm$$

. . . . . lx, 10, 12

$N_{\Sigma}(m)$ A modelling matrix used in the high-level SSM,

$$N_{\Sigma}(m) \triangleq \frac{1}{m}\begin{bmatrix}1 & 1 & 1 & \dots & 1\end{bmatrix} \in \mathcal{M}_{1,m}(\mathbb{R})$$

. . . . . xxxiv, xxxv, xli, lx, lxx, lxxiii, 80–82, 84, 85, 90, 91, 95, 107, 110, 115

$N_{\Delta}(m)$ A modelling matrix used in the high-level SSM,

$$N_{\Delta}(m) \triangleq \frac{1}{m}\begin{bmatrix} m-1 & -1 & -1 & \dots & -1 \\ -1 & m-1 & -1 & \dots & -1 \\ -1 & -1 & m-1 & \dots & -1 \\ \vdots & \vdots & \vdots & \ddots & \vdots \\ -1 & -1 & -1 & \dots & m-1 \end{bmatrix} \in \mathcal{M}_{m}(\mathbb{R})$$

. . . . . xxxiii, xxxiv, xli, lx, lxix, lxxii, lxxiv, 81, 83–85, 91, 94, 115

O

ω Electrical frequency (rad/s) standing for the angular speed of the rotating Park reference frame with respect to the natural $\{1, 2, \dots, m\}$ static reference frame xxxii, lxvii, 92, 93, 95, 108–110

ω_c Electrical frequency (rad/s) standing for the angular speed of the rotating Park reference frame with respect to the natural $\{1, 2, \dots, m\}$ static reference frame for the circulating current $\mathbf{I_c}$ . . . . . lxxix, 92, 197

ω_o Electrical frequency (rad/s) standing for the angular speed of the rotating Park reference frame with respect to the natural $\{1, 2, \dots, m\}$ static reference frame for the output current $\mathbf{I_o}$,

$$\omega_o \triangleq 2\pi f_o$$

. . . lx, lxvii, lxxii, lxxiv, lxxx, 92, 94, 116, 119–121, 128, 153, 196, 197, 206, 218, 219, 243

P

p Letter standing for the positive pole of the DC bus, used to describe the connection of a given to the positive pole of the DC bus . . xlix, lii–liv, lxvi, lxxii, lxxiii, lxxvi, 12, 13, 196

P_{AC} Electric active power provided to the AC-side grid,

$$P_{AC} \triangleq \sum_{y=y_1}^{y_m} v_y i_y = \mathbf{V_y}^T \mathbf{I_y} \in \mathbb{R}$$

. . . . . lx, lxi, 112, 113, 217

p_{CC} The closed-loop poles for the four current types dynamics. 187, 189, 195

p_j The closed-loop poles when using a control allocation with integral compensator architecture. 157

P_{DC} Electric power supplied by the DC bus to the MMC,

$$P_{DC} \triangleq v_p i_p + v_n i_n = \mathbf{V_x}^T \mathbf{I_x} = (v_p - v_n)\, m i_s \in \mathbb{R}$$

. . . . . lxi, 112–114

p_{EC} The closed-loop poles for the energy dynamics. 195

P_{MMC}^{loss} Electric power losses within the MMC . . . . . lxi, 112, 113, 197

P_o Electric active power at the output of the MMC,

$$P_o \triangleq P_{AC} + P_o^{loss} \in \mathbb{R}$$

. . . . . lxi, 112, 113, 194, 197

P_o^{loss} Joules losses in the AC network at the output of the MMC,

$$P_o^{loss} \triangleq R_o \sum_{y=y_1}^{y_m} {i_y}^2 = R_o \mathbf{I_y}^T \mathbf{I_y} \in \mathbb{R}$$

. . . . . lxi, 112, 113

$\tilde{p}_{xyj}(i_{xy}^*, v_{C_{xyj}})$ Binary variable that describes the capacitor state of the SM $\#xyj$. If -i_{xy}^* intends to charge de capacitor of the SM, no problem is encountered, the capacitor is considered available to be charged. If -i_{xy}^* intends to discharge the capacitor, this capacitor can only be discharged if its voltage is positive. Thus $\tilde{p}_{xyj}$ is defined:

$$\tilde{p}_{xyj} \triangleq \left[\left(i_{xy}^* < 0\right) + \left(i_{xy}^* > 0\right)\left(v_{C_{xyj}} > 0\right)\right]$$

As a result, $\hat{p}_{xyj} = 1$ means that the capacitor is available to be charged or discharged by the current $-i_{xy}^*$ and $\hat{p}_{xyj} = 0$ means the capacitor is empty and cannot be discharged anymore . . . . . lvi, lxvi

P_s Electric power at the input of the MMC,

$$P_s \triangleq P_{DC} - P_s^{loss} \in \mathbb{R}$$

. . . . . lxi, 112, 114

$P_{\bar{s}}$ Virtual electric power used in the power-energy model,

$$P_{\bar{s}} \triangleq P_{MMC}^{loss} + P_{AC} + P_o^{loss} = P_{MMC}^{loss} + P_o \in \mathbb{R}$$

. . . . . xxii, xlii, lxi, 113, 114

P_s^{loss} Joules losses in the DC link between the DC supply and the MMC,

$$P_s^{loss} \triangleq R_s({i_p}^2 + {i_n}^2) = R_s \mathbf{I_x}^T \mathbf{I_x} = 2R_s m^2 {i_s}^2 \in \mathbb{R}$$

. . . . . lxi, 112, 113

$[P(\theta)]$ Transformation matrix from the reference frame $\{\alpha, \beta, 0\}$ to the $\{d, q, 0\}$ synchronous rotating reference frame,

$$[P(\theta)] \triangleq \begin{bmatrix} \cos(\theta) & -\sin(\theta) & 0 \\ \sin(\theta) & \cos(\theta) & 0 \\ 0 & 0 & 1 \end{bmatrix} \in \mathcal{M}_3(\mathbb{R})$$

. . . . . xxxiii–xxxv, xli, xliv, xlviii, li, lxi, lxii, lxxi–lxxiv, 90, 92–95, 133

$[P(\theta)_{12}^{m}]$ Transformation matrix from the reference frame $\{\alpha_1, \beta_1, \alpha_2, \beta_2, 0\}$ to the $\{d_1, q_1, d_2, q_2, 0\}$ synchronous rotating reference frame. In the case where $m \geq 5$ this matrix is defined:

$$[P(\theta)] \triangleq \begin{bmatrix} \cos(\theta) & -\sin(\theta) & 0 & 0 & 0 \\ \sin(\theta) & \cos(\theta) & 0 & 0 & 0 \\ 0 & 0 & \cos(2\theta) & -\sin(2\theta) & 0 \\ 0 & 0 & \sin(2\theta) & \cos(2\theta) & 0 \\ 0 & 0 & 0 & 0 & 1 \end{bmatrix} \in \mathcal{M}_5(\mathbb{R})$$

For the definition of $\left[C_{K_{12}}^{m}\right]$ in the cases where $m \leq 5$, see Section 3.E.2.3 . . . xxxiv, xxxv, xli, xliv, xlviii, li, lxxi, lxxiii, lxxiv, 106–110, 133

P The discrete time polynomial representing the power-energy allocation equation that stands for the targeted MMC power balance in closed-loop that the control $\mathbf{U_{PE}}$ has to solve,

$$P(\mathbf{U_{PE}}) \triangleq \mathbf{a_{d_{PE}}} - M'_{PE}\mathbf{U_{PE}}^2 - M_{PE}\mathbf{U_{PE}}$$

. . . . . xxxviii, lxii, 194

$\hat{p}_{xyj}(i^*_{xy}, v_{C_{xyj}})$ Binary variable that describes the capacitor state of the SM $\#xyj$. If i^*_{xy} intends to charge de capacitor of the SM, no problem is encountered, the capacitor is considered available to be charged. If i^*_{xy} intends to discharge the capacitor, this capacitor can only be discharged if its voltage is positive. Thus $\hat{p}_{xyj}$ is defined:

$$\hat{p}_{xyj} \triangleq \left[\left(i^*_{xy} > 0\right) + \left(i^*_{xy} < 0\right)\left(v_{C_{xyj}} > 0\right)\right]$$

As a result, $\hat{p}_{xyj} = 1$ means that the capacitor is available to be charged or discharged by the current $+i^*_{xy}$ and $\hat{p}_{xyj} = 0$ means the capacitor is empty and cannot be discharged anymore . . . . . lvi, lxvi, 54, 55

P^{loss}_{xyj} Joule losses is the SM $\#xyj$. . . . . lxii, 53, 58–60, 62, 64

P^{loss}_{xy} Total Joules losses in the submodules from the arm $\#xy$,

$$P^{loss}_{xy} \triangleq \sum_{j=1}^{N} P^{loss}_{xyj}$$

. . . . . lxii, 64

Q

q Variable standing for the number of commutation cells in the selected submodule topology,

$$q \triangleq \begin{cases} 1, \text{ if the considered topology is the half-bridge submodule} \\ 2, \text{ if the considered topology is the full-bridge submodule} \end{cases}$$

. . . . . xlviii, l, li, liii, lxii, lxx, lxxi, 62, 64, 65, 116, 117, 121, 186, 206, 218, 243

Q_{AC} Electric reactive power provided to the AC-side grid 217

R

R MMC arm resistance . . . . . lxiv, lxv, 13, 22, 25, 79–83, 121, 206, 218, 243

R_a Resistance parameter for the low-level model, it encapsulates a larger expression and its purpose is to simplify mathematical model manipulations in F.2,

$$R_a = (R_{T_l} + R'_{D_l})(i^*_{xy} > 0) + (R_{D_l} + R'_{T_l})(i^*_{xy} < 0)$$

R_a^f ..... lxii, lxvii, lxxv, lxxx
Resistance parameter for the low-level model, it encapsulates a larger expression and its purpose is to simplify mathematical model manipulations in F.2,

$$R_a^f = R_f//(R_{T_l} + R'_{D_l})(i^*_{xy} > 0) + R_f//(R'_{T_l} + R_{D_l})(i^*_{xy} < 0)$$

R_α ..... lxiii, lxvii, lxxv, lxxx
Resistance parameter for the low-level model, it encapsulates a larger expression and its purpose is to simplify mathematical model manipulations in F.2,

$$R_\alpha = (R_{T_l} + R'_{D_l})(i^*_{xy} > 0) + (R_{D_l} + R'_{D_u})(i^*_{xy} < 0)$$

R_α^f ..... lxiii, lxxv, lxxx
Resistance parameter for the low-level model, it encapsulates a larger expression and its purpose is to simplify mathematical model manipulations in F.2,

$$R_\alpha^f = R_f//(R_{T_l} + R'_{D_l})(i^*_{xy} > 0) + R_f(i^*_{xy} < 0)$$

R'_α ..... lxiii, lxxv, lxxx
Resistance parameter for the low-level model, it encapsulates a larger expression and its purpose is to simplify mathematical model manipulations in F.2,

$$R'_\alpha = (R_{D_u} + R'_{D_l})(i^*_{xy} > 0) + (R_{D_l} + R'_{T_l})(i^*_{xy} < 0)$$

R'^f_α ..... lxiii, lxxv, lxxx
Resistance parameter for the low-level model, it encapsulates a larger expression and its purpose is to simplify mathematical model manipulations in F.2,

$$R'^f_\alpha = R_f(i^*_{xy} > 0) + R_f//(R'_{T_l} + R_{D_l})(i^*_{xy} < 0)$$

R_b ..... lxiii, lxxv, lxxx
Resistance parameter for the low-level model, it encapsulates a larger expression and its purpose is to simplify mathematical model manipulations in F.2,

$$R_b = (R_{D_u} + R'_{D_l})(i^*_{xy} > 0) + [R_{T_u}(v_{C_{xyj}} > 0) + R_{D_l}(v_{C_{xyj}} = 0) + R'_{T_l}](i^*_{xy} < 0)$$

R_β ..... lxiii, lxvii, lxxv
Resistance parameter for the low-level model, it encapsulates a larger expression and its purpose is to simplify mathematical model manipulations in F.2,

$$R_\beta = (R_{D_u} + R'_{D_l})(i^*_{xy} > 0) + (R_{T_u} + R'_{D_u})(i^*_{xy} < 0)$$

R_β^f ..... lxiii, lxxv
Resistance parameter for the low-level model, it encapsulates a larger expression and its purpose is to simplify mathematical model manipulations in F.2,

$$R_\beta^f = R_f(i^*_{xy} > 0) + R_f//(R'_{D_u} + R_{T_u})(i^*_{xy} < 0)$$

R'_β ..... lxiii, lxxv
Resistance parameter for the low-level model, it encapsulates a larger expression and its purpose is to simplify mathematical model manipulations in F.2,

$$R'_\beta = (R_{D_u} + R'_{T_u})(i^*_{xy} > 0) + (R_{D_l} + R'_{D_u})(i^*_{xy} < 0)$$

..... lxiii, lxxv

$R'_{\beta}{}^{f}$ Resistance parameter for the low-level model, it encapsulates a larger expression and its purpose is to simplify mathematical model manipulations in F.2,

$$R'_{\beta}{}^{f} = R_f//(R_{D_u} + R'_{T_u})(i^*_{xy} > 0) + R_f(i^*_{xy} < 0)$$

. . . . . lxiv, lxxv

R^f_b Resistance parameter for the low-level model, it encapsulates a larger expression and its purpose is to simplify mathematical model manipulations in F.2,

$$R^f_b = R_f$$

. . . . . lxiv, lxvii, lxxv

R_c Resistance parameter for the low-level model, it encapsulates a larger expression and its purpose is to simplify mathematical model manipulations in F.2,

$$R_c = [R_{Tl}+R'_{T_u}(v_{C_{xyj}} > 0)+R'_{D_l}(v_{C_{xyj}} = 0)](i^*_{xy} > 0)+(R_{D_l}+R'_{D_u})(i^*_{xy} < 0)$$

. . . . . lxiv, lxvii, lxxv

R^{eq}_c Equivalent resistance that is seen by the circulating current $\mathbf{I_c}$ when the converter is operating,

$$R^{eq}_c = R$$

. . . . . xxxi, xxxii, lxiv, lxxix, 82–85, 91–95, 108, 110

R^f_c Resistance parameter for the low-level model, it encapsulates a larger expression and its purpose is to simplify mathematical model manipulations in F.2,

$$R^f_c = R_f//(R_{D_u} + R'_{T_u})(i^*_{xy} > 0) + R_f//(R'_{D_u} + R_{T_u})(i^*_{xy} < 0)$$

. . . . . lxiv, lxvii, lxxv

R_d Resistance parameter for the low-level model, it encapsulates a larger expression and its purpose is to simplify mathematical model manipulations in F.2,

$$R_d = (R_{D_u} + R'_{T_u})(i^*_{xy} > 0) + (R_{T_u} + R'_{D_u})(i^*_{xy} < 0)$$

. . . . . lxiv, lxvii

R_{D_l} Conduction resistance of the lower diode from the first cell of any SM . . . . . lxii–lxiv, 58

R'_{D_u} Conduction resistance of the upper diode from the second cell of Full-Bridge Submodules (SM-FBs) . . . . . lxiii, lxiv, 58

R_f Conduction resistance of the security switch used under faulty conditions . . . lxiii, lxiv, 58

R_γ Resistance parameter for the low-level model, it encapsulates a larger expression and its purpose is to simplify mathematical model manipulations in F.2,

$$R_\gamma = (R_{D_u} + R'_{D_l})(i^*_{xy} > 0) + (R_{D_l} + R'_{D_u})(i^*_{xy} < 0)$$

. . . . . lxiv, lxxx

R^f_γ Resistance parameter for the low-level model, it encapsulates a larger expression and its purpose is to simplify mathematical model manipulations in F.2,

$$R^f_\gamma = R_f$$

. . . . . lxiv, lxxx

R_m^{eq} Equivalent resistance that is seen by the common mode current I_m when the converter is operating,

$$R_m^{eq} = mR_s + R + 2R_o$$

..... xxxi, xxxii, lxv, lxxix, lxxx, 80, 81, 83–85, 90, 91, 94, 95, 107, 109, 110

R_o AC network phase line resistance lxi, lxv, lxxii, 13, 22, 25, 79, 80, 83, 112, 121, 206, 218, 243

R'_{D_l} Conduction resistance of the lower diode from the second cell of any SM-FBs lxii–lxiv, 61

R'_{T_l} Conduction resistance of the lower transistor from the second cell of SM-FBs lxii, lxiii, 61

R_s DC bus resistance... xxii, xxxv, lviii, lxi, lxv, 13, 25, 79–83, 112–114, 121, 206, 218, 243

R_s^{eq} Equivalent resistance that is seen by the source current I_s when the converter is operating,

$$R_s^{eq} = mR_s + R$$

..... xxxi, xxxii, lxv, lxxx, 81, 82, 84, 85, 91, 95, 107, 108, 110

R_{T_l} Conduction resistance of the lower transistor from the first cell of any SM... lxii–lxiv, 58

R_{T_u} Conduction resistance of the upper transistor from the first cell of any SM... lxiii, lxiv, 58

R_{xyj}^{FB} Conduction resistance of the SM $\#xyj$ for the case of SM-FB. Equation (A.52) gives the definition of ths resistance..... lxvii, lxxv, lxxx, 59, 61–64

R_{xyj}^{HB} Conduction resistance of the SM $\#xyj$ for the case of SM-HB. Equation (2.7) gives the definition of ths resistance..... 57–59, 61, 62, 64

R_{arm}^{loss} Equivalent conduction resistance of an entire arm..... 60

S

S_{xyj}^{b} Blocking state of the first cell from the SM $\#xyj$. This state forces the two transistors of the first cell from the SM to reach OFF state.... lvi, lxvi–lxviii, lxxv, lxxx, 20, 53–56, 58, 61, 68

$S_{xyj}^{b'}$ Blocking state of the second cell from the SM $\#xyj$. This state forces the two transistors of the second cell from the SM to reach OFF state. This second cell is available only when using SM-FB..... lvi, lxvi–lxviii, lxxv, lxxx, 61, 68

$\mathbf{S_{xy}^{es}}$ Vector containing the entire set of switching states from the submodules of the arm $\#xy$ and is therefore considered as a control vector for the low-level part of the system. It contains all the S_{xyj}s as well as the S'_{xyj}s of this arm. In this vector the S_{xyj}s and S'_{xyj}s are organized in a different way than in $\mathbf{S_{xy}^{e}}$,

$$\mathbf{S_{xy}^{es}} \triangleq [S_{xy1}, \ldots, S_{xyN}, S'_{xy1}, \ldots, S'_{xyN}]^T \in \mathbb{R}^{2N}$$

..... xxxix, lxv

$\mathbf{S_{xy}^{e}}$ Vector containing the entire set of switching states from the submodules of the arm $\#xy$. It contains all the S_{xyj}s as well as the S'_{xyj}s of this arm. In this vector the S_{xyj}s and S'_{xyj}s are organized in a different way than in $\mathbf{S_{xy}^{es}}$,

$$\mathbf{S_{xy}^{e}} \triangleq [S_{xy1}, S'_{xy1}, S_{xy2}, S'_{xy2}, \ldots, S_{xyN}, S'_{xyN}]^T \in \mathbb{R}^{2N}$$

..... xxxix, lxv, lxviii, 64–66

S^f_{xyj} Faulty state of the SM $\#xyj$. This state drives the switch that allows to fully disconnect the associated SM from the arm to which it belongs . . . . . lvi, lxvi–lxviii, lxxv, lxxx, 20, 53–56, 58, 61, 239

$\sigma(x)$ Function that associates the type of pole (positive or negative) to an integer value (1 or -1),

$$\sigma(x) \triangleq \begin{cases} +1, \text{ if } x = p \\ -1, \text{ if } x = n \end{cases}$$

. Note that $\sigma(x)^2 = 1$ xxx, xxxi, liii, lviii, lxvi, lxxiii, 12, 62, 64–66, 68, 180, 181

S_o Electric apparent power at the output of the MMC 121

S^{FB}_{xyj} Global state of the **SM-FB** $\#xyj$. This binary variable represents the entire state of the considered full-bridge submodule, taking into account the state of the transistors, the blocking state and the faulty state,

$$\begin{aligned} S^{FB}_{xyj} &= S^{FB}_{xyj}\left(S_{xyj}, S^b_{xyj}, S'_{xyj}, S^{b'}_{xyj}, S^f_{xyj}\right) \\ &\triangleq \Big[\left(S_{xyj}\,\hat{p}_{xyj}(i^*_{xy}, v_{C_{xyj}}) - S'_{xyj}\,\tilde{p}_{xyj}(i^*_{xy}, v_{C_{xyj}})\right)\overline{S^b_{xyj}}\,\overline{S^{b'}_{xyj}} \\ &\quad + \left((i^*_{xy} > 0)\overline{S_{xyj}}' - (i^*_{xy} < 0){S_{xyj}}'\right) S^b_{xyj}\overline{S^{b'}_{xyj}} \\ &\quad + \left((i^*_{xy} > 0)S_{xyj} - (i^*_{xy} < 0)\overline{S_{xyj}}\right)\overline{S^b_{xyj}}S^{b'}_{xyj} \\ &\quad + sign(i^*_{xy})S^b_{xyj}S^{b'}_{xyj}\Big]\overline{S^f_{xyj}} \end{aligned}$$

. . . . . lvi, lxvi, lxviii, 56, 59, 61–64

S^{HB}_{xyj} Global state of the **SM-HB** $\#xyj$. This binary variable represents the entire state of the considered half-bridge submodule, taking into account the state of the transistors, the blocking state and the faulty state,

$$S^{HB}_{xyj} = S^{HB}_{xyj}\left(S^{f,b,-}_{xyj}\right) \triangleq \left[S_{xyj}\overline{S^b_{xyj}}\hat{p}_{xyj}(i^*_{xy}, v_{C_{xyj}}) + (i^*_{xy} > 0)S^b_{xyj}\right]\overline{S^f_{xyj}}$$

. . . . . lxvi, 55, 58, 61

S_{xyj} Switching state of the first cell from the SM $\#xyj$. This state drives the two transistors of the first cell from the SM in opposition . . . . . xxxix, lxv, lxvi, 12, 19–21, 27, 53–56, 58, 61, 63, 238

S'_{xyj} Switching state of the second cell from the SM $\#xyj$. This state drives the two transistor of the second cell from the SM in opposition. This second cell is available only when using SM-FB . . . xxxix, lxv, lxvi, 12, 21, 53, 61, 63, 238

T

t Variable standing for the current time . . . . . lv, 13, 68, 144, 196, 197, 243, 244

T_c The sampling period of the control system . . . . . xxx, xxxi, xxxiii, xxxix, xl, xliii, xlvi, lv, lviii, lxviii, 66–68, 113, 144, 153, 165, 180, 181, 187, 189, 193–195, 198, 213

T_{CL} The closed-loop transfer function of some system. When no disturbance is applied to the system:

$$\mathbf{Y}(z) = T_{CL}(z)\mathbf{Y}^{ref}(z)$$

. . . . . lxvi, 151, 152, 155–159, 161, 162, 167

t_{end} The end time of the simulations and the emulations . . 121, 206, 218–220, 223, 231, 243

θ Electrical angle between the rotating Park reference frame and the natural $\{1, 2, \ldots, m\}$ static reference frame,

$$\theta \triangleq \int \omega dt$$

. . xxxiii–xxxv, xli, xliv, xlviii, li, lxi, lxii, lxvii, lxxi–lxxiv, 90–95, 106–110, 133

θ_m Inter-phase electrical angle in a m-phase balanced polyphase system,

$$\theta_m \triangleq \frac{2\pi}{m}$$

. . . . . xxxvii, lxvii, 89, 99, 101, 105

θ_o Electrical angle between the rotating Park reference frame for the output current $\mathbf{I_o}$ and the AC-side phase #1 angular position,

$$\theta_o \triangleq \int \omega_o dt$$

. . . . . lxvii, 92

Θ_{xy} Matrix containing the entire set of θ_{xyj}s and of the submodules from the arm $\#xy$,

$$\Theta_{xy} \triangleq \begin{bmatrix} \begin{bmatrix} 0 & \theta_{xy1} \\ 0 & 0 \end{bmatrix} & & & \\ & \begin{bmatrix} 0 & \theta_{xy2} \\ 0 & 0 \end{bmatrix} & & \\ & & \ddots & \\ & & & \begin{bmatrix} 0 & \theta_{xyN} \\ 0 & 0 \end{bmatrix} \end{bmatrix} \in \mathcal{M}_{2N}(\mathbb{R})$$

. . . . . lxvii, 64

θ_{xyj} Parameter of the submodule $\#xyj$. This parameter is needed to define the resistance R_{xyj}^{FB} of the full-bridge submodule,

$$\theta_{xyj} = \overline{S_{xyj}^{b}}\,\overline{S_{xyj}^{b'}}\left[\left(R_a^f - 2R_b^f + R_c^f - R_a + R_b + R_c - R_d\right)S^f + (R_a - R_b - R_c + R_d)\right]$$

. . . . . lxvii, 63, 64

T_o The fondamental period of the $\mathbf{I_o}$, $\mathbf{V_y}$, $\underline{V_{AC}}$ and $\underline{V_o'}$ signals . xlv, 206, 218, 243

T_s The switching period of the pulse width modulation xlv, 21, 165, 198, 206, 218, 243

T_{step} The computation time step for the simulations and the emulations . . 121, 206, 218, 243

T_{SU} The closed-loop sensitivity function of some system. When no output reference is applied to the system:

$$\mathbf{Y}(z) = T_{SU}(z)\delta\mathbf{U}(z)$$

. . . . . lxvii, 151, 152, 155–159, 161, 168

$\mathbf{T_{xy}}$ Vector containing the entire set of τ_{xyj}s of the submodules from the arm $\#xy$,

$$\mathbf{T_{xy}} \triangleq [\tau_{xy1}, \tau_{xy2}, \ldots, \tau_{xyN}]^T \in \mathbb{R}^N$$

. Note that **this vector is null** in nominal operation of the MMC when no fault is experienced in the submodules . xxx, xxxi, xxxiii, xlii, lxvii, 64–66, 68, 180, 181

τ_{xyj} Parameter of the submodule $\#xyj$. This parameter is needed to define the global state S_{xyj}^{FB} of the full-bridge submodule,

$$\tau_{xyj} = \left[-(i_{xy}^* < 0)\overline{S_{xyj}^b}S_{xyj}^{b'} + (i_{xy}^* > 0)S_{xyj}^b\overline{S_{xyj}^{b'}} + sign(i_{xy}^*)S_{xyj}^bS_{xyj}^{b'}\right]\overline{S_{xyj}^f}$$

. . . . . lxvii, lxviii, 63, 64

U

$\mathbf{U}$ The control vector in a state-space model. $\mathbf{U} \in \mathbb{R}^{n_u}$ xxix, xl, lxviii, 34, 37–42, 62, 144–152, 154, 155, 158, 163, 165, 166, 169, 170, 179, 211–213, 241, I

$\overline{\mathbf{U}}$ The auxiliary control vector. It is used when solving the control allocation optimization problem. $\overline{\mathbf{U}} = \mathbf{U} - \mathbf{U}_{min} \in \mathbb{R}^{n_u}$ . . . . . lxviii, 149

$\mathbf{U_{MMC}}$ Control vector of the global high-level-low-level state-space model describing the dynamic behavior of the voltages and currents of the entire MMC,

$$\mathbf{U_{MMC}} \triangleq \mathbf{U_{LL}} \in \mathbb{R}^{4mN}$$

. . . . . lxviii, 192

$\mathbf{U_{HL}}$ Control vector for the high-level SSM,

$$\mathbf{U_{HL}} \triangleq \begin{bmatrix}\mathbf{V_{py}}\\ \mathbf{V_{ny}}\end{bmatrix} = \mathbf{V} = [v_{py_1}, \ldots, v_{py_m}, v_{ny_1}, \ldots, v_{ny_m}]^T \in \mathbb{R}^{2m}$$

. . . . . xl, lxviii, 84–86, 185, 186

$\mathbf{U_{HL}^{dq0}}$ Control vector for the high-level SSM in the Park reference frame,

$$\mathbf{U_{HL}^{dq0}} \triangleq \begin{bmatrix}\mathbf{V_{py}^{dq0}}\\ \mathbf{V_{ny}^{dq0}}\end{bmatrix} = [v_{py}^d, v_{py}^q, v_{py}^0, v_{ny}^d, v_{ny}^q, v_{ny}^0]^T \in \mathbb{R}^6$$

. . . . . lxviii, 95

$\mathbf{U_{HL}^{dq012}}$ Control vector for the high-level SSM in the Park 12 reference frame,

$$\mathbf{U_{HL}^{dq012}} \triangleq \begin{bmatrix}\mathbf{V_{py}^{dq012}}\\ \mathbf{V_{ny}^{dq012}}\end{bmatrix} = \mathbf{V^{dq012}} \in \mathbb{R}^{2m'}$$

. . . . . xl, xli, lxviii, 109, 110, 187–189, 229, 230

$\mathbf{U_{LL}}$ Control vector for the low-level SSM containing the entire set of duty cycles from the MMC,

$$\mathbf{U_{LL}} \triangleq \mathbf{D^e} \in \mathbb{R}^{4mN}$$

. . . . . xl, xli, lxviii, 182, 192

$\mathbf{U_{LL}^{xy}}$ Control vector for the low-level SSM containing the entire set of D_{xyj}s and D'_{xyj}s of the submodules from the arm $\#xy$,

$$\mathbf{U_{LL}^{xy}} \triangleq \mathbf{D_{xy}^e} = \langle \mathbf{S_{xy}^e} \rangle_{T_c}$$

. . . . . xli, xlii, lxviii, 66, 68, 181

$\mathbf{U}_{max}$ The control vector upper boundary . . . 34, 37, 40, 41, 46, 62, 145, 146, 148–151, 165, 166, 169, 170, 241, I

$\mathbf{U}_{min}$ The control vector lower boundary . . . . . lxviii, 34, 37, 40, 41, 46, 62, 145, 146, 148–151, 165, 166, 169, 170, 241, I

$\mathbf{U}_p$ The control vector preferred value 38, 41, 46, 147

$\mathbf{U_{PE}}$ Control vector for the power-energy SSM,

$$\mathbf{U_{PE}} \triangleq i_s \in \mathbb{R}$$

. . . . . lxii, lxix, 113, 193, 194

V

$\mathbf{V}$ All arms voltage vector,

$$\mathbf{V} \triangleq \begin{bmatrix} \mathbf{V_{py}} \\ \mathbf{V_{ny}} \end{bmatrix} \in \mathbb{R}^{2m}$$

. . . . . lxviii, lxix, 186, 191

$\hat{V}_{AC}$ Amplitude of the phase voltage across the AC network li, lxix, lxxiv, 116, 117, 119, 121, 196, 206, 218, 243

$\underline{V_{AC}}$ Complex phasor describing the phase voltage across the AC network,

$$\underline{V_{AC}} \triangleq \hat{V}_{AC}\, e^{-j\varphi_v}$$

. . . . . xlv, lxvii, lxix, lxxii

$\mathbf{V_c}$ Voltage controlling the circulating current flowing within the legs of the MMC,

$$\mathbf{V_c} \triangleq -\frac{1}{2} N_\Delta(m)\,(\mathbf{V_{py}} - \mathbf{V_{ny}}) = \begin{bmatrix} v_{c_{y_1}} \\ v_{c_{y_2}} \\ \cdots \\ v_{c_{y_m}} \end{bmatrix}$$

. . . . . lxix, 83, 115

$\mathbf{v_C}$ Vector containing the entire set of capacitor voltages of the MMC,

$$\mathbf{v_C} \triangleq \begin{bmatrix} \mathbf{v_{C_{py_1}}} \\ \vdots \\ \mathbf{v_{C_{xy}}} \\ \vdots \\ \mathbf{v_{C_{py_m}}} \\ \mathbf{v_{C_{ny_1}}} \\ \vdots \\ \mathbf{v_{C_{ny_m}}} \end{bmatrix} \in \mathbb{R}^{2mN}$$

. . . . . lxix, lxxvi, 191, 192, 197

$\hat{V}_c$ Amplitude of $\mathbf{V_c}$ in steady-state . . . . . xxii, 118

v_C^{max} Maximum voltage across the capacitors of the submodules,

$$v_C^{max} \triangleq (1 + \alpha_C^{max}) v_C^{nom}$$

. . . . . xxxii, lxix, 240

v_C^{nom} Nominal voltage across the capacitors of the submodules,

$$v_C^{nom} \triangleq \frac{V_{DC}}{N}$$

. . . . . xxxii, lxix, 12, 13, 115, 206, 218, 240, 241

$\mathbf{v}_{\mathbf{C}}^{ref}$ Vector containing the entire set of capacitor voltages references of the MMC,

$$\mathbf{v}_{\mathbf{C}}^{ref} \triangleq \begin{bmatrix} \mathbf{v}_{\mathbf{C_{py_1}}}^{ref} \\ \vdots \\ \mathbf{v}_{\mathbf{C_{xy}}}^{ref} \\ \vdots \\ \mathbf{v}_{\mathbf{C_{py_m}}}^{ref} \\ \mathbf{v}_{\mathbf{C_{ny_1}}}^{ref} \\ \vdots \\ \mathbf{v}_{\mathbf{C_{ny_m}}}^{ref} \end{bmatrix} \in \mathbb{R}^{2mN}$$

. . . . . xxiv, lxx, lxxvii, 196, 197, 206, 216

$\mathbf{v}_{\mathbf{C_{xy}}}$ Vector containing the entire set of capacitor voltages of the submodules from the arm $\#xy$,

$$\mathbf{v}_{\mathbf{C_{xy}}} \triangleq [v_{C_{xy1}}, v_{C_{xy2}}, \ldots, v_{C_{xyN}}]^T \in \mathbb{R}^N$$

. . . . xxx, xxxiii, lviii, lxix, lxx, lxxvii, lxxviii, 64–66, 68, 180, 181, 183, 208, 219

$v_{C_{xyj}}$ Voltage across the capacitor $\#xyj$. xxi, lvi, lxi–lxiv, lxvi, lxxvii, 12, 13, 20, 21, 28, 53–60, 62, 64–66, 196, 205, 240, 241

$\mathbf{v}_{\mathbf{C_{xy}}}^{ref}$ Vector containing the entire set of capacitor voltage references of the submodules from the arm $\#xy$ . . . . . xxx, xxxiii, lxx, 180, 181, 183, 208, 240, 241

V_{DC} Voltage supply across the DC bus connected to the MMC. xlviii, l, li, liii, lviii, lix, lxix–lxxi, 12, 13, 21, 28, 114–117, 120, 121, 128, 186, 196, 205, 206, 216, 218, 239–244

$\mathbf{V}^{\mathbf{dq012}}$ All arms voltage vector in the Park 12 reference frame,

$$\mathbf{V}^{\mathbf{dq012}} \triangleq \begin{bmatrix} \mathbf{V}_{\mathbf{py}}^{\mathbf{dq012}} \\ \mathbf{V}_{\mathbf{ny}}^{\mathbf{dq012}} \end{bmatrix} \in \mathbb{R}^{2m'}$$

. . . . . lxviii, lxx, 188

V_m Voltage controlling the common mode current flowing between the DC-side and AC-side neutral points when those are connected,

$$V_m \triangleq -\frac{1}{2} N_\Sigma(m) \left(\mathbf{V_{py}} + \mathbf{V_{ny}}\right) = v_m$$

. . . . . lxx, 81, 82, 115

$\hat{V}_m$ Amplitude of V_m in steady-state . . . . . xxii, 118

$\mathbf{V_{max}}$ All arms voltage vector upper boundary,

$$\mathbf{V_{max}} \triangleq \begin{bmatrix} \mathbf{V_{py}}_{max} \\ \mathbf{V_{ny}}_{max} \end{bmatrix} = \begin{bmatrix} V_{DC}\mathbb{I}_{m,1} \\ (q-1)V_{DC}\mathbb{I}_{m,1} \end{bmatrix} \in \mathbb{R}^{2m}$$

. . . . . lxx, 186, 188

$\mathbf{V}_{\mathbf{max}}^{\mathbf{dq012}}$ All arms voltage vector upper boundary in the Park 12 reference frame,

$$\mathbf{V}_{\mathbf{max}}^{\mathbf{dq012}} \triangleq \begin{bmatrix} V_{DC}/k \\ \cdots \\ V_{DC}/k \\ 2/k_0\ V_{DC}/k \end{bmatrix} \in \mathbb{R}^{m'}$$

. . . . . lxx, 188, 229, 230

$\mathbf{V_{min}}$ All arms voltage vector lower boundary,

$$\mathbf{V_{min}} \triangleq \begin{bmatrix} \mathbf{V_{py}}_{min} \\ \mathbf{V_{ny}}_{min} \end{bmatrix} = \begin{bmatrix} (1-q)V_{DC}\mathbb{I}_{m,1} \\ -V_{DC}\mathbb{I}_{m,1} \end{bmatrix} \in \mathbb{R}^{2m}$$

. . . . . lxxi, 186, 188

$\mathbf{V_{min}^{dq012}}$ All arms voltage vector lower boundary in the Park 12 reference frame,

$$\mathbf{V_{min}^{dq012}} \triangleq \begin{bmatrix} -V_{DC}/k \\ \cdots \\ -V_{DC}/k \\ -2/k_0\ V_{DC}/k \end{bmatrix} \in \mathbb{R}^{m'}$$

. . . . . lxxi, 188, 229, 230

v_n Voltage between the DC bus neutral point n_{DC} and its negative pole . . . xxii, xxxv, lviii, lxi, lxxiii, 13, 22, 25, 79–83, 112–114, 116, 121, 206, 218

$v_{n_{AC}}$ AC network neutral point voltage . . . . . lxxi, 79, 80

$V_{n_{AD}}$ Voltage between the AC network neutral point n_{AC} and DC bus neutral point n_{DC},

$$V_{n_{AD}} \triangleq v_{n_{AD}} = v_{n_{AC}} - v_{n_{DC}}$$

. . . . . xli, l, lxxi, 79–81, 83–85, 90, 91, 95, 107, 110, 115, 117

$v_{n_{DC}}$ DC bus neutral point voltage . . . . . lxxi, 79, 80

$\mathbf{V_{ny}}$ Negative pole arm voltage vector,

$$\mathbf{V_{ny}} \triangleq [v_{ny_1}, \ldots, v_{ny_m}]^T \in \mathbb{R}^m$$

. . . . . lxviii–lxxiii, 80–85, 90, 91, 94, 107–109, 185, 186

v_{ny} Voltage across the arm $\#ny$,

$$v_{ny} \triangleq -\sum_{j=1}^{N} v_{nyj}$$

. . . . . xxii, xxxviii, lvi, lviii, lxxi, 22, 25, 79–84, 95, 110, 116, 120, 122, 128

$\mathbf{V_{ny}^{\alpha\beta 0}}$ Negative pole arm voltage vector in the $\{\alpha, \beta, 0\}$ reference frame,

$$\mathbf{V_{ny}^{\alpha\beta 0}} \triangleq [C_K]\mathbf{V_{ny}} = [v_{ny}^{\alpha}, v_{ny}^{\beta}, v_{ny}^{0}]^T \in \mathbb{R}^3$$

. . . . . lxxi, lxxii, 91

$\mathbf{V_{ny}^{\alpha\beta 0^{12}}}$ Negative pole arm voltage vector in the $\{\alpha_1, \beta_1, \alpha_2, \beta_2, 0\}$ reference frame,

$$\mathbf{V_{ny}^{\alpha\beta 0^{12}}} \triangleq \left[C_{K_{12}}^{m}\right]\mathbf{V_{ny}} = [v_{ny}^{\alpha_1}, v_{ny}^{\beta_1}, v_{ny}^{\alpha_2}, v_{ny}^{\beta_2}, v_{ny}^{0}]^T \in \mathbb{R}^5$$

. lxxi

$\mathbf{V_{ny}^{dq0}}$ Negative pole arm voltage vector in the $\{d, q, 0\}$ synchronous rotating frame,

$$\mathbf{V_{ny}^{dq0}} \triangleq [P(-\theta)]\mathbf{V_{py}^{\alpha\beta 0}} = [P(-\theta)][C_K]\mathbf{V_{ny}} = [v_{ny}^{d}, v_{ny}^{q}, v_{ny}^{0}]^T \in \mathbb{R}^3$$

. . . . . lxviii, lxxi, lxxii, 90, 91, 94

$\mathbf{V_{ny}^{dq012}}$ Negative pole arm voltage vector in the $\{d1, q1, d2, q2, 0\}$ synchronous rotating frame,

$$\mathbf{V_{ny}^{dq012}} \triangleq [P(-\theta)_{12}^{m}]\mathbf{V_{ny}^{\alpha\beta 0^{12}}} = [P(-\theta)_{12}^{m}]\left[C_{K_{12}}^{m}\right]\mathbf{V_{ny}} = [v_{ny}^{d_1}, v_{ny}^{q_1}, v_{ny}^{d_2}, v_{ny}^{q_2}, v_{ny}^{0}]^T \in \mathbb{R}^5$$

$\mathbf{V_{ny}^{dq0_n}}$ Negative pole arm voltage vector in the $\{d, q, 0\}$ synchronous rotating frame at n times the $\mathbf{I_o}$ fondamental frequency,

$$\mathbf{V_{ny}^{dq0_n}} \triangleq [P(-n\theta)]\mathbf{V_{ny}^{\alpha\beta 0}} = [P(-n\theta)][C_K]\mathbf{V_{ny}} = [P((1-n)\theta)]\,\mathbf{V_{ny}^{dq0}} \in \mathbb{R}^3$$

v_{nyj} Voltage across the SM $\#yj$ among $[\![1; N]\!]$ of the arm $\#n$ of the leg $\#y$ among $\{y_1, \ldots, y_m\}$

$\mathbf{V_{ny}^{ref}}$ Negative pole arm voltage reference vector,

$$\mathbf{V_{ny}^{ref}} \triangleq [v_{ny_1}^{ref}, \ldots, v_{ny_m}^{ref}]^T \in \mathbb{R}^m$$

$\mathbf{V_o}$ Voltage controlling the output currents flowing through the AC-side load,

$$\mathbf{V_o} \triangleq -\frac{1}{2}N_\Delta(m)\,(\mathbf{V_{py}} + \mathbf{V_{ny}}) = \begin{bmatrix} v_{o_{y_1}} \\ v_{o_{y_2}} \\ \cdots \\ v_{o_{y_m}} \end{bmatrix}$$

$\hat{V}_o$ Amplitude of $\mathbf{V_o}$ in steady-state

$\underline{V_o'}$ Complex phasor describing the phase voltage across the AC network and the AC load,

$$\underline{V_o'} \triangleq (R_o + j\omega_o L_o)\underline{I_{AC}} + \underline{V_{AC}} = (R_o + j\omega_o L_o)2\underline{I_o} + \underline{V_{AC}}$$

v_p Voltage between the DC bus neutral point n_{DC} and its positive pole

$\mathbf{V_{py}}$ Positive pole arm voltage vector,

$$\mathbf{V_{py}} \triangleq [v_{py_1}, \ldots, v_{py_m}]^T \in \mathbb{R}^m$$

v_{py} Voltage across the arm $\#py$,

$$v_{py} \triangleq \sum_{j=1}^{N} v_{pyj}$$

$\mathbf{V_{py}^{\alpha\beta 0}}$ Positive pole arm voltage vector in the $\{\alpha, \beta, 0\}$ reference frame,

$$\mathbf{V_{py}^{\alpha\beta 0}} \triangleq [C_K]\mathbf{V_{py}} = [v_{py}^{\alpha}, v_{py}^{\beta}, v_{py}^{0}]^T \in \mathbb{R}^3$$

$\mathbf{V_{py}^{\alpha\beta 0^{12}}}$ Positive pole arm voltage vector in the $\{\alpha_1, \beta_1, \alpha_2, \beta_2, 0\}$ reference frame,

$$\mathbf{V_{py}^{\alpha\beta 0^{12}}} \triangleq \left[C_{K_{12}}^m\right]\mathbf{V_{py}} = [v_{py}^{\alpha_1}, v_{py}^{\beta_1}, v_{py}^{\alpha_2}, v_{py}^{\beta_2}, v_{py}^{0}]^T \in \mathbb{R}^5$$

$\mathbf{V_{py}^{dq0}}$ Positive pole arm voltage vector in the $\{d, q, 0\}$ synchronous rotating frame,

$$\mathbf{V_{py}^{dq0}} \triangleq [P(-\theta)]\mathbf{V_{py}^{\alpha\beta 0}} = [P(-\theta)][C_K]\mathbf{V_{py}} = [v_{py}^{d}, v_{py}^{q}, v_{py}^{0}]^T \in \mathbb{R}^3$$

$\mathbf{V_{py}^{dq012}}$ Positive pole arm voltage vector in the $\{d1, q1, d2, q2, 0\}$ synchronous rotating frame,

$$\mathbf{V_{py}^{dq012}} \triangleq [P(-\theta)_{12}^{m}]\mathbf{V_{py}^{\alpha\beta 0^{12}}} = [P(-\theta)_{12}^{m}][C_{K_{12}}^{m}]\mathbf{V_{py}} = [v_{py}^{d_1}, v_{py}^{q_1}, v_{py}^{d_2}, v_{py}^{q_2}, v_{py}^{0}]^T \in \mathbb{R}^5$$

$\mathbf{V_{py}^{dq0_n}}$ Positive pole arm voltage vector in the $\{d, q, 0\}$ synchronous rotating frame at n times the $\mathbf{I_o}$ fondamental frequency,

$$\mathbf{V_{py}^{dq0_n}} \triangleq [P(-n\theta)]\mathbf{V_{py}^{\alpha\beta 0}} = [P(-n\theta)][C_K]\mathbf{V_{py}} = [P((1-n)\theta)]\,\mathbf{V_{py}^{dq0}} \in \mathbb{R}^3$$

v_{pyj} Voltage across the SM $\#yj$ among $[\![1; N]\!]$ of the arm $\#p$ of the leg $\#y$ among $\{y_1, \ldots, y_m\}$

$\mathbf{V_{py}^{ref}}$ Positive pole arm voltage reference vector,

$$\mathbf{V_{py}^{ref}} \triangleq [v_{py_1}^{ref}, \ldots, v_{py_m}^{ref}]^T \in \mathbb{R}^m$$

$\mathbf{V}^{ref}$ All arms voltage reference vector,

$$\mathbf{V}^{ref} \triangleq \begin{bmatrix} \mathbf{V_{py}^{ref}} \\ \mathbf{V_{ny}^{ref}} \end{bmatrix} \in \mathbb{R}^{2m}$$

V_s Voltage controlling the DC-source current supplying the MMC,

$$V_s \triangleq -\frac{1}{2} N_\Sigma(m)\,(\mathbf{V_{py}} - \mathbf{V_{ny}}) = v_s$$

$\hat{V}_s$ Amplitude of V_s in steady-state

$\mathbf{V_x}$ Vector which compnents are the voltages between the DC bus neutral point n_{DC} and the positive and the negative pole,

$$\mathbf{V_x} \triangleq \begin{bmatrix} v_p \\ v_n \end{bmatrix}$$

v_x One of the two compnents of $\mathbf{V_x}$,

$$v_x \triangleq \begin{cases} v_p, \text{ if } x = p \\ v_n, \text{ if } n = n \end{cases}$$

v_{xy} Voltage across the arm $\#xy$,

$$v_{xy} \triangleq \sigma(x) \sum_{j=1}^{N} v_{xyj}$$

v_{xyj} Voltage across the SM $\#yj$ among $[\![1; N]\!]$ of the arm $\#x$ among $\{n, p\}$, of the leg $\#y$ among $\{y_1, \ldots, y_m\}$

v_{xy}^{ref} Voltage reference across the arm $\#xy$ ..... xxx, xxxi, 180, 181, 183, 244

$\mathbf{V_y}$ Vector which components are the phase voltages across the AC network,

$$\mathbf{V_y} \triangleq \begin{bmatrix} v_{y_1} \\ v_{y_2} \\ \vdots \\ v_{y_j} \\ \vdots \\ v_{y_m} \end{bmatrix}$$

xli, xlv, lx, lxvii, lxxiv, 80, 81, 83–85, 90, 91, 94, 95, 107, 109, 110, 112, 113, 115, 189

v_y Phase voltage across the AC network,

$$v_y = \hat{V}_{AC} \sin\left(\omega_o t - \varphi_y - \varphi_v\right)$$

..... lx, lxxiv, 13, 22, 25, 79, 80, 83, 112, 116, 119, 196, 205

$\mathbf{V_{y\Delta}}$ AC-side voltage influencing the behavior of the output current $\mathbf{I_o}$,

$$\mathbf{V_{y\Delta}} \triangleq N_\Delta(m)\mathbf{V_y}$$

..... lxxiv, 109

$\tilde{\mathbf{V}}_{\mathbf{y\Delta}}^{\mathbf{dq}012}$ AC-side voltage influencing the behavior of the output current $\mathbf{I_o}$ in the $\{d_1, q_1, d_2, q_2, 0\}$ reference frame,

$$\tilde{\mathbf{V}}_{\mathbf{y\Delta}}^{\mathbf{dq}012} \triangleq \begin{bmatrix} 1 & 0 & 0 & 0 & 0 \\ 0 & 1 & 0 & 0 & 0 \\ 0 & 0 & 1 & 0 & 0 \\ 0 & 0 & 0 & 1 & 0 \end{bmatrix} [P(-\theta)_{12}^m][C_{K_{12}}^m]\mathbf{V_{y\Delta}}$$

..... lxxiv, 109

$\tilde{\mathbf{V}}_{\mathbf{y\Delta}}^{\mathbf{dq}0}$ AC-side voltage influencing the behavior of the output current $\mathbf{I_o}$ in the $\{d, q, 0\}$ reference frame,

$$\tilde{\mathbf{V}}_{\mathbf{y\Delta}}^{\mathbf{dq}0} \triangleq \begin{bmatrix} 1 & 0 & 0 \\ 0 & 1 & 0 \end{bmatrix} [P(-\theta)][C_K]\mathbf{V_{y\Delta}}$$

..... lxxiv, 94

W

$\mathbf{w}$ High-level-low-level control current and voltage reference tracking objective weighting factor,

$$\mathbf{w} \triangleq \begin{bmatrix} \mathbf{w_{v_C}} \\ w_m \\ w_s \\ \mathbf{w_c} \\ \mathbf{w_o} \end{bmatrix}$$

..... xxx, lvii, lxxiv, 192

$\mathbf{w_I}$ High-level control current reference tracking objective weighting factor,

$$\mathbf{w_I} \triangleq \begin{bmatrix} w_m \\ w_s \\ \mathbf{w_c} \\ \mathbf{w_o} \end{bmatrix}$$

. . . . . xxx, xl, lvii, lxxiv, 186–188, 229, 230

$\mathbf{w_c}$ High-level control circulating current reference tracking objective weighting factor,

$$\mathbf{w_c} \triangleq \begin{bmatrix} w_{c_{y_1}} \\ w_{c_{y_2}} \\ \cdots \\ w_{c_{y_j}} \\ \cdots \\ w_{c_{y_{m-1}}} \end{bmatrix}$$

. . . . . lxxiv, lxxv, 186, 187, 192

w_m High-level control common mode current reference tracking objective weighting factor . . . . . lxxiv, 186, 187, 192

$\mathbf{w_o}$ High-level control output current reference tracking objective weighting factor,

$$\mathbf{w_o} \triangleq \begin{bmatrix} w_{o_{y_1}} \\ w_{o_{y_2}} \\ \cdots \\ w_{o_{y_j}} \\ \cdots \\ w_{o_{y_{m-1}}} \end{bmatrix}$$

. . . . . lxxiv, lxxv, 186, 187, 192

w_s High-level control source current reference tracking objective weighting factor lxxiv, 186, 187, 192

ω_p The preference weighting factor in the control allocation problem that takes into account a secondary allocation objective 147, 170, 171

w_{v_C} low-level control secondary objective, capacitor balancing, weighting factor . xxx, lvii, lviii, lxxiv, 180–182, 192

W_{xy} Matrix containing the entire set of w_{xyj}s and w'_{xyj}s of the submodules from the arm $\#xy$,

$$W_{xy} \triangleq \begin{bmatrix} w_{xy1} & w'_{xy1} & & & & & \\ & & w_{xy2} & w'_{xy2} & & & \\ & & & \ddots & \ddots & & \\ & & & & & w_{xyN} & w'_{xyN} \end{bmatrix} \in \mathcal{M}_{N,2N}(\mathbb{N})$$

. . . . . lxxv, 64

w_{xyj} Parameter of the submodule $\#xyj$. This parameter is needed to define the resistance R^{FB}_{xyj} of the full-bridge submodule,

$$\begin{aligned} w_{xyj} = &\left[(R_b - R_a)\,\overline{S^b}\,\overline{S^{b'}} + (R_\beta - R_\alpha)\,\overline{S^b}\,S^{b'}\right]\overline{S^f} \\ &+ \left[\left(R^f_b - R^f_a\right)\overline{S^b}\,\overline{S^{b'}} + \left(R^f_\beta - R^f_\alpha\right)\overline{S^b}\,S^{b'}\right]S^f \end{aligned}$$

. . . . . lxxv, 63, 64

w'_{xyj} Parameter of the submodule $\#xyj$. This parameter is needed to define the resistance R^{FB}_{xyj} of the full-bridge submodule,

$$\begin{aligned} w'_{xyj} = &\left[(R_c - R_a)\,\overline{S^b}\,\overline{S^{b'}} + \left(R'_\beta - R'_\alpha\right)S^b\,\overline{S^{b'}}\right]\overline{S^f} \\ &+ \left[\left(R^f_c - R^f_a\right)\overline{S^b}\,\overline{S^{b'}} + \left(R'^f_\beta - R'^f_\alpha\right)S^b\,\overline{S^{b'}}\right]S^f \end{aligned}$$

. . . . . lxxv, 63, 64

X

X The state vector in a state-space model. $\mathbf{X} \in \mathbb{R}^{n_x}$ . . . lxxvi, 144, 145, 151, 152, 155, 158, 165, 169, 170

x Variable used to specify the arm connection type to the DC bus. x either takes the value p (arm connected to the positive pole) or n (arm connected to the negative pole). . . . . xxx–xxxiii, xxxv, xxxix, xli, xlii, xlix, liii–lvi, lviii, lxi, lxii, lxv–lxviii, lxx, lxxiii–lxxviii, lxxx, 11–13, 62, 64–66, 68, 180, 181

$\mathbf{X}^*$ The desired state vector, it can be see as a reference to track. $\mathbf{X}^* \in \mathbb{R}^{n_x}$ lxxvi, 169, 170

$\mathbf{X_{MMC}}$ State vector of the global high-level-low-level state-space model describing the dynamic behavior of the voltages and currents of the entire MMC,

$$\mathbf{X_{MMC}} \triangleq \begin{bmatrix} \mathbf{v_C} \\ I_m \\ I_s \\ \tilde{\mathbf{I}}_\mathbf{c} \\ \tilde{\mathbf{I}}_\mathbf{o} \end{bmatrix} \in \mathbb{R}^{2m(N+1)}$$

. . . . . xxx, lxxvi, lxxvii, 192

$\mathbf{X_{HL}}$ State vector for the high-level SSM,

$$\mathbf{X_{HL}} \triangleq \begin{bmatrix} I_m \\ I_s \\ \mathbf{I_c} \\ \mathbf{I_o} \end{bmatrix} \in \mathbb{R}^{2m+2}$$

. . . . . lxxvi, 84–86

$\mathbf{X_{HL}^{dq0}}$ State vector for the high-level SSM in the Park reference frame,

$$\mathbf{X_{HL}^{dq0}} \triangleq \begin{bmatrix} I_m^{dq0} \\ I_s^{dq0} \\ \tilde{\mathbf{I}}_\mathbf{c}^{\mathbf{dq0}} \\ \tilde{\mathbf{I}}_\mathbf{o}^{\mathbf{dq0}} \end{bmatrix} \in \mathbb{R}^6$$

. . . . . lxxvi, lxxviii, 95

$\mathbf{X_{HL}^{dq012}}$ State vector for the high-level SSM in the Park 12 reference frame,

$$\mathbf{X_{HL}^{dq012}} \triangleq \begin{bmatrix} I_m^{dq012} \\ I_s^{dq012} \\ \tilde{\mathbf{I}}_\mathbf{c}^{\mathbf{dq012}} \\ \tilde{\mathbf{I}}_\mathbf{o}^{\mathbf{dq012}} \end{bmatrix} \in \mathbb{R}^{2m'}$$

. . . . . xxx, lxxvi, lxxviii, 109, 110, 187, 188

$\tilde{\mathbf{X}}_\mathbf{HL}$ Reduced state vector for the high-level SSM, containing the controllable and observable state variables,

$$\tilde{\mathbf{X}}_\mathbf{HL} \triangleq C_{HL}\mathbf{X_{HL}} \in \mathbb{R}^{2m}$$

. . . . . xxx, lxxvi, 86, 185, 186

$\mathbf{x_k^c}$ Static virtual basis $\mathcal{B}^c$ vector . . . . . xxvi, xxxiii, 98–100, 104, 106

$\mathbf{x}_{\mathbf{k}}^{\mathbf{m}}$ Natural basis $\mathcal{B}^m$ vector ..... xxxv, xliv, xlix, 97, 99, 101, 105

$\mathbf{X}_{\mathbf{LL}}^{\mathbf{xy}}$ State vector for the low-level SSM containing the entire set of $v_{C_{xyj}}$s of the submodules from the arm $\#xy$,

$$\mathbf{X}_{\mathbf{LL}}^{\mathbf{xy}} \triangleq [\mathbf{v}_{\mathbf{C_{xy}}}] \in \mathbb{R}^N$$

..... xxx, xxxi, lviii, lxxvii, 65, 66, 68

X_{PE} State vector for the power-energy SSM,

$$X_{PE} \triangleq E_{MMC} \in \mathbb{R}$$

..... xxxi, lxxvii, lxxviii, 113, 193, 194

$\mathbf{x}$ The decision variable vector in the LP, and in the QP. $\mathbf{x}_{max}$ and $\mathbf{x}_{min}$ are its upper and lower boundaries ..... lxxvii, 149, 150

$\mathbf{X_R}$ The integral compensator vector in the control allocation with integral compensator. $\mathbf{X_R} \in \mathbb{R}^{n_y}$ ..... lxxvii, 155, 158

Y

$\mathbf{Y}$ The output vector in a state-space model. $\mathbf{Y} \in \mathbb{R}^{n_y}$ xlii, xliii, lxvi, lxvii, lxxvii, 144, 145, 151, 152, 155–160, 162, 183

y Variable used to specify the leg number. y takes its value among $\{y_1, \ldots, y_m\}$ xxx–xxxiii, xxxv, xxxix, xli, xlii, xlix, l, lii–lvi, lviii, lix, lxi, lxii, lxv–lxviii, lxx–lxxv, lxxvii, lxxviii, lxxx, 11, 13, 22, 77, 79

$\mathbf{Y}^*$ The desired output vector in a reference state-space model. $\mathbf{Y}^* \in \mathbb{R}^{n_y}$ lxxvii, 145, 183

$\mathbf{Y_{MMC}}$ Output vector of the global high-level-low-level state-space model describing the dynamic behavior of the voltages and currents of the entire MMC,

$$\mathbf{Y_{MMC}} \triangleq \mathbf{X_{MMC}} \in \mathbb{R}^{2m(N+1)}$$

..... lxxvii, 192

$\mathbf{Y}_{\mathbf{MMC}}^*$ Desired output vector of the global high-level-low-level control allocation. This vector is defined after the closed-loop reference model of the current:

$$\mathbf{Y}_{\mathbf{MMC}}^*(k+1) \triangleq F_{MMC,M}\mathbf{Y_{MMC}} + G_{MMC,M}\mathbf{Y}_{\mathbf{MMC}}^{ref}$$

..... xxx, lxxvii, 192

$\mathbf{Y}_{\mathbf{MMC}}^{ref}$ Output reference vector for the global high-level-low-level control allocation,

$$\mathbf{Y}_{\mathbf{MMC}}^{ref} \triangleq \begin{bmatrix} \mathbf{v}_{\mathbf{C}}^{ref} \\ I_m^{ref} \\ I_s^{ref} \\ \tilde{\mathbf{I}}_{\mathbf{c}}^{ref} \\ \tilde{\mathbf{I}}_{\mathbf{o}}^{ref} \end{bmatrix} \in \mathbb{R}^{2m(N+1)}$$

..... lxxvii, 192

$\mathbf{Y_{HL}}$ Output vector for the high-level SSM,

$$\mathbf{Y_{HL}} \triangleq \begin{bmatrix} I_m \\ I_s \\ \tilde{\mathbf{I}}_{\mathbf{c}} \\ \tilde{\mathbf{I}}_{\mathbf{o}} \end{bmatrix} \in \mathbb{R}^{2m}$$

. . . . . lxxvii, lxxviii, 84–86, 185

$\mathbf{Y^*_{HL}}$ Desired output vector for the high-level control allocation. This vector is defined after the closed-loop reference model of the current:

$$\mathbf{Y^*_{HL}}(k+1) = F_{HL,M}\mathbf{Y_{HL}}(k) + G_{HL,M}\mathbf{Y^{ref}_{HL}}(k)$$

. . . . . xxx, lxxviii, 185

$\mathbf{Y^{dq0}_{HL}}$ Output vector for the high-level SSM in the Park reference frame,

$$\mathbf{Y^{dq0}_{HL}} \triangleq \mathbf{X^{dq0}_{HL}} = \begin{bmatrix} I_m^{dq0} \\ I_s^{dq0} \\ \tilde{\mathbf{I}}_\mathbf{c}^{\mathbf{dq0}} \\ \tilde{\mathbf{I}}_\mathbf{o}^{\mathbf{dq0}} \end{bmatrix} \in \mathbb{R}^6$$

. . . . . lxxviii, 95

$\mathbf{Y^{dq012}_{HL}}$ Output vector for the high-level SSM in the Park 12 reference frame,

$$\mathbf{Y^{dq012}_{HL}} \triangleq \mathbf{X^{dq012}_{HL}} = \begin{bmatrix} I_m^{dq012} \\ I_s^{dq012} \\ \tilde{\mathbf{I}}_\mathbf{c}^{\mathbf{dq012}} \\ \tilde{\mathbf{I}}_\mathbf{o}^{\mathbf{dq012}} \end{bmatrix} \in \mathbb{R}^{2m'}$$

. . . . . xxxi, lxxviii, 109, 110, 187, 230

$\mathbf{Y^{dq012*}_{HL}}$ Desired output vector for the high-level control allocation in the Park 12 reference frame. This vector is defined after the closed-loop reference model of the current:

$$\mathbf{Y^{dq012*}_{HL}}(k+1) = F^{dq012}_{HL,M}\mathbf{Y^{dq012}_{HL}}(k) + G^{dq012}_{HL,M}\mathbf{Y^{dq012^{ref}}_{HL}}(k)$$

. . . . . xxx, lxxviii, 187, 188

$\mathbf{Y^{dq012^{ref}}_{HL}}$ Output reference vector for the high-level SSM in the Park 12 reference frame,

$$\mathbf{Y^{dq012^{ref}}_{HL}} \triangleq \begin{bmatrix} I_m^{dq012_{ref}} \\ I_s^{dq012_{ref}} \\ \tilde{\mathbf{I}}_\mathbf{c}^{\mathbf{dq012_{ref}}} \\ \tilde{\mathbf{I}}_\mathbf{o}^{\mathbf{dq012_{ref}}} \end{bmatrix} \in \mathbb{R}^{2m'}$$

. . . . . xxxi, lxxviii, 187, 230

$\mathbf{Y^{ref}_{HL}}$ Output reference vector for the high-level SSM,

$$\mathbf{Y^{ref}_{HL}} \triangleq \begin{bmatrix} I_m^{ref} \\ I_s^{ref} \\ \tilde{\mathbf{I}}_\mathbf{c}^{\mathbf{ref}} \\ \tilde{\mathbf{I}}_\mathbf{o}^{\mathbf{ref}} \end{bmatrix} \in \mathbb{R}^{2m}$$

. . . . . lxxviii, 185

$\mathbf{Y^{xy}_{LL}}$ Output vector for the low-level SSM containing a set of electrical signals from the arm $\#xy$,

$$\mathbf{Y^{xy}_{LL}} \triangleq [\mathbf{v_{C_{xy}}}] \in \mathbb{R}^N$$

. . . . . lxxviii, 65, 66

$\mathbf{Y_{PE}}$ Output vector for the power-energy SSM,

$$\mathbf{Y_{PE}} \triangleq X_{PE} \in \mathbb{R}$$

. . . . . lxxviii, lxxix, 113, 193, 194

$\mathbf{Y}^{*}_{\mathbf{PE}}$ Desired output vector for the power-energy control allocation. This vector is defined after the closed-loop reference model of the energy:

$$\mathbf{Y}^{*}_{\mathbf{PE}}(k+1) \triangleq F_{PE,M}\mathbf{Y}_{\mathbf{PE}}(k) + G_{PE,M}\mathbf{Y}^{ref}_{\mathbf{PE}}(k)$$

. . . . . xxxi, lxxix, 193, 194

$\mathbf{Y}^{ref}_{\mathbf{PE}}$ Output reference vector for the power-energy SSM . . . . . lxxix, 193, 194

$\mathbf{Y}^{ref}$ The output vector reference in a state-space model. $\mathbf{Y}^{ref} \in \mathbb{R}^{n_y}$ . . . xlii, xliii, lxvi, lxxix, 145, 151, 152, 155–160, 183

Z

z_j The closed-loop zeros when using a control allocation with integral compensator architecture. 157

$Z_c(t)$ Impedance seen by the current $\mathbf{I_c}$,

$$Z_c(t) \triangleq R_c^{eq} + L_c^{eq}\frac{d\cdot}{dt}$$

. . . . . lxxix, 115

$\underline{Z_c}$ Impedance seen by the current $\mathbf{I_c}$ in steady-state,

$$\underline{Z_c} \triangleq R_c^{eq} + jL_c^{eq}\omega_c$$

. lxxix

Z_c Norm of the impedance seen by the current $\mathbf{I_c}$ in steady-state,

$$Z_c \triangleq |\underline{Z_c}| = \sqrt{{R_c^{eq}}^2 + {L_c^{eq}}^2{\omega_c}^2}$$

. . . . . xlviii, lxxix, 117

$Z^{dq012}_{HL,M}$ The discrete time matrix involved in tuning the disturbance rejection pole placement of the high-level reference state-space model of the currents for the control allocation with integral compensator in the Park 12 reference frame. $Z^{dq012}_{HL,M} \in \mathbb{R}^{2m' \times 2m'}$ . . . . . xxxi, lxxix, 230

Z_M The discrete time zero matrix in a reference state-space model. $Z_M \in \mathbb{R}^{n_y \times n_y}$ xxiii, lxxix, 160, 161, 166–168, 170, 173

Z_m Impedance seen by the current I_m in steady-state,

$$Z_m \triangleq R_m^{eq}$$

. . . . . l, lxxix, 117

$Z_m(t)$ Impedance seen by the current I_m,

$$Z_m(t) \triangleq R_m^{eq} + L_m^{eq}\frac{d\cdot}{dt}$$

. . . . . lxxix, 115

$Z_o(t)$ Impedance seen by the current $\mathbf{I_o}$,

$$Z_o(t) \triangleq R_o^{eq} + L_o^{eq}\frac{d\cdot}{dt}$$

. . . . . lxxix, 115

$\underline{Z_o}$ Impedance seen by the current $\mathbf{I_o}$ in steady-state,

$$\underline{Z_o} \triangleq R_o^{eq} + jL_o^{eq}\omega_o$$

. lxxx

Z_o Norm of the impedance seen by the current $\mathbf{I_o}$ in steady-state,

$$Z_o \triangleq |\underline{Z_o}| = \sqrt{R_o^{eq2} + L_o^{eq2}\omega_o{}^2}$$

. . . . . li, lxxx, 117

$Z_s(t)$ Impedance seen by the current I_s,

$$Z_s(t) \triangleq R_s^{eq} + L_s^{eq}\frac{d\cdot}{dt}$$

. . . . . lxxx, 115

Z_s Impedance seen by the current I_s in steady-state,

$$Z_s \triangleq R_s^{eq}$$

. . . . . liii, lxxx, 117

$\mathbf{Z_{xy}}$ Vector containing the entire set of z_{xyj}s of the submodules from the arm $\#xy$,

$$\mathbf{Z_{xy}} \triangleq \mathbb{J}_{1,N} \cdot [z_{xy1}, z_{xy2}, \ldots, z_{xyN}]^T \in \mathbb{R}$$

. . . . . xxx, lxxx, 64

z_{xyj} Parameter of the submodule $\#xyj$. This parameter is needed to define the resistance R_{xyj}^{FB} of the full-bridge submodule,

$$\begin{aligned} z_{xyj} = &\left[R_a \overline{S^b}\,\overline{S^{b'}} + R'_\alpha S^b\,\overline{S^{b'}} + R_\alpha \overline{S^b}\,S^{b'} + R_\gamma S^b\,S^{b'}\right]\overline{S^f} \\ &+ \left[R_a^f \overline{S^b}\,\overline{S^{b'}} + R'_\alpha{}^f S^b\,\overline{S^{b'}} + R_\alpha^f \overline{S^b}\,S^{b'} + R_\gamma^f S^b\,S^{b'}\right] S^f \end{aligned}$$

. . . . . lxxx, 63, 64

General Introduction

Context of the study

In order to distribute electrical energy to a large number of entities in the territory, it is necessary to increase the power that the transmission networks are able to convey. In order to guarantee this electrical supply with the best performance and therefore low losses in the lines - which are proportional to the square of the current - the transmissions are made in high-voltage. In order to adapt the voltage levels between these lines and the low-voltage electrical systems, converters are required. Among the candidate topologies, the modular multilevel converter (MMC) appears to be a privileged solution because of its modular structure. This modularity allows it to be adapted to any voltage level without changing the stress of the semiconductors, starting from the same elementary brick called submodule (SM). This means that the same topology can be used for a converter with a nominal power of 10 kW as for a 1 GW converter, for example, while using semiconductors with the same operating region. This topology being a multilevel converters, it presents beneficial features such as a better harmonic quality or a very good efficiency due - in part - to the low switching frequency, especially for topologies with a large number of submodules.

Although they have advantages from an electrical point of view, as the number of voltage levels increases, these multilevel converters show an increasing number of degrees of freedom to control them. Thus, multilevel converters represent a challenge for the control of electrical systems using them because the number of control variables is then higher than the objectives to be reached, making them redundant systems also called overactuated systems. In the context of the control of such systems, there is a family of control methods that are particularly well suited to deal with these problems: control allocation methods. They first appeared in the 1980s in aeronautics to take advantage of the multiplicity of aerodynamic and redundant surfaces that an aircraft has in order to control its trajectory (flaps, ailerons, rudders,..). They have been progressively applied in different fields. These methods have thus proven themselves in an industrial context while being the subject of research work leading to the integration of optimization algorithms into these control methods. The purpose of optimization is to take maximum advantage of the multiplicity of control variables of the system considered. If it is now possible to use real time optimization algorithms for the control of electrical systems, thanks to the increase in the capabilities of real time computers which now reach the high requirements in terms of computation speed that are those of electrical systems, requirements that are lower when one is interested in the motion control of an aircraft, a ship or a robot. This last point explains the fact that the possibility of using online optimization allocation methods for electrical systems is quite recent.

The proposed topic for this work concerns the development and the implementation in real time of these control allocation methods using online optimization for an electrical system involving an MMC. This can then be delineated in various exploration axes:

- Design of a control allocation method for the MMC
- Real time development of the control law designed in order to guarantee an execution in a bounded time

- Real time implementation on a 10 kW MMC
- Evaluation of the reconfiguration capabilities of the control by MMC allocation

The development of the allocation method will be given a methodological aspect in the perspective of generalizing the control allocation to electrical systems as a whole.

Class of problems considered

Introducing the considered control problems

From a formal point of view, the control allocation problems of redundant or overactuated systems for which the actuators have limitations, also called control saturations, are considered here in a general way. The overactuated character is given to systems with more control variables than state variables to control.

This class of problems is reduced, in the case of the present work, to electrical systems that are powered by static converters.

Existing works on solving these problems

The idea at the origin of the control allocation methods which deal with the resolution of these control problems appeared for the first time in 1983 [Cun83; Ryn83]. The objective is then not only to use the redundant aerodynamic surfaces of the aircraft when the main surfaces are faulty but to take advantage of all these surfaces also when all the actuators of the aircraft are fully functional. In a more general way, considering any system, this objective represents the will to efficiently allocate the set of multiple control variables in order to guarantee the achievement of the required performances automatically. The principle of control allocation was born.

The first methods for solving control allocation problems were not long in coming. These first works are based on the principle of model inversion [Bro85]: from a control model of the system with more inputs than outputs, the allocation equation is established. This relationship is then inverted to determine which inputs give the desired reference values for the outputs [KH83; Lal85; MGB89; SGE90; Dur93]. Although these methods can be efficient and computationally non-demanding, the main drawback is that the control saturations are taken into account non-optimally. Solutions and new methods based on inversion have been proposed to deal with this problem of managing saturations [Ada+92; BE92; VB94] but without taking them into account beforehand. The consequence is that when the limits of the region of operation are reached or even exceeded, the solutions of the model inversion-based algorithms are suboptimal and do not always guarantee an allocation that achieves its objectives.

To cope with this problem of taking into account the saturations, control allocation methods using optimization and constrained optimization appear [Par89; Bod02; Här03; Poo+04; Joh+08]. The optimization algorithms have then the capability to take into account both the control model and the saturations of the control variables as constraints to the optimization problem to be treated. Thus, it is possible to fully consider the operating limits of the system to be controlled, which represents a major advance compared to model inversion-based methods. However, the drawback of these optimization methods is that they require more computational resources in real time to find an optimal solution. New allocation methods using optimization are then introduced but this time the optimization is not anymore done online but offline. However, a procedure for calculating and updating the solution in real time is implemented : [TJ05a; Lia+07;

TN11; TYK17]. The advantage over online optimization allocation methods is a certain guarantee of optimality of the solution obtained in real time while the optimization is solved offline. However, this advantage comes at the cost of a higher mathematical complexity for the development of the allocation method.

The now rapid expansion of artificial intelligence has also spread to control allocation methods. However the first allocation methods using artificial intelligence are not so young. First works were done in the 1990s [Gro94] in the laboratory of Dr. Wayne C. Durham. For now, it is possible to classify the works in two branches. As in the case of [Gro94], the first methods to be developed are those using a neural network which aims at learning the optimal relationship between the requested action vector and the value to allocate to the command [Sku+18; Hua+18; Kha+22]. These allocation methods will be based on a single simple neural network. But there is another trend that is emerging: the use of Reinforcement Learning methods for control allocation [SB18]. The idea here is to use two neural networks that feed each other: the Actor-Critic model. This allows, in real time, both to learn the dynamic behavior of the system and to steer it in an optimal way by maximizing a given reward function. Overall, the use of artificial intelligence for control allocation still has a large horizon of perspectives since it has been little explored for the moment.

Although these control methods were born in the field of aeronautics [Ryn83; SGE90; Dur93; DLB01], they have spread to other fields usually related to motion like spacecrafts [Par89; Jin+06; Boa+10], ground vehicules [WH00; Tag+09] and robots [KH83; Fen+10], or also ships [Sør97; Joh+03] and underwater vessels [FS91]. This spread to motion control fields is partly due to the initial formulation of the allocation, made for the case of generalized force vectors that are desired to achieve. However, since a few years, we can account for the fact that those methods are spreading to another domain: electrical engineering [Bou+15; Kre19; LFB21b; LFB22c; LBF22]. If work on the topic of control allocation in electrical engineering has only recently appeared, this is also due to the improvement of real time computing capabilities which are now sufficient to adress the use of optimization algorithms executed in real time at the scale of the sampling period of these systems. Indeed, the sampling period of a static converter control system is very short compared to a motion control system: from 1 ms to 1 µs, which is equivalent to a switching period of 1 kHz to 1 MHz [Let+19], depending on the semiconductor technologies used.

The work presented here is part of the development of allocation methods for the domain of electrical engineering, although a significant part of the work is methodological and general on the topic of control allocation.

Outline and contributions of the Thesis

The contribution of the work presented in this thesis manuscript to solving the class of problems aforementioned is made of the 5 following chapters:

- *Chapter 1 - State-of-the-Art on the Modular Multilevel Converter and Control Allocation Methods*, presents the state-of-art of control-oriented methods to model the Modular Multilevel Converter (MMC) as well as the methods to control this converter. The second part presents the state-of-art of the control allocation methods and how the MMC can benefit from those control methods.

- *Chapter 2 - Contributions to the Scalable Modelling of Modular Multilevel Converters*, details the contribution to the modelling of the MMC for control purposes. Models of the internal dynamics of the MMC arms are proposed, describing the behavior of arm voltages and submodules capacitor voltages depending on the states from the switches. The goal of this chapter is to introduce the new voltage models that provide more scalability to the control systems in power electronics while taking into account part of their losses.

- *Chapter 3 - Contributions to the Scalable Modelling of Polyphase Systems*, details the contribution to the modelling of the MMC for control purposes as the previous chapter, but focuses on other dynamics of the MMC: those of the currents. In this chapter the relationships between arm voltages and currents are derived. A new Park transform is proposed in order to reduce the complexity of the control-oriented model. The objective of this chapter is to introduce the new current models that provide more scalability to the control systems in power electronics while being of fixed size and complexity. *Published work related to this topic: [LFB21a; LFB21b; LFB22c]*

- *Chapter 4 - Contributions to Improving the Control Allocation Methods*, explores novel control allocation (CA) methods with the objective to increase the range of systems where they can be implemented. Aiming at a wider usage of control allocation in power electronics. A new reference model control allocation architecture with the upgrade of an integral compensator that significantly improves the control performances of the allocation methods is proposed. The specific feature is that the addition of the integrator is transparent to the closed-loop reference tracking dynamics: no pole or zero is added, and the dynamic behavior remains that of the aforementioned reference model. This non-trivial progress is obtained with just few modifications to existing methods and can readily be added to existing allocation algorithms. *Published work related to this topic: [LBF22]*

- *Chapter 5 - Scalable Control Allocation Methods for the Modular Multilevel Converter*, presents the main contributions of the study which is about the control of the MMC using allocation methods. A variety of real time optimization allocation architectures are developed and proposed for the low-level voltage control as well as for the high-level current control and global energy balancing. The tests prooving the reliability are done thanks to a real time hardware-in-the-loop (HIL) procedure. The control system shows the ability to ensure circulating current supression as well as injection, output current reference tracking, and effective capacitor balancing. The goal of this chapter is to emphasize the fact that, with a unique control allocation algorithm using online optimization, it is possible to control any polyphase system having any number of phases but still keep a constant execution duration in real time. Moreover, the fault tolerant control capabilities of the allocation methods are mobilized in the case of a faulty submodule and show that the use of allocation in power electronics can ensure the continuity of operation for electrical systems at rated power. *Published work related to this topic: [LFB22a; LFB22b]*

List of Publications

The contributions presented in this manuscript have been the topic of communications and knowledge dissemination, the list of which is given below:

International peer-reviewed journals - Published papers

[LFB22] G. Le Goff, M. Fadel, and M. Bodson. "_Scalable Control-Oriented Model of the Modular Multilevel Converter for Polyphase Systems". *IEEE Transactions on Industry Applications (TIA)*. 2022. Conference Name: IEEE Transactions on Industry Applications, ISSN: 1939-9367. DOI: 10.1109/TIA.2022.3152470.

Conferences with proceedings and peer review - Published papers

[LBF22] G. Le Goff, M. Bodson, and M. Fadel. "Model Reference Control of Constrained Overactuated Systems with Integral Compensation". *2022 IEEE 61st Conference on Decision and Control (CDC)*. ISSN: 2576-2370. 2022, DOI: 10.1109/CDC51059.2022.9992648.

[LFB21a] G. Le Goff, M. Fadel, and M. Bodson. "Modélisation Analytique Modulaire du Convertisseur Modulaire Multiniveaux (MMC)". *Symposium de Génie Electrique 2020 (SGE)*. Nantes, France: IREENA, 2021.

[LFB21b] G. Le Goff, M. Fadel, and M. Bodson. "Modular polyphased full order current state-space model of the modular multilevel converter". *2021 IEEE 19th International Power Electronics and Motion Control Conference (PEMC)*. 2021, DOI: 10.1109/PEMC48073.2021.9432502.

[LFB22a] G. Le Goff, M. Fadel, and M. Bodson. "-Scalable Optimal Control Allocation: Linear and Quadratic Programming Methods Applied to Active Capacitor Balancing in Modular Multilevel Converters". en. *IFAC-PapersOnLine*. 18th IFAC Workshop on Control Applications of Optimization CAO 2022. 2022, ISSN: 2405-8963. DOI: 10.1016/j.ifacol.2022.09.004.

[LFB22b] G. Le Goff, M. Fadel, and M. Bodson. "Scalable Control Allocation: Real-time Optimized Current Control in the Modular Multilevel Converter for Polyphase Systems". *2022 International Symposium on Power Electronics, Electrical Drives, Automation and Motion (SPEEDAM)*. Sorrento, Italy, 2022, DOI: 10.1109/SPEEDAM53979.2022.9842095.

Feel free to follow my reserach updates at the links below:
ORCID - Research Gate - Google Scholar - HAL Personal Open Archive Repository

1 State-of-the-Art on the Modular Multilevel Converter and Control Allocation Methods

Contents

1.A Introduction

The MMC is a converter appeared at the beginning of the 21st century. By its modularity, it brings significant performance advantages for the conversion of electrical energy to the point of participating in the acceleration of the deployment of High-Voltage Direct Current (HVDC) networks. The modularity is accompanied by a large number of degrees of freedom to control it, which makes it a system particularly suited for control methods that are tailored to deal with overactuated systems.

The state of the art will therefore first address the topic of the MMC and the context in which it appeared to then focus on the control-oriented modelling methods of this converter with a

view to comparing the most suitable modelling methods for the Control Allocation (CA) that will be implemented next. A third part will focus on the control methods adapted to guarantee the different performance challenges of the MMC and a last part will present an overview of the control allocation methods.

1.B The Modular Multilevel Converter

1.B.1 Emergence of the Modular Multilevel Converter

Beginnings of the electrification: predominance of AC

The advent of electrification in the world first went through a power battle in the 1880s between the Direct Current (DC) and the Alternating Current (AC) which resulted in the predominant choice of AC for several reasons. Among these reasons at the time, the safety of a double zero crossing at each period of the fundamental which allows one to remove more easily a body which is being electrified than in the case of the DC where a constant level of voltage is maintained. Another reason is the lack of conversion equipment to modulate and manage the electrical power in DC. At the end of the second half of the 19th century, power electronics had not yet seen the birth of the mercury arc valves which only arrived in 1902 and the other great inventions of the 20th century such as the transistor which appeared in 1947 [83] or the Insulated-Gate Bipolar Transistors (IGBTs) in the 1980s [Pea10]. Indeed, thanks to the transformers, whose design is simple and reliable, the conversion of electricity at different voltage levels is easily done in AC. The existence of asynchronous machines, which are robust, easy to start, and do not require power electronics to provide mechanical power, are mostly used in the development of industries, which is an additional reason for the adoption of AC.

In order to meet the electricity needs across large distances, installations capable of transporting a large electrical power are necessary. Since losses are proportional to the square of the current, high voltage with a lower current is preferred to low voltage. Thus, high voltage transmissions have rapidly developed, requiring conversion devices between the voltage level generated by the generation systems and the network. The cost of a transmission line depends on both the cost of the conversion stations and the line itself. In HVDC, the stations are expensive to maintain, whereas in HVAC, the conversion stations are more reliable, efficient and simple in design, which motivates the deployment of the AC network.

HVDC becomes competitive with HVAC

Advances in power electronics over the last century and the last decades have made HVDC transmission competitive with HVAC transmission, each of which has advantages and drawbacks compared to the other. Although the strengths of the transmission in AC are 1) the simplicity of design, the robustness, the ease of maintenance of the stations, 2) the simplicity of modulation of the voltage level by the transformers, 3) the simpler and less expensive breaker circuits, 4) the protection of the people; the HVDC competes with 1) a better efficiency of the lines without skin effect, 2) an easier stabilization of the network, in particular on long distances to interconnect distant sources, as off-shore ones, 3) the capacity to interconnect networks AC of different frequency and phase, or 4) the absence of reactive power [MU07]. The limit distance of the transmission beyond which the HVDC is cheaper than the HVAC is between 600 km and 800 km for overhead lines and around 50 km for submarine ones. Thus the first commercial line was commissioned in 1954 in Sweden [Pea10]. Gotland HVDC Link is a 96 km submarine line

which used 20 MW - 100 kV mercury-arc-valve-based conversion stations.

From CSC to VSC

Since then, several lines of HVDC have seen the light of day using different technologies of switches and converters [FAD09]. It is possible to classify the converters used in two categories, the Current Source Converters (CSCs) and the Voltage Source Converters (VSCs). The emergence of the CSC was first made thanks to the thyristors, then it is the high-power Gate Turn-Off Thyristors (GTOs) which allowed the VSC to appear. The invention of the IGBT then accelerated the development of the VSC. Compared to the CSC, the VSC has several advantages, such as 1) the possibility of active and reactive power control in the four quadrants, 2) the bidirectionality of the power exchange which is done by simple inversion of the sign of the current which requires less expensive cables, 3) a better reliability of the switching and thus a better quality of the waveforms and 4) a better controllability with fully controllable semiconductors at the firing and at the blocking [FAD09]. These various beneficial features led to the first commercial use of the VSC in the context of the HVDC in 1997 in Sweden as shown in the table from [FAD09] which presents a range of VSC-HVDC conversion system projects.

Improving the VSC features with multilevel converters like the MMC

However, compared to the CSC, the traditional 2-level VSC has a physical limit which does not allow it to extend to any voltage level DC. Indeed its topology imposes to have semiconductors able to stand the voltage of the bus to which it is connected. The more it will be required to design a very high voltage line, the more it is necessary to have semiconductors able to stand strong constraints in current and voltage. A solution that appears in the early 21st century to increase the amount of voltage and power converted while exposing the semiconductors to a constant level of voltage stress is the MMC [Mar02; LM03]. The MMC is part of the family of the multilevel converters made of several switching cells.

Multilevel converters have significant advantages over classical converters for high-power applications. They make it possible to lower the stress on the switching cells as well as the total harmonic distortion [ALW07]. The original MMC has a topology made of identical series-connected submodules [LM03] that gives the converter its scalability feature. Indeed, it is very well suited for high-power and high-voltage applications when compared to other multilevel topologies like flying-capacitor converters or the neutral-point-clamped converters which are built from an imbrication of switching cells [Lad+12]. Moreover, [Els+20] shows the versatility benefit of this topology for rapid energy supply. Compared to the traditionnal 2-level VSC, where the failure of one semiconductor affects the entire converter, under the failure one (or more, to some extent) submodule(s) the MMC is able of ensuring a service continuity [Sel+19].

Thus, all these characteristics of the MMC make that it has enabled an acceleration of the development of HVDC transmission systems [Sha+16c]. In less than 10 years, the first MMC-based commercial line was built in the United States, the Trans Bay Cable with a power rating of 400 MW and a DC bus of $\pm$200 kV. Since then, several projects of converter stations based on the MMC have emerged in the world as [Per+15] reports. One can quote for example the INELFE between France and Spain [Per+12; Saa+13b; Saa+14].

The progress concerning the MMC shows its ability to be implemented on a larger scale than in a single transmission between two networks, but within the framework of Multi-Terminal Direct

Current (MTDC) as a conversion element for a better stability of the network DC [Tal+17]. The works of [SCF15; Tal+18] put forward its capacity - thanks to the capacitors which it contains - to exert a role of buffer with a very good dynamic response between a network AC and the MTDC. Indeed, under some energy varations in the MMC, the DC bus remains stable and that the transients due to these charges and discharges are well absorbed. In [Tal+18], a non-dead band voltage droop control is used in simulation and experimentally on a reduced model showing the power flow management and stabilization capabilities of the bus.

1.B.2 Introducing the Modular Multilevel Converter

Before starting with the first mathematical notations, note that general recurring notations are present in the document, see *the general notations* for more details.

1.B.2.1 Topology of the Modular Multilevel Converter

The Modular Multilevel Converter (MMC), is a static converter allowing the conversion of direct current into alternating current and vice versa, a three-phase representation of this converter associated with its DC bus and its AC network is depicted on the Figure 1.2. This MMC has the remarkable characteristic of being modular, i.e. it is made up of elementary bricks, called submodules, whose number can be increased to reach high voltage, and thus power, levels. Let N be the number of submodules in a arm of the MMC and m the number of phases of the AC network connected to the converter, the converter then has a total of $n_{SM} = 2mN$ submodules. In the same arm, N of them are stacked in a series-connection. In the original topology from [Mar02; LM03], those switching cells are identical. Each SM itself is a static DC to DC converter operating between a voltage source, which is a capacitor, and the current source imposed by the arm on which the submodule is located.

Submodule topologies

Each submodule being itself a DC-DC converter, it is conceptually endowed with at least one switching cell and thus with a switching state to drive for the control system. This means that the ability of the MMC to scale up to a high voltage level, which is accompanied by a proportional increase in the number of submodule, increases the number of degrees of freedom that the control system must be able to manage to ensure the proper operation of the converter.

In the first years after the appearance of the MMC the question of the control complexity and the cost in semiconductors proved to be decisive and thus naturally encouraged the use of the half-bridge submodules as Figure 1.1 (a) presents the functional diagram. However, the use of the full-bridge Figure 1.1 (b) gives the submodule additional capabilities such as 1) bipolarity which allows it to both enforce a negative voltage on the arm but also to open the connection of the arm and eliminate its current, 2) a wider region of operation of the converter [Mar10]. Nevertheless the addition of a switching cell necessarily leads to an increase in losses. So choosing between half-bridge and full-bridge is a compromise.

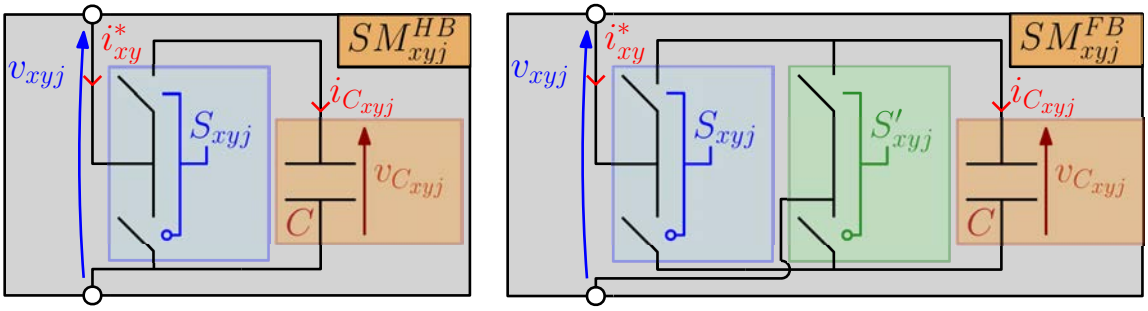

(a) SM-HB (b) SM-FB

Figure 1.1: Simplified electric diagrams for the control of the two most common types of SM. (a) SM-HB, (b) SM-FB.

From these first two topologies, others have been proposed in the pursuit of either a gain in functionality, such as a better ability to manage faults, or a gain in performance, such as a reduction in losses for example. This is typically the case of the double-clamped submodule [Mar11] improved in semi-full-bridge submodule [Ilv+15a] for voltage bipolarity of the cell. The introduction of a supplementary switch to the full-bridge submodule brings the double-zero submodule [DKM17] which enables lower losses. Nevertheless, there is still work to be done to tackle the challenges still present such as the reduction of the size of the capacitors, the management of the operation in case of failure or the reduction of the losses. In terms of losses, [Mar18] proposes a comparison of a batch of different topologies including those just mentioned. This comparison allows one to classify the full-bridge submodule as the one with the most losses and the half-bridge submodule as the second one with the least losses. The work of [YSD17] reports a variety of possible topologies for submodules.

Among all these topologies, accordingly with the control objective that is set here - whose inherent complexity of the methods used is naturally important - the choice is made to select on the submodules having the least control variables: the half-bridge submodule with one duty cycle and the full-bridge submodule which has two. Although the SM-FB has more switches than the SM-HB, making its control more complex, it simplifies the balancing of the capacitor voltage, the study will therefore focus on these two usual SM topologies.

Adopted formalism

The literature is full of different formalisms to approach the modelling of the MMC such as the original formalism of [LM03] tracked by [Mar10; Mar11; DKM17; Mar18] which has been progressively modified and improved to take into account the different specificities and behaviors of the physical quantities associated with the converter in [PR11; PRB14; Liz+15; Per+15; BFB19]. Another formalism present in the book [Sha+16a], of good quality and relatively complete on the topics related to MMC, is carried and used by various authors of which [Ilv+11; Lad+12; Pou+15; Ber15; YSD17; Sel+19]. As a choice of notations is necessary, the first trend directly issued from the original works which allows a more harmonious representation of the currents and voltages at work in the MMC will be favored here. More specifically, the formalism adopted here is the one which is the closest to [PRB14; Liz+15].

The Figure 1.1 shows these two topologies by focusing on the submodule $\#\{x, y, j\}$ i.e. the SM $\#j$ of arm $\#x$ of the leg $\#y$. In these two cases, the SM contains only one DC voltage source

which is materialized by the capacitor. The notations used to denote electrical signals at the switching cell scale are shown in Figure 1.1. The voltage $v_{C_{xyj}}$ is the voltage across the capacitor of any $\#x, y, j$ SM while v_{xyj} is that across the module itself. Similarly, the current flowing through the capacitor is noted $i_{C_{xyj}}$ and i^*_{xy} is that which flows through the module. Comparing the position of the submodule in the Figure 1.2 with the electric diagram of the Figure 1.1, it is observed that for the submodule belonging to the arm of the positive pole: $i^*_{xy} = i_{xy}$; while for those belonging to the negative pole: $i^*_{xy} = -i_{xy}$. For this reason, the function $\sigma(x)$ is introduced, it is equal to $+1$ for $x = p$ and to -1 for $x = n$. In this way these different cases for i^*_{xy} are summarized by: $i^*_{xy} = \sigma(x)\ i_{xy}$. It is emphasized that, in nominal operation, whatever the state of the switches S_{xyj} - and S'_{xyj} for the full-bridge case - the current i^*_{xy} will always flow through the module and will not be cut off. In other words, each SM is transparent to the current i^*_{xy}. This property of transparency is fundamental for the operation of the MMC. From this behavior, the circulating currents originate, see paragraph 1.B.2.2 for more details.

The MMC containing n_{SM} submodules, it therefore contains a total of n_{SM} capacitors whose voltage levels must be controlled for at least three reasons: 1) the need to ensure the voltage protection of the semi-conductors, 2) the need to gurantee the operating zone of the converter at its nominal state, and 3) the necessity to maintain a stable quantity of stored energy in the MMC. Let V_{DC} be the voltage available at the terminals of the DC network connected to the converter, and v_C^{nom} be the nominal voltage at the terminals of the capacitors. The latter is chosen in order to guarantee a nominal operation for the MMC. The analysis of the operating region of the MMC enables one to derive the maximum and minimum voltage values from v_{xy}. In the current case study, it is assumed that the maximum of v_{xy} reaches V_{DC}. For that need, with a total of N submodules per arm, the capacitor voltages must be balanced around V_{DC}/N [Sha+16c].

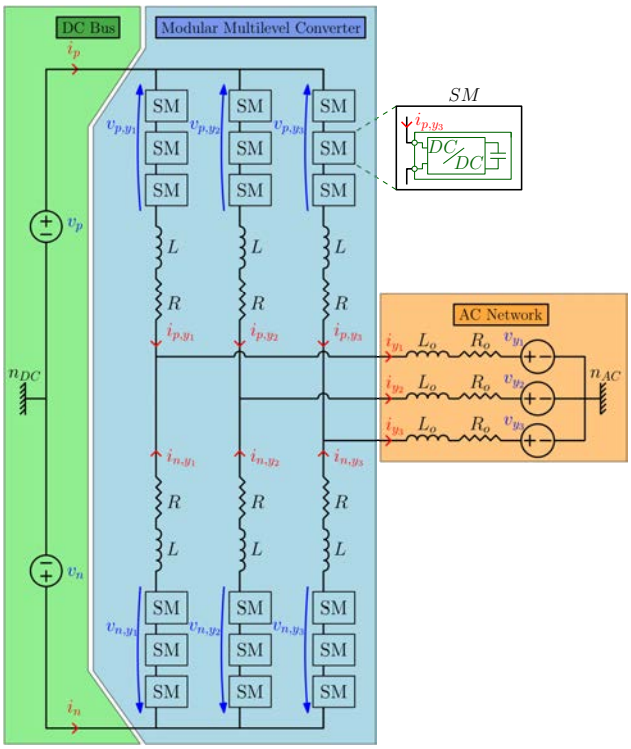

Figure 1.2: MMC electrical system diagram in its 3-phase, 3 submodules per arm configuration.

It is noted that the configuration $m = 3$ and $N = 3$ is one of those of the MMC experimental setup available at the LAPLACE. Details on the design of this converter are presented in [Ser14].

[Sel+19] uses the same converter but in a different configuration of the submodules. The Table 19 displays its main parameters.

About the notations shown on the Figure 1.2, x is used to indicate the type of arm. There are two types of arms possible: either the arm attached to the positive pole of the DC bus, then noted p, or the arm attached to the negative pole of this same bus, then noted n. The variable x then always takes one of these two values according to the leg considered. To designate a leg of the converter, the notation y is used. As there are as many legs as there are phases in the output AC network, the phases and the legs are designated the same way. Having m legs and phases, y will always take a value in $\{y_1, \ldots, y_m\}$.

- For the MMC, the variable v_{xy} is then defined as being the voltage at the terminals of the arm $\#xy$ and i_{xy} is the current flowing through this same leg. The arm inductance is necessary to curb the circulating currents of the converter during its operation [Mar18], and its sizing is related to short-circuit current limitation. The impedance of the arm is materialized by R and L.
- For the DC bus, the voltages v_p and v_n stand for the continuous supply of the bus. In nominal operation it is specified that $v_n = -v_p$ and that $V_{DC} = v_p - v_n$. The currents i_p and i_n are injected by the DC bus in the converter. In some cases it will be considered that this bus can display an impedance, it is characterized by R_s and L_s.
- For the AC-side network, the voltages v_y show the possibility for this network to be active, as in the case of a electric motor or a grid. In the case of a passive network, the AC load made of R_o and L_o sees the current i_y flow through it.

As the connection between the neutral points is considered as a changeable parameter, two neutral points are considered: n_{AC} for the AC network and n_{DC} for the DC network.

In nominal operation it is considered that all the capacitors of the converter are balanced at the voltage level v_C^{nom}. The energy contained in the MMC in nominal operation is then expressed:

$$E_{MMC} = \sum_{y=y_1}^{y_m} \sum_{x=n}^{p} \sum_{j=1}^{N} C \frac{{v_{C_{xyj}}}^2}{2} = \frac{mC}{N} {V_{DC}}^2 \tag{1.1}$$

In the whole document, unless otherwise specified, the models will be derived in instantaneous quantities for the electrical signals, current and voltage, as well as the switching states. Therefore, the notations t for time as a variable is voluntarily omitted in order to lighten the equations.

1.B.2.2 Operating specificities of the MMC

The particularity of the MMC, which is at the same time what makes its strength, is to be made of submodules. Indeed, the presence of these submodules gives it a very different behavior from the usual DC-AC voltage source static converters.

The submodules: an elementary brick which gives its modularity to the MMC

A major functionality that is provided to the MMC by the presence of these SMs is its modularity. In the case of the MMC, its particular topology entails that each switching cell has for voltage source a capacitor. In normal operation this capacitor is balanced at its nominal voltage. Thus, whether the cell is in the OFF state (Figure 1.3), or in the ON state (Figure 1.4), the switches

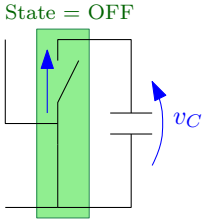

Figure 1.3: Simplified diagram of the SM-HB in OFF state.

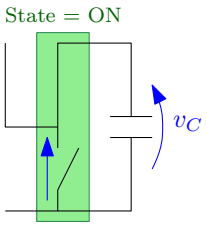

Figure 1.4: Simplified diagram of the SM-HB in ON state.

will experience a voltage $v_{switch} = v_C$ across their terminals. To ensure that the maximum voltage rating of the switches is respected, the capacitor voltage must not exceed this maximum voltage value. This means that the capacitors have a protective role to ensure for the switches.

In the following, it is assumed that a control law effectively balances the capacitors and thus maintains the capacitor voltages v_C around their nominal value, which is generally obtained when using control laws of the MMC already available in the literature. A series connection of two submodules will not change the maximum voltage to which the switches will be subjected: they will all see the voltage v_C of their own capacitor at the most. Thus, it is possible to put in series a stack of those submodules without having to change the voltage rating of the switches used. Such a stacking allows one to reach and convert voltage levels that are multiple of the voltage limit of the switches: the latter do not see the whole bus at their terminals but only v_C, contrary to the case of the usual 2-level 3-leg VSC. This is what gives the modular character of the MMC. From the same type of submodule it will be possible to design a 10 kW MMC with a 1.2 kV DC bus as well as to design a 1 MW DC with a 120 kV DC bus: the only difference will be the number of submodule used but not their voltage and current ratings that will remain the same. In the first case, with capacitors balancing at 300 V, one would need $N = 4$ submodules per arm. And in the second case, with the same submodule, one would need $N = 400$ per arm. In both cases, the maximum current delivered by the DC bus would be 8.33 A and the maximum current flowing through the arms of the converter would be the same, without modifying the maximum current that the switches within the submodules must withstand.

The different MMCs use various topologies of submodule which are not always directly akin to the SM-HB as mentionned previously. However, the concept of modularity presented here is also applicable to them without loss of generality.

The submodules: a freedom for the currents within the arms

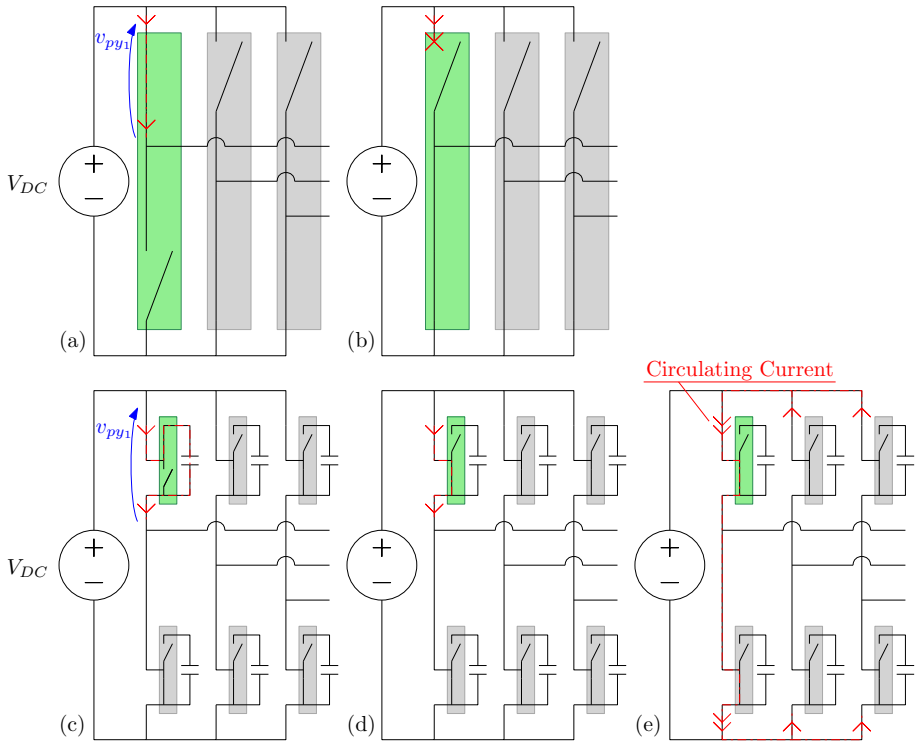

Figure 1.5: Comparing the functionnal behavior of the MMC with a conventionnal 2-level 3-leg VSC. (a) and (b) represent a 3-phase inverter. (c) to (e) represent a single SM per arm MMC in the 3-phase case.

To analyze the functionnal behavior of the MMC, focus is on the top left arm of both converters colored in green and pictured in Figure 1.5. The considered MMC has a single SM per arm which is unusual but done on purpose in order to emphasize the behavior principle. Throughout the figure, a full switching cell is shown in a green or gray rectangle. In the case of the VSC, a switching cell is located on both sides of the same leg and the middle point of this cell is connected to the AC network to be supplied. In the case of the MMC, a same switching cell is entirely arranged on one single side of a leg of the converter, and all the circuit connections it has are made with the same arm. This major difference explains the behavior observed in Figure 1.5 (c)-(d) & Figure 1.5 (a)-(b): For the usual 3-phase VSC, in one of the two possible states of the switching cell, current flows through the arm (a), and in the complementary state, no current flows through this same arm (b). Whereas for the MMC whatever the state of the cell considered, a current will always flow through the arm (c)-(d). The cell does not have the ability to interrupt the current flowing through the arm to which it belongs. This means that, unlike the VSC, during the operation of the MMC, a current will always be able to flow through an arm and this whatever the arm that one considers in the MMC. The fact of adding SMs does not change this behavioral property which is preserved. If all the arms conduct current at all times, then so do the whole legs and a current will always be able to circulate between the positive pole and the negative pole via the legs of the MMC as represented in Figure 1.5 (e). This current is then named circulating current. This explains the appearance of the circulating current between the legs of the MMC, current which is a singular phenomenon of this converter.

1.B.2.3 High-level operation of the MMC

The existence of circulating currents within the MMC, as highlighted by the Figure 1.5, comes in addition to the other currents that usually flow through a DC-DC converter such as the DC bus current, the AC network current or the common mode current in the case where the neutrals are connected. In order to analyze how the MMCs interfaces with the networks it connects, the interest is then focused on the path followed by each current in the MMC.

Modelling choices are necessary to keep a overall consitency. In this way, accordingly with [PRB14; Liz+15], it is decided to let $6\,i_m$ be the total current flowing through the neutrals, $3\,i_s$ be the total current delivered by the DC bus to the MMC, i_{c_y} be the current circulating in each arm of the MMC and $2\,i_{o_y}$ be the current distributed by a leg of the MMC to the AC network. According to the KCL, assuming the different impedances balanced between the phases and between the arms, one finds the current distribution from Figure 1.6 [Liz+15].

From this Figure 1.6, it is possible to infer the various contributions to the current carried by each arm by using the superposition theorem. Indeed, when focusing on an arm $\{x, y\}$, its current i_{xy} will be made of the current that flows through the neutrals (a), the current that comes from the DC source (b), the current that can flow between the arm of the converter (c) and the current distributed to the AC network (d). The following formulas can then be deduced, paying particular attention to the directions of the currents when performing the superposition:

$$\forall y \in \{y_1, y_2, y_3\}, \begin{cases} i_{py}(t) = i_m(t) + i_s(t) + i_{c_y}(t) + i_{o_y}(t) \\ i_{ny}(t) = i_m(t) - i_s(t) - i_{c_y}(t) + i_{o_y}(t) \end{cases} \tag{1.2}$$

It is thus observed that each of the currents in the arms will be composed of a maximum of four components when the neutrals are connected and three otherwise, as in the case of [Fre+16b; Bou17; Ber+18]. An important point to note is that the circulating current has no direct influence on the currents at the interfaces of the MMC: i_s and i_{o_y}. It is thus really a current proper to the

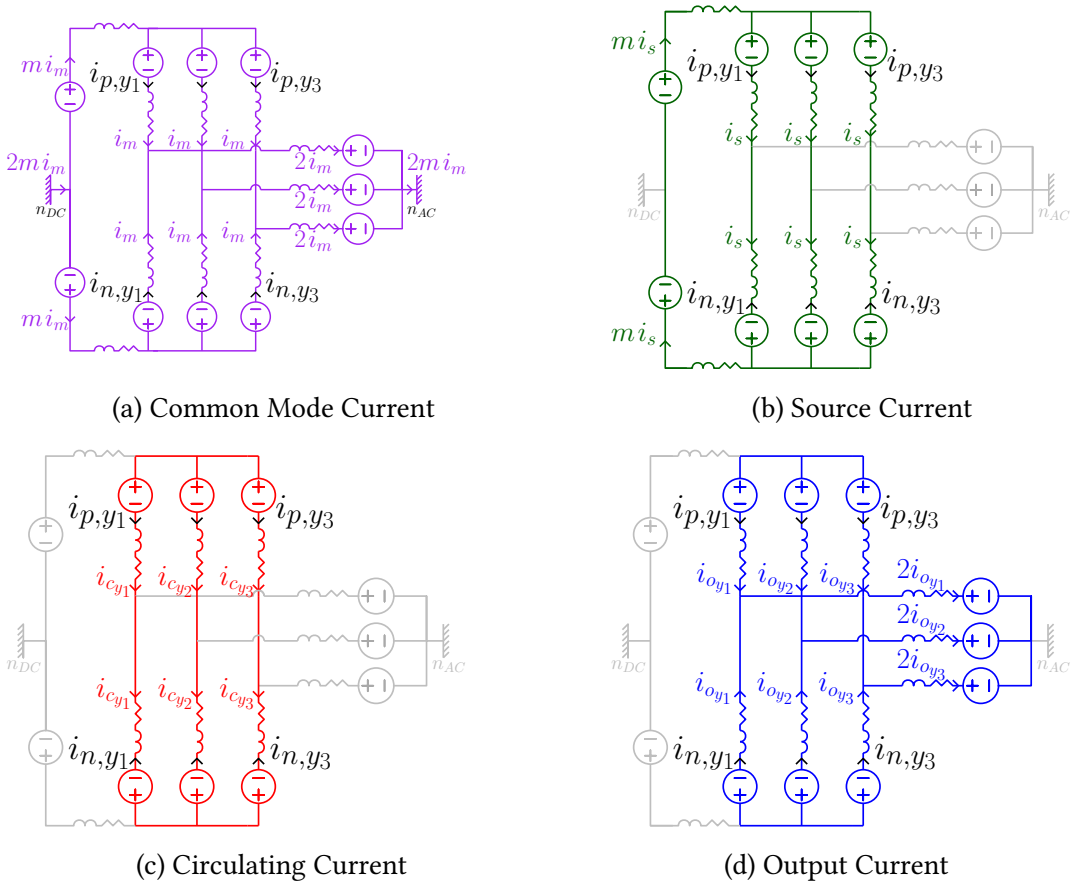

(a) Common Mode Current

(b) Source Current

(c) Circulating Current

(d) Output Current

Figure 1.6: Illustration of the currents involved in the conversion performed by the MMC

converter itself and these two last ones represent only the conversion of energy carried out by the MMC as it is the case in a usual converter.

1.C | Control-oriented modelling for the MMC

The topology of the MMC having been introduced as well as its singularities of design which give it its characteristics of operation, range of the various models available to describe the behavior of this converter is presented in this section.

1.C.1 | Variety of modelling catagories and levels

The modelling of the MMC, like many modern technological systems, can be categorized according to the utilisation purpose of the developed models:

- Knowledge models whose objective is to understand, generally with an advanced level of detail, the functioning of the modeled system.
- The design models whose aim is to perform the sizing of the considered system.
- The control models whose purpose is to allow the realization of algorithms allowing to steer the system.

Each of these categories is a more or less complex and accurate representation of reality that

influences the computation or simulation time. Making a choice is finding the adapted trade-off between these three characteristics, according to the modelling requirements a category rather than another will be used. Within the framework of the work carried out here, the objective is the control of the MMC.

The MMC, which is a converter built from elementary bricks, can be described as a converter with two hierarchical levels of conversion: a first conversion DC-DC takes place at the level of the switching cell of the submodules which - together with those of the other submodules - contribute to generate a voltage at the terminals of each arm. These voltages are, in turn, responsible for the realization of the second conversion DC-AC, called high-level. This hierarchization of the conversion enables the classification of a variety of modelling levels of the MMC which goes from the switching cell, like the Detailed Model (DM), to the converter in a wider vision like the average model.

1.C.2 From the semiconductor to the arm modelling methods

From the closest model to the physical phenomenon represented to the lightest model to be executed, this section draws up a range of modelling methods able to represent the switching cells of the submodules in the framework of the MMC.

Physics model

In the case of the PM, the semiconductors are represented by a detailed equivalent electric circuit which reproduces the behavior of the electric quantities at work in the considered switch. Each diode and IGBT are then substituted by other electronic components on the basis of few assumptions. [Str97] proposes this type of modelling for the case of the IGBT based on solving diffusion equation for the electric charges in semiconductor media. The level of detail of this model makes it possible to represent the losses within the converter, however the detail is such that for the MMC which has as many switches as it has submodules, using such an approach proves to be very heavy.

Detailed model

This representation is established from the Physics Model (PM) and constitutes a simplification. This reduction of complexity is done by obtaining a reduction of the representation made of each of the semiconductors. A set IGBT-diode is then replaced by an equivalent circuit made of a reduced set of electronic components [SC98]. Able to represent some nonlinearities of the cell as well as its losses [Per+12], this model is obtained from the datasheet of the semiconductors and represents the submodule with a good accuracy. However, it is lighter to use and to simulate than the PM.

Equivalent model

This modelling approach amounts to extracting an equivalent of Thevenin or Norton from the switching cell. This representation is obtained by analyzing the nodes of the electrical circuit [GGJ11; Saa+13a]. This greatly reduces the complexity of the electric circuit model. Having a model of MMCs where each submodule is replaced by a voltage source with its series impedance

or a current source with its parallel impedance represents an important simplification leading to a strong decrease of the simulation time [Zam17].

Average model

Through assumptions the average model of the switching cell is obtained from the DM [MC76; BMB14]. This shift to the average value drastically reduces the mathematical complexity and the order of the model. This simplification, which is based on assumptions that can be more or less strong depending on the operating parameters of the converter, leads to a loss of accuracy. This representation does not take into account the resistance and therefore cannot describe the losses in the converter. On the other hand, such a model complexity reduction has the major feature to make possible the design of higher-level control laws for the represented converters, and also brings a strong reduction of the simulation time [Per13; LRV10; CVR12].

This Average Model (AVM) method, applied to a submodule, can just as easily be applied to the arm level of the MMC [CVR12]. This reduces the hierarchy of the two conversion stages mentioned to a single stage. This averaging principle, applied to the next higher level, can represent the MMC only with a modulation index between the DC supply voltage and that of the AC network to which it is connected [Saa+14; DKM17; Mar18].

In the case where the AVM is used at the scale of an arm of the MMC, it has the remarkable property that the greater the number N of submodules, the more accurate this model is [Saa+14]. In other words, it is particularly suitable for multilevel converters such as the MMC which are precisely designed with this desire for modularity and increased voltage level. At the higher scale of the MMC the AVM does not depend on the number of submodules.

Comparison of the modelling approaches

For our control purpose, the PM represents a level of detail that is too important and that leads to a computation time that is prohibitive to use it for such a purpose. In the context of control-oriented modelling for the arms and the submodules this approach will not be retained.

A comparative study proposed by [Saa+14] allows us to highlight the fact that AVM is much faster to simulate the behavior of the MMC than EM, itself faster than DM. However, in terms of accuracy, the trend is reversed. However for the high-level control point of view, the AVM is shown to be sufficiently accurate for the MMC.

From the modelling methods presented here which are realized in the case of a nominal operation of the submodules, [Zam17] brings the increase of the harmonious and aggregated consideration of additional switches which are essential in practice to ensure the starting procedure of the converter or the isolation of the submodules in the case of semiconductor faults. With similar tests to those from [Saa+14], the augmented versions of the AVM, EM and DM, [Zam17] show the same ranking regarding the computation time and accuracy of the approaches.

In light of the performance of the various models and the control perspective which is that of the current study, it is therefore the AVM approach that is selected here for its low computation time and its good accuracy. However, obtaining the AVM requires a first necessary step of DM.

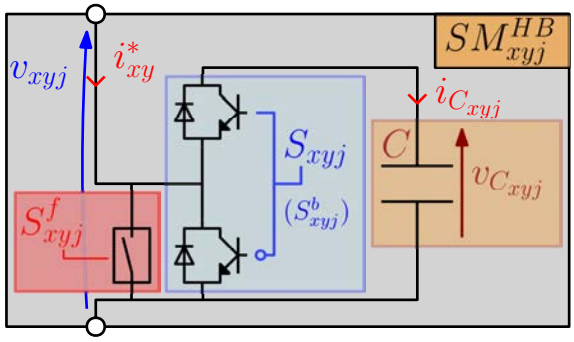

Figure 1.7: Electrical diagram of the SM-HB with the detail of the blocking and faulty switches as in [Zam17; Zha+16]

1.C.2.1 Average model development for the MMC

DM for the SM-HB taking into account blocked and faulty operating conditions

Some work has proposed first models taking into account the operation of the submodule in case of a fault or in the blocked state where the submodule lose controllability of the submodule [Saa+16]. Compared to previous works, [Zam17] improves these models and proposing a version that aggregates all the cases of operation of the SM into a single mathematical model.

In order to go into the development of the submodules model, the Figure 1.7 introduces a detailed representation of the internal constitution of the half-bridge submodules according to [Zam17]. The switching cell must allow the flow of an alternating current; and the DC voltage source, materialized by the capacitor considered polarized, will feature at its terminals a voltage that is always positive or zero. A third switch is added to the cell input, this switch has a safety function. This particular switch makes it possible to isolate the cell from the arm to which it belongs when it is faulty.

A submodule will have several operating states that are at the origin of the energy conversion that the MMC can perform [Saa+16; Zha+16; Zam+16a]. These operating states are the following ones:

- Connected, or Inserted: In this state, the capacitor is connected to the arm, it is called *inserted*. This corresponds to the case where the upper transistor is closed and the lower transistor open. According to the notations on the Figure 1.7, this corresponds to the case where $S_{xyj} = 1$.
- Disconnected, or Bypassed: In this state, the capacitor is disconnected from the arm, it is called *bypassed*. In this state the upper transistor is open and the lower transistor closed. According to the notations on Figure 1.7, this corresponds to the case where $S_{xyj} = 0$.
- Blocked: In the blocked state both the upper and lower transistors are open. Depending on the sign of the current i^*_{xy}, the capacitor can only charge or remain at a constant charge level since the diodes prevent the capacitors from discharging. As explained by [Sha+16b], this mode is used to energize the MMC at the time of its startup for example, where it is necessary to charge all the capacitors before being able to enter the normal operation mode. In operation, this mode can also be used for a few tens of milliseconds when faults occur on the network to protect the transistors from possible short-circuit currents. The diodes in antiparallel of the transistors have therefore generally a higher current rating than the associated transistors in order to bear this current increase. According to the notations on the Figure 1.7, this state does not correspond to any possible value of S_{xyj}, it is thus necessary to introduce another binary

variable: S^b_{xyj} with b for *blocked*. For the model the choice is made that when $S^b_{xyj} = 1$, the blocked state is active and the two transistors of the cell are forced open. The value of S_{xyj} then has no influence on the state of the SM. On the contrary, when $S^b_{xyj} = 0$, the blocked state is not activated and the state of the SM can then be controlled by S_{xyj}. This mode of operation has already been used in detailed models of submodules [Den+15; Saa+16; Zha+16].

- Faulty: This faulty state is a particular state of the whole SM and not only of a switching cell as it is the case for the other binary variables. A SM will be forced into this state when it presents a faulty operation. S^f_{xyj}, with f for *faulty*, stands for the state of a very reliable switch with a high switching speed, i.e. a sub-vacuum switch. In the event that a fault occurs in one of the SMs during operation of the MMC, this fault can be detected and the associated SM can then be isolated by closing that switch. This then ensures that the faulty SM will no longer interfere with the operation of the MMC. The use of the fault switch therefore allows for risk-free operation since the current of the arm to which the faulty SM belongs can continue to flow in the converter, ensuring the operation continuity of the MMC [Din+08]. When $S^f_{xyj} = 1$, the associated SM will be considered as faulty and the switch driven by S^f_{xyj} will be closed. Neither S_{xyj}, nor S^b_{xyj} will then have inluence on the behavior of the SM. In the opposite case where $S^f_{xyj} = 0$, the fault switch is open.

The three types of variables S_{xyj}, S^b_{xyj} and S^f_{xyj} they are binary variables representing the state of the considered submodule, a truth table, Table 2.1, is drawn up like those of [Saa+16; LB16] to represent the various possible cases.

S^f_{xyj}	S^b_{xyj}	S_{xyj}		$i_{C_{xyj}}$	v_{xyj}
0	0	0		0	0
0	0	1		i^*_{xy}	$v_{C_{xyj}}$
0	1	-		$i^*_{xy} \cdot (i^*_{xy} > 0)$	$v_{C_{xyj}} \cdot (i^*_{xy} > 0)$
0	1	-		$i^*_{xy} \cdot (i^*_{xy} > 0)$	$v_{C_{xyj}} \cdot (i^*_{xy} > 0)$
1	-	-		0	0

Table 1.1: Truth table - Behavior of the SM-HB

From this truth table it is possible to extract, by application of the laws of KIRCHHOFF to the electric circuit Figure 1.1 (a) in each case, the logical function expressing the capacitor current and the voltage at the terminals of the selected submodule as a function of the different states S_{xyj}, S^b_{xyj} and S^f_{xyj}. This logic function, whose development is proposed in details in Appendix D to adopt the formalism used here, corresponds to the analytical DM of [Zam+16a; Zam17] but without taking into account the conduction resistances here.

$$\begin{cases} i_{C_{xyj}} = C\,\frac{dv_{C_{xyj}}}{dt} = i^*_{xy}\,\left[S_{xyj}\overline{S^b_{xyj}} + (i^*_{xy} > 0)S^b_{xyj}\right]\overline{S^f_{xyj}} \\ v_{xy} = \sum_j^N v_{xy} = \sum_j^N v_{C_{xyj}}\,\left[S_{xyj}\overline{S^b_{xyj}} + (i^*_{xy} > 0)S^b_{xyj}\right]\overline{S^f_{xyj}} \in \left[0; v_{C_{xyj}}\right] \end{cases} \tag{1.3}$$

DM and AVM for the SM-FB

The work of [Zam+16a] focuses on a single type of submodule, however that of [Saa+16] proposes a study of the operation of full-bridge submodules in the case of deadlock that [LB16] extends to include fault consideration. Truth tables to describe the behavior that the SM-FB adopts in the different cases are introduced, but do not present a practical analytical formulation to use as [Zam17] does for the case of the half-bridge submodule.

Thus the behavior of full-bridge submodule is expressed from the direct application of the laws of KIRCHHOFF to the Figure 1.1 (b) in the case of nominal operation:

$$\begin{cases} i_{C_{xyj}} = C\,\frac{dv_{C_{xyj}}}{dt} = i^*_{xy}\,\left(S_{xyj} - S'_{xyj}\right) \\ v_{xy} = \sum_j^N v_{xyj} = \sum_j^N v_{C_{xyj}}\,\left(S_{xyj} - S'_{xyj}\right) \in \left[0; v_{C_{xyj}}\right] \end{cases} \tag{1.4}$$

The AVM of the SM-FB is determined in the manner of [WM73; MC76; BMB14]. This model here amounts to averaging DM across the switching period T_s. Assuming that the latter is short enough compared to the dynamics of the electrical quantities of the submodule, there comes the model proposed by [Yan+19]:

$$\begin{cases} i_{C_{xyj}} = C\,\frac{dv_{C_{xyj}}}{dt} = i^*_{xy}\,\left(D_{xyj} - D'_{xyj}\right) \\ v_{xy} = \sum_j^N v_{xyj} = \sum_j^N v_{C_{xyj}}\,\left(D_{xyj} - D'_{xyj}\right) \in \left[-v_{C_{xyj}}; v_{C_{xyj}}\right] \end{cases} \tag{1.5}$$

Whatever the type of submodules, the modulation index m_{xy} of an arm is a particularly useful tool during the implementation of the control to decouple the low-level part from the high-level part as explained in more detail later. This index can be defined for each of the submodules of the converter in a general way from the relation:

$$v_{xy} = m_{xy} \sum_{j=1}^{N} v_{C_{xyj}} \tag{1.6}$$

In the case where the arm-AVM is given an equivalent model of the capacitor behavior by series association of the capacitor dynamics in each arm. It is possible to see each arm as an equivalent capacitor of capacitance $C_{eq} = C/N$ as proposed by [Sha+16b; BSD16]. The relation $v_{xy} = m_{xy} v^{eq}_{C_{xy}}$ then allows one to define the modulation index in this case. If the capacitors are considered nominally balanced at all time, then $v_{xy} = m_{xy} V_{DC}$ comes.

1.C.3 | From the arm to the whole converter modelling methods

The modelling methods used to go from the semiconductor to the converter arm level are, for some - such as the arm-AVM [Per+12; Saa+14; Den+15; Zam17] or the arm-EM [Ste+21] - the starting point of a larger modelling that takes into account the whole converter and thus represents the behavior of the different types of currents that flow through it. Thus these approaches which initially focus on the modelling of the submodule can be extended to the arms and even to the MMC like the AVM [Per+12; Saa+14; Ste+21] which is derived from the DM of the submodules. As a result, the boundary between modelling from the semiconductor to the arm and modelling from the arm to the whole converter is sometimes difficult to distinguish, depending on the objective of the modelling approach.

In the case of models dedicated to the computer simulation of the MMC for example, it could be wished to have an aggregated model which does not make a distinction between the two levels but which provides the value of the various electrical quantities in play with a good compromise between precision and speed of execution.

Whereas, **in the case of a control-oriented modelling** approach, it may be preferable to decompose the system into several levels that are simpler to control, [HA09; PRB14; Sha+16b;

Gey16; Cif+21], rather than addressing the whole complexity of the system in one go. Compared to this last solution of performing the control of the MMC in a condensed way [RGM15; BFB19; MAR19] the majority tendency remains the decomposition of the control in several stages.

The name low-level control then designates the control of the arms and the submodules while the high-level control designates the control of the currents as well as the powers and, by extension, the energy converted and contained in the MMC. This distinction with the notion of level can therefore also be extended to the high-level modelling and the low-level modelling.

After having presented an overview of the existing low-level modelling approaches, the interest is now focusing on high-level modelling of the MMC.

State-space modelling of the MMC

With the large number of capacitors, switching cells and their arrangement which implies a large number of currents to be controlled, the MMC represents a large number of physical quantities, of states which evolve in the course of time and whose internal dynamics interact together. This converter is a MIMO whose modelling in the state space appears as naturally relevant.

The variety of these models shows a diversity of choice in the representation of the currents. The detailed decomposition of the latter could be given in Section 1.B.2.3. In the case of this decomposition and of a nominal operation of the converter in steady state, the bus current is a current of continuous nature as well as the common mode current, while the circulating current as well as the output current are currents of alternating nature [Sha+16b].

This decomposition is not tracked by all, and in particular the common mode current is poorly represented because of the configurations of the MMC on which the work focuses where a connection between the neutral DC and AC does not exist [RWB11; WBB14; CD15].

In some cases also, the current called *circulating* corresponds to the association of the current noted i_{c_y} here with the bus current DC: i_s. In other words, in this case the current called *circulating* has for continuous component i_s and for alternating component i_{c_y} [Ilv+12; Ber+18; Lyu+18]. The same can be said for the current *output* which then aggregates the current i_{o_y} with the common mode current i_m.

However, whatever the current decomposition adopted by the variety of available models, the common ground to all these models remains the only current that can be observed in the set of MMCs and which is the basis of its operating principle: the arm current, represented by i_{xy} here. The simple application of the Kirchhoff Voltage Law (KVL) on the two circuits of the Figure 1.2 which connect the y_1 leg of the DC bus to the AC network without any impedance at the input nor at the output shows that for each of the three legs:

$$\forall y \in \{y_1, y_2, y_3\}, \begin{cases} v_p = v_y + \left(R_o + L_o \frac{d}{dt}\right) i_y + \left(R + L \frac{d}{dt}\right) i_{py} + v_{py} \\ v_n = v_y + \left(R_o + L_o \frac{d}{dt}\right) i_y + \left(R + L \frac{d}{dt}\right) i_{ny} + v_{ny} \end{cases} \tag{1.7}$$

This is in line with [Har+13]. Among the set of state models used for the MMC there are a number that take advantage of the arm-AVM [RWB11; Ras+09; MLE10; Rak+13; CD15; VHS15]. The modelling proposed by [BFB19] allows a formulation where the converter behavior is linearized in the state space under time separation assumptions. This results in a decoupled approach to the control of the MMC which yet shows good performances.

Another possibility is to use the switched principle as proposed by [WBB14], or the state-space

model taking advantage of the periodicity of the current and voltage signals to simplify the state model and obtain a steady-state version as proposed by [Mün+10].

The SSMs are also an interesting way to represent the MMC in the will to study more in details its dynamic behavior, and more particularly that of the currents. The harmonic SSM is precisely a tool for this purpose [Lyu+18; Ma+19].

The analyses proposed by [Ilv+12; Lyu+18] taking advantage of high-level models based on the principle of arm-AVM allow to highlight the harmonic content of the different types of currents which flow through the MMC. By making the assumptions that the capacitors are balanced on the scale of the fundamental period of the output currents, that the output current has only one fundamental component [Ilv+12] shows several interesting results by solving the differential equations of the currents in frequency form. The first of these findings is that the existence of the fundamental component of the output current implies the existence of the second order harmonic component of the circulating current, the latter is of variable amplitude depending on the output current. The study shows by recurrence relation that the circulating current can not have harmonic components of odd rank. In the case where the circulating current would present a fundamental component, this one influences the energy balance between the positive and negative arms according to its phase. There is a value of the phase for which the balance is maintained. The analysis shows that these behaviors are experimentally verified and highlights the fact that the presence of losses in the converter is a necessary condition to attenuate the harmonic components at the resonant frequencies of the converter.

Analytically it is shown that the harmonic components of order higher than two of the circulating current will be significantly lower, which is experimentally confirmed in the same study. [Lyu+18] also proposes a study of the harmonic content which reaches the same conclusions based on a harmonic state-space model.

Modelling in the synchronous rotating reference frame

As in many electrical systems, modelling in the Park reference frame has a certain number of beneficits due to the fact that sinusoidal quantities are continuous in steady state such that the model is said to be Steady-State Time Invariant (SSTI). Compared to a representation in the natural base, this one is more complex mathematically but allows for example to reach certain dynamic and static performances more easily than a control realized in the initial stationary reference frame.

As the work of [Ilv+12; Lyu+18] shows, the main harmonic content of currents and voltages within the MMC contains continuous, fundamental, and second-order harmonic components. This harmonic content is such that it is not possible to represent the electrical quantities faithfully with sufficient accuracy by directly applying the traditional Park transformation [Par29; Par33]. A dedicated Park transformation must be formatted to obtain a model of the MMC in a Synchronous Rotating Reference Frame (SRRF).

However, it is possible to use the usual transformation for the MMC in the case where the behavior of the circulating currents and the capacitor voltages second order harmonics are not those that are of interest. These quantities being the ones carrying the second order harmonics, neglecting them allows one to have only continuous and fundamental components. This opens the way to the application of the usual transformations of Park. In this case where the internal dynamics are neglected, this approach is rather suitable when one wants to solely model the network behavior along with that from the bus [Liu+14; LV14; Tri+16]. As the internal dynamics

of the MMC are not represented, it is desirable to use them only in an operating case with slow dynamics.

However, work has been done to model the MMC by adopting a higher level of detail, accompanied by an effort to shape an adapted PARK transformation, in order to represent the internal dynamics of the converter. To do so, the basic idea is to shape a transform of PARK whose rotation angle is synchronized on the frequency of the second harmonic. Accordingly, the work of [FJ15; BDS16; JJ16; LGZ16; Ber+18] models the second order harmonic behavior of arm voltage as well as the circulating current second order harmonic component in a correctly synchronized SRRF. [SB20] derives a formulation that performs a reduction of the model order compared to previous models.

The AVM model proposed by [Fre+16a] in the PARK reference frame is a first solution to take into account the nonlinearity of the MMC, but the second order harmonic components are not considered. The work of [Ber+18] performs the development of a arm-AVM model in a specific SRRF with few assumptions which allows one to represent at the same time the intrinsic nonlinearity of the coupling between currents and voltages capacitors in the MMC but also all the harmonic components of the various electrical quantities and in particular the third order harmonics too, allowing to represent a potential injection of harmonics to extend the operating zone of the converter. This leads to a SSTI state-space model. This work, which aggregates a good part of the SRRF state-space models obtained until now, does not represent some quantities such as the common mode current or the impedance of the DC bus - which adds a coupling between the currents - and the neutral point voltage.

Matrix decoupled modelling in the stationary reference frame

Some state-space modelling approaches have been able to decouple the behavior of the different types of currents involved in the MMC such as [Bou17] by usual mathematical operations, or [Fre+16a] and [Ber+18] via a PARK transform. However, they thus do not represent all four possible types of currents explicitly and distinctly. Compared to these works, those of [PRB14; Liz+15] propose a heavier and higher order matrix representation than the previous state models. These models are then able to represent all types of currents in a decoupled manner which allows a better visualization and understanding of the interactions at work in the MMC. These approaches also allow the representation of the neutral point voltage of the AC network.

Initially it is this decoupling matrix approach that is selected as the basis for developing the models that are introduced here because it has the beneficial feature of explicitly distinguishing the different internal electrical quantities of the MMC.

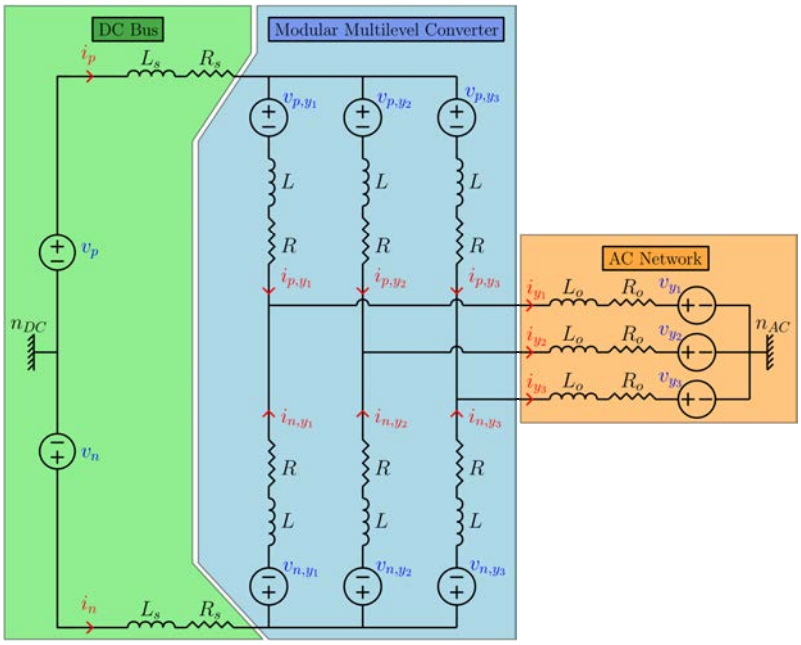

Figure 1.8: MMC electrical system diagram in its 3-phase configuration, arm-AVM is considered as well as a DC bus impedance.

The system considered in the case of [PRB14] is more complete than the previous system with the consideration of an impedance at the bus as shown on Figure 1.8. By applying the KIRCHHOFF's laws the following equations is obtained:

$$\begin{aligned}\begin{bmatrix} v_p & v_p & v_p \\ v_n & v_n & v_n \end{bmatrix} &= \left(R_s + L_s\tfrac{d}{dt}\right)\begin{bmatrix} i_p & i_p & i_p \\ i_n & i_n & i_n \end{bmatrix} + \left(R + L\tfrac{d}{dt}\right)\begin{bmatrix} i_{py_1} & i_{py_2} & i_{py_3} \\ i_{ny_1} & i_{ny_2} & i_{ny_3} \end{bmatrix} \\ &+ \begin{bmatrix} v_{py_1} & v_{py_2} & v_{py_3} \\ v_{ny_1} & v_{ny_2} & v_{ny_3} \end{bmatrix} + \left(R_o + L_o\tfrac{d}{dt}\right)\begin{bmatrix} i_{y_1} & i_{y_2} & i_{y_3} \\ i_{y_1} & i_{y_2} & i_{y_3} \end{bmatrix} + \begin{bmatrix} v_{y_1} & v_{y_2} & v_{y_3} \\ v_{y_1} & v_{y_2} & v_{y_3} \end{bmatrix}\end{aligned} \tag{1.8}$$

From this equation the decoupling of the currents is obtained by a product with carefully selected matrices, a differential equation is then obtained to represent each of the four types of current:

$$\begin{cases} \left[(3R_s + R + 2R_o) + (3L_s + L + 2L_o)\,\tfrac{d}{dt}\right]\begin{bmatrix} i_m & i_m & i_m \\ i_m & i_m & i_m \end{bmatrix} = P_2\begin{bmatrix} v_p & v_p & v_p \\ v_n & v_n & v_n \end{bmatrix} \\ \qquad - \begin{bmatrix} v_{y_1} & v_{y_2} & v_{y_3} \\ v_{y_1} & v_{y_2} & v_{y_3} \end{bmatrix} P_3 - P_2\begin{bmatrix} v_{py_1} & v_{py_2} & v_{py_3} \\ v_{ny_1} & v_{ny_2} & v_{ny_3} \end{bmatrix} P_3 \\ \left[(3R_s + R) + (3L_s + L)\,\tfrac{d}{dt}\right]\begin{bmatrix} i_s & i_s & i_s \\ i_s & i_s & i_s \end{bmatrix} = Q_2\begin{bmatrix} v_p & v_p & v_p \\ v_n & v_n & v_n \end{bmatrix} - Q_2\begin{bmatrix} v_{y_1} & v_{y_2} & v_{y_3} \\ v_{y_1} & v_{y_2} & v_{y_3} \end{bmatrix} P_3 \\ \left[(R + 2R_o) + (L + 2L_o)\,\tfrac{d}{dt}\right]\begin{bmatrix} i_{o_{y1}} & i_{o_{y2}} & i_{o_{y3}} \\ i_{o_{y1}} & i_{o_{y2}} & i_{o_{y3}} \end{bmatrix} = -\begin{bmatrix} v_{y_1} & v_{y_2} & v_{y_3} \\ v_{y_1} & v_{y_2} & v_{y_3} \end{bmatrix} Q_3 \\ \qquad - P_2\begin{bmatrix} v_{py_1} & v_{py_2} & v_{py_3} \\ v_{ny_1} & v_{ny_2} & v_{ny_3} \end{bmatrix} Q_3 \\ \left[R + L\tfrac{d}{dt}\right]\begin{bmatrix} i_{c_{y1}} & i_{c_{y2}} & i_{c_{y3}} \\ i_{c_{y1}} & i_{c_{y2}} & i_{c_{y3}} \end{bmatrix} = -Q_2\begin{bmatrix} v_{py_1} & v_{py_2} & v_{py_3} \\ v_{ny_1} & v_{ny_2} & v_{ny_3} \end{bmatrix} Q_3 \end{cases} \tag{1.9}$$

With decoupling matrices:

$$P_2 = \begin{bmatrix} 0.5 & 0.5 \\ 0.5 & 0.5 \end{bmatrix} \quad Q_2 = \mathbb{I}_2 - P_2 \quad P_3 = \begin{bmatrix} 1/3 & 1/3 & 1/3 \\ 1/3 & 1/3 & 1/3 \\ 1/3 & 1/3 & 1/3 \end{bmatrix} \quad Q_3 = \mathbb{I}_3 - P_3 \tag{1.10}$$

This matrix representation being of higher order than the traditional state models of the MMC, their use in the context of a converter control algorithm can be bulkier than necessary.

Beside this work focused on three-phase systems, [Sha+16b] proposes a beginning of generalization to polyphase systems by considering that the equation (1.7) can be applied for any number of legs in the MMC. However this equation is not extended in his case to a complete model of representation of the MMC in the polyphase case and some electrical quantities are not represented. [KM18] propose a more global approach of representation of a wider class of converters of type MMC, their generalization of the model adapts then to any number of phases of the AC network but also to any number of poles of the DC bus. This amounts to modelling a class of multilevel converters with a very important versatility. This work is indeed very enriching with the implementation of a cascade control law for matrix MMC. However, compared to the MMC which is treated here, the development of a model with such a level of generalization is done by derivations which are not explicit enough to analyze the singular and internal behaviors of the converter.

Operating region

Regarding the region of operation of the MMC, [Sha+16c] provides an analysis of the limits from the converter in terms of achievable input and output voltages depending on the choice of submodules. It is reasonable to assume that a MMC with a hybridization of these two types of submodule has an intermediate operating zone between that of an -only MMC and an -only.

The work of [DQV19] introduces a more detailed study in the Park SRRF from a arm-AVM model. The study of the Limits of the Operating Zone (LOZ) is done from three limits: those of the DC bus, those of the maximum operating capacities of the arms of the converter, and those of the AC-side network. This allows us to establish limits in the plane of the active and reactive powers of the AC-side network according to the internal impedances of the arms. This study highlights the need for trade-offs when sizing the inductances: decreasing them increases the region of operation in the active and reactive power plane, but increasing them allows one to limit the currents in the arms, which is needed for safe operation.

Of the models proposed here for the *from arms to the whole MMC* level, which is the high-level, the choice is made to focus on a decoupled model of the currents, relying on (1.9), in order to be able to fully and transparently study, analyze, observe and control each of the current types that flow through the converter during its operation.

1.D Control of the MMC

1.D.1 Control architecture of the MMC

The book of [Sha+16a] which gives quite detailed elements concerning the modelling and sizing of the converter also gives a general framework on how to approach the control of this converter

and the associated control issues that [Zha+21] complements with more recent advances.

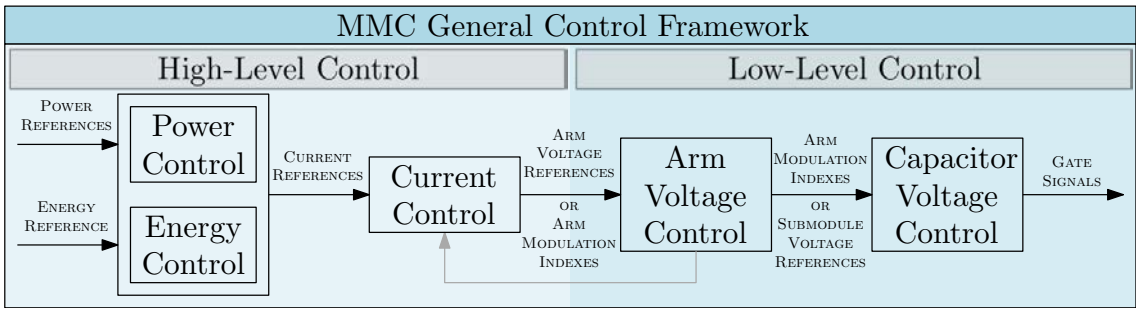

Figure 1.9: Modular multilevel converter general control framework.

The chapter [Sha+16b] describes the different control objectives that the control algorithm MMC faces. As shown in Figure 1.9:

1. The realization of control orders sent in the form of duty cycles or directly from the switching states.
2. The balancing of each submodules capacitor in order to guarantee that the nominal operating region of the converter is reached.
3. Ensure the control of the different types of currents involved in the operation of the MMC.
4. To guarantee the global energy balance between the arms of the same legs and for the legs between them.
5. A last optional objective is to guarantee the reference tracking of the various powers that one wishes to convert by means of the MMC. This objective is general to any type of converter and can be realized without having to adopt a form dedicated to the MMC.

Traditionally, it is the first two objectives that are associated with the low-level control and the following ones with the high-level control although for the high-level control it will often be a question of the third and fourth objectives or even only the third one.

To understand the architecture it is important to note that the list of these different control objectives does not presuppose that the control of the MMC is done by nested controllers, each of which has the role of guaranteeing one of the objectives, in other words it is possible to conceive an architecture of control of the MMC by grouping some of these objectives in a single controller. Moreover, some works assume either that the low-level control is already externally designed and focus on the high-level control [Bou17; Ber+18; Fre+18], or the opposite and focus mainly on the low-level control [Gao+11; Saa+15; Ilv+15b].

Each of these control objectives will be described here by presenting a range of methods used for each. In the classification proposed here, it is considered that the interface between the high-level control and the low-level control is made by a set of quantities at the arm scale. Either the modulation index m_{xy} of each of the arms or the voltage v_{xy} desired at their terminals.

1.D.1.1 Low-level control

The aim of the low-level control is, from the control requirement sent by the high-level control in the form of either modulation indexes m_{xy} or arm voltages v_{xy}, to go as far as the determination of the switching states S_{xyj} to be sent to the gate-drivers of the semiconductors to ensure the

balance of the capacitors while guaranteeing that the references received from the high-level control are reached. Conventionally, in order to carry out all the intermediate calculations, the low-level control is divided into several functions to be guaranteed [Sha+16a; Zam17], as shown on Figure 1.10.

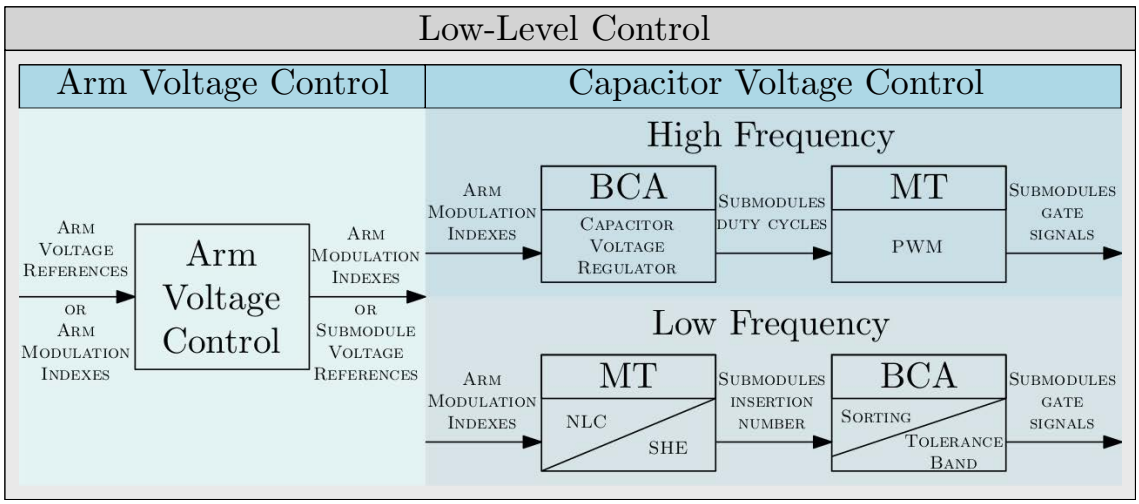

Figure 1.10: Modular multilevel converter low-level control framework with detailed classification of capacitor voltage control schemes.

Arm voltage control

This first function of the low-level control has for role to pass from the level of the arm to the level of the submodules by determining the modulation index m_{xy} from the reference of v_{xy}.

To do this there are different techniques, the first is the *direct voltage control*: $m_{xy} = v_{xy}/V_{DC}$. For the high-level control this is equivalent to having done a simple arm-AVM modelling where it is considered that the behavior of the capacitors is part of an external study, it is assumed that all the capacitors are balanced at their nominal value V_{DC}/N. The beneficial aspect of this formulation is the simplicity of calculation while guaranteeing an asymptotic stability, however parasitic voltages appear in the MMC.

In the case of the *closed-loop voltage control*, the true total voltage available in the capacitors of the arm is taken into account. This solution is implemented by the calculation $m_{xy} = v_{xy}/\sum_{j=1}^{N} v_{C_{xyj}}$. This approach is also relatively simple mathematically if sensors on the set of capacitors are available, which gives it *closed-loop* character. In the case where the measurement of the voltages is not available, a solution of estimation or observation is necessary, it is then qualified of *open-loop voltage control*. In both cases the parasitic voltages are reduced or even cancelled [Ang+11; Ant+14; Har+15]. However, it should be noted that *closed-loop* requires an additional Energy Control (EC) to ensure stability. Hybrid methods combining measurements and direct algebraic relations have also been proposed [Sha+16b].

Capacitor voltage control

As presented on Figure 1.10, the *capacitor voltage control* is functionally made up of a Balancing Control Algorithm (BCA) role and a Modulation Technique (MT) role. As its name indicates, the role of the BCA is to guarantee on the scale of the submodules that the capacitor voltages remain

balanced around their reference value. The goal of the MT is to determine how to modulate the use of the submodules in each of the arms of the converter. Depending on the switching frequency range of the switches, the topology of the *capacitor voltage control* is different. The advantage of being able to operate at low frequency for a multilevel converter such as the MMC is to be able to reduce its switching losses while guaranteeing - by its multilevel character - a good harmonic quality. For such a topology of VSC which can convert up to GW, in order of magnitude, the losses mitigation is a crucial element because even 0.5% of losses on 1 GW it already represents 5 MW.

High-frequency In the case of high frequency, the MT which will be used belongs to the Pulse Width Modulation (PWM) family. This has the consequence of allowing the BCA to work on the duty cycles and not on the state of the switches directly. In this case, from the knowledge of the modulation index of each arm m_{xy}, the duty cycle D_{xyj} of each one of the submodules of the converter are determined in different ways.

Within the framework of the high-frequency modulation technique, the BCA - when it is necessary - is carried out before the MT, see Figure 1.10. From the knowledge of the reference of v_{xy} or of m_{xy}, its objective is to bring the adapted correction to generate duty cycles by guaranteeing the balancing of the capacitors, to then send them to the MT. In [Ser14; Liz+15; Tal+18] an algorithm of BCA of this type where the modulations indices m_{xy} received from the high-level control are corrected by the injection of a small δm_{xy} is proposed. A PI-controller aims at compensating the error on the capacitor voltages which generates a new $m_{xy}{}'$ to ensure an active balancing of the capacitors. This approach is then experimentally verified by [Ser14; Liz+15; Tal+18] on small MMCs.

It has been shown that by using a PSPWM approach to perform voltage reference tracking, capacitor balancing is also guaranteed without any additional control device under certain conditions, the main one being to have a switching frequency high enough compared to the AC network fundamental frequency [Ilv+15b]. Even if this ability has only been proven with this level of detail for this technique of PWM, this does not prevent the use of other methods of PWM by accompanying the MT with an BCA upstream. In this case the MT takes as input the arm voltage reference or the m_{xy} index and determines the switching states.

Low-frequency In the case of the low frequency the MT will determine the index of insertion starting from the index of modulation m_{xy}, this index of insertion represents the necessary number of submodules to include in the arm in order to reach the reference of v_{xy}. Knowing this index of the total number of submodules to insert in the arm, the BCA will judiciously choose the submodules to switch, see Figure 1.10.

One of the most popular methods of achieving the BCA in the MMC is the Nearest Level Control (NLC). The idea of this method is to select the integer number of submodules to be inserted in the arm to reach at the terminals of this last one the voltage closest to the arm voltage reference [LM03] associated from the knowledge of the modulation index of the arm. The study proposed by [TX11] shows the efficiency and the limits of this method as a function of N and of the switching frequency f_s, the larger N will be, the better will be the quality of the arm voltage reference tracking but this must be accompanied by an increase in f_s to be able to make full use of the $N+1$ voltage levels. Compared to a modulation of type PWM, the greater N will be, the less the benefit of using an PWM to have a good harmonic quality will be interesting because it is accompanied by more losses by switching, a method of type NLC will be able to reach a very good harmonic quality with much less losses [Saa15].

The work of [WLK21] presents an interesting general review of Selective Harmonic Elimination

(SHE) methods for capacitor balancing in multilevel converters of which the MMC is a part. The beneficial aspect of these methods, as their name indicates, is to allow the selection of the harmonic content which aims at taking full advantage of the particular capacity of multilevel converters to allow a clear improvement of the harmonic content of waveforms. Compared to the NLC, the latter will determine at a given moment the ideal number of submodules to insert in the from the reference of v_{xy} which is given, whereas the SHE will not only look at the scale of the instant but will have a longer term vision on a horizon of a fundamental period for example and according to the amplitude of the reference of v_{xy}, will associate with each instant of this fundamental period a number of submodules to be inserted with the aim of guaranteeing a certain harmonic content.

To carry out the insertion of the number of submodules necessary as requested by the NLC, it is easy to understand that one cannot simply choose to insert the submodules starting from the first one in the arm and insert them all until the requested count is reached. To do so would have the consequence of ending up unbalancing the capacitors, so a *sorting* of the submodules to be inserted in priority according to the state of their capacitor is introduced by [LM03]. The idea is the following: from the knowledge of the sign of the current arm, when an submodule has to be switched, the choice is made so that the submodules presenting the capacitor voltages the most deviated from their references are inserted if it makes it possible to correct their deviation from the reference. This algorithm of BCA is a solution which was improved afterwards as with the *predictive sorting* [Ilv+15c] where to choose if a submodule is inserted or not the first step is to calculate a prediction of the value that its capacitor voltage will reach by the next sampling period. The submodule is then inserted only if this predicted value is close enough to the reference. This solution makes it possible, for example, to reduce the switching frequency and the amplitude of the voltage ripples compared to the previous method. Other algorithms have been proposed such as that from [Saa+15], based on a sorting of extreme values only. This allows one to strongly reduce the total number of switchings of a same arm.

Another family of technique of BCA is the *tolerance band*. It is a popular method in power electronics because it allows one to simplify the control of these systems by taking into account only one control and modulation step at the same time. The general principle is to switch the switches when it is necessary, i.e. when the quantity to be controlled goes out of the *tolerance band*, which does not guarantee a constant switching frequency. The idea in the context of the MMC is to define a zone in which the voltages at the terminals of the capacitors are desired to remain, and the submodules will be inserted according to whether or not they belong to this zone. Several methods of this type have been proposed for the MMC, focusing sometimes on the average value of the voltages, sometimes on the instantaneous value [Has+15; Has+16]. The suggestion of [Zam+16b; Zam17] is to use the size of the tolerance band as a control input to adapt in real time, which allows one to contain the voltage ripple around the same value whatever the operating point of the converter.

1.D.1.2 High-level control

Overall the high-level control is conceptually simpler because there is less overlap of roles as is the case for the low-level control between the Short and the BCA.

Current control

The objective of the current control stage is to ensure the reference tracking of the different currents in the MMC. This means guaranteeing that the currents I_m, I_s, $\mathbf{I_c}$ and $\mathbf{I_o}$ track their reference by acting directly on the arm voltage references [MLE10; Har+13; Sha+16b; Bou17] or directly on the arm modulation indices m_{xy} for models employing a more complete arm-AVM model [Fre+16b; Ber+18; Ber+19].

Depending on the type of modelling used, if all four types of currents are decoupled, then a current control architecture with four controllers is possible [PRB14; Liz+15]. The configuration of the MMC allows one to associate I_m and $\mathbf{I_o}$ because I_m is the homopolar component that flows towards the AC network, as well as I_s with $\mathbf{I_c}$ because I_s is the DC component of the current that flows in the legs from one side to the other. Thus another architectural possibility is to have two controllers, one for the $\{I_m, \mathbf{I_o}\}$ set and another for the $\{I_s, \mathbf{I_c}\}$ association as implemented by [Ber+18; Har+13; Har+15]. As a result, the Current Control (CC) is reduced to two controllers, one to control the current delivered by the MMC on the AC network and another to control the currents which flow through the arms of the converter. However, an additional controller can be added to act specifically on the continuous component of $\{I_s, \mathbf{I_c}\}$, i.e. on I_s which - being the current taken from the DC bus - is a main actor in the total energy contained in the converter, in order to manage the latter [BSD15; Fre+18; Ber+19].

To ensure the role of the controllers of each of these different types of currents a variety of methods have been proposed, ranging from the most common forms in the industry with the PI-controller [Ser14; Sha+16b; Fre+16a; Ber+18] to the most demanding forms in terms of complexity of real time calculation with the MPC [DGM14; Gey16; Gey+18; FJB19; Yin+20] passing through the PR-controller [Teo+06; Har+15], the IMC [Li+17; Liu+17], the LQR [MLE10; Mün+10; Rak+13; Rak+20], the SMC [Zam17; YSP19], the DBC [Wan+21], and also the CA [Bou17]. These controllers are implemented with different bases, in the stationnary reference frame [Har+13; Saa+13b; Sha+16b; Bou17; Jin+21] or in the synchronous rotating reference frame as for [MLE10; Per+12; Li+17; Ber+18; Rak+20]. This variety of current control approaches represent different methods to guarantee the current reference tracking of different types of currents with different performances and different computation times but a current reference selection is necessary.

Output current reference selection Regarding the AC-side ouput current, it is easy to understand that it can be responsible for the active and reactive power supplied to the AC network. Its reference can therefore be simply determined arbitrarily or by a power calculation. However it can also be used to act on the voltage available at the input of the MMC on the DC bus as shown by [Fre+16a].

Circulating current reference selection This circulating current $\mathbf{I_c}$ being present only in the legs of the converter, it does not directly impact either the current I_s coming from the DC bus, nor the AC output current $\mathbf{I_o}$ and I_m, but it appears in the current of the arm i^*_{xy} in the same way as the latter three. The presence of $\mathbf{I_c}$ in the arm current increases the amplitude of the latter and thus the conduction losses in the arms. As a consequence, an important part of the work on the topic of MMC current control has sought to eliminate this circulating current to such an extent that the name Circulating Current Supression Control (CCSC) has been coined [TXX11; BDS16; Sun+18; Den+20].

The capacity of the active balancing capacitors, which depends directly on this arm current, can be modified according to the circulating current which is a component of it. In other words, the Circulating Current Injection (CCI) can act on the performances of the BCA. The study

of [Ilv+12] confirms it by showing that the presence of a fundamental harmonic component of circulating current is able to act on the balance of the capacitive energy contained in the arms of the same leg, but this component is not the only one to influence the balancing.

In some operating cases it is judicious to inject current into the converter arms in order to act on the balancing of the capacitors [FG19; Pou+15] or for applications such as the supply of variable-speed drives [Den+20]. For example in its experimental test the injection technique from [Pou+15] reduces the ripple of around 30% and [FG19] manages to reduce the voltage ripple from more than one third, with a 2^{nd} order harmonic injection. The work from [Ber15] offers to use offline optimization methods to determine the best CCI to be achieved with respect to a given criterion related to the energy balance of the MMC. The research activities concerning the control methods of the circulating currents are still a active theme today involving trending mathematical approches like [Wu+22].

Energy control

The role of the EC is to guarantee a high-level balancing of the energy contained in the arms. The role of the BCA is to balance the capacitors at the submodules level according to the current i_{xy} available in the arms as seen previously. However, in order to improve the guarantee that the BCA will have sufficient current i_{xy} available to guarantee a sustained balancing of the capacitors, the EC is implemented. Depending on the currents that the CC drives, the EC will use currents for which no reference is yet imposed, and choose one that will allow them to guarantee the BCA the adequate current i_{xy} for capacitor balancing.

Source current reference selection Typically, the main goal of the CC will be to guarantee reference tracking for the current $\mathbf{I_o}$, the circulating current $\mathbf{I_c}$ will follow a CCSC or CCI scheme and the common mode current I_m - when its existence is possible - will have a zero reference in order to guarantee the balancing of the capacitors. The closed-loop can then play on the reference of the current I_s taken by the converter on the bus in order to guarantee the maintenance of the global level of energy in the converter at its reference level, as is done by [Liz+15; Fre+18].

The use of a closed-loop EC is not mandatory for certain configurations of the converter. Indeed, as shown by [Fre+18] with its first control architecture which does not have one, it is possible to ensure a stability of the voltages at the level of the capacitors in steady-state, but without a EC the value reached by the capacitors in steady-state varies according to the current called by the AC network. [Ber+18] obtains the same result of being able to guarantee a perennial balancing of the global energy contained in the MMC with an open-loop EC.

For global energy balancing in the converter, the above approaches realize a control of the total energy amount of the converter. However, other approaches propose to perform energy balancing in the arms with the notion of *vertical* and *horizontal* or $\Sigma - \Delta$ control of the energies [AÄN09; Har+15]. The idea is to make sure that the energy difference between two arm of the same leg balances around zero and that the total energy contained in the leg follows the nominal reference. From an energetic point of view, this approach is in direct bijection with the solution where an energy control is ensured in each arm. But the beneficial aspect of this approach is to be able to decouple the control of the Δ energies from the Σ energies, in fact, the circulating current will be responsible for the exchange of energy between the arms of the same leg whereas the current I_s acts on the total energy of the leg.

1.D.2 | Families of control architectures for the MMC

As mentioned at the beginning of Section 1.D.1, the control architecture of the MMC must ensure a certain number of roles that we have just identified and specified. These roles can be performed sequentially in the same order as presented by Figure 1.9 but it is possible to adopt joint or globalized control approaches where the management of several electrical quantities is done simultaneously. The Figure 1.11 shows some of the other major approaches that can be considered.

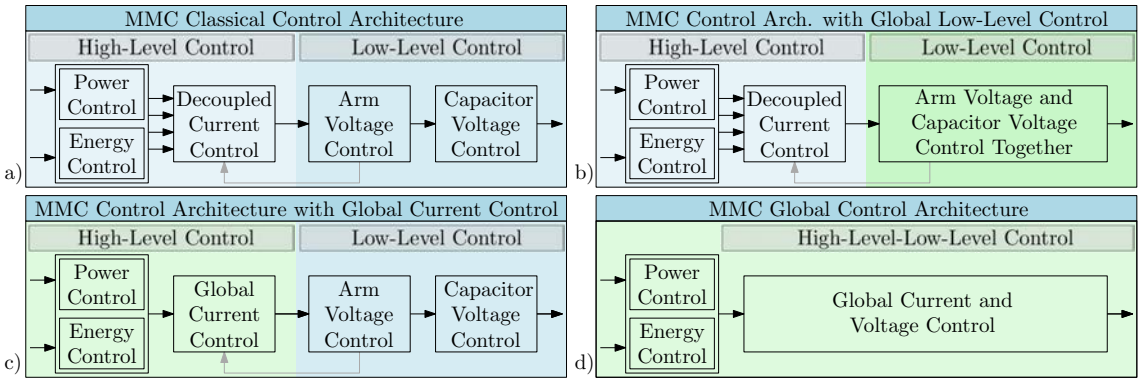

Figure 1.11: Modular multilevel converter major control architectures.

Among these four architectures, the a) is the most used and the most encountered, both in the literature [Ser14; PRB14; Liz+15; Sha+16b; Ber+18] and industrially, because it is the one that presents the easiest implementation. However, the other architectures have undeniable beneficial effects on the ability to guarantee a better control performance of the MMC thanks to the mutualized consideration of the different electrical quantities and dynamics that interact in the converter. More details are given in the work of [Gey16] for the case of architecture c), and in those of [RGM15; MAR19] for architecture d). The work from [BFB19] provides a low-level control solution that has the shape of that from architecture b).

1.D.3 | MMC fault tolerant control

As the MMC is a topology that has the capabilities of having a large number of submodules, one can legitimately wonder if such a converter can have a fault tolerant behavior and if it is capable of reconfiguration in case of faults. [LLB13] proposes a nice nomenclature of the set of faults that can happen at the level of a MMC-based power conversion system ranging from faults at the submodules level (e.g., a semiconductor short circuit) to faults at the converter and system level (e.g., DC pole-to-ground). More details about this topic are given in Section 5.E.

1.E | Control allocation methods for overactuated systems

The control allocation problems can be characterized by the fact of willing to control a system having more control variables (*inputs*) than state variables to be controlled (*outputs*), while taking into account constraints on the control variables (*input saturations*). Physically this means that the same output can be influenced by several inputs, the system is then qualified as *overactuated* or that these inputs are *redundant*. This general definition appeared a posteriori [Dur93] but it describes well the control problem which is at the origin of the control allocation [Cun83].

As highlighted by [Cun83], at that time, to control the trajectory of an airplane, the practice was to use the aerodynamic surfaces of the airplane which one knows, by expertise or piloting experience, the effect they have on the flight dynamics. For example, to apply a rotation around the pitch axis, the pilot uses the elevator, for roll: the ailerons and for yaw: the rudder. This works effectively in practice, however with the means of study that have been developed since the advent of aviation, it is observed with the help of models and tests that each of these aerodynamic surfaces will not only generate a moment along one single axis but an effort along several of these axes.

During the development of aircraft in the 21st century, guided by the desire to ensure safe flight, aircraft manufacturers have designed aircraft with a certain level of redundancy for the most critical parts. This is to ensure continuity of operation even when some of the subsystems fail. Thus, aircraft have been equipped with a multitude of aerodynamic surfaces to ensure flight path control even when an actuator failure occurs. Some aircraft with more sophisticated designs may even have more actuators and degrees of freedom for their control such as flaps, spoilers, and slats; V-tails that give coupled lateral and longitudinal forces, or tiltable propellers, and thrust vector jets for example. In normal flight, the aircraft uses the main flight surfaces and when one of them fails, the corresponding secondary flight surface is used. In the 1980s, a double observation was made: 1) the aircraft has flight surfaces that are capable of generating an effort that does not have a single component along one of the flight axes but a main component with additional components of lower amplitude, 2) the aircraft has redundant flight surfaces of which only a part is used when it is in normal operation.

It is then that the reflection proposed by [Ryn83] comes in: couldn't is be possible to use all the flight surfaces - primary and secondary - in the different flight modes - normal and faulty - and thus take advantage of the secondary surfaces, most often unused, also in normal flight mode ? By distributing the effort in this way, the load of the main surfaces would be less for the same mission profile, which could be beneficial for the onboard energy consumption. Moreover, knowing the effort components that each aerodynamic surface is capable of generating, it would be interesting to have a combined use, and determined intelligently, of these surfaces in order not to generate useless efforts that it is then necessary to compensate by the use of another flight surface. To seek to use all the redundant aerodynamic surfaces together with a single objective of tracking a flight trajectory is therefore the first problem of control allocation that is stated: the system has more control variables *control surfaces multiplicity* than output variables to control *flight trajectory* and these control variables have saturations *deflection limitations* [Lal85; SGE90]. The goal is therefore to control an overactuated system by taking into account the constraints of the control variables [Dur93].

1.E.1 | The control allocation problem

More formally, by setting $\mathbf{U} \in \mathbb{R}^{n_u}$ the control vector - also called the vector of real control inputs -, $\mathbf{a_d} \in \mathbb{R}^{n_a}$ the desired action vector - also called the vector of virtual inputs - and $\mathcal{M} : \mathbb{R}^{n_u} \mapsto \mathbb{R}^{n_a}$ the function representing the effectiveness of the control, i.e., the influence of the control $\mathbf{U}$ on the system to be controlled. The objective of the allocation methods is to find the control $\mathbf{U}$ that verifies the allocation equation while respecting the constraints of the command. The Control Allocation Problem (CAP) is then stated:

$$CAP : \{\mathcal{M}(\mathbf{U}) = \mathbf{a_d} \mid \mathbf{U}_{min} \leq \mathbf{U} \leq \mathbf{U}_{max}\} \tag{1.11}$$

control allocation refers to a family of control methods that have taken different formalisms in the literature : [Lal85; Bod02; JFB04; Gro94] but in general these approaches all converge towards

the same formulation which is described by (1.11).

1.E.2 The control allocator

Allocation problems are encountered when it is necessary to distribute the effort required to achieve a control objective among a set of control variables. This type of problem was first encountered in aeronautics when the guidance indicates a trajectory to follow and that to follow this trajectory it is necessary to generate a moment and a thrust. To generate this effort, the role of the allocator is to distribute it to all the control surfaces and thrusters, taking into account their limitations. It then sends each of the control input values to the devices which will steer the control surfaces and drive the thrusters correctly. It is then understood that solving the allocation problem is at the heart of a more global flight control law which will indicate the effort to be provided.

We therefore designate as *allocator* or *control allocator* the device which, within the control architecture of the system, will have the role of solving the CAP.

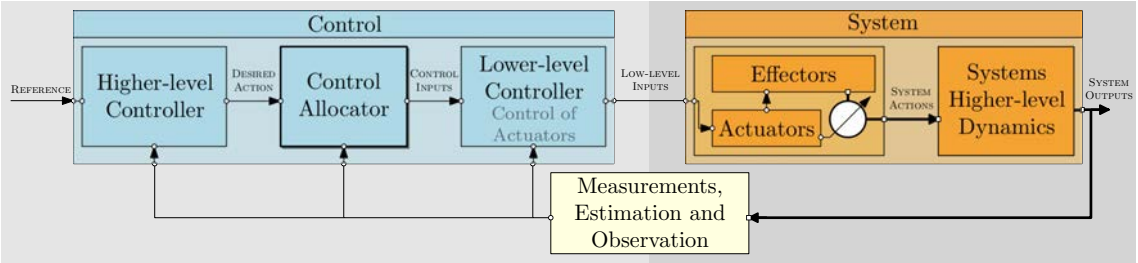

Figure 1.12: Control allocation general framework.

The Figure 1.12 proposes a block diagram illustrating the integration of the allocator in a general control architecture of a dynamic system. The role of each block is presented below. The Figure 1.13 gives an application example of this control architecture using allocation methods.

Higher-level controller From the reference tracking objective imposed externally on the whole control law, the higher-level control must determine the desired action vector necessary to achieve the requested tracking performance. This desired action vector is sometimes called virtual effort because it aggregates under a single mathematical entity a set of internal behaviors of the converter which, from a higher-level point of view, are not interesting to be taken separately and a single variable to represent them is sufficient. **Application:** in electrical engineering one can take the example of a circuit feeding a resistive-inductive load from several buck converters connected in series as shown on the right side from Figure 1.13. The higher-level controller would be the current controller that, from the knowledge of the current reference, computes the desired total voltage which is not a voltage that can be acted upon directly, one is obliged to pass through a localized action on each of the output voltages of the buck converters to achieve this. This total voltage is not a voltage directly controllable. Thus, it can be considered as a virtual voltage, and from the high-level point of view it is the total voltage that matters for the current and not each of the independent voltages.

Control allocator In order to guarantee that the desired action vector is reached, the allocator will then distribute the requested control effort among the control inputs while making sure that they do not exceed their saturation. In some cases rate limitations are also taken into account. It is important to note that initially the allocator has no vocation to deal with the dynamics of

actuators or effectors, so one will traditionally see allocation presented as a *static* process and the works that take into account the behavior of actuators and effectors will generally specify that they do *dynamic* allocation[1]. **In the proposed example**, the purpose of the allocator is to distribute the total voltage desired across the load between each of the buck converters, it can then determine each of the three voltages, or the duty cycles taking into account the fact that the sources are not all identical, in both cases those are *static* allocators. At this point we face the following problem: all the converters must generate a total voltage of v^{ref}. And we have several duty cycles to achieve this control objective. Therefore, the case of a control allocation problem defined by (1.11) is found. A trivial solution would be to make each converter generate $v^{ref}/3$ but this is without taking into account the parameters of each of them which will never be identical in practice. By taking into account the voltage E_k of each source, the resistance R_k associated with them and the imposed duty cycle boundaries, one soon realizes that the solution is non-trivial. In order to bring the allocator to choose physically interesting solution one can also add a criterion on the ohmic losses in each resistance R_k.

Lower-level controller In allocation terminology, the devices that modulate each of the distributed efforts are called *actuators*. The control commands sent by the allocator to each of the actuators must be guaranteed to be tracked and regulated. For this, an internal control loop of each of the actuators is necessary. This is the role of the lower-level control. **For the given example**, this corresponds to the realization of the duty cycles with a PWM technique.

Actuators and Effectors In the vocabulary of the CA, the *effectors* are organs capable of generating efforts that the *actuators* then modulate. The control orders sent by the control algorithm will then be received and carried out by the actuators by channelling the effort supplied to them by the effectors. **In our example**, the effectors are the voltage sources and the actuators are the switching cells of the buck converters that modulate the voltage of each source to generate the output voltages.

System dynamics The effort thus generated by the combination of actuators and effectors will act on the system dynamics in order to reach the initial control objective. **For the considered electrical system**, this amounts to acting on the current through the total voltage generated at the terminals of the load.

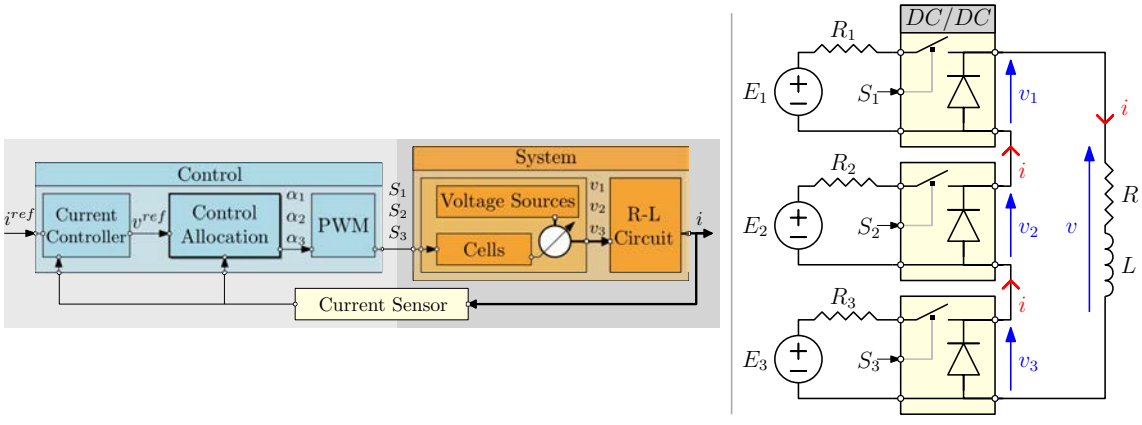

Figure 1.13: Suggestion of a control architecture based on control allocation for a 3-input 1-output electrical system example.

The diagram of the allocator within a control architecture of any system, shown on Figure 1.12,

[1] The use of the term *dynamic* accompanying the notion of allocation is not consensual and involves a diversity of at least four different definitions specified in paragraph 1.E.3.5.

is a general representation allowing to identify the role of the allocation methods in the traditional case. However, it is worth noting that this architecture is not rigid. First, this architecture is modular. In other words, several loops containing each one an allocator can be implemented. Secondly, the allocator is not constrained to hold an intermediate position. Depending on the system to be controlled, the allocator will hold a higher or lower position in the control architecture hierachy. For example, in our electrical system, it is as if the allocator determined the state of the switches directly and not the duty cycles.

Before going into more detail on the different families of allocation methods, it is valuable to highlight the review work on the CA methods, which gives an overview of the different works in the field of these control methods before getting into their development and use. The work of [JF13] provides an overview of the different methods as well as the solving algorithms that are used depending on the nature of linearity of the system under study. A range of technological fields of application of these methods is also proposed. The study of [Bod02] presents in detail a variety of Model Inversion Based (MIB) and Error Minimization Online (EMOn) methods with optimization-based solving algorithms using Linear Programming (LP) and Quadratic Programming (QP). A comparison of the approaches allows us to identify the benefits and drawbacks of each. Finally, the work of [Här03] gives application examples of the CA to small systems while still overactuated. This allows a visual understanding of how the allocation works.

1.E.3 Families of CA methods

1.E.3.1 Model-Inversion-Based methods

The definition of the CAP from (1.11) is valid for both linear and nonlinear systems, but early work focuses on solving the allocation problem in the linear case or, at a minimum, in the nonlinear case linearized around an equilibrium point. In these two cases (1.11) becomes:

$$\{M\mathbf{U} = \mathbf{a_d} \mid \mathbf{U}_{min} \leq \mathbf{U} \leq \mathbf{U}_{max}\} \tag{1.12}$$

Where $M \in \mathbb{R}^{n_a \times n_u}$ stands for the effectiveness of the control in the case of a linear or linearized system.

From inverse to generalized-inverse methods

The first allocation methods capable of solving (1.12) did not take long to arrive in the 1980s, indeed a simple inversion of the matrix M makes it possible to calculate $\mathbf{U}$, hence the name MIB:

$$\mathbf{U} = inv(M)\ \mathbf{a_d} \tag{1.13}$$

Where $inv(.)$ represents the matrix inversion operation here. However M is not always invertible since the case $n_u = n_a$ is, by definition, quite rare in allocation problems. The first allocation methods that appeared were therefore based on the inversion of the matrix M, however in the case of overactuated systems one will be much more often in the case where $n_u > n_a$. The allocation methods based on the Pseudo-Inverse (PI) of matrices are then implemented [KH83; Lal85; MGB89; SGE90] to take into account the cases where M is not square or not of full rank.

$$\mathbf{U} = M^{+}\ \mathbf{a_d} \tag{1.14}$$

With $M^{+} = M^{T}\left(MM^{T}\right)^{-1}$ the pseudo-inverse matrix of M in the case where it is of full rank. This solving by matrix inversion does not necessarily allow one to see immediately that $\mathbf{U}$ is

then the solution of a rather simple quadratic programming problem [FS91] which is put in the form:

$$\min_{\mathbf{U}} J = \frac{1}{2}\mathbf{U}^T\mathbf{U} \;\; under \;\; the \;\; constraint \;\; M\mathbf{U} = \mathbf{a_d} \tag{1.15}$$

The quadratic optimization performed is then an optimization aiming at minimizing a least-squares cost function which depends on the control. Formulations of the pseudo-inversion method progressively lead to a more complex optimization:

$$\min_{\mathbf{U}} J = \frac{1}{2}(\mathbf{U}-\mathbf{U}_p)^T W(\mathbf{U}-\mathbf{U}_p) \;\; under \;\; the \;\; constraint \;\; M\mathbf{U} = \mathbf{a_d} \tag{1.16}$$

Where $\mathbf{U}_p$ is a value of the control vector that it is desired to prioritize, to achieve a given behavior that minimizes energy consumption for example, and $W \in \mathbb{R}^{n_u \times n_u}$ is a positive definite weighting matrix that prioritizes the different control inputs, which gives the name Weighted Pseudo-Inverse (WPI) to the allocations using it. The solving is done by Generalized Pseudo-Inverse (GPI) from optimality conditions using LAGRANGE multipliers [Dur93; Enn98; SGE90; VB94] and gives the following solution in the case where M is full-rank:

$$\mathbf{U} = \mathbf{U}_p + N\left(\mathbf{a_d} - M\mathbf{U}_p\right) \tag{1.17}$$

With $N = W^{-1}M^T\left(MW^{-1}M^T\right)^{-1}$. For the case where M is rank-deficient, several methods have been investigated such as *damped least-squares inverse* or the *singular value decomposition*. The first solution uses a small slack variable ε that must be strictly positive when M is rank-deficient, and N is updated to $N = W^{-1}M^T\left(MW^{-1}M^T + \varepsilon\mathbb{I}\right)^{-1}$. As well as the *damped least-squares inverse* method, according to [Lev17], this *singular value decomposition* method can also be used when M is of full rank. However in the case where it is necessary to update M in real time for time varying systems, it is faster to make a QR decomposition for that to make a pseudo-inversion [Här03].

All these methods are based on the principle of inversion illustrated by the equation (1.13), so if a desired action $\mathbf{a_d}$ by the system has too great an amplitude, it is possible that the control $\mathbf{U}$ will also reach a very great amplitude at the risk of exceeding the limits admissible by the actuators. The quick solution to this problem is simply to clip the components u_i that exceed their boundaries on right on their boundaries. But this leads to obtaining an action vector $\mathbf{a}$ which is different from the desired action vector $\mathbf{a_d}$ since the values finally given to $\mathbf{U}$ are not those coming from (1.13) but the latter to which a post-processing has been applied to ensure that the bounds are not exceeded so there is no longer any guarantee that the allocation equation (1.12) is verified.

Redistributed-pseudo-inverse methods

New allocation methods are then introduced which are based on the principle of redistributing the missing effort $\delta\mathbf{a} = \mathbf{a_d} - \mathbf{a}$ on the other control variables u_i which are not yet saturated. These methods are based on the fact that when the control variables u_i start to reach their saturations, they do not all reach their limits at the same time, there are still $u_{j\neq i}$ which are still free. The principle consists therefore in using these control variables $u_{j\neq i}$ initially calculated ideally by (1.13) and which, being not saturated, still represent a degree of freedom. They are then adjusted to try to get as close as possible to the cancellation of δa, which is $\mathbf{a} = \mathbf{a_d}$.

Adaptive weighted pseudo-inverse A first solution directly in continuity with the previous ones, that [BM02; YSX16] implement, is to use a pseudo-inverse by adapting the weighting matrix

W in the course of time to take into account the limitations of the control and the rate constraints, it can be considered as an adaptive WPI.

Redistributed pseudo-inverse Another solving algorithm is studied by [Dur93; VB94; IP06; Shi+10; ASC19]. In this case the determination of the control is done in several steps, the first step of the redistributed pseudo-inverse method is to perform a pseudo-inversion or a generalized inversion in order to solve the unconstrained control allocation problem. If the obtained solution does not saturate then it is kept which is optimal from the point of view of the preceding criteria and the allocation is done, in the contrary case, a second stage takes place: the saturating u_i are frozen at the exceeded bound and the u_i still free are used to reduce the gap between the references to be reached and what the staturated u_i already allow. This step is then repeated until the first of the two conditions having all the u_i saturated or $\delta \mathbf{a} = 0$ being satisfied.

Daisy chaining Another method is introduced as an alternative to the RPI [Ada+92; BE96; BE92]. The u_i are grouped by packs, each pack is assigned a priority number. The allocation is then calculated so that the group with the highest priority satisfies the allocation equation, if this is the case without saturation of the u_i, then iterations are stop there and the u_i of the other packs will not have been used. In the opposite case, when some u_i of the first pack saturate, the current pack is frozen and the algorithm moves on to the next priority pack: they must be calculated to satisfy the allocation equation, taking into account the fact that the u_i of the first pack now have values which are assigned to them. If the u_i in this pack are saturated, then the logic is continued by moving on to a new pack, otherwise the alogirthm stops here and send the control.

Exact null-space Another solution analyzed by [KH83; BD95a; MLY20] tries to take advantage of the null space of M to allow itself a virtual saturation which has no effect on the generated action vector. The first step also consists in applying the generalized inversion, then in the case where the control exceeds its saturations, the computed control receives the add-on $\delta \mathbf{U} = \alpha \; ker(M)$ to make the allocated control $\mathbf{U} = pinv(M) \; \mathbf{a_d} + \alpha \; ker(M)$ complies with its bounds without affecting the achievement of $\mathbf{a_d}$ since $M \; ker(M) = 0$. The scalar α is then determined so that the control $\mathbf{U}$ applied to the system remains between its bounds. However this is only possible if $ker(M)$ has the power to act on all the u_i that reach their limits, and that the unsaturating of one of the u_i by adding $\delta \mathbf{U}$ does not saturate another component of the control vector.

With these redistribution methods better results are obtained than with the simple inversion methods since one can have a better guarantee that the desired action will be reached. But overall, the inversion methods take into account the bounds on the control variables, which decreases their efficiency. The iterative mechanism of RPI gives suboptimal solutions and one cannot guarantee the optimality of the solutions because one bounds oneself by successive steps on the freedoms of u_i [Bod02]. Concerning the DC, the solutions that is found with this method are necessarily sub-optimal because of the fact of fully exploiting several subsets of u_i and not all the u_i in one go [Här03].

Generally speaking, concerning this family of CA methods, the methods based on the principle of model inversion are rather simple and quick to implement, which explains why they are the most popular family of methods in the literature and are still used today [WY22]. However, although some of them are associated with an optimization criterion, they do not present a real optimality to determine the control to allocate in real time compared to the other available methods because they do not take into account the constraints *a priori* [Bod02; Här03]. However, redistribution

methods are slightly more efficient because they aim to take these into account, but their iterative process makes them slower and more complex to develop. *These identified characteristics allow to fill the comparative Figure 1.15.*

1.E.3.2 | Minimization online methods

To improve the efficiency of the allocation, methods based on online optimization appear, helped by the increase of the performances of the real time computers. The objective of these methods is to take into account the constraints of the control *a priori*, and therefore to consider the allocation problem (1.12) as a whole from the start and not just the allocation equation separately from the limitations of the control. Since one cannot guarantee that the allocation equation will always be verified, because of the bounds of the ordering variables, it is necessary to allow for a deviation from the realization of (1.12), the ordering deviation $\mathbf{e}$ is then introduced:

$$\mathbf{e} = M\mathbf{U} - \mathbf{a_d} \tag{1.18}$$

The first objective of the optimization is to minimize a criterion function of $\mathbf{e}$ under the constraint of the bounds of the control as well as the model of the system, in other words, the capacities of the control $\mathbf{U}$ to achieve $\mathbf{a_d}$.

Direct allocation methods

A possible approach to realize this optimization in real time is the Direct Allocation (DA) [Dur93] it consists in making sure that the $\mathbf{a}$ reached is at least collinear to $\mathbf{a_d}$. The determination of the control solution $\mathbf{U}$ is done in two steps: the first is to find $\mathbf{U}$ solution of the allocation equation by the methods of PI, WPI, or GPI. If $\mathbf{U}$ does not saturate then it is applied, otherwise this solution $\mathbf{U}$ is forgotten and the following optimization is solved in real time:

$$\begin{cases} \max_{\mathbf{U},\alpha} J = \alpha \\ u.c. \quad M\mathbf{U} = \alpha\, \mathbf{a_d} \\ \qquad \mathbf{U}_{min} \leq \mathbf{U} \leq \mathbf{U}_{max} \\ \qquad 0 \leq \alpha \leq 1 \end{cases} \tag{1.19}$$

This idea of conservation of the vector orientation is quite interesting in the case of the notion of generated effort and of CA used for motion control. Because in the case of saturation and failure to reach the effort vector required to give the system a certain acceleration, the fallback solution will be one that gives an effort in the same orientation and therefore an acceleration that goes in the direction required even if it is less than that desired by the higher-level control.

Compared to the first solving algorithm [Dur93] improvements have been made that are based on various data structures, enumerations and representations [Dur94a; BD95b; Dur94b; Dur99] and also LP [Bod02; PB05]. However, when using this method, it is necessary that $\mathbf{U} = 0$ either feasible and if ever two u_i have a collinear effect on the respect of the allocation equation then it will be necessary to modify their weighting in the criterion in order not to encounter an indetermination [Här03]. In the case of nonlinear systems, the formulation is relatively similar [VD01; DS02; BD04b], but the use of other optimization algorithms allow the consideration of nonlinear constraints and criteria.

Error minimization online methods

In the case of the EMOn, the determination of the control $\mathbf{U}$ is done directly by real time optimization at each sampling period of a criterion which depends directly on the deviation from the allocation equation $\mathbf{e}$:

$$\begin{cases} \max_{\mathbf{U},\mathbf{e}} J = f(\mathbf{e}) \\ u.c. \quad M\mathbf{U} = \mathbf{a_d} \\ \qquad \mathbf{U}_{min} \leq \mathbf{U} \leq \mathbf{U}_{max} \end{cases} \tag{1.20}$$

But a second optimization criterion can be formulated to represent the preference that $\mathbf{U}$ take the value $\mathbf{U}_p$: $J = g(\mathbf{e}, \mathbf{U}_p)$ [Bod02]. Functions $f(\cdot)$ and $g(\cdot)$ depend on the programming formulation choice, the most proven possibilities are discribed below.

Linear programming A first approach is with the use of LP [Par89; Bod02]. This corresponds to a cost function using $l1$-norm, ∞-norm or a combination of both, the optimization is then put in the form by reformulations into the standard LP forms via the introduction of slack variables. The most common solvers are the Simplex, Active-Set and Interior-Point methods [NW99]. A motivation for the choice of $l1$-norm is that in general, a LP can be solved faster than a QP [Bod02; Här03]. [Bod02] develops a Simplex algorithm dedicated to CA by caring about the cycling behavior that may appear [Dan51] and implementents an anti-cycling procedure. It then shows that the complexity is undoubtedly within the capabilities of current embedded computer hardware technology. When comparing LP with QP, $l2$-norm as well as ∞-norm will tend to use more u_i and in a balanced way while the $l1$-norm will tend to use as little as possible of u_i and at the maximum of their potential [Här03; FBA09; FB10; BF11]. The $l1/\infty$-norm mix appears to be more robust to actuator failures and less sensitive to nonlinearities of the system. $l1$-norm and $l1/\infty$-norm show similar computation time, which is explained by the fact that both are based on LP [FB10].

Quadratic programming With the $l2$-norm, the control allocation problems leads to a QP that are solved with numerical algorithms like Active-Set or Interior-Point [Här03; PB05; PB06]. An iterative Fixed-Point Method has also shown to be efficient in some cases [Bur+01]. However, the Fixed-Point Method has shown to be recursive and long to converge in addition to being very sensitive to $\mathbf{a_d}$ [Bod02; Här03; FB10]. The Active-Set is an iterative algorithm which, starting from the unconstrained solution, searches for the optimum solution iteratively by activating the violated constraints and deactivating those corresponding to search directions [NW99]. Active-Set has a very good convergence rate which is helped by the warm restart capability of [Här02a; Här03], and provides quality suboptimal solutions. About Interior-Point now, the more decision variables there are, the faster Interior-Point is compared to Active-Set, and its convergence rate appears to be more constant according to the number of variables [Här03; FB10; PB05]. In addition to these algorithms whose performance has been proven, new ones have recently appeared in CA [Liu+21] using the Operator Splitting Quadratic Programming [Ste+20] whose comparison with previous algorithms in CA may be an interesting prospect for investigation.

Nonlinear programming The use of nonlinear programming for control allocation was proposed in [JFB04; Poo+04]. In [JFB04] it was shown how formulations similar to (1.20) could be addressed by locally approximating the cost function by a quadratic cost function, and linearizing the constraints. Compared to conventional control laws, [Bur+01] shows that this control allocation approach is more effective. control allocation with nonlinear models are studied using NLP in [Ma+08]. A Nonlinear Programming (NLP) approach to nonlinear constrained control allocation is performed in [TJ05b], which uses a multi-parametric NLP solver that shows computational effectivness.

Although developing a generic nonlinear CA algorithm capable of adapting to any cost criterion, model and type of constraints, it is relevant to study dedicated control allocation formulations for specific subclasses of systems, nonlinearities and constraints. By designing a CA algorithm tailored to systems with given properties it is possible to have allocation solvers that converge to optimal solutions much faster without excessive computational effort.

Mixed integer linear programming In some cases of systems, it happens that it is possible to formulate the allocation problem in the form of a MILP using piecewise linear functions [BD04a]. In this case it is a Branch-and-Bounds, mixed-integer program is much more difficult to solve than a LP. However, efficient simplifying approaches have been proposed such as enumeration methods of discrete possibilities in association with QP. It enables to solve practical nonconvex control allocation problems [Joh+08; RS09]. MILP is particularly suitable when system has discrete control as in a spacecraft with reaction jets that are on/off input variables [DGN09].

This family of methods involving online optimization are more complex to develop and slower to execute in real time compared to the family of inversion methods, however they are ahead of them on the overall efficiency to solve (1.12) since they take into account the constraints from the formulation of the online optimization. *These identified characteristics allow to fill the comparative Figure 1.15.*

The work on allocation methods has now reached a stage where, starting from simple and fast methods, it is now possible thanks to online optimization methods to solve (1.12) fully and efficiently. So the control allocation problem initially raised would finally be solved after about twenty years of work ? No, because the methods using optimization algorithms are quite efficient but the real time execution represents a certain cost in computational resources. The question then arises as to whether it would not be possible to design a new family of allocation methods that would guarantee the optimality of the solution while requiring less computing capacity in real time.

1.E.3.3 Error minimization offline methods

The Error Minimization Offline (EMOff) allocation methods are developed in order to ensure the optimality of the solutions with less computation in real time. The principle of these methods is to start from a model of the dynamics of the system that is sufficiently faithful to then formulate the optimization to be carried out and then solve it analytically in order to deduce a deterministic expression for the calculation of the control $\mathbf{U}$. However, although the model of the system used is faithful, it is always possible to have small deviations from reality, disturbances or modelling uncertainties that alter the performance of the system. Thus, after analytically calculating the solution of the optimization, the implementation also takes into account a procedure of updating the control in real time in order to make it converge, in spite of the possible disturbances, towards the optimum which is then adapted according to the state of the system [Joh04; Lia+07; TJ08; TYK17; CB19]. This convergence is then guaranteed by the intermediary of a function of Lyapunov judiciously chosen and which is expressed from the Karush Khun Tucker (KKT) conditions of optimality [Kar39; KT51]. Avec with such a method, the convergence to the optimum should be asymptotic, however these methods are adapted to ensure a convergence in a finite and controlled time to the optimum [Lia+07; Ben+09].

Dynamic optimization seeking [Joh04] formulates the nonlinear optimization control allocation as a control LYAPUNOV-function and use LYAPUNOV-design methods. The effects of internal dynamics and minimum phase properties are studied in [Ben+09]. Disadvantages of the dynamic optimization seeking methods include possible convergence problems in case of non-convex cost function and constraints, similar to the NLP approach.

Adaptive control allocation [TJ05a; TJ08] propose an adaptive approach where uncertain parameters in the model are stably adapted using an adaptation law that is designed by augmenting the control LYAPUNOV-function in a standard way. This framework was further extended by [TJ07; Lia+09]. [TYK17] shows that the proposed adaptive control allocation method will not violate the ordering constraints. An advance of the method is proposed for a discretized implementation by [TY21].

Although very efficient from the point of view of the solution obtained compared to (1.12) and requiring little computation time in real time, compared to the different families of methods presented, these are among the most complex to develop and implement. *These identified characteristics allow to fill the comparative Figure 1.15.*

1.E.3.4 Artificial intelligence methods

The now rapid expansion of the development of artificial intelligence has also spread to the allocation methods with the Artificial Intelligence (AI) control allocation. However the first allocation methods using artificial intelligence are not so young, first works date from the 1990s [Gro94] in the laboratory of Dr. Wayne C. Durham. For the moment it is possible to classify the works in two branches.

Articifial neural network allocation As in the case of [Gro94], the first methods to be developed are those using a neural network whose goal is to learn the optimal relation between the requested action and the value to be allocated to the control [Sku+18; Hua+18; Kha+22]. These allocation methods are based on a single neural network. The results obtained by [Sku21] do not show much difference on the application case compared to the GPI, the advantage of the ANNA remains however to be trained offline and can thus be fast to be executed in real time, which is confirmed by [Kha+22]. However if an actuator becomes faulty online, the ANNA is not able to adapt on its own, it should first have been trained offline with that actuator down. Moreover, with the proposed formulation the input saturations can be violated online even if the ANNA was trained not to, so the constraints would need to be enforced in this case. [Kha+22] makes a comparison of this method with the EMOn QP, the efficiencies are comparable but the trained network is much faster to converge to the optimal solution in real time for this class of systems whose nonlinearity is considered.

Reinforcement learning allocation But there is another trend that is emerging: the use of reinforcement learning [SB18] for the CA. The idea here is to use two neural networks that feed each other: the l'*Actor-Critic*. This allows, in real time, both to learn the dynamic behavior of the system and to optimally steer by maximizing a reward function, which is similar to the opposite of the cost function to be minimized for the optimization-based allocation methods seen previously. Overall, the use of artificial intelligence for the CA still has some potential since it has been little explored so far [VK19; KLL20]. The method of [KLL20] starts by establishing a

state model of the allocator, the state vector of the allocator is then used to design an optimization criterion that depends on the control and an additional penalty representing the constraints to be satisfied. Together, the state model of the allocator and the optimization criterion form a dynamic programming problem. The solution is then done by model-free RLA in real time which aims at learning the best allocator state-space model input vector.

From the studies carried out so far, it is shown that these methods are efficient to solve (1.12) and require very little computation time in real time. They nevertheless require a training time that the other families do not have. These approaches remain among the most complex to develop and implement.

However, at the moment, the methods of artificial intelligence based on CA present too few elements of comparison with the other families of methods to draw general comparative conclusions, which opens perspectives of investigations and improvement of the existing. Their efficiency compared to other methods remains to be proven. *These identified characteristics allow to fill the comparative Figure 1.15.*

1.E.3.5 | Dynamic control allocation

Until now, the families of methods presented have been presented without any particular distinction between *static* CA and *dynamic* CA. This is because for the majority of the presented methods, they are formulated in the form of *static* allocation but can be just as well implemented in the case of one of the possible forms of *dynamic*. However, it is necessary to draw the attention of the reader to the fact that the notion of *dynamic* allocation can represent a wide range of definitions. In the context of allocation, *dynamic* is used to mean:

- The fact that the dynamic lower-level of actuators and effectors is taken into account [TJ07; TJ08; TJ10]. The objective is then to always determine the same control but taking into account the lower-level dynamic behavior to better anticipate the actions to be taken on the system.
- In the case where the allocator has its own dynamics in the form of a state model for example [Zac09; Boa+10; KLL20; Lim+21b; Lim+21a].
- In the case where the allocation equation contains a desired action vector that aggregates past values of the system behavior over a given time horizon to determine the future control to allocate [Här02b].
- That the allocation, which is well implemented on a static system model, is accompanied by a law of dynamic update of parameters in real time, as it is the case for [TN11] based on the work of [Joh04].
- That the optimization carried out is done in real time, on line, in concordance with the works of Bellman on the dynamic programming [Bel56] as [KLL20] does.

A dynamic control allocation approach is presented in [Zac09]. It is designed to allocate the control effort while the superfluous input variables are allocated through a dynamic allocator state-space model that can be tuned for optimizing secondary objectives and constraints. The work from [Lim+21b; Lim+21a] extends this dynamic allocation method to a more general scenario, including the capability to deal with a wider class of cases and implementing an optimization that makes it possible to minimize energy consumption in the actuators. This extension is made

possible thanks to the co-design of an allocator along with an anti-windup strategy for the global controller of the system.

1.E.4 | Comparison and combination of the CA with the MPC

When the focus is on allocation methods and more particularly on methods of type EMOn, the control allocation then appears as a real time optimization control method in the same way as the Model Predictive Control (MPC). It may therefore be interesting to highlight the differences between these two approaches to control.

On the one hand the MPC [Ric+78; GPM89] first is based on a method of control by on-line optimization with taking into account the dynamics of the system to make a prediction on a given horizon and steer the system in an optimal way towards its objective with this capacity of anticipation. The optimization is done at the current control time taking into account the predicted behavior on several future sampling periods and the addressed system does not necessarily present any input redundancy. On the other hand, the CA is initially characterized by the distribution of effort among the redundant control inputs at the current sampling time, and when dynamics are taken into account, the prediction is done with a time step horizon. The direct consequence is that the CA has much less decision variables than an MPC driving the same system, making its real time execution much faster than the MPC. For the same real time computer, using the CA is possible for systems with a larger bandwidth than the MPC is able to handle.

Comparatively, the strength of the CA is to be able to quickly distribute the control efforts among a large number of redundant control inputs, while the strength of the MPC is to anticipate the dynamic evolution of the system with an adjustable prediction quality. As a consequence, work has been proposed to associate the two approaches of control by optimization in the form of the Model Predictive Control Allocation (MPCA) with the objective of coupling the prediction capacity on a long horizon with the capacity to quickly find a trade-off optimizing the use of the control inputs.

Some MPCA taking explicitly into account the dynamics of the system have been introduced [Luo+04; Luo+05; Bor+05; Luo+07]. It has also been shown by [Han+11] that the use of QP for MPCA allows the implementation with current off-the-shelf computer technology. With the prediction horizon the MPCA has shown to be an interesting approach for fault-tolerant control allocation [JBL08]. Recent work using MPCA show a clean, pedagogical and explicit realization which can allow a first approach to the implementation of the MPCA [Kha+20; Kis+19].

1.E.5 | Control allocation features

Key features

In general, the strengths that have been highlighted in this presentation that characterize the allocation methods are the following ones. They are graphically summarized by Figure 1.14.

- Ability to distribute the required control objective among all input control variables.
- Capability to allocate optimally while fully accommodating to the constraints.
- Optimal real time control ability that is fast and within the current capabilities of embedded computer hardware.

- Possibility to tune the desired dynamics through a reference model in closed-loop [Bod02; LBF22].
- The capability to provide fault tolerant control by adapting the control allocation law or by reconfiguring the allocator in case of a fault.

Control allocation is also an effective approach for Fault-Tolerant Control (FTC). Once faults are identified, they can be modeled as a reconfiguration of the allocation equation, either by changing M or $\mathbf{a_d}$ or the bounds $\mathbf{U}_{min}$ and $\mathbf{U}_{max}$, or both. For example, in the case of an actuator constrained in a certain fault state, this configuration can be taken into account by setting the lower and upper constraint limits to the enforced value of the actuator. Another solution could be to act on $\mathbf{U}_p$ which could then be set to the enforced actuator state as in [Sch+04]. Another possibility, when the WPI method is used, is to adapt the W weighting to ensure that the faults are distributed appropriately among the fault-free effectors without reconfiguring the high level controller [AE08]. Another reconfiguration method based on pseudo-inversion is implemented by [MLY20] which takes advantage of the null-space.

The suggestion from [ASC19] to use the RPI in a modular way makes it possible to ensure a fault tolerant functionality without having to reconfigure the control agorithm, in essence the formulation works in both cases, healthy and faulty. A robust control method aims at guaranteeing the closed-loop stability even in case of a fault. Moreover, it has been shown that the fault tolerant control can deal with weakly input redundant systems.

Some have even suggested to take into account the actuators dynamics in their reconfiguration algorithm [CJ14]. A finite-time control reconfiguration technique that ensure performances recovering despite actuators faults is then introduced. In [CPJ18] a complete architecture is formulated, for the class of input affine nonlinear systems, with fault detection and confinement allowing to design a reduced order allocator when fault occurs. A different FTC with adaptive control allocation using a Lyapunov function was developed in [CB21].

Based on a formulation of the EMOn QP allocator which takes into account a real time adaptation from the beginning, [LZS21] introduces an algorithm whose one of the advantages is its capability of addressing unknown actuator faults online without reconfiguring the controller.

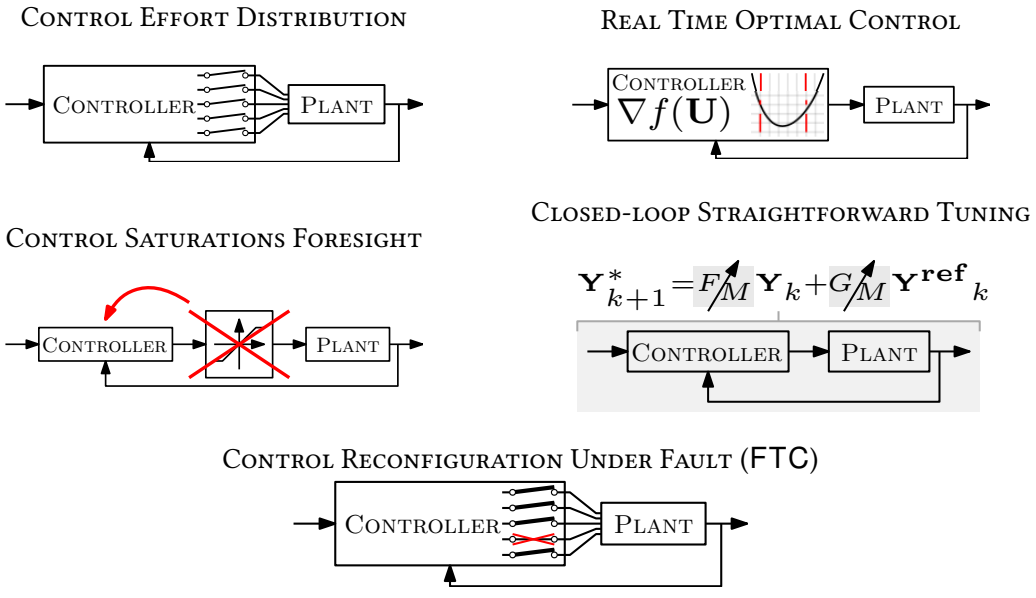

Figure 1.14: Graphical representation of the key features from the control allocation methods.

Comparison of the control allocation families

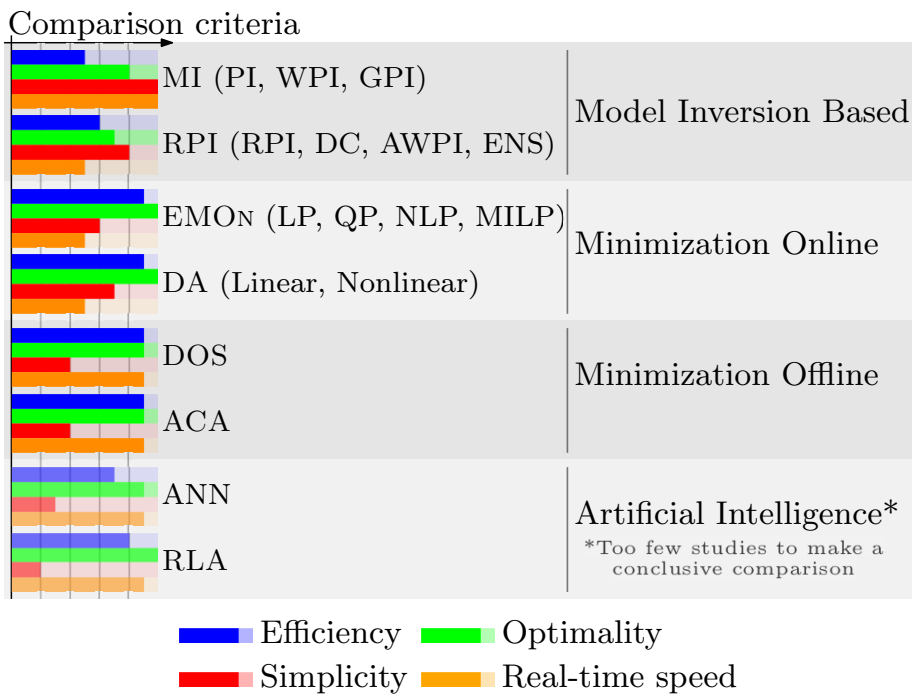

Figure 1.15: Main control allocation families characteristics comparison.

From the characteristic elements given in the description of the methods above, a general comparison of the different families of methods is possible on the criteria of **Efficiency** which represents the global efficiency of the method to solve the CAP (1.11)[1], de **Optimality** which represents the optimization character of the method, at which point it uses an optimization to determine the order[2], of **Simplicity** which qualifies the complexity to develop and implement the method in real time, and of **Real time speed** which represents the computation time needed by the allocator in the embedded computer hardware.

From the elements of comparison proposed by Figure 1.15, the methods of EMOn present a better efficiency than the inversion methods and an efficiency comparable to the offline optimization methods and seem for the moment to be as comparable or even superior to those using artificial intelligence. As far as optimality is concerned, the EMOn are the most optimal with a computation of the control that is entirely based on an optimization. They are however more complex to develop than the inversion methods, simpler than the two other families. Concerning the speed of calculation, the necessary iterations in real time make them the slowest methods. These EMOn methods thus appear to be a good compromise between efficiency, optimality, and simplicity of implementation compared to the other methods. Moreover, although they are generally the slowest in real time, the works implementing them have shown that embedded computer technologies are capable of executing them sufficiently quickly compared to the control objectives.

[1] For example, one can have a method without optimization such as the RPI which takes into account the constraints *a posteriori*, which is more efficient than the PI for example which just clips the exceeding control variables to its boundaries.

[2] For example, the EMOn QP corresponds to an optimization of a linear criterion on the allocation error but the WPI also corresponds to a quadratic optimization on the control variable, hence the necessity to introduce **Efficiency** as an additional criterion.

1.E.6 | Current trends in contol allocation

Methodological trends

In terms of the development of methods for CA, those that are currently the most novel are those using AI algorithms. The use of artificial intelligence to solve the control allocation problem being new, this constitutes an area of investigation for which there are problems to be solved such as the respect of constraints in real time or opportunities for performance improvement compared to the current state of these methods. Comparison work with current methods also remains to be done to fully evaluate these new approaches to solving the CAP (1.11).

Technological fields trends

Concerning the use of allocation methods in physical systems, the domain of predilection of the CA remains the aeronautics from the begining [Cun83; Lal85] up to now [TYK17; KW21; San+21; PBW22; Yan+22]. In general, the CA has been mainly used in the field of motion control until now with applications in space [Par89; Jin+06; DGN09; Boa+10; Shi+12; Wei+21], ships [Sør97; Joh+03; Sør11; Sku+18; Liu+21], in the underwater vehicles [FS91; SPA02; IP22] for the ground vehicles [WH00; TJ05b; Tag+09; CW12; Wei+22] and robots [KH83; Kha+20]. However, recently, these allocation methods are spreading to other domains than motion control such as electrical engineering.

The first works in this domain focused on the 2-level 4-leg [Bou+15; BBF18; BFB19], which introduce for the first time in this domain the allocation methods using more particularly the EMOn LP by the Simplex algorithm of which a form dedicated to the CA is programmed for a real time execution on FPGA. This work makes it possible to introduce a new PWM method which, depending on the setting of the real time optimization, allows a trade-off between already known PWM techniques [BFB16]. The results of this work are partly gathered in [Bou17] which proposes an explicit pedagogical approach to visualize how it is possible to take advantage of allocation methods for the control of redundant electrical systems such as the flying capacitor converter too. [BFB19] proposes a first cascade implementation of the control allocation law for the MMC. It shows that in simulation the EMOn LP with a Simplex solver is able to meet the challenge of hierarchical ordering in a particular case of MMC.

More recently [Kre19; Kre+21] studied a redundant heterogeneous DC power supply by using the methods of EMOn QP with a Active-Set solver. This work proposes a different approach to the control of a multi-terminal power system, compared to droop-control [Gue+11] and to balanced current sharing [Cid+11] methods where the reference tracking objectives of voltage and current are seen as competing objectives, the allocation in the case of the [Kre19] system introduces a different approach where they are seen as complementary objectives. Consequently, it is possible to satisfy them simultaneously. The allocation is then used to decide how to perform the current sharing between the different power sources of a single load. It is shown that, depending on the setting of the different criteria in the cost function of the optimization, it is possible to tune the current sharing behavior that one wishes to minimize the conduction losses for example. Experimental validation shows the value of the introduced approach.

It is also interesting to note a recent development in the field of nuclear fusion with [GS21] which proposes the implementation of an allocator to distribute the control effort of an internal control loop of the ITER. A first allocation method of type EMOn QP is proposed then a method of EMOff ACA method using a Lyapunov function to dynamically adapt the allocation

is implemented.

1.F | Conclusion

With the first developments of the control allocation methods in electrical engineering which show to be functional and effective to answer the encountered control problems, they bring new results in simulation and experimentally which attest an improvement compared to the existing control laws.

The control issues that the MMC must face, such as current reference tracking, the global energy balancing and the capacitor voltage balancing, are complex and coupled. The modular structure of the MMC first and then the modelling work give it a large number of control variables that are the switches - or duty cycles - of the submodules. The more submodules an MMC has, the more degrees of freedom are available to control the power flowing through the system. To generate a voltage at the terminals of an arm of the converter, several solutions of cooperative contribution of the submodules of this arm are possible, a redundancy of the actuators - that are the submodules - is identified. To generate a given output current, several arm configuration solutions are also possible. Thus the allocation methods, whose main feature is to control overactuated systems, are particularly suitable for the control of the MMC.

The development of allocation methods in the framework of the MMC is thus a relevant and ongoing field of study to be addressed which has the potential to bring a particularly adapted answer to the control problem of such a converter, modular and scalable in voltage and power, presenting a significant number of redundant degrees of freedom. Consequently, the work presented here is entitled:

Scalable Control Allocation Methods for the Modular Multilevel Converter
from Modelling to Real Time Implementation

The family of EMOn having shown to be a good trade-off between the different control allocation methods, they are the ones mainly used in this study. However, the MIB methods are also used for their simplicity in a first approach. Concerning the EMOn methods, the choices are the LP and the QP which are solved in real time. For the LP, it is the Simplex solver from [Bod02] which is used as well as the Interior-Point from [PB05]. In the case of the QP, it is first the Active-Set *Weigthed Least Squares* of [Här03] then the Interior-Point of [PB06] which are implemented. These two last algorithms are currently freely available online in the archive [Här] Among the algorithms of the archive, the *Weigthed Least Squares* is chosen for the performances which it shows compared to the other available formulations.

2 Contributions to the Scalable Modelling of Modular Multilevel Converters

Contents

As it was presented in Chapter 1, the modelling of the considered converter involves two challenges:

- The low-level modelling describing the relation between the switching states of the submodules of the MMC and the various electrical signals - with the capacitor voltage, as the main one - as well as the arm voltages.
- The high-level modelling describing the relation between the arm voltages and the four types of currents flowing through the converter. This modelling step can also take into account the relationship between these currents and the different powers involved in the power conversion.

As shown on Figure 2.1, each of those two modelling objectives are adressed in two steps. The first of these two goals is addressed in this chapter, while the second is addressed in Chapter 3. The order in which these two modelling steps are presented follows the physical causality of the system: from the low-level control variables that are the switch states to the converted electrical powers.

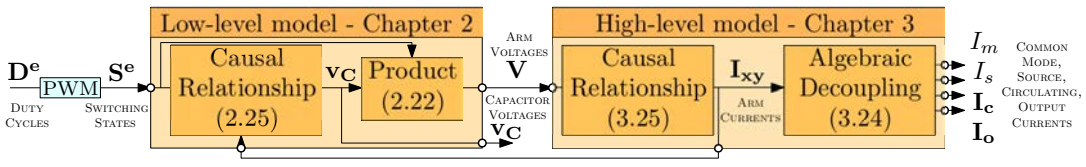

Figure 2.1: Overview of the modelling objectives from Chapter 2 and Chapter 3.

2.A | Research axis: towards a generalization of the models

The choice of contributions to the modelling of the MMC has been turned towards the exploration of new models more general than those available in the literature. One of the interesting features made possible by such models is the development of generic control algorithms that are able to adapt to different systems without having to make major modifications to the control system.

Low-level model

About the low-level part first, willing to describe the dynamics of the most common submodule types in the MMC that the objective to have a single model able to model their behaviors was formulated. [Mar18] presents a variety of different SM topologies that exist and have been designed to give the converter different operating properties. However, the SM-HB and SM-FB topologies are, for now, the most widespread in the MMC because of their design, operation and control simplicity [Mar02; LM03]. The role of Section 2.B is to develop these models to the level of detail necessary for the low-level control of the converter.

Outline

Section 2.B, will detail the low-level MMC modelling step by first establishing a functional model. Then, the detail of its physical representation will be increased. The final step will derive a generalized scalable model ready to be used for the control. The models developed here will be used afterwards in Chapter 5 to design the CA. Finally, Section 2.C will conclude this chapter.

2.B | Low-level modelling: from the cell to the converter arm voltages

Even if there is a generalization goal in the proposed models, there is a significant diversity of usable submodules as examples are given in Chapter 1, this diversity of SM topologies is too large to be able to make a general analytical detailed model of the submodules. Topology choice is therefore necessary although restrictive for the generalization of the low-level model. The general objective of the work presented in this manuscript is to develop a new control method for the MMC. The choice is therefore made to start showing the efficiency of these methods on simple topologies of MMC to then open the perspective of a use of these methods on more complex topologies, the developments will thus focus on submodule topologies which are today those most present in the MMC. It happens that they are also the ones that appeared first: the SM-HB and the SM-FB. Both of their electrical diagrams are shown on Figure 1.1.

Eventually, switching states will have to be controlled in order to impose a given behavior to the submodules, depending on the voltage level that it is desired to have across the capacitors or the voltage level across the submodules. The objective of the control model developed here is to describe the influence of the switching states specific to the submodules on the electrical signals associated with the latter.

The modelling approach will display a gradual complexity, the SM-HB will first be approached and a functional detailed model without semiconductor resistance will be established, then it will be the turn of the SM-FB. Then the functional physical detailed modelling with consideration of a part of the losses in the form of a conduction resistance will be derived for both types of

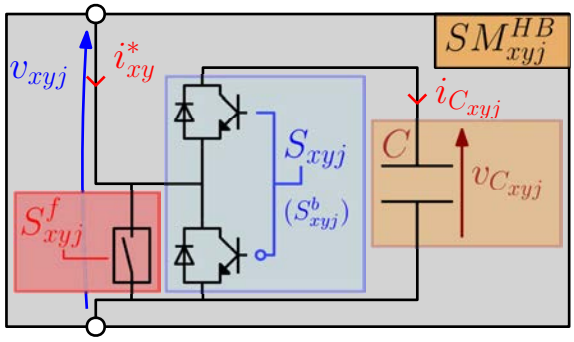

Figure 2.2: Electrical diagram of the SM-HB with the detail of the blocking and faulty switches.

submodules. For each level of complexity of the models, it will be sought to express $i_{C_{xyj}}$, $v_{C_{xyj}}$, v_{xyj}, v_{xy}, and even P^{loss}_{xyj} when the model allows it, according to the state of the switching cells of the different submodules: S_{xyj} and S'_{xyj}.

2.B.1 Submodules functional detailed models

2.B.1.1 Functional detailed model of the half bridge submodule

The model that is proposed in the first approach is intended here to be an improvement of the model proposed by [Zam17]. Indeed, in the case of the model (1.3) presented in Chapter 1, a simulation which would use this entirely analytical detailed model is not able to fully represent the behavior of the capacitors in the case where a negative current is imposed on them even though the voltage at the terminals of the capacitor is zero. While keeping an analytical approach, the functional detailed model, i.e. without resistance, proposed here takes into account this aspect but also provides a condensing procedure of the model which will be followed throughout the chapter in order to be able to provide the control algorithm with a formulation that is easy to manipulate.

In order to go into the development of the submodules model, Figure 2.2 introduces a more detailed representation of the internal constitution of the half-bridge submodules as used by [Zam17].

As introduced in [Saa+16], the following different states of the half-bridge submodule are considered:

- Connected, or Inserted: In this state, the capacitor is connected to the arm, $S_{xyj} = 1$.
- Disconnected, or Bypassed: In this state, the capacitor is disconnected from the arm, $S_{xyj} = 0$.
- Blocked: In the blocked state, $S^b_{xyj} = 1$, both the upper and lower transistors are open, and S_{xyj} losses controllability of the submodule.
- Faulty: This faulty state is a particular state of the whole SM and not only of a switching cell as it is the case for the other binary variables. In this state $S^f_{xyj} = 1$, and neither S^b_{xyj} nor S_{xyj} have the possibility to influence the behavior of the submodule

In normal operation, neither the blocked state (S^b_{xyj}) nor the fault state (S^f_{xyj}) will be activated. An algorithm for supervising the state of the SMs and the current flowing through the MMC will be able to decide in real time to act on these states if necessary. The control algorithm for the state of the switching cells (S_{xyj}) will have to adapt to what is forced by the supervision algorithm

in order to continue to guarantee the best possible reference tracking for the arm voltages while guaranteeing the balancing of the capacitors.

The three types of variables S_{xyj}, S^b_{xyj} and S^f_{xyj} are variables which are used to impose an operating state to the associated SM. They are thus all three control variables of the SM. Although they are control variables, the value assigned to them will be determined by a supervision algorithm which will decide what to do for special operations. What is considered as the low-level control is therefore the algorithm computing the value to assign to S_{xyj} while taking into account the values of S^b_{xyj} and S^f_{xyj} already assigned by the supervison algorithm considered as being part of an upper level in the hierarchy of the control architecture.

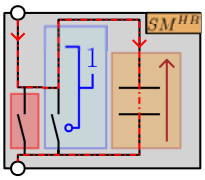

Figure 2.3: SM-HB in its active state.

From the influence of the variables S_{xyj}, S^b_{xyj}, S^f_{xyj} and the associated switches on the behavior of the submodule, it is possible to derive the evolution of the electrical signals $i_{C_{xyj}}$, $v_{C_{xyj}}$, v_{xyj} and v_{xy} which are directly linked to the considered SM and its state. For that, the use of a truth table will make it possible to extract a formula of the submodule state in the form of a logical equation.

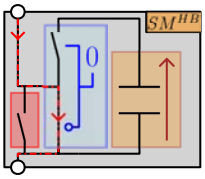

Figure 2.4: SM-HB in its passive state.

For example, for the state characterized by $S_{xyj} = 1$, $S^b_{xyj} = 0$ and $S^f_{xyj} = 0$ which is shown on Figure 2.3, it comes from the KCL that the current flowing through the capacitor will be $i_{C_{xyj}} = i^*_{xy}$ as long as the capacitor is not discharged and from the KVL the voltage across the submodule will be $v_{xyj} = v_{C_{xyj}}$. For the dual state which is represented on Figure 2.4 and characterized by $S_{xyj} = 0$, $S^b_{xyj} = 0$ and $S^f_{xyj} = 0$, the current through the capacitor will be zero $i_{C_{xyj}} = 0$ as well as the voltage across the submodule $v_{xyj} = 0$. In normal operation of the submodule, the latter will be in one of those two states. By applying Kirchhoff's laws to the half-bridge submodule in the different possible combinations of the variables S_{xyj}, S^b_{xyj} and S^f_{xyj}, all the different states are analyzed. The result of this process is given in Table 2.1.

S^f_{xyj}	S^b_{xyj}	S_{xyj}		$i_{C_{xyj}}$	v_{xyj}
0	0	0		0	0
0	0	1		$i^*_{xy} \cdot \hat{p}_{xyj}(i^*_{xy}, v_{C_{xyj}})$	$v_{C_{xyj}} \cdot \hat{p}_{xyj}(i^*_{xy}, v_{C_{xyj}})$
0	1	-		$i^*_{xy} \cdot (i^*_{xy} > 0)$	$v_{C_{xyj}} \cdot (i^*_{xy} > 0)$
0	1	-		$i^*_{xy} \cdot (i^*_{xy} > 0)$	$v_{C_{xyj}} \cdot (i^*_{xy} > 0)$
1	-	-		0	0

Table 2.1: Truth table - Behavior of the SM-HB

Newly introduced notations in the table make it possible to simplify it[1][2]. The behavior of the submodule requires some clarification in the case where it is faulty ($S^f_{xyj} = 1$) and the variable S_{xyj} is in full control of the state of the switching cell ($S^b_{xyj} = 0$). In this operating case, if the capacitor is charged at the moment when S_{xyj} switches from 0 to 1, a strong current will appear in the capacitor, allowing it to discharge, and this during a very short transient whose duration

[1] In order to describe the state of availability of the capacitor the binary variable $\hat{p}_{xyj}(i^*_{xy}, v_{C_{xyj}})$ is used. When it is in the 1 state, the capacitor can be charged or discharged, when it is in the 0 state, the capacitor is completely discharged and cannot be discharged any more. Thus this variable is defined by $\hat{p}_{xyj}(i^*_{xy}, v_{C_{xyj}}) \triangleq \left[(i^*_{xy} > 0) + (i^*_{xy} < 0)\,(v_{C_{xyj}} > 0)\right]$.

[2] Binary variables standing for of the sign of the current and the voltage are introduced:

$$(i^*_{xy} > 0) = \begin{cases} 1, \text{if } i^*_{xy} > 0 \\ 0, \text{if } i^*_{xy} \leq 0 \end{cases} \Longrightarrow (i^*_{xy} > 0) = (sign(i^*_{xy}) + 1)\,\frac{sign(i^*_{xy})}{2} \tag{2.1}$$

$$(i^*_{xy} < 0) = \begin{cases} 1, \text{if } i^*_{xy} < 0 \\ 0, \text{if } i^*_{xy} \geq 0 \end{cases} \Longrightarrow (i^*_{xy} < 0) = (sign(i^*_{xy}) - 1)\,\frac{sign(i^*_{xy})}{2} \tag{2.2}$$

The variables $(v_{C_{xyj}} > 0)$ and $(v_{C_{xyj}} < 0)$ are defined analogously.

depends on the product of the safety switch resistance with the capacitance of the capacitor. The current and voltage in the capacitor will then stabilize at zero after the short transient. This transient will also influence v_{xyj} which will present a strong increase at the switching instant before coming back to its previous level in steady-state. The dynamics of these electrical signals is considered sufficiently fast compared to the sampling period of the control so that for the establishment of a control model, the current through the capacitor and the voltage at its terminals can be considered zero. Thus, the truth table presents null values for $i_{C_{xyj}}$ and $v_{C_{xyj}}$ for $S^f_{xyj} = 1$ and $S^b_{xyj} = 0$.

The principles of logic equation synthesis applied to the truth table as a whole makes it possible to derive more comprehensive equations than that of (1.3) for the half-bridge submodule[1]. It is worth noting that the voltage v_{xyj} is then bounded between 0 and $v_{C_{xyj}}$ for the half-bridge submodule case:

$$\begin{cases} i_{C_{xyj}} = C\,\frac{dv_{C_{xyj}}}{dt} = i^*_{xy}\left[S_{xyj}\,\overline{S^b_{xyj}}\,\hat{p}_{xyj}(i^*_{xy}, v_{C_{xyj}}) + (i^*_{xy} > 0)\,S^b_{xyj}\right]\,\overline{S^f_{xyj}} \\ v_{xyj} = v_{C_{xyj}}\left[S_{xyj}\,\overline{S^b_{xyj}}\,\hat{p}_{xyj}(i^*_{xy}, v_{C_{xyj}}) + (i^*_{xy} > 0)\,S^b_{xyj}\right]\,\overline{S^f_{xyj}} \end{cases} \tag{2.3}$$

In order to lighten this model, a binary variable representing the global state of the considered submodule is introduced:

$$S^{HB}_{xyj} = S^{HB}_{xyj}\left(S_{xyj}, S^b_{xyj}, S^f_{xyj}\right) \triangleq \left[S_{xyj}\overline{S^b_{xyj}}\hat{p}_{xyj}(i^*_{xy}, v_{C_{xyj}}) + (i^*_{xy} > 0)S^b_{xyj}\right]\overline{S^f_{xyj}} \tag{2.4}$$

Taking advantage of the notation introduced by (2.4), substitutions can be made in (2.3):

FUNCTIONAL DETAILED MODEL OF THE HALF-BRIDGE SUBMODULE

$$\begin{cases} i_{C_{xyj}} = C\,\frac{dv_{C_{xyj}}}{dt} = i^*_{xy}\,S^{HB}_{xyj} \\ v_{xyj} = v_{C_{xyj}}\,S^{HB}_{xyj} \in \left[0; v_{C_{xyj}}\right] \end{cases} \tag{2.5}$$

with the global state of the half-bridge submodule S^{HB}_{xyj} defined by equation (2.4).

Equation (2.5) then defines the low-level functional detailed model of the half-bridge submodule. From this first half-bridge submodule functional model, the one focusing on the full-bridge submodule is going to be designed by applying the same approach while being based on a truth table.

2.B.1.2 Functional detailed model of the full bridge submodule

The same reasoning as for the half-bridge submodule is extended to the case of the full-bridge submodule. Its explicit derivation is given in Appendix E.1. Figure 11 shows the full-bridge submodule in the case where all binary states are represented, applying the KIRCHHOFF laws in this case, bring the following model (2.6).

[1] It is reminded that the notation $\overline{x}$ for a logical variable x represents its logical inverse, $\overline{x}$ is also sometimes noted $not(x)$.

FUNCTIONAL DETAILED MODEL OF THE FULL-BRIDGE SUBMODULE

$$\begin{cases} i_{C_{xyj}} = C\,\frac{dv_{C_{xyj}}}{dt} = i^*_{xy}\,S^{FB}_{xyj} \\ v_{xyj} = v_{C_{xyj}}\,S^{FB}_{xyj} \in \left[-v_{C_{xyj}}; v_{C_{xyj}}\right] \end{cases} \tag{2.6}$$

with the global state of the full-bridge submodule S^{FB}_{xyj} defined by equation (A.38).

2.B.2 Submodules functional detailed models with conduction losses

The choice to realize a model taking into account the conduction resistances of the semiconductors constituting the submodules comes from the will to have a representation of the energy consumption of the submodules during their use.

2.B.2.1 Functional physical detailed model of the half bridge submodule

The realization of the augmented model is based on the representation of the half-bridge submodule available on Figure 2.5 which takes into account the conduction resistance of each semiconductor. These resistances are named according to the type of semiconductor (T for transistor and D for diode) and whether it is located at the upper side or lower side of the cell (respectively u or l) as shown in Figure 2.5.

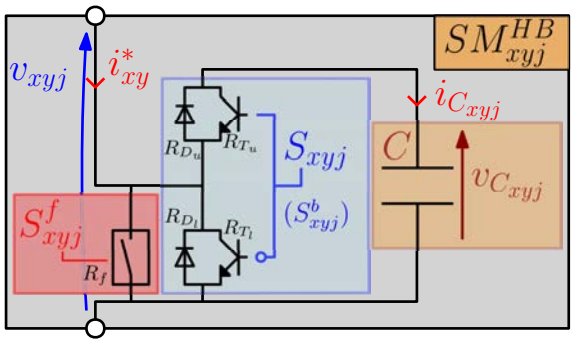

Figure 2.5: Electrical diagram of the SM-HB with the detail of the conduction resistances of each semiconductor.

The same approach as previously carried out, for the case of the functional detailed model, is used in order to establish the path of the current according to the state of the three binary variables defining the state of the SM. The use of KIRCHHOFF's laws to establish Table 2.1 are applied here on the electrical diagram augmented with resistors, Figure 2.5, taking into account the semiconductor details. To evaluate the sequence of semiconductors through which the current passes, it is considered that $v_{C_{xyj}}$ is positive or null. Depending on the sign of the current i^*_{xy} the path taken will also change.

For example, in the normal operating case, i.e. when $S^f_{xyj} = 0$ and $S^b_{xyj} = 0$, the system adopts one of the operating cases depicted by Figures 2.6 to 2.10. In the case where $S_{xyj} = 0$, it is the lower transistor T_l which is closed, so if the current i^*_{xy} is positive then it flows through this transistor and meet its resistance; in the opposite case where i^*_{xy} is negative, the antiparallel diode D_l conducts the current. The case where $S_{xyj} = 1$ is slightly more complex because it depends on the capacitor state of charge. In this case, the upper transistor T_u of the cell is closed.

If i^*_{xy} is positive, the upper diode D_u conducts the current through the capacitor and makes it possible to charge it. However, if i^*_{xy} is negative, the capacitor will only be able to discharge if it still contains charges and has a positive voltage at its terminals. In this situation, it is the upper transistor T_u which will conduct the current. If the voltage in the capacitor becomes zero, the current can no longer flow through it. The semiconductor capable of conducting the current is the lower diode D_l.

The two cases presented as examples above correspond to the first two lines of Table 2.2.

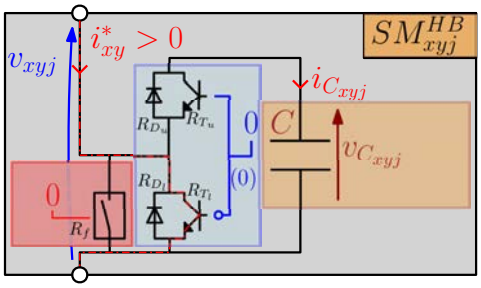

Figure 2.6: SM-HB in the passive state, current path for $i^*_{xy} > 0$.

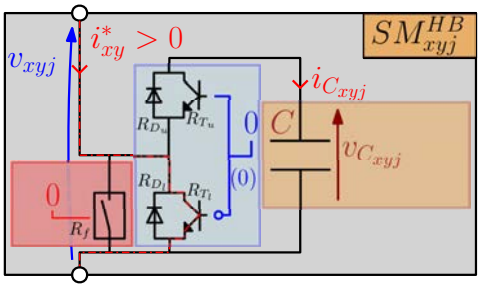

Figure 2.7: SM-HB in the passive state, current path for $i^*_{xy} < 0$.

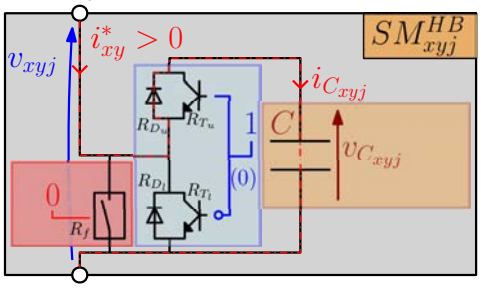

Figure 2.8: SM-HB in the active state, current path for $i^*_{xy} > 0$.

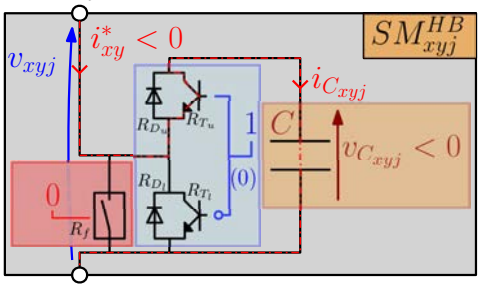

Figure 2.9: SM-HB in the active state, current path for $i^*_{xy} < 0$ and $v_{C_{xyj}} > 0$.

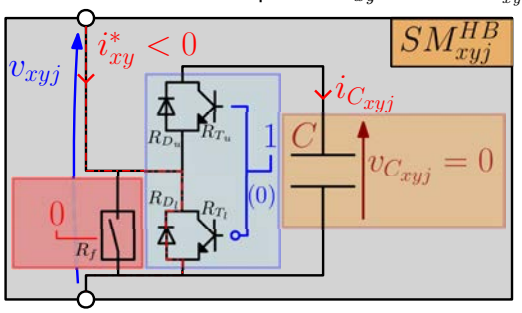

Figure 2.10: SM-HB in the active state, current path for $i^*_{xy} < 0$ and $v_{C_{xyj}} = 0$.

From the knowledge of the path covered by the current, the resistance R^{HB}_{xyj} that the latter presents to the flow of the current i^*_{xy} is deduced. Table 2.2 is then obtained.

By applying the principles of logic function design to Table 2.2, the logical expression for the resistance R^{HB}_{xyj} from the half-bridge submodule under consideration to the passage of the current

S^f_{xyj}	S^b_{xyj}	S_{xyj}		R^{HB}_{xyj}
0	0	0		$R_{T_l}(i^*_{xy}>0)+R_{D_l}(i^*_{xy}<0)$
0	0	1		$R_{D_u}(i^*_{xy}>0)+[R_{T_u}(v_{C_{xyj}}>0)+R_{D_l}(v_{C_{xyj}}=0)](i^*_{xy}<0)$
0	1	0		$R_{D_u}(i^*_{xy}>0)+R_{D_l}(i^*_{xy}<0)$
0	1	1		$R_{D_u}(i^*_{xy}>0)+R_{D_l}(i^*_{xy}<0)$
1	0	0		$\left(\frac{R_f R_{T_l}}{R_f+R_{T_l}}\right)(i^*_{xy}>0)+\left(\frac{R_f R_{D_l}}{R_f+R_{D_l}}\right)(i^*_{xy}<0)$
1	0	1		R_f
1	1	0		$R_f(i^*_{xy}>0)+\left(\frac{R_f R_{D_l}}{R_f+R_{D_l}}\right)(i^*_{xy}<0)$
1	1	1		$R_f(i^*_{xy}>0)+\left(\frac{R_f R_{D_l}}{R_f+R_{D_l}}\right)(i^*_{xy}<0)$

Table 2.2: Truth table - Resistance of the SM-HB.

i^*_{xy} is deduced.

$$\begin{aligned}R^{HB}_{xyj} \triangleq\ & \Big[\big[(R_{T_l}(i^*_{xy}>0)+R_{D_l}(i^*_{xy}<0))\overline{S_{xyj}}\\ &+(R_{D_u}(i^*_{xy}>0)+[R_{T_u}(v_{C_{xyj}}>0)+R_{D_l}(v_{C_{xyj}}=0)](i^*_{xy}<0))S_{xyj}\big]\,\overline{S^b_{xyj}}\\ &+\left[R_{D_u}(i^*_{xy}>0)+R_{D_l}(i^*_{xy}<0)\right]S^b_{xyj}\Big]\,\overline{S^f_{xyj}}\\ &+\Big[\Big[\left(\left(\tfrac{R_f R_{T_l}}{R_f+R_{T_l}}\right)(i^*_{xy}>0)+\left(\tfrac{R_f R_{D_l}}{R_f+R_{D_l}}\right)(i^*_{xy}<0)\right)\overline{S_{xyj}}+R_f S_{xyj}\Big]\,\overline{S^b_{xyj}}\\ &+\left[R_f(i^*_{xy}>0)+\left(\tfrac{R_f R_{D_l}}{R_f+R_{D_l}}\right)(i^*_{xy}<0)\right]S^b_{xyj}\Big]\,S^f_{xyj}\end{aligned} \tag{2.7}$$

The consequence of taking into account these conduction resistances implies the modification of the voltage at the terminals of the half-bridge submodule. This voltage, until now expressed by (2.4), must now take into account ohmic voltage drops:

$$v_{xyj} = v_{C_{xyj}} S^{HB}_{xyj} + R^{HB}_{xyj} i^*_{xy} \tag{2.8}$$

The knowledge of the conduction resistance of the half-bridge submodule makes it possible to determine the conduction losses in the latter. The conduction losses dissipated power is then:

$$P^{loss}_{xyj} = R^{HB}_{xyj}\ {i^*_{xy}}^2 \tag{2.9}$$

Finally, taking into account the semiconductor conduction resistance in the half-bridge submodule case results in a slight modification of (2.3):

FUNCTIONAL PHYSICAL DETAILED MODEL OF THE HALF-BRIDGE SUBMODULE

$$\begin{cases} i_{C_{xyj}} = C\,\frac{dv_{C_{xyj}}}{dt} = i^*_{xy}\ S^{HB}_{xyj} \\ v_{xyj} = v_{C_{xyj}}\ S^{HB}_{xyj} + R^{HB}_{xyj}\ i^*_{xy} \in \left[R^{HB}_{xyj} i^*_{xy}; R^{HB}_{xyj} i^*_{xy} + v_{C_{xyj}}\right] \\ P^{loss}_{xyj} = R^{HB}_{xyj}\ {i^*_{xy}}^2 \end{cases} \tag{2.10}$$

with the global state of the half-bridge submodule S^{HB}_{xyj} defined by equation (2.4) and the resistance of the SM is R^{HB}_{xyj}, defined by (2.7).

2.B.2.2 Functional physical detailed model of the full bridge submodule

The study of the full-bridge submodule case is done by taking advantage of the one carried out for the half-bridge submodule. Compared to the half-bridge submodule, the additional switching cell results in four new conduction resistances associated with the semiconductors of the second cell as highlighted in Figure 12. As for the functional detailed model, the derivations for the full-bridge submodule similar to those of the half-bridge submodule, thus the detailed development is given in Appendix E.2.

FUNCTIONAL PHYSICAL DETAILED MODEL OF THE FULL-BRIDGE SUBMODULE

$$\begin{cases} i_{C_{xyj}} = C\,\frac{dv_{C_{xyj}}}{dt} = i^*_{xy}\,S^{FB}_{xyj} \\ v_{xyj} = v_{C_{xyj}}\,S^{FB}_{xyj} + R^{FB}_{xyj}\,i^*_{xy} \in \left[R^{HB}_{xyj} i^*_{xy} - v_{C_{xyj}}; R^{HB}_{xyj} i^*_{xy} + v_{C_{xyj}}\right] \\ P^{loss}_{xyj} = R^{FB}_{xyj}\,{i^*_{xy}}^2 \end{cases} \tag{2.11}$$

with the global state of the full-bridge submodule S^{FB}_{xyj} defined by equation (A.38) and the resistance of SM is R^{FB}_{xyj}, defined by (A.52).

At this stage, the models taking into account the resistances of the semiconductors have been developed for the two types of submodules studied. The next modelling step is to determine which of the models is the most general, but first a comparison of the models is provided.

2.B.3 Putting the developed models into perspective

Tables 2.3 and 2.4 show comparison between the models proposed here and some of the most relevant works in the literature with respect to the objectives of having a control-oriented model of the submodules. The choice of the comparison criteria in the tables is guided by the use that this study wishes to make of the models, which are not intended to be used for simulation but for development of an algorithm to ensure capacitor voltage balancing and arm voltage reference tracking as well.

Compared to the models proposed in the literature, the models introduced here are considered as detailed models because they represent the behavior of the submodules with the consideration of the switching states directly. However, the first formulations introduced do not represent the equivalent resistance to the conduction of the submodules and are instead condensed - with the use of the global submodule state - with the objective of being used for control. For this reason, they are called *functional*. The next two models take into account a finer description of the conduction resistance of the submodules while keeping this condensed aspect for the control, they are then named *functional physical*.

With the developments proposed so far in this chapter, a will of unification and progression of the models to reach the same level of physical representation for both submodule types has been tracked as shown by Tables 2.3 and 2.4. From the models that are both able to 1) represent the operation of the submodule in a condensed way as a function of the global state of the submodule from a single analytical equation, 2) to take into account the blocked and faulty states 3) for the two most common types of submodules, and 4) to describe more precisely than before the conduction resistances. The next step is to unify the four proposed models into a unique one, to extend it to the arm of the MMC and to derive the AVM.

Splitting the table in two parts is solely due to table width concerns compared to the page limits

	Models from the literature					Developed models	
Criterion	[Per+12]	[Saa+14]	[Den+15]	[Zha+16]	[Yan+19]	FDM	FPDM
Model type	DM, AVM	DM, EM, AVM	AVM	DM, AVM	DM, AVM	DM (AVM in Section 2.B.5.2)	
SM type	SM-HB	SM-HB	None	SM-HB	SM-FB	both	both
Truth table	No	No	No	No	No	Yes	Yes
Quantities analytically described	v_{xy}	i_C, v_C, v, v_{xy}	v_C	None	i_C, v	v_C,i_C,v	v_C,i_C,v,P_{SM}^{loss}
Preventing from $v_C < 0$	Not analytically	No	Not anal.	Not anal.	No	Yes	Yes
Blocked state modeled	Yes	Yes	Yes	Yes	Yes	Yes	Yes
Faulty state modeled	No	No	No	Yes	No	Yes	Yes
SM resistance modeled	None	Equivalent R_{ON}	Eq. R_{ON}	None	None	None	Comprehensive R_{ON}
Unique equation for each quantity	No	No	No	No	No	Yes	Yes
Model condensed	No	No	No	No	No	Yes	Yes

Table 2.3: Comparison of the characteristics of the proposed low-level models with the literature - Part #1

	Models from the literature				Developed models	
Criterion	[LB16]	[Saa+16]	[Zam17]	[Ste+21]	FDM	FPDM
Model type	EM	DM, EM	DM, EM, AVM	DM, EM, EM, AVM	DM (AVM in Section 2.B.5.2)	
SM type	both	both	SM-HB	both & hybrid combination	both	both
Truth table	Yes	Yes	Yes	No	Yes	Yes
Quantities analytically described	v_C	i_C, v_C, v	v_C, v, R_{arm}^{loss}	v_C,i_C,v	v_C,i_C,v	v_C,i_C,v,P_{SM}^{loss}
Preventing from $v_C < 0$	No	Not anal.	No	Not anal.	Yes	Yes
Blocked state modeled	Yes	Yes	Yes	Yes	Yes	Yes
Faulty state modeled	Yes	No	Yes	No	Yes	Yes
SM resistance modeled	R_{disc}	Eq. R_{ON}	Eq. R_{ON}	Eq. R_{ON}	None	Comprehensive R_{ON}
Unique equation for each quantity	Yes	No	Yes	No	Yes	Yes
Model condensed	No	No	No	No	Yes	Yes

Table 2.4: Comparison of the characteristics of the proposed low-level models with the literature - Part #2

2.B.4 | Arm generalized model

2.B.4.1 | Low-level most general model of the submodule

It seems intuitive that the most general model between that of the full-bridge submodule and that of the full-bridge submodule is the model associated with the topology containing the most switching cells.

When replacing S'_{xyj} and $S^{b'}_{xyj}$ by zero in the full-bridge submodule model, the following observation is done:

$$\boxed{S^{FB}_{xyj}\left(S_{xyj}, S^{b}_{xyj}, 0, 0, S^{f}_{xyj}\right) = S^{HB}_{xyj}\left(S_{xyj}, S^{b}_{xyj}, S^{f}_{xyj}\right)} \tag{2.12}$$

Moreover, when we also substitute the resistances of the second cell by zero in the full-bridge submodule conduction resistance model, it is obtained that:

$$\boxed{R^{FB}_{xyj}\left(S_{xyj}, S^{b}_{xyj}, S'_{xyj}=0, S^{b'}_{xyj}=0, S^{f}_{xyj}, R'_{D_l}=0, R'_{T_l}=0\right) = R^{HB}_{xyj}\left({S_{xyj}}^{f}, S^{b}_{xyj}, S_{xyj}\right)} \tag{2.13}$$

From the previous explanations which led to the equations (2.12) and (2.13), it is obtained that the full-bridge submodule model is more general than the half-bridge submodule model, Therefore, the most general model of submodule is represented by (A.42). The transition from the full-bridge model to the half-bridge model is done seamlessly by the cancellation of some parameters, as described by the flowchart Figure 2.11.

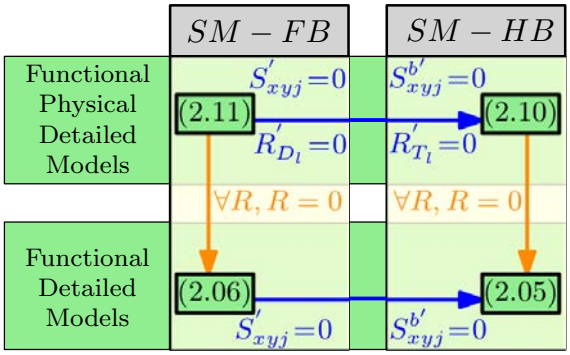

Figure 2.11: Flowchart of the transition from the full-bridge submodule model to the half-bridge submodule model.

Remark: It is important to note that, in this model, all the losses resulting from the operation of semiconductors are not taken into account, indeed only the conduction losses are considered and the switching losses are not modeled.

2.B.4.2 | Developing the arm generalized model

In order for the control allocation to benefit from the redundancy that the submodules feature in the generation of a voltage across an arm, the control-oriented arm model is derived.

In the MMC, an arm is made of a total of N submodules connected in series as well as an impedance made up of an inductance mainly, whose role is to limit the currents circulating in the converter, and of a resistance as shown in Figure 1.2. Figure 2.12 focuses on one of the arm

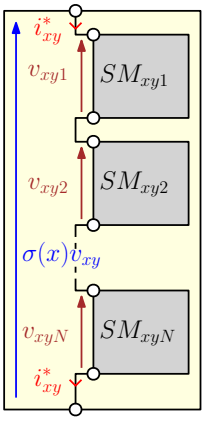

Figure 2.12: Simplified electrical diagram of any arm of the MMC.

alone, the expression of the voltage v_{xy} across all the submodule of this arm is then obtained trivially:

$$v_{xy} = \sigma(x) \sum_{j=1}^{N} v_{xyj} \tag{2.14}$$

It is noted that the use of $\sigma(x)$[1] is necessary because the sign of this sum will not be the same as that of the v_{xyj}, whether one is interested in the arms connected to the positive pole of the DC bus or those connected to the negative pole. It is pointed out that, for the case of the half-bridge submodule, the voltage v_{xyj} is between 0 and $v_{C_{xyj}}$, while for the case of the full-bridge submodule, this same voltage is between $-v_{C_{xyj}}$ and $v_{C_{xyj}}$. This implies that v_{xy} bounds will not be the same depending on the type of submodule used. In order to keep unified notations, the variable q is introduced, its definition is given by equation (2.16). By using this newly introduced variable, it is possible to formulate the boundaries of v_{xyj}: $v_{xyj} \in \left[R^{HB}_{xyj} i^*_{xy} + (1-q)v_{C_{xyj}}; R^{HB}_{xyj} i^*_{xy} + v_{C_{xyj}}\right]$, and thus deduce those of v_{xy}:

$$v_{xy} \in \left[\sum_{j=1}^{N} R^{HB}_{xyj} i^*_{xy} + (1-q)v_{C_{xyj}}; \sum_{j=1}^{N} R^{HB}_{xyj} i^*_{xy} + v_{C_{xyj}}\right] \tag{2.15}$$

In this way, the FPDM of the full-bridge submodule (A.42) can be augmented with this information about v_{xy}:

$$q \triangleq \begin{cases} 1, \text{ for SM-HB} \\ 2, \text{ for SM-FB} \end{cases} \tag{2.16}$$

q is the variable standing for the number of commutation cells in a given submodule topology.

FUNCTIONAL PHYSICAL DETAILED MODEL OF THE FULL-BRIDGE SUBMODULE AND THE ARM

$$\begin{cases} i_{C_{xyj}} = C\,\frac{dv_{C_{xyj}}}{dt} = i^*_{xy}\,S^{FB}_{xyj} \\ v_{xyj} = v_{C_{xyj}}\,S^{FB}_{xyj} + R^{FB}_{xyj}\,i^*_{xy} \in \left[R^{HB}_{xyj} i^*_{xy} - v_{C_{xyj}}; R^{HB}_{xyj} i^*_{xy} + v_{C_{xyj}}\right] \\ v_{xy} = \sigma(x)\,\sum_{j=1}^{N} v_{xyj} \in \left[\sum_{j=1}^{N} R^{HB}_{xyj} i^*_{xy} + (1-q)v_{C_{xyj}}; \sum_{j=1}^{N} R^{HB}_{xyj} i^*_{xy} + v_{C_{xyj}}\right] \\ P^{loss}_{xyj} = R^{FB}_{xyj}\,{i^*_{xy}}^2 \end{cases} \tag{2.17}$$

with the global state of the full-bridge submodule S^{FB}_{xyj} defined by equation (A.38) and the resistance of the SM is R^{FB}_{xyj}, defined by (A.52).

The model embodied by equation (2.17) is now complete since it contains all the elements necessary to design the arm voltage control of the converter. Indeed, this equation describes both the influence of the control variables, which are the states of the switches, on the internal electrical states of the submodule and formulates the limits of the electrical states, information which the control law will need. Although the equations of the model (2.17) indicate the influence of the control variables on the electrical states, the current formalism does not yet allow the implementation of the control allocation. To do so, a matrix model is necessary and must take the form of the control allocation problem reiterated in the margin. A transformation step of the model will then take place in order to turn it into the adequate formulation.

Finding $\mathbf{U}$ in $\mathbf{U}_{min} \leq \mathbf{U} \leq \mathbf{U}_{max}$ such that $\mathcal{M}(\mathbf{U}) = \mathbf{a_d}$. Equation defining the general formulation of the control allocation problem.

2.B.5 Low-level generalized matrix model

In order to be able to implement the control allocation method, a matrix model of the submodule is developed for the most general case of submodule, i.e. for the full-bridge submodule. This

[1] It is recalled that $\sigma(x) = 1/\sigma(x)$, the notation used on Figure 2.12 is consitent with the equation (2.14)

matrix model can be readily reduced to the half-bridge submodule case, as explained previously.

Generalized matrix model for the global state of the submodule

As indicated by (A.38), the state of the SM depends on five binary variables, only two of which can be controlled by the low-level control of the SM: S_{xyj} and S'_{xyj}. The other variables are managed externally by a supervision algorithm that deals with startup procedures and faults. For the development of the low-level control algorithm, a formulation that brings out the control variables is derived. The global state of the submodule is shown, by Appendix F.1, to be able to take the form:

$$S^{FB}_{xyj} = \begin{bmatrix} l_{xyj} & l'_{xyj} \end{bmatrix} \begin{bmatrix} S_{xyj} \\ S'_{xyj} \end{bmatrix} + \begin{bmatrix} \tau_{xyj} \end{bmatrix} = \underset{\text{Nominal Operation}}{\begin{bmatrix} 1 & -1 \end{bmatrix}} \begin{bmatrix} S_{xyj} \\ S'_{xyj} \end{bmatrix} = S_{xyj} - S'_{xyj} \tag{2.18}$$

The equation (2.18) is thus a matrix model that directly links the control variables from the submodule to its state. However, the submodule resistance also depends on the different binary variables associated with the switches, thus it is also necessary to go through the transformation into a matrix model for the equation defining R^{FB}_{xyj}. The variables l_{xyj}, l'_{xyj} and τ_{xyj} are integer parameters depending on the blocked state and faulty state binary variables. In nominal operating case - where every submodule is healthy and no blocking is enforced - the equation is simplified as expressed above.

Generalized matrix model for the conduction resistance of the submodule

The same approach is thus applied in Appendix F.2 for the conduction resistance, that adopts also this matrix form:

$$R^{FB}_{xyj} = \begin{bmatrix} w_{xyj} & w'_{xyj} \end{bmatrix} \begin{bmatrix} S_{xyj} \\ S'_{xyj} \end{bmatrix} + \begin{bmatrix} \theta_{xyj} \end{bmatrix} S_{xyj} S'_{xyj} + \begin{bmatrix} z_{xyj} \end{bmatrix} \tag{2.19}$$

It is noted that the full-bridge submodule resistance model thus adopts a nonlinear form unlike the case of the global full-bridge submodule state according to the equation (2.18). The variables w_{xyj}, w'_{xyj},θ_{xyj} and z_{xyj} are resistances that depend on the blocked state and faulty state binary variables. The simplified formula in nominal operation is not relevant to show since it is still bulky.

2.B.5.1 Generalized matrix model of the arms

The two previous paragraphs allowed to establish the matrix model at the scale of the submodule, it is now necessary to move on to the complete arm. The objective is therefore to establish a model linking the control variables of each submodule to the evolution of the electrical signals of the entire arm composed of all these submodules. The developments carried out here, are based on the results represented by the equations (2.18) and (2.19) and (2.17). The latter is recalled below

and focuses on describing the behavior of a single submodule:

$$\begin{cases} i_{C_{xyj}} = C\,\frac{dv_{C_{xyj}}}{dt} = i^*_{xy}\,S^{FB}_{xyj} \\ v_{xyj} = v_{C_{xyj}}\,S^{FB}_{xyj} + R^{FB}_{xyj}\,i^*_{xy} \in \left[R^{HB}_{xyj} i^*_{xy} - v_{C_{xyj}}; R^{HB}_{xyj} i^*_{xy} + v_{C_{xyj}}\right] \\ v_{xy} = \sigma(x)\,\sum_{j=1}^{N} v_{xyj} \in \left[\sum_{j=1}^{N} R^{HB}_{xyj} i^*_{xy} + (1-q) v_{C_{xyj}}; \sum_{j=1}^{N} R^{HB}_{xyj} i^*_{xy} + v_{C_{xyj}}\right] \\ P^{loss}_{xyj} = R^{FB}_{xyj}\,{i^*_{xy}}^2 \end{cases} \tag{2.20}$$

To go from the model of a single submodule to the model of a whole arm, the development proposed in Appendix F.2.1 is based on a matrix concatenation: the models of the N submodules of the arm are put one after the other. This leads directly to the following arm model 2.21. Figure 2.13 is provided with (2.21) and (2.22) in order to visualize the quantities involved in the functional physical detailed model of the arm.

FUNCTIONAL PHYSICAL DETAILED MODEL OF THE ARM

$$\begin{cases} \mathbf{i_{C_{xy}}} = C\,\dot{\mathbf{v}}_{\mathbf{C_{xy}}} = i^*_{xy}\left(L_{xy}\mathbf{S^e_{xy}} + \mathbf{T_{xy}}\right) \\ v_{xy} = \sigma(x)\left[\left({\mathbf{v_{C_{xy}}}}^T L_{xy} + i^*_{xy} W_{xy}\right)\mathbf{S^e_{xy}} + i^*_{xy}{\mathbf{S^e_{xy}}}^T\,\Theta_{xy}\mathbf{S^e_{xy}} + \left({\mathbf{v_{C_{xy}}}}^T\,\mathbf{T_{xy}} + i^*_{xy}\mathbf{Z_{xy}}\right)\right] \\ v_{xy} \in \left[\sum_{j=1}^{N} R^{HB}_{xyj} i^*_{xy} + (1-q) v_{C_{xyj}}; \sum_{j=1}^{N} R^{HB}_{xyj} i^*_{xy} + v_{C_{xyj}}\right] \\ P^{loss}_{xy} = \left(W_{xy}\mathbf{S^e_{xy}} + {\mathbf{S^e_{xy}}}^T\,\Theta_{xy}\mathbf{S^e_{xy}} + \mathbf{Z_{xy}}\right)\,{i^*_{xy}}^2 \end{cases} \tag{2.21}$$

Where L_{xy} contains the concatenation of all l_{xyj}s and l'_{xyj}s, $\mathbf{T_{xy}}$ the concatenation of τ_{xyj}s, $\mathbf{Z_{xy}}$ that of z_{xyj}s, W_{xy} that of w_{xyj}s and w'_{xyj}s, and Θ_{xy} that of θ_{xyj}s. For the electrical signals such as $\mathbf{i_{C_{xy}}}$, $\mathbf{v_{C_{xy}}}$ and $\mathbf{S^e_{xy}}$ that are the most important quantities of the model here, Figure 2.13 details their definition.

The model described by equation (2.21) embeddeds a degree of generality as has been emphasized during the developments of this section. In its ability to describe the conduction losses as well as the influence of the ohmic drops on the voltage of the arm, this model has the potential to be used beneficially to design a control which aims at minimizing the conduction losses.

However, leading to such a nonlinear model is a finding that has not been anticipated. Thus, in a first approach using allocation methods for the MMC, this capacity of the model proposed here will not be used in order to perform a proof-of-concept of first relatively sober allocation algorithms. This obviously does not prevent the community from taking advantage of the model representing the conduction losses to design a more fancy control of the MMC. In this way, from now on, the future developments which are going to come closer to the formulation of the control law, will focus on the model without taking into account the resistances. To this extent, it is sufficient to remove the resistive terms W_{xy}, Θ_{xy} and $\mathbf{Z_{xy}}$ from the equation (2.21).

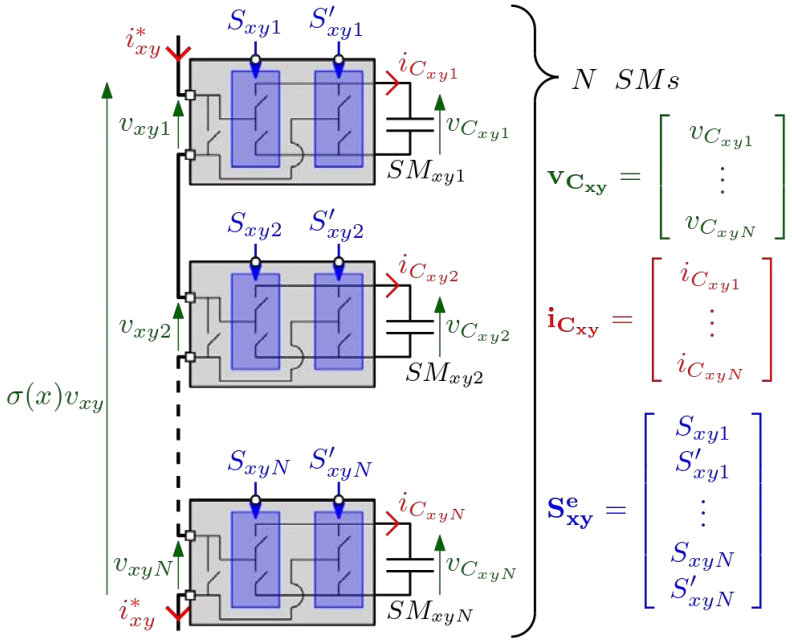

Figure 2.13: Functional diagram of an arm from the MMC

FUNCTIONAL DETAILED MODEL OF THE ARM

$$\begin{cases} \mathbf{i_{C_{xy}}} = C\frac{d\mathbf{v_{C_{xy}}}}{dt} = i^*_{xy}\left(L_{xy}\mathbf{S^e_{xy}} + \mathbf{T_{xy}}\right) \\ v_{xy} = \sigma(x)\left[\left(\mathbf{v_{C_{xy}}}^T L_{xy}\right)\mathbf{S^e_{xy}} + \left(\mathbf{v_{C_{xy}}}^T\mathbf{T_{xy}}\right)\right] \\ v_{xy} \in \left[\sum_{j=1}^{N}(1-q)v_{C_{xyj}}; \sum_{j=1}^{N} v_{C_{xyj}}\right] \end{cases} \tag{2.22}$$

2.B.5.2 Generalized state-space model of the arms

According to (2.22), the state variables whose dynamics are described by low-level the model are the voltages across the capacitors contained in the vector $\mathbf{v_{C_{xy}}}$. It is then decided to define the state vector for the low-level model as the one containing the voltages across the capacitors:

$$\mathbf{X^{xy}_{LL}} = [\mathbf{v_{C_{xy}}}] \tag{2.23}$$

In order to control the current flowing through the converter, the control of the voltage v_{xy} across the arm of the converter is necessary, so the output vector takes the form:

$$\mathbf{Y^{xy}_{LL}} = [v_{xy}, \mathbf{v_{C_{xy}}}^T]^T \tag{2.24}$$

According to (2.22), the state-space model can be put into the form:

$$\dot{\mathbf{v}}_{\mathbf{C_{xy}}} = \frac{i^*_{xy}}{C} L_{xy}\mathbf{S^e_{xy}} + \frac{i^*_{xy}}{C}\mathbf{T_{xy}} \tag{2.25}$$

In this state-space equation $\mathbf{S^e_{xy}}$ stands for the switching states, however the control that will be performed will use a PWM technique. The low-level control algorithm will compute the duty cycles which will then be transformed into binary signals for the gate drivers of the switches thanks to the PWM. The SSM that it is necessary to derive for the control is a model whose control vector must be made of the duty cycles of the switching cells and not the states of their

switches directly. To do this, (2.25) is averaged over the sampling period, the low-level arm-AVM [MC76; BMB14] is then formulated. $\mathbf{D^e_{xy}}$ is then defined as the vector containing the duty cycles of the switches, it is expressed as follows:

$$\mathbf{D^e_{xy}} \triangleq \langle \mathbf{S^e_{xy}} \rangle_{T_c} \tag{2.26}$$

Where (2.28) recalls the definition of the average of a signal over a time window. Switching from the instantaneous model (2.25) to the average value model is achieved by:

$$\langle \dot{\mathbf{v}}_{\mathbf{C_{xy}}} \rangle_{T_c} = \frac{\langle i^*_{xy} \rangle_{T_c}}{C} L_{xy} \mathbf{D^e_{xy}} + \frac{\langle i^*_{xy} \rangle_{T_c}}{C} \mathbf{T_{xy}} \tag{2.27}$$

The average of a signal $x(t)$ over a time window Δt is defined according to:

$$\langle x(\nu) \rangle_{\Delta t} = \frac{1}{\Delta t} \int_{\nu}^{\nu+\Delta_t} x(t)\, dt \tag{2.28}$$

The state-space model is therefore defined thanks to the following differential equation:

$$\dot{\mathbf{X}}^{\mathbf{xy}}_{\mathbf{LL}} = [\langle \dot{\mathbf{v}}_{\mathbf{C_{xy}}} \rangle_{T_c}] = \frac{\langle i^*_{xy} \rangle_{T_c}}{C} L_{xy} \mathbf{D^e_{xy}} + \frac{\langle i^*_{xy} \rangle_{T_c}}{C} \mathbf{T_{xy}} = A^{xy}_{LL} \mathbf{X^{xy}_{LL}} + B^{xy}_{LL} \mathbf{U^{xy}_{LL}} + \mathbf{E^{xy}_{LL}} \tag{2.29}$$

with: $A^{xy}_{LL} = \mathbb{O}_{N,N}$, $B^{xy}_{LL} = \frac{i^*_{xy}}{C} L_{xy}$, $\mathbf{U^{xy}_{LL}} = \mathbf{D^e_{xy}}$ et $\mathbf{E^{xy}_{LL}} = \frac{i^*_{xy}}{C} \mathbf{T_{xy}}$. By expanding each factor of v_{xy} in (2.22) after transforming it into an AVM, it is obtained that:

$$\begin{aligned} \langle v_{xy} \rangle_{T_c} &= \sigma(x) \left[\langle \mathbf{v_{C_{xy}}} \rangle^T_{T_c} L_{xy} \mathbf{S^e_{xy}} + \langle \mathbf{v_{C_{xy}}} \rangle^T_{T_c} \mathbf{T_{xy}} \right] \\ &= \sigma(x) \mathbf{T_{xy}}^T \langle \mathbf{v_{C_{xy}}} \rangle_{T_c} + \sigma(x) \langle \mathbf{v_{C_{xy}}} \rangle^T_{T_c} L_{xy} \mathbf{S^e_{xy}} \\ &= \sigma(x) \mathbf{T_{xy}}^T \mathbf{X^{xy}_{LL}} + \sigma(x) \mathbf{X^{xy}_{LL}}^T L_{xy} \mathbf{U^{xy}_{LL}} \end{aligned} \tag{2.30}$$

The output vector can then be expressed as follows by taking advantage of the previous developments:

$$\mathbf{Y^{xy}_{LL}} = \begin{bmatrix} \langle v_{xy} \rangle_{T_c} \\ \langle \mathbf{v_{C_{xy}}} \rangle_{T_c} \end{bmatrix} = \begin{bmatrix} \sigma(x) \mathbf{T_{xy}}^T \mathbf{X^{xy}_{LL}} + \sigma(x) \mathbf{X^{xy}_{LL}}^T L_{xy} \mathbf{U^{xy}_{LL}} \\ \mathbf{X^{xy}_{LL}} \end{bmatrix} \tag{2.31}$$

This can then be factorized according to the different vectors of the SSM:

$$\mathbf{Y^{xy}_{LL}} = \begin{bmatrix} \langle v_{xy} \rangle_{T_c} \\ \langle \mathbf{v_{C_{xy}}} \rangle_{T_c} \end{bmatrix} = \begin{bmatrix} \sigma(x) \mathbf{T_{xy}}^T \\ \mathbb{I}_N \end{bmatrix} \mathbf{X^{xy}_{LL}} + \begin{bmatrix} \sigma(x) \mathbf{X^{xy}_{LL}}^T L_{xy} \mathbf{U^{xy}_{LL}} \\ \mathbb{O}_{N,1} \end{bmatrix} \tag{2.32}$$

The finally developed model showcase several interesting features. Indeed, this model is non-causal by the presence of the direct feedthrough between the output $\langle v_{xy} \rangle_{T_c}$ and the control $\mathbf{U^{xy}_{LL}}$. Moreover an additive nonlinearity in the form of a state-input product is involved. These different particularities will be treated in the section dedicated to the design of the low-level control.

2.B.5.3 Generalized control allocation-oriented model of the arms

Initially, the elements that will be the object of the low-level control are the global voltage level in an arm v_{xy} as well as the balancing of each of the capacitor voltages $v_{C_{xyj}}$ of this arm. The goal will be to make sure that the voltage v_{xy} reaches its reference while each $v_{C_{xyj}}$ remains as constant as possible around its reference, thus ensuring a good balancing. From the previously established (2.29) and (2.30), it comes that:

$$\begin{bmatrix} \langle v_{xy} \rangle_{T_c} \\ \frac{d\langle \mathbf{v_{C_{xy}}} \rangle_{T_c}}{dt} \end{bmatrix} = \begin{bmatrix} \sigma(x) \mathbf{T_{xy}}^T \mathbf{X^{xy}_{LL}} + \sigma(x) \mathbf{X^{xy}_{LL}}^T L_{xy} \mathbf{U^{xy}_{LL}} \\ \frac{\langle i^*_{xy} \rangle_{T_c}}{C} L_{xy} \mathbf{U^{xy}_{LL}} + \frac{\langle i^*_{xy} \rangle_{T_c}}{C} \mathbf{T_{xy}} \end{bmatrix} \tag{2.33}$$

The control method that will be implemented will use a real time computer, the control will be discrete. To be able to implement this type of control it is necessary that the model has been

discretized. The only differential relation here is that of (2.29). The dynamic matrix being zero, this relation is of the general form:

$$\dot{\mathbf{X}} = B\mathbf{U} + \mathbf{E} \tag{2.34}$$

This is a direct differential relation without linking the state variable to its derivative. Such a State-Space Model (SSM) can be discretized precisely using the matrix exponential by taking advantage of the development carried out in appendix section A for the case where the dynamic matrix A is null, see equation (A.9). To enable this derivation, it is considered that the voltage v_{xy} and the current i^*_{xy} are constant throughout the sampling period of the control. It is important to note that these signals will both have fundamental components at 50 Hz while the sampling frequency will be 4 kHz. This factor 80 between the two allows us to assert that the assumption made about the constancy of v_{xy} and i^*_{xy} at the scale of the sampling period is realistic from a physical point of view.

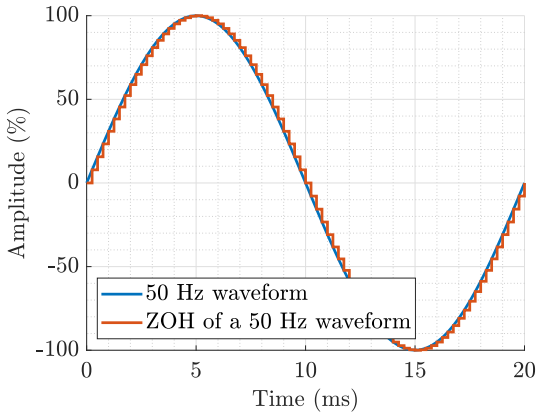

Figure 2.14: 50 Hz waveform and its associated 4 kHz sampled signal.

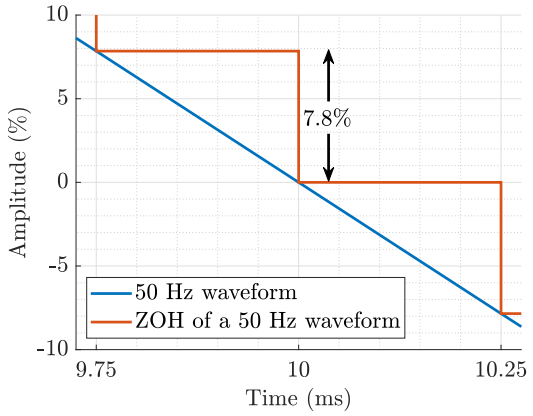

Figure 2.15: Zoom in the location in time where the temporal variation of the signal to sample is the strongest.

The Figure 2.14 shows the waveform of a sinusoidal signal at 50 Hz at the moment when its variation is the strongest, that is to say at the time when the signal crosses 0 because its normalized derivative is then 1, that is to say the maximum for a sinusoidal signal. Figure 2.15 zooms in between two sampling periods at 4 kHz. This figure shows that the maximum difference observed between the real signal at 50 Hz and the corresponding signal sampled and blocked at 4 kHz is 7.8 % of the signal amplitude. This deviation is considered sufficiently small to make the assumption that at the sampling period scale the control law can consider the quantities v_{xy} and i^*_{xy} constant.

Assumption 1. *It is assumed that the sampling period of the control is short enough so that at this time scale the waveforms of the electrical quantities evolving in the MMC are considered constant.*

Thus, as long as this assumption holds, $\langle i^*_{xy} \rangle_{T_c} = i^*_{xy}(k)$ et $\langle v_{xy} \rangle_{T_c} = v_{xy}(k)$ since the average of a constant signal is the signal itself. Moreover, the control itself is considered sampled and blocked on the whole sampling period. This is also consistent because there will be only one determination and one assignment of the duty cycles per sampling period. It is then shown by equation (A.10) that the discretization by matrix exponential gives an identical result to the explicit approximation of Euler:

$$\frac{\mathbf{X}(k+1) - \mathbf{X}(k)}{T_c} = B\mathbf{U}(k) + \mathbf{E} \tag{2.35}$$

with k standing for the current time instant and $k+1$ the next instant at T_c later. Here T_c is the sampling period at which the control will be computed and applied to the system. The above result is true, provided that $B\mathbf{U}+\mathbf{E}$ is constant from time $t = k\,T_c$ to time $t+dt = (k+1)T_c$, which is the case according to the assumption made. This result can be applied to (2.33) which is discretized:

$$\begin{bmatrix} v_{xy}(k)/\sigma(x) \\ \frac{\mathbf{v_{C_{xy}}}(k+1)-\mathbf{v_{C_{xy}}}(k)}{T_c} \end{bmatrix} = \begin{bmatrix} \mathbf{T_{xy}}^T\mathbf{X_{LL}^{xy}}(k) + \mathbf{X_{LL}^{xy}}(k)^T L_{xy}\mathbf{U_{LL}^{xy}}(k) \\ \frac{i^*_{xy}(k)}{C}L_{xy}\mathbf{U_{LL}^{xy}}(k) + \frac{i^*_{xy}(k)}{C}\mathbf{T_{xy}} \end{bmatrix} \tag{2.36}$$

It is reminded that $\sigma(x)^2 = 1$, the following simplification is then obtained:

$$\begin{bmatrix} \sigma(x)v_{xy}(k) \\ \mathbf{v_{C_{xy}}}(k+1) - \mathbf{v_{C_{xy}}}(k) \end{bmatrix} = \begin{bmatrix} \mathbf{T_{xy}}^T\mathbf{X_{LL}^{xy}}(k) + \mathbf{X_{LL}^{xy}}(k)^T L_{xy}\mathbf{U_{LL}^{xy}}(k) \\ \frac{T_c}{C}i^*_{xy}(k)(L_{xy}\mathbf{U_{LL}^{xy}}(k) + \mathbf{T_{xy}}) \end{bmatrix} \tag{2.37}$$

The factorization of the different products as a function of the control allows one to highlight the effectiveness of the control on the different electrical quantities of the submodule. This factorization leads to the following formulation:

$$\begin{bmatrix} \sigma(x)v_{xy}(k) \\ \mathbf{v_{C_{xy}}}(k+1) - \mathbf{v_{C_{xy}}}(k) \end{bmatrix} = \begin{bmatrix} \mathbf{T_{xy}}^T\mathbf{X_{LL}^{xy}}(k) \\ \frac{T_c}{C}i^*_{xy}(k)\mathbf{T_{xy}} \end{bmatrix} + \begin{bmatrix} \mathbf{X_{LL}^{xy}}(k)^T L_{xy} \\ \frac{T_c}{C}i^*_{xy}(k)L_{xy} \end{bmatrix} \mathbf{U_{LL}^{xy}}(k) \tag{2.38}$$

Isolating the control effectivness in the left member of the equation, it follows that:

$$\begin{bmatrix} \mathbf{X_{LL}^{xy}}(k)^T L_{xy} \\ \frac{T_c}{C}i^*_{xy}(k)L_{xy} \end{bmatrix} \mathbf{U_{LL}^{xy}}(k) = \begin{bmatrix} \sigma(x)v_{xy}(k) \\ \mathbf{v_{C_{xy}}}(k+1) - \mathbf{v_{C_{xy}}}(k) \end{bmatrix} - \begin{bmatrix} \mathbf{T_{xy}}^T\mathbf{X_{LL}^{xy}}(k) \\ \frac{T_c}{C}i^*_{xy}(k)\mathbf{T_{xy}} \end{bmatrix} \tag{2.39}$$

It is mentionned that, in normal operation, without blocking the switching cells via the variables S^b_{xyj} and $S^{b'}_{xyj}$, the vector $\mathbf{T_{xy}}$ is zero.

2.C | Conclusions about the low-level modelling

From this chapter, the low-level model has been developed in order to generalize the existing models while providing a more complete description. The developed models focus on the two most common topologies of submodules in the MMCs used today: the half-bridge submodule and the full-bridge submodule.

The developed models are able to describe both the functional behavior of the submodule but also to represent a larger part of the physical details of the submodule, for the half-bridge submodule as well as the full-bridge submodule. In particular, the models go as far as representing the conduction losses in the semiconductors. A generalized model, able to fit any of these two types of submodules, with or without taking into account the conduction losses has been developed. The generality of the models is also given by their scalability: they can be used in the case of a MMC having any number of submodules.

The models proposed here have been developed for the MMC control purpose, they are therefore behavioral models. Their complexity is therefore reduced compared to a knowledge model, in order to be used in a control law design process. During the development, it was observed that the generalized model exhibits nonlinearities, and that taking into account more physical details brings additional nonlinearities. The possibility to linearize the model has been verified and justified in the framework of the parameters of the MMC setup at the LAPLACE. Therefore, in a first approach, the control of the MMC which is developed in this work is done using the linearization of the generalized model. The formulation of the model dedicated to the control methods developed here is embodied by equation (2.39) and is used in Chapter 5.

Thanks to the models developed here, it is now possible to design low-level control[1] of a MMC having any number of submodules while taking into account, or not, the conduction losses in the switches. Although in the context of this study, which is a first approach to allocation-based control methods for the MMC, focus is on a linearized version of the models, low-level models of the MMC that contain nonlinearities can be used to design control systems for the MMC with full consideration of these nonlinearities. This features an interesting work perspective whose results can be compared with the control methods introduced here in Chapter 5.

[1] The low-level control stands for the control of the voltages across the capacitors and the voltages across the arms.

3 Contributions to the Scalable Modelling of Polyphase Systems

Contents

As previously explained in the introduction of Chapter 2, the modelling of the considered converter has two challenges that are shown on Figure 2.1: the low-level and the high-level control-oriented models. Since the first modelling challenge is adressed in Chapter 2, this Chapter 3 focuses on the second challenge which is to describe the relationship between the arm voltages of the MMC and the four types of currents flowing through the latter.

3.A Research axis: towards a generalization of the models

The choice of contributions to the modelling of the MMC has been turned towards the exploration of new models more general than those available in the literature. One of the interesting features made possible by such models is the possibility to develop generic control algorithms that are able to seamlessly adapt to different systems without having to make major modifications to the control system.

High-level model motivations: a generalization to polyphase systems

The interest for electrical polyphase systems is proven, and several reasons for this can be highlighted. The first reason is related to the torque quality properties of electrical machines, which influences vibrations, losses and acoustic noice for example. Indeed, the more phases an electrical machine has, the lower the amplitude of the torque ripples on its mechanical shaft will be [Asl+11; PK06; Zhe+12; Wu+14]. The control of these machines can moreover be the topic of performance research in the aim to lower torque ripples [Tia+17; KS11]. The fact that an electric motor has more phases also makes it possible to guarantee better service continuity when one or more phases have a fault that prevents them from operating nominally; possibilities for operation in the event of faults and in degraded mode are ensured [MAC04; Loc+06; BBM10; Adi+21]. Another reason for increasing the number of phases can come from global sizing methods for electric motors achieved by the optimization of several criteria by tweaking a variety of parameters of which the number of phases is a part. [Le +18] has shown that such a sizing method could lead to the industrialization of a machine with 7 phases. Increasing the number of phases of an electric machine can also have a significant advantage on the conduction losses. Indeed, assuming that the electric motor is designed to guarantee a given maximum torque, having more phases will require a lower maximum current per phase to guarantee this same torque. The increase of m will induce a linear increase of the number of sources producing conduction losses but the maximum current being lower, the conduction losses being proportional to their square, their sum will finally be lower. Increasing the number of phases therefore allows the power of the motor to be distributed among these phases, thus reducing the power rating of each phase [Lev08]. This reduction of the current required in each phase can also be of interest for the design of the converter feeding the machine. The semiconductor sizing constraints are then reduced.

The article [Lev08] presents a rather detailed survey on polyphase machines and their interests since their advent in the 1960s which, completed by the information of [DG18], adds a chronology

to the various advantages introduced above and presents the various research themes of which polyphase machines are the main topic since then. These themes range from the sizing of these machines to their control, through the modelling of these machines and the analysis of their physical characteristics.

Polyphase motors with more than a few phases have already been studied such as: 5-phase [Liu+16; Zho+17; Tia+17], 6-phase [Zhe+12; Wu+14], 7-phase [Loc+06], 9-phase [Li+14; YCC16]. Motors with more than 10 phases can be of interest in the field of marine transport, for example, for the acoustic qualities given by such machines. As examples, one can cite the submarine Scorpene from Naval Group-AREVA-Jeumont (based on a 13-phase permanent magnet motor) [Gro], Permasyn from Siemens (based on a 12-phase permanent magnet motor) [Sie] or also a 15-phase induction machine for ship propulsion [TSN04] and even up to 20 phases [WSH04]. Machines with up to several dozen phases have already been made for one or more of the reasons that have been outlined [PG14; Pat+16; Bac+15]. Thus, interest in polyphase systems is established and it dates back to the 1960s.

Knowing that the MMC is a modular topology in power rating by its ability to stack the elementary bricks which are the SMs, it can be interesting to give it even more modularity by looking at the aspect which concerns the increase in the number of legs of this topology of converter. Increasing the number of legs does not present a structural risk for the integrity of the semiconductors as long as the increase in the number of phases is accompanied by a proportional increase in the power rating that it is desired to convert. Having a control model of such a converter, modular in the number of submodule and in the number of legs, would make it possible to adapt to a very large class of electrical systems and a very large power range. The applications of the MMC have indeed already a very wide range of power: from a few kilowatts [Ser14] to several gigawatts like for the INELFE.

For the high-level part, the emphasis is therefore placed on developing models capable of taking into account the fact that the MMC can be used in the context of a electrical polyphase system containing any number of submodules. The control-oriented high-level models that are detailed in this chapter will aim to be scalable to both the number N of submodules contained in an arm of the converter and to the number m of phases of the AC network. These models will be derived in the state-space. This choice comes from the control allocation method which traditionally uses state-space models to develop its control laws [Lal85; MGB89; Bod02].

Outline

In order to have a control-oriented model adapted to the methods that will be used in Chapter 5, a current state-space model will be developed. The first modelling step of Section 3.B will aim at describing the dynamic behavior of each type of current. A state-space model gathering the different currents together will then be established in Section 3.C. In order to reduce the complexity of the model then obtained, a new formulation of the state-space model is derived in Section 3.D, applying a first Park tranform. Due to a lack of accuracy of this first reduced order model, a new Park transformation is designed and proposed in Section 3.E, it is a new general Park tranform that can be adapted to any polyphase system. Section 3.F takes advantage of this new Park transform in order to develop a reduced order invariant model of the currents which embodies a very good trade-off between accuracy and complexity. The different models introduced are then tested and compared with the existing one and with a simulation software dedicated to electrical engineering: PLECS®, in Section 3.H. The results then obtained allow to guarantee the ability to use the proposed models in a control purpose while featuring outstanding characteristics.

The two sufficiently accurate models will be used in Chapter 5 to develop the CA for the MMC. Finally, Section 3.J will conclude this chapter.

3.B High-level modelling: from the converter arm voltages to the currents

3.B.1 Modelling goals and assumptions

The primary objective of high-level modelling is the scalability of the proposed model to the number of phases from the AC network at the output of the converter. Figure 1.2 showing the three-phase topology, is increased to obtain the topology of the MMC in the case of a m-phase AC network which is schemed on Figure 3.1 with the addition of the DC-side impedance.

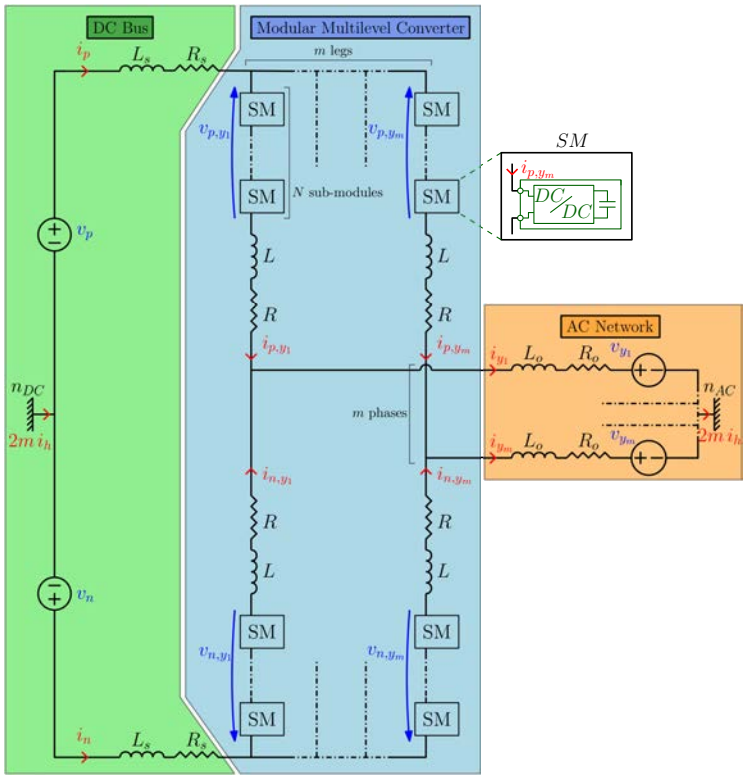

Figure 3.1: Electrical diagram of the MMC topology in the m-phase case, each leg contains N submodules by arm

In the low-level model it is of interest to express the internal electrical quantities of the submodules as well as the voltages between the terminals of the arm as a function of the switching states of these submodules which will be then considered as the effectors for the low-level. In the high-level model the aim is at describing the behavior of more global electrical quantities like the currents, resulting from the interaction between the various arms of the MMC. Those global electrical quantities are expressed as a function of the arm voltages which will then be considered as the effectors for the high-level.

In the approach implemented here, the dynamics of the currents and of the capacitor voltages are considered sufficiently different to assume that it is possible to focus on the control of the currents independently of that of the voltages in a first approach. Therefore, a model of type arm-AVM with an averaging performed at the scale of the switching period is adopted in a simplified

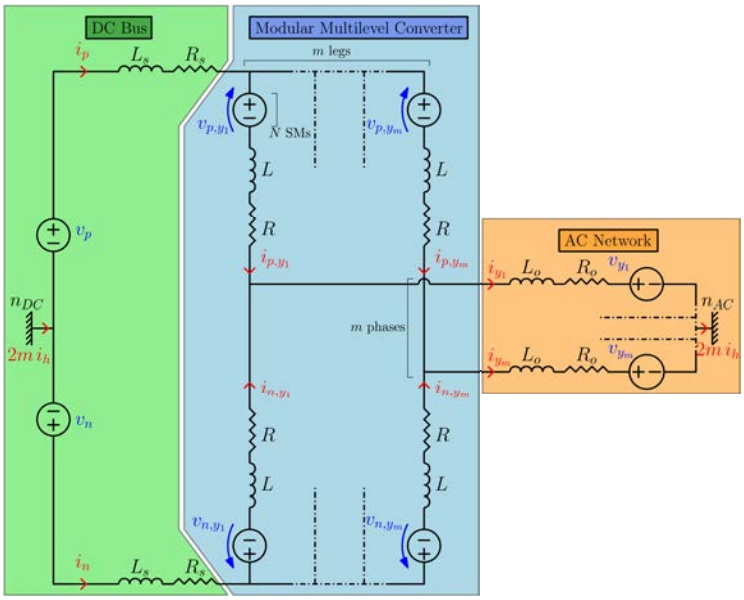

Figure 3.2: Electrical diagram of the MMC topology in the m-phase case, each leg contains N submodules which are considered to be continuously variable voltage sources according to Assumption 2

formulation which does not take into account the internal dynamics of each capacitor, nor those of a possible arm-equivalent capacitor. As a consequence, this high-level model considers each arm as a simple variable voltage source.

Assumption 2. *All submodules are considered to be continuously variable voltage sources.*

Assumption 2 is considered true for the model derivations in this chapter. Considering that each submodule is a variable voltage source means considering that the voltages across the arms, v_{xy}, are themselves continuously variable voltages according to the definition of v_{xy}. Each arm features then, from a high-level point of view, a variable voltage source. The developed high-level model is thus independent of the number of submodules, making it adaptable and insensitive to N. Figure 3.2 presents the electrical diagram of the m-phase topology taking into account this assumption.

3.B.2 Special caracteristics of high-level operation

As described in Section 1.B.2.3, the currents that appear during the operation of the MMC can be split into four different types: 1) the DC supply current, 2) the AC-side output current, 3) the circulating current and 4) the common mode current in the case the neutrals are connected. In order to analyze the dynamic behavior of each of these currents, the high-level model will aim at describing each current independently of the influence of the others. To do so, the interest is then focused on the path followed by each current in the MMC as described by Figure 1.6. So as to generalize the modelling of the MMC to the polyphase case, Figure 1.6 is extended to the m-phase case with Figure 3.3 by simply adding as many legs as the number of desired phases.

In order to stay consitent with state-of-the-art models [PRB14; Liz+15], it is decided to let $2m\,i_m$ be the total current flowing through the neutrals, $m\,i_s$ be the total current delivered by the DC bus to the MMC, i_{c_y} be the current flowing from each arm of the MMC and $2\,i_{o_y}$ be the current distributed by a leg of the MMC to the AC network. According to the KCL and the superposition

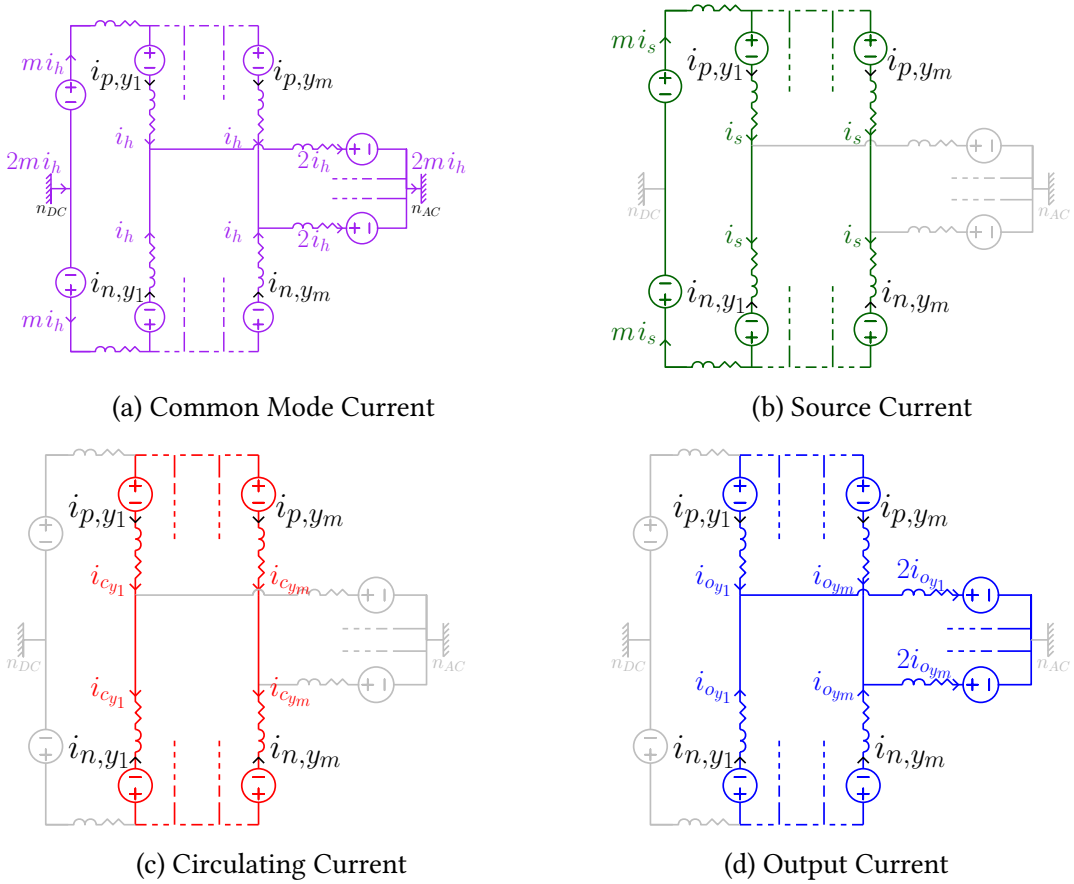

(a) Common Mode Current

(b) Source Current

(c) Circulating Current

(d) Output Current

Figure 3.3: Illustration of the currents involved in the conversion performed by the MMC

theorem, the i_{xy} formulas can then be deduced:

$$\forall y \in \{y_1, \ldots, y_m\}, \begin{cases} i_{py}(t) = i_m(t) + i_s(t) + i_{c_y}(t) + i_{o_y}(t) \\ i_{ny}(t) = i_m(t) - i_s(t) - i_{c_y}(t) + i_{o_y}(t) \end{cases} \tag{3.1}$$

In order not to make the writing more cumbersome, the notation of the time dependence is voluntarily omitted but the focus is always on the instantaneous value of the currents:

$$\forall y \in \{y_1, \ldots, y_m\}, \begin{cases} i_{py} = i_m + i_s + i_{c_y} + i_{o_y} \\ i_{ny} = i_m - i_s - i_{c_y} + i_{o_y} \end{cases} \tag{3.2}$$

By sum and difference of the relations from (3.2):

$$\forall y \in \{y_1, \ldots, y_m\}, \begin{cases} i_{py} + i_{ny} = 2(i_m + i_{o_y}) \\ i_{py} - i_{ny} = 2(i_s + i_{c_y}) \end{cases} \tag{3.3}$$

By observing the positive pole, first, then the negative pole of the DC bus, Figure 3.2 allows the following observation:

$$\begin{cases} i_p = \sum_{y=y_1}^{y_m} i_{py} \\ i_n = \sum_{y=y_1}^{y_m} i_{ny} \end{cases} \tag{3.4}$$

Summing the expression (3.3) over all phases and putting to use the definitions introduced by (3.4), it follows that:

$$\begin{cases} \sum_{y=y_1}^{y_m} i_{py} + i_{ny} = i_p + i_n = 2mi_m + 2\sum_{y=y_1}^{y_m} i_{o_y} \\ \sum_{y=y_1}^{y_m} i_{py} - i_{ny} = i_p - i_n = 2mi_s + 2\sum_{y=y_1}^{y_m} i_{c_y} \end{cases} \tag{3.5}$$

Structurally, through the KCL, Figure 3.3 (c) and Figure 3.3 (d) highlight the fact that the circulating currents as well as the output currents are null sum, thus:

$$\begin{cases} \sum_{y=y_1}^{y_m} i_{o_y} = 0 \\ \sum_{y=y_1}^{y_m} i_{c_y} = 0 \end{cases} \tag{3.6}$$

Equation (3.5) can then be directly reformulated taking into account this freshly obtained result:

$$\begin{cases} i_p + i_n = 2m\, i_m \\ i_p - i_n = 2m\, i_s \end{cases} \tag{3.7}$$

By sum and difference of the formulas from (3.7), then dividing them by 2:

$$\begin{cases} i_p = m(i_m + i_s) \\ i_n = m(i_m - i_s) \end{cases} \tag{3.8}$$

This equation (3.8) is set aside for later use.

Decoupling equations for single component currents

Applying the KCL at the connection between each converter arm and the associated AC grid phase, Figure 3.2, shows that:

$$\forall y \in \{y_1, \ldots, y_m\}, i_y = i_{py} + i_{ny} \tag{3.9}$$

By putting (3.3) to use, it is found that:

$$\forall y \in \{y_1, \ldots, y_m\}, i_y = 2(i_m + i_{o_y}) \tag{3.10}$$

The concatenation of (3.8) and (3.10), gives:

$$\begin{cases} i_p = m(i_m + i_s) \\ i_n = m(i_m - i_s) \\ \forall y \in \{y_1, \ldots, y_m\}, i_y = 2(i_m + i_{o_y}) \end{cases} \tag{3.11}$$

It is possible to reformulate (3.7) using the definitions of (3.4) as:

$$\begin{cases} 2m\, i_m = i_p + i_n = \sum_{y=y_1}^{y_m} i_{py} + i_{ny} \\ 2m\, i_s = i_p - i_n = \sum_{y=y_1}^{y_m} i_{py} - i_{ny} \end{cases} \tag{3.12}$$

Equation (3.12) is set aside for future derivations while a new development takes place.

Decoupling equations for the output current

For upcoming models it is necessary to look at the following different formulas:

- $\forall j \in [\![1; m]\!],\ \ (m-1) i_{y_j} - \sum_{k \neq j}^{m} i_{y_k}$
- $\forall j \in [\![1; m]\!],\ \ (m-1)(i_{p,y_j} - i_{n,y_j}) - \sum_{k \neq j}^{m} (i_{p,y_k} - i_{n,y_k})$

From the i_y expression of (3.11) which is true for any y, it can be shown that:

$$\forall j \in [\![1; m]\!],\ \ (m-1) i_{y_j} - \sum_{k \neq j}^{m} i_{y_k} = (m-1) 2(i_m + i_{o_{y_j}}) - \sum_{k \neq j}^{m} 2(i_m + i_{o_{y_k}}) \tag{3.13}$$

Since i_m, in the second sum, does not depend on the summation index, it can be removed from the sum. It is noted that the sum contains a total of only $(m-1)$ terms. Thus, it follows that:

$$\forall j \in [\![1;m]\!],\ \ (m-1)i_{y_j} - \sum_{k\neq j}^{m} i_{y_k} = 2(m-1)i_{o_{y_j}} - 2\sum_{k\neq y}^{m} i_{o_{y_k}} \tag{3.14}$$

By (3.6), selecting the j-th current among the m available currents gives:

$$\sum_{k=1}^{m} i_{o_{y_k}} = 0 \Longleftrightarrow i_{o_{y_j}} = -\sum_{k\neq j}^{m} i_{o_{y_k}} \tag{3.15}$$

By substituting $i_{o_{y_j}}$ for $-\sum_{k\neq j}^{m} i_{o_{y_k}}$ in (3.14) it is deduced that:

$$(m-1)i_{y_j} - \sum_{k\neq j}^{m} i_{y_k} = 2(m-1)i_{o_{y_j}} + 2i_{o_{y_j}} = 2m\, i_{o_{y_j}} \tag{3.16}$$

This gives, according to (3.4) and (3.9):

$$mi_{y_j} - \sum_{k=1}^{m} i_{y_k} = 2m\, i_{o_{y_j}} \Longleftrightarrow m(i_{p,y_j} + i_{n,y_j}) - (i_p + i_n) = 2m\, i_{o_{y_j}} \tag{3.17}$$

So it is finally achieved:

$$\forall y \in \{y_1, \ldots, y_m\},\quad m(i_{py} + i_{ny}) - (i_p + i_n) = 2m\, i_{o_y} \tag{3.18}$$

This equation (3.18) is essential for the development of the output current model.

Decoupling equations for the circulating current

By substituting $(i_{py} - i_{ny})$ from (3.3), it follows that:

$$\begin{aligned} \forall j \in [\![1;m]\!],\ \ &(m-1)(i_{p,y_j} - i_{n,y_j}) - \textstyle\sum_{k\neq j}^{m}(i_{p,y_k} - i_{n,y_k}) \\ &= (m-1)2(i_s + i_{c_{y_j}}) - \textstyle\sum_{k\neq j}^{m} 2(i_s + i_{c_{y_k}}) \\ &= 2(m-1)i_{c_{y_j}} - 2\textstyle\sum_{k\neq j}^{m} i_{c_{y_k}} \end{aligned} \tag{3.19}$$

The same reasoning as previously followed for the output current will take place here again. By Figure 3.3 (c), the KCL:

$$\sum_{k=1}^{m} i_{c_{y_k}} = 0 \Longleftrightarrow i_{c_{y_j}} = -\sum_{k\neq j}^{m} i_{c_{y_k}} \tag{3.20}$$

Taking advantage of this equation, it is possible to substitute $-\sum_{k\neq j}^{m} i_{c_{y_k}}$ from (3.19) by $i_{c_{y_j}}$, it is thus deduced that:

$$(m-1)(i_{p,y_j} - i_{n,y_j}) - \sum_{k\neq j}^{m}(i_{p,y_k} - i_{n,y_k}) = 2(m-1)i_{c_{y_j}} + 2i_{c_{y_j}} = 2m\, i_{c_{y_j}} \tag{3.21}$$

This gives, by (3.12):

$$m(i_{p,y_j} - i_{n,y_j}) - (i_p - i_n) = 2m\, i_{c_{y_j}} \tag{3.22}$$

So it is finally obtained:

$$\forall y \in \{y_1, \ldots, y_m\},\quad m(i_{py} - i_{ny}) - (i_p - i_n) = 2m\, i_{c_y} \tag{3.23}$$

which is also an essential equation for future developments.

Decoupling equations for the four current types

To sum it up, equations (3.12), (3.18), and (3.23) allow to state that:

$$\forall y \in \{y_1, \dots, y_m\}, \begin{cases} 2m\, i_m = i_p + i_n = \sum_{y=y_1}^{y_m} (i_{py} + i_{ny}) \\ 2m\, i_s = i_p - i_n = \sum_{y=y_1}^{y_m} (i_{py} - i_{ny}) \\ 2m\, i_{o_y} = m(i_{py} + i_{ny}) - (i_p + i_n) \\ 2m\, i_{c_y} = m(i_{py} - i_{ny}) - (i_p - i_n) \end{cases} \tag{3.24}$$

This result is the starting point that makes it possible to derive decoupled differential equations to describe the dynamics of each current type independently of the others.

3.B.3 Decoupled generalized polyphase full order model of the currents

Initially the model will be established for only one phase and thus only one arm of the MMC without loss of generality for the other phases built the same way, this model will be thereafter extended to the m phases of the system. When focusing on a single phase of the MMC, its diagram becomes the one displayed on Figure 3.2.

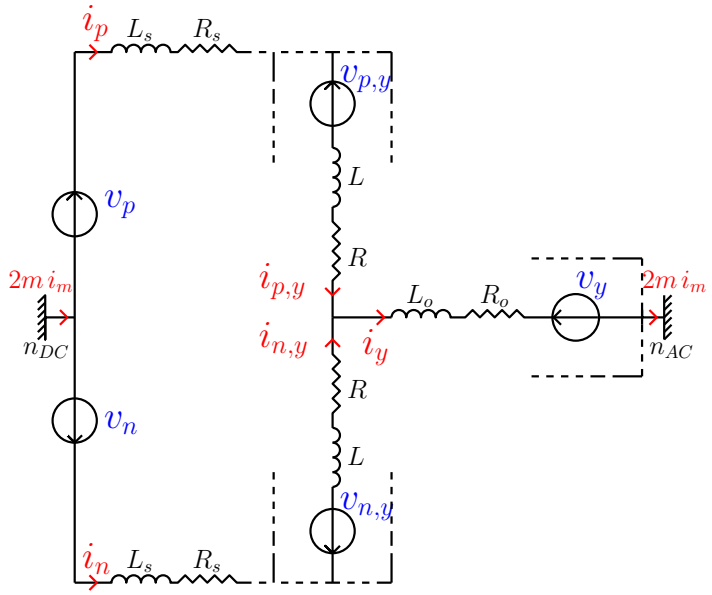

Figure 3.4: Electric diagram of a single leg of a m-phase MMC.

By using the KIRCHHOFF laws applied to the path where the currents flow through the upper side of the electric circuit and to the path where they flow through its lower side, it is possible to show that:

$$\forall y \in \{y_1, \dots, y_m\}, \\ \begin{cases} v_p = v_y + (R_o + L_o s) i_y + (R + Ls) i_{py} + v_{py} + (R_s + L_s s) i_p + v_{n_{AD}} \\ v_n = v_y + (R_o + L_o s) i_y + (R + Ls) i_{ny} + v_{ny} + (R_s + L_s s) i_n + v_{n_{AD}} \end{cases} \tag{3.25}$$

where s is the LAPLACE variable representing the time derivation operator $\frac{d\cdot}{dt}$, and $v_{n_{AD}} = v_{n_{AC}} - v_{n_{DC}}$. From this, it can be deduced that:

$$\forall x \in \{n, p\}, \forall y \in \{y_1, \dots, y_m\}, \\ (\alpha_{x,y}) : \quad v_x = v_y + (R_o + L_o s) i_y + (R + Ls) i_{xy} + v_{xy} + (R_s + L_s s) i_x + v_{n_{AD}} \tag{3.26}$$

The objective of the following development is to be able to describe the dynamics of each current type that it is possible to observe on Figure 3.3. To do this, the differential equation $(\alpha_{x,y})$ which describes the dynamics of the electrical quantities in the MMC will be used. To guess which developments to address, the precious help from (3.24) is recalled here:

$$\forall y \in \{y_1, \dots, y_m\}, \begin{cases} 2m\, i_m = i_p + i_n = \sum_{y=y_1}^{y_m} (i_{py} + i_{ny}) \\ 2m\, i_s = i_p - i_n = \sum_{y=y_1}^{y_m} (i_{py} - i_{ny}) \\ 2m\, i_{o_y} = m(i_{py} + i_{ny}) - (i_p + i_n) \\ 2m\, i_{c_y} = m(i_{py} - i_{ny}) - (i_p - i_n) \end{cases} \tag{3.27}$$

Since equation $(\alpha_{x,y})$ contains the current i_{xy}, it is intuitive to think that in order to formulate the dynamics of the different types of currents found in (3.24), it will be necessary to combine different $(\alpha_{x,y})$ equations.

Model for the common mode current (i_m, I_m)

As suggested by the first relation of (3.27) which deals with the common mode current, the dynamic behavior of i_m will be found by deriving the dynamics of the current $\sum_{y=y_1}^{y_m}(i_{py}+i_{ny})$. The first step is therefore to develop the dynamics of $(i_{py} + i_{ny})$. The current i_{py} appears in the equation $(\alpha_{p,y})$ and i_{ny} in $(\alpha_{n,y})$, it may be interesting to start by developing the following addition: $(\alpha_{p,y}) + (\alpha_{n,y})$, which gives:

$$\begin{aligned} v_n + v_p \;=\; & 2v_y + [(R + 2R_o) + (L + 2L_o)s](i_{py} + i_{ny}) \\ & + (R_s + L_s s)(i_p + i_n) + 2v_{n_{AD}} + (v_{py} + v_{ny}) \end{aligned} \tag{3.28}$$

By summing over all phases $\sum_{y=y_1}^{y_m} (\alpha_{p,y}) + (\alpha_{n,y})$, the dynamics of $\sum_{y=y_1}^{y_m}(i_{py} + i_{ny})$ are obtained. From the previous equation, $\sum_{y=y_1}^{y_m} (\alpha_{p,y}) + (\alpha_{n,y})$ gives:

$$\begin{aligned} m(v_n + v_p) \;=\; & 2\sum_{y=y_1}^{y_m} v_y + [(R + 2R_o) + (L + 2L_o)s](i_p + i_n) \\ & + m(R_s + L_s s)(i_p + i_n) + 2m\, v_{n_{AD}} + \sum_{y=y_1}^{y_m}(v_{py} + v_{ny}) \end{aligned} \tag{3.29}$$

Moreover by (3.27) it is known that $i_p + i_n = 2m\, i_m$, so by substituting $2m\, i_m$ for $i_p + i_n$ in (3.29) and dividing it by $2m$, it follows that:

$$\begin{aligned} \tfrac{(v_n+v_p)}{2} \;=\; & \tfrac{1}{m}\sum_{y=y_1}^{y_m} v_y + [(mR_s + R + 2R_o) + (mL_s + L + 2L_o)s] i_m \\ & + v_{n_{AD}} + \tfrac{1}{2m}\sum_{y=y_1}^{y_m}(v_{py} + v_{ny}) \end{aligned} \tag{3.30}$$

In order to simplify and unify the equations from the model, it is decided to use the following notations:

$$\begin{aligned} & R_m^{eq} = mR_s + R + 2R_o \quad \text{and} \quad L_m^{eq} = mL_s + L + 2L_o \\ & N_\Sigma(m) = \tfrac{1}{m}[1, \dots, 1] \in \mathcal{M}_{1,m}(\mathbb{R}) \\ & I_m = [i_m] \\ & \mathbf{V_x} = [v_p, v_n]^T \\ & \mathbf{V_y} = [v_{y_1}, \dots, v_{y_m}]^T \\ & V_{n_{AD}} = [v_{n_{AD}}] = [v_{n_{AC}} - v_{n_{DC}}] \\ & \mathbf{V_{py}} = [v_{py_1}, \dots, v_{py_m}]^T \\ & \mathbf{V_{ny}} = [v_{ny_1}, \dots, v_{ny_m}]^T \end{aligned} \tag{3.31}$$

The use of these notations leads to the following equation[1]:

[1] The colors used for this equation and in the upcoming ones (3.32), (3.47) and (3.55) are deliberately reminiscent of those of Figure 3.3 because it is then possible to make the link between the path covered by each current type and the equivalent impedance associated with them in the resulting model.

$$(R_m^{eq} + L_m^{eq}s)I_m = -\frac{1}{2}N_\Sigma(m)\left(\mathbf{V_{py}} + \mathbf{V_{ny}}\right) + \left(N_\Sigma(2)\mathbf{V_x} - N_\Sigma(m)\mathbf{V_y} - N_\Sigma(1)V_{n_{AD}}\right) \tag{3.32}$$

The voltage V_m is then defined as the voltage driving the common mode current because for the high-level model it is the voltages v_{py} and v_{ny} which are the control variables of the currents, themselves contained in the vectors $\mathbf{V_{py}}$ and $\mathbf{V_{ny}}$:

$$V_m = -\frac{1}{2}N_\Sigma(m)\left(\mathbf{V_{py}} + \mathbf{V_{ny}}\right) \tag{3.33}$$

The expression of $N_\Sigma(m)$ which will be often used thereafter is detailed here:

$$N_\Sigma(m) = \frac{1}{m}\begin{bmatrix}1 & 1 & 1 & \dots & 1\end{bmatrix} \in \mathcal{M}_{1,m}(\mathbb{R}) \tag{3.34}$$

It is important to note that when the DC and AC neutrals are not connected, the I_m current is forced to zero and that a voltage can appear between the neutrals. Equation (3.32), allowing to describe this voltage, then becomes:

$$V_{n_{AD}} = -\frac{1}{2}N_\Sigma(m)\left(\mathbf{V_{py}} + \mathbf{V_{ny}}\right) + \left(N_\Sigma(2)\mathbf{V_x} - N_\Sigma(m)\mathbf{V_y}\right) \tag{3.35}$$

Model for the source current (i_s, I_s)

The approach taken for the common mode current will take place here as well. As suggested by the second formula from (3.27) which involves the source current, the i_s dynamics will be obtained by deriving the dynamics from $(i_{py} - i_{ny})$. The first step is thus to determine the dynamics of $(i_{py} - i_{ny})$. The current i_{py} appears in the equation $(\alpha_{p,y})$ and i_{ny} in $(\alpha_{n,y})$, thus the derivation starts by developing the following relationship: $(\alpha_{p,y}) - (\alpha_{n,y})$, which gives:

$$v_p - v_n = (R + Ls)(i_{py} - i_{ny}) + (R_s + L_s s)(i_p - i_n) + (v_{py} - v_{ny}) \tag{3.36}$$

By summing over all phases $\sum_{y=y_1}^{y_m}(\alpha_{p,y}) - (\alpha_{n,y})$, the dynamics of $\sum_{y=y_1}^{y_m}(i_{py} - i_{ny})$ are obtained. From the previous equation, $\sum_{y=y_1}^{y_m}(\alpha_{p,y}) - (\alpha_{n,y})$ gives:

$$m(v_p - v_n) = (R + Ls)(i_p - i_n) + m(R_s + L_s s)(i_p - i_n) + \sum_{y=y_1}^{y_m}(v_{py} - v_{ny}) \tag{3.37}$$

Moreover by (3.27) it is obtained that $i_p - i_n = 2m\, i_s$, so by substituting $2m\, i_s$ for $i_p - i_n$ in (3.37) and dividing by $2m$, it follows that:

$$\frac{(v_p - v_n)}{2} = [(mR_s + R) + (mL_s + L)s]i_s + \frac{1}{2m}\sum_{y=y_1}^{y_m}(v_{py} - v_{ny}) \tag{3.38}$$

To simplify the expression obtained, it is decided to set:

$$\begin{aligned} &R_s^{eq} = mR_s + R \quad \text{and} \quad L_s^{eq} = mL_s + L \\ &N_\Delta(m) = \tfrac{1}{m}[m\mathbb{I}_m - \mathbb{J}_m] \in \mathcal{M}_m(\mathbb{R}) \\ &I_s = [i_s] \end{aligned} \tag{3.39}$$

Where $\mathbb{J}_m$ is the matrix of size $(m \times m)$ filled with 1's. Using these new notations then shows that:

$$(R_s^{eq} + L_s^{eq} s) I_s = -\frac{1}{2} N_\Sigma(m) \left(\mathbf{V_{py}} - \mathbf{V_{ny}}\right) + \left([1 \;\; 0] \cdot N_\Delta(2) \mathbf{V_x}\right) \tag{3.40}$$

In the same way that V_m was previously defined, V_s is the driving voltage for the source current:

$$V_s = -\frac{1}{2} N_\Sigma(m) \left(\mathbf{V_{py}} - \mathbf{V_{ny}}\right) \tag{3.41}$$

Model for the circulating current $(i_{c_y}, \mathbf{I_c})$

The same approach used for the common mode current as well as for the DC bus current will be applied once again for the circulating currents. However, the approach here will be significantly more complex since the inspiring expression here is less obvious. As suggested by the fourth formula from (3.27) which deals with the circulating current, the dynamics of i_{c_y} will be derived by developing the dynamics of $m(i_{py} - i_{ny}) - (i_p - i_n)$ either the dynamics of $m(i_{py} - i_{ny}) - \sum_{y=y_1}^{y_m}(i_{py} - i_{ny})$. The first step is to formulate the dynamics of $m(i_{py} - i_{ny})$. The current i_{py} appears in equation $(\alpha_{p,y})$ and i_{ny} in $(\alpha_{n,y})$, thus one must start by developing the following relationship: $m\left[(\alpha_{p,y}) - (\alpha_{n,y})\right]$, which gives:

$$m(v_p - v_n) = m(R + Ls)(i_{py} - i_{ny}) + m(R_s + L_s s)(i_p - i_n) + m(v_{py} - v_{ny}) \tag{3.42}$$

It is now necessary to look at the second part: $-\sum_{y=y_1}^{y_m}(i_{py} - i_{ny})$. From the previous developments $\sum_{y=y_1}^{y_m}(\alpha_{p,y}) - (\alpha_{n,y})$ has already been computed as shown by (3.37), so a multiplication by -1 brings $-\sum_{y=y_1}^{y_m}(\alpha_{p,y}) - (\alpha_{n,y})$:

$$-m(v_p - v_n) = -(R_s^{eq} + L_s^{eq} s)(i_p - i_n) - \sum_{y=y_1}^{y_m}(v_{py} - v_{ny}) \tag{3.43}$$

The sum of these two previous equations gives $m\left[(\alpha_{p,y}) - (\alpha_{n,y})\right] - \sum_{y=y_1}^{y_m}(\alpha_{p,y}) - (\alpha_{n,y})$ which governs the dynamics of $m(i_{py} - i_{ny}) - \sum_{y=y_1}^{y_m}(i_{py} - i_{ny}) = m(i_{py} - i_{ny}) - (i_p - i_n)$:

$$0 = (R + Ls)\left(m(i_{py} - i_{ny}) - (i_p - i_n)\right) + \left(m(v_{py} - v_{ny}) - \sum_{y=y_1}^{y_m}(v_{py} - v_{ny})\right) \tag{3.44}$$

It is decided to set the simplifying notations:

$$\begin{array}{l} R_c^{eq} = R \quad \text{and} \quad L_c^{eq} = L \\ N_\Delta(y, m) = \frac{1}{m}[-1, \ldots, -1, m-1, -1, \ldots, -1] \in \mathcal{M}_{1,m}(\mathbb{R}) \text{ with } m-1 \text{ in position } \#y \\ \mathbf{I_c} = [i_{c_{y_1}}, \ldots, i_{c_{y_m}}]^T \end{array} \tag{3.45}$$

By (3.27) it has been shown that $2m\, i_{c_y} = m(i_{py} - i_{ny}) - (i_p - i_n)$, so substituting $m(i_{py} - i_{ny}) - (i_p - i_n)$ by $2m\, i_{c_y}$, dividing it by $2m$ and using the notations defined above, it is shown that:

$$0 = (R_c^{eq} + L_c^{eq} s) i_{c_y} + \frac{1}{2} N_\Delta(y, m) \left(\mathbf{V_{py}} - \mathbf{V_{ny}}\right) \tag{3.46}$$

This equation being true $\forall y \in \{y_1, \ldots, y_m\}$, it is extended to yield then:

$$(R_c^{eq} + L_c^{eq}s)\mathbf{I_c} = -\frac{1}{2}N_\Delta(m)\,(\mathbf{V_{py}} - \mathbf{V_{ny}}) \tag{3.47}$$

As for the two previous currents, the control voltage of the current under scrutiny is defined:

$$\mathbf{V_c} = -\frac{1}{2}N_\Delta(m)\,(\mathbf{V_{py}} - \mathbf{V_{ny}}) \tag{3.48}$$

The expression of $N_\Delta(m)$ which will be often used thereafter is detailed here:

$$N_\Delta(m) = \begin{bmatrix} N_\Delta(y_1,m) \\ N_\Delta(y_2,m) \\ N_\Delta(y_3,m) \\ \vdots \\ N_\Delta(y_m,m) \end{bmatrix} = \frac{1}{m}\begin{bmatrix} m-1 & -1 & -1 & \dots & -1 \\ -1 & m-1 & -1 & \dots & -1 \\ -1 & -1 & m-1 & \dots & -1 \\ \vdots & \vdots & \vdots & \ddots & \vdots \\ -1 & -1 & -1 & \dots & m-1 \end{bmatrix} \in \mathcal{M}_m(\mathbb{R}) \tag{3.49}$$

Model for the output current $(i_{o_y}, \mathbf{I_o})$

The same approach as that used for the circulating current will be taken here for the output current. As suggested by the third formula of (3.27) which involves the output current, the dynamics from i_{o_y} will be developed by deriving the dynamics of the current $m(i_{py} + i_{ny}) - (i_p + i_n)$ that is the dynamics of $m(i_{py} + i_{ny}) - \sum_{y=y_1}^{y_m}(i_{py} + i_{ny})$. The first step is to find the dynamics of $m(i_{py} + i_{ny})$. The current i_{py} appears in the equation $(\alpha_{p,y})$ and i_{ny} in $(\alpha_{n,y})$, one must begin by developing the following relationship: $m\,[(\alpha_{p,y}) + (\alpha_{n,y})]$, which gives:

$$\begin{array}{rcl} m(v_p + v_n) & = & 2mv_y + m[(R + 2R_o) + (L + 2L_o)s](i_{py} + i_{ny}) \\ & & +m(R_s + L_s s)(i_p + i_n) + 2mv_{n_{AD}} + m(v_{py} + v_{ny}) \end{array} \tag{3.50}$$

It is now necessary to look at the second part: $-\sum_{y=y_1}^{y_m}(i_{py} + i_{ny})$. From the previous developments $\sum_{y=y_1}^{y_m}(\alpha_{p,y}) + (\alpha_{n,y})$ has already been computed as shown by (3.29), so a multiplication by -1 brings $-\sum_{y=y_1}^{y_m}(\alpha_{p,y}) + (\alpha_{n,y})$:

$$-m(v_p + v_n) = -2\sum_{y=y_1}^{y_m} v_y - (R_m^{eq} + L_m^{eq}s)(i_p + i_n) - 2mv_{n_{AD}} - \sum_{y=y_1}^{y_m}(v_{py} + v_{ny}) \tag{3.51}$$

The sum of these two previous equations gives $m\,[(\alpha_{p,y}) + (\alpha_{n,y})] - \sum_{y=y_1}^{y_m}(\alpha_{p,y}) + (\alpha_{n,y})$ which governs the dynamics of $m(i_{py} + i_{ny}) - \sum_{y=y_1}^{y_m}(i_{py} + i_{ny}) = m(i_{py} + i_{ny}) - (i_p + i_n)$:

$$\begin{array}{c} 0 = 2\left(mv_y - \sum_{y=y_1}^{y_m} v_y\right) + [(R + 2R_o) + (L + 2L_o)s]\,(m(i_{py} + i_{ny}) - (i_p + i_n)) + \\ \left(m(v_{py} + v_{ny}) - \sum_{y=y_1}^{y_m}(v_{py} + v_{ny})\right) \end{array} \tag{3.52}$$

Notations are then introduced:

$$\begin{array}{l} R_o^{eq} = R + 2R_o \text{ and } L_o^{eq} = L + 2L_o \\ \mathbf{I_o} = [i_{o_{y_1}}, \dots, i_{o_{ym}}]^T \end{array} \tag{3.53}$$

By (3.27) one gets $2mi_{o_y} = (m(i_{py} + i_{ny}) - (i_p + i_n)$. Substituting $m(i_{py} + i_{ny}) - (i_p + i_n)$ by $2m\,i_{o_y}$, dividing by $2m$, and using the notations newly defined shows that:

$$0 = N_\Delta(y,m)\mathbf{V_y} + (R_o^{eq} + L_o^{eq}s)i_{o_y} + \frac{1}{2}N_\Delta(y,m)\,(\mathbf{V_{py}} + \mathbf{V_{ny}}) \tag{3.54}$$

This equation being true $\forall y \in \{y_1, \ldots, y_m\}$, it is extended to achieve that:

$$(R_o^{eq} + L_o^{eq}s)\mathbf{I_o} = -\frac{1}{2}N_\Delta(m)\left(\mathbf{V_{py}} + \mathbf{V_{ny}}\right) + \left(-N_\Delta(m)\mathbf{V_y}\right) \tag{3.55}$$

As for the other types of currents, the voltage driving the output currents of the converter is defined as follows:

$$\mathbf{V_o} = -\frac{1}{2}N_\Delta(m)\left(\mathbf{V_{py}} + \mathbf{V_{ny}}\right) \tag{3.56}$$

3.C | Development of the General Polyphase Full Order Current State-Space Model

3.C.1 | State-space model representing all current types

It is possible to group the equations (3.32), (3.40), (3.47), and (3.55) in order to have the behavior of all the currents directly in one mathematical object. By isolating the currents in each of the left-hand members of these four equations, and using the fact that the identity matrix is its own inverse, it is obtained that:

$$\begin{cases} sI_m = -\frac{R_m^{eq}}{L_m^{eq}}I_m - \frac{1}{2L_m^{eq}}N_\Sigma(m)\left(\mathbf{V_{py}} + \mathbf{V_{ny}}\right) + \frac{1}{L_m^{eq}}\left(N_\Sigma(2)\mathbf{V_x} - N_\Sigma(m)\mathbf{V_y} - N_\Sigma(1)V_{n_{AD}}\right) \\ sI_s = -\frac{R_s^{eq}}{L_s^{eq}}I_s - \frac{1}{2L_s^{eq}}N_\Sigma(m)\left(\mathbf{V_{py}} - \mathbf{V_{ny}}\right) + \frac{1}{L_s^{eq}}\left([1\ \ 0]\cdot N_\Delta(2)\mathbf{V_x}\right) \\ s\mathbf{I_c} = -\frac{R_c^{eq}}{L_c^{eq}}\mathbf{I_c} - \frac{1}{2L_c^{eq}}N_\Delta(m)\left(\mathbf{V_{py}} - \mathbf{V_{ny}}\right) \\ s\mathbf{I_o} = -\frac{R_o^{eq}}{L_o^{eq}}\mathbf{I_o} - \frac{1}{2L_o^{eq}}N_\Delta(m)\left(\mathbf{V_{py}} + \mathbf{V_{ny}}\right) + \frac{1}{L_o^{eq}}\left(-N_\Delta(m)\mathbf{V_y}\right) \end{cases} \tag{3.57}$$

The variables for which it is desired to know the dynamic behavior are the currents, so the currents are concatenated in the state vector for the model high-level: $\mathbf{X_{HL}} = \left[I_m\ \ I_s\ \ \mathbf{I_c}^T\ \ \mathbf{I_o}^T\right]^T$. The quantities which will then control these different current variables are the voltages v_{py} and v_{ny} grouped in the vectors $\mathbf{V_{py}}$ and $\mathbf{V_{ny}}$. These voltages will then be associated in the form of the current control vector: $\mathbf{U_{HL}} = \left[\mathbf{V_{py}}^T\ \ \mathbf{V_{ny}}^T\right]^T$. From (3.57), it is possible to formulate the state-space model representing the dynamics of the four current types:

GPFOCSSM

$$\begin{cases} \dot{\mathbf{X}}_{\mathbf{HL}} = A_{HL}\mathbf{X_{HL}} + B_{HL}\mathbf{U_{HL}} + \mathbf{E_{HL}} \\ \mathbf{Y_{HL}} = C_{HL}\mathbf{X_{HL}} + D_{HL}\mathbf{U_{HL}} \end{cases} \tag{3.58}$$

This is equivalent to (3.59), which defines the model:

$$
\begin{cases}
\dot{\mathbf{X}}_{\mathbf{HL}} = \begin{bmatrix} \dot{I}_m \\ \dot{I}_s \\ \dot{\mathbf{I}}_{\mathbf{c}} \\ \dot{\mathbf{I}}_{\mathbf{o}} \end{bmatrix} = \begin{bmatrix} -\frac{R_m^{eq}}{L_m^{eq}} & & & \\ & -\frac{R_s^{eq}}{L_s^{eq}} & & \\ & & -\frac{R_c^{eq}}{L_c^{eq}}\mathbb{I}_m & \\ & & & -\frac{R_o^{eq}}{L_o^{eq}}\mathbb{I}_m \end{bmatrix} \begin{bmatrix} I_m \\ I_s \\ \mathbf{I}_{\mathbf{c}} \\ \mathbf{I}_{\mathbf{o}} \end{bmatrix} \\
\qquad -\frac{1}{2}\begin{bmatrix} N_\Sigma(m)/L_m^{eq} & N_\Sigma(m)/L_m^{eq} \\ N_\Sigma(m)/L_s^{eq} & -N_\Sigma(m)/L_s^{eq} \\ N_\Delta(m)/L_c^{eq} & -N_\Delta(m)/L_c^{eq} \\ N_\Delta(m)/L_o^{eq} & N_\Delta(m)/L_o^{eq} \end{bmatrix} \begin{bmatrix} \mathbf{V}_{\mathbf{py}} \\ \mathbf{V}_{\mathbf{ny}} \end{bmatrix} \\
\qquad + \begin{bmatrix} N_\Sigma(2)/L_m^{eq} \\ [1\ \ 0]\cdot N_\Delta(2)/L_s^{eq} \\ 0 \\ 0 \end{bmatrix} \mathbf{V}_{\mathbf{x}} + \begin{bmatrix} -N_\Sigma(m)/L_m^{eq} \\ 0 \\ 0 \\ -N_\Delta(m)/L_o^{eq} \end{bmatrix} \mathbf{V}_{\mathbf{y}} + \begin{bmatrix} -N_\Sigma(1)/L_m^{eq} \\ 0 \\ 0 \\ 0 \end{bmatrix} V_{n_{AD}} \\
\mathbf{Y}_{\mathbf{HL}} = \begin{bmatrix} I_m \\ I_s \\ \tilde{\mathbf{I}}_{\mathbf{c}} \\ \tilde{\mathbf{I}}_{\mathbf{o}} \end{bmatrix} = \begin{bmatrix} 1 & & & & \\ & 1 & & & \\ & & \mathbb{I}_{m-1} & \mathbb{O}_{m-1,1} & \\ & & & \mathbb{I}_{m-1} & \mathbb{O}_{m-1,1} \end{bmatrix} \begin{bmatrix} I_m \\ I_s \\ \mathbf{I}_{\mathbf{c}} \\ \mathbf{I}_{\mathbf{o}} \end{bmatrix} + \begin{bmatrix} \mathbb{O}_{2m,2m} \end{bmatrix} \begin{bmatrix} \mathbf{V}_{\mathbf{py}} \\ \mathbf{V}_{\mathbf{ny}} \end{bmatrix}
\end{cases}
\tag{3.59}
$$

The state-space model can then be defined from the following matrices and vectors:

$$
\begin{aligned}
A_{HL} &= \begin{bmatrix} -\frac{R_m^{eq}}{L_m^{eq}} & & & \\ & -\frac{R_s^{eq}}{L_s^{eq}} & & \\ & & -\frac{R_c^{eq}}{L_c^{eq}}\mathbb{I}_m & \\ & & & -\frac{R_o^{eq}}{L_o^{eq}}\mathbb{I}_m \end{bmatrix} \in \mathcal{M}_{2m+2}(\mathbb{R}) \\
B_{HL} &= -\frac{1}{2}\begin{bmatrix} N_\Sigma(m)/L_m^{eq} & N_\Sigma(m)/L_m^{eq} \\ N_\Sigma(m)/L_s^{eq} & -N_\Sigma(m)/L_s^{eq} \\ N_\Delta(m)/L_c^{eq} & -N_\Delta(m)/L_c^{eq} \\ N_\Delta(m)/L_o^{eq} & N_\Delta(m)/L_o^{eq} \end{bmatrix} \in \mathcal{M}_{2m+2,2m}(\mathbb{R}) \\
C_{HL} &= \begin{bmatrix} 1 & & & & \\ & 1 & & & \\ & & \mathbb{I}_{m-1} & \mathbb{O}_{m-1,1} & \\ & & & \mathbb{I}_{m-1} & \mathbb{O}_{m-1,1} \end{bmatrix} \in \mathcal{M}_{2m,2m+2}(\mathbb{R}) \\
D_{HL} &= \begin{bmatrix} \mathbb{O}_{2m,2m} \end{bmatrix} \in \mathcal{M}_{2m}(\mathbb{R}) \\
\mathbf{E}_{\mathbf{HL}} &= \begin{bmatrix} N_\Sigma(2)/L_m^{eq} \\ [1\ \ 0]\cdot N_\Delta(2)/L_s^{eq} \\ 0 \\ 0 \end{bmatrix} \mathbf{V}_{\mathbf{x}} + \begin{bmatrix} -N_\Sigma(m)/L_m^{eq} \\ 0 \\ 0 \\ -N_\Delta(m)/L_o^{eq} \end{bmatrix} \mathbf{V}_{\mathbf{y}} + \begin{bmatrix} -N_\Sigma(1)/L_m^{eq} \\ 0 \\ 0 \\ 0 \end{bmatrix} V_{n_{AD}} \in \mathbb{R}^{2m+2} \\
\mathbf{U}_{\mathbf{HL}} &= [v_{py_1}, \ldots, v_{py_m}, v_{ny_1}, \ldots, v_{ny_m}]^T \in \mathbb{R}^{2m}
\end{aligned}
\tag{3.60}
$$

The choice of this output vector is made knowing that the electrical systems represented by the circulating currents (i_{c_y}) and the output currents (i_{o_y}) are both balanced since the model has been derived from the decomposition represented on Figure 3.3. Therefore the sum of the circulating currents is null as is the sum of the output currents. There is thus a circulating current and an output current that it will not be possible to control. The choice is then made to discard the currents $i_{c_{ym}}$ and $i_{o_{ym}}$ from the vector $\mathbf{Y}_{\mathbf{HL}}$. Hence the fact that the matrix C_{HL} has empty columns.

3.C.2 | Controllable and observable current state-space model

Considering the controllability property for multi-input multi-output systems [Ros70] applied to $\{A_{HL}, B_{HL}\}$, it is possible to show that only $2m$ states among $2m+2$ are controllable. Indeed, the sum of the circulating and output currents is zero, so that they cannot be independently controlled. However, a reduced form of GPFOCSSM can easily be obtained that is controllable. The new state-space vector $\tilde{\mathbf{X}}_{\mathbf{HL}}$ is the same as $\mathbf{X}_{\mathbf{HL}}$, but with $i_{o_{ym}}$ and $i_{c_{ym}}$ removed, which is obtained by multiplying the state vector by C_{HL} with:

$$\tilde{\mathbf{X}}_{\mathbf{HL}} = C_{HL}\mathbf{X}_{\mathbf{HL}} \tag{3.61}$$

It is possible to notice that ${C_{HL}}^T$ is the pseudo-inverse matrix of C_{HL} defined so that:

$${C_{HL}}^T \cdot C_{HL} = \mathbb{I}_{2m+2} \quad \Longrightarrow \quad \mathbf{X}_{\mathbf{HL}} = {C_{HL}}^T \tilde{\mathbf{X}}_{\mathbf{HL}} \tag{3.62}$$

Thus:

$$A_{HL}\mathbf{X}_{\mathbf{HL}} = A_{HL}{C_{HL}}^T \tilde{\mathbf{X}}_{\mathbf{HL}} \tag{3.63}$$

Therefore:

$$\begin{aligned} \dot{\tilde{\mathbf{X}}}_{\mathbf{HL}} &= C_{HL}\dot{\mathbf{X}}_{\mathbf{HL}} \\ &= \left(C_{HL}A_{HL}{C_{HL}}^T\right)\tilde{\mathbf{X}}_{\mathbf{HL}} + \left(C_{HL}B_{HL}\right)\mathbf{U}_{\mathbf{HL}} + \left(C_{HL}\mathbf{E}_{\mathbf{HL}}\right) \\ &= \quad \tilde{A}_{HL}\tilde{\mathbf{X}}_{\mathbf{HL}} \quad + \quad \tilde{B}_{HL}\mathbf{U}_{\mathbf{HL}} \quad + \quad \tilde{\mathbf{E}}_{\mathbf{HL}} \end{aligned} \tag{3.64}$$

Keeping the same output vector gives:

$$\begin{aligned} \mathbf{Y}_{\mathbf{HL}} &= C_{HL}\mathbf{X}_{\mathbf{HL}} + D_{HL}\mathbf{U}_{\mathbf{HL}} \\ &= \mathbb{I}_{2m}\tilde{\mathbf{X}}_{\mathbf{HL}} + D_{HL}\mathbf{U}_{\mathbf{HL}} \\ &= \tilde{C}_{HL}\tilde{\mathbf{X}}_{\mathbf{HL}} + \tilde{D}_{HL}\mathbf{U}_{\mathbf{HL}} \end{aligned} \tag{3.65}$$

This state-space realization of the GPFOCSSM with matrices $\{\tilde{A}_{HL}, \tilde{B}_{HL}, \tilde{C}_{HL}, \tilde{D}_{HL}\}$ is controllable, observable, and therefore minimal. Thus, this generalized state-space model can direclty be used for control design of the currents for the MMC. And this will be the state-space model used for further developments of the control. Its definition can be sumed by the following equation (3.66) which defines the minimal state-space model:

GPFOCSSM - Minimal Realization

$$\begin{cases} \dot{\tilde{\mathbf{X}}}_{\mathbf{HL}} = \tilde{A}_{HL}\tilde{\mathbf{X}}_{\mathbf{HL}} + \tilde{B}_{HL}\mathbf{U}_{\mathbf{HL}} + \tilde{\mathbf{E}}_{\mathbf{HL}} \\ \mathbf{Y}_{\mathbf{HL}} = \tilde{C}_{HL}\tilde{\mathbf{X}}_{\mathbf{HL}} + \tilde{D}_{HL}\mathbf{U}_{\mathbf{HL}} \end{cases} \tag{3.66}$$

with

$$\begin{aligned} \tilde{A}_{HL} &= C_{HL}A_{HL}{C_{HL}}^T \\ \tilde{B}_{HL} &= C_{HL}B_{HL} \\ \tilde{\mathbf{E}}_{\mathbf{HL}} &= C_{HL}\mathbf{E}_{\mathbf{HL}} \\ \tilde{C}_{HL} &= \mathbb{I}_{2m} \\ \tilde{D}_{HL} &= D_{HL} \end{aligned} \tag{3.67}$$

Note that in both state-space models, the same control vector is used. Applying the derivations given in Appendix B to the state-space model gives:

$$\tilde{C}_{HL}\tilde{G}_{HL}\mathbf{U}_{\mathbf{HL}}(k) = \mathbf{Y}_{\mathbf{HL}}(k+1) - \tilde{C}_{HL}\tilde{F}_{HL}\tilde{\mathbf{X}}_{\mathbf{HL}}(k) - \tilde{C}_{HL}\tilde{H}_{HL}\tilde{\mathbf{E}}_{\mathbf{HL}}(k) \tag{3.68}$$

3.C.3 Conclusions about the GPFOCSSM

The work of modelling the behavior of currents that has been carried out so far has made it possible to provide a first model of currents that can be adapted to any number of phases because, as can be seen, the equations (3.58) and (3.66) which represent this model, as well as the matrices (3.60) and (3.67) which define it, depend on the parameter m in size and value. This model thus fulfills the objective of scalability and can be qualified as "polyphase". This state-space model is - compared to those which will follow - qualified by the term "full order" because the state vector contains all the currents which can flow through the MMC during its operation. Embedding a certain level of generalization about the modelling possibilities of the DC bus as well as the AC network, it can be qualified as "general". It is from these various characteristics that this model is thus named General Polyphase Full Order Current State-Space Model (GPFOCSSM). From now on and in the following work it is its acronym GPFOCSSM which will be mainly used to refer to it.

The model that has been developed for the high-level in section 3.C has the advantage of being independent of the number of submodules N and is modular to the number of phases in the AC network m. The state-space model matrices increase in size with the number of phases in the AC network, e.g., the number of rows and columns in the control matrix is proportional to twice the number of phases: $(2m \times 2m)$ in the case of the minimal representation. Thus, as the number of phases increases in the system, the control algorithm that would take advantage of the GPFOCSSM would see its complexity grow rapidly as the number of phases is increased. In the case of a state feedback the gain matrix would have a total of $4m^2$ terms. It would therefore be consistent to observe an increase in real time control computation time that is quadratic with the number of phases in the system. It could therefore be very beneficial - both for the real time control computation and the system simulation time - to have a state-space model high-level that is independent of the number of phases m.

A first idea can come by intuition from the known behavior of the studied system. Knowing that I_s is the source current DC which feeds the converter, it should rather have a single component of continuous nature, while the $\mathbf{I_o}$, which is the AC-side current, should feature a fundamental alternating component. The circulating currents $\mathbf{I_c}$ being of null sum, it would be consistent to see it take an alternating behavior with a fundamental component as well and the common mode current I_m should also be continuous as well as I_s. Knowing this behavior for the MMC, the idea can be to apply a change of basis to the GPFOCSSM currently established in the natural basis. This change of basis would then allow to have a state-space representation describing the behavior of the system only on the areas from the state-space actually reached by the state variables.

3.D Development of the General Polyphase Fixed-Size Reduced Order Current State-Space Model

3.D.1 PARK transform in the m-phase case

3.D.1.1 Foundations of the transformation

To perform a base change, several solutions are possible, but there is one that is usually applied in the case of three-phase systems: the PARK transformation [Par29; Par33; Cla43; Con51; MBB11]. The objective here is to use a PARK transform in the polyphase case to bring down from m phases to 3 phases reducing then the order of the high-level model of our system and this whatever the number of phases of the AC network m. This type of model in the PARK reference frame, also called Synchronous Rotating Frame or SRRF, has already been studied in the context of the MMC for the case of a three-phase AC network. This was done without taking into account the behavior of the common mode current or the voltage between the neutral points by [Fre+16a; Ber+18]. The desire here is therefore to partly rely on this work to extend the model established in the PARK frame of the three-phase MMC to the m-phase case.

The first approach of basis change proposed here operates a transformation from the Stationary Reference Frame (SRF), also called Stationary Frame, to the SRRF. In this basis change, the choice is made to consider that the model can be reduced - while keeping a satisfactory accuracy - to the continuous components and to the fundamental components of the various waveforms of the currents which flow through the MMC. The simulations which are carried out in the last part of this chapter make it possible to analyze if the precision of such a model is sufficient.

Assumption 3. *Only the continuous and fundamental components of the currents flowing through the MMC are considered, the other components are assumed null*[1].

This assumption is the keystone of the GPFSROCSSM model and the Assumption 9 is considered true only in the framework of this model.

As the following development sets up, each current of an alternating nature will have a PARK transformation applied by rotation at a single frequency. This means that, **for the case of** $m \leq 3$, only the fundamental or the largest amplitude harmonic will be considered and not the whole harmonic content of the latter. **In the case where** $m > 3$ the PARK transform set up here will only be able to take into account the fundamental component of each of the currents. This dependence on the number of phases is explained in detail by [SBH03; SKB04; Kes03]. The reduced order model obtained will not be as general as the full order model in terms of describing the values that the different types of currents can take, but it is a first step that will be improved later to take into account additional harmonics of the circulating currents and the output currents in particular for the case where $m > 3$.

Another assumption, necessary for the development of the model GPFSROCSSM, is laid:

Assumption 4. *The poles of the DC bus, the legs of the MMC and the AC network phases all feature a symmetrical load.*

Each of the current types $\mathbf{I_c}$ and $\mathbf{I_o}$ constitute two electrical systems of polyphase currents. As seen on Figure 3.3, these two types of currents are structurally null-sum and the model described

[1] This assumption, which may appear strong from the knowledge of the harmonic content from the arm currents, will be discussed further, especially concerning the circulating currents.

by (3.60) shows that all circulating currents see the same impedance. The same is true for the output currents. Thus, the circulating currents and the output currents form two electrical systems on a symmetrical load and thus verify this assumption.

3.D.1.2 Development of basis changes

From the m-phase $(1, 2, \ldots, m)$ stationary frame to the $(\alpha, \beta, 0)$ stationary frame

From [Kes03] in the case where the harmonic content of the waveforms is limited to the fundamental components, it is possible to consider only a single reference frame $(\alpha, \beta, 0)$ to represent all the information contained in the electrical waveforms. This last one will be able to represent the selected waveforms without any loss of information [Kes03]. A phasor will then be made up to stand for the representation of the polyphase waveforms in the $(\alpha, \beta, 0)$ framework. The α axis will be the real axis, the β axis, the imaginary axis and the 0 axis will allow to represent the homopolar component for the case where the electrical system would showcase an unbalanced operation. By setting x_k as the electrical signal $x(t)$ in the phase $\#k$ of the polyphase network, $\theta_m = \frac{2\pi}{m}$, $a = e^{j\theta_m}$ and $\underline{x}^{\alpha\beta}$ the phasor in the $(\alpha, \beta, 0)$ reference frame, the pentaphase formulation presented in [TWL98; Gat00] is generalized to the m-phase case:

$$\begin{aligned} \underline{x}^{\alpha\beta} &= K \cdot \left(x_1 + a x_2 + a^2 x_3 + \ldots + a^{m-1} x_m\right) = x_\alpha + j x_\beta \\ x_0 &= \frac{K}{k_0} \cdot (x_1 + x_2 + x_3 + \ldots + x_m) \end{aligned} \tag{3.69}$$

with x_0 the zero sequence component directly related to the sum of the different components in the initial stationary frame. If the electrical system is not balanced, the sum of all its components will not be null, inducing a non-zero value for the homopolar component. The introduction of the coefficients K and k_0 is intended to let the user choose the conservation type: amplitude [Cla43], or power [Con51]. Let $\mathbf{X}^{\alpha\beta 0} = [x_\alpha \; x_\beta \; x_0]^T$ and $\mathbf{X^m} = [x_1 \; x_2 \; x_3 \ldots x_m]^T$, By the introduced transformation, it thus comes:

$$\mathbf{X}^{\alpha\beta 0} = \begin{bmatrix} \mathfrak{Re}\left(\underline{x}^{\alpha\beta}\right) \\ \mathfrak{Im}\left(\underline{x}^{\alpha\beta}\right) \\ x_0 \end{bmatrix} = K \begin{bmatrix} x_1 + \cos(\theta_m) x_2 + \cos(2\theta_m) x_3 + \ldots + \cos((m-1)\theta_m) x_m \\ 0 + \sin(\theta_m) x_2 + \sin(2\theta_m) x_3 + \ldots + \sin((m-1)\theta_m) x_m \\ x_1/k_0 + x_2/k_0 + x_3/k_0 + \ldots + x_m/k_0 \end{bmatrix} \tag{3.70}$$

With a matrix product, it is trivially deduced that:

$$\mathbf{X}^{\alpha\beta 0} = K \begin{bmatrix} 1 & \cos(\theta_m) & \cos(2\theta_m) & \ldots & \cos((m-1)\theta_m) \\ 0 & \sin(\theta_m) & \sin(2\theta_m) & \ldots & \sin((m-1)\theta_m) \\ 1/k_0 & 1/k_0 & 1/k_0 & \ldots & 1/k_0 \end{bmatrix} \mathbf{X^m} \tag{3.71}$$

The transformation matrix is then named $[C_K]$:

$$[C_K] \triangleq K \begin{bmatrix} 1 & \cos(\theta_m) & \cos(2\theta_m) & \ldots & \cos((m-1)\theta_m) \\ 0 & \sin(\theta_m) & \sin(2\theta_m) & \ldots & \sin((m-1)\theta_m) \\ 1/k_0 & 1/k_0 & 1/k_0 & \ldots & 1/k_0 \end{bmatrix} \tag{3.72}$$

This gives: $\mathbf{X}^{\alpha\beta 0} = [C_K]\mathbf{X^m}$. However $[C_K]$ is a rectangular matrix, but it is possible to show by simple matrix product that:

$$[C_K] \cdot [C_K]^T = K^2 m \begin{bmatrix} 1/2 & 0 & 0 \\ 0 & 1/2 & 0 \\ 0 & 0 & 1/{k_0}^2 \end{bmatrix} = K^2 \frac{m}{2} \mathbb{I}_3 \quad \uparrow_{k_0 = \sqrt{2}} \tag{3.73}$$

The choice of $k_0 = \sqrt{2}$ is thus made for both types of transformations although in some cases of the CLARKE transformation the choice of $k_0 = 2$ is made to conserve the amplitude of the homopolar component. This leads to the definition of the pseudo-inverse matrix of $[C_K]$:

$$[C_K]^+ \triangleq \frac{2}{K^2 m}[C_K]^T \Longrightarrow \mathbf{X^m} = [C_K]^+ \mathbf{X}^{\alpha\beta 0} = \frac{2}{K^2 m}[C_K]^T \mathbf{X}^{\alpha\beta 0} \tag{3.74}$$

The determination of K will not be detailed here, but in the case of the CONCORDIA transformation, this coefficient will be determined to ensure the conservation of electric powers. In this case, it is possible to show that it is necessary to have $K = \sqrt{2/m}$. In the case of the CLARKE transformation, this coefficient will be chosen to ensure the conservation of the amplitudes of the wave forms. In this case, it is necessary to have $K = 2/m$.

From the $(\alpha, \beta, 0)$ stationary frame to the synchronous rotating frame $(d, q, 0)$

The second part of the PARK transform is the usual change of reference frame by rotation:

$$\mathbf{X}^{\alpha\beta 0} = \begin{bmatrix} \cos(\theta) & -\sin(\theta) & 0 \\ \sin(\theta) & \cos(\theta) & 0 \\ 0 & 0 & 1 \end{bmatrix} \cdot \mathbf{X^{dq0}} = [P(\theta)] \cdot \mathbf{X^{dq0}} \tag{3.75}$$

where the matrix $[P(\theta)]$ is invertible with the remarkable property that $[P(\theta)]^{-1} = [P(-\theta)]$. The angle θ is that of the rotation to be imposed between the two reference frames, oriented from the stationary frame towards the rotating frame. In the case of the static converter studied, this angle will be associated with the frequency of the alternating currents which evolve within it.

3.D.2 Decoupled generalized polyphase fixed-size reduced order model of the currents

Model for the common mode current (i_m, I_m)

To derive the model of the currents in the PARK reference frame, the starting points are the differential equations governing the dynamics of each current type formulated in the GPFOCSSM model. For the common mode current this calls for (3.32):

$$R_m^{eq} I_m + L_m^{eq} s I_m = -\frac{1}{2} N_\Sigma(m) \left(\mathbf{V_{py}} + \mathbf{V_{ny}}\right) + \left(N_\Sigma(2)\mathbf{V_x} - N_\Sigma(m)\mathbf{V_y} - N_\Sigma(1) V_{n_{AD}}\right) \tag{3.76}$$

The model (3.76) is a particular case of the general equation (A.81) proposed in the appendix. Appendix G provides a detailed development of the change of basis that must be made in order to shift the current model into the PARK reference frame. Thus, by applying this development to equation (3.76), the model of the common mode current in the synchronous rotating reference frame is deduced. Notations to unify the models of the different types of currents are introduced:

$$\begin{cases} I_m^{dq0} = I_m \\ B_\Sigma^{dq0} = \frac{k_0}{mK}\begin{bmatrix} 0 & 0 & -1/2 \end{bmatrix} \\ \mathbf{V_{py}^{dq0}} = [P(-\theta)][C_K]\mathbf{V_{py}} \\ \mathbf{V_{ny}^{dq0}} = [P(-\theta)][C_K]\mathbf{V_{ny}} \end{cases} \tag{3.77}$$

The use of these new notations finally gives:

$$(R_m^{eq} + L_m^{eq}s)I_m^{dq0} = B_\Sigma^{dq0}\left(\mathbf{V_{py}^{dq0}} + \mathbf{V_{ny}^{dq0}}\right) + (N_\Sigma(2)\mathbf{V_x} - N_\Sigma(m)\mathbf{V_y} - N_\Sigma(1)V_{n_{AD}}) \quad (3.78)$$

Model for the source current (i_s, I_s)

The current model of the DC bus will have the same modelling approach applied to it since the current I_s is also a scalar with the same way as I_m. Thus, the starting point is equation (3.40):

$$R_s^{eq}I_s + L_s^{eq}sI_s = -\frac{1}{2}N_\Sigma(m)\left(\mathbf{V_{py}} - \mathbf{V_{ny}}\right) + ([1\ \ 0] \cdot N_\Delta(2)\mathbf{V_x}) \quad (3.79)$$

According to the Park transform derivations from Appendix G, it can be directly deduced - using the notation $I_s^{dq0} = I_s$ - that:

$$(R_s^{eq} + L_s^{eq}s)I_s^{dq0} = B_\Sigma^{dq0}\left(\mathbf{V_{py}^{dq0}} - \mathbf{V_{ny}^{dq0}}\right) + ([1\ \ 0] \cdot N_\Delta(2)\mathbf{V_x}) \quad (3.80)$$

Model for the circulating current $(i_{c_y}, \mathbf{I_c})$

The circulating current $\mathbf{I_c}$, like the output alternating current $\mathbf{I_o}$, is a polyphase current with m components. The Park transformation can therefore be fully applied to it. The use of Appendix G is applied in details here since the circulating current has some specificities. To do this, the equation governing the dynamics of the circulating current (3.47) is recalled:

$$R_c^{eq}\mathbf{I_c} + L_c^{eq}s\mathbf{I_c} = -\frac{1}{2}N_\Delta(m)\left(\mathbf{V_{py}} - \mathbf{V_{ny}}\right) \quad (3.81)$$

The notations $B_\Delta^m = -\frac{1}{2}N_\Delta(m)$ and $\mathbf{\Phi_c} = L_c^{eq}\mathbf{I_c}$ are introduced:

$$R_c^{eq}\mathbf{I_c} + s\mathbf{\Phi_c} = B_\Delta^m\left(\mathbf{V_{py}} - \mathbf{V_{ny}}\right) \quad (3.82)$$

By substituting the vectors of the natural stationary reference frame by those of the new stationary reference frame $\{\alpha, \beta, 0\}$:

$$R_c^{eq}[C_K]^+\mathbf{I_c^{\alpha\beta0}} + s[C_K]^+\mathbf{\Phi_c^{\alpha\beta0}} = [C_K]^+B_\Delta^{\alpha\beta0}[C_K] \cdot [C_K]^+\left(\mathbf{V_{py}^{\alpha\beta0}} - \mathbf{V_{ny}^{\alpha\beta0}}\right) \quad (3.83)$$

The matrix $[C_K]$ being constant as a function of time, the permutation with the scalar variable of Laplace is possible, it is deduced:

$$[C_K]^+R_c^{eq}\mathbf{I_c^{\alpha\beta0}} + [C_K]^+s\mathbf{\Phi_c^{\alpha\beta0}} = [C_K]^+B_\Delta^{\alpha\beta0}\left(\mathbf{V_{py}^{\alpha\beta0}} - \mathbf{V_{ny}^{\alpha\beta0}}\right) \quad (3.84)$$

With the left multiplication by $[C_K]$, it follows that:

$$R_c^{eq}\mathbf{I_c^{\alpha\beta0}} + s\mathbf{\Phi_c^{\alpha\beta0}} = B_\Delta^{\alpha\beta0}\left(\mathbf{V_{py}^{\alpha\beta0}} - \mathbf{V_{ny}^{\alpha\beta0}}\right) \quad (3.85)$$

Following the shift to the $(\alpha, \beta, 0)$ reference frame, the rotation towards the $(d, q, 0)$ reference frame will be operated. It is decided to set θ the angle between the rotating frame and the initial

stationary frame in the general case. The PARK reference frame will thus rotate at the frequency ω, this frequency will take the value ω_c, which is the frequency of the currents $\mathbf{I_c}$ with respect to the stationary reference frame, when the interest is focused on the PARK model of the circulating current. The detailed analysis by [Ilv+12] of the potential harmonic content from the different current types involved in the conversion performed by the MMC is very enlightening. This study indicates that, under normal operation conditions of the MMC, the circulating current consists of a series of harmonics of even order with ω_o for fundamental frequency of the output current $\mathbf{I_o}$, so that the harmonic content of the circulating current is composed of the frequencies: $2\omega_o, 4\omega_o, \ldots, 2k\omega_o$, $k \in \mathbb{N}^*$. However, the study shows that the harmonics of rank higher than 2 are of very low amplitude compared to that of rank 2 in the common configuration of MMCs and that in all cases the amplitude of the $\mathbf{I_c}$ harmonics decreases as the harmonic order increases, which is confirmed by [Lyu+18]. In the example presented by [Ilv+12] the amplitude of the 4^{th} harmonic is about 47 times smaller than the 2^{nd} harmonic. Therefore, based on these studies, most of the circulating current will be considered to be contained in its 2^{nd} order harmonic. It is concluded that the change of reference frame from the stationary frame $(\alpha, \beta, 0)$ to the PARK synchronous rotating reference frame will be performed by the matrix $[P(-\theta_c)]$ with $\theta_c = 2\theta_o = 2\int \omega_o dt$, for the case of the circulating current. The inverse change of reference frame is determined by the matrix $[P(\theta_c)]$.

But according to [Kes03], the transformation operated by $[C_K]$ only allows one to conserve the fundamental components of each current in the $(\alpha, \beta, 0)$ reference frame for **a number of phases** $m > 3$ as it will be detailed in the following section. **For the case where** $m = 3$, all harmonic components are conserved by $[C_K]$. Even though the largest amplitude harmonic of the circulating current is considered to be the one of second order, in this first model, only the fundamental component will be considered. A verification of the accuracy of this model for the control purpose of the MMC will be performed, to assess how necessary the representation of this 2^{nd} harmonic of the circulating current is. This consideration implies that the change of reference frame from $(\alpha, \beta, 0)$ to the PARK reference frame will be performed by $[P(-\theta)]$ for the case $m > 3$, whereas $[P(-n\theta)]$ $(n = 2)$ will be used for the case $m = 3$, having set $\theta = \theta_o$. This choice made here is also made by [Ber+18] which also features a model of the MMC in the synchronous rotating reference frame, but limited to the case of three-phase AC networks and without consideration of the possible common mode current or the DC bus coupling impedance. The change of reference frame applying the rotation is then operated:

$$R_c^{eq} P(n\theta)\mathbf{I_c^{dq0}} + s\left([P(n\theta)]\mathbf{\Phi_c^{dq0}}\right) = [P(n\theta)]B_\Delta^{dq0_n}[P(-n\theta)]\cdot[P(n\theta)]\left(\mathbf{V_{py}^{dq0_n}} - \mathbf{V_{ny}^{dq0_n}}\right) \tag{3.86}$$

By the fact that R_c^{eq} is a scalar and the inverse matrix of $[P(\theta)]$ is $[P(-\theta)]$, it follows that:

$$[P(n\theta)]R_c^{eq}\mathbf{I_c^{dq0}} + s\left([P(n\theta)]\mathbf{\Phi_c^{dq0}}\right) = [P(n\theta)]B_\Delta^{dq0_n}\left(\mathbf{V_{py}^{dq0_n}} - \mathbf{V_{ny}^{dq0_n}}\right) \tag{3.87}$$

With a simple derivation of a product of time dependent functions, it is obtained that:

$$[P(n\theta)]R_c^{eq}\mathbf{I_c^{dq0}} + s[P(n\theta)]\cdot\mathbf{\Phi_c^{dq0}} + [P(n\theta)]\cdot s\mathbf{\Phi_c^{dq0}} = [P(n\theta)]B_\Delta^{dq0_n}\left(\mathbf{V_{py}^{dq0_n}} - \mathbf{V_{ny}^{dq0_n}}\right) \tag{3.88}$$

By matrix multiplication on the left by $[P(-n\theta)]$, the previous equation turns into:

$$R_c^{eq}\mathbf{I_c^{dq0}} + [P(-n\theta)]s[P(n\theta)]\cdot\mathbf{\Phi_c^{dq0}} + s\mathbf{\Phi_c^{dq0}} = B_\Delta^{dq0_n}\left(\mathbf{V_{py}^{dq0_n}} - \mathbf{V_{ny}^{dq0_n}}\right) \tag{3.89}$$

The term $[P(-n\theta)]s[P(n\theta)]\cdot\mathbf{\Phi_c^{dq0}}$ of this equation must then be made explicit in order to obtain a complete analytical form. The determination of the time derivative of $[P(n\theta)]$ is then necessary. This derivative can be computed by the separation of variables:

$$s[P(n\theta)] = \frac{d[P(n\theta)]}{dt} = \frac{d\theta}{dt}\cdot\frac{d[P(n\theta)]}{d\theta} \tag{3.90}$$

This separation of variables allows an efficient determination of the $[P(n\theta)]$ time derivative:

$$s[P(n\theta)] = \frac{d\theta}{dt} \cdot \frac{d}{d\theta} \begin{bmatrix} \cos(n\theta) & -\sin(n\theta) & 0 \\ \sin(n\theta) & \cos(n\theta) & 0 \\ 0 & 0 & 1 \end{bmatrix} = \omega \cdot n \begin{bmatrix} -\sin(n\theta) & -\cos(n\theta) & 0 \\ \cos(n\theta) & -\sin(n\theta) & 0 \\ 0 & 0 & 0 \end{bmatrix} \tag{3.91}$$

The expression of the term $[P(-n\theta)]s[P(n\theta)]$ is then deduced by matrix product:

$$\begin{aligned} [P(-n\theta)]s[P(n\theta)] &= n\omega \cdot \begin{bmatrix} \cos(n\theta) & \sin(n\theta) & 0 \\ -\sin(n\theta) & \cos(n\theta) & 0 \\ 0 & 0 & 1 \end{bmatrix} \begin{bmatrix} -\sin(n\theta) & -\cos(n\theta) & 0 \\ \cos(n\theta) & -\sin(n\theta) & 0 \\ 0 & 0 & 0 \end{bmatrix} \\ &= n\omega \cdot \begin{bmatrix} 0 & -1 & 0 \\ 1 & 0 & 0 \\ 0 & 0 & 0 \end{bmatrix} \end{aligned} \tag{3.92}$$

The term $[P(-n\theta)]s[P(n\theta)] \cdot \mathbf{\Phi_c^{dq0}}$ can then be expressed as:

$$[P(-n\theta)]s[P(n\theta)] \cdot \mathbf{\Phi_c^{dq0}} = n\omega \begin{bmatrix} -\Phi_c^q \\ \Phi_c^d \\ 0 \end{bmatrix} \tag{3.93}$$

From the definition of the change of basis operated here, the magnetic flux circulating in the Park reference frame $\mathbf{\Phi_c^{dq0}}$ is found from the following transformation:

$$\mathbf{\Phi_c^{dq0}} = [P(-n\theta)][C_K]\mathbf{\Phi_c} = L_c^{eq}[P(-n\theta)][C_K]\mathbf{I_c} = L_c^{eq} \begin{bmatrix} I_c^d \\ I_c^q \\ I_c^0 \end{bmatrix} = \begin{bmatrix} \Phi_c^d \\ \Phi_c^q \\ \Phi_c^0 \end{bmatrix} \tag{3.94}$$

This equation allows one to obtain the relationship defining Φ_c^d and Φ_c^q. Thus, by substitution of their respective formulas in (3.93), it is deduced that:

$$[P(-n\theta)]s[P(n\theta)] \cdot \mathbf{\Phi_c^{dq0}} = n\omega L_c^{eq} \begin{bmatrix} -I_c^q \\ I_c^d \\ 0 \end{bmatrix} \tag{3.95}$$

Knowing the explicit expression of $[P(-n\theta)]s[P(n\theta)] \cdot \mathbf{\Phi_c^{dq0}}$, a substitution in equation (3.89) is made. The equation governing the dynamics of the circulating currents thus becomes:

$$R_c^{eq}\mathbf{I_c^{dq0}} + s\mathbf{\Phi_c^{dq0}} + n\omega L_c^{eq} \begin{bmatrix} -I_c^q \\ I_c^d \\ 0 \end{bmatrix} = B_\Delta^{dq0_n} \left(\mathbf{V_{py}^{dq0_n}} - \mathbf{V_{ny}^{dq0_n}} \right) \tag{3.96}$$

with:

$$\begin{cases} \mathbf{I_c^{dq0}} = [P(-n\theta)][C_K]\mathbf{I_c} = \begin{bmatrix} I_c^d \\ I_c^q \\ I_c^0 \end{bmatrix} \\ \mathbf{\Phi_c^{dq0}} = L_c^{eq}\mathbf{I_c^{dq0}} = L_c^{eq} \begin{bmatrix} I_c^d \\ I_c^q \\ I_c^0 \end{bmatrix} \\ B_\Delta^{dq0_n} = [P(-n\theta)][C_K]B_\Delta^m[C_K]^+ P(n\theta) = \begin{bmatrix} -1/2 & 0 & 0 \\ 0 & -1/2 & 0 \\ 0 & 0 & 0 \end{bmatrix} \\ \qquad = [P(-\theta)][C_K]B_\Delta^m[C_K]^+[P(\theta)] = \begin{bmatrix} -1/2 & 0 & 0 \\ 0 & -1/2 & 0 \\ 0 & 0 & 0 \end{bmatrix} = B_\Delta^{dq0} \end{cases} \tag{3.97}$$

The expression of B_{Δ}^{dq0} highlights the fact that by acting on the control voltages which are $\mathbf{V_{py}^{dq0_n}}$ and $\mathbf{V_{ny}^{dq0_n}}$, it is not possible to act on the homopolar component of the circulating current. But, as it is possible to see on Figure 3.3 (c), the circulating currents are structurally forced to be null sum: $\sum_{y=1}^{m} i_{c_y} = 0$. The homopolar component of the circulating currents, I_c^0, is therefore structurally null whatever the operating mode of the converter. This guarantees that the third and last line of equation (3.96) is useless, so it is possible to remove it from the model to reduce its size. The variables are then redefined as:

$$\begin{cases} \tilde{\mathbf{I}}_{\mathbf{c}}^{\mathbf{dq0}} = \begin{bmatrix} I_c^d \\ I_c^q \end{bmatrix} \\ \tilde{B}_{\Delta}^{dq0} = \begin{bmatrix} -1/2 & 0 & 0 \\ 0 & -1/2 & 0 \end{bmatrix} \\ \mathbf{V_{py}^{dq0_n}} = [P(-n\theta)][C_K]\mathbf{V_{py}} = [P((1-n)\theta)][P(-\theta)][C_K]\mathbf{V_{py}} = [P((1-n)\theta)]\mathbf{V_{py}^{dq0}} \\ \mathbf{V_{ny}^{dq0_n}} = [P(-n\theta)][C_K]\mathbf{V_{ny}} = [P((1-n)\theta)][P(-\theta)][C_K]\mathbf{V_{ny}} = [P((1-n)\theta)]\mathbf{V_{ny}^{dq0}} \end{cases} \tag{3.98}$$

By using these notations, the final equation describing the dynamics of the current $\mathbf{I_c}$ in the reference frame of Park is expressed as:

$$(R_c^{eq} + L_c^{eq}s)\tilde{\mathbf{I}}_{\mathbf{c}}^{\mathbf{dq0}} + n\omega_o L_c^{eq} \begin{bmatrix} -I_c^q \\ I_c^d \end{bmatrix} = \tilde{B}_{\Delta}^{dq0} P((1-n)\theta) \left(\mathbf{V_{py}^{dq0}} - \mathbf{V_{ny}^{dq0}} \right) \tag{3.99}$$

It is interesting to note that from equation (3.47) describing the behavior of the circulating current in the framework of the GPFOCSSM, switching to equation (3.99) allows one to perform a reduction of order by shifting from a representation of m currents to only 2 currents. This simplification is therefore relatively strong.

Model for the ouput current $(i_{o_y}, \mathbf{I_o})$

The output alternating current $\mathbf{I_o}$, is a polyphase current embedding m components. This transformation will be applied to equation (3.55) previously found for the output current in the framework of the GPFOCSSM model:

$$R_o^{eq}\mathbf{I_o} + L_o^{eq}s\mathbf{I_o} = -\frac{1}{2}N_{\Delta}(m)\left(\mathbf{V_{py}} + \mathbf{V_{ny}}\right) + \left(-N_{\Delta}(m)\mathbf{V_y}\right) \tag{3.100}$$

Applying the Park transform to this model as detailed in Appendix G, gives the following result with the dedicated notations:

$$\begin{cases} \tilde{\mathbf{I}}_{\mathbf{o}}^{\mathbf{dq0}} = \begin{bmatrix} I_o^d \\ I_o^q \end{bmatrix} = \begin{bmatrix} 1 & 0 & 0 \\ 0 & 1 & 0 \end{bmatrix} [P(-\theta)][C_K]\mathbf{I_o} \\ \tilde{\mathbf{V}}_{\mathbf{y\Delta}}^{\mathbf{dq0}} = \begin{bmatrix} V_y^d \\ V_y^q \end{bmatrix} = \begin{bmatrix} 1 & 0 & 0 \\ 0 & 1 & 0 \end{bmatrix} [P(-\theta)][C_K]N_{\Delta}(m)\mathbf{V_y} \\ \qquad = -2\tilde{B}_{\Delta}^{dq0}[P(-\theta)][C_K]N_{\Delta}(m)\mathbf{V_y} \end{cases} \tag{3.101}$$

This finally leads to:

$$(R_o^{eq} + L_o^{eq}s)\tilde{\mathbf{I}}_{\mathbf{o}}^{\mathbf{dq0}} + \omega_o L_o^{eq} \begin{bmatrix} -I_o^q \\ I_o^d \end{bmatrix} = \tilde{B}_{\Delta}^{dq0} \left(\mathbf{V_{py}^{dq0}} - \mathbf{V_{ny}^{dq0}} \right) - \begin{bmatrix} V_y^d \\ V_y^q \end{bmatrix} \tag{3.102}$$

As in the case of the circulating current, the output currents are structurally forced to be null-sum: $\sum_{y=1}^{m} i_{o_y} = 0$ as shown by Figure 3.3 (d). As a result, it was possible to decrease the size of

the model to get (3.102). As for the case of the circulating current $\mathbf{I_c}$, the equation representing the dynamics of the output current $\mathbf{I_o}$ is strongly reduced in order: from m for (3.55) to 2 for (3.102).

3.D.3 Current fixed-size reduced order state-space model

It is possible to combine the equations (3.78), (3.80), (3.99), and (3.102) in order to have the behavior of all the currents directly into a single state-space model. The state vector is thus define as $\mathbf{X_{HL}^{dq0}} = \begin{bmatrix} I_m^{dq0} & I_s^{dq0} & \tilde{\mathbf{I}}_\mathbf{c}^{\mathbf{dq0}T} & \tilde{\mathbf{I}}_\mathbf{o}^{\mathbf{dq0}T} \end{bmatrix}^T$ and the state-space model is found:

$$\begin{cases} \dot{\mathbf{X}}_{\mathbf{HL}}^{\mathbf{dq0}} = A_{HL}^{dq0}\ \mathbf{X}_{\mathbf{HL}}^{\mathbf{dq0}} + B_{HL}^{dq0}\ \mathbf{U}_{\mathbf{HL}}^{\mathbf{dq0}} + \mathbf{E}_{\mathbf{HL}}^{\mathbf{dq0}} \\ \mathbf{Y}_{\mathbf{HL}}^{\mathbf{dq0}} = C_{HL}^{dq0}\ \mathbf{X}_{\mathbf{HL}}^{\mathbf{dq0}} \end{cases} \tag{3.103}$$

Defined by

$$A_{HL}^{dq0} = \begin{bmatrix} -\frac{R_m^{eq}}{L_m^{eq}} & & & & & \\ & -\frac{R_s^{eq}}{L_s^{eq}} & & & & \\ & & -\frac{R_c^{eq}}{L_c^{eq}} & n\omega & & \\ & & -n\omega & -\frac{R_c^{eq}}{L_c^{eq}} & & \\ & & & & -\frac{R_o^{eq}}{L_o^{eq}} & \omega \\ & & & & -\omega & -\frac{R_o^{eq}}{L_o^{eq}} \end{bmatrix} \in \mathcal{M}_{6,6}(\mathbb{R})$$

$$B_{HL}^{dq0} = \begin{bmatrix} B_\Sigma^{dq0}/L_m^{eq} & B_\Sigma^{dq0}/L_m^{eq} \\ B_\Sigma^{dq0}/L_s^{eq} & -B_\Sigma^{dq0}/L_s^{eq} \\ \tilde{B}_\Delta^{dq0} P((1-n)\theta)/L_c^{eq} & -\tilde{B}_\Delta^{dq0} P((1-n)\theta)/L_c^{eq} \\ \tilde{B}_\Delta^{dq0}/L_o^{eq} & \tilde{B}_\Delta^{dq0}/L_o^{eq} \end{bmatrix} \in \mathcal{M}_{6,6}(\mathbb{R})$$

$$C_{HL}^{dq0} = \begin{bmatrix} 1 & & & \\ & 1 & & \\ & & \mathbb{I}_2 & \\ & & & \mathbb{I}_2 \end{bmatrix} \in \mathcal{M}_{6,6}(\mathbb{R}) \tag{3.104}$$

$$\mathbf{E}_{\mathbf{HL}}^{\mathbf{dq0}} = \begin{bmatrix} N_\Sigma(2)/L_m^{eq} \\ [1\ \ 0] \cdot N_\Delta(2)/L_s^{eq} \\ \mathbb{O}_{2,2} \\ \mathbb{O}_{2,2} \end{bmatrix} \mathbf{V_x} + \begin{bmatrix} -N_\Sigma(m)/L_m^{eq} \\ \mathbb{O}_{1,m} \\ \mathbb{O}_{2,m} \\ 2\tilde{B}_\Delta^{dq0}[P(-\theta)][C_K]/L_o^{eq} \end{bmatrix} \mathbf{V_y} + \begin{bmatrix} -N_\Sigma(1)/L_m^{eq} \\ \mathbb{O}_{1,1} \\ \mathbb{O}_{2,1} \\ \mathbb{O}_{2,1} \end{bmatrix} V_{n_{AD}} \in \mathcal{M}_{6,1}(\mathbb{R})$$

$$\mathbf{U}_{\mathbf{HL}}^{\mathbf{dq0}} = [{v_{py}}^d, {v_{py}}^q, {v_{py}}^0, {v_{ny}}^d, {v_{ny}}^q, {v_{ny}}^0]^T \in \mathcal{M}_{6,1}(\mathbb{R})$$

The resulting state-space model is fully controllable and observable. The above minimal representation can therefore be used to control the currents in the MMC. Applying the development proposed in appendix B, this state-space model shows:

$$C_{HL}^{dq0} G_{HL}^{dq0} \mathbf{U}_{\mathbf{HL}}^{\mathbf{dq0}}(k) = \mathbf{Y}_{\mathbf{HL}}^{\mathbf{dq0}}(k+1) - C_{HL}^{dq0} F_{HL}^{dq0} \mathbf{X}_{\mathbf{HL}}^{\mathbf{dq0}}(k) - C_{HL}^{dq0} H_{HL}^{dq0} \mathbf{E}_{\mathbf{HL}}^{\mathbf{dq0}}(k) \tag{3.105}$$

3.D.4 | Conclusions about the GPFSROCSSM

This change of basis approach results in a state-space model of significantly lower order than the previous one (3.60). Not only is the resulting model of reduced order, but this order is constant regardless of the number of phases in the output AC network. This property gives the model the "fixed-order" character while preserving its "generalized" property. It is from these different characteristics, as well as those of the GPFOCSSM model that it capitalizes from, that this model is named General Polyphase Fixed-Size Reduced Order Current State-Space Model (GPFSROCSSM). From now on and in the following work, it is its acronym GPFSROCSSM which will be mainly used to refer to it.

Thanks to this new modelling step, the high-level model of the currents has been reduced from $2m$ to $4+2$. The first observation is that the order of the model could be reduced in a substantial way, and it is in this way that the new model meets the objectives initially stated. Moreover, the order of the model now obtained is independent of the number m of phases. This represents a strong feature of the proposed model. As highlighted by the state-space model matrices defined by (3.104), the latter has parameters that depend on m, which makes it a model that is always modular and scalable as a function of the number m of phases and submodules N, yet without its order depending on it. With such a model it is now possible to represent a MMC being connected to an AC network having any number of phases while featuring a constant complexity. In the case of a state feedback the gain matrix would have a total of 36 terms. It would therefore be consistent to observe a relatively constant computation time for real time control as the number of phases in the system increases.

Although it has the strong benefit of being constant in size, this model has an aspect that could lead to a lack of precision in the representation of the circulating current. Indeed this model does not allow, for electrical systems with more than three phases, to model more than the fundamental components of each type of alternating current. However, it has been shown by [Ilv+12] and confirmed by [Lyu+18] (see Section 3.D.2) that the circulating current has as its largest component its 2^{nd} order harmonic components. It would therefore be interesting to be able to develop a model able to represent the fundamental and 2^{nd} harmonic components for the four types of currents including the circulating current, whatever the number of phases in the system. To answer this issue one idea is to suggest a change of basis which is able to represent both the fundamental components of the currents and the 2^{nd} harmonic components with the same accuracy. This change of basis would then allow to have a state-space representation describing the behavior of the system on areas of the state-space which cover more realistically those actually reached by the state variables.

3.E | Biharmonic PARK transform for polyphase systems

3.E.1 | Foundations of the PARK transform operated

The new transformation of PARK which will be implemented to derive the reduced order model with the consideration of an extended harmonic content is possible under certain assumptions.

The first assumption concerns the harmonic content of the represented signals. Indeed, the electric signals must present a fundamental and second order harmonic component for systems of **more than five phases**. For systems of **five phases or less**, this second condition is that the electrical signals must have only two harmonic components, which can be any of them. As a matter of fact, the following assumption, more complete than the assumption 9 made in the previous PARK transformation, is considered:

Assumption 5. *For $m < 5$: The currents flowing through the MMC are entirely described at most by one continuous component and two harmonic components, the other components are considered null. For $m \geq 5$: The harmonic components mentioned above are limited to the fundamental and 2^{nd} order harmonic components.*

The harmonic content of these currents has been analyzed by [Ilv+12; Lyu+18] showing that the harmonic components of greatest amplitude are those of first and second order, in other words, the fundamental and the 2^{nd} harmonic. The hypothesis made is therefore verified by the currents to be represented and the PARK transform can therefore by applied on the model describing the dynamics of the currents. Representing only first and second order harmonics, means that it will be impossible to perform a third harmonic injection for voltage operating zone enlargement as done in [HG84; NÄJ12], this is a choice in this first approach of MMC high-level model PARK transform for polyphase systems.

The second assumption deals with the symmetry of the loads, indeed, as for the case of the previous transformation of PARK, the assumption 4 is considered. The circulating and output currents make two electrical systems of polyphase currents. As seen in Figure 3.3, these two current types are structurally null-sum and the model described by (3.60) shows that all circulating currents see the same impedance. The same is true for the output currents. Thus, the circulating currents and the output currents form two electrical systems on a symmetrical load and thus verify this assumption.

3.E.2 | Development of basis changes

3.E.2.1 | Design of the appropriate PARK transform

The new PARK transform proposed here builds on the work from [SBH03; SKB04; Kes03; SK10], which will allow for the development of a more accurate state-space model of the currents due to the inclusion of a larger harmonic content.

In order to design the PARK transform capable of taking into account the whole harmonic content in the m-phase case, i.e. the most general PARK transform, [Kes03] relies on the diagonalization of the inductance matrix in the case of an m-phase electrical system with mutual inductances between each of the phases. It is noted $\mathcal{B}^m$ the basis associated with the m-phase stationary reference frame and $\mathbf{x}_\mathbf{k}^\mathbf{m}$ the vectors of the initial basis for $k \in [\![1; m]\!]$. For example, for the three-phase case, one has the current $i_1(t)$ in phase $\#1$, the current $i_2(t)$ in phase $\#2$ and the current

$i_3(t)$ in phase #3, so in the basis $\mathcal{B}^m$ the current vector representing the set of currents in the three phases is written as $\mathbf{i^m}$:

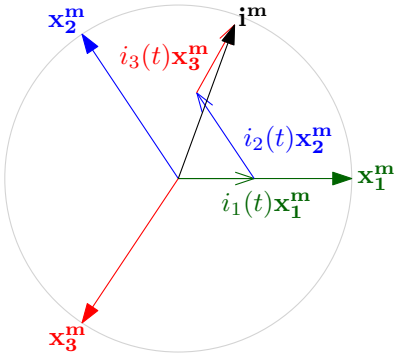

Figure 3.5: Representation of a current in the natural basis $\mathcal{B}^m$ for the three-phase case.

$$\mathbf{i^m} = \begin{bmatrix} i_1(t) \\ i_2(t) \\ i_3(t) \end{bmatrix} = i_1(t) \cdot \mathbf{x_1^m} + i_2(t) \cdot \mathbf{x_2^m} + i_3(t) \cdot \mathbf{x_3^m} \tag{3.106}$$

Let λ be the linear map which represents the relationship between magnetic magnetic flux in the electric circuit and the associated current, by setting $\mathbf{\Phi^m}$ the magnetic magnetic flux, the flux-current relationship is thus expressed:

$$\mathbf{\Phi^m} = \lambda(\mathbf{i^m}) \tag{3.107}$$

In the initial m-phase reference frame, the flux-current relationships are simple to formulate because they are based directly on the physical behavior of the induction process. These relations can also take into account the mutual induction phenomena between phases. To represent all the flux-current relationships it is then possible to use a matrix formulation which represents the influence of each current on each phase magnetic flux. The associated matrix will be noted L^m and stands for the flux-current relationship in the natural basis. According to the definition of λ, it follows that then:

$$L^m = mat(\lambda, \mathcal{B}^m) \tag{3.108}$$

As there are mutual inductances between the phases, L^m is not diagonal. The work of [Kes03] aims then at diagonalizing the inductance matrix, here called L^m, in the general case of a m-phase electric system. This diagonalization is done in several steps:

- Determination of the eigenvalues Λ_i of the inductance matrix L^m.
- Determination of the eigenvectors $\mathbf{c_i}$ associated with each of the eigenvalues Λ_i.
- The eigenvectors $\mathbf{c_i}$ having with complex coordinates in the initial basis $\mathcal{B}^m$, new eigenvectors with real coordinates $\mathbf{x_k^c}$ are obtained by linear combination of the $\mathbf{c_i}$.
- The bases $\mathcal{B}_p^c$ of the eigensubspaces are then built from these real eigenvectors $\mathbf{x_k^c}$. Each eigensubspace E_p^c is associated to a fictitious or virtual electrical system $\{\alpha_p, \beta_p\}$.
- The transition matrix $[C_K^m]$ from the initial basis $\mathcal{B}^m$ to the basis of the fictitious electrical systems $\mathcal{B}^c$ is then derived. $\mathcal{B}^c$ is then named base of Clarke or Concordia according to the type of transformation chosen.

From the eigenvalues to the basis change matrix

When determining the eigenvalues Λ_i, it is possible to observe a certain cyclicity. Indeed it is observed that $\Lambda_{m-i+2} = \Lambda_i$ for $i \in [\![2; m]\!]$ Therefore, if a new eigenvector is obtained by linear

combination of $\mathbf{c_i}$ and $\mathbf{c_{m-i+2}}$ then it will also be associated to the eigenvalue Λ_i. It is also shown that:

$$\mathbf{c_i} = c_1 \begin{bmatrix} 1 \\ e^{j\theta_m(i-1)} \\ e^{j\theta_m(i-1)2} \\ e^{j\theta_m(i-1)3} \\ \vdots \\ e^{j\theta_m(i-1)(m-2)} \\ e^{j\theta_m(i-1)(m-1)} \end{bmatrix} \tag{3.109}$$

Where c_1 is a constant factor which will be determined according to the choice of the transformation of CLARKE or that of CONDORDIA, and $\mathbf{c}_1$ is defined as follows:

$$\mathbf{c}_1 = c_1 \begin{bmatrix} 1 \\ 1 \\ \vdots \\ 1 \end{bmatrix} \tag{3.110}$$

The eigenvectors $\mathbf{c_i}$ and $\mathbf{c_{m-i+2}}$ are both complex-valued in $\mathcal{B}^m$, but it is preferable to have real-valued eigenvectors. One reason for this preference is the desire to design a current control algorithm that uses real gains although the realization of complex gain correctors is possible and efficient [Bod20]. Using the EULER formulas, it is possible to show that:

$$\begin{cases} \mathbf{c_i} + \mathbf{c_{m-i+2}} = 2c_1 \cdot \sum_{k=1}^{m} \cos(\theta_m(i-1)(k-1))\mathbf{x_k^m} \\ \mathbf{c_i} - \mathbf{c_{m-i+2}} = 2jc_1 \cdot \sum_{k=1}^{m} \sin(\theta_m(i-1)(k-1))\mathbf{x_k^m} \end{cases} \tag{3.111}$$

New real coordinate eigenvectors are introduced and defined as follows:

$$\begin{aligned} &\text{For } k=1,\ \mathbf{x_1^c} = \mathbf{c}_1 \\ &\forall k \in [\![2;m]\!],\ \mathbf{x_k^c} = \begin{cases} \mathbf{x_k^{c+}} = \frac{\mathbf{c_i}+\mathbf{c_{m-i+2}}}{\sqrt{2}}, \text{ if } k \text{ is even and it comes that } i = 1 + k/2 \\ \mathbf{x_k^{c-}} = \frac{\mathbf{c_i}-\mathbf{c_{m-i+2}}}{j\sqrt{2}}, \text{ if } k \text{ is odd and it comes that } i = 1/2 + k/2 \end{cases} \end{aligned} \tag{3.112}$$

As a result, it is interesting to note that:

$$\begin{aligned} &\text{For } k=1,\ \mathbf{x_1^c} = \mathbf{c}_1 \\ &\forall k \in [\![2;m]\!], \text{ so that } k = 2p, \qquad \mathbf{x_k^c} = \mathbf{x_k^{c+}} = \frac{\mathbf{c_{p+1}}+\mathbf{c_{m-p+1}}}{\sqrt{2}} \\ &\qquad \text{it comes that: } k+1 = 2p+1,\ \mathbf{x_{k+1}^c} = \mathbf{x_{k+1}^{c-}} = \frac{\mathbf{c_{p+1}}-\mathbf{c_{m-p+1}}}{j\sqrt{2}} \end{aligned} \tag{3.113}$$

The relationship between i and k as a function of phase number parity is clarified in equation (3.116). For $k \in [\![2;m]\!]$, all $\mathbf{x_k^c}$ will be grouped two by two to constitute a vector subspace associated to the same eigenvalue. In the case where m is even, $\mathbf{x_m^c}$ is not obtained from a linear combination of two $\mathbf{c_i}$ but it comes directly from the relation: $\mathbf{x_m^c} = \mathbf{c_{m/2+1}}$, it is thus not issued from the association of two $\mathbf{c_i}$. It can however be noted that in the case where m is even, $\mathbf{x_m^c}$ is then orthogonal to $\mathbf{x_1^c}$. In the odd case, $\mathbf{x_1^c}$ will be alone, with no orthogonal vector that can be associated to it. Any vector subspace E_p^c will be generated by a $\mathbf{x_k^{c+}}$ whose coordinates are in cosine and the associated $\mathbf{x_{k+1}^{c-}}$ whose coordinates are in sine in the basis $\mathcal{B}^m$, the associations $\{\mathbf{x_k^{c+}}, \mathbf{x_{k+1}^{c-}}\}$ will thus constitute the bases $\mathcal{B}_p^c$. It is interesting to note that all the bases $\mathcal{B}_p^c$ are therefore orthogonal, which is trivial to show by scalar product of $\mathbf{x_{k+1}^{c-}}$ with $\mathbf{x_k^{c+}}$. The new base of the space will therefore be:

$$\mathcal{B}^c = \{\mathcal{B}_1^c, \mathcal{B}_2^c, \ldots, \mathcal{B}_J^c\} \tag{3.114}$$

with $J = (m+1)/2$ if m is odd and $J = m/2$ if m is even. Which can be summarized by:

$$\mathcal{B}^c = \begin{cases} \{\{\mathbf{x_1^c}\}, \{\mathbf{x_2^c}, \mathbf{x_3^c}\}, \ldots, \{\mathbf{x_{m-1}^c}, \mathbf{x_m^c}\}\}, \text{if } m \text{ is odd} \\ \{\{\mathbf{x_1^c}\}, \{\mathbf{x_2^c}, \mathbf{x_3^c}\}, \ldots, \{\mathbf{x_{m-2}^c}, \mathbf{x_{m-1}^c}\}, \{\mathbf{x_m^c}\}\}, \text{if } m \text{ is even} \end{cases} \tag{3.115}$$

To illustrate the creation process of the bases of the vector subspaces $\{\mathbf{x_k^{c+}}, \mathbf{x_{k+1}^{c-}}\} = \{\mathbf{x_k^c}, \mathbf{x_{k+1}^c}\}$ from the eigenvectors $\mathbf{c_i}$ as a function of the number m of phases, Table 3.1 is drawn. Although

	$\mathbf{c_i}$							
	$i=1$	$i=2$	$i=3$	$i=4$	$i=5$	$i=6$	$i=7$	$i=8$
$m=1$	$\mathbf{c}_1$							
$m=2$	$\mathbf{c}_1$	$\mathbf{c}_2$						
$m=3$	$\mathbf{c}_1$	$\mathbf{c}_2$	$\mathbf{c}_3$					
$m=4$	$\mathbf{c}_1$	$\mathbf{c}_2$	$\mathbf{c}_3$	$\mathbf{c}_4$				
$m=5$	$\mathbf{c}_1$	$\mathbf{c}_2$	$\mathbf{c}_3$	$\mathbf{c}_4$	$\mathbf{c}_5$			
$m=6$	$\mathbf{c}_1$	$\mathbf{c}_2$	$\mathbf{c}_3$	$\mathbf{c}_4$	$\mathbf{c}_5$	$\mathbf{c}_6$		
$m=7$	$\mathbf{c}_1$	$\mathbf{c}_2$	$\mathbf{c}_3$	$\mathbf{c}_4$	$\mathbf{c}_5$	$\mathbf{c}_6$	$\mathbf{c}_7$	
$m=8$	$\mathbf{c}_1$	$\mathbf{c}_2$	$\mathbf{c}_3$	$\mathbf{c}_4$	$\mathbf{c}_5$	$\mathbf{c}_6$	$\mathbf{c}_7$	$\mathbf{c}_8$

Table 3.1: Table, for $m[1;8]$, grouping the $\mathbf{c_i}$s to form the real eigenvectors $\mathbf{x_k^c}$

the table is limited to 8 phases, the appearance pattern of the different colors continues for a higher number of phases. The first step consists in gathering the eigenvectors $\mathbf{c_i}$ and $\mathbf{c_{m-i+2}}$ because it is together that they will generate, by linear combination, the real eigenvectors $\mathbf{x_k^c}$ and $\mathbf{x_{k+1}^c}$. In the table, each combination is represented by a color, for example for $m = 5$ phases, $\mathbf{c}_2$ and $\mathbf{c}_5$ will be associated to form $\mathbf{x_2^c}$ and $\mathbf{x_3^c}$, so they take the same color. It is observed that for the cases where the number of phases is even, $\mathbf{c_{m/2+1}}$ will be associated to no other eigenvector to conceive a $\mathbf{x_k^c}$ by linear combination, hence the fact of having only one vector carrying the pink color for cases where there is an even number of phases. Once the eigenvector associations are made, they are used to generate the real eigenvectors:

$$\begin{aligned}
&m=1 : \{\mathbf{c}_1\} \longrightarrow \{\mathbf{x_1^c}\} \\
&m=2 : \{\mathbf{c}_1\}; \{\mathbf{c}_2\} \longrightarrow \{\mathbf{x_1^c}\}; \{\mathbf{x_2^c}\} \\
&m=3 : \{\mathbf{c}_1\}; \{\mathbf{c}_2, \mathbf{c}_3\} \longrightarrow \{\mathbf{x_1^c}\}; \{\mathbf{x_2^c}, \mathbf{x_3^c}\} \\
&m=4 : \{\mathbf{c}_1\}; \{\mathbf{c}_2, \mathbf{c}_4\}; \{\mathbf{c}_3\} \longrightarrow \{\mathbf{x_1^c}\}; \{\mathbf{x_2^c}, \mathbf{x_3^c}\}; \{\mathbf{x_4^c}\} \\
&m=5 : \{\mathbf{c}_1\}; \{\mathbf{c}_2, \mathbf{c}_5\}; \{\mathbf{c}_3, \mathbf{c}_4\} \longrightarrow \{\mathbf{x_1^c}\}; \{\mathbf{x_2^c}, \mathbf{x_3^c}\}; \{\mathbf{x_4^c}; \mathbf{x_5^c}\} \\
&m=6 : \{\mathbf{c}_1\}; \{\mathbf{c}_2, \mathbf{c}_6\}; \{\mathbf{c}_3, \mathbf{c}_5\}; \{\mathbf{c}_4\} \longrightarrow \{\mathbf{x_1^c}\}; \{\mathbf{x_2^c}, \mathbf{x_3^c}\}; \{\mathbf{x_4^c}; \mathbf{x_5^c}\}; \{\mathbf{x_6^c}\} \\
&m=7 : \{\mathbf{c}_1\}; \{\mathbf{c}_2, \mathbf{c}_7\}; \{\mathbf{c}_3, \mathbf{c}_6\}; \{\mathbf{c}_4, \mathbf{c}_5\} \longrightarrow \{\mathbf{x_1^c}\}; \{\mathbf{x_2^c}, \mathbf{x_3^c}\}; \{\mathbf{x_4^c}; \mathbf{x_5^c}\}; \{\mathbf{x_6^c}; \mathbf{x_7^c}\}
\end{aligned} \tag{3.116}$$

This association between the initial eigenvectors and the real eigenvectors highlights the fact that if an electrical signal has a component along $\mathbf{c_i}$ then this component will be found on the associated eigenvectors $\mathbf{x_k^c}$ and $\mathbf{x_{k+1}^c}$. Compared to the more classical PARK transformation encountered in three-phase, each pair $\{\mathbf{x_k^c}; \mathbf{x_{k+1}^c}$ is in fact a pair $\{\mathbf{x}_{\alpha_n}; \mathbf{x}_{\beta_n}$ with n the index that can cover the set of groups of two associated vectors of the new basis. And the vector $\mathbf{x_1^c}$ represents the homopolar component, it can be noted $\mathbf{x}_0$.

From equation (3.115) introducing the definition of the basis $\mathcal{B}^c$, it is then possible to formulate the vectors of the new basis $\mathcal{B}^c$ as a function of the vectors of the initial basis $\mathcal{B}^m$. This gives:

- m odd:

$$\begin{cases} \mathbf{x_1^c} = c_1 \sum_{k=1}^{m} \mathbf{x_k^m} \\ \mathbf{x_2^c} = \sqrt{2} c_1 \sum_{k=1}^{m} \cos(\theta_m (k-1)) \mathbf{x_k^m} \\ \mathbf{x_3^c} = \sqrt{2} c_1 \sum_{k=1}^{m} \sin(\theta_m (k-1)) \mathbf{x_k^m} \\ \mathbf{x_4^c} = \sqrt{2} c_1 \sum_{k=1}^{m} \cos(\theta_m (k-1)2) \mathbf{x_k^m} \\ \mathbf{x_5^c} = \sqrt{2} c_1 \sum_{k=1}^{m} \sin(\theta_m (k-1)2) \mathbf{x_k^m} \\ \vdots \\ \mathbf{x_{m-1}^c} = \sqrt{2} c_1 \sum_{k=1}^{m} \cos(\theta_m (k-1)(m-1)/2) \mathbf{x_k^m} \\ \mathbf{x_m^c} = \sqrt{2} c_1 \sum_{k=1}^{m} \sin(\theta_m (k-1)(m-1)/2) \mathbf{x_k^m} \end{cases} \tag{3.117}$$

- m even:

$$\begin{cases} \mathbf{x_1^c} = c_1 \sum_{k=1}^{m} \mathbf{x_k^m} \\ \mathbf{x_2^c} = \sqrt{2} c_1 \sum_{k=1}^{m} \cos(\theta_m (k-1)) \mathbf{x_k^m} \\ \mathbf{x_3^c} = \sqrt{2} c_1 \sum_{k=1}^{m} \sin(\theta_m (k-1)) \mathbf{x_k^m} \\ \mathbf{x_4^c} = \sqrt{2} c_1 \sum_{k=1}^{m} \cos(\theta_m (k-1)2) \mathbf{x_k^m} \\ \mathbf{x_5^c} = \sqrt{2} c_1 \sum_{k=1}^{m} \sin(\theta_m (k-1)2) \mathbf{x_k^m} \\ \vdots \\ \mathbf{x_{m-2}^c} = \sqrt{2} c_1 \sum_{k=1}^{m} \cos(\theta_m (k-1)(m-2)/2) \mathbf{x_k^m} \\ \mathbf{x_{m-1}^c} = \sqrt{2} c_1 \sum_{k=1}^{m} \sin(\theta_m (k-1)(m-2)/2) \mathbf{x_k^m} \\ \mathbf{x_m^c} = c_1 \sum_{k=1}^{m} \cos(\theta_m (k-1)m/2) \mathbf{x_k^m} = c_1 \sum_{k=1}^{m} (-1)^{k-1} \mathbf{x_k^m} \end{cases} \tag{3.118}$$

It is decided to set $K = c_1\sqrt{2}$. From these expressions, the determination of the transition matrix $[C_K^m] = \mathcal{M}_{\{\mathcal{B}^c, \mathcal{B}^m\}}$ from the basis $\mathcal{B}^m$ to the basis $\mathcal{B}^c$ is therefore trivial:

- m odd:

$$\begin{bmatrix} \mathbf{x_1^c} \\ \mathbf{x_2^c} \\ \mathbf{x_3^c} \\ \mathbf{x_4^c} \\ \mathbf{x_5^c} \\ \vdots \\ \mathbf{x_{m-1}^c} \\ \mathbf{x_m^c} \end{bmatrix} = K \begin{bmatrix} 1/\sqrt{2} & 1/\sqrt{2} & 1/\sqrt{2} & \dots & 1/\sqrt{2} \\ 1 & \cos(\theta_m) & \cos(2\theta_m) & \dots & \cos(\theta_m(m-1)) \\ 0 & \sin(\theta_m) & \sin(2\theta_m) & \dots & \sin(\theta_m(m-1)) \\ 1 & \cos(2\theta_m) & \cos(4\theta_m) & \dots & \cos(\theta_m(m-1)2) \\ 0 & \sin(2\theta_m) & \sin(4\theta_m) & \dots & \sin(\theta_m(m-1)2) \\ \vdots & & & & \\ 1 & \cos(\theta_m(m-1)/2) & \cos(2\theta_m(m-1)/2) & \dots & \cos(\theta_m(m-1)(m-1)/2) \\ 0 & \sin(\theta_m(m-1)/2) & \sin(2\theta_m(m-1)/2) & \dots & \sin(\theta_m(m-1)(m-1)/2) \end{bmatrix} \begin{bmatrix} \mathbf{x_1^m} \\ \mathbf{x_2^m} \\ \mathbf{x_3^m} \\ \mathbf{x_4^m} \\ \mathbf{x_5^m} \\ \vdots \\ \mathbf{x_m^m} \end{bmatrix} \tag{3.119}$$

- m even:

$$\begin{bmatrix} \mathbf{x_1^c} \\ \mathbf{x_2^c} \\ \mathbf{x_3^c} \\ \mathbf{x_4^c} \\ \mathbf{x_5^c} \\ \vdots \\ \mathbf{x_{m-2}^c} \\ \mathbf{x_{m-1}^c} \\ \mathbf{x_m^c} \end{bmatrix} = K \begin{bmatrix} 1/\sqrt{2} & 1/\sqrt{2} & 1/\sqrt{2} & \dots & 1/\sqrt{2} \\ 1 & \cos(\theta_m) & \cos(2\theta_m) & \dots & \cos(\theta_m(m-1)) \\ 0 & \sin(\theta_m) & \sin(2\theta_m) & \dots & \sin(\theta_m(m-1)) \\ 1 & \cos(2\theta_m) & \cos(4\theta_m) & \dots & \cos(\theta_m(m-1)2) \\ 0 & \sin(2\theta_m) & \sin(4\theta_m) & \dots & \sin(\theta_m(m-1)2) \\ \vdots & & & & \\ 1 & \cos(\theta_m(m-2)/2) & \cos(2\theta_m(m-2)/2) & \dots & \cos(\theta_m(m-1)(m-2)/2) \\ 0 & \sin(\theta_m(m-2)/2) & \sin(2\theta_m(m-2)/2) & \dots & \sin(\theta_m(m-1)(m-2)/2) \\ 1/\sqrt{2} & -1/\sqrt{2} & 1/\sqrt{2} & \dots & -1/\sqrt{2} \end{bmatrix} \begin{bmatrix} \mathbf{x_1^m} \\ \mathbf{x_2^m} \\ \mathbf{x_3^m} \\ \mathbf{x_4^m} \\ \mathbf{x_5^m} \\ \vdots \\ \mathbf{x_m^m} \end{bmatrix} \tag{3.120}$$

Whatever m, it is possible to show the following result by matrix product:

$$[C_K^m] \cdot [C_K^m]^T = \frac{K^2 m}{2} \mathbb{I}_m \tag{3.121}$$

This result allows one to easily determine the matrix operating the inverse base change $\mathcal{M}_{\{\mathcal{B}^m,\mathcal{B}^c\}}$. $[C_K^m]$ being a square matrix $(m \times m)$, its inverse is thus defined:

$$[C_K^m]^{-1} \triangleq \frac{2}{K^2 m}[C_K^m]^T \tag{3.122}$$

The introduced basis change then allows one to diagonalize the inductance matrix and gives the following result, since the eigenvectors $\mathbf{x_j^c}$ derived by linear combination of the $\mathbf{c_i}$ that are associated to the same eigenvalues:

$$L_c = mat(\lambda, \mathcal{B}^c) = \begin{cases} diag(\Lambda_1, \Lambda_2, \Lambda_2, \ldots, \Lambda_{(m+1)/2}, \Lambda_{(m+1)/2}), \text{ cas } m \text{ impair} \\ diag(\Lambda_1, \Lambda_2, \Lambda_2, \ldots, \Lambda_{m/2}, \Lambda_{m/2}, \Lambda_1), \text{ cas } m \text{ pair} \end{cases} \tag{3.123}$$

with $diag(\mathbf{v})$ the diagonal matrix that contains on its diagonal elements the components of vector $\mathbf{v}$.

Analysis of the harmonic content embedded by the eigenvectors

The Park transform which has just been explained is well known in the literature. However, it can be interesting to highlight its characteristics. The characteristics which are of particular interest here are those which concern the capacity of the transformation to preserve a sufficient precision in the description of the signal waveforms on which the base change is carried out.

To evaluate how well the transformation preserves the information of the transformed signals, an analysis consists in evaluating the projection of the harmonic components on the eigenvectors of the basis $\mathcal{B}^c$. To do so, any electrical signal (current, voltage or magnetic flux) is considered with n harmonic components, it is named $\mathbf{f_m}$ in the initial basis so that:

$$\mathbf{f_m} = \begin{bmatrix} f_1(t) \\ f_2(t) \\ \vdots \\ f_m(t) \end{bmatrix} \tag{3.124}$$

Each coordinate of $\mathbf{f_m}$ in the $\mathcal{B}^m$ basis is considered to have a harmonic content consisting of n components featuring a cyclicity, which means that $\forall k \in [\![1, m]\!]$:

$$f_k(t) = f_k^1(t) + f_k^2(t) + \ldots + f_k^h(t) + \ldots + f_k^n(t) \tag{3.125}$$

with $f_k^h(t)$ the $\#h^{th}$ order harmonic component of $f_k(t)$. This decomposition being possible for all coordinates of $\mathbf{f_m}$, the following result is then obtained. The notation of the time dependence (t) is voluntarily omitted for more clarity:

$$\mathbf{f_m} = \begin{bmatrix} f_1(t) \\ f_2(t) \\ \vdots \\ f_m(t) \end{bmatrix} = \begin{bmatrix} f_1^1 \\ f_2^1 \\ \vdots \\ f_m^1 \end{bmatrix} + \begin{bmatrix} f_1^2 \\ f_2^2 \\ \vdots \\ f_{m^2} \end{bmatrix} + \begin{bmatrix} f_1^3 \\ f_2^3 \\ \vdots \\ f_m^3 \end{bmatrix} + \ldots + \begin{bmatrix} f_1^h \\ f_2^h \\ \vdots \\ f_m^h \end{bmatrix} + \ldots + \begin{bmatrix} f_1^n \\ f_2^n \\ \vdots \\ f_m^n \end{bmatrix} \tag{3.126}$$

Noting $\mathbf{f_m^h}$ the set of harmonic components of rank $\#h$ in the $\mathcal{B}^m$ basis of $\mathbf{f_m}$, it then comes:

$$\mathbf{f_m} = \mathbf{f_m^1} + \mathbf{f_m^2} + \mathbf{f_m^3} + \ldots + \mathbf{f_m^h} + \ldots + \mathbf{f_m^n} \tag{3.127}$$

To carry out the analysis of the harmonic content which is preserved by the change of basis, the interest is now focused on the whole set of harmonic components of any rank $\#h$: $\mathbf{f_m^h}$. The

objective will then be to compute the scalar product between $\mathbf{f_m^h}$ and $\mathbf{c_i}$ to evaluate the result of the projection of the harmonic components of the electric signals in the new basis $\mathcal{B}^c$. The calculation of this scalar product is already presented in [SKB04; Kes03] and gives the following result:

$$\mathbf{f_m^h} \cdot \mathbf{c_i} \neq 0 \iff \exists\ u \in \mathbb{N},\ \ h - i + 1 = u \cdot m \tag{3.128}$$

This result means that the scalar product of $\mathbf{f_m^h}$ with $\mathbf{c_i}$ will give a non-zero result if and only if the rank $\#h$ of the considered harmonic verifies a specific relationship with i and m. More precisely, the computed scalar product can be interpreted as the projection of the vector $\mathbf{f_m^h}$ on the base constituted by the $\mathbf{c_i}$ vectors. The result of this projection indicates that each $\mathbf{c_i}$ will be able to carry the harmonics of rank $h = u \cdot m + i - 1$, and thus that some harmonics will not be carried by this same $\mathbf{c_i}$. For example, for $m = 5$ phases, the vector $\mathbf{c}_3$ will be able to carry the harmonics of rank $h = 5u + 3 - 1 = 5u + 2$ with u integer, that is to say the harmonics of rank $\{2, 7, 12, 17, \ldots\}$. The Table 3.2 of the harmonics carried by each $\mathbf{c_i}$ can then be drawn up.

Ranks h	$\mathbf{c_i}$							
	$i=1$	$i=2$	$i=3$	$i=4$	$i=5$	$i=6$	$i=7$	$i=8$
$m=1$	u							
$m=2$	$2u$	$2u+1$						
$m=3$	$3u$	$3u+1$	$3u+2$					
$m=4$	$4u$	$4u+1$	$4u+2$	$4u+3$				
$m=5$	$5u$	$5u+1$	$5u+2$	$5u+3$	$5u+4$			
$m=6$	$6u$	$6u+1$	$6u+2$	$6u+3$	$6u+4$	$6u+5$		
$m=7$	$7u$	$7u+1$	$7u+2$	$7u+3$	$7u+4$	$7u+5$	$7u+6$	
$m=8$	$8u$	$8u+1$	$8u+2$	$8u+3$	$8u+4$	$8u+5$	$8u+6$	$8u+7$

Table 3.2: Table for $m \in [\![1; 8]\!]$ of harmonic distributions over the eigenvectors $\mathbf{c_i}$

This table shows that whatever the number of phases, if the entire set of eigenvectors $\mathbf{c_i}$ is considered, then all the harmonics of the electrical signals will be represented. In other words, since the change of basis introduced and operated by equation (3.120) is established from a linear combination of the eigenvectors $\mathbf{c_i}$, this change of basis will present no loss of information. Thus all the harmonic content will be represented in the new basis $\mathcal{B}^c$. Applied for the first few integer values of u, this table becomes Table 3.3.

Ranks h	$\mathbf{c_i}$						
	$i=1$	$i=2$	$i=3$	$i=4$	$i=5$	$i=6$	$i=7$
$m=1$	$1,2,3$						
$m=2$	$2,4,6$	$1,3,5$					
$m=3$	$3,6,9$	$1,4,7$	$2,5,8$				
$m=4$	$4,8,12$	$1,5,9$	$2,6,10$	$3,7,11$			
$m=5$	$5,10,15$	$1,6,11$	$2,7,12$	$3,8,13$	$4,9,14$		
$m=6$	$6,12,18$	$1,7,13$	$2,8,14$	$3,9,15$	$4,10,16$	$5,11,17$	
$m=7$	$7,14,21$	$1,8,15$	$2,9,16$	$3,10,17$	$4,11,18$	$5,12,19$	$6,13,20$

Table 3.3: Table for $m \in [\![1; 7]\!]$ of harmonic distributions over the eigenvectors $\mathbf{c_i}$ for $u \in 0, 1, 2$

This last table allows one to determine that, depending on the number of phases, the same harmonic component will not be carried by the same eigenvector $\mathbf{c_i}$. Thus, if it is desired to keep the representation of certain harmonics only - whatever the number of phases -, it is not the same set of eigenvectors that will be selected.

As [Ilv+12; Lyu+18] have shown, the harmonic content of the currents that flow within the MMC will be mostly composed of the fundamental at the frequency of the AC grid at the output of the MMC and the second order harmonic. The transformation performed by $[C_K^m]$ allows one to represent all the harmonic content in the new base, some components of which are not significant here. And this transformation will not reduce the order of the current model since $[C_K^m]$ is square of size $(m \times m)$. In order to have a model of the currents with a not too high order, the objective is to design a change of basis, to go towards the PARK reference frame, which represents only the significant components of the currents, i.e., the continuous and fundamental components as well as the second order harmonics.

In order to design this new transformation which should be generalizable as a function of m, the fundamental components and 2^{nd} rank harmonics are isolated in Table 3.2 and thus give rise to the new Table 3.4, with in purple the eigenvectors carrying both the fundamental components and the second order harmonics.

Ranks h	$\mathbf{c_i}$						
	$i=1$	$i=2$	$i=3$	$i=4$	$i=5$	$i=6$	$i=7$
$m=1$	u						
$m=2$	$2u$	$2u+1$					
$m=3$	$3u$	$3u+1$	$3u+2$				
$m=4$	$4u$	$4u+1$	$4u+2$	$4u+3$			
$m=5$	$5u$	$5u+1$	$5u+2$	$5u+3$	$5u+4$		
$m=6$	$6u$	$6u+1$	$6u+2$	$6u+3$	$6u+4$	$6u+5$	
$m=7$	$7u$	$7u+1$	$7u+2$	$7u+3$	$7u+4$	$7u+5$	$7u+6$

Table 3.4: Table for $m \in [\![1;7]\!]$ of harmonic distributions over the eigenvectors $\mathbf{c_i}$

If an eigenvector $\mathbf{c_i}$ is identified as being able to carry the harmonic component of rank $\#h$, then it will also be necessary to take the eigenvector $\mathbf{c_{m-i+2}}$ associated with it, to build the real eigenvectors $\mathbf{x_k^c}$ and $\mathbf{x_{k+1}^c}$. From Table 3.4, it is possible to isolate the set of $\mathbf{c_i}$ that will be selected to create the new transformation, knowing that the $\mathbf{c}_1$ vector will be kept to represent the homopolar component in case it is involved.

Ranks h	$\mathbf{c_i}$						
	$i=1$	$i=2$	$i=3$	$i=4$	$i=5$	$i=6$	$i=7$
$m=1$	u						
$m=2$	$2u$	$2u+1$					
$m=3$	$3u$	$3u+1$	$3u+2$				
$m=4$	$4u$	$4u+1$	$4u+2$	$4u+3$			
$m=5$	$5u$	$5u+1$	$5u+2$	$5u+3$	$5u+4$		
$m=6$	$6u$	$6u+1$	$6u+2$		$6u+4$	$6u+5$	
$m=7$	$7u$	$7u+1$	$7u+2$			$7u+5$	$7u+6$

Table 3.5: Table for $m \in [\![1;7]\!]$ of harmonic distributions in the eigenvectors $\mathbf{c_i}$ that are kept

Several particular cases appear before arriving, for $m=5$, at a pattern that repeats itself for the largest numbers of phases. This disjunction of cases is done in the following way:

In purple are the pairs of eigenvectors carrying both the fundamental components and the second order harmonics. Once the transition matrix from the $(1,2,\ldots,m)$ initial stationary frame to the $(\alpha_1,\beta_1,\alpha_2,\beta_2,0)$ stationary frame is determined for the different values of m, the transformation

	Composition of the bases $\mathcal{B}^c$		
	Selected $\mathbf{c_i}$	$\mathcal{B}^c$ shaped	Common notation
$m=1$	$\{\mathbf{c}_1\}$	$\{\mathbf{x}_1^\mathbf{c}\}$	$\{\mathbf{x}_0\}$
$m=2$	$\{\mathbf{c}_1\},\{\mathbf{c}_2\}$	$\{\mathbf{x}_1^\mathbf{c}\},\{\mathbf{x}_2^\mathbf{c}\}$	$\{\mathbf{x}_0\},\{\mathbf{x}_{0*}\}$
$m=3$	$\{\mathbf{c}_1\},\{\mathbf{c}_2;\mathbf{c}_3\}$	$\{\mathbf{x}_1^\mathbf{c}\},\{\mathbf{x}_2^\mathbf{c};\mathbf{x}_3^\mathbf{c}\}$	$\{\mathbf{x}_0\},\{\mathbf{x}_{\alpha_1};\mathbf{x}_{\beta_1}\}$
$m=4$	$\{\mathbf{c}_1\},\{\mathbf{c}_2;\mathbf{c}_4\},\{\mathbf{c}_3\}$	$\{\mathbf{x}_1^\mathbf{c}\},\{\mathbf{x}_2^\mathbf{c};\mathbf{x}_3^\mathbf{c}\},\{\mathbf{x}_4^\mathbf{c}\}$	$\{\mathbf{x}_0\},\{\mathbf{x}_{\alpha_1};\mathbf{x}_{\beta_1}\},\{\mathbf{x}_{0*}\}$
$m\geq 5$	$\{\mathbf{c}_1\},\{\mathbf{c}_2;\mathbf{c_m}\},\{\mathbf{c}_3,\mathbf{c_{m-1}}\}$	$\{\mathbf{x}_1^\mathbf{c}\},\{\mathbf{x}_2^\mathbf{c};\mathbf{x}_3^\mathbf{c}\},\{\mathbf{x}_4^\mathbf{c},\mathbf{x}_5^\mathbf{c}\}$	$\{\mathbf{x}_0\},\{\mathbf{x}_{\alpha_1};\mathbf{x}_{\beta_1}\},\{\mathbf{x}_{\alpha_2},\mathbf{x}_{\beta_2}\}$

Table 3.6: Table, for $\forall m\in\mathbb{N}^*$, of eigenvectors selected to preserve the continuous, fundamental and second order harmonic components by PARK transformation.

to the $(d_1,q_1,d_2,q_2,0)$ rotating frame will have to perform a change of basis by rotation taking into account the harmonics carried by the vectors of the basis associated to the $(\alpha_1,\beta_1,\alpha_2,\beta_2,0)$ frame.

3.E.2.2 From the m-phase $(1,2,\dots,m)$ stationary frame to the $(\alpha_1,\beta_1,\alpha_2,\beta_2,0)$ stationary frame

From the list of eigenvectors which are selected to build the new basis, it is possible to determine the different basis change matrices allowing to keep the desired harmonic components according to the number of phases. For the following, it is decided to use $k_0=\sqrt{2}$.

The focus is on the general case $m\geq 5$ here. However, the cases where $m<5$ are detailed in Appendix H.1. For this general case, it comes the following matrix when choosing to put the homopolar component at the bottom:

$$\begin{aligned}
\mathbf{x}_{\alpha_1}&=\mathbf{x}_2^\mathbf{c}=\sqrt{2}c_1\textstyle\sum_{k=1}^m\cos(\theta_m(k-1))\mathbf{x_k^m}\\
\mathbf{x}_{\beta_1}&=\mathbf{x}_3^\mathbf{c}=\sqrt{2}c_1\textstyle\sum_{k=1}^m\sin(\theta_m(k-1))\mathbf{x_k^m}\\
\mathbf{x}_{\alpha_2}&=\mathbf{x}_4^\mathbf{c}=\sqrt{2}c_1\textstyle\sum_{k=1}^m\cos(2\theta_m(k-1))\mathbf{x_k^m}\\
\mathbf{x}_{\beta_2}&=\mathbf{x}_5^\mathbf{c}=\sqrt{2}c_1\textstyle\sum_{k=1}^m\sin(2\theta_m(k-1))\mathbf{x_k^m}\\
\mathbf{x}_0&=\mathbf{x}_1^\mathbf{c}=\mathbf{c}_1=c_1\textstyle\sum_{k=1}^m\mathbf{x_k^m}
\end{aligned}\tag{3.129}$$

with $\theta_m=2\pi/m$. This gives the transformation matrix:

$$[C_{K12}^{m\geq 5}]=K\begin{bmatrix}
1 & \cos(\theta_m) & \cos(2\theta_m) & \cos(3\theta_m) & \cos(4\theta_m) & \dots & \cos((m-1)\theta_m)\\
0 & \sin(\theta_m) & \sin(2\theta_m) & \sin(3\theta_m) & \sin(4\theta_m) & \dots & \sin((m-1)\theta_m)\\
1 & \cos(2\theta_m) & \cos(4\theta_m) & \cos(6\theta_m) & \cos(8\theta_m) & \dots & \cos(2(m-1)\theta_m)\\
0 & \sin(2\theta_m) & \sin(4\theta_m) & \sin(6\theta_m) & \sin(8\theta_m) & \dots & \sin(2(m-1)\theta_m)\\
1/k_0 & 1/k_0 & 1/k_0 & 1/k_0 & 1/k_0 & \dots & 1/k_0
\end{bmatrix}\tag{3.130}$$

It is then possible to show the following relation knowing that $k_0=\sqrt{2}$:

$$[C_{K12}^m]^+\triangleq\frac{2}{K^2m}[C_{K12}^m]^T\tag{3.131}$$

It is thus with this transformation matrix that the shift from the initial stationary frame $(1,2,\dots,m)$ to the stationary frame $(\alpha_1,\beta_1,\alpha_2,\beta_2,0)$ is operated:

$$\mathbf{X}^{\{\alpha_1,\beta_1,\alpha_2,\beta_2,0\}}=\mathbf{X}^{\alpha\beta012}=[C_{K12}^m]\mathbf{X^m}\tag{3.132}$$

For the inverse transformation the following relation will be used:

$$\mathbf{X^m}=[C_{K12}^m]^+\mathbf{X}^{\alpha\beta0^{12}}=\frac{2}{K^2m}[C_{K12}^m]^T\mathbf{X}^{\alpha\beta012}\tag{3.133}$$

For a power conservation - Concordia - the choice is $K = \sqrt{2/m}$, for the amplitude conservation - Clarke - one should choose $K = 2/m$.

3.E.2.3 From the $(\alpha_1, \beta_1, \alpha_2, \beta_2, 0)$ stationary frame to the $(d_1, q_1, d_2, q_2, 0)$ synchronous rotating frame

The cases with $m < 5$ are detailed in Appendix H.2. In the case with 5 phases or more, the fundamental components are carried by $\mathbf{x}_{\alpha_1}$ and $\mathbf{x}_{\beta_1}$, while the second order harmonic components are carried by $\mathbf{x}_{\alpha_2}$ and $\mathbf{x}_{\beta_2}$. The vectors $\mathbf{x}_{\alpha_1}$ and $\mathbf{x}_{\beta_1}$ form a pair $\{\mathbf{x}^{\mathbf{c}}_{\mathbf{k}}; \mathbf{x}^{\mathbf{c}}_{\mathbf{k+1}}\}$ of orthogonal vectors on which a rotation can be operated, it is the same for $\mathbf{x}_{\alpha_2}$ and $\mathbf{x}_{\beta_2}$:

$$\begin{aligned}
\mathbf{x}_{\mathbf{d}_1} &= \cos(\theta)\mathbf{x}_{\alpha_1} + \sin(\theta)\mathbf{x}_{\beta_1} \\
\mathbf{x}_{\mathbf{q}_1} &= -\sin(\theta)\mathbf{x}_{\alpha_1} + \cos(\theta)\mathbf{x}_{\beta_1} \\
\mathbf{x}_{\mathbf{d}_2} &= \cos(2\theta)\mathbf{x}_{\alpha_2} + \sin(2\theta)\mathbf{x}_{\beta_2} \\
\mathbf{x}_{\mathbf{q}_2} &= -\sin(2\theta)\mathbf{x}_{\alpha_2} + \cos(2\theta)\mathbf{x}_{\beta_2} \\
\mathbf{x}_0 &= \mathbf{x}_0
\end{aligned} \tag{3.134}$$

In matrix form:

$$\begin{bmatrix} \mathbf{x}_{\mathbf{d}_1} \\ \mathbf{x}_{\mathbf{q}_1} \\ \mathbf{x}_{\mathbf{d}_2} \\ \mathbf{x}_{\mathbf{q}_2} \\ \mathbf{x}_0 \end{bmatrix} = \begin{bmatrix} \cos(\theta) & \sin(\theta) & 0 & 0 & 0 \\ -\sin(\theta) & \cos(\theta) & 0 & 0 & 0 \\ 0 & 0 & \cos(2\theta) & \sin(2\theta) & 0 \\ 0 & 0 & -\sin(2\theta) & \cos(2\theta) & 0 \\ 0 & 0 & 0 & 0 & 1 \end{bmatrix} \begin{bmatrix} \mathbf{x}_{\alpha_1} \\ \mathbf{x}_{\beta_1} \\ \mathbf{x}_{\alpha_2} \\ \mathbf{x}_{\beta_2} \\ \mathbf{x}_0 \end{bmatrix} = [P(-\theta)^{m\geq 5}_{12}] \begin{bmatrix} \mathbf{x}_{\alpha_1} \\ \mathbf{x}_{\beta_1} \\ \mathbf{x}_{\alpha_2} \\ \mathbf{x}_{\beta_2} \\ \mathbf{x}_0 \end{bmatrix} \tag{3.135}$$

Finally, whatever the number of phase, it is possible to verify that the matrix $[P(-\theta)^m_{12}]$ will always be invertible which will allow to operate the transformations in the following way:

$$\mathbf{X}^{\{\mathbf{d}_1,\mathbf{q}_1,\mathbf{d}_2,\mathbf{q}_2,0\}} = \mathbf{X}^{\mathbf{dq}0^{12}} = [P(-\theta)^m_{12}]\, \mathbf{X}^{\alpha\beta 0^{12}} \tag{3.136}$$

The inverse transformation is then performed by:

$$\mathbf{X}^{\alpha\beta 0^{12}} = [P(-\theta)^m_{12}]^{-1} \mathbf{X}^{\mathbf{dq}0^{12}} = [P(\theta)^m_{12}]\, \mathbf{X}^{\mathbf{dq}0^{12}} \tag{3.137}$$

It is noted that, as a function of the number m of phases, the size of the transformation matrices will change, and the size of the vectors in the Park reference frame will also change accordingly. Denoting m' the size of the vectors obtained after the full transformation to this last reference frame, Figure 14 shows the evolution of this size as a function of the number of phases.

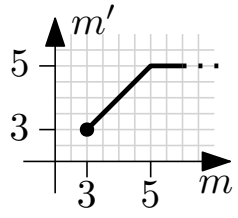

$$m' = \begin{cases} m, \text{ if } m \leq 5 \\ 5, \text{ if } m \geq 5 \end{cases} \tag{3.138}$$

Figure 3.6: Definition of m' as a function of m.

3.F | Development of the General Polyphase Fixed-Size Reduced Order BiHarmonic Content Current State-Space Model

3.F.1 | Decoupled generalized polyphase fixed-size reduced order biharmonic content model of the currents

The order reduction of the GPFOCSSM model of the currents developed in section 3.C is done here in several steps, each corresponding to a type of current. The common mode current is the first to be dealt with as for the two previous state-space models. The transformation matrices that are used to operate the change of basis, from the initial stationary reference frame to the PARK 12 synchronously rotating one, change as the number of phases increases as it was shown in the previous section. For this reason it is chosen to describe the development approach of the reduced order model only for the case where $m \geq 5$. Note that the method to be applied for the cases where $m < 5$ will be the same.

3.F.1.1 | Model for the common mode current (i_m, I_m)

The differential equation governing the behavior of the common mode current in the new reference frame is obtained from that established in the natural basis (3.76):

$$R_m^{eq} I_m + L_m^{eq} s I_m = B_\Sigma^m \left(\mathbf{V_{py}} + \mathbf{V_{ny}}\right) + \left(N_\Sigma(2)\mathbf{V_x} - N_\Sigma(m)\mathbf{V_y} - N_\Sigma(1)V_{n_{AD}}\right) \tag{3.139}$$

Even though the PARK transform derived in Appendix G is explicitly done for the first PARK transform, the same developement holds for the PARK 12 transform as explained at the end of Appendix G. Applying the change of basis method as it is detailed in Appendix G, gives the following result with the dedicated notations:

$$\begin{cases} I_m^{dq012} = I_m \\ B_\Sigma^{dq012} = \frac{k_0}{mK}\begin{bmatrix} 0 & 0 & 0 & 0 & -1/2 \end{bmatrix} \\ \mathbf{V_{py}^{dq012}} = \left[P(-\theta)_{12}^m\right]\left[C_{K_{12}}^m\right]\mathbf{V_{py}} \\ \mathbf{V_{ny}^{dq012}} = \left[P(-\theta)_{12}^m\right]\left[C_{K_{12}}^m\right]\mathbf{V_{ny}} \end{cases} \tag{3.140}$$

The use of these new notations finally gives:

$$(R_m^{eq} + L_m^{eq} s) I_m^{dq012} = B_\Sigma^{dq012}\left(\mathbf{V_{py}^{dq012}} + \mathbf{V_{ny}^{dq012}}\right) + \left(N_\Sigma(2)\mathbf{V_x} - N_\Sigma(m)\mathbf{V_y} - N_\Sigma(1)V_{n_{AD}}\right) \tag{3.141}$$

3.F.1.2 | Model for the source current (i_s, I_s)

To determine the dynamics of the source current, the procedure is identical to that used for the common mode current, since the source current also has only one component. In order to reduce the equation then obtained, the simplification introduced by Appendix G is taken advantage of, so that:

$$R_s^{eq} I_s + L_s^{eq} s I_s = B_\Sigma^{dq012}\left(\mathbf{V_{py}^{dq012}} - \mathbf{V_{ny}^{dq012}}\right) + \left(\begin{bmatrix} 1 & 0 \end{bmatrix} \cdot N_\Delta(2)\mathbf{V_x}\right) \tag{3.142}$$

To harmonize the equation, the following notation is then defined $I_s^{dq012} = I_s$. By using this definition, it is thus obtained:

$$(R_s^{eq} + L_s^{eq}s)I_s^{dq012} = B_\Sigma^{dq012}\left(\mathbf{V_{py}^{dq012}} - \mathbf{V_{ny}^{dq012}}\right) + ([1\ \ 0] \cdot N_\Delta(2)\mathbf{V_x}) \tag{3.143}$$

3.F.1.3 | Model for the circulating current $(i_{c_y}, \mathbf{I_c})$

The development that is carried out here is analogous to the one that is carried out in the previous change of basis for the case of the current flowing in Equation 3.D.2. This development will be based on equation (3.82) which represents the behavior of the circulating current in the natural basis:

$$R_c^{eq}\mathbf{I_c} + s\mathbf{\Phi_c} = B_\Delta^m\left(\mathbf{V_{py}} - \mathbf{V_{ny}}\right) \tag{3.144}$$

Applying the change of basis method as it is detailed in Appendix G, gives the following result with the newly introduced notations:

$$\begin{cases} \mathbf{I_c^{dq012}} = [P(-\theta)_{12}^m]\left[C_{K_{12}}^m\right]\mathbf{I_c} = \begin{bmatrix} I_c^{d_1} \\ I_c^{q_1} \\ I_c^{d_2} \\ I_c^{q_2} \\ I_c^0 \end{bmatrix} \text{ and } \mathbf{\Phi_c^{dq012}} = L_c^{eq}\mathbf{I_c^{dq012}} = L_c^{eq}\begin{bmatrix} I_c^{d_1} \\ I_c^{q_1} \\ I_c^{d_2} \\ I_c^{q_2} \\ I_c^0 \end{bmatrix} \\ B_\Delta^{dq012} = [P(-\theta)_{12}^m]\left[C_{K_{12}}^m\right]B_\Delta^m\left[C_{K_{12}}^m\right]^+[P(\theta)_{12}^m] = \begin{bmatrix} -1/2 & 0 & 0 & 0 & 0 \\ 0 & -1/2 & 0 & 0 & 0 \\ 0 & 0 & -1/2 & 0 & 0 \\ 0 & 0 & 0 & -1/2 & 0 \\ 0 & 0 & 0 & 0 & 0 \end{bmatrix} \end{cases} \tag{3.145}$$

By the expression of B_Δ^{dq012}, it is found that by acting on the control voltages, which are $\mathbf{V_{py}^{dq012}}$ and $\mathbf{V_{ny}^{dq012}}$, it is not possible to act on the homopolar component of the circulating current which will be structurally null as in the case of the model of this current presented in Section 3.D.2. Here also the last line of the equation is considered useless, leading to the model which is free of it with the following notations:

$$\begin{cases} \tilde{\mathbf{I}}_\mathbf{c}^{\mathbf{dq012}} = \begin{bmatrix} I_c^{d_1} \\ I_c^{q_1} \\ I_c^{d_2} \\ I_c^{q_2} \end{bmatrix} \text{ and } \tilde{B}_\Delta^{dq012} = \begin{bmatrix} -1/2 & 0 & 0 & 0 & 0 \\ 0 & -1/2 & 0 & 0 & 0 \\ 0 & 0 & -1/2 & 0 & 0 \\ 0 & 0 & 0 & -1/2 & 0 \end{bmatrix} \end{cases} \tag{3.146}$$

This gives the final equation:

$$(R_c^{eq} + L_c^{eq}s)\tilde{\mathbf{I}}_\mathbf{c}^{\mathbf{dq012}} + \omega L_c^{eq}\begin{bmatrix} -I_c^{q_1} \\ I_c^{d_1} \\ -2I_c^{q_2} \\ 2I_c^{d_2} \end{bmatrix} = \tilde{B}_\Delta^{dq012}\left(\mathbf{V_{py}^{dq012}} - \mathbf{V_{ny}^{dq012}}\right) \tag{3.147}$$

This model is therefore able to represent both the alternating components of the circulating current at frequency ω but also the second order harmonic components of this current.

3.F.1.4 | Model for the output current $(i_{o_y}, \mathbf{I_o})$

In order to apply the change of basis towards the PARK 12 reference frame to the output current model, the approach is based on equation (3.148):

$$R_o^{eq}\mathbf{I_o} + s\mathbf{\Phi_o} = B_\Delta^m\left(\mathbf{V_{py}} + \mathbf{V_{ny}}\right) - \mathbf{V_{y\Delta}} \tag{3.148}$$

The rest of the development is patterned after the one done in the previous section for the circulating current, Section 3.F.1.3, according to the method given in Appendix G. For the modelling needs, new notations are introduced:

$$\begin{cases} \tilde{\mathbf{I}}_\mathbf{o}^{\mathbf{dq}012} = \begin{bmatrix} I_o^{d_1} \\ I_o^{q_1} \\ I_o^{d_2} \\ I_o^{q_2} \end{bmatrix} \text{ and } \tilde{B}_\Delta^{dq012} = \begin{bmatrix} -1/2 & 0 & 0 & 0 & 0 \\ 0 & -1/2 & 0 & 0 & 0 \\ 0 & 0 & -1/2 & 0 & 0 \\ 0 & 0 & 0 & -1/2 & 0 \end{bmatrix} \\ \tilde{\mathbf{V}}_{\mathbf{y\Delta}}^{\mathbf{dq}012} = \begin{bmatrix} V_y^{d_1} \\ V_y^{q_1} \\ V_y^{d_2} \\ V_y^{q_2} \end{bmatrix} = 2\tilde{B}_\Delta^{dq012}[P(-\theta)_{12}^m]\left[C_{K_{12}}^m\right]\mathbf{V_y} \end{cases} \tag{3.149}$$

The use of these notations finally leads to:

$$(R_o^{eq} + L_o^{eq}s)\tilde{\mathbf{I}}_\mathbf{o}^{\mathbf{dq}012} + \omega L_o^{eq}\begin{bmatrix} -I_o^{q_1} \\ I_o^{d_1} \\ -2I_o^{q_2} \\ 2I_o^{d_2} \end{bmatrix} = \tilde{B}_\Delta^{dq012}\left(\mathbf{V}_\mathbf{py}^{\mathbf{dq}012} + \mathbf{V}_\mathbf{ny}^{\mathbf{dq}012}\right) - \begin{bmatrix} V_y^{d_1} \\ V_y^{q_1} \\ V_y^{d_2} \\ V_y^{q_2} \end{bmatrix} \tag{3.150}$$

3.F.2 | Current fixed-size reduced order biharmonic state-space model

From the knowledge of equations (3.141), (3.143), (3.147) and (3.150), describing the dynamics of each type of current in the PARK 12 reference frame, it is possible to build a state-space model that assembles the behavior of these different currents. For that purpose, the state vector is defined: $\mathbf{X}_\mathbf{HL}^{\mathbf{dq}012} = \left[I_m^{dq012} \quad I_s^{dq012} \quad \tilde{\mathbf{I}}_\mathbf{c}^{\mathbf{dq}012^T} \quad \tilde{\mathbf{I}}_\mathbf{o}^{\mathbf{dq}012^T}\right]$. The state-space model is defined by:

GPFSROBHCCSSM

$$\begin{cases} \mathbf{X}_\mathbf{HL}^{\mathbf{dq}012} = A_{HL}^{dq012}\ \mathbf{X}_\mathbf{HL}^{\mathbf{dq}012} + B_{HL}^{dq012}\ \mathbf{U}_\mathbf{HL}^{\mathbf{dq}012} + \mathbf{E}_\mathbf{HL}^{\mathbf{dq}012} \\ \mathbf{Y}_\mathbf{HL}^{\mathbf{dq}012} = C_{HL}^{dq012}\ \mathbf{X}_\mathbf{HL}^{\mathbf{dq}012} \end{cases} \tag{3.151}$$

with:

$$A_{HL}^{dq012} = \begin{bmatrix} -\frac{R_m^{eq}}{L_m^{eq}} & & & & & & & & & \\ & -\frac{R_s^{eq}}{L_s^{eq}} & & & & & & & & \\ & & -\frac{R_c^{eq}}{L_c^{eq}} & \omega & & & & & & \\ & & -\omega & -\frac{R_c^{eq}}{L_c^{eq}} & & & & & & \\ & & & & -\frac{R_c^{eq}}{L_c^{eq}} & 2\omega & & & & \\ & & & & -2\omega & -\frac{R_c^{eq}}{L_c^{eq}} & & & & \\ & & & & & & -\frac{R_o^{eq}}{L_o^{eq}} & \omega & & \\ & & & & & & -\omega & -\frac{R_o^{eq}}{L_o^{eq}} & & \\ & & & & & & & & -\frac{R_o^{eq}}{L_o^{eq}} & 2\omega \\ & & & & & & & & -2\omega & -\frac{R_o^{eq}}{L_o^{eq}} \end{bmatrix} \in \mathcal{M}_{10}(\mathbb{R})$$

$$B_{HL}^{dq012} = \begin{bmatrix} B_\Sigma^{dq012}/L_m^{eq} & B_\Sigma^{dq012}/L_m^{eq} \\ B_\Sigma^{dq012}/L_s^{eq} & -B_\Sigma^{dq012}/L_s^{eq} \\ \tilde{B}_\Delta^{dq012}/L_c^{eq} & -\tilde{B}_\Delta^{dq012}/L_c^{eq} \\ \tilde{B}_\Delta^{dq012}/L_o^{eq} & \tilde{B}_\Delta^{dq012}/L_o^{eq} \end{bmatrix} \in \mathcal{M}_{10}(\mathbb{R})$$

$$C_{HL}^{dq012} = \begin{bmatrix} 1 & & & \\ & 1 & & \\ & & \mathbb{I}_4 & \\ & & & \mathbb{I}_4 \end{bmatrix} \in \mathcal{M}_{10}(\mathbb{R})$$

$$\mathbf{E_{HL}^{dq012}} = \begin{bmatrix} N_\Sigma(2)/L_m^{eq} \\ [1\ \ 0] \cdot N_\Delta(2)/L_s^{eq} \\ \mathbb{O}_{4,2} \\ \mathbb{O}_{4,2} \end{bmatrix} \mathbf{V_x} + \begin{bmatrix} -N_\Sigma(m)/L_m^{eq} \\ \mathbb{O}_{1,m} \\ \mathbb{O}_{4,m} \\ 2\tilde{B}_\Delta^{dq012}[P(-\theta)_{12}^m]\left[C_{K_{12}}^m\right]/L_o^{eq} \end{bmatrix} \mathbf{V_y} + \begin{bmatrix} -N_\Sigma(1)/L_m^{eq} \\ \mathbb{O}_{1,1} \\ \mathbb{O}_{4,1} \\ \mathbb{O}_{4,1} \end{bmatrix} V_{n_{AD}} \in \mathcal{M}_{10,1}(\mathbb{R})$$

$$\mathbf{U_{HL}^{dq012}} = [{v_{py}}^{d_1}, {v_{py}}^{q_1}, {v_{py}}^{d_2}, {v_{py}}^{q_2}, {v_{py}}^{0}, {v_{ny}}^{d_1}, {v_{ny}}^{q_1}, {v_{ny}}^{d_2}, {v_{ny}}^{q_2}, {v_{ny}}^{0}]^T \in \mathcal{M}_{10,1}(\mathbb{R}) \tag{3.152}$$

The resulting state-space model is fully controllable and observable. This minimal representation can therefore be adopted to design the control system of the currents in the MMC. This model is then of reduced order compared to the state-space model (3.58) shown previously, but of higher order than the state-space model (3.103) because the harmonic content taken into account here is more important. Applying the development provided in Appendix B to the state-space model here, it follows that:

$$\begin{aligned} &C_{HL}^{dq012} G_{HL}^{dq012} \mathbf{U_{HL}^{dq012}}(k) \\ &\quad = \mathbf{Y_{HL}^{dq012}}(k+1) - C_{HL}^{dq012} F_{HL}^{dq012} \mathbf{X_{HL}^{dq012}}(k) - C_{HL}^{dq012} H_{HL}^{dq012} \mathbf{E_{HL}^{dq012}}(k) \end{aligned} \tag{3.153}$$

3.F.3 | Conclusions about the GPFSROBHCCSSM

Compared to the previously developed model, GPFSROCSSM, the model presented here allows one to take into account the second order harmonics of the currents in addition to the fundamental and continuous components. This brings to a total of 2 the number of harmonics that can be represented for each type of current. Hence the fact of giving the name "biharmonic" to the model introduced in this section, which thus bears the name General Polyphase Fixed-Size Reduced Order BiHarmonic Content Current State-Space Model (GPFSROBHCCSSM). The associated Park reference frame is able to represent both the harmonic components of first order (fundamental) and second order harmonic components, hence the name of this reference frame "Park 12". With this model, it is possible to consider only a reduced harmonic spectrum of the currents. The reduced order model thus obtained is not as general as the full order model GPFOCSSM in terms of description of the values that the different types of currents can take, but it is a step that will present a better description than the previous reduced order model GPFSROCSSM, and an important step forward for the modelling of the type of system under study.

The elements that motivated the development of this model initially were to have a model representing both the continuous, fundamental and 2^{nd} order harmonic components. This objective was reached as well as the one to have a constant order state model (constant order for $m \geq 5$ and lower order for $m < 5$). The order of the state model is then $2m'$ compared to $2m$ for the model GPFOCSSM and $4+2$ for GPFSROCSSM. The higher the state-space model order, the more accurate but also more complex is the model. The GPFSROBHCCSSM is a scalable model that makes it possible to represent a MMC connected to an AC network having any number of phases while having a constant complexity.

Thanks to this control model several features are now available. Indeed, this model allows the development of generic current control algorithms: a single control law can be designed from this state-space model which will be suitable for any number of phases. The only modification required is to specify the right number of phases in the parameters of the control agorithm and the entire controller will update itself accordingly without having to undergo changes in the code. This paves the way for the development of scalable controls with nearly constant execution time for electrical polyphase systems. This ability given by the GPFSROBHCCSSM is used in Section 5.D where different control laws using this state-space model are tested.

The modelling objectives having been reached, the GPFSROBHCCSSM model obtained here concludes the whole control-oriented modelling approach of the converter under study. The strong feature, and to be emphasized, to which the whole process has led is the ability of the current state-space model in the Park 12 reference frame to be scalable to any number of phases while representing only the necessary harmonic content of the currents and being of constant size as the number of phases is increased. The model development approach will now give way to a study of the converter taking advantage of these models. This study has several aspects, including the evaluation of the accuracy of the different models for control purposes, or the analysis of the operating region of the converter in steady state.

3.G | Development of the power-energy model of the converter

3.G.1 | Foundations of the high-level power-energy model

From a system point of view, the MMC can be seen as a capacitor whose voltage level is linearly dependent on that of the DC bus. Moreover, if the user wishes to impose a power set-point to be delivered to the AC network, it is necessary that the system is able to control the amount of power to be drawn from the DC bus in order to guarantee the proper balancing of the capacitors as well as the achievement of the desired power level in the AC network. The energy modelling of the MMC is therefore a necessity in order to control these power exchanges.

The modelling is based on a study inspired by [Bou17] which presents an interesting way to manage power flows using the MIB control allocation.

3.G.2 | High-level power-energy state-space model

The power balance of the MMC in inverter operation can be represented by the following diagram:

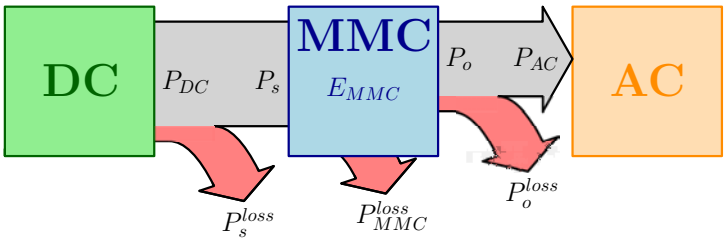

Figure 3.7: Diagram of the energy network involving the MMC whose powers are signed in inverter convention.

By a power balance, it is thus deduced that:

$$\begin{cases} \frac{dE_{MMC}}{dt} = P_{DC} - P_s^{loss} - P_{MMC}^{loss} - P_o^{loss} - P_{AC} = P_s - P_o - P_{MMC}^{loss} \\ P_s = P_{DC} - P_s^{loss} \\ P_o = P_{AC} + P_o^{loss} \end{cases} \tag{3.154}$$

with P_{DC} the power supplied by the DC bus, P_{AC} the power absorbed by the AC-side active network, P_s^{loss} the conduction losses on the DC link at the input of the MMC, P_o^{loss} the conduction losses in the AC network at the output of the MMC and P_{MMC}^{loss} the total losses of the MMC. These different powers are determined by:

$$\begin{cases} P_{DC} = v_p i_p + v_n i_n = \mathbf{V_x}^T \mathbf{I_x} \\ P_s^{loss} = R_s({i_p}^2 + {i_n}^2) = R_s \mathbf{I_x}^T \mathbf{I_x} \\ P_{AC} = \sum_{y=y_1}^{y_m} v_y i_y = \mathbf{V_y}^T \mathbf{I_y} \\ P_o^{loss} = R_o \sum_{y=y_1}^{y_m} {i_y}^2 = R_o \mathbf{I_y}^T \mathbf{I_y} \end{cases} \tag{3.155}$$

with:

$$\begin{cases} \mathbf{V_x} = [v_p \ \ v_n]^T \\ \mathbf{I_x} = [i_p \ \ i_n]^T \\ \mathbf{V_y} = [v_{y_1}, \ldots, v_{y_m}]^T \\ \mathbf{I_y} = [i_{y_1}, \ldots, i_{y_m}]^T \end{cases} \tag{3.156}$$

The DC bus voltages $\mathbf{V_x}$ are imposed externally, as are the AC voltages $\mathbf{V_y}$. The alternating current $\mathbf{I_y}$ is directly controlled by the current control stage. The only variable on which it is possible to act so as to guarantee the right amount of energy in the MMC thus remains the current drawn by the MMC from the DC bus. It is therefore this current $\mathbf{I_x}$ which will be the control variable to ensure the reference tracking of E_{MMC}.

The energy control stage will be of higher hierarchy than the current control stage, so the development of the control model from E_{MMC} will be done considering that the current control stage is fully operational. The operation that it is desired to achieve with the current control is first to guarantee the electrical balance of the AC network, and therefore a null i_m current. The control of the currents being considered effective within the framework of this development, i_m will thus be considered null. By Figure 3.3, it is deduced that by having a null common mode current, it follows that $i_p = -i_n$. It is then assumed that $I_{DC} = i_p$. According to (3.11) with i_m null, one finds: $i_p = mi_s$ and $I_{DC} = mi_s$. The model of the powers related to the bus DC thus becomes:

$$\begin{cases} P_{DC} = (v_p - v_n)mi_s \\ P_s^{loss} = 2R_s m^2 {i_s}^2 \end{cases} \tag{3.157}$$

Assuming that the system has enough sensors to measure the different electrical quantities that output P_{MMC}^{loss}, P_o^{loss} and P_{AC}, it is possible to express the dynamics of E_{MMC} in terms of I_{DC}. By denoting $P_{\bar{s}} = P_{MMC}^{loss} + P_o^{loss} + P_{AC} = P_{MMC}^{loss} + P_o$, it is obtained that:

$$\frac{dE_{MMC}}{dt} = P_{DC} - P_s^{loss} - P_{\bar{s}} = (v_p - v_n)mi_s - 2R_s m^2 {i_s}^2 - P_{\bar{s}} \tag{3.158}$$

In the state-space, by setting $X_{PE} = E_{MMC}$ and $\mathbf{U_{PE}} = i_s$ it comes thus:

$$\begin{cases} \dot{X}_{PE} = A_{PE}X_{PE} + B_{PE}\mathbf{U_{PE}} + B'_{PE}{\mathbf{U_{PE}}}^2 + \mathbf{E_{PE}} \\ \mathbf{Y_{PE}} = C_{PE}X_{PE} + D_{PE}\mathbf{U_{PE}} \end{cases} \tag{3.159}$$

Defined by:

$$\begin{aligned} &\mathbf{Y_{PE}} = X_{PE} = E_{MMC} \\ &A_{PE} = 0 \\ &B_{PE} = m(v_p - v_n) \\ &B'_{PE} = -2m^2 R_s \\ &\mathbf{E_{PE}} = -P_{\bar{s}} \\ &C_{PE} = 1 \\ &D_{PE} = 0 \\ &\mathbf{U_{PE}} = i_s \end{aligned} \tag{3.160}$$

In order to implement the control allocation of the energy, discretization of the state-space model is necessary. For a better accuracy, an exact discretization by exponential matrix model is performed. By stating T_c the sampling period with k denoting the current time instant so that $t = kT_c$ and $k+1$ denoting the next time instant $t + dt = (k+1)T_c$ at which it is desired to know the state vector, the beneficial use of Appendix A shows that:

$$\begin{cases} X_{PE}(k+1) = X_{PE}(k) + T_c B_{PE}\mathbf{U_{PE}}(k) + T_c B'_{PE}\mathbf{U_{PE}}(k)^2 + T_c\mathbf{E_{PE}}(k) \\ \mathbf{Y_{PE}}(k) = C_{PE}X_{PE}(k) + D_{PE}\mathbf{U_{PE}}(k) \end{cases} \tag{3.161}$$

Combining the two state-space model equations, knowing that D_{PE} is zero, yields:

$$\begin{aligned} &\mathbf{Y_{PE}}(k+1) \\ &\quad = C_{PE}X_{PE}(k) + T_c C_{PE}B_{PE}\mathbf{U_{PE}}(k) + T_c C_{PE}B'_{PE}\mathbf{U_{PE}}(k)^2 + T_c C_{PE}\mathbf{E_{PE}}(k) \end{aligned} \tag{3.162}$$

That is, isolating the terms depending on the order on the left:

$$\begin{aligned} T_c C_{PE}B_{PE}\mathbf{U_{PE}}(k) + T_c C_{PE}B'_{PE}\mathbf{U_{PE}}(k)^2 \\ = \mathbf{Y_{PE}}(k+1) - C_{PE}X_{PE}(k) - T_c C_{PE}\mathbf{E_{PE}}(k) \end{aligned} \tag{3.163}$$

Remark:

The model developed here shows that the current i_s will take values during the operation of the converter that will verify the nonlinear equation (3.158). In other words i_s will be a root of the polynomial $P_{PE}(i_s)$:

$$P_{PE}(i_s) = -2R_s m^2 {i_s}^2 + (v_p - v_n) m i_s - P_{\bar{s}} - \dot{E}_{MMC} \tag{3.164}$$

The determination of the roots of this polynomial, in the case where $P_{\bar{s}} + \dot{E}_{MMC} \geq 0$, can be represented by Figure 3.8. This solution leads to two roots which are represented by i_{s_1} and i_{s_2} on this figure. The first root i_{s_1} represents the power equilibrium where the current i_s is the lowest.

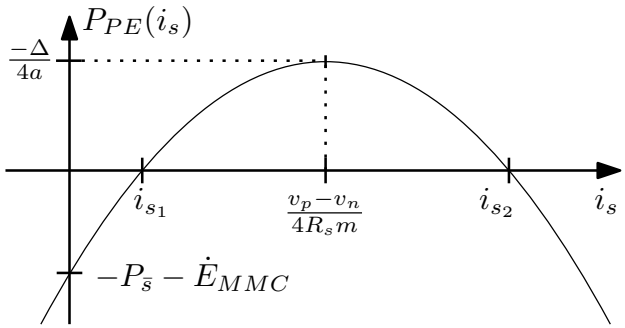

Figure 3.8: Representation of $P_{PE}(i_s)$ for $P_{\bar{s}} + \dot{E}_{MMC} \geq 0$. It is noted that $a = -2R_s m^2$, $b = (v_p - v_n)m$, $c = -P_{\bar{s}} - \dot{E}_{MMC}$ and $\Delta = b^2 - 4ac$.

In this case, the power P_{s1} absorbed by the MMC corresponds to the equilibrium necessary to maintain the energy balance within the converter while guaranteeing the power supply on the AC side. This is for low conduction losses on the DC link. The second root i_{s_2} represents the power balance where the current i_s is the most important. In this case, the power P_{DC2} supplied by the bus DC to the MMC is quite important, but the conduction losses in ${i_s}^2$ are so that the power absorbed by the MMC P_{s2} is identical to the case of the root i_{s_1}: $P_{s2} = P_{s1}$, guaranteeing also the equilibrium of the power balance. But this is obtained at the cost of significantly higher conduction losses on the link.

Contrary to the open-loop specification of the I_s control voltage $V_s = -V_{DC}/2$ in [Ber+18] where no DC bus impedance is considered, a control law at the power-energy level is therefore necessary here to steer the system towards an operation around the equilibrium point where the conduction losses on the DC link are the lowest.

3.G.3 Conclusions about the power-energy model

The power-energy model was designed to formulate the power balance of the MMC in order to control the energy contained in the converter by acting on the reference of the current to be drawn from the DC bus. This objective was effectively reached and this model made it possible to highlight the need for a control stage ensuring an operation minimizing the conduction losses in the bus.

This non-linear state-space model will be beneficial for the design of CA methods for the energy contained in the converter.

3.H | Accuracy assement of the models introduced

A power-energy model of the converter close to the one developed here has already been used in a control law. The evaluation of the accuracy of this model is therefore not considered as a priority here, considering that the model has already been evaluated. Regarding the low-level and high-level models proposed here, being new, none of them has been tested yet. An evaluation procedure for these two modelling levels has been set up. However, it is chosen here to present only one of them: the one for the current state-space models. This choice does not change the quality of the low level model which will be revealed indirectly during its use in the control laws developed afterwards.

The objective being to verify the accuracy of the proposed models for control purposes, the ideal approach is to test these models on the entire operating region of the converter. An analysis of the limits of this operating zone is therefore necessary at first. From the knowledge of these limits, it will be possible to evaluate the accuracy of the models on the operating region of the converter. This evaluation will use a commercial software dedicated to the simulation of electrical systems and circuits as the benchmark standard.

3.H.1 | Analysis of the operating zone limits of the MMC

High-level models in steady-state for the operating limits analysis

The GPFOCSSM model describes the dynamics of the different types of currents as a function of the voltages across the arms. It is also possible to use this model to evaluate the behavior of these same currents in steady state. As the arm voltages are the input variables of the current state-space model, from the knowledge of the arm voltage limits, it is possible to determine the current limits.

By doing this derivation, the current limits are obtained from those on the control voltages. The region of operation of the currents bounded by these limits can then be referred to as the control-limited zone of operation. Generally, the boundaries of the operating zone of the converter will be referred to as the LOZ.

In order to determine the values that can be reached by each of the four types of currents in this zone of operation, the analysis is based on (3.57). Defining $Z_i(t) = R_i^{eq} + L_i^{eq}\frac{d.}{dt}$ for the four types of currents $i \in \{m, s, c, o\}$, it then comes:

$$\begin{cases} Z_m(t)I_m = V_m + (N_\Sigma(2)\mathbf{V_x} - N_\Sigma(m)\mathbf{V_y} - N_\Sigma(1)V_{n_{AD}}) \\ Z_s(t)I_s = V_s + ([1\ \ 0] \cdot N_\Delta(2)\mathbf{V_x}) \\ Z_c(t)\mathbf{I_c} = \mathbf{V_c} \\ Z_o(t)\mathbf{I_o} = \mathbf{V_o} + (-N_\Delta(m)\mathbf{V_y}) \end{cases} \tag{3.165}$$

The analysis of the zone of operation from the MMC proposed here is done within the framework of a certain number of assumptions which make it possible to set up a first approach which can be extended thereafter.

Assumption 6. *The converter opertates in steady state. This means that all the capacitors are balanced at voltage:*

$$v_C^{nom} = \frac{V_{DC}}{N}$$

This also means that the voltages $\mathbf{V_{xy}}$ across the arm of the converter will all have the same minimum and maximum achievable amplitude at all times.

Assumption 7. *The power DC supply is in nominal operation, which is embodied by:*

$$v_p = -v_n = \frac{V_{DC}}{2}$$

Assumption 8. *The AC voltage system is in nominal operation, which means that:*

$$v_y = \hat{V}_{AC} \cdot \sin(\omega_o t - \varphi_y - \varphi_v) = \hat{V}_{AC} \cdot \cos(\omega_o t - \varphi_y - \varphi_v - \pi/2)$$

with φ_v defining the origin phase of these voltages.

Assumption 9. *The waveforms of the currents and voltages involved in the operation of the converter are made up solely of continuous and fundamental components.*

This last assumption here is the strongest because, as highlighted previously, the circulating current $\mathbf{I_c}$ also has - at least - second order harmonics. If the analysis of the LOZ does not take into account these harmonic components of second order here, it is to derive this operating zone analysis with a first simplified study, because taking into account several harmonic components makes the LOZ analysis much more complex. Indeed, this can involve strong nonlinearities which is not the case when a unique alternating component is considered in addition to the continuous component. However, it will be shown in the following work that the analyzed model does not lose its capability to represent these second order harmonics with a sufficient accuracy to allow the design of current control laws.

The detailed derivations of the operation zone are given in Appendix I. However, from Assumption 9 the arm voltages are defined to have both a continuous and fundamental component:

$$\forall y \in \{y_1, \ldots, y_m\}, \begin{cases} v_{py} = \frac{V_{DC}}{2}\left[m_p - d_p \cdot \cos(\omega_o t - \varphi_y)\right] = m_{py} \cdot V_{DC} \\ v_{ny} = -\frac{V_{DC}}{2}\left[m_n + d_n \cdot \cos(\omega_o t - \varphi_y)\right] = m_{ny} \cdot V_{DC} \end{cases} \tag{3.166}$$

Figure 3.9 represents those arm voltage signals.

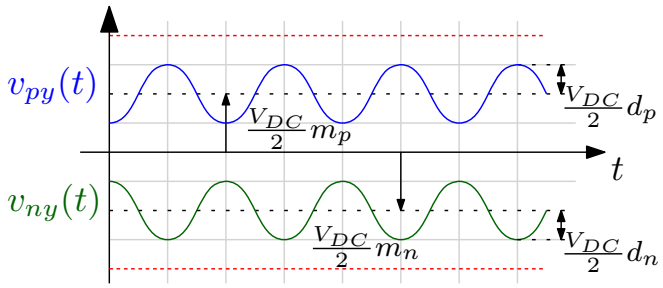

Figure 3.9: Illustrative waveforms for v_{py} and v_{ny}.

According to the choice of submodule type, the maximum and minimum reachable values of the arm voltages change. Those limitations can be expressed by the following equation where $q = 1$ for half-bridge submodules and $q = 2$ for full-bridge submodules:

$$\begin{cases} \forall y \in \{y_1, \ldots, y_m\}, (1-q)V_{DC} \leq v_{py} \leq V_{DC} \\ \forall y \in \{y_1, \ldots, y_m\}, -V_{DC} \leq v_{ny} \leq (q-1)V_{DC} \end{cases} \tag{3.167}$$

It is possible to visualize those constraints in the following way in terms of continuous and fundamental components limitations in Figure 3.10. Those limitations can than be translated into the limits of the control voltage of each type of current as shown on Figure 3.11

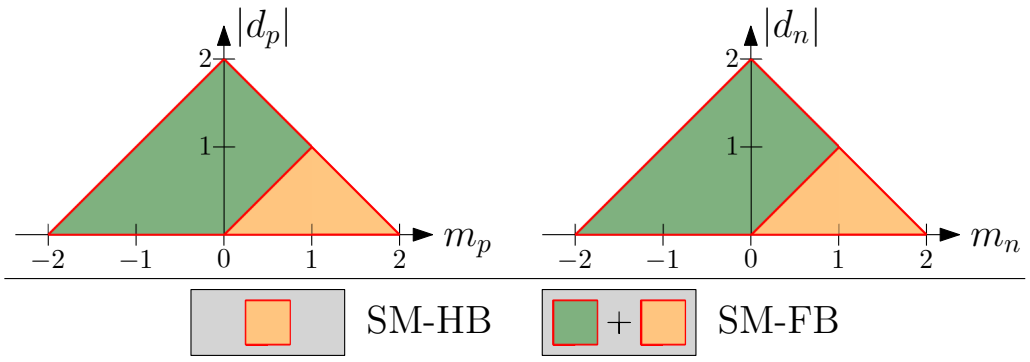

Figure 3.10: Control-limited operating zone in the maps $(m_p, |d_p|)$ and $(m_n, |d_n|)$

Using the model of the currents (3.165), it is then possible to determine the maximum current magnitudes when control voltages reach their limits:

$$\begin{cases} \hat{I}_m^{max} = \frac{1}{Z_m}\left(\frac{q}{2}V_{DC} - V_{n_{AD}}\right) \\ \hat{I}_s^{max} = \frac{1}{Z_s}\left(q - \frac{1}{2}\right)V_{DC} \\ \hat{I}_c^{max} = \frac{1}{Z_c}\frac{q}{2}V_{DC} \\ \hat{I}_o^{max} = \frac{1}{Z_o}\left|\frac{q}{2}V_{DC} - \hat{V}_{AC}\cdot e^{-j\varphi_v}\right| \end{cases} \quad \begin{cases} \hat{I}_m^{min} = \frac{1}{Z_m}\left(-\frac{q}{2}V_{DC} - V_{n_{AD}}\right) \\ \hat{I}_s^{min} = -\frac{1}{Z_s}\frac{1}{2}V_{DC} \\ \hat{I}_c^{min} = -\frac{1}{Z_c}\frac{q}{2}V_{DC} \\ \hat{I}_o^{min} = \frac{1}{Z_o}\left|-\frac{q}{2}V_{DC} + \hat{V}_{AC}\cdot e^{-j\varphi_v}\right| \end{cases} \tag{3.168}$$

Remark: It is important to note that these expressions represent the maximum magnitudes of the four types of currents in the case where the voltages driving them to reach their own limits. These are current limits obtained from the control point of view and not from the physical point of view. Indeed, additional physical limits, such as the current allowed by the semiconductors or a power limit imposed by the DC bus power, may shrink the operating zone described by Figure 20 and equation (3.168).

Applying those formulas to the MMC experimental setup from the LAPLACE and taking into account the physical limitations, the following table specifying the maximum amplitude of each current is deduced[1]:

Control-limited current boundaries with physical limitations		
Current	Lower boundary	Upper boundary
$\hat{I}_m$	$\hat{I}_m^{min} = -3.743$ A	$\hat{I}_m^{max} = +3.743$ A
$\hat{I}_s$	$\hat{I}_s^{min} = -5.57$ A	$\hat{I}_s^{max} = +5.57$ A
$\hat{I}_c$	$\hat{I}_c^{min} = -14$ A	$\hat{I}_c^{max} = +14$ A
$\hat{I}_o$	$\hat{I}_o^{min} = -3.749$ A	$\hat{I}_o^{max} = +3.749$ A

Table 3.7: Table of current boundaries by projection into the space of feasible powers, voltages and currents

3.H.2 | Accuracy assement of the high-level models

The operation limits of the converter being determined, it will now be possible to carry out simulations - on the whole operating zone of the MMC - in order to fully check the accuracy of the developed models. To do this, a verification procedure is set up.

[1] Table 19 holds the parameters from the MMC hardware setup considered.

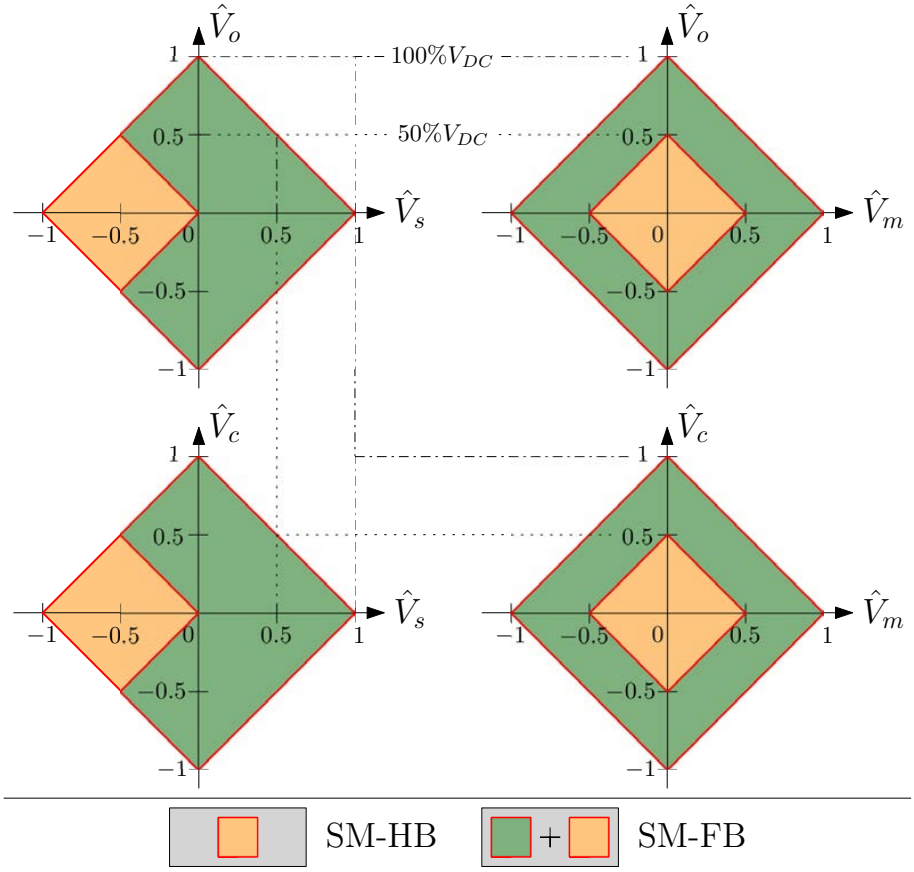

Figure 3.11: Control-limited operating zone in the maps $(\hat{V}_o, \hat{V}_s)$, $(\hat{V}_o, \hat{V}_m)$, $(\hat{V}_c, \hat{V}_s)$ and $(\hat{V}_c, \hat{V}_m)$

3.H.2.1 Accuracy verification procedure of the high-level models

To ensure that the developed models correctly represent the behavior of the MMC currents, an accuracy verification procedure is set-up using Matlab®. The state-space model is coded in Simulink® using a *Matlab-Function* able to adapt itself depending on the number of MMC legs and neutral points connection, as shown in Figure 3.12. In parallel, the electrical diagram of Figure 3.2 is also simulated with the PLECS®-Blockset in Simulink®for $m \in \{3, 10, 14, 21\}$, the 7-phase case is shown in Figure 3.13.

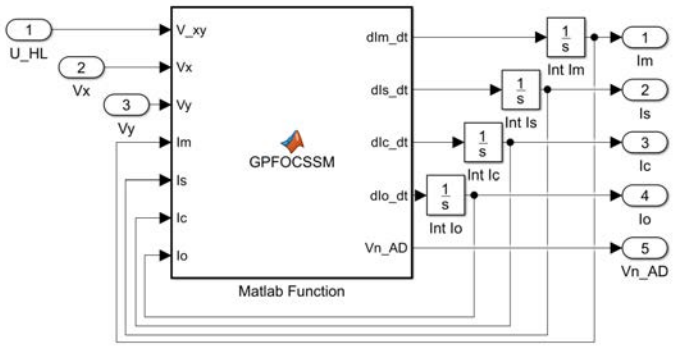

Figure 3.12: State-space model *Matlab-Function* used in Simulink®.

The model as well as the electrical circuit are simulated jointly, both are fed with the same input voltage signals. At the end of the simulation, the difference between the currents computed by

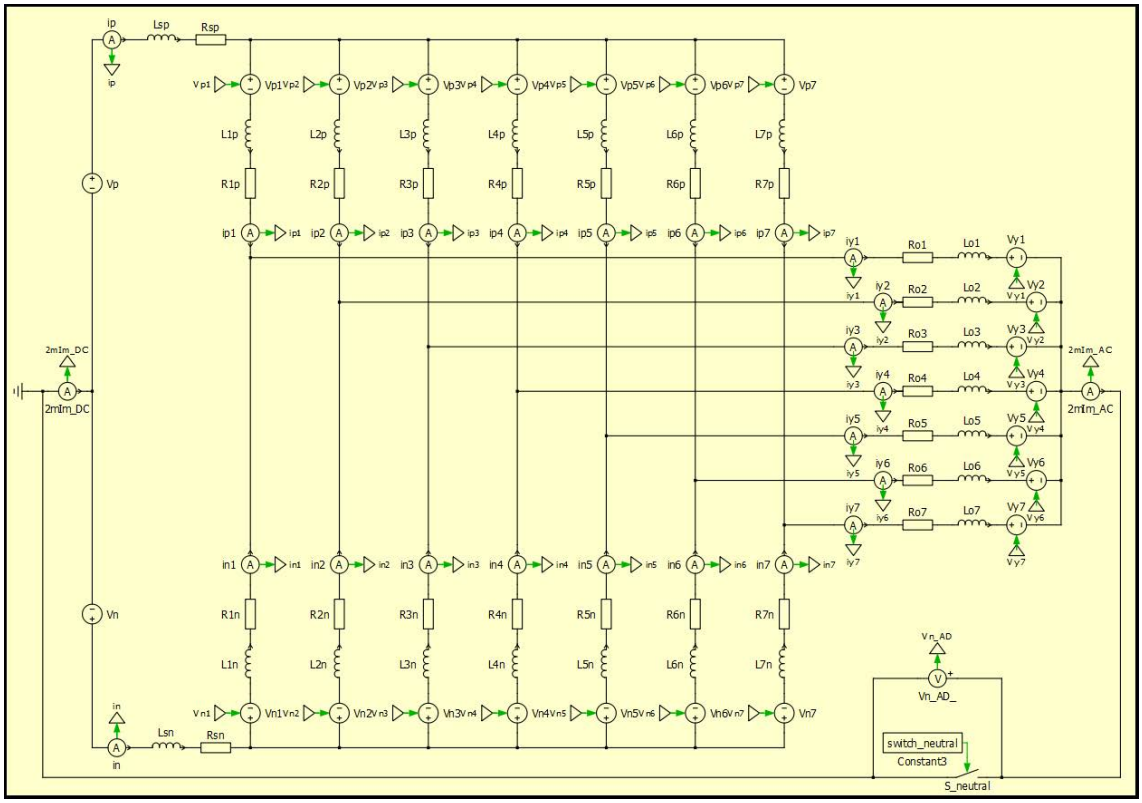

Figure 3.13: Electrical circuit drawn in PLECS® Blockset - here for $m = 7$. The same is done for $m \in \{3, 10, 14, 21\}$.

PLECS® and computed by the model is evaluated as shown on Figure 3.14. In the accuracy tests to follow, the plots will highlight the difference between the two sets of electrical signals, and more specifically ϵ_{I_m}, ϵ_{I_s}, $\epsilon_{\mathbf{I_c}}$ and $\epsilon_{\mathbf{I_o}}$.

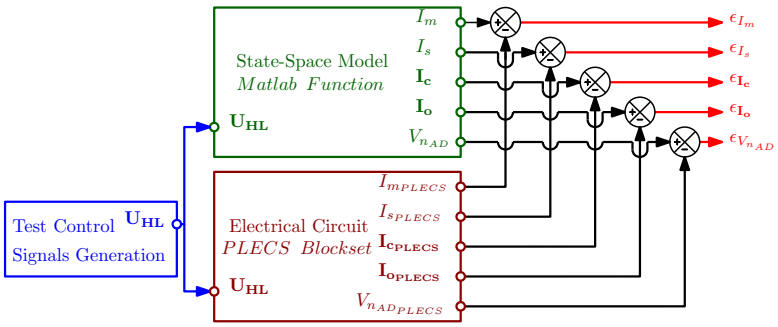

Figure 3.14: Validation principle of the state-space model in Simulink®

To verify the model, the most general operation simulation is considered. This operating behavior is characterized by an active AC grid, the AC and DC neutrals connected and non-zero control signals. The three requirements are respectively implemented in the m-phase case with:

- $\forall y \in \{y_1, \ldots, y_m\}, v_y = \hat{V}_{AC} \sin(\omega_o t - \varphi_y - \varphi_v)$. It is recalled that $\varphi_{y_j} = 2\pi(j-1)/m$ and that φ_v is the phase of the AC grid voltage.
- An electrical link in the PLECS® diagram between the AC and DC neutrals to connect them[1].

[1] Connecting neutrals implies that $v_{n_{AC}} = v_{n_{DC}}$, thus $V_{n_{AD}} = 0$ for the model and the circuit simulator, so that $\epsilon_{V_{n_{AD}}} = 0$. This null difference is not shown in the upcoming curves, so that 4 out of 5 difference curves are presented.

And using (3.32) rather than (3.35) for the GPFOCSSM.

- $\forall x \in \{p, n\}, \forall y \in \{y_1, \ldots, y_m\}, v_{x,y} \neq 0$.

The question then arises as the choice of non-zero input voltage signals $v_{x,y}$. The goal for those voltage signals is to enable the test of the models on various operating points ensuring that all currents can - at some point - be non-zero. In other words, the control signals have to influence the waveforms of all four current types. It turns out that the previous definition of the arm voltage signals (3.166) already enable this feature[1][2]:

$$\forall y \in \{y_1, \ldots, y_m\}, \begin{cases} v_{py} = \frac{V_{DC}}{2}\left[m_p - d_p \cos(\omega_o t - \varphi_y)\right] \\ v_{ny} = -\frac{V_{DC}}{2}\left[m_n + d_n \cos(\omega_o t - \varphi_y)\right] \end{cases} \tag{3.170}$$

where the parameters m_p, d_p, m_n and d_n have to be carefully chosen in order for v_{py} and v_{ny} to remain within their boundaries. In [LFB21b], those parameters took the values 1, M, $1/2$ and $M/2$, respectively, enabling a preliminary accuracy assessment on particular operating points. To improve the accuracy assessment, an objective is to simulate the model on a set of points covering the entire operating space.

The analysis of the operating zone performed in Section 3.H.1 determined the limits that the parameters m_p, d_p, m_n, and d_n can reach. These limits are represented in Figure 3.10. This figure shows the entire zone of operation that can be explored to verify the accuracy of the models. A set of operating points is chosen to cover the operating zone from the control point of view, as shown on Figure 3.15[3]. Simulations are performed for 5 different number of phases: 3, 7, 10, 14 and 21 phases.

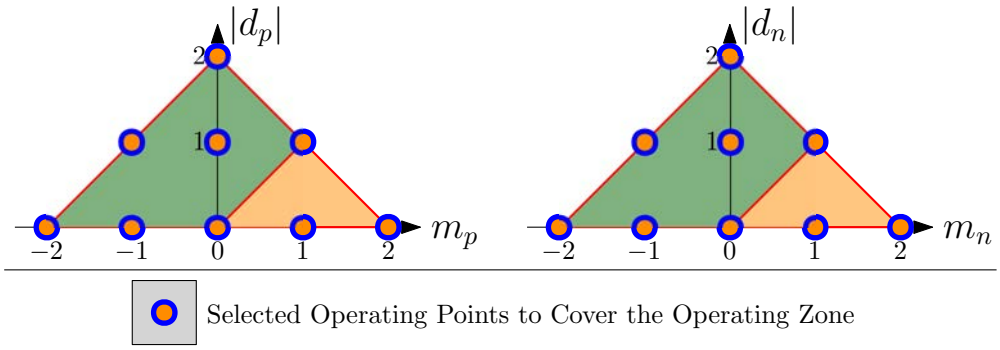

Figure 3.15: Selected operating points in the in the $(m_p, |d_p|)$ and $(m_n, |d_n|)$ spaces for simulations covering the entire operating region.

Having 9 operating points covering the entire zone chosen in the $(m_p, |d_p|)$ space and 9 others chosen in the $(m_n, |d_n|)$ space give a total of 81 possible combinations. Thus, 81 simulations are done for each number of phases in the selected list of phase numbers, which makes a total of 405 simulations for each high-level model. Each simulation will output the waveforms of each current and will, for each type of current, compute the maximum difference between the selected high-level model and PLECS® over the entire simulation time. Once those 405 simulations are

[1] It is mentionned that (3.170) will not always define the arm voltage signals since in the test case from Section 3.H.2.4 it will also take into account a 2^{nd} order harmonic component.

[2] For example, in the 3-phase case, the arm voltages are:

$$\forall j \in \{1, 2, 3\}, \begin{cases} v_{py_j} = \frac{V_{DC}}{2}\left[m_p - d_p \cdot \cos\left(\omega_o t - \frac{2\pi}{3}(j-1)\right)\right] \\ v_{ny_j} = -\frac{V_{DC}}{2}\left[m_n + d_n \cdot \cos\left(\omega_o t - \frac{2\pi}{3}(j-1)\right)\right] \end{cases} \tag{3.169}$$

[3] Not only the operating region is covered but also the time domains: simulations are carried out in transient as well as in steady-state.

Meaning	Symbol	Value
MMC Hardware Parameters		
DC bus		
DC Bus voltage	V_{DC}	600 V
Half-bus voltage	$v_p = -v_n$	$V_{DC}/2 = 300$ V
DC Bus impedance	R_s, L_s	50 mΩ, 2 mH
MMC		
Rated power	$S_o{}^{nom}$	10 kVA
Submodules type	q	1 (half-bridge submodule)
Switching frequency and period	f_s, T_s	4 kHz, 250 µs
Arm resistance and inductance	R, L	10 mΩ, 5 mH
AC network		
Number of phases	m	7
AC active voltage amplitude	$\hat{V}_{AC}$	150 V
AC active voltage phase	φ_v	0 rad
AC grid frequency and period	f_o, T_o	50 Hz, 20 ms
AC grid frequency	ω_o	$2\pi f_o \simeq 314$ rad/s
AC load resistance and inductance	R_o, L_o	40 Ω, 5 mH
Simulation Hardware Parameters		
Computation Hardware Parameters		
CPU Type	–	Intel Xeon
CPU Clock	–	3.00 GHz
CPU Cache / RAM	–	11.6 Gb / 64 Gb
Simulation Parameters		
Simulation time step	T_{step}	$T_s/25 = 10$ µs
Simulation end time	t_{end}	$14 \cdot T_o = 280$ ms

Table 3.8: Open-Loop Simulation & MMC Parameters

completed, the maximum difference is extracted for each type of current. Finally, it is possible to compute the maximum difference between the high-level models and PLECS® over the entire operating zone for each type of current.

The first simulations presented aim to visualize the waveforms of the different currents for particular operating points. Once the behavior of the different currents has been observed, it is possible to move on to the series of 405 simulations which are summarized with thanks to several figures focusing on the presentation of the maximum deviations between the models and PLECS® and not the whole temporal waveforms of the currents.

3.H.2.2 Evaluation of the high-level models' accuracy on a particular set of operating points

Simulations were carried out for several operating cases and, in particular, for several values of the number of m of phases. To highlight the interest of the model developed here, the curves obtained for the case where $m = 7$ are shown. The parameters of the MMC correspond to those displayed in Table 3.8.

The control signals defined in (3.170) were applied in simulation for seven phases with $m_p = 1$, $d_p = 1$, $m_n = 1/2$ and $d_n = 0.97$, resulting in the curves of Figure 3.16 for GPFOCSSM and

GPFSROCSSM, and Figure 3.17 for GPFSROCSSM and GPFSROBHCCSSM. In order to trigger transient conditions, the v_{xy} signals take 50% of the value given by (3.170) over the first half of the simulation before a sudden change is applied in the middle of the simulation to make them reach 100% of the expected value. This simulation scenario is run for all three models. In order to compare the models, all currents are plotted in the natural basis. For the models developed in the PARK reference frame, an inverse transformation is applied to have the current waveforms in each phase.

Remark: Note that important circulating currents may appear. This is due to the unusual forms of v_{py} and v_{ny} using different modulation indices. The reader is reminded that this behavior is intended in order to test the accuracy of the model with non-zero circulating currents.

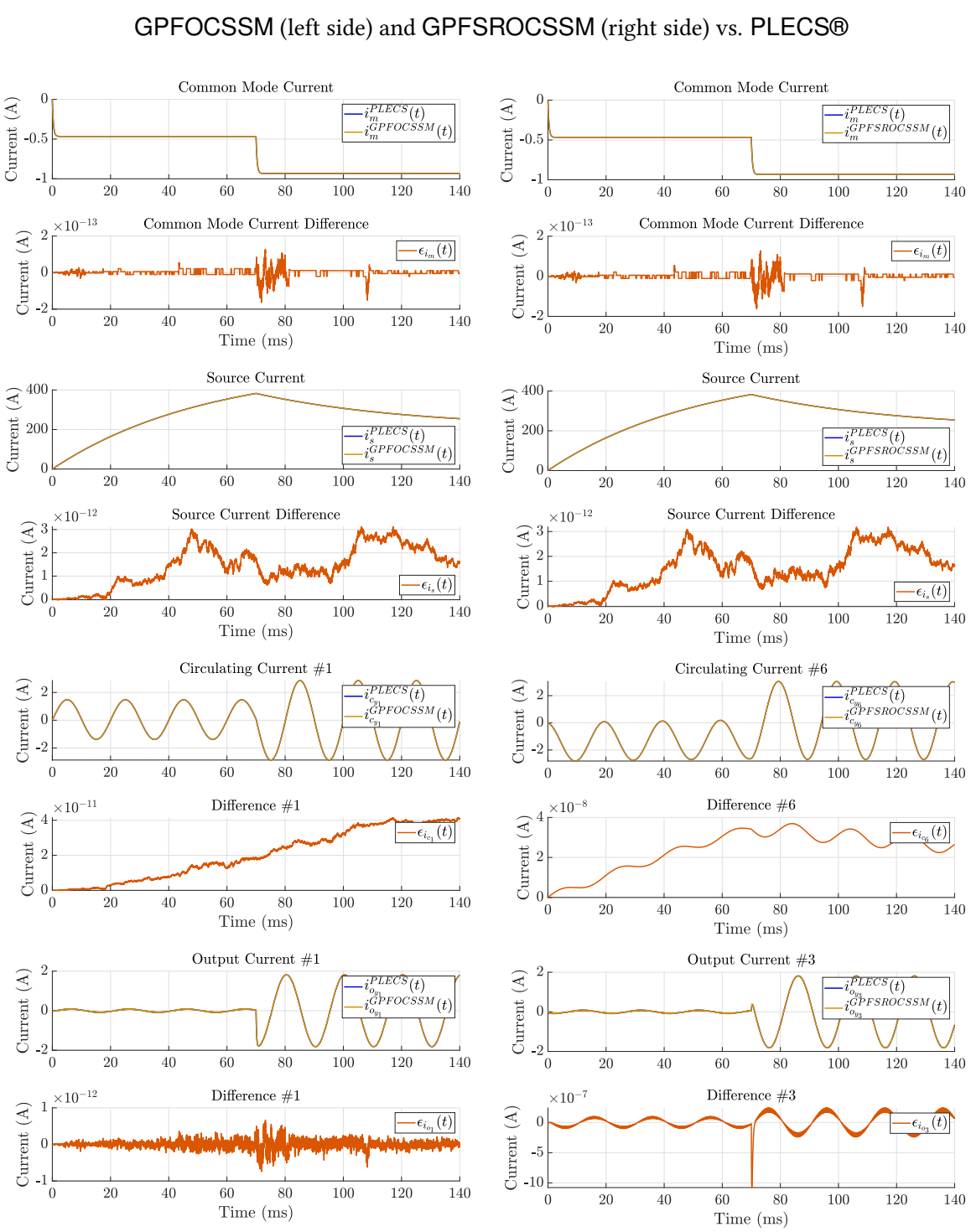

Figure 3.16: Behavior of the currents according to the high-level models GPFOCSSM and GPFSROCSSM in comparison with PLECS® for a set of operating points - Case $m = 7$. For each graph, top plot: currents from one of the model and PLECS®, bottom plot: the difference between the two.

To clarify the reading not all seven circulating currents and output currents are presented, only those having the largest difference are shown.

For each type of current, the bottom plot shows the difference between the current from the state-space model and the same current from PLECS®. Figure 3.16 shows the different current waveforms in steady-state as well as in transient conditions for the GPFOCSSM and the

GPFSROCSSM. The figure highlights that the maximum difference between GPFOCSSM and PLECS® is on the circulating current $\mathbf{I_c}$. The deviation is of the order of $7.43 \cdot 10^{-12}$A which is very low compared to the magnitude of the current signals. For the case of the GPFSROCSSM, the maximum deviation with PLECS® is reached by the output current $\mathbf{I_o}$ and is about $-10.2 \cdot 10^{-7}$A which is also very little compared to the waveforms amplitude. Note that for both models, transient conditions triggered at $t = 70$ ms have very little effect on the model accuracy.

This result validates both state-space models in steady-state as well as in transient for the operating points reached during the displayed simulation.

It is worth comparing the current waveforms of GPFOCSSM with that of GPFSROCSSM. The first point to mention is that for both currents having a single component (I_m and I_s) the behavior of both models are identical. But GPFOCSSM is more accurate than GPFSROCSSM for the currents having atlernating components ($\mathbf{I_c}$ and $\mathbf{I_o}$). This difference is explained by the fact that the PARK transform used to derive the GPFSROCSSM filters a part of the AC spectrum of the signals that the GPFOCSSM does not filter.

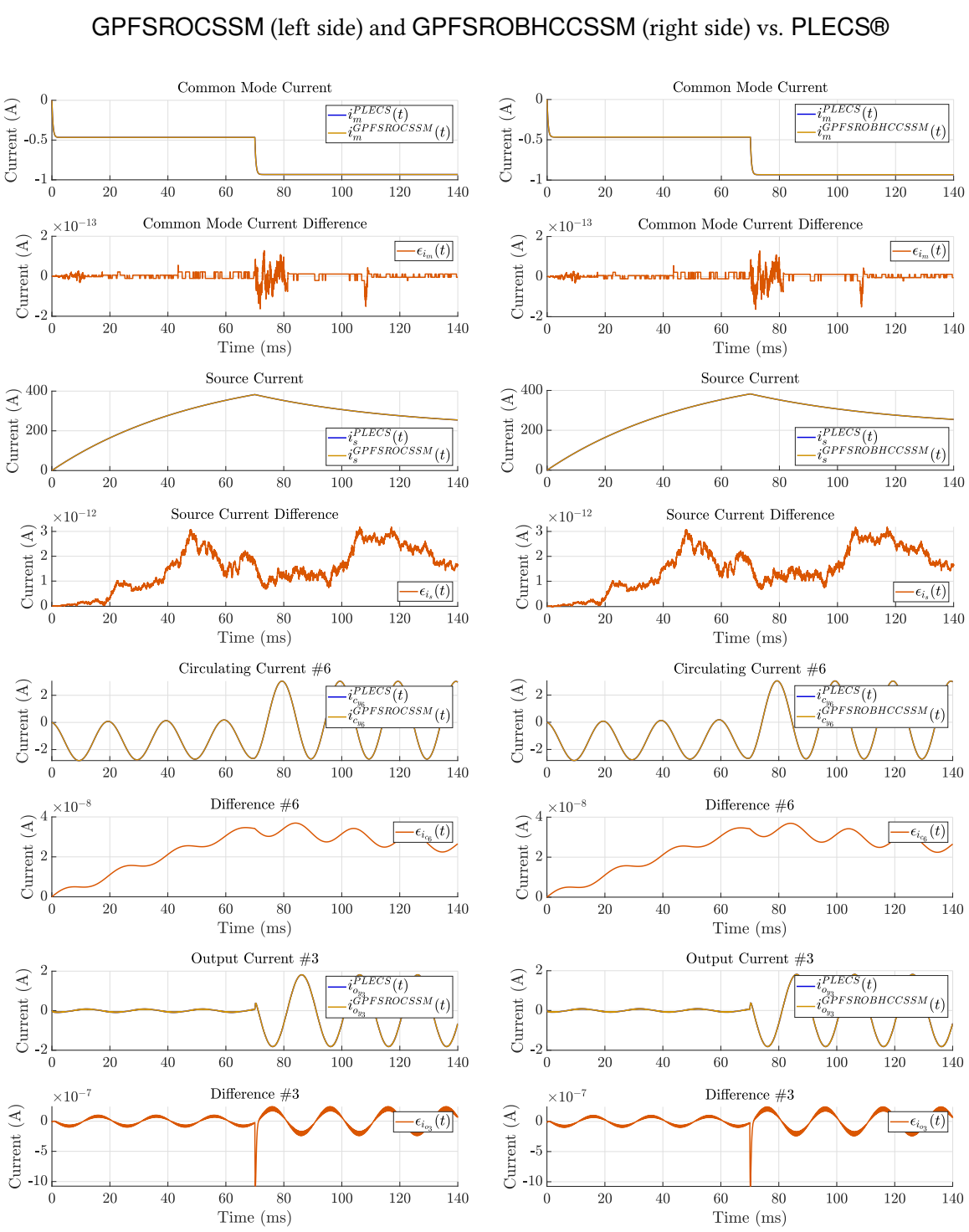

Figure 3.17: Behavior of the currents according to the high-level models GPFSROCSSM and GPFSROBHCCSSM in comparison with PLECS® for a set of operating points - Case $m = 7$. For each graph, top plot: currents from one of the model and PLECS®, bottom plot: the difference between the two.

Figure 3.17 shows the different current waveforms in steady-state as well as in transient conditions for the GPFSROCSSM[1] and the GPFSROBHCCSSM. The waveforms depicted on the figure show that the maximum difference between GPFSROBHCCSSM and PLECS® is on

[1]The results displayed for the GPFSROCSSM are the same figures as in Figure 3.16, they are plotted here again for comparison purposes with GPFSROBHCCSSM.

the output current $\mathbf{I_o}$. The deviation is of the order of $-10.2 \cdot 10^{-7}$A which is very low compared to the magnitude of the current signals. Note that for GPFSROBHCCSSM, transient conditions triggered at $t = 70$ ms have, here also, little effect on the model accuracy.

This result validates the state-space model in steady-state as well as in transient for the operating points reached during the simulation.

When comparing the current waveforms of GPFSROCSSM with those of GPFSROBHCCSSM, it is noticed that, for all types of currents, both models seem to feature the exact same accuracy. This is explained by the fact that both models are derived thanks to a PARK transform that filters the signals. But the PARK transform used to derive GPFSROCSSM is not the same than for GPFSROBHCCSSM, thus differences between the current waveforms should be observed[1]. This is true and this would be the case if 2^{nd} order harmonic components were part of the v_{xy} signals, but only continuous components and fundamental ones are included in v_{xy} for this simulation, thus both PARK transforms have the same filtering effect on the electrical waveforms. This explains the fact that current signals of GPFSROBHCCSSM are similar to those from GPFSROCSSM here.

The results shown in Section 3.H.2.2 are obtained using a particular set of operating points. In order to validate the proposed state-space models in a more comprehensive manner, it is necessary to simulate the model for a set of operating points that covers the entire operating zone as shown in Figure 3.10. This objective will be now adressed.

3.H.2.3 Evaluation of the high-level models' accuracy over the entire operating region

Accordingly with the testing procedure described in Section 3.H.2.1, a set of 81 simulations covering the entire operating zone of the converter is run for each high-level model and for each polyphase system in the set $m \in \{3, 7, 10, 14, 21\}$. After each set of simulations covering the operating zone the maximum difference between PLECS® and the models is saved for each current type. Thus, the maximum difference is diplayed in Figure 3.18.

[1] It is recalled that PARK 12 transform represents the continuous, fundamental and 2^{nd} order harmonic components of the signals in the synchronous rotating frame whereas the simple PARK transform first introduced only conveys the continuous and fundamental components.

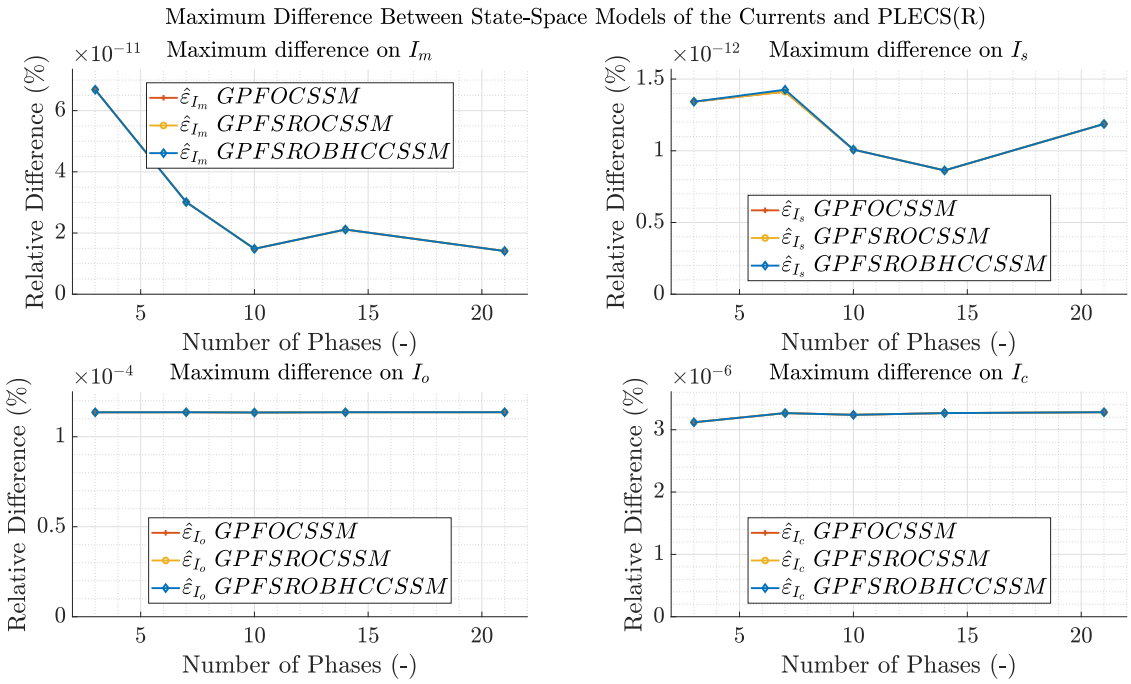

Figure 3.18: Evolution of the maximum deviation for each current and each model with respect to PLECS® over a total of $3 \times 5 \times 81 = 1215$ simulations.

The maximum difference between the models and the simulation software over the set of polyphase systems is then easily deduced and summarized in Table 3.9.

Summary of the simulation results (Continuous and fundamental components)				
Model	Maximum relative difference $\hat{\epsilon}_{\%}$ and its type			
	I_m	I_s	$\mathbf{I_c}$	$\mathbf{I_o}$
GPFOCSSM	$6.68 \cdot 10^{-11}$ %	$1.41 \cdot 10^{-12}$ %	$3.28 \cdot 10^{-6}$ %	$1.14 \cdot 10^{-4}$ %
GPFSROCSSM	$6.68 \cdot 10^{-11}$ %	$1.41 \cdot 10^{-12}$ %	$3.28 \cdot 10^{-6}$ %	$1.14 \cdot 10^{-4}$ %
GPFSROBHCCSSM	$6.68 \cdot 10^{-11}$ %	$1.43 \cdot 10^{-12}$ %	$3.28 \cdot 10^{-6}$ %	$1.14 \cdot 10^{-4}$ %

Table 3.9: Summary table of the maximum deviations of the models after open-loop simulations over the entire operating zone.

Each plot shows the relative difference between PLECS® and the three state-space models versus the number of phases.

The important information to note here is that among all current types, the maximum deviation of the models with PLECS® is about $1.14 \cdot 10^{-4}\%$. This is reached for the output current $\mathbf{I_o}$. This difference is also the maximum deviation of the models over the entire operating zone of the converter, meaning that any deviation of any of the models at any operating point will be lower than $1.14 \cdot 10^{-4}\%$ which is a very small upper boundary of the deviation. Further, the evolution of the difference versus the number of phases shows that maximum difference stays very small even for higher number of phases.

It is worth pointing out the fact that all three models have nearly the same maximum deviation to PLECS® for any current type and any number of phases. This means that at some point on the operating zone each one of the currents reach the same maximum deviation.

The results displayed here allow us not only to validate all three models on the entire operating zone of the MMC for any number of phases, but also to use those three state-space models in order to design the current control system aiming at ensuring the reference tracking of the currents for any number of phases and for references waveforms with continuous components and fundamental alternating ones.

Since those simulations only include continuous components and fundamental ones in the waveforms, simulations with 2^{nd} order harmonic components are needed to validate the models since the circulating current $\mathbf{I_c}$ feature 2^{nd} order harmonic components that have to be described by the models. Simulations including a second harmonic component will now be presented.

3.H.2.4 Evaluation of the high-level models to represent a second order harmonic component

In order to evaluate the ability of the different models to accurately represent the harmonic content of the currents and, more specifically, to determine how strong Assumption 9 is, tests are performed in simulation following the procedure previously described in Section 3.H.2.1. The arm voltage signals are then defined by equation (3.172) in order to embed a second order harmonic content[1]:

$$\forall y \in \{y_1, \dots, y_m\}, \begin{cases} v_{py} = \frac{V_{DC}}{2}\left(m_p - d_p \cdot \cos(\omega_o t - \varphi_y) - {d_p}' \cdot \cos(2\omega_o t - 2\varphi_y)\right) \\ v_{ny} = -\frac{V_{DC}}{2}\left(m_n + d_n \cdot \cos(\omega_o t - \varphi_y) + {d_n}' \cdot \cos(2\omega_o t - 2\varphi_y)\right) \end{cases} \tag{3.172}$$

The terms $\cos(2\omega_o t - 2\varphi_y)$ will be responsible for the emergence of the second order harmonic for the circulating currents and the AC output currents, the other types of currents will not be influenced by the appearance of this harmonic in the control signals. For this reason, the upcoming curves will neither show the common mode current nor the DC source current which are constant in steady state.

The analysis, offered in Section 3.E.2.1, of the harmonic content represented in the Park reference frame as a function of the number of phases indicates that for $m = 3$ the Park transform 3.D.1, used to derive GPFSROCSSM, embeds the whole harmonic content. Thus, for $m = 3$, the three high-level models will provide very good accuracy for the whole harmonic content defined by (3.172). However, the same analysis indicates that for a larger number of phases, the harmonic content embedded by the different Park transforms used will not be the same. The goal being to compare these models, and thus to highlight their differences, the simulations are made for a larger number of phases. It is chosen to consider a number of phases $m = 7$. Within the framework of the simulations carried out here, the parameters of the MMC are voluntarily chosen to be more general than those of the MMC available at LAPLACE in order to test the model in more operating cases, these parameters are displayed in Table 3.8.

Several simulations of the three models are then performed. Having chosen $m = 7$, the vectors $\mathbf{I_c}$ and $\mathbf{I_o}$ both include 7 components. To ease the reading of the results, only one of these components is presented here for each model and each current. The component shown is then the one which, among all the components of the considered current, presents the largest deviation

[1] For example, in the 3-phase case, the arm voltages are:

$$\forall j \in \{1, \dots, 3\}, \begin{cases} v_{py_j} = \frac{V_{DC}}{2}\left[m_p - d_p \cdot \cos\left(\omega_o t - \frac{2\pi}{3}(j-1)\right) - {d_p}' \cdot \cos\left(2\omega_o t - \frac{4\pi}{3}(j-1)\right)\right] \\ v_{ny_j} = -\frac{V_{DC}}{2}\left[m_n + d_n \cdot \cos\left(\omega_o t - \frac{2\pi}{3}(j-1)\right) + {d_n}' \cdot \cos\left(2\omega_o t - \frac{4\pi}{3}(j-1)\right)\right] \end{cases} \tag{3.171}$$

with PLECS®. Figure 3.19 shows these results for one of the simulations performed.

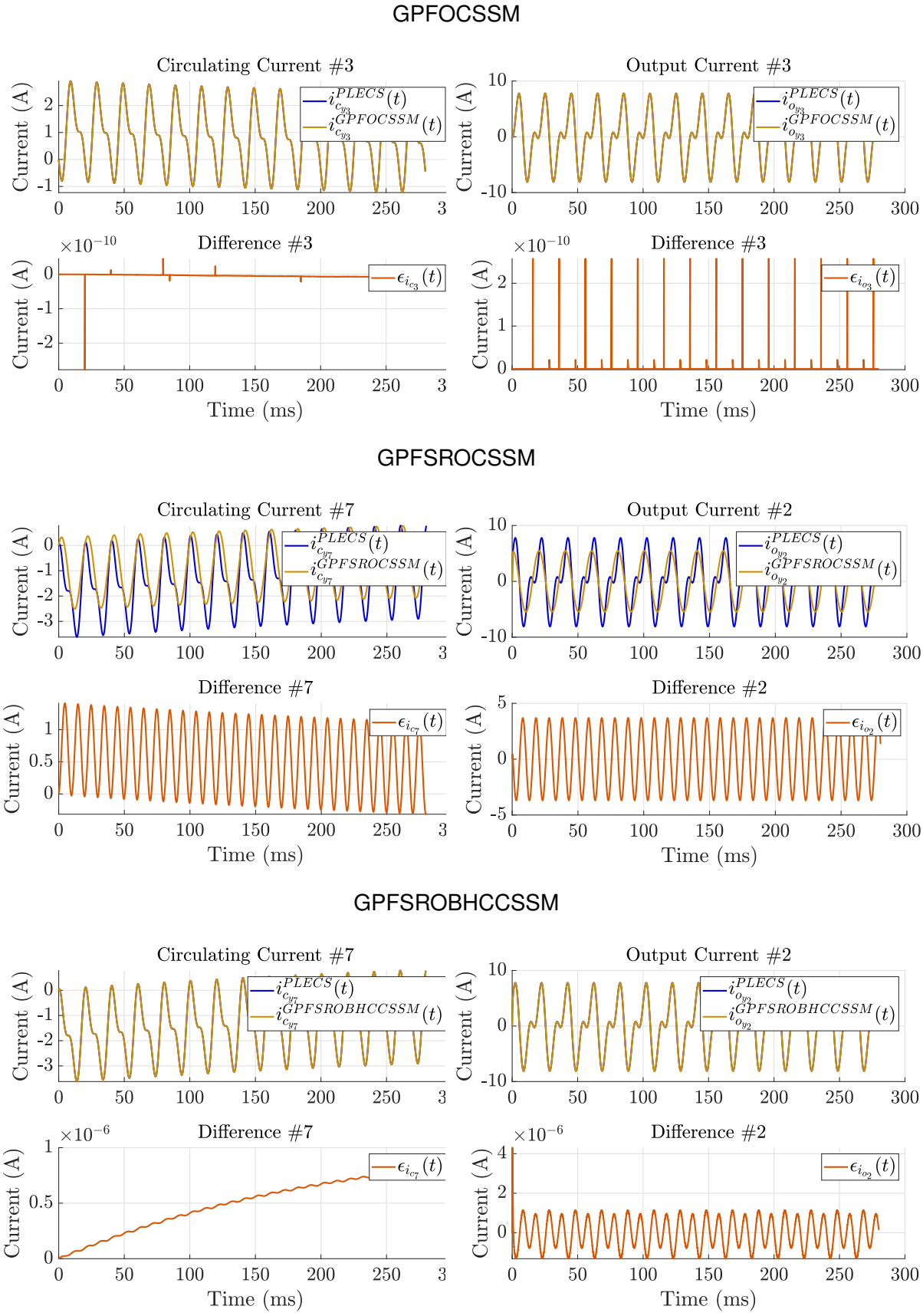

Figure 3.19: Behavior of the currents from the three high-level models GPFOCSSM, GPFSROCSSM and GPFSROBHCCSSM in comparison with PLECS® for a 2^{nd} order harmonic injection - **7-phase** case. For each graph, top plot: currents from one of the model and PLECS®, bottom plot: the difference between the two.

The deviations between each of the models and PLECS® are evaluated for the circulating and AC output currents. The largest error values are summarized in Table 3.10.

Summary of the simulation results (Fondamental component + 2^{nd} harmonic)	
Model	Maximum relative difference $\hat{\epsilon}_{\%}$ and its type
GPFOCSSM	$2.4 \cdot 10^{-8}$ % sur $\mathbf{I_c}$
GPFSROCSSM	48 % sur $\mathbf{I_o}$
GPFSROBHCCSSM	$5.5 \cdot 10^{-5}$ % sur $\mathbf{I_o}$

Table 3.10: Summary table of open loop simulation results for #2 harmonic injection

Without precise measurement of the difference between GPFSROCSSM and PLECS®, the simple view of the curves representing the currents in Figure 3.19 shows that this model does not represent the second order harmonics of the currents with sufficient accuracy, unlike the GPFOCSSM and GPFSROBHCCSSM models, whose error with respect to PLECS® is much less than 10^{-3}%. This highlights the fact that Assumption 9 is very strong. The precise measurement of the difference, which is then maximum for $\mathbf{I_o}$, shows a deviation of about half the amplitude of the latter (48 %). This confirms the lack of precision of GPFSROCSSM.

Looking specifically at the circulating current #7 plot for the GPFSROBHCCSSM model, it is reasonable to wonder if the difference between PLECS® and the model is bounded. A long simulation on this same operating point confirms that the model converges and that this difference stabilizes. To verify that this property does not depend on the operating point, a long simulation of 5600 ms on another operating point has been performed to verify this specific point. The result is presented in Figure 3.20. It shows that this difference converges and stabilizes also for other operating points.

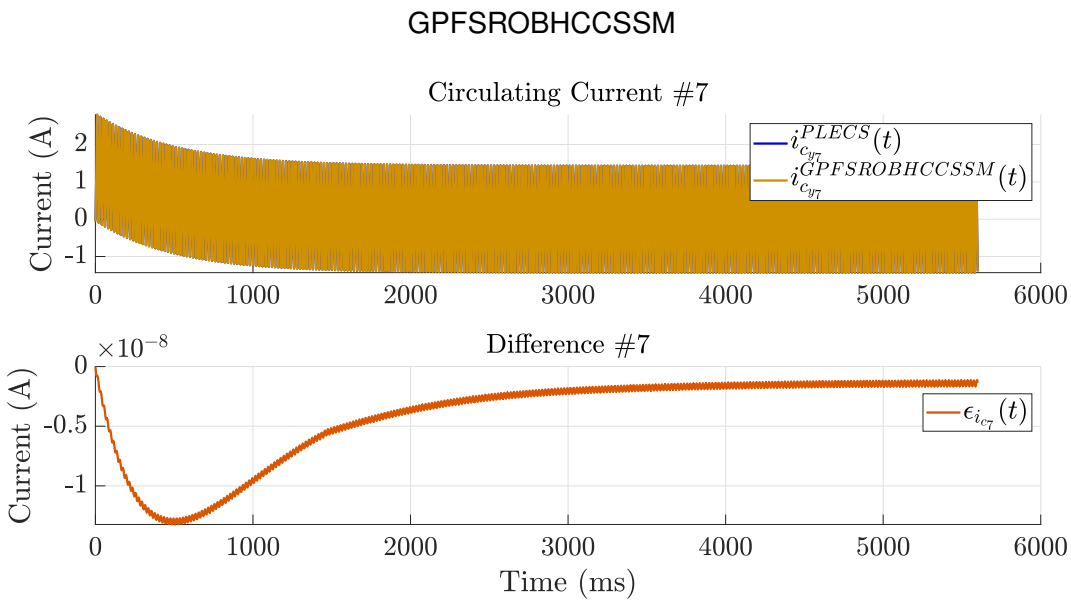

Figure 3.20: Circulating current behavior according to GPFSROBHCCSSM for a long simulation - 7-phase case. Top plot: currents from the model and PLECS®. Bottom plot: the difference between the two.

These tests confirm that the GPFSROBHCCSSM model is able to represent the second order harmonics of the currents, that is to say, to reach the objectives for which it was developed based on the GPFSROCSSM. The models GPFOCSSM and GPFSROBHCCSSM will thus be the only ones to be used thereafter to implement a control of the currents involved in the conversion

operated by the MMC because they are the only ones to be able to represent the second order harmonic components, and thus the circulating current, with sufficient accuracy.

3.H.2.5 Evaluation of the computation time from the high-level models

After focusing on the accuracy of the high-level models, the analysis of the simulation time of those models is interesting since it can bring a qualitative indication on the computation time needed by a current control system in real time which is based on the derived models. Thus, the simulation time of each model is measured for the models as well as for PLECS®, the data are plotted in Figure 3.21. The parameters from the computation hardware used for those simulations are detailed at the bottom of Table 3.8.

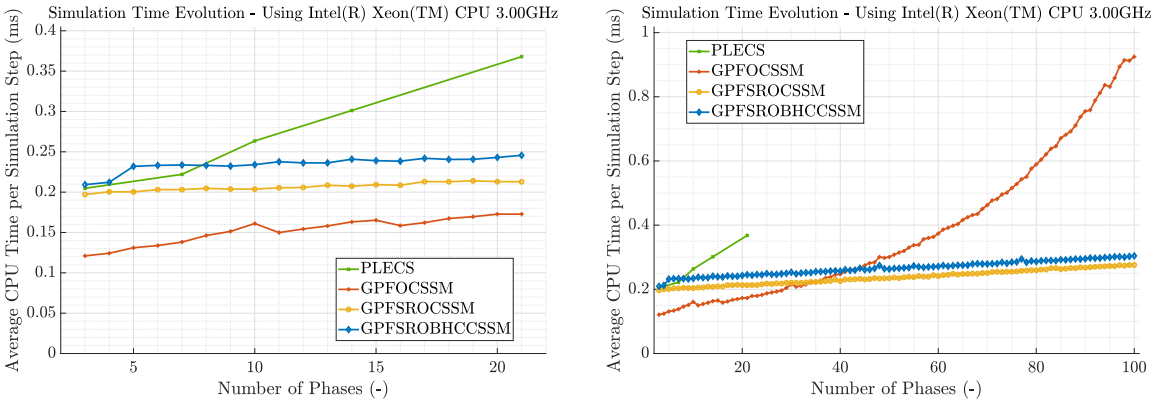

Figure 3.21: Evolution of the simulation time of each high-level model versus the number of phases and comparison with PLECS®.

Average CPU time per simulation step - Curve fitting		
	Fitting model	Norm of residuals
PLECS®	$9.44 \cdot m + 168$ µs	$14.82 \cdot 10^{-3}$
GPFOCSSM	$9.57 \cdot 10^{-2} \cdot m^2 - 2.21 \cdot m + 170$ µs	$165.2 \cdot 10^{-3}$
GPFSROCSSM	$0.792 \cdot m + 197$ µs	$13.06 \cdot 10^{-3}$
GPFSROBHCCSSM	$0.776 \cdot m + 226$ µs	$33.18 \cdot 10^{-3}$

Table 3.11: Average CPU time models derived from curve fitting using Figure 3.21 data.

The simulation time measured is divided by the number of simulation time steps in order to have an average value of the computation time needed for a single simulation step. Since the PLECS® electrical diagrams are drawn for specific values of m between 3 and 21, first simulations are done up to $m = 21$. As the high-level models adapt to any number of phases, simulations of the models are then extended to 100 phases. Figure 3.21 shows the evolution of the average CPU time needed to compute a simulation step versus the number of phases in both cases, i.e. up to 21 phases and then up to 100.

The first observation is that from $m = 3$ and above, all models are faster then PLECS® except for GPFSROBHCCSSM which is slower for $m \leq 7$ but still very close from the PLECS® computation time. The fact that the simulation sofware is slower then the models is explained by the fact that the models developed in this work are dedicated to a specific converter whereas PLECS® is able to simulate any converter topology. This means that in this work it will be faster to run all the simulations needed using the high-level models rather then PLECS®.

The second observation is that the simulation time of the GPFOCSSM increases quadratically with the number of phases while the simulation time of the two other models grows linearly with m. In order to explain this property, one must compare the computation time of the models when currents are computed for the same reference frame which is the case for the simulations[1]. This second observation can be explained by the size of the dynamic matrix of those models seen from the natural basis. Indeed, the GPFOCSSM has a $(2\ m \times 2\ m)$ dynamic matrix, the GPFSROCSSM has a $(2\ m \times 6)$ dynamic matrix in $\mathcal{B}^m$ and GPFSROBHCCSSM has a $(2\ m \times 10)$ dynamic matrix in $\mathcal{B}^m$. The number of terms in the GPFOCSSM dynamic matrix is therefore $4\ m^2$ which means that when the number of phases is increased, the number of multiplications done by the computer increases with m^2. As the number of operations increases quadratically, so does the computation time. Unlike the GPFOCSSM, model GPFSROCSSM (respectively GPFOCSSM) has a dynamic matrix seen from $\mathcal{B}^m$ that embeds $12\ m$ (respectively $20\ m$) terms. This number grows linearly with the number of phases. Thus, the number of multiplications and then the computation time needed by GPFSROCSSM and GPFSROBHCCSSM, grow linearly with m. The fact that GPFSROBHCCSSM dynamic matrix in $\mathcal{B}^m$ has $20\ m$ terms unlike GPFSROCSSM with $12\ m$ terms explains that the computation time needed GPFSROBHCCSSM is higher than that from GPFSROCSSM. The different observations made here are confirmed by Table 3.11 where the fitting features a very nice accuracy with small norm for the residuals.

From the knowledge of the evolution of the computation time of each high-level model with the number of phases, it is possible to expect that the current control system using models GPFSROCSSM and GPFSROBHCCSSM will feature a control computation time that varies very little when m is increased, unlike when using GPFOCSSM. This variation will be smaller as the slope of the fitting models in Table 3.11 are smaller.

Conjecture 1. *A control system using GPFSROCSSM or GPFSROBHCCSSM will feature a slowly varying computation time as the number of phases increases.*

Note that this assertion is successfully evaluated and proven in Chapter 5 for the GPFSROBHCCSSM.

The dependency carried out here thus makes it possible to show the low sensitivity of the reduced fixed order models on the number m of phases, which makes it possible to guarantee certain properties of this model which are presented in the Tables 3.12 and 3.13.

[1] For the GPFOCSSM, since the model is developed in the natural basis $\mathcal{B}^m$, no basis changes need to be applied to the currents after they are determined by the model. This is not the case for the other two models since they both are located in a Park reference frame. An inverse transformation must then be applied to the currents to bring them back into the natural basis $\mathcal{B}^m$ in order to compare them. In the case of the GPFSROCSSM, this transformation involves a product with the matrices $[C_K]^+[P(\theta)]$ of size $(m \times 3)$. In the case of the GPFSROBHCCSSM, this transformation proceeds by a product with the matrices $\left[C^m_{K_{12}}\right]^+[P(\theta)^m_{12}]$ of size $(m \times m')$. These changes of basis are applied only to the currents of alternating nature $\mathbf{I_c^{dq}}^{012}$ and $\mathbf{I_o^{dq}}^{012}$, the other currents being identical whatever the basis in which they remain. In the case where these changes of basis would be directly applied to the dynamic matrices of the state-space models, this amounts to bringing back these dynamic matrices in part in the basis $\mathcal{B}^m$. Thus GPFSROCSSM which has a dynamic matrix of size (6×6) in the Park reference frame ends up having a matrix equivalent to the calculations to be made which is of size $(2m \times 6)$ in the basis $\mathcal{B}^m$ and GPFSROBHCCSSM which has a dynamic matrix of size (10×10) in the reference frame of Park ends up having a matrix equivalent to the calculations to be made which is of size $(2m \times 10)$ in the basis $\mathcal{B}^m$.

3.H.3 Conclusions about the accuracy assement of the high-level models

From the tests which were carried out to compare the models with a simulation sofware dedicated to electrical circuits PLECS® with an aim of validating these models, it was highlighted that even if the models show deviations to the circuit simulator, these deviations remain sufficiently small and allow to conclude that the GPFOCSSM as well as the reduced order models GPFSROCSSM and GPFSROBHCCSSM are of very good precision, and this, whatever the number m of phases when representing the continuous and fundamental components of the currents. The maximum deviation encountered during these tests is $1.14 \cdot 10^{-4}$ %. This maximum deviation is reached by the alternating current at the output of the MMC $\mathbf{I_o}$. If 2^{nd} order harmonics are added to the fundamental components, it is found that the GPFSROCSSM has a very strong deviation. This error is due to the fact that this model is derived from a Park transformation which considers only the fundamental components, the observed deviation is thus normal. The full order model GPFOCSSM and the reduced order model GPFSROBHCCSSM represent much better the 2^{nd} order harmonic components since their maximum deviation is about $5.5 \cdot 10^{-5}$ %. This maximum error is reached by the alternating current at the output of the MMC $\mathbf{I_o}$.

The General Polyphase Full Order Current State-Space Model (GPFOCSSM) and the General Polyphase Fixed-Size Reduced Order BiHarmonic Content Current State-Space Model (GPFSROBHCSSM) will therefore be used to develop the current control allocation of the MMC. The General Polyphase Fixed-Size Reduced Order Current State-Space Model (GPFSROCSSM) will not be used to implement the control of the currents because it has a too large error in the representation of the 2^{nd} order harmonic components of the currents.

However, there is a perspective of further study of the LOZ. Indeed, here the study is limited to considering that the $\mathbf{V_{xy}}$ are made of a constant component and a harmonic component of first order (fundamental) whereas in reality the second order harmonic component which is added to it is useful for describing the circulating current as it was seen in the development of the high-level model. If the LOZ analysis of the system did not take into account these second order harmonic components here, it is to perform a first operation zone analysis with a simplified study. The choice of a simplified study is done because taking into account several harmonic components makes the LOZ analysis much more complex. The complexity of embedding at least two harmonic components is due to the appearance of strong nonlinearities in the amplitude of the waveforms which are not featured in the case where only one AC component is considered in addition to the DC component, see Appendix C. An approach that would perhaps allow this LOZ analysis to be carried out while reducing the nonlinear property would be to derive this analysis in the Park 12 rotating frame.

Although the analysis proposed here does not allow to evaluate the accuracy of the high-level models in an operating case that corresponds perfectly to all the operating cases of the MMC, this evaluation is done for an important number of operating points with constant and alternating components, in steady state and in transient conditions. This is considered sufficient to assert that the models developed are sufficiently accurate in order to develop converter control laws based on them.

3.I Models' new features review compared to the state-of-art

This section aims to provide a summary of the characteristics of the models developed in order to implement the control allocation method. First, a summary of the characteristics of the three

high-level models representing the dynamics of the currents will be proposed, then a perspective with models already available in the literature will be drawn up.

3.I.1 | Features from the high-level models

Scalability

Property 1. *The models GPFOCSSM, GPFSROCSSM and GPFSROBHCCSSM are all three scalable to an MMC having any number of submodules and any number of phases m.*

Generality

Property 2. *The models GPFOCSSM, GPFSROCSSM and GPFSROBHCCSSM are all three adaptable to a MMC connected to a DC bus featuring an impedance or not, connected to a network AC having an impedance or not and being an active load or not.*

Accuracy

Property 3. *The models GPFOCSSM, GPFSROCSSM and GPFSROBHCCSSM have different accuracies:*

- *GPFOCSSM represents the total harmonic content of the currents.*
- *GPFSROCSSM represents only the continuous and fundamental harmonic components of the currents for $m > 3$. For $m = 3$ all the harmonic content of the currents is represented.*
- *GPFSROBHCCSSM represents only the continuous, fundamental and $\#2$ harmonic components of the currents for $m > 5$. For $m \leq 5$ all the harmonic content of the currents is represented.*

Sensitivity of the complexity when scaling up

Property 4. *The models GPFOCSSM, GPFSROCSSM and GPFSROBHCCSSM feature a complexity that evolves differently as a function of the number m of phases:*

- *GPFOCSSM has a complexity which evolves quadratically as a function of m. This complexity implies a computation time that evolves significantly as a function of the number of phases compared to the other models.*
- *GPFSROCSSM and GPFSROBHCCSSM both have a complexity that evolves linearly as a function of m. It is observed in simulation that the computation time of both models grows very slightly as a function of the number of phases, making them almost insensitive to the number of phases.*

3.I.2 | Putting the developed models into perspective

In order to analyze the interest of the models developed here, a comparative table is drawn up. The modelling of the MMC is not a new research topic to date, the multitude of models available in the literature would make the comparison very complex and the summary table would take too much space. For this reason, a choice of models was made to carry out this analysis. This choice

was made by selecting the works introducing the best suitable models for the implementation of a control allocation. Indeed, this table allows one to highlight the contributions of the introduced models compared to the already available models which show predispositions as for their use in an algorithm of control allocation.

➤ As presented in the state of the art concerning control allocation methods, these methods are initially based on a state-space model of the system to be controlled. Whether or not the allocation control method uses optimization algorithms, the lower the order of the state-space model, the smaller the time required to compute the control to be allocated. It is therefore desirable to use control models in the form of a state-space model with the lowest possible order. This already gives two criteria for comparing models: the fact of being **in the form of a state-space equation** and the fact of having a **low order for this state model**.

➤ To understand the proposed model it is necessary to have its **derivations**, which is an additional comparison criterion.

➤ Moreover, one of the main objectives of this research work is to have a control as general as possible which takes advantage of models which can **readily adapt** themselves to the modifications of the structure of the MMC, that is to say, a model of **all types of currents** which can **adapt to the modification of the number N of submodules**, **to the number m of phases** of the AC network at the output of the MMC, **to the input DC bus**, to the fact that the **AC network may be active**, and to the **connection of the AC and the DC neutral points**. This gives 7 additional criteria.

➤ Putting these new criteria against the two criteria that are given directly by the control allocation method, knowing that increasing m and N can lead to an increase in the order of the state-space model, the best would be to have a state-space model that is insensitive to both m and N in order to better satisfy the low order criterion of the state-space model. This generates two new criteria: **insensitivity to m and N**.

➤ To be able to judge the quality of the models, it is important to know their precision. This accuracy can be represented by the **harmonic content** that these models represent, which is then also a criterion for comparison.

It is thus from these various criteria, then displayed in Tables 3.12 and 3.13, that the models are compared. The last column of the table contains the optimal values of each criterion, they constitute together the desired characteristics of the goal model so as to reach the following main objectives: to easily adapt to control allocation methods and to satisfy the objective of scalability and adaptability of the model.

Previous works have decoupled the dynamics of the four different current types for three-phase electrical systems like in [PRB14; Liz+15] where a matrix model is derived. Taking inspiration from these studies and [KM18], a first novelty of the present model is to derive a non-matrix decoupled model of the currents extended to the polyphase (m-phase) case. The approaches of [Fre+16a; Bou17; KM18] produce a state-space model representing the dynamics of only three out of the four possible current types. Compared to [KM18], the contribution of [LFB21b] presents a more limited, but also more explicit derivation of the converter model[1], in addition to considering the presence of a common mode current. Table 3.12 and Table 3.13 summarize the comparison of characteristics from the proposed high-level models with the literature.

[1] The work is more limited since the focus is only on the MMC here unlike [KM18], but the explicit charateristic is due to the fact that the models are derived in details here whereas [KM18] only introduces the general concept.

In conclusion, this table shows that the main novelties of the models developed here are first 1) the adaptability to the number m of phases[1], 2) the ability to take into account I_m, 3) the adaptability of the connection of neutrals AC and DC, 4) the ability to take into account the various possible cases of AC and DC networks. With the reduced order models the additional contributions are 5) the low sensitivity of the state models to the number of phases, as shown by the evolution of the simulation time on Figure 3.21, and its low order. However, compared to the full order model, the fixed-size reduced order models feature a lower harmonic content representation which then makes them less accurate.

It is also noted that from the various models available in the literature, none really approaches the characteristics of the goal model sought. Among the developed models, it is the reduced order model GPFSROBHCCSSM which is the closest to the goal model, it has thus great chances to be used in a privileged way in this work, for the current control of the MMC.

To put it in a nutshell, the novelties of the state-space models introduced in this work, is to have a state-space model which readily adapts to m without loss of generality on the possibilities of the DC bus, the AC network and the connection between the two. Out of the three high-level models, the two fixed-size reduced order models feature a very low complexity and thus a computation time almost insesitive to the number of phases.

[1] This adaptation capability to the number of phases is already used beneficially for the simulations presented above since the *Matlab-Functions* which have been programmed to implement the models in simulation, are precisely the same whether one is in the three-phase, seven-phase or more case.

Splitting the table in two parts is solely due to table width concerns compared to the page limits.

	Models from the literature			Developed models			Goal model
Criterion	[Fre+16a]	[Ber+18]	[Liz+15]	GPFOCSSM	GPFSROCSSM	GPFSROBHCCSSM	Goal model
State-space model	Yes	Yes	No	Yes	Yes	Yes	Yes
Model derivations	Explicit	Explicit	Explicit	Explicit	Explicit	Explicit	Explicit
Model reference frame	SRRF	SRRF	SRF	SRF	SRRF	SRRF	No pref.
Scalability to m	No	No	No	Yes	Yes	Yes	Yes
Sensitivity to m	N/A	N/A	N/A	Yes	Low	Low	No
Order of the model	$3, m = 3$	$5, m = 3$	$24, m = 3$	$2m$	6	$2m'$	Constant low
Scalability to N	Yes	Yes	Yes	Yes	Yes	Yes	Yes
Sensitivity to N	No	No	No	No	No	No	No
Currents represented	No I_m	No I_m	All	All	All	All	All
Harmonic content for $m = 3$	Full	Full	Full	Full	Full	Full	Full
Harmonic content for $m > 3$	N/A	N/A	N/A	Full	DC + Fond.	DC + Fond. + 2^{nd} Harmo.	Full
Neutral points connection	Fixed	Fixed	Versatile	Versatile	Versatile	Versatile	Versatile
Possible active nature of AC-side	Yes	Yes	Yes	Yes	Yes	Yes	Yes
DC-side impedance is modelled	No	No	Yes	Yes	Yes	Yes	Yes
Readily adaptive to any MMC	No	No	No	Yes	Yes	Yes	Yes

Table 3.12: Comparison of the characteristics of the proposed scalable state-space model with the literature - Table #1

N/A: Not applicable

	Models from the literature			Developed models			Goal model
Criterion	[Bou17]	[PRB14]	[KM18]	GPFOCSSM	GPFSROCSSM	GPFSROBHCCSSM	Goal model
State-space model	Yes	No	Yes	Yes	Yes	Yes	Yes
Model derivations	Explicit	Explicit	Implicit	Explicit	Explicit	Explicit	Explicit
Model reference frame	SRF	SRF	SRF	SRF	SRRF	SRRF	No pref.
Scalability to m	No	No	Yes	Yes	Yes	Yes	Yes
Sensitivity to m	N/A	N/A	Yes	Yes	Low	Low	No
Order of the model	$7, m = 3$	$24, m = 3$	$2m - 1$	$2m$	6	$2m'$	Constant low
Scalability to N	Yes	Yes	Yes	Yes	Yes	Yes	Yes
Sensitivity to N	No	No	No	No	No	No	No
Currents represented	No I_m	All	No I_m	All	All	All	All
Harmonic content for $m = 3$	Full	Full	Full	Full	Full	Full	Full
Harmonic content for $m > 3$	N/A	N/A	Not specified	Full	DC + Fond.	DC + Fond. + 2^{nd} Harmo.	Full
Neutral points connection	Fixed	Versatile	Versatile	Versatile	Versatile	Versatile	Versatile
Possible active nature of AC-side	No	Yes	Yes	Yes	Yes	Yes	Yes
DC-side impedance is modelled	Yes	Yes	Yes	Yes	Yes	Yes	Yes
Readily adaptive to any MMC	No	No	No	Yes	Yes	Yes	Yes

Table 3.13: Comparison of the characteristics of the proposed scalable state-space model with the literature - Table #2

N/A: Not applicable

3.J | Conclusions about the high-level modelling

Along the approach proposed in this chapter, different state-space models describing the behavior of currents in the MMC have been developed. The developments carried out have been achieved with a double objective of generalization of the models while trying to guarantee a low complexity for the latter.

In line with this aim, a first generalized state-space model of the currents which fits a MMC having any number of phases, to the characteristics of the DC bus, to those of the AC network, to the type of connection between neutrals has been developed: the GPFOCSSM. It allowed us to reach one of the first modelling objectives: the generalization of the current model to a large set of electrical network topologies taking advantage of the MMC. The analysis of this model allowed us to put forward the fact that its complexity is very important, this is why a second model was developed.

The second model, GPFSROCSSM, was developed from the first GPFOCSSM to which a Park transformation was applied to reduce its order. The GPFSROCSSM is based in a synchronous rotating frame. It has the generality characteristics of the first model but also the fact of being of low complexity. Simulations and analysis of this second model were then carried out. They have highlighted the fact that this model, being of too low complexity, represents the behavior of the currents with too little accuracy and information, leading to strong deviations on the calculation of the currents flowing through the converter. The two modelling objectives are achieved with this GPFSROCSSM. However, the model is too inaccurate to be used in the design of a control algorithm, a third model was then developed.

This third model was derived by applying a more sophisticated Park transform to the GPFOCSSM. First, this Park transform was designed to ensure that the model in the synchronous rotating frame represents the dominant harmonic components of the different currents involved in the MMC. This transformation was tailored to act as a filter that selects the very specific harmonic content that represents the currents with sufficient accuracy. The GPFSROBHCCSSM model, then achieved after applying the transformation, also features the generality properties of the GPFOCSSM, to which is added the fact of having a model of low complexity while describing the state vector with a sufficient accuracy to be able to use this model in a current control law design approach. It is noted that the complexity of the latter increases very slowly as systems with a higher number of phases are modelled.

Before being able to use the models in a current control design approach, the developed high-level models were subjected to various simulation tests to compare them with a software dedicated to the simulation of electrical systems. These tests have shown differences in accuracy between the models, from the most accurate to the least accurate they come in order: GPFOCSSM, GPFSROBHCCSSM and finally GPFSROCSSM. The simulation time of each model was also evaluated during these numerous simulations, showing also differences between the models. The most accurate model, GPFOCSSM, is also the slowest to simulate, especially since its complexity increases quadratically with the number of phases. For the two remaining models, their computation time changes linearly with the number of phases. It has been observed and explained that GPFSROCSSM is faster to run than GPFSROBHCCSSM. Figure 3.22 summarizes these different comparative elements in a qualitative way. It is found that the GPFSROBHCCSSM is a good trade-off between accuracy and low computation time.

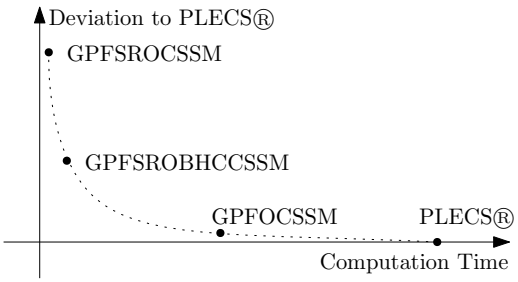

Figure 3.22: Comparison of the high-level models according to the accuracy and computation time criteria.

The developed state-space model that is readily scalable to any number of phases paves the path for new possibilities. 1) It is now possible to readily analyze the evolution of the open-loop dynamic characteristics of the four types of currents versus the number of phases, for any type of neutral connection and any nature of the AC-side, and thus prove the stability of the state-space system. 2) Using the model in steady-state, it is now feasible to predict the evolution of the operating zone of the four types of currents (maximum reachable values of the currents) versus the number of phases as it was done in Section 3.H.1. 3) Current-level simulations can be performed faster than PLECS®. 4) The developed model enables the design of generic[1] control algorithms for the currents within the MMC featuring a low computation time online that varies very little with the number of phases. Thanks to this last feature, it will be sufficient to specify to the control algorithm the parameters of the MMC, of the AC network and of the DC bus without having to undergo major changes in the system model and control algorithm structure.

The modelling work done in this chapter has brought very interesting results and new possibilities. However, some perspectives are still to be explored. An interesting study would be to investigate the LOZ when 2^{nd} order harmonic components are added to the v_{xy} waveforms. This would allow to have an analysis of the operating zone of the MMC for all the operating cases of the latter. The interest of such a work is to easily determine the bounds of the four types of currents flowing through the MMC in nominal operating cases.

[1] Algorithms that ensure current-control for any number of phases with very little change in computation time in the AC-side are said to be scalable and generic.

4 Contributions to Improving the Control Allocation Methods

Contents

The objective of this chapter is to describe the different methodological contributions that have been made to the control allocation. The general theme of these works is focused on an adaptation of allocation methods for the control of electrical systems. The use of these methods for the control of the MMC have for objective to ensure given performances from the automatic control point of view such as a settling time, an overshoot or an accuracy. These performances, not being always guaranteed, suggested to explore the development of new allocation methods to be able to correct the obtained behavior and to reach the performance objectives.

4.A Research axis: extending the features of the Control Allocation methods

Although the study proposed in this chapter is first motivated by the need for the control system of the MMC to meet the specified performances, it is part of a wider approach to improve the allocation methods. Indeed, the objective here is to give new features to the allocation methods which contribute to extend their possible field of utilization and to develop their competitiveness compared to the other existing control methods.

Outline

The first part of this chapter, Section 4.B, will discuss views on the formulations of the existing allocation methods with the aim of deriving a generalized and versatile formalism that will be used later on to design the converter control algorithms. The second part, Section 4.C, will focus on adding new features to the allocation methods that requires few modifications to the current methods and yet significantly improves their performance in an elegant way.

4.B General formalism for the control allocation methods

4.B.1 Definition of the control allocation problem

Let a state-space model be defined by[1]:

$$\begin{cases} \mathbf{X}_{k+1} = F\mathbf{X}_k + H\left[b\left(\mathbf{U}_k\right) + \mathbf{E}_k\right] \\ \mathbf{Y}_k = C\mathbf{X}_k \end{cases} \tag{4.1}$$

where $\mathbf{X} \in \mathbb{R}^{n_x}$ is the state vector, $\mathbf{U} \in \mathbb{R}^{n_u}$ is the control vector, $\mathbf{Y} \in \mathbb{R}^{n_y}$ is the output vector, and $\mathbf{E} \in \mathbb{R}^{n_x}$ is a known additive perturbation that can be related to a nonlinearity of the system for example. The matrices $F \in \mathbb{R}^{n_x \times n_x}$ and $C \in \mathbb{R}^{n_y \times n_x}$, are the state matrix and the output matrix, respectively. The matrix $H \in \mathbb{R}^{n_x \times n_x}$ and the function $b : \mathbb{R}^{n_u} \mapsto \mathbb{R}^{n_x}$ represent the influence of the control vector $\mathbf{U}$ on the system. Note that the product $H\ b(\cdot)$ becomes the input matrix $G = H\ B$ when the influence of the control on the system is linear. If one combines the two equations of this discrete state-space model (4.1), $\mathbf{Y}_{k+1}$ is derived:

$$\mathbf{Y}_{k+1} = CF\mathbf{X}_k + CHb\left(\mathbf{U}_k\right) + CH\mathbf{E}_k \tag{4.2}$$

Isolating the control term in the left side of this equation gives:

$$CHb\left(\mathbf{U}_k\right) = \mathbf{Y}_{k+1} - CF\mathbf{X}_k - CH\mathbf{E}_k \tag{4.3}$$

This equation reads:

$$\mathcal{M}\left(\mathbf{U}_k\right) = \mathbf{a}_k \tag{4.4}$$

with:

$$\mathbf{a}_k = \mathbf{Y}_{k+1} - CF\mathbf{X}_k - CH\mathbf{E}_k \tag{4.5}$$

where $\mathcal{M}(\cdot) = CHb(\cdot)$ is the effectiveness function and $\mathbf{a}_k$ is the action vector generated at time $t = kT_c$ by applying $\mathbf{U}_k$ to the system. The case, where the state-space model is defined by (4.6), will be that of the low-level and the high-level.

$$\begin{cases} \dot{\mathbf{X}} = A\mathbf{X} + B\mathbf{U} + \mathbf{E} \\ \mathbf{Y} = C\mathbf{X} \end{cases} \tag{4.6}$$

In this case, the function $b(\cdot)$ is updated as $b(\mathbf{U}) = B\mathbf{U}$. Thus, (4.3) becomes:

$$CG\mathbf{U}_k = \mathbf{Y}_{k+1} - CF\mathbf{X}_k - CH\mathbf{E}_k \tag{4.7}$$

with $G = HB$. This equation reads:

$$M\mathbf{U}_k = \mathbf{a}_k \tag{4.8}$$

[1] Appendix A details how this form is derived from a continuous-time state-space model

where $M = CG = CHB$ is the effectiveness matrix. The equation (4.3) - or (4.7) when applicable - represents the influence of the control vector $\mathbf{U}$ on the system under consideration, and where $\mathbf{a}_k$ is the consequence of applying such a control vector to the system.

By closing the loop it will be wished that the output $\mathbf{Y}$ of the system tracks its reference $\mathbf{Y}^{ref}$ while guaranteeing certain performances in terms of static error, overshoot, or settling time. This is embodied by the definition of the reference model (4.9).

Definition 1. *The performance objective that the control allocation methods aim to track is defined by the following* ***reference model****:*

$$\mathbf{Y^*}_{k+1} = F_M \mathbf{Y}_k + G_M \mathbf{Y^{ref}}_k \tag{4.9}$$

where F_M and G_M are respectively the dynamic and control matrices of this so-called ***reference model****.*

Applying the control $\mathbf{U}_k$ at time k will transform $\mathbf{Y}_k$ into $\mathbf{Y}_{k+1}$ as described by (4.2); and $\mathbf{a}_k$ represents this transformation, as defined by (4.5). Now, let $\mathbf{Y^*}_{k+1}$ be the output that it is desired to reach a time $k+1$ as a consequence of applying $\mathbf{U}_k$ at time k. The related action vector that represents the transformation of $\mathbf{Y}_k$ into $\mathbf{Y^*}_{k+1}$ is noted $\mathbf{a_d}_k$, and is called the **desired action vector**. Thus, in a analogous way to the definition made of $\mathbf{a}$ by (4.5), the desired action vector $\mathbf{a_d}$ can thus be introduced in order to represent the targeted behavior encapsulated into the reference model (4.9):

$$\begin{aligned} \mathbf{a_d}_k &= \mathbf{Y^*}_{k+1} - CF\mathbf{X}_k - CH\mathbf{E}_k \\ &= (F_M \mathbf{Y}_k + G_M \mathbf{Y^{ref}}_k) - C\left(F\mathbf{X}_k + H\mathbf{E}_k\right) \end{aligned} \tag{4.10}$$

The control algorithm will therefore try to ensure that this desired action is reached, in other words the control allocation will seek the control $\mathbf{U}$ that guarantees $\mathbf{a} = \mathbf{a_d}$, which is formulated by:

$$\begin{aligned} & \mathbf{a}_k = \mathbf{a_d}_k \\ \iff & \mathcal{M}\left(\mathbf{U}_k\right) = \mathbf{a_d}_k \\ \iff & CHb\left(\mathbf{U}_k\right) = (F_M \mathbf{Y}_k + G_M \mathbf{Y^{ref}}_k) - C\left(F\mathbf{X}_k + H\mathbf{E}_k\right) \end{aligned} \tag{4.11}$$

This equation represents the control objective and is called the **control allocation equation** or **allocation equation**.

Definition 2. *The control allocation equation is defined by:*

$$\mathcal{M}(\mathbf{U}) = \mathbf{a_d} \tag{4.12}$$

The control vector will therefore have to be a solution of the latter while respecting the limitations imposed by the system operating limits. Thus, the condition $\mathbf{U}_{min} \leq \mathbf{U} \leq \mathbf{U}_{max}$ must also be taken into account when the control algorithm aims to solve (4.12). This allows one to fully define the control allocation problem:

Definition 3. *The control allocation problem is mathematically defined by:*

$$\{\mathcal{M}(\mathbf{U}) = \mathbf{a_d} \mid \mathbf{U}_{min} \leq \mathbf{U} \leq \mathbf{U}_{max}\} \tag{4.13}$$

Taking into account the saturations of the control variables it is possible that (2) may not always be verified. Indeed, if the desired action vector reaches a too large magnitude, the required $\mathbf{U}$ that verifies the allocation equation may exceed its boundaries, making the computed control unfeasible. In this case, before applying the control to the system, the latter would be clipped to its boundaries. In order to take into account the possibility that the allocation equation may not always be feasible, a control error is introduced. This $\mathbf{e}$ measures how far the computed input is from verifying the allocation equation:

Definition 4. *The control allocation problem error is defined according to:*

$$\mathbf{e} = \mathcal{M}(\mathbf{U}) - \mathbf{a_d} \tag{4.14}$$

4.B.2 Optimization formulation of the control allocation problem

At this stage $\mathbf{e}$ is only defined as a simple deviation but it represents an interesting tool to solve the control problem that is set. As it has been seen in the state of the art, the solution of casting on the bounds of the admissible control zone the determined exceeding control vector is not ideal. This is due to the fact that in some cases it is possible to distribute the required effort over several control vector variables in order to satisfy the allocation equation while complying with the control bounds. To give the control law this ability to distribute the requested effort, it is necessary to take into account the limitations of the control *a priori*. The use of optimization methods is particularly suitable for this purpose. The task to be carried out is then to determine $\mathbf{U}$ which minimizes $\mathbf{e}$ while respecting the control saturations. This is formalized in the following way:

Definition 5. *The control allocation optimization problem is defined by:*

$$\begin{cases} \min_{\mathbf{U},\mathbf{e}} J_l = ||\mathbf{e}||_l^l \\ under\ the\ constraints\ (u.c.)\ : \\ \mathcal{M}(\mathbf{U}) - \mathbf{e} = \mathbf{a_d} \\ \mathbf{U}_{min} \leq \mathbf{U} \leq \mathbf{U}_{max} \\ -\mathbf{e}_{max} \leq \mathbf{e} \leq \mathbf{e}_{max} \end{cases} \tag{4.15}$$

where $\mathbf{e}_{max}$ is an upper bound on the achievable error, for exemple $||\mathbf{a_d}||_l^l$, and l is a given norm to be chosen. For example, [Bod02; PB05; FB10] use the $l1$-norm, [FB10] uses the $l\infty$-norm, and [PB06; FB10] use the $l2$-norm. It is important to note that here $\mathbf{e}$ holds the role of slack variable allowing to guarantee the feasibility of the optimization. This slack variable is therefore also a decision variable of the optimization problem which must be determined and to which bounds are associated.

However, in some cases of overactuated systems, the degree of overactuation[1] is such that there may be several solutions to the allocation equation that are within the limitations. Another reason for modifying this cost function is the fact that there are system operations that are desirable to prioritize. In these cases, it may be interesting to extend the optimization criterion J_l to select one of the solutions of (4.12) in order to steer the behavior of the system towards the most preferred.

[1] The overactuation degree stands for the difference between the size of the input vector and that of the output.

For example, for an airplane, it is possible to compare two combinations of aileron deflection angles: 1) in the first case, the left aileron has a deflection of $+4°$ and the symmetrical right aileron has the opposite deflection of $-4°$. The roll moment applied to the airplane is then null, but obtaining such a deflection consumes energy. 2) the left and right ailerons have the same deflection of $0°$. The reaction on the plane is the same as in the previous case but this time the deflections are zero and the actuators consume no energy. In both cases the desired behavior is obtained: a zero roll moment, which amounts to the fact that the allocation equation is verified at every time but there is a solution $\mathbf{U}$ that consumes more energy than the other. To notify the optimization that it prefers an input that consumes less energy, one solution is to specify the preference vector that embodies the operation that one wishes to prefer when there are several possible solutions to the allocation equation. The implementation of this preference vector is done as follows in the optimization criterion:

$$\begin{aligned} J_l &= ||\mathcal{M}(\mathbf{U}) - \mathbf{a_d}||_l^l + \omega_p ||\mathbf{U} - \mathbf{U}_p||_l^l \\ &= ||\mathcal{M}(\mathbf{U}) - \mathbf{a_d}||_l^l + ||\omega_p{}^{\frac{1}{l}} (\mathbf{U} - \mathbf{U}_p)||_l^l \end{aligned} \tag{4.16}$$

where $\omega_p \in \mathbb{R}^+$ allows one to set the weight of the preference criterion in the optimization algorithm. The larger it will be, the more the optimization algorithm will aim at enforcing $\mathbf{U} = \mathbf{U}_p$ by leaving the verification of the allocation equation aside. In order not to deviate too much from the initial objective of the allocation, i.e. to cancel $\mathbf{e}$, ω_p should be chosen to be less than 1. It is possible that it may be desirable not only to favor a control vector but also a behavior of the system directly. The objective would not necessarily be to prefer a certain $\mathbf{U}_p$ but rather an action vector $\mathbf{a_p}$. In this case, the cost function adopts a more general form:

$$\begin{aligned} J_l &= ||\mathcal{M}(\mathbf{U}) - \mathbf{a_d}||_l^l + \omega_p ||\mathcal{M}_p(\mathbf{U}) - \mathbf{a_p}||_l^l \\ &= ||\mathcal{M}(\mathbf{U}) - \mathbf{a_d}||_l^l + ||\omega_p{}^{\frac{1}{l}} (\mathcal{M}_p(\mathbf{U}) - \mathbf{a_p})||_l^l \end{aligned} \tag{4.17}$$

This last formulation generalizes (4.16) since it is sufficient to set $\mathcal{M}_p(\cdot) = \mathbb{I}_{n_u}$ and $\mathbf{a_p} = \mathbf{U}_p$ to get back to it. The inclusion of the weighting coefficient ω_p within the second criterion norm is possible as (4.16) and (4.17) show. By analytical definition of the norm (4.19), this allows one to simplify the expression of the optimization criterion:

$$J_l = \left|\left| \begin{bmatrix} \mathcal{M}(\mathbf{U}) - \mathbf{a_d} \\ \omega_p{}^{\frac{1}{l}} (\mathcal{M}_p(\mathbf{U}) - \mathbf{a_p}) \end{bmatrix} \right|\right|_l^l \tag{4.18}$$

This can be directly put in the form:

$$J_l = \left|\left| \hat{\mathcal{M}}(\mathbf{U}) - \hat{\mathbf{a}}_\mathbf{d} \right|\right|_l^l \tag{4.20}$$

with $\hat{\mathcal{M}}(\mathbf{U}) = \begin{bmatrix} \mathcal{M}(\mathbf{U}) \\ \omega_p{}^{\frac{1}{l}} \mathcal{M}_p(\mathbf{U}) \end{bmatrix}$ and $\hat{\mathbf{a}}_\mathbf{d} = \begin{bmatrix} \mathbf{a_d} \\ \omega_p{}^{\frac{1}{l}} \mathbf{a_p} \end{bmatrix}$. The resulting form in (4.20) shows that the addition of a preference criterion to the cost function is done in a way that allows the latter to keep the original formalism of the control allocation optimization problem stated by Definition 5 with the only difference that the equation $\hat{\mathcal{M}}(\mathbf{U}) - \hat{\mathbf{e}} = \hat{\mathbf{a}}_\mathbf{d}$ replaces $\mathcal{M}(\mathbf{U}) - \mathbf{e} = \mathbf{a_d}$. By doing so, the online optimization control algorithms will always adopt the generic form of control allocation problem into which it is possible to turn a large class of allocation problems that may or may not have a preference criterion.

Definition of the l-norm of $\mathbf{e} \in \mathbb{R}^{n_a}$:

$$||\mathbf{e}||_l = \left(\sum_{n_a} |e_i|^l \right)^{\frac{1}{l}} \tag{4.19}$$

4.B.3 | Solving methods for the control allocation problem

As it has been presented in details in the part dedicated to the state of the art, there are three main families of methods for solving the so-called allocation problem: 1) the model-inversion based

methods MIB, 2) the error minimization online methods EMOn and 3) the error minimization offline methods EMOff. In the context of the work done in this research project, the focus is on the second family of methods. The idea is to use optimization algorithms run in real time to solve the control allocation problem which takes the form of control allocation optimization problem. To do so, different algorithms that are able to execute rapidly in real time have already been implemented to drive different systems that generally belong to the transportation category. In the framework of these motion control systems, the required performances in terms of settling time are of the order of a second, whereas the work carried out here focuses on power electronics where the order of magnitude of the settling time is around a millisecond. This means that there is no guarantee that optimization algorithms implemented in real time to drive motion control systems can also be implemented in power electronics where the control required performance imposes stronger time constraints on the microcontroller clock.

The work of [Bou+15] has shown that it is possible to use the Simplex algorithm in real time to perform the allocation computation for a static converter having $n_u = 4$ control variables and $n_a = 3$ components for the desired action vector. This algorithm will therefore be implemented here as well. Quadratic optimization algorithms such as Interior-Point or Active-Set have - at the beginning of the work presented here - not yet been used to control a static converter. Given the current advances in the performance of real time computing devices, the idea will be to evaluate whether the use of such optimization algorithms is possible for the control of the MMC. The optimization algorithms that will be used here will be developed by adapting already available algorithms that have been used in the framework of the control allocation for other systems. By choosing to use such programs that have already proven themselves in the context of allocation methods, the chances of a successful EMOn method for controlling the MMC increase. The work of [Bod02] gave rise to an advanced Simplex algorithm which takes into account policies for preventing the cycling phenomenon [Dan51]. This algorithm adopting a form dedicated to allocation will be used here as well as the Interior-Point from [PB05] also able to solve LP optimization problems. The study of [Här03] has allowed to gather two QP algorithms: first an Active-Set developed within the framework of these same researches as well as an Interior-Point resulting from the work of [PB06]. These two algorithms as well as others have been gathered in the archive available online [Här]. The work of [Här03] has carried out a comparison of the different Active-Set algorithms dedicated to the control allocation contained in this archive, allowing to identify the *WLS* (Weigthed Least Squares) as the best trade-off between convergence speed and optimality of the resulting solution. For the case of Active-Set it will thus be the formulation *WLS* of the archive which will be used here, as for the Interior-Point it will be the only algorithm available in the archive which will be implemented here.

For the control of the MMC studied here, the allocation methods using optimization will be used for control loops which aim at driving physical quantities whose dynamics can be represented by a state space model with linear control action. This means that optimization allocation algorithms will have to deal with systems such as $b(\mathbf{U}) = B\mathbf{U}$. In this case, the control allocation optimization problem updates to the form:

$$\begin{cases} \min_{\mathbf{U},\mathbf{e}} J_l = ||\mathbf{e}||_l^l \\ u.c. : \\ M\mathbf{U} - \mathbf{e} = \mathbf{a_d} \\ \mathbf{U}_{min} \leq \mathbf{U} \leq \mathbf{U}_{max} \\ -\mathbf{e}_{max} \leq \mathbf{e} \leq \mathbf{e}_{max} \end{cases} \tag{4.21}$$

From this formulation, it is possible to define the form that the allocation problem will take for the different selected optimization algorithms.

Linear programming

For the LP case, the chosen norm becomes the $l1$-norm. Thus, the objective function is updated: $J_l = ||\mathbf{e}||_1^1 = |\mathbf{e}| = \sum_{n_a} |e_i|$. In its standard form, the Simplex is suitable to solve the following optimization problem:

$$\begin{cases} \min_{\mathbf{x}} J_{LP} = \mathbf{c}^T\mathbf{x} \\ u.c. : \\ \mathcal{A}\,\mathbf{x} = \mathbf{b} \\ 0 \leq \mathbf{x} \leq \mathbf{x}_{max} \end{cases} \tag{4.22}$$

Compared to (4.21), the decision variable $\mathbf{x}$ will contain the input vector $\mathbf{U}$ as well as the error vector $\mathbf{e}$. For a given system, there is no guarantee that the lower bound of its control vector will be the null vector, so a change of variable needs to be applied to (4.21) to bring it closer to the standard form of LP. A first change of variable is made on $\mathbf{U}$ such that $\mathbf{U} = \overline{\mathbf{U}} + \mathbf{U}_{min}$. This updates the boundaries of the control into $0 \leq \overline{\mathbf{U}} \leq \mathbf{U}_{max} - \mathbf{U}_{min}$. The error variable $\mathbf{e}$ is decomposed into $\mathbf{e} = \mathbf{e}^+ - \mathbf{e}^-$ with $\mathbf{e}^+, \mathbf{e}^- \geq 0$ so as to ease the derivation of the cost function. In the case where the deviation e_i is positive, ${e_i}^+ = e_i \geq 0$ and ${e_i}^- = 0$; and when e_i is negative: ${e_i}^- = e_i \geq 0$ and ${e_i}^+ = 0$. Thus the cost function is adapted:

$$J_l = |\mathbf{e}| = \sum_{n_a} |e_i| = \sum_{n_a} |{e_i}^+ - {e_i}^-| = \underset{\substack{\uparrow \\ \mathbf{e}^+, \mathbf{e}^- \geq 0}}{\sum_{n_a}} {e_i}^+ + {e_i}^- = [1 \ \dots \ 1 \ 1 \ \dots \ 1] \cdot \begin{bmatrix} \mathbf{e}^+ \\ \mathbf{e}^- \end{bmatrix} \tag{4.23}$$

Applying the introduced changes of variables, (4.21) becomes:

$$\begin{cases} \min_{\mathbf{U},\mathbf{e}} J_l = ||\mathbf{e}||_1^1 \\ u.c. : \\ M\overline{\mathbf{U}} - \mathbf{e}^+ + \mathbf{e}^- = \mathbf{a_d} - M\mathbf{U}_{min} \\ 0 \leq \mathbf{U} \leq \mathbf{U}_{max} - \mathbf{U}_{min} \\ 0 \leq \mathbf{e}^+ \leq \mathbf{e}_{max} \\ 0 \leq \mathbf{e}^- \leq \mathbf{e}_{max} \end{cases} \tag{4.24}$$

The decision variable vector of the optimization then appears easily when comparing (4.24) with (4.22): $\mathbf{x} = \begin{bmatrix} \overline{\mathbf{U}} & \mathbf{e}^+ & \mathbf{e}^- \end{bmatrix}^T$. Thus, (4.24) embraces the form of (4.22) whose parameters are then:

$$\begin{array}{l} \mathbf{x} = \begin{bmatrix} \overline{\mathbf{U}} & \mathbf{e}^+ & \mathbf{e}^- \end{bmatrix}^T \in \mathbb{R}^{n_u+2n_a} \\ \mathbf{c}^T = \begin{bmatrix} \mathbb{O}_{1,n_u} & 1 \dots 1 & 1 \dots 1 \end{bmatrix} \in \mathbb{R}^{n_u+2n_a} \\ \mathcal{A} = \begin{bmatrix} M & -\mathbb{I}_{n_a} & +\mathbb{I}_{n_a} \end{bmatrix} \in \mathcal{M}_{n_a,n_u+2n_a}(\mathbb{R}) \\ \mathbf{b} = \begin{bmatrix} \mathbf{a_d} - M\,\mathbf{U}_{min} \end{bmatrix} \in \mathbb{R}^{n_a} \\ \mathbf{x}_{max} = \begin{bmatrix} \mathbf{U}_{max} - \mathbf{U}_{min} & \mathbf{e}_{max} & \mathbf{e}_{max} \end{bmatrix} \in \mathbb{R}^{n_u+2n_a} \end{array} \tag{4.25}$$

The Simplex or the Interior-Point algorithm solves the optimization problem (4.25) at each control sampling period. Once per sampling period, the optimization will output the solution $\overline{\mathbf{U}}^*$, and the control vector to be applied to the system will be derived as $\mathbf{U}^* = \overline{\mathbf{U}}^* + \mathbf{U}_{min}$.

Quadratic programming

For the case of QP, the chosen norm becomes the $l2$-norm. Thus the objective function is updated: $J_l = ||\mathbf{e}||_2^2 = \sum_{n_a} {e_i}^2$. The control allocation oriented algorithms available to date are

tailored to solve the following optimization problem:

$$\begin{cases} \min_{\mathbf{x}} J_{QP} = \frac{1}{2}\mathbf{x}^T\mathcal{H}\mathbf{x} + \mathbf{c}^T\mathbf{x} + f \\ u.c. : \\ \mathcal{A}\,\mathbf{x} = \mathbf{b} \\ \mathbf{x}_{min} \leq \mathbf{x} \leq \mathbf{x}_{max} \end{cases} \tag{4.26}$$

Compared to (4.21), the decision variable $\mathbf{x}$ will contain the input vector $\mathbf{U}$ as well as the error vector $\mathbf{e}$. But contrary to the case of the LP, it is not necessary to carry out a change of variable because the form that can be solved by the QP algorithms admits the possibility of having decision variables with negative values. Thus the cost function can be directly put in the appropriate form:

$$J_l = ||\mathbf{e}||_2^2 = \sum_{n_a} {e_i}^2 = \mathbf{e}^T\mathbb{I}_{n_a}\mathbf{e} = \frac{1}{2}\mathbf{e}^T\left(2\mathbb{I}_{n_a}\right)\mathbf{e} \tag{4.27}$$

By comparing (4.21) with (4.26), the decision vector is readily determined: $\mathbf{x} = \begin{bmatrix}\mathbf{U} & \mathbf{e}\end{bmatrix}^T$. Thus, (4.21) embraces the form of (4.26) whose parameters are then:

$$\begin{array}{l} \mathbf{x} = \begin{bmatrix}\mathbf{U} & \mathbf{e}\end{bmatrix}^T \in \mathbb{R}^{n_u+n_a} \\ \mathcal{H} = 2\begin{bmatrix}\mathbb{O}_{n_u} & \\ & \mathbb{I}_{n_a}\end{bmatrix} \in \mathcal{M}_{n_u+n_a}(\mathbb{R}) \\ \mathbf{c}^T = \begin{bmatrix}\mathbb{O}_{1,n_u+n_a}\end{bmatrix} \in \mathbb{R}^{n_u+n_a} \qquad f = 0 \\ \mathcal{A} = \begin{bmatrix}M & -\mathbb{I}_{n_a}\end{bmatrix} \in \mathcal{M}_{n_a,n_u+n_a}(\mathbb{R}) \\ \mathbf{b} = \begin{bmatrix}\mathbf{a_d}\end{bmatrix} \in \mathbb{R}^{n_a} \\ \mathbf{x}_{min} = \begin{bmatrix}\mathbf{U}_{min} & -\mathbf{e}_{max}\end{bmatrix} \in \mathbb{R}^{n_u+n_a} \\ \mathbf{x}_{max} = \begin{bmatrix}\mathbf{U}_{max} & \mathbf{e}_{max}\end{bmatrix} \in \mathbb{R}^{n_u+n_a} \end{array} \tag{4.28}$$

The QP algorithms solve the optimization problem (4.28) at each control sampling period like in the case of the LP. At each sampling period, a value of the input vector $\mathbf{U}^*$ is determined that can directly be applied to the system.

Remark: Note that whether one uses the LP or the QP in order to solve the control allocation optimization problem, the optimization algorithms are designed such that it is sufficient to provide them with M, $\mathbf{a_d}$, $\mathbf{U}_{min}$ and $\mathbf{U}_{max}$. Hence the fact that implementing EMOn control allocation methods is made easy.

Real time classical control allocation architecture

Let $\mathbb{S}$ be the system defined by the state-space equation (4.1). This system is considered to be controlled by a control allocation algorithm, the resulting closed-loop is displayed on Figure 4.1. It is mentioned that the control computations are done with discrete controllers since the allocation will require an optimization executed in real time on an embeded computer.

Note that what is considered here as *classical* control allocation is a control allocation which in essence is built to perform the allocation from a reference model. Not all versions of the control allocation take into account a reference model, as it is the case in the work of [Dur93]. However, from the first formulations of model inversion-based allocation methods [SGE90], a reference model is already used in the allocation process. It is in this sense that the name *classical* is given to control allocation here. Taking into account this reference model also allows a broader study in our case.

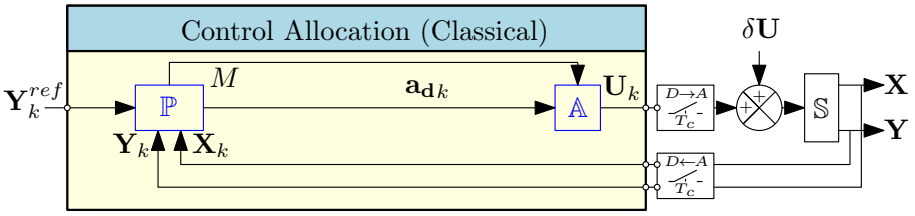

Figure 4.1: Control allocation classical architecture.

As the block diagram shows, the control allocation can be conceptually divided into two blocks in real time:

- A first step $\mathbb{P}$ for $\mathbb{P}$*reparation* or $\mathbb{P}$*reparator* block that updates the value of $\mathbf{a_d}$ at each time step and M in case the considered system is nonlinear or temporally varying and requires an update of M also. The model of the system used in order to compute M and $\mathbf{a_d}$, according to (4.8) and (4.10) respectively, can also adapt to system variations, which means that the control system is capable of reconfiguration. Even though in the major cases the limitations of a system may not vary over time, it is still possible to use this preparation step to update $\mathbf{U}_{min}$ and $\mathbf{U}_{max}$ as well if needed.
- A second step $\mathbb{A}$ for $\mathbb{A}$*llocation* or $\mathbb{A}$*llocator* that will determine the control vector $\mathbf{U}$ to apply to the system from the knowledge of M, $\mathbf{a_d}$ and the control boundaries. This block is the core of the control allocation. It uses a method from one of the three families (MIB, EMOn or EMOff) in order to compute the control. In the case of the work presented here, this block mainly uses the EMOn method, implementing the LP and QP as explained in the two previous paragraphs.

To analyze the behavior of the system in closed-loop according to the classical control allocation, an assumption is made:

Assumption 10. *The Allocation block in Figure 4.1 guarantees the verification of* (2) *at any time. Let* $M\mathbf{U}_k = \mathbf{a_d}_k$ *be true for all time step* k.

The definition of the classical control allocation architecture can then be stated by specifying that this definition requires the allocation equation to be fully verified at all time.

Definition 6. *The classical control allocation method is defined according to the following when Assumption 10 holds true:*

$$\begin{cases} M\,\mathbf{U}_k = \mathbf{a_d}_k \\ \mathbf{a_d}_k = \underbrace{\left[F_M\mathbf{Y}_k + G_M\mathbf{Y^{ref}}_k\right]}_{\text{Reference Model}} - C\left(F\mathbf{X}_k + H\mathbf{E}_k\right) \end{cases} \tag{4.29}$$

The ***reference model*** (4.9) *stands for the dynamic behavior that one wants to give to the system in closed-loop, it can be freely tuned to place desired poles for example.*

Assuming that Assumption 10 holds, it is possible to prove that:

Theorem 1 (Classical control allocation closed-loop behavior)**.** *The transfer function matrix linking the output reference* $\mathbf{Y}^{ref}$ *and the input matched disturbance* $\delta\mathbf{U}$ *to* $\mathbf{Y}$ *in closed-loop is* $\mathbf{Y}(z) = T_{CL}(z)\mathbf{Y}^{ref}(z) + T_{SU}(z)\delta\mathbf{U}(z)$*, where the closed-loop transfer function is* $T_{CL}(z) = \left[z\mathbb{I}_{n_y} - F_M\right]^{-1} G_M$ *and the sensitivity matrix is* $T_{SU}(z) = \left[z\mathbb{I}_{n_y} - F_M\right]^{-1} M$*. The closed-loop*

dynamics are of order n_y and are governed by the F_M and G_M matrices from the reference model (4.9). *This matrix F_M specifies the poles in closed-loop and no zero influences the dynamics. The static gain is specified by G_M.*

Proof. According to the state-space model of the system under consideration (4.1) in addition with the input matched disturbance $\delta\mathbf{U}$ depicted on Figure 4.1, it is shown that:

$$\mathbf{Y}_{k+1} = CF\mathbf{X}_k + CG\left(\mathbf{U}_k + \delta\mathbf{U}_k\right) + CH\mathbf{E}_k \tag{4.30}$$

Assumption 10 holding true, substituting $CG\mathbf{U}_k$ for $M\mathbf{U}_k$ from 4.11 in (4.30) gives:

$$\mathbf{Y}_{k+1} = C(F\mathbf{X}_k + H\mathbf{E}_k) + \mathbf{a_d}_k + M\delta\mathbf{U}_k = F_M\mathbf{Y}_k + G_M\mathbf{Y}_k^{ref} + M\delta\mathbf{U}_k \tag{4.31}$$

By applying the z-transform with zero initial conditions, this equation becomes:

$$\left[z\mathbb{I}_{n_y} - F_M\right]\mathbf{Y}(z) = G_M\mathbf{Y}^{ref}(z) + M\delta\mathbf{U}(z) \tag{4.32}$$

Thus, the closed-loop behavior is found:

$$\mathbf{Y}(z) = \left[z\mathbb{I}_{n_y} - F_M\right]^{-1} G_M\mathbf{Y}^{ref}(z) + \left[z\mathbb{I}_{n_y} - F_M\right]^{-1} M\delta\mathbf{U}(z) \tag{4.33}$$

The transfer matrices are obtained:

$$\begin{array}{l} T_{CL}(z) = \left[z\mathbb{I}_{n_y} - F_M\right]^{-1} G_M \\ T_{SU}(z) = \left[z\mathbb{I}_{n_y} - F_M\right]^{-1} M \end{array} \tag{4.34}$$

When no disturbance is acting on the system, the closed-loop behavior becomes:

$$\mathbf{Y}(z) = \left[z\mathbb{I}_{n_y} - F_M\right]^{-1} G_M\mathbf{Y}^{ref}(z) = T_{CL}(z)\mathbf{Y}^{ref}(z) \tag{4.35}$$

■

Equation (4.35) shows that the closed-loop behavior is the one of the reference model (4.9), which means having n_y poles and no zero in closed-loop. It is also of interest to evaluate the ability of such control allocation to ensure a null static error.

Theorem 2 (Classical control allocation static error and disturbance rejection)**.** *The use of the classical control allocation architecture ensures zero static error under the condition that $G_M = \mathbb{I}_{n_y} - F_M$ when no disturbance is in play. No disturbance rejection is ensured for a step-input disturbance: $\varepsilon_\mathbf{s} = 0$ for $\mathbf{y}^{ref}(t) = \mathcal{H}(t)\ \mathbf{Y}_0 \in \mathbb{R}^{n_y}$ and $\delta\mathbf{u}(t) = \mathcal{H}(t)\ \delta\mathbf{U}_0 \in \mathbb{R}^{n_u}$ where $\mathcal{H}(t)$ is the Heaviside step function. $\mathbf{Y}_0$ and $\delta\mathbf{U}_0$ are vectors containing constant components over time.*

Proof. For a step-input reference $\mathbf{y}^{ref}(t) = \mathcal{H}(t)\ \mathbf{Y}_0$, the z-transform gives $\mathbf{Y}^{ref}(z) = z\ \mathbf{Y}_0\ (z-1)^{-1}$ and accordingly, the step-input disturbance $\delta\mathbf{u}(t) = \mathcal{H}(t)\ \delta\mathbf{U}_0$ brings $\delta\mathbf{U}(z) = z\ \delta\mathbf{U}_0\ (z-1)^{-1}$. From Theorem 1, $\mathbf{Y}^{ref}(z)$ can thus be derived:

$$\mathbf{Y}(z) = T_{CL}(z)\mathbf{Y}^{ref}(z) + T_{SU}(z)\delta\mathbf{U}(z) \tag{4.36}$$

The use of the final value theorem enables to derive the static error:

$$\begin{array}{l} \varepsilon_\mathbf{s} = \lim_{z\to1}(z-1)\left(\mathbf{Y}^{ref}(z) - \mathbf{Y}(z)\right) \\ \quad = \lim_{z\to1}(z-1)\left[(\mathbb{I}_{n_y} - T_{CL}(z))\mathbf{Y}^{ref}(z) - T_{SU}(z)\delta\mathbf{U}(z)\right] \\ \quad = \lim_{z\to1} z\left[(\mathbb{I}_{n_y} - T_{CL}(z))\mathbf{Y}_0 - T_{SU}(z)\delta\mathbf{U}_0\right] \\ \quad = \left[(\mathbb{I}_{n_y} - \left[\mathbb{I}_{n_y} - F_M\right]^{-1} G_M)\mathbf{Y}_0 - \left[\mathbb{I}_{n_y} - F_M\right]^{-1} M\delta\mathbf{U}_0\right] \end{array} \tag{4.37}$$

Thus, when no distrubance is considered, the static error becomes:

$$\varepsilon_{\mathbf{s}} = \left(\mathbb{I}_{n_y} - \left[\mathbb{I}_{n_y} - F_M\right]^{-1} G_M\right) \mathbf{Y}_0 = 0 \quad \underset{G_M = \mathbb{I}_{n_y} - F_M}{\uparrow} \tag{4.38}$$

Assume that $G_M = \mathbb{I}_{n_y} - F_M$, the substitution in the previous equation turns the static error into zero. However, when the disturbance is considered, whatever may the reference model matrices be, the static error remains non-zero:

$$\varepsilon_{\mathbf{s}} = -\left[\mathbb{I}_{n_y} - F_M\right]^{-1} M \delta \mathbf{U}_0 \tag{4.39}$$

■

The first observation is that classical allocation control methods guarantee a null static error only when the system does not encounter any disturbance and the relation $G_M = \mathbb{I}_{n_y} - F_M$ between the reference model matrices is satisfied.

In the first control allocation implementations for the control of the MMC, the method used will be initially based on classical allocation methods. However, in view of the properties of these methods that have just been highlighted, a performance improvement work is proposed. This enhancement will be evaluated in the context of the MMC in order to quantify the benefit of its use.

4.C Control allocation methods with a transparent integral compensator

As shown by Theorem 2, the conditions allowing classical allocation methods to guarantee a zero static deviation are quite restrictive: one must both tune the reference model (4.9) properly but also have a system which is not subject to external input matched disturbances. In a large part of physical systems it is however possible to encounter external disturbances influencing the behavior of the system. In the privileged application fields of the control allocation to date, there is one where this applies particularly: aeronautics. Indeed, an airplane can be subjected to wind gusts acting on its trajectory and making it deviate from its objective. It would be then interesting to have a control allocation architecture which in its essence feature the possibility to counteract those disturbances.

During the various tests carried out in simulation and in HIL, it was observed that the tracking of the currents in the MMC, explained in detail in Chapter 5, was not always guaranteed with the desired performances when having adapted the classical allocation methods. For example, with respect to the accuracy of the current control, it was observed that a static deviation of about 5% remained in steady-state. The control being a discrete control, the zero-order-hold has the effect of introducing a delay in the closed-loop, having as a consequence to negatively influence the performances of the control such as the static deviation. However, given the sampling period, this difference should be relatively small and less than 5%. Given the known sampling period $T_c = 250$ µs and the fundamental frequency of the currents $\omega_o = 2\ \pi\ 50$ rad/s, the maximum current error related to the delay introduced by the zero-order-hold is evaluated to be around 0.3%. This makes a difference of 4.7%, with the measured error, that is to say a non negligible margin of improvement.

To contribute to extend the operating conditions in which the control allocation can guarantee a null static error and reduce the error observed in the current control of the MMC, the idea

proposed here is therefore to add an integral action to the control allocation methods with the objective that it integrates *fully* and *readily* to the already existing methods; in order to design a control allocation which has an integral compensator directly built-in. Allocation methods essentially do not use integral actions. However, some works have proposed their addition in an externalized way. The addition of an integrator in control laws using control allocation was considered in [VB94; Buf97; Zac09; Kre+21]. Compared to these works, the novelty of the approach presented here is the implementation of an integrator direclty into the control method without inducing any changes to the initial closed-loop dynamic behavior.

The work done in the context of adding an integral action has led to the design of different control allocation architectures, the most successful of which are proposed in this document. Regarding the results obtained with the latter, exploration perspectives are still the subject of active work. The first architecture that is introduced is the CAI-II for which a detailed analysis of the closed-loop behavior will be conducted before presenting a first tuning method. Then the CAI-IPII architecture will be proposed to explore the possibility of giveing new operating properties. The relationship between the CAI-II and the CAI-IPII will then be highlighted before proceeding to simulations of these architectures. The benefits of the control allocation with integral compensator over classical control allocation are demonstrated using the simulation of a system involving multiple power electronic converters. The choice of not doing simulations on the MMC directly is part of the will to perform a first proof-of-concept on a simpler system but which also has an overactuated character that the allocation methods are well suited to deal with.

4.C.1 Control allocation with integral compensator - indirect injection

The first idea to improve the performance is to add an integral action. After several tests it was identified that the best strategy was the indirect injection of the integral action into the control allocation. This indirect injection represents the fact that the vector produced by the integral action is added to the desired action vector $\mathbf{a_d}$, as opposed to the direct injection which would add this same integral action to the control vector $\mathbf{U}$ before sending it to the system. In this way, the architecture with indirect injection is drawn Figure 4.2. Note that switching from control allocation to control allocation with integral compensator does not change the input and output signals that the controller needs: from a higher level control point of view, adding the integral action to the control allocation is done seamlessly.

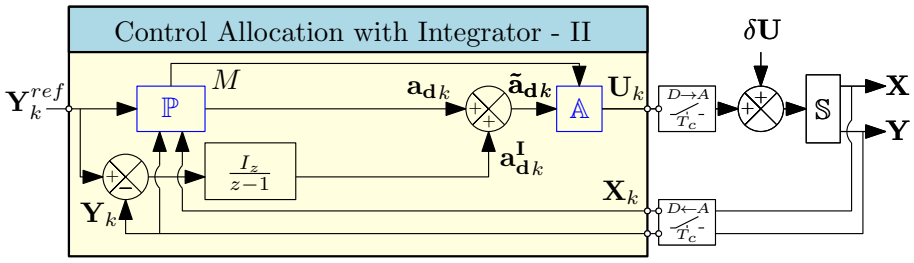

Figure 4.2: Control allocation with integral compensator - indirect injection architecture. Blocks that are shared with the classical control allocation architecture are in blue.

The integration of this integral action modifies the objective that the $\mathbb{A}$ allocation must guarantee. Indeed, it is no longer the allocation equation from Definition 2 that must be satisfied, but the latter is updated as follows:

Definition 7. *The control allocation with integral compensator equation is defined by:*

$$\mathcal{M}(\mathbf{U}) = \tilde{\mathbf{a}}_{\mathbf{d}} = \mathbf{a}_{\mathbf{d}} + \mathbf{a}_{\mathbf{d}}^{\mathbf{I}} \tag{4.40}$$

To perform the analysis of the closed-loop system using the CAI-II, the complementary assumption to the Assumption 10 is stated here:

Assumption 11. *The Allocation block in Figure 4.2 and Figure 4.3 guarantees the verification of Definition 7 at any time. Let $M\mathbf{U}_k = \tilde{\mathbf{a}}_{\mathbf{d}k} = \mathbf{a}_{\mathbf{d}k} + \mathbf{a}_{\mathbf{d}k}^{\mathbf{I}}$ be true for all time step k.*

From the architecture of Figure 4.2, it is then possible to deduce the definition of the CAI-II by taking advantage of the previous assumption and the definition of the updated allocation equation:

Definition 8. *The novel CAI-II method is defined according to the following:*

$$\begin{cases} M\,\mathbf{U}_k = \mathbf{a}_{\mathbf{d}k} + \mathbf{a}_{\mathbf{d}k}^{\mathbf{I}} = \tilde{\mathbf{a}}_{\mathbf{d}k} \\ \mathbf{a}_{\mathbf{d}k} = \left[F_M \mathbf{Y}_k + G_M {\mathbf{Y}^{ref}}_k\right] - C\left(F\mathbf{X}_k + H\mathbf{E}_k\right) \\ \mathbf{a}_{\mathbf{d}k}^{\mathbf{I}} = I_z \mathbf{X}_{\mathbf{R}k} \\ \mathbf{X}_{\mathbf{R}k+1} = \mathbf{X}_{\mathbf{R}k} + \left({\mathbf{Y}^{ref}}_k - \mathbf{Y}_k\right) \end{cases} \tag{4.41}$$

Closed-loop behavior analysis of the CAI-II

Taking advantage of the presentation made of the CAI-II, the analysis of the transfer functions in closed-loop is conducted to evaluate the response to an output reference as well as to an input matched disturbance.

Theorem 3 (Novel CAI-II closed-loop behavior)**.** *The transfer function matrix linking the output reference $\mathbf{Y}^{ref}$ and the input matched disturbance $\delta\mathbf{U}$ to $\mathbf{Y}$ in closed-loop is $\mathbf{Y}(z) = T_{CL}(z)\mathbf{Y}^{ref}(z) + T_{SU}(z)\delta\mathbf{U}(z)$ where the closed-loop transfer function is $T_{CL}(z) = \left[z^2\mathbb{I}_{n_y} - (F_M + \mathbb{I}_{n_y})z + (F_M + I_z)\right]^{-1}\left[(z-1)G_M + I_z\right]$ and the sensitivity matrix is $T_{SU}(z) = \left[z^2\mathbb{I}_{n_y} - (F_M + \mathbb{I}_{n_y})z + (F_M + I_z)\right]^{-1}(z-1)M$. The closed-loop dynamics are of order $2n_y$ and are governed by the F_M, G_M and I_z matrices.*

Proof. According to the state-space model of the system under consideration (4.1) in addition with the input matched disturbance $\delta\mathbf{U}$ depicted on Figure 4.2, it is shown that:

$$\mathbf{Y}_{k+1} = CF\mathbf{X}_k + CG\left(\mathbf{U}_k + \delta\mathbf{U}_k\right) + CH\mathbf{E}_k \tag{4.42}$$

Assumption 11 holding true, substituting $CG\mathbf{U}_k$ for $M\mathbf{U}_k$ from (4.41) in (4.42) gives:

$$\mathbf{Y}_{k+1} = C(F\mathbf{X}_k + H\mathbf{E}_k) + \mathbf{a}_{\mathbf{d}k} + \mathbf{a}_{\mathbf{d}k}^{\mathbf{I}} + M\delta\mathbf{U}_k = F_M\mathbf{Y}_k + G_M\mathbf{Y}_k^{ref} + \mathbf{a}_{\mathbf{d}k}^{\mathbf{I}} + M\delta\mathbf{U}_k \tag{4.43}$$

By applying the z-transform with zero initial conditions to this equation and to the definition of $\mathbf{a}_{\mathbf{d}k+1}^{\mathbf{I}}$ in (4.41), this equation becomes:

$$\left[z\mathbb{I}_{n_y} - F_M\right]\mathbf{Y}(z) = G_M\mathbf{Y}^{ref}(z) + (z-1)^{-1}I_z\left(\mathbf{Y}^{ref}(z) - \mathbf{Y}(z)\right) + M\delta\mathbf{U}(z) \tag{4.44}$$

Applying a left multiplication by $(z-1)$ reads:

$$\left[(z-1)\left[z\mathbb{I}_{n_y} - F_M\right] + I_z\right]\mathbf{Y}(z) = \left[(z-1)G_M + I_z\right]\mathbf{Y}^{ref}(z) + (z-1)M\delta\mathbf{U}(z) \tag{4.45}$$

Thus, the closed-loop behavior is found:

$$\mathbf{Y}(z) = T_{CL}(z)\mathbf{Y}^{ref}(z) + T_{SU}(z)\delta\mathbf{U}(z) \tag{4.46}$$

where the transfer matrices are defined:

$$\begin{aligned} T_{CL}(z) &= \left[z^2\mathbb{I}_{n_y} - (F_M + \mathbb{I}_{n_y})z + (F_M + I_z)\right]^{-1}\left[(z-1)G_M + I_z\right] \\ T_{SU}(z) &= \left[z^2\mathbb{I}_{n_y} - (F_M + \mathbb{I}_{n_y})z + (F_M + I_z)\right]^{-1}(z-1)M \end{aligned} \tag{4.47}$$

When no disturbance is acting on the system, the closed-loop behavior becomes:

$$\mathbf{Y}(z) = \left[z^2\mathbb{I}_{n_y} - (F_M + \mathbb{I}_{n_y})z + (F_M + I_z)\right]^{-1}\left[(z-1)G_M + I_z\right]\mathbf{Y}^{ref}(z) \tag{4.48}$$

■

The closed-loop transfer function then shows that the addition of the integral action leads to the appearance of zeros in closed-loop, which is normal and expected with the added integral action. The placement of these zeros can then be adjusted by G_M and I_z. However it is important to note that I_z, along with F_M, is also used to adjust the pole placement of the closed-loop. More details are given in the next paragraph about pole placement and setting the F_M, G_M and I_z matrices accordingly to the desired poles.

Obtaining the transfer functions in closed-loop allows, as for the classical control allocation, to evaluate the disturbances rejection and static error cancellation capabilities, the following theorem specifies its characteristics.

Theorem 4 (Novel CAI-II static error and disturbance rejection)**.** *The use of the control allocation with integral compensator indirect injection architecture ensures zero static error and disturbance rejection is ensured for a step-input disturbance:* $\varepsilon_{\mathbf{s}} = 0$ *for* $\mathbf{y}^{ref}(t) = \mathcal{H}(t)\ \mathbf{Y}_0 \in \mathbb{R}^{n_y}$ *and* $\delta\mathbf{u}(t) = \mathcal{H}(t)\ \delta\mathbf{U}_0 \in \mathbb{R}^{n_u}$ *where* $\mathcal{H}(t)$ *is the* Heaviside *step function.* $\mathbf{Y}_0$ *and* $\delta\mathbf{U}_0$ *are vectors containing constant components over time.*

Proof. For a step-input reference $\mathbf{y}^{ref}(t) = \mathcal{H}(t)\ \mathbf{Y}_0$, the z-transform gives $\mathbf{Y}^{ref}(z) = z\ \mathbf{Y}_0\ (z-1)^{-1}$ and accordingly, the step-input disturbance $\delta\mathbf{u}(t) = \mathcal{H}(t)\ \delta\mathbf{U}_0$ brings $\delta\mathbf{U}(z) = z\ \delta\mathbf{U}_0\ (z-1)^{-1}$. From Theorem 3, $\mathbf{Y}^{ref}(z)$ can thus be derived:

$$\mathbf{Y}(z) = T_{CL}(z)\mathbf{Y}^{ref}(z) + T_{SU}(z)\delta\mathbf{U}(z) \tag{4.49}$$

The use of the final value theorem enables to derive the static error:

$$\begin{aligned} \varepsilon_{\mathbf{s}} &= \lim_{z\to 1}(z-1)\left(\mathbf{Y}^{ref}(z) - \mathbf{Y}(z)\right) \\ &= \lim_{z\to 1}(z-1)\left[(\mathbb{I}_{n_y} - T_{CL}(z))\mathbf{Y}^{ref}(z) - T_{SU}(z)\delta\mathbf{U}(z)\right] \\ &= \lim_{z\to 1} z\left[(\mathbb{I}_{n_y} - T_{CL}(z))\mathbf{Y}_0 - T_{SU}(z)\delta\mathbf{U}_0\right] \\ &= \left[(\mathbb{I}_{n_y} - {I_z}^{-1}I_z)\mathbf{Y}_0 - 0\cdot M\delta\mathbf{U}_0\right] = 0 \end{aligned} \tag{4.50}$$

Thus, the proposed method removes the static error and ensures disturbance rejection. ■

Contrary to the classical allocation method, it is therefore possible to conclude that the addition of an integral compensator modifies the closed-loop behavior in such a way that the cancellation of the static deviation as well as the disturbance rejection is ensured under very little requirements. It is possible to set the parameters G_M and F_M defining the reference model independently.

As for the control allocation previously, the static error rejection guaranteed by this theorem is nevertheless conditioned by the fact that the desired action vector does not become unrealizable, in which case the analysis performed is no longer valid.

A first tuning method approach for the CAI-II

The properties concerning the static error and the disturbance are obtained without any condition on the tunable parameters of the architecture: F_M, G_M and I_z. A first simple method to adjust these matrices is proposed here to take advantage of this freedom and the influence of these gains on the behavior of the closed-loop is also evaluated.

For this simplified approach, it is considered that the matrices F_M, G_M and I_z are diagonal and their terms are respectively noted f_j, g_j and I_{z_j}. Each of these matrices has n_y diagonal terms.

Using the definition (4.41), it is possible to formulate $\mathbf{a}^{\mathbf{I}}_{\mathbf{d}\,k+1}$. Moreover, the proof of Theorem 3 gives the expression of $\mathbf{Y}_{k+1}$. The combination of these two equations allows one to deduce the state space model of the closed-loop system:

$$\begin{bmatrix} \mathbf{Y}_{k+1} \\ \mathbf{a}^{\mathbf{I}}_{\mathbf{d}\,k+1} \end{bmatrix} = \begin{bmatrix} F_M & \mathbb{I}_{n_y} \\ -I_z & \mathbb{I}_{n_y} \end{bmatrix} \begin{bmatrix} \mathbf{Y}_k \\ \mathbf{a}^{\mathbf{I}}_{\mathbf{d}\,k} \end{bmatrix} + \begin{bmatrix} G_M \\ I_z \end{bmatrix} {\mathbf{Y}^{ref}}_k = F_{CL} \begin{bmatrix} \mathbf{Y}_k \\ \mathbf{a}^{\mathbf{I}}_{\mathbf{d}\,k} \end{bmatrix} + G_{CL} {\mathbf{Y}^{ref}}_k \tag{4.51}$$

F_M and I_z being diagonal matrices, the poles of the closed-loop are trivially determined from F_{CL}. The latter being of size $2n_y$, the $2n_y$ poles are defined by:

$$\forall j \in [\![1; n_y]\!],\ {p_j}_{1,2} = \frac{(1+f_j) \pm \sqrt{(1-f_j)^2 - 4I_{z_j}}}{2} \tag{4.52}$$

Using the closed-loop state-space model is another approach to determining the transfer function. This transfer function reveals the presence of zeros in the closed-loop. In the case of diagonal matrices, these zeros are expressed:

$$\forall j \in [\![1; n_y]\!],\ z_j = 1 - \frac{I_{z_j}}{g_j} \tag{4.53}$$

From the expression of the poles and zeros obtained, it appears that the three matrices F_M, G_M and I_z make it possible to adjust the dynamics of the system. In the current stage the architecture has $3n_y$ gains to set for these last three matrices and $3n_y$ poles and zeros, so it would seem possible to realize a complete pole and zero placement. Suppose then that it is desired to impose the poles ${p_j}^*_{1,2}$ and the zeros ${z_j}^*$ in closed-loop. The setting of the matrix gains is then done in the following way:

$$First\ Tuning : \begin{cases} f_j = 2\,\mathfrak{Re}({p_j}^*_{1,2}) - 1 \\ I_{z_j} = \mathfrak{Im}({p_j}^*_{1,2})^2 + \left(1 - \mathfrak{Re}({p_j}^*_{1,2})\right)^2 \\ g_j = \frac{I_{z_j}}{1-{z_j}^*} \end{cases} \tag{4.54}$$

With such a setting it is therefore possible to place the poles on the whole complex plane. However, only a placement of real zeros is possible. It is important to note that regarding T_{CL} and T_{SU}, this setting of the matrix gains will impose both the tracking dynamics as well as the disturbance rejection dynamics which have the same poles.

It is specified that the tuning method of the gains of the CAI-II will be beneficially used to implement the control allocation with integral compensator for the control of the currents (high-level

control) of the MMC in the following chapter Chapter 5.

As it has been shown, the architecture proposed here constrains to have a certain pole placement identical for the tracking dynamics of the disturbance rejection dynamics, it is then proposed to explore another architecture of control allocation with integral compensator.

4.C.2 Control allocation with integral compensator - integral proportionnal indirect injection

The modification of the CAI-II which is proposed here is to add a proportional gain judiciously placed with the objective - for the integral action - of not bringing a zero in closed-loop. Therefore the gain K_z is placed after a summator achieving the difference between the output of the integral action and the measurement made of the output of the system $\mathbf{Y}$ as presented in Figure 4.3.

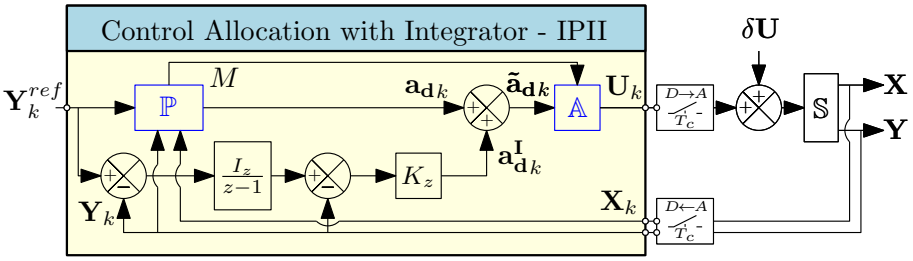

Figure 4.3: Control allocation with integral compensator - integral proportionnal indirect injection architecture. Blocks shared with the classical control allocation architecture are in blue.

In a similar way to the definition of the CAI-II, based on its block-diagram and under the Assumption 11, the new architecture CAI-IPII is defined:

Definition 9. *The novel CAI-IPII method is defined according to the following:*

$$\begin{cases} M\ \mathbf{U}_k = \mathbf{a_d}_k + \mathbf{a}^{\mathbf{I}}_{\mathbf{d}k} = \tilde{\mathbf{a}}_{\mathbf{d}k} \\ \mathbf{a_d}_k = \left[F_M \mathbf{Y}_k + G_M {\mathbf{Y}^{ref}}_k\right] - C\left(F\mathbf{X}_k + H\mathbf{E}_k\right) \\ \mathbf{a}^{\mathbf{I}}_{\mathbf{d}k} = K_z\left(I_z \mathbf{X}_{\mathbf{R}k} - \mathbf{Y}_k\right) \\ \mathbf{X}_{\mathbf{R}k+1} = \mathbf{X}_{\mathbf{R}k} + \left({\mathbf{Y}^{ref}}_k - \mathbf{Y}_k\right) \end{cases} \tag{4.55}$$

Closed-loop behavior analysis of the CAI-IPII

From the definition of the CAI-IPII, the analysis of the transfer functions in closed-loop is done to evaluate the behavior obtained for the system and how it differs from the one given by the CAI-II.

Theorem 5 (Novel CAI-IPII closed-loop behavior)**.** *The transfer function matrix linking the output reference $\mathbf{Y}^{ref}$ and the input matched disturbance $\delta\mathbf{U}$ to $\mathbf{Y}$ in closed-loop is $\mathbf{Y}(z) = T_{CL}(z)\mathbf{Y}^{ref}(z) + T_{SU}(z)\delta\mathbf{U}(z)$ where the closed-loop transfer function is $T_{CL}(z) = \left[z^2\mathbb{I}_{n_y} - (F_M - K_z + \mathbb{I}_{n_y})z + (F_M + K_z(I_z - \mathbb{I}_{n_y}))\right]^{-1}\left[(z-1)G_M + K_z I_z\right]$ and the sensitivity matrix is $T_{SU}(z) = \left[z^2\mathbb{I}_{n_y} - (F_M - K_z + \mathbb{I}_{n_y})z + (F_M + K_z(I_z - \mathbb{I}_{n_y}))\right]^{-1}(z-1)M$. The closed-loop dynamics are of order $2n_y$ and are governed by the F_M, G_M and I_z matrices.*

Proof. According to the state-space model of the system under consideration (4.1) in addition with the input matched disturbance $\delta\mathbf{U}$ depicted on Figure 4.3, the approach adopted for the

demonstration of the current theorem is exaclty the same than for Theorem 3. From the sole knowledge of (4.55), the Assumption 11, and applying the z-transform, the closed-loop behavior is found to be:

$$\mathbf{Y}(z) = T_{CL}(z)\mathbf{Y}^{ref}(z) + T_{SU}(z)\delta\mathbf{U}(z) \tag{4.56}$$

where the transfer matrices are defined:

$$\begin{aligned} T_{CL}(z) &= \left[z^2\mathbb{I}_{n_y} - (F_M - K_z + \mathbb{I}_{n_y})z + (F_M + K_z(I_z - \mathbb{I}_{n_y}))\right]^{-1}\left[(z-1)G_M + K_z I_z\right] \\ T_{SU}(z) &= \left[z^2\mathbb{I}_{n_y} - (F_M - K_z + \mathbb{I}_{n_y})z + (F_M + K_z(I_z - \mathbb{I}_{n_y}))\right]^{-1}(z-1)M \end{aligned} \tag{4.57}$$

When no disturbance is acting on the system, the closed-loop behavior becomes:

$$\begin{aligned} \mathbf{Y}(z) = \left[z^2\mathbb{I}_{n_y} - (F_M - K_z + \mathbb{I}_{n_y})z + (F_M + K_z(I_z - \mathbb{I}_{n_y}))\right]^{-1} \\ \cdot\left[(z-1)G_M + K_z I_z\right]\mathbf{Y}^{ref}(z) \end{aligned} \tag{4.58}$$

■

The closed-loop transfer function then shows that the addition of the integral action leads to the appearance of zeros in the closed-loop for the CAI-IPII too. The placement of these zeros can then be set by G_M, K_z and I_z. But the matrices K_z and I_z are also involved in the pole placement with F_M. The following paragraph provides a tuning method for these matrices that gives the closed-loop a strong property that is beneficial for the use of such an integral action in the context of the control of a system not only by allocation but more generally, by reference model.

The evaluation of the disturbance rejection and static error cancellation capabilities is made possible by the following theorem which explains the essential information.

Theorem 6 (Novel CAI-IPII static error and disturbance rejection)**.** *The use of the control allocation with integral compensator proportional integral indirect injection architecture ensures zero static error and disturbance rejection is ensured for a step-input disturbance:* $\varepsilon_{\mathbf{s}} = 0$ *for* $\mathbf{y}^{ref}(t) = \mathcal{H}(t)\ \mathbf{Y}_0 \in \mathbb{R}^{n_y}$ *and* $\delta\mathbf{u}(t) = \mathcal{H}(t)\ \delta\mathbf{U}_0 \in \mathbb{R}^{n_u}$ *where* $\mathcal{H}(t)$ *is the* Heaviside *step function.* $\mathbf{Y}_0$ *and* $\delta\mathbf{U}_0$ *are vectors containing constant components over time.*

Proof. For a step-input reference $\mathbf{y}^{ref}(t) = \mathcal{H}(t)\ \mathbf{Y}_0$, the z-transform gives $\mathbf{Y}^{ref}(z) = z\ \mathbf{Y}_0\ (z-1)^{-1}$ and accordingly, the step-input disturbance $\delta\mathbf{u}(t) = \mathcal{H}(t)\ \delta\mathbf{U}_0$ brings $\delta\mathbf{U}(z) = z\ \delta\mathbf{U}_0\ (z-1)^{-1}$. From Theorem 5, $\mathbf{Y}^{ref}(z)$ can thus be derived:

$$\mathbf{Y}(z) = T_{CL}(z)\mathbf{Y}^{ref}(z) + T_{SU}(z)\delta\mathbf{U}(z) \tag{4.59}$$

The use of the final value theorem enables to derive the static error:

$$\begin{aligned} \varepsilon_{\mathbf{s}} &= \lim_{z\to 1}(z-1)\left(\mathbf{Y}^{ref}(z) - \mathbf{Y}(z)\right) \\ &= \lim_{z\to 1}(z-1)\left[(\mathbb{I}_{n_y} - T_{CL}(z))\mathbf{Y}^{ref}(z) - T_{SU}(z)\delta\mathbf{U}(z)\right] \\ &= \lim_{z\to 1} z\left[(\mathbb{I}_{n_y} - T_{CL}(z))\mathbf{Y}_0 - T_{SU}(z)\delta\mathbf{U}_0\right] \\ &= \left[(\mathbb{I}_{n_y} - (K_z I_z)^{-1}(K_z I_z))\mathbf{Y}_0 - 0\cdot M\delta\mathbf{U}_0\right] = 0 \end{aligned} \tag{4.60}$$

Thus, the proposed method removes the static error and ensures disturbance rejection. ■

According to the analysis conducted so far, the CAI-IPII features the same properties than the CAI-II: null static error is ensured and step-input disturbance rejection as well, with no requirements on matrices F_M, G_M, K_z and I_z. The only requirement to meet in order to preseve these properties, is to not saturate the control. However, compared to CAI-II, the CAI-IPII seems to have an additional degree of freedom for the adjustment of the control system: K_z. The question then arises as to whether it would be possible to tune the CAI-IPII in order to provide the system with a given additional feature.

Tuning method turning the CAI-IPII integral action into a transparent compensator

The introduction of K_z having been suggested with the objective of guaranteeing an addition of integral action with no zero, the question arises as to whether it would be possible to make the system adopt the behavior of the reference model in closed-loop, see Definition 1, represented by the following equation (4.61) instead of the full behavior described by (4.58):

$$\left[z\mathbb{I}_{n_y} - F_M\right] \mathbf{Y}(z) = (\mathbb{I}_{n_y} - F_M)\mathbf{Y}^{ref}(z) \tag{4.61}$$

This behavior being that which it is desired to reach, the matrix F_M is thus already determined and imposed in order to guarantee the dynamics that one wants to give to the system.

In closed-loop the behavior of the system with no disturbance is fully described by (4.58) which can be put in the form:

$$\begin{aligned}\left[z^2\mathbb{I}_{n_y} - (F_M - K_z + \mathbb{I}_{n_y})z + (F_M + K_z(I_z - \mathbb{I}_{n_y}))\right] \mathbf{Y}(z) \\ = \left[(z-1)G_M + K_z I_z\right] \mathbf{Y}^{ref}(z) \\ = \left[zG_M + (K_z I_z - G_M)\right] \mathbf{Y}^{ref}(z)\end{aligned} \tag{4.62}$$

The equation (4.61) represents only a behavior governed by n_y poles. It is thus necessary to increase the form representing the desired dynamics to match the possible dynamics (4.62). To do so, the matrix $Z_M \in \mathbb{R}^{n_y \times n_y}$ is introduced, and (4.61) is then updated by multiplying to the left by $\left[z\mathbb{I}_{n_y} - Z_M\right]$:

$$\begin{aligned}&\left[z\mathbb{I}_{n_y} - Z_M\right]\left[z\mathbb{I}_{n_y} - F_M\right] \mathbf{Y}(z) = \left[z\mathbb{I}_{n_y} - Z_M\right](\mathbb{I}_{n_y} - F_M)\mathbf{Y}^{ref}(z) \\ &\qquad\qquad \Longleftrightarrow \\ &\left[z^2\mathbb{I}_{n_y} - (Z_M + F_M)z + Z_M F_M\right] \mathbf{Y}(z) = \left[z(\mathbb{I}_{n_y} - F_M) - Z_M(\mathbb{I}_{n_y} - F_M)\right] \mathbf{Y}^{ref}(z)\end{aligned} \tag{4.63}$$

Note that the transition in the direction from (4.63) to (4.61), which appears to be a pole-zero cancellation of the $z\mathbb{I}_{n_y} - Z_M$ terms on both sides, is possible under the condition that the eigenvalues of Z_M are chosen to be stable and well-damped.

To make the behavior that can be specified through (4.62) take the form (4.61), it is necessary that all factors in front of the monomials of the polynomials of the left and right members of the equations (4.62) and (4.63) be equal. This corresponds to a total of 4 pairs of terms to equalize term by term, that is to say 4 equations for the 3 unknowns[1] G_M, K_z and I_z. It is therefore necessary to determine the 3 unknowns and then to check if the 4^{th} equation is satisfied. By identifying in the left member of the equations (4.61) and (4.62) two first gains are determined, the third gain G_M is determined by equalizing the factors of z in the right member:

$$Transparent\ Tuning : \begin{cases} K_z = \mathbb{I}_{n_y} - Z_M \\ I_z = \mathbb{I}_{n_y} - F_M \\ G_M = \mathbb{I}_{n_y} - F_M \end{cases} \tag{4.64}$$

The 4^{th} equation is then verified:

$$K_z I_z - G_M = (\mathbb{I}_{n_y} - Z_M)(\mathbb{I}_{n_y} - F_M) - (\mathbb{I}_{n_y} - F_M) = -Z_M(\mathbb{I}_{n_y} - F_M) \tag{4.65}$$

Since $-Z_M(\mathbb{I}_{n_y} - F_M)$ corresponds to the last factor in (4.63), it is possible to state that if the gains of the control architecture verify the setting (4.64), then the tracking dynamics adopted in closed-loop are the one described by (4.63), which simplifies to (4.61). This result allows us to deduce the following property:

[1] It is assumed that F_M is already imposed by the dynamics that it is desired for the closed-loop system, see (4.61)

Property 5 (Control allocation with a transparent integral compensator). *Tuning the gains of the control allocation with integral compensator architecture such that* $K_z = \mathbb{I}_{n_y} - Z_M$ *and* $G_M = I_z = \mathbb{I}_{n_y} - F_M$ *turns the closed-loop dynamic behavior of the system into:* $\mathbf{Y}(z) = \left[z\mathbb{I}_{n_y} - F_M\right]^{-1}(\mathbb{I}_{n_y} - F_M)\mathbf{Y}^{ref}(z) = T_{CL}(z)\mathbf{Y}^{ref}(z)$ *under the condition that the eigenvalues of* Z_M *are chosen to be stable and well-damped. The integral action eliminates static error and rejects distrubances without adding any zero and the closed-loop behavior remains unchanged, i.e. the exact same closed-loop behavior than that of the reference model desired (see Definition 1) is preserved. As a matter of fact, the integral compensator becomes transparent to the reference tracking when added to the classical control allocation.*

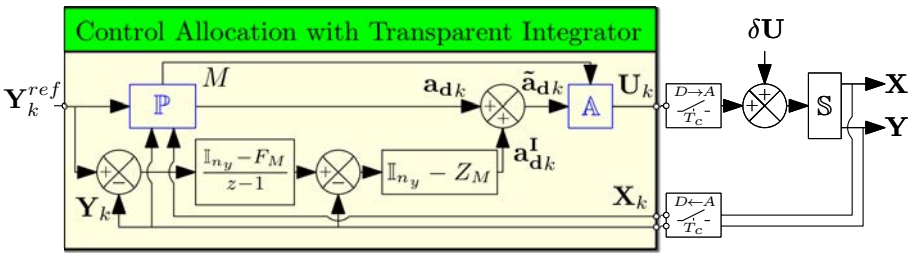

Figure 4.4: Control allocation with transparent integral compensator architecture. Blocks shared with the classical control allocation architecture are in blue.

This setting, which makes the integrator invisible from the outside, is shown in the figure below Figure 4.4. With such a setting, the sensitivity function obtained is expressed as follows:

$$T_{SU}(z) = \left[z\mathbb{I}_{n_y} - Z_M\right]^{-1}\left[z\mathbb{I}_{n_y} - F_M\right]^{-1}(z-1)M \tag{4.66}$$

This shows that it is possible to tune the disturbance rejection dynamics differently from the tracking dynamics by acting on Z_M while respecting the stability conditions.

To summarize this tuning method of the CAI-IPII, the main contributions of the latter are outlined:

- Addition of an integral action that eliminates static error and rejects distrubances
- The integral compensation added is transparent, meaning no zero is added and the closed-loop behavior remains unchanged
- This enhancement of the control allocation is readily done: it can be seamlessly integrated to any existing classical control allocation method
- The disturbance rejection response can be tuned to feature a different dynamic than that of the reference model

Since this tuning method of the CAI-IPII provides strong particular features to the control allocation with integral compensator, it is decided to name it CAI-TII and its related control allocation architecture is fully defined by Figure 4.4.

Relationship between CAI-II and CAI-IPII

Looking at the architectures of Figure 4.2 and Figure 4.3 it is legitimate to ask what is the link between these two possibilities of adding an integral compensator to the control allocation. According to Theorem 3 the closed-loop transfer function for the CAI-II is expressed:

$$T_{CL}{}^{II}(z) = \left[z^2\mathbb{I}_{n_y} - (F_M{}^{II} + \mathbb{I}_{n_y})z + (F_M{}^{II} + I_z{}^{II})\right]^{-1}\left[(z-1)G_M{}^{II} + I_z{}^{II}\right] \tag{4.67}$$

Theorem 5 shows that the closed-loop transfer function for the CAI-IPII is expressed:

$$T_{CL}{}^{IPII}(z) = \left[z^2\mathbb{I}_{n_y} - ({F_M}^{IPII} - {K_z}^{IPII} + \mathbb{I}_{n_y})z + ({F_M}^{IPII} + {K_z}^{IPII}({I_z}^{IPII} - \mathbb{I}_{n_y}))\right]^{-1} \cdot \left[(z-1){G_M}^{IPII} + {K_z}^{IPII}{I_z}^{IPII}\right] \tag{4.68}$$

By comparing the two transmittances it is observed that by choosing the gain matrices such that:

$$\begin{cases} {I_z}^{II} = {K_z}^{IPII}{I_z}^{IPII} \\ {F_M}^{II} = {F_M}^{IPII} - {K_z}^{IPII} \\ {G_M}^{II} = {G_M}^{IPII} \end{cases} \tag{4.69}$$

The transfer functions of the two proposed architectures are found to be equivalent.

This equivalence is explained by the fact that in the $\mathbb{P}$ block of the two architectures, the reference model - defined from F_M and G_M - employs gains that can be freely set. And the addition of K_z appears as a matrix modifying F_M because $-K_z$ is then also in factor of $\mathbf{Y}$. With the gain K_z the factor in front of $\mathbf{Y}$ is changed from F_M to $F_M - K_z$. The setting of F_M and K_z being free, having K_z does not give more freedom to the setting of the closed-loop. On the other hand, K_z will transform the term I_z into K_zI_z. Since I_z is already a free real matrix, adding K_z as a factor does not bring more freedom either. However, conceptually the addition of K_z still has an advantage, it allows one to keep in the $\mathbb{P}$ block the computation of $\mathbf{a_d}$ using the reference model defined from F_M which represents the behavior that it is wished to impose in closed-loop. Without K_z, it would have been necessary to modify the term F_M of this reference model according to (4.69) and it would also have been necessary to modify I_z accordingly.

Thus, to be able to carry out the tuning allowing to reach the CAI-TII behavior, the architecture CAI-IPII will be preferred because it is conceptually more direct. However starting with the architecture CAI-II is a part of the exploration step carried out to answer the raised problem since it introduces a first form of integral compensator direclty built-in the already existing control allocation methods.

4.C.3 Case study: comparing control allocation with CAI-TII on a simple MISO-system

The simulation approach proposed here aims at highlighting the improvements brought by the control allocation with integral compensator compared to the classical methods of control allocation. Among the different architectures of control allocation with integral compensator proposed, CAI-II and CAI-IPII being equivalent, it is the CAI-IPII which is implemented here. The chosen tuning method is the one allowing to give to the control allocation with integral compensator the transparency property, see Property 5. Thus it is the formulation CAI-TII which is compared to the classic control allocation because it is the one which presents the most differences comparatively.

The goal being here to justify the benefits of using the control allocation with integral compensator rather than just the control allocation in a distinct way, the simulations will be performed on a MISO system with 2 redundant inputs. This corresponds to the simplest possible overactuated system, allowing to focus on the behavior of the control allocation.

4.C.3.1 | Introducing the system: a DC-DC conversion system for a single load

In power electronics, to ensure the supply continuity of a DC load, it is possible to design a redundant energy conversion system to supply this load. The redundancy can be done for example by associating sources in parallel, in the case of a system having a single DC load in the form of a RC circuit, the power supply case ensuring a minimum of redundancy calls for two DC - DC converters as presented in Figure 4.5. This type of parallelized interconnection system of multiple converters is becoming increasingly popular for the benefits it provides: increased reliability due to redundancy and stress distribution of components [TV97], ease of maintenance and repair, improved thermal management [HT07], and reduced output ripple by interleaving the phases of PWM. [Cid+11]. Such a system has already been the topic of the use of allocation methods to design its control law as shown by the work of [Kre+21], the global control architecture is then obtained without integrating any integral action at the allocation level.

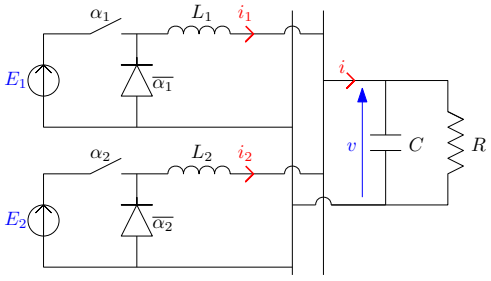

Figure 4.5: Electrical diagram of the 2-input 1-output system for control allocation with integral compensator testing.

$$\forall j \in \{1,2\},\ \frac{di_j}{dt} = \frac{\alpha_j E_j}{L_j} - \frac{v}{L_j} \tag{4.70}$$

$$\frac{dv}{dt} = -\frac{v}{RC} + \frac{i}{C} = -\frac{v}{RC} + \frac{i_1 + i_2}{C} \tag{4.71}$$

By applying Kirchhoff's laws, it is possible to derive the dynamics of each current, i_1 and i_2, as a function of the duty cycles of the two buck converters as well as the dynamics governing the behavior of the voltage v across the load. These dynamics are described by (4.70) and (4.71). The goal of such a system is to guarantee a continuous power supply for the load fed by these converters, so this system must be able to ensure the stability of the voltage v which is then the voltage of the DC bus on which the load is connected. The voltage v is then considered as the output of the system, from which the following state model is deduced:

$$\frac{d}{dt}\begin{bmatrix} i_1 \\ i_2 \\ v \end{bmatrix} = \begin{bmatrix} 0 & 0 & -1/L_1 \\ 0 & 0 & -1/L2 \\ 1/C & 1/C & -1/(RC) \end{bmatrix} \begin{bmatrix} i_1 \\ i_2 \\ v \end{bmatrix} + \begin{bmatrix} E_1/L_1 & 0 \\ 0 & E_2/L2 \\ 0 & 0 \end{bmatrix} \begin{bmatrix} \alpha_1 \\ \alpha_2 \end{bmatrix} \tag{4.72}$$

The quantities on which the control acts here are directly the duty cycles, thus: $\mathbf{U} = [\alpha_1\ \alpha_2]^T$.

Control architecture of the system under consideration

The global control objective of this system is to ensure the stability of the DC bus which means to guarantee the regulation of the voltage v at its reference level v^{ref}. To do so, the architecture will have to adapt the current i by taking it from the voltage sources E_1 and E_2 through the buck converters.

On the one hand, due to the behavior of the system itself and on the other hand due to the dynamics involved in the system, a decoupling of the control of this system is made possible.

Indeed, it is considered here that the time constant RC, and partly the capacitance C, which specifies the rapidity of the voltage dynamics v is slower by at least one order of magnitude than the current dynamics i in open-loop. Moreover, it is decided to tune a closed-loop bandwidth at least one order of magnitude slower for the dynamics of v than for that of i. By doing so, the different dynamics involved in the power converter are decoupled and the current control law can be designed separately from that of the voltage.

With a ratio of one order of magnitude between the different dynamics of the system, we consider that this gap is sufficient to make the Assumption 12.

Assumption 12. *Each control loop considers its downstream loop as instantaneously guaranteeing the tracking of the setpoint sent to it and the upstream loop as being infinitely slower. As a consequence, the possible interactions between the different dynamics involved in the considered system are not taken into account for the design of the control system.*

This allows one to decompose the control architecture as shown in Figure 4.6 into two stages, 1) the outer stage has to control the voltage level v in the bus by specifying to the lower stage the total current reference i^{ref} that it needs in order to guarantee the voltage level v^{ref}, 2) the inner stage that distributes the total current among the different converters and ensures that each current i_j tracks its reference i_j^{ref}. In comparison, this lower stage considers that the quantity v has a very slow evolution.

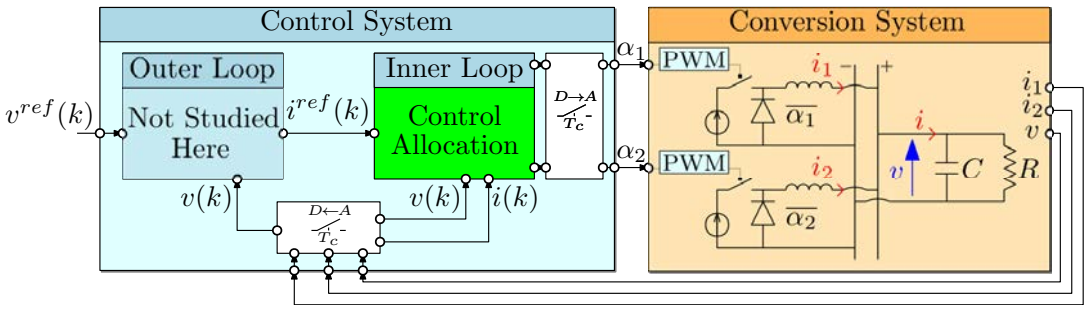

Figure 4.6: Global control architecture of the 2-bucks-1-load system.

The choice to implement the control of this system in two nested loops is also taken because it will allow one to isolate the core of the system which presents an input redundancy; internal loop which thus showcase the particular characteristics to be the privileged place of use of a control allocation method.

Focus on the control allocation for the inner loop

Consequently, in the will to evaluate the particular capabilities of the control allocation with integral compensator, the study and the tests focus on the internal control loop only, see Figure 4.7.

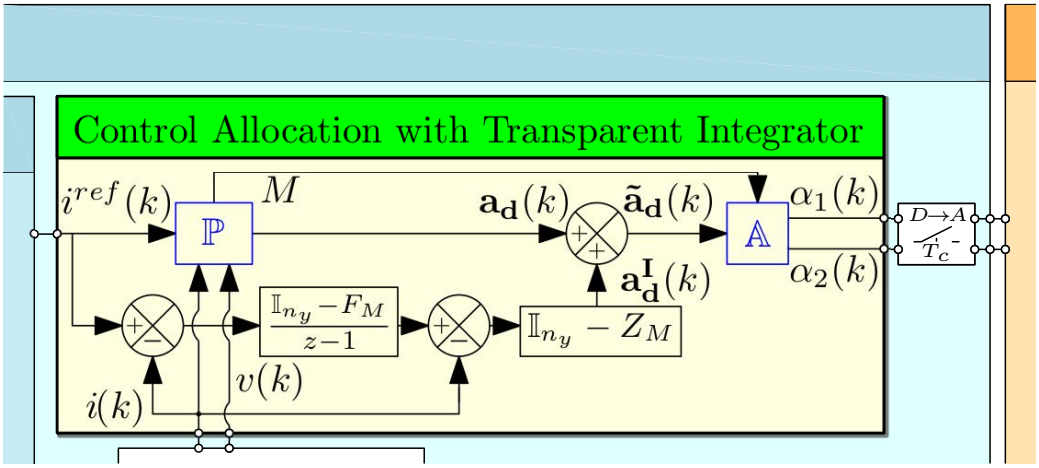

Figure 4.7: 2-bucks-1-load system control architecture inner loop zoom-in.

To do this, the voltage v is then considered constant at the time scale of the inner loop dynamics, and the state-space model representing the dynamics that the inner loop will be in charge of controlling is thus adapted from (4.70). By choosing the state vector $\mathbf{X} = [i_1 \ i_2]^T$ and $\mathbf{U} = [\alpha_1 \ \alpha_2]^T$, the following state-space model is obtained. The current that governs the voltage appearing on the load is the total current that the buck converters can deliver. Its reference is speficied by the outer control loop; for the inner loop it thus stands as the output to control.

$$\begin{cases} \dot{\mathbf{X}} = \begin{bmatrix} E_1/L_1 & 0 \\ 0 & E_2/L_2 \end{bmatrix} \mathbf{U} + \begin{bmatrix} -1/L_1 \\ -1/L_2 \end{bmatrix} v = B\mathbf{U} + \mathbf{E} \\ \mathbf{Y} = i_1 + i_2 = [1 \ \ 1]\mathbf{X} = C\mathbf{X} \end{cases} \tag{4.73}$$

The discretization of (4.73), by using the development from Appendix A, gives (4.74) with $F = \mathbb{I}_2$, $G = BT_s$ and $H = T_s$.

$$\begin{cases} \mathbf{X}(k+1) = \begin{bmatrix} 1 & 0 \\ 0 & 1 \end{bmatrix} \mathbf{X}(k) + T_s \begin{bmatrix} E_1/L_1 & 0 \\ 0 & E_2/L_2 \end{bmatrix} \mathbf{U}(k) + \begin{bmatrix} -T_s/L_1 \\ -T_s/L_2 \end{bmatrix} v(k) \\ \qquad\qquad = \quad F\mathbf{X}(k) \quad + \qquad G\mathbf{U}(k) \qquad + \quad H\mathbf{E}(k) \\ \mathbf{Y}(k) = [1 \ \ 1]\mathbf{X}(k) = C\mathbf{X}(k) \end{cases} \tag{4.74}$$

Having only one output in this system: $n_y = 1$, the input-ouput reference model dynamics in closed-loop will be of order 1, meaning that $F_M \in \mathbb{R}$ and $G_M \in \mathbb{R}$.

By taking advantage of the development of Appendix B, the control allocation problem dedicated to the considered system is deduced, the control problem which will be addressed by the control allocation methods at each time step k is thus the following[1]:

$$\begin{gathered} \left\{ \begin{bmatrix} \frac{E_1}{L_1} & \frac{E_2}{L_2} \end{bmatrix} \begin{bmatrix} \alpha_1(k) \\ \alpha_2(k) \end{bmatrix} = \frac{1}{T_c}\left((F_M - 1)i(k) + G_M i^{ref}(k)\right) - \left(\frac{L_1+L_2}{L_1 L_2}\right) v(k) \;\middle|\; \begin{matrix} 0 \le \alpha_1(k) \le 1 \\ 0.3 \le \alpha_2(k) \le 0.7 \end{matrix} \right\} \\ \Longleftrightarrow \\ \{ M\mathbf{U} = \mathbf{a_d} \quad | \quad \mathbf{U}_{min} \le \mathbf{U} \le \mathbf{U}_{max} \} \end{gathered} \tag{4.75}$$

[1] The duty cycle boundaries are intentionally selected different to account for some operating zone restrictions and are specified in Table 4.1

Compared to the classical control allocation, the control allocation with integral compensator will solve the following control problem that takes into account the integral action within the allocation equation:

$$\left\{ M\mathbf{U} = \mathbf{a_d} + \mathbf{a_d^I} = \tilde{\mathbf{a}}_\mathbf{d} \quad | \quad \mathbf{U}_{min} \leq \mathbf{U} \leq \mathbf{U}_{max} \right\} \tag{4.76}$$

It is decided to use QP to solve the control problem, thus the control algorithm is going to solve the optimization problem minimizing the following cost function:

$$J_2 = ||\mathbf{e}||_2^2 = \begin{cases} ||M\mathbf{U} - \mathbf{a_d}||_2^2, \text{ for the CA case} \\ ||M\mathbf{U} - \tilde{\mathbf{a}}_\mathbf{d}||_2^2, \text{ for the CAI-IPII case} \end{cases} \tag{4.77}$$

In order to implement the classical and integral control allocation methods, one needs to choose the dynamics to impose on the closed-loop system through the parameters F_M, G_M, K_z and I_z. First, F_M is chosen according to the desired reference model. In this case, the desired 5% settling time in closed-loop is $T_{5\%} = 2.1$ ms for the reference tracking dynamics. Having only one output in this system: $n_y = 1$, the input-ouput dynamics in closed-loop will be of order 1. Thus, the closed-loop stable pole placement is deduced: $p_M = -1429$ rad/s which is 0.8669 in z-domain. The other pole Z_M influencing the disturbance rejection response is chosen a little faster than F_M: $Z_M = k_{ZF} F_M$ with $k_{ZF} \in [0; 1[$. The gains G_M, K_z and I_z are thus determined by applying the transparent control allocation with integral compensator tuning method detailed in Section 4.C.2, equation (4.64). Their values are given in Table 4.1.

The entire set of parameters needed for the simulation of the system are given in Table 4.1. It is pointed out that the characteristics of the two converters are assumed to be different so as to evaluate the control effort distribution capabilities of the control allocation methods used.

Meaning	Values
System Parameters	
Buck converters inductances	$L_1 = 1$ mH, $L_2 = 2$ mH
Buck converters voltage sources	$E_1 = E_2 = 24$ V
Duty cycles boundaries	$0 \leq \alpha_1 \leq 1, 0.3 \leq \alpha_2 \leq 0.7$
Stabilized voltage across the load	$v = 12$ V
Load resistor	$R = 3\ \Omega$
Load capacitor	$C = 5$ mF
Control Allocation with Integrator - Tuning Parameters	
Settling time	$T_{5\%} = 2.1$ ms
Control sampling time	$T_c = 0.1$ ms
Closed-loop poles (s-domain)	$p_M = -1429$ rad/s
Closed-loop poles (z-domain)	$F_M = e^{T_s p_M} = 0.8669$
Disturbance rejection poles (z-domain)	$Z_M = k_{ZF}\ F_M$
Closed-loop reference gain	$G_M = 1 - F_M = 0.1331$
Proportionnal gain	$K_z = 1 - Z_M = 0.2632$
Integral gain	$I_z = 1 - F_M = 0.1331$

Table 4.1: Simulation test parameters for the 2-buck converters 1-load system

In the tests presented here, the classical allocation method as well as the one with integrator uses the Interior-Point algorithm from [PB06] to compute the optimal solution $\mathbf{U}^* = [\alpha_1^* \ \alpha_2^*]^T$ in real time.

4.C.3.2 | Simulation results and analysis

A simulation test procedure is therefore proposed to compare the different control allocation architectures introduced in this chapter. The series of tests that will be carried out aims at evaluating different behavioral characteristics in closed-loop that have been highlighted during the analysis of the tracking performances and the disturbance rejection performances.

In order to trigger the dynamics of tracking and perturbation rejection, each of the simulations performed follows the same scheme. It starts by applying a step output reference to the system: $i^{ref}(t) = i_0^{ref} \cdot \mathcal{H}(t - t_{step})$, which appears at $t_{step} = 3$ ms, then a step disturbance is applied on the system. It is defined by $\delta\alpha_1(t) = -0.25\ \alpha_1^{max} \cdot \mathcal{H}(t - t_{dist})$ and $\delta\alpha_2(t) = -0.25\ \alpha_2^{max} \cdot \mathcal{H}(t - t_{dist})$, it appears at $t_{dist} = 15$ ms. The reference step first and then the disturbance allow one to quantify the tracking and regulation performances.

These tests are performed using the Matlab®-Simulink®. A continuous time state space model computes the system behavior and Matlab functions are used to close the loop and determine, at each sampling period, the control to apply to the system input.

Comparing CA with CAI-IPII

The first test aims at comparing the CA with the CAI-IPII set to present Property 5 of transparency in operating conditions where the parameters settings of the control law follows the prescriptions given previously in Table 4.1. It is specified that for this test, the parameter k_{ZF} is 0.85 which gives $Z_M = 0.7368$ and i_0^{ref} is chosen at 16 A. The result of these simulations is presented in Figure 4.8.

The first observation is that, for the CA as for the CAI-IPII, the performance in terms of settling time is globally guaranteed since for both architectures the output reaches the $\pm 5\%$ zone of its final value in about 2.1 ms or less. The difference in settling time between the two architectures can be explained by the fact that the commands reach their saturations - the CA thus has a settling time slightly slower than the desired performance: 2.2 ms - and by the presence of a zero for the CAI-IPII. This zero, which is slightly faster than F_M, influences the tracking when the control saturates because the linearity assumptions that guaranteed the zero-pole cancellation of the $z\mathbb{I}_{n_y} - Z_M$ term in the CAI-IPII transfer function $T_{CL}(z)$ are no longer satisfied.

The second observation is the fact that with the setting $G_M = \mathbb{I}_{n_y} - F_M$, the CA guarantees a zero static deviation when no disturbance is imposed on the system, which illustrates Theorem 2. When the perturbation appears however, the zero static deviation is reached only by using the CAI-IPII, contrary to that the CA does not ensure any perturbation rejection. Theorem 6 is thus also illustrated by this test.

The second test aims at comparing the influence of the setting $G_M = \mathbb{I}_{n_y} - F_M$ for the CA with the influence of this same setting for the CAI-IPII. To do this, a first simulation is performed for the CA with $G_M = \mathbb{I}_{n_y} - F_M$ and a second with $G_M = 0.5\ (\mathbb{I}_{n_y} - F_M)$. These same simulations are also executed for the CAI-IPII. For this last architecture, this test will allow one to evaluate the respect of Property 5 and of Theorem 6, while for the CA it is Theorem 2 which will be tested. The setting of Z_M and i_0^{ref} is the same as before. Simulation results are shown in Figure 4.9.

For both control architectures the case where $G_M = 0.5\ (\mathbb{I}_{n_y} - F_M)$ is displayed in dotted line. The plots associated with the CA confirm, in accordance with Theorem 2 that the condition to have a null static error is indeed to have no disturbance on the system and the setting $(\mathbb{I}_{n_y} - F_M)$

contrary to CAI-IPII. Indeed, the curves associated with the latter show that whatever the setting of G_M, and with or without disturbance, the zero static error is guaranteed.

It is however observed that in the case where G_M is different from $\mathbb{I}_{n_y} - F_M$, the tracking dynamics of CAI-IPII are modified. This is due to the fact that G_M no longer satisfies the transparent tuning conditions (4.64) and Z_M then influences the tracking dynamics. In the framework of this particular system this influence is here relatively weak since the settling time is modified by 0.1 ms.

Analysis of the CAI-IPII closed-loop behavior

For the purpose of this analysis, the simulations are all performed with the setting $G_M = \mathbb{I}_{n_y} - F_M$.

In the first test the influence of the Z_M setting on the CAI-IPII is observed. A first setting of the gain $Z_M = 0.4F_M$ is simulated. Then it is the turn of the setting $Z_M = 0.85F_M$. In these two cases, the reference current step is set to $i_0^{ref} = 10$ A. Figure 4.10 presents the simulations done.

The results highlight the fact that the matrix Z_M only influences the disturbance rejection, which is in agreement with the transmittance T_{SU}(z) obtained in the case of a transparent truning (4.66). It is noted that the control does not reach its saturations during this tests.

For the second test the only difference with the previous test is the setting of the output reference step that becomes $i_0^{ref} = 20$ A. The results are in Figure 4.11.

Contrary to the previous test, it is found that the choice of Z_M influences the tracking dynamics in addition to the disturbance rejection dynamics. This is explained by the fact that the control saturates. Indeed, when the control saturates, Assumption 11 is no longer true because a desired action vector of too great an amplitude is requested from the allocation which cannot achieve it and approaches it at best by reaching the saturations of the control. This assumption not being verified anymore, Property 5 which relies on Theorem 5 is not verified and Z_M acts on the tracking dynamics. As a consequence, a modification of the settling time of the order of 0.1 ms is observed.

In the third test the influence of parametric uncertainties in the model of the system on the CAI-IPII is observed. In this test, $Z_M = 0.85F_M$ and the output reference is set to be $i_0^{ref} = 16$ A. For this test, the CAI-IPII uses the matrices from the model (4.74) to determine the control vector to allocate in real time. However, the model used for the simulation is set differently. To each matrix of the simulation model, a parameter variation is applied. For example, the control will use the state matrix F when the simulation uses $(1 + \lambda_{unc})F$ instead. This modification is applied to the entire set of matrices needed for the state-space model. The term $\lambda_{unc} \in \mathbb{R}$ stands for the parametric variation factor. λ_{unc} only has to be different from zero to force the simulation model to be different from the control model. In the current test, three simulations are run: one for $\lambda_{unc} = 0$, another for $\lambda_{unc} = -1/3$ and a last one for $\lambda_{unc} = +1/3$. Figure 4.12 presents the simulations results.

Although parametric differences influence the dynamics of the closed-loop, the CAI-IPII still guarantees zero static error and disturbance rejection. This means that the important benefit of using CAI-IPII over CA can also be ensured when experiencing some parametric uncertainties.

Analysis of the CAI-IPII closed-loop behavior of the state and output-transparent improvement of the state behavior

However, after this series of various tests where only the control variables and the output of the system are observed on the figures, it is decided to look at the behavior of the state variables. In this effort, Figure 4.13 (left side) shows the state variables behavior, associated with Figure 4.9, diplaying the results from the CAI-IPII. The control law uses the CAI-IPII algorithm implemented so far which solves the control allocation problem (4.76):

$$\left\{ M\mathbf{U} = \mathbf{a_d} + \mathbf{a_d^I} = \tilde{\mathbf{a}}_\mathbf{d} \quad | \quad \mathbf{U}_{min} \leq \mathbf{U} \leq \mathbf{U}_{max} \right\} \tag{4.78}$$

As shown by the simulations, see Figure 4.14 (top), the behavior obtained for the total current, which is the output of the system, is in accordance with the requirements on dynamic and static performance. However, Figure 4.13 (left side) shows that although the behavior of the output corresponds to the expectations, it is reached thanks to currents that diverge for each of the converters. This behavior is not realistic regarding the physical system which is sized to support a maximum and minimum current not to be exceeded.

In order to obtain a behavior that is consistent with these limitations, a new control allocation problem must be formulated. In order to give - in addition - the ability to the control algorithm to choose a solution that is of interest for the global physical behavior of the system, this new formulation is designed wisely. To this aim, a second criterion is added in the objective to minimize the ohmic losses in the system. The minimization of the ohmic losses is equivalent to minimizing the square of the currents:

$$\min i_1^2 + i_2^2 \tag{4.79}$$

However, this second criterion can be formalized in the following way to get closer to a state formulation:

$$\min i_1^2 + i_2^2 \Longleftrightarrow \min \left(\begin{bmatrix} i_1 \\ i_2 \end{bmatrix} - \begin{bmatrix} 0 \\ 0 \end{bmatrix} \right)^T \cdot \left(\begin{bmatrix} i_1 \\ i_2 \end{bmatrix} - \begin{bmatrix} 0 \\ 0 \end{bmatrix} \right) \Longleftrightarrow \min \left|\left| \begin{bmatrix} i_1 \\ i_2 \end{bmatrix} - \begin{bmatrix} 0 \\ 0 \end{bmatrix} \right|\right|_2^2 \tag{4.80}$$

The control algorithm will determine, at the time k, the control so that the square of the currents is minimized. The application of this control to the system will act upon the currents in such a way as to make them reach a value at the time $k+1$. It is therefore the currents at time $k+1$ that one will try to minimize by acting at time k. The secondary criterion thus takes the form:

$$\min_{\mathbf{U}(k)} \left|\left| \begin{bmatrix} i_1(k+1) \\ i_2(k+1) \end{bmatrix} - \begin{bmatrix} 0 \\ 0 \end{bmatrix} \right|\right|_2^2 \Longleftrightarrow \min_{\mathbf{U}(k)} ||\mathbf{X}(k+1) - 0||_2^2 \tag{4.81}$$

Seeking to minimize the ohmic losses is in fact the same as choosing the reference $\mathbf{X}^*(k+1) = 0$ for the state. Thus the secondary criterion becomes:

$$\min_{\mathbf{U}(k)} ||\mathbf{X}(k+1) - \mathbf{X}^*(k+1)||_2^2 \tag{4.82}$$

Taking into account the dynamic model of the system (4.74) then allows to substitute $\mathbf{X}(k+1)$ by its expression as a function of $\mathbf{U}(k)$:

$$\min_{\mathbf{U}(k)} ||\mathbf{X}(k+1) - \mathbf{X}^*(k+1)||_2^2 \Longleftrightarrow \min_{\mathbf{U}(k)} ||F\mathbf{X}(k) + G\mathbf{U}(k) + H\mathbf{E}(k) - \mathbf{X}^*(k+1)||_2^2 \tag{4.83}$$

This can trivially be put in the following form:

$$\min_{\mathbf{U}(k)} ||G\mathbf{U}(k) - [\mathbf{X}^*(k+1) - F\mathbf{X}(k) - H\mathbf{E}(k)]||_2^2 \Longleftrightarrow \min_{\mathbf{U}(k)} ||M_p\mathbf{U}(k) - \mathbf{a_p}(k)||_2^2 \quad (4.84)$$

In the allocation formalism, the elements that represent this secondary preference criterion are therefore defined as follows:

$$\begin{aligned} M_p(k) &= G \\ \mathbf{a_p}(k) &= \mathbf{X}^*(k+1) - F\mathbf{X}(k) - H\mathbf{E}(k) \end{aligned} \quad (4.85)$$

Keeping in mind that this loss minimization objective is secondary, the complete optimization criterion that the CAI-IPII algorithm must address is updated from (4.77) to become the following. The weighting factor ω_p is used to adjust the priority of the secondary criterion to specify that the primary objective still remains the reference tracking for the system output:

$$\hat{J}_2 = ||M\mathbf{U} - \tilde{\mathbf{a}}_\mathbf{d}||_2^2 + \omega_p||M_p\mathbf{U} - \mathbf{a_p}||_2^2 \quad (4.86)$$

Taking advantage of the developments proposed in Section 4.B.2, this new criterion is equivalent to the formulation:

$$\hat{J}_2 = \left|\left|\begin{bmatrix} M\mathbf{U} - \tilde{\mathbf{a}}_\mathbf{d} \\ \sqrt{\omega_p}\,(M_p\mathbf{U} - \mathbf{a_p}) \end{bmatrix}\right|\right|_2^2 = \left|\left|\hat{M}\mathbf{U} - \hat{\mathbf{a}}_\mathbf{d}\right|\right|_2^2 \quad (4.87)$$

The implemented CAI-IPII algorithm will then solve the new control allocation problem:

$$\left\{\hat{M}\mathbf{U} = \hat{\mathbf{a}}_\mathbf{d} \quad | \quad \mathbf{U}_{min} \leq \mathbf{U} \leq \mathbf{U}_{max}\right\} \quad (4.88)$$

In summary, the control allocation with integral compensator is programmed to solve two different optimizations. The first one, whose results are displayed in Figure 4.14 (bottom left corner) and in Figure 4.13 (left side), minimizes J_2 which is recalled below and does not take into account any secondary criteria.

$$J_2 = ||M\mathbf{U} - \tilde{\mathbf{a}}_\mathbf{d}||_2^2 \quad (4.89)$$

The second one, whose results are displayed in Figure 4.14 (bottom right corner) and in Figure 4.13 (right side), minimizes $\hat{J}_2$ (4.87) which takes into account a criterion on the minimization of the gap between the state and its reference. Minimizing this deviation is the same as minimizing the ohmic losses here.

This test has for objective to show the benefit and the influence of adding a secondary optimization criterion focusing on losses minimization. For both of the CAI-IPII algorithms here, with and without losses minimization, the testing conditions are exactly the same with $G_M = \mathbb{I}_{n_y} - F_M$, $Z_M = 0.7368$ and $i_0^{ref} = 16$ A. Note that the weighting factor, for the algorithm with the secondary objective, is set to $\omega_p = 0.001$. The CAI-IPII is CAI-TII-tuned in both cases. For the remaining parameters, the values from Table 4.1 are selected. Comparative simulation results can be seen on Figures 4.13 and 4.14.

The first thing one can notice is that the modification of the optimization criterion, even with a very low weighting, will have a significant influence on the state of the system and will really allow it to reach an operating point that minimizes the ohmic losses. Indeed, in simulation, the

final value of the state leads to $i_1^2+i_2^2=(30.56)^2+(-14.56)^2\simeq 1146\ A^2$ for the initial CAI-IPII against $i_1^2+i_2^2=(7.89)^2+(8.11)^2\simeq 128.0\ A^2$ only, for the CAI-IPII with losses minimization.

A particularly noteworthy feature is therefore that this very slight modification of the optimization criterion ($\omega_p = 0.001$) will have a strong influence on the internal behavior of the system without any impact on the output. As shown in Figure 4.14 (top), the two CAI-IPII algorithms lead to the same behavior for the output of the system, both in terms of static and dynamic performances. This modification of the optimization criterion of the allocator will thus bring a strong operational improvement while being transparent with respect to the output. In such a system where it is desired to spend a minimum of energy to achieve the control objectives, the algorithm with loss minimization will be preferred.

Conclusions about the simulations

Finally, through these tests the proposed control architectures of CA and CAI-IPII have been tested in the applicable zone as well as beyond the application limits of the Theorems characterizing their closed-loop behaviors. It could be shown that in the case of the current system, even if the operation requires the control variables to reach their bounds or that the transparent tuning conditions are not verified, the CAI-IPII manages to guarantee very good tracking and disturbance rejection performances which outperform the CA. This also confirms in simulation the theoretically proven features.

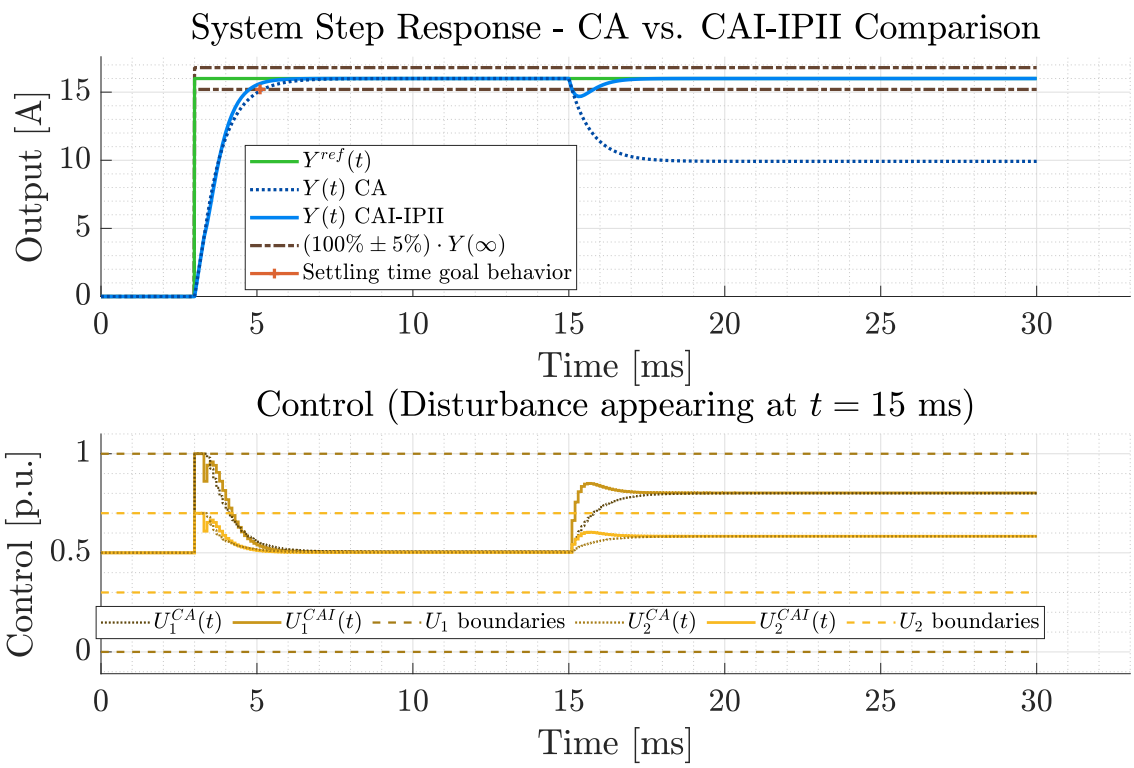

Figure 4.8: Comparing classical control allocation and control allocation with integral compensator for $G_M = \mathbb{I}_{n_y} - F_M$. The CAI-IPII is CAI-TII-tuned.

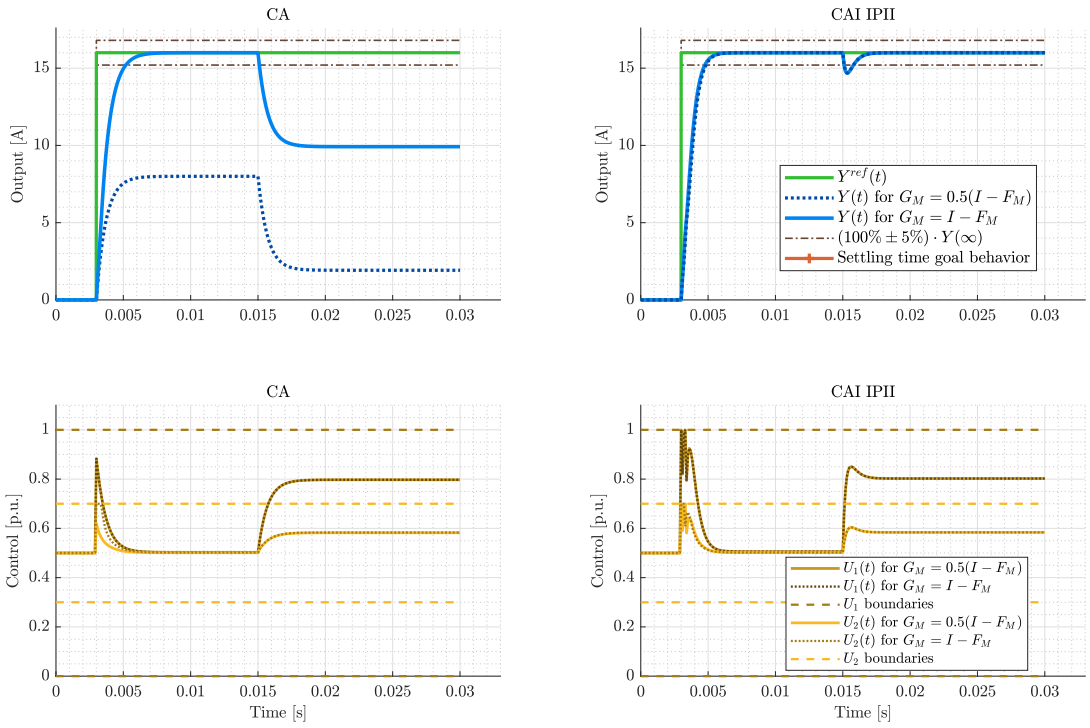

Figure 4.9: Comparing classical control allocation and control allocation with integral compensator under two different G_M values.

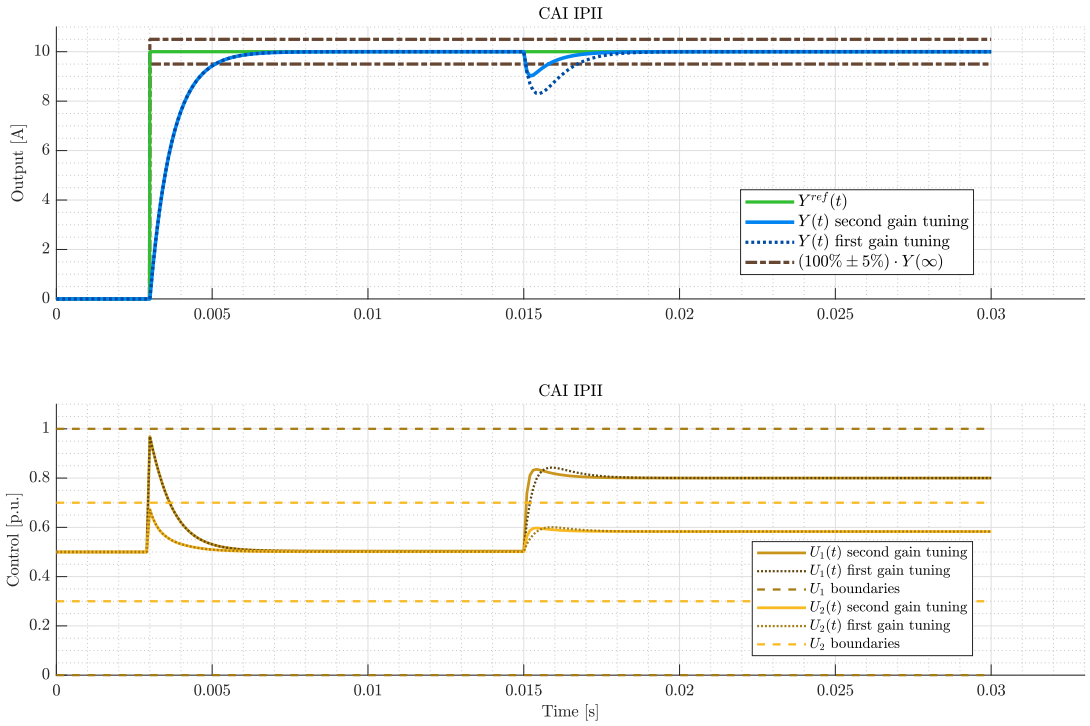

Figure 4.10: Comparing two tunings of control allocation with integral compensator for two different Z_M when control does not reach its saturations. The CAI-IPII is CAI-TII-tuned in both cases.

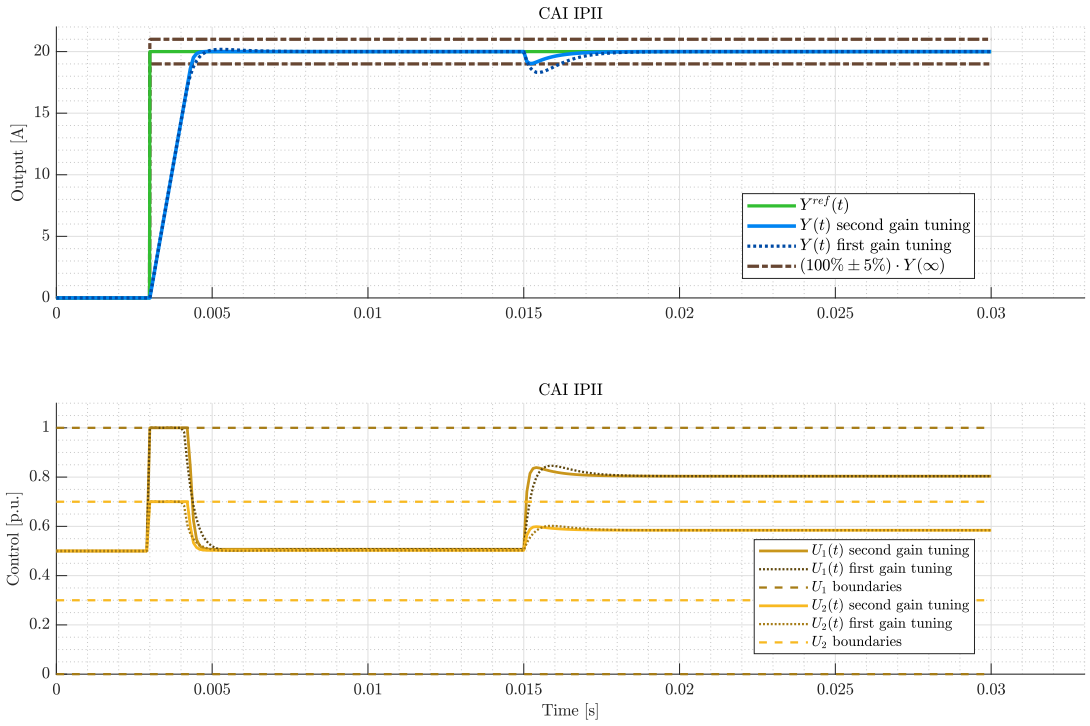

Figure 4.11: Comparing two tunings of control allocation with integral compensator for two different Z_M when control reaches its saturations. The CAI-IPII is CAI-TII-tuned in both cases.

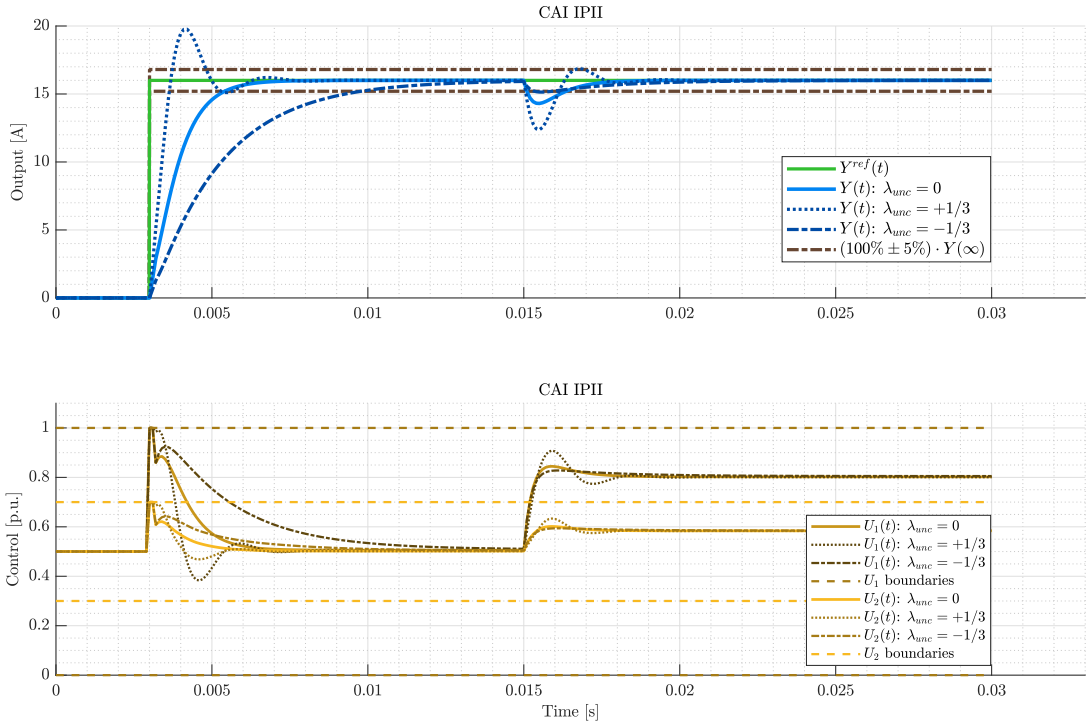

Figure 4.12: Comparing two parametric variation behaviors to the perfect-model-knowledge one. The CAI-IPII is CAI-TII-tuned in both cases.

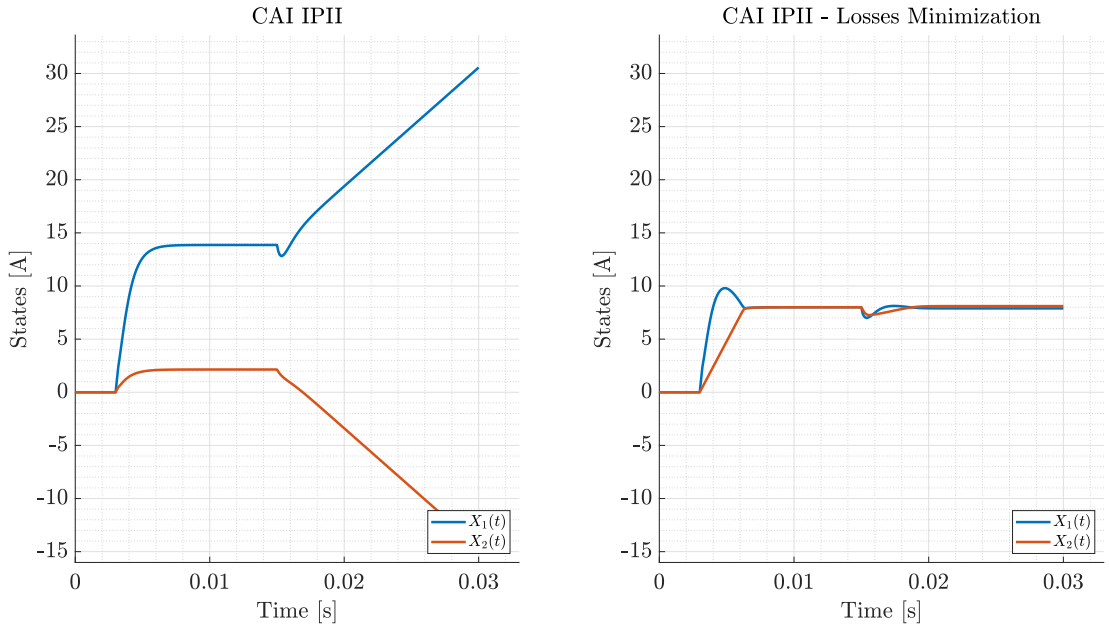

Figure 4.13: Comparing control allocation with integral compensator for two different optimisation cost functions. State variables of the system for the one without losses minimization (left side), and state variables of the system for the one including losses minimization (right side). The CAI-IPII is CAI-TII-tuned in both cases.

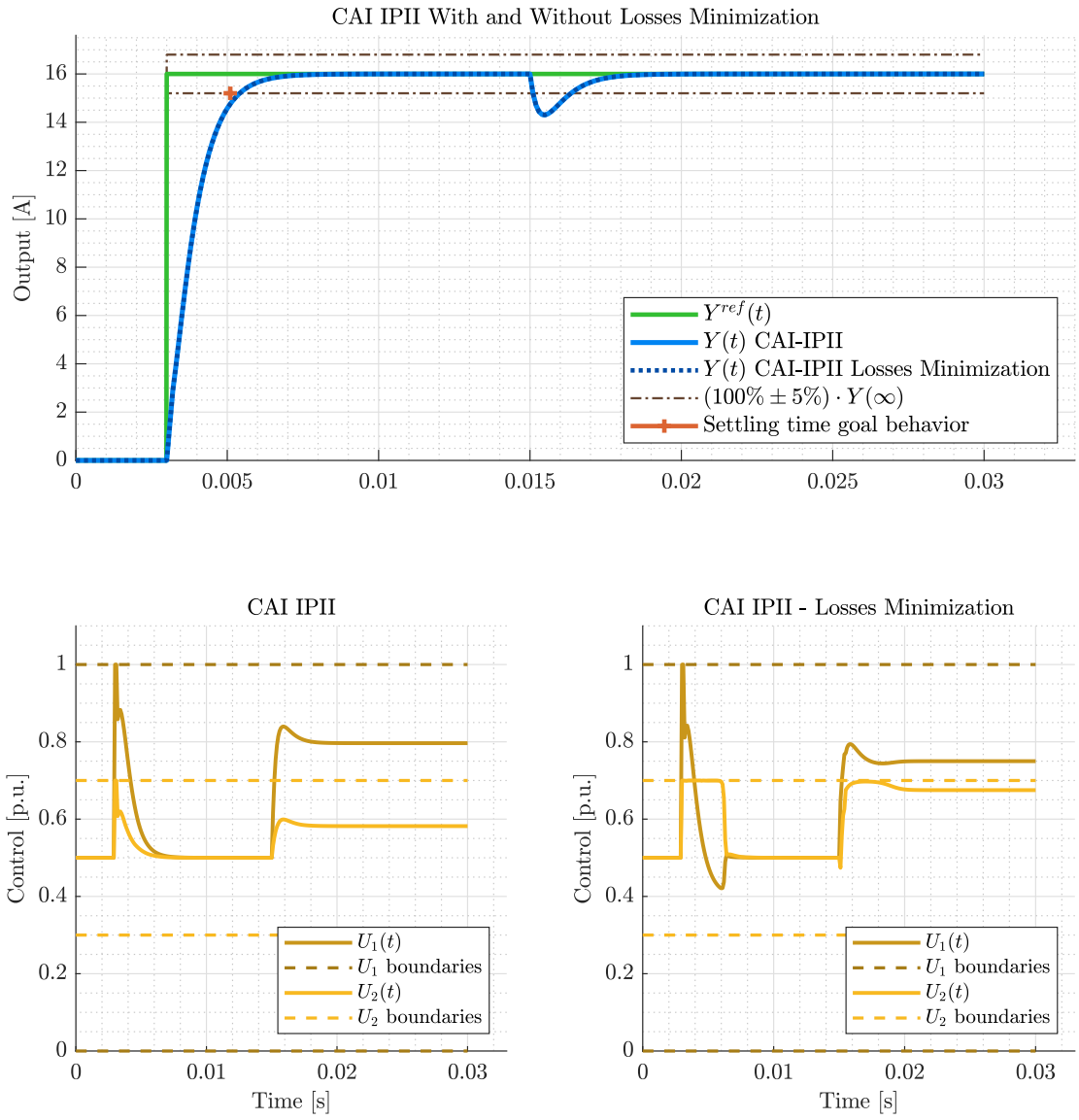

Figure 4.14: Comparing control allocation with integral compensator for two different optimisation cost functions. Control variables of the system for the one without losses minimization (bottom left corner), and control variables of the system for the one including losses minimization (bottom right corner). Output of the system for both (top). The CAI-IPII is CAI-TII-tuned in both cases.

4.D Conclusion about the contribution to the development of control allocation methods

In this chapter, a generalized formulation of the allocation methods using optimization which may or may not take into account a secondary preference criterion in the cost function have been shown to be able to be brought back to a same common formulation of the allocation equation. This generic formulation is the one that is used afterwards for the development of the control methods for the MMC.

The control allocation methods that will be implemented for the control of the MMC are those based on an online optimization principle. Optimization algorithms, that have already been proven to work effectively for control allocation purposes, have been presented here for the LP and the QP. The associated optimization algorithms are readily available online in the archive [Här] for the QP.

Classical control allocation methods have shown to be able to ensure a null static error only under strong and restrictive conditions: the control law must be precisely tuned and no disturbance must be applied to the system. A novel reference model based control allocation method including a built-in integral compensator was then proposed and its features have been proven theoretically and through simulations:

- Static error cancellation and disturbance rejection even under small parametric uncertainties,
- Closed-loop dynamics seamlessly specified through a multivariable reference model,
- Ability to tune the disturbance rejection dynamics differently than the reference tracking ones,
- Readily combined with existing methods for an important performance gain and little change of the control allocation algorithm.
- A major feature of the control allocation with integral compensator, detailed by Property 5, is that adding the integrator is transparent for the closed-loop response: no supplementary zero or pole appears due to the integrator and the same reference model is followed.

Those features are combined with the intrinsic features from the control allocation, graphically summarized by Figure 1.14, such as the optimal distribution of the control effort among the available control variables. Simulations showed that even when saturations were reached under transient conditions, the static deviation cancellation and disturbance rejection properties are preserved.

Note that the valuable work introduced here can also be seen as a multivariable model reference control scheme where the vectorial integrator is transparent and the closed-loop dynamic behavior is easily tuned.

As seen in simulation, reaching the limitations of the control changes the dynamics of the closed-loop compared to the initially specified performances, which is normal and expected. However, this paves the way to an interesting perspective of exploring anti-windup methods to improve the closed-loop behavior when using the control allocation with integral compensator. Existing literature on the theme of anti-windup in the context of allocation methods [Zac09; Boa+10; Lim+21a; Lim+21b] can be used to guide the first works in this axis.

5 Scalable Control Allocation Methods for the Modular Multilevel Converter

Contents

The objective of this chapter is to present the different works that led to the development of a control allocation architecture of the MMC and the different challenges that were taken on the way of this design. The theme of this work is focused on an adaptation of allocation methods for the control of the MMC first. Using the control allocation methods has for objective to ensure given performances from the automatic control point of view such as a settling time, an overshoot or an accuracy so that the converter operates properly. The control system of the MMC has to meet several goals and ensure the control of several physical quantities that are the starting point of the architectures introduced in this chapter.

5.A Research axis: towards a scalable, generic and versatile control allocation architecture for the MMC

This chapter is part of the will to contribute to a more generalized adoption of MMCs in electrical energy conversion systems. The conceptual position adopted here is to consider that the sizing and control of systems are two topics that are part of the same workflow, studied in parallel and not sequentially. When studied sequentially, the first step is the sizing that produces the system that must then be controlled, which is the second step. When studied together in parallel, the sizing and the control of the system are co-designed by taking into account the sizing and operating constraints from the beginning [Fat+01; RP02]. The co-design of systems has shown overall significant operational performance improvement compared to sequential design and is a trending topic [Gar19; Mab+22].

By designing a control algorithm scalable to the number of phases and submodule of the MMC, it is then possible to consider m and N as sizing parameters because knowing that the control is able to adapting to m and N gives more freedom from the beginning of the design phase of the electrical conversion system.

The MMC being already modular by its number of submodules, would it be possible to give it even more modularity by showing that the control of such converters with a large number of phases is possible and functional when using online optimization methods ?

The objective of the current chapter is therefore to design a control allocation by real time optimization of the MMC that is both scalable to the number m of phases, to the number N of submodules and that guarantees good performance to ensure the compliant operation of the MMC. One of the design objectives of this control architecture will be to evaluate the possibilities of achieving a generic control seamlessly adapting to the MMC to be controlled while maintaining the same control quality.

Outline

First, in Section 5.B, the control allocation methods for voltages and currents are developed. They are then gathered in a global control architecture of the MMC. Following this, several simulation and Hardware-In-the-Loop (HIL) studies are presented to evaluate the performances and specificities of allocation methods for the control of the MMC. In Section 5.C, focusing on the low-level control, a comparison is made between the optimization types used to perform the EMOn aiming to ensure the capacitor active balancing. Regarding Section 5.D, dedicated to the high-level control, the efficiency and the versatility of the allocation methods coupled to the models used to ensure the control of the currents are shown. After having shown that the control allocation methods are able to meet the control challenges of the MMC by taking advantage of the numerous degrees of freedom to control it, Section 5.E focuses on the possibility of using the control allocation methods to optimally steer the system with the remaining input variable when some of those degrees of freedom are lost: the FTC of the MMC, using control allocation. Perspectives for future explorations are then shared in the conclusion of this chapter.

5.B Control architecture of the MMC based on allocation methods

As seen in the state of the art, the MMC is a singular converter which brings into play different specificities during its operation such as the circulating currents different from the traditional

VSCs. This makes a total of four different types of currents on which the MMC acts. Thus, the control architecture must be able to drive these four types of currents by acting on the voltages across the arms of the converter in order to ensure a proper energy DC-AC conversion operation.

Each of the submodules is comprised of a capacitor. The maximum voltage that the switches of a submodule will experience is the voltage across the capacitor[1]. To protect the switches, the control must balance the capacitors. Ensuring such an operation also guarantees the continuity of the operating zone of the converter at its maximum level according to Section 3.H.1. Therefore, the MMC control architecture will also aim to control the voltages in the capacitors by acting directly on the duty cycles of the cells to which they belong.

As stated in Section 3.G.2, the global energy balancing of the MMC will only be guaranteed by having a dedicated device ensuring that the power balance of the system is satisfied. Since the power balance of the converter leads to a non-linear model, this control stage is necessary to ensure the convergence towards the appropriate operating point for the DC bus. The control architecture of the MMC will therefore also have the objective of selecting the right current to draw from the DC bus in order to maintain the level of energy contained in the converter.

These different control objectives allow to outline the functional control architecture which is represented by Figure 5.1.

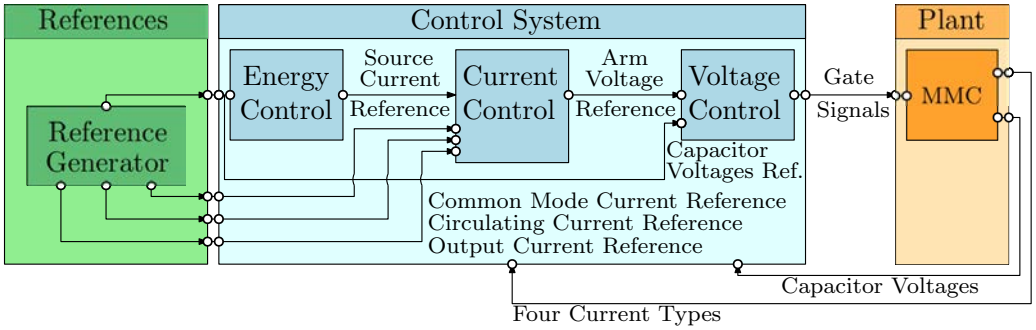

Figure 5.1: MMC general control architecture. The block dedicated to *Voltage Control* is considered to be the low-level control, and the high-level control is made of the *Energy Control* and the *Current Control*.

5.B.1 | Low-level control

Since allocation methods are able to solve a problem in the form control allocation problem, they require a formulation of the control objective under the form $\mathcal{M}(\mathbf{U}) = \mathbf{a_d}$. To adopt it, the control-oriented models from Chapter 2 are used.

In all cases, the voltage control allocation of the system embodies the scheme described by Figure 1.11 b), which means that the control allocation ensures the role of the *arm voltage control* and that of the *balancing control algorithm* simultaneously.

Even if this may seem complex at first, the interest of dealing with coupled control objectives simultaneously is beneficial. Indeed, focusing on the voltage control, the models have shown that the switching states operate simultaneously on the arm voltage as well as on the evolution of the voltages across the capacitors. It therefore seems relevant to have a single controller that takes

[1] In operation, the switches may be opened or closed. In closed state, the voltage across the switch is null. In open state the latter is equal to the capacitor voltage. This means that the maximum voltage that the switches will experience during operation is that of the capacitor. This implies that, in order to ensure proper operation of the converter, it is necessary to guarantee a voltage level in the capacitor that is less than or equal to the maximum voltage limit for which the switch is designed.

into account the saturations of the switching states to satisfy both the objective of tracking arm voltages and that of tracking capacitor voltages references. This is instead of considering the two objectives separately and forcing priority order between the objectives that is not necessarily in the best interest of the operation of the converter.

5.B.1.1 Low-level control for an arm

According to 2.B.4.1, the behavior of the arms can be represented by a generalized model which will be adapted according to the type of submodules. The generalized control allocation-oriented model of the arms in its discrete verison is recalled according to (2.39):

It is reminded that $\sigma(x) = 1/\sigma(x)$

$$\begin{bmatrix} \sigma(x)\mathbf{v_{C_{xy}}}(k)^T L_{xy} \\ \frac{T_c}{C} i^*_{xy}(k) L_{xy} \end{bmatrix} \mathbf{D^e_{xy}}(k) = \begin{bmatrix} v_{xy}(k) \\ \mathbf{v_{C_{xy}}}(k+1) - \mathbf{v_{C_{xy}}}(k) \end{bmatrix} - \begin{bmatrix} \sigma(x)\mathbf{T_{xy}}^T \mathbf{v_{C_{xy}}}(k) \\ \frac{T_c}{C} i^*_{xy}(k)\mathbf{T_{xy}} \end{bmatrix} \tag{5.1}$$

For a vector of duty cycles $\mathbf{D^e_{xy}}$ applied to the system at time k, the first consequence is the voltage $v_{xy}(k)$ which then appears at this same instant across the arm $\#xy$; the second consequence is the variation imposed on $\mathbf{v_{C_{xy}}}(k)$ which gives rise to $\mathbf{v_{C_{xy}}}(k{+}1)$ at the next instant.

According to the architecture of Figure 5.1, the primary objective of the voltage control is to ensure the arms voltage reference tracking. Thus, for a voltage reference v^{ref}_{xy} determined by the current control stage at time k, the voltage control stage must find $\mathbf{D^e_{xy}}$ that satisfies:

$$v^{ref}_{xy}(k) = \sigma(x)\mathbf{v_{C_{xy}}}(k)^T L_{xy} \mathbf{D^e_{xy}}(k) + \sigma(x)\mathbf{T_{xy}}^T \mathbf{v_{C_{xy}}}(k) \tag{5.2}$$

However, as the general control architecture shows, the purpose of this voltage control stage is also to ensure the capacitor voltage balancing. In other words, for a capacitor voltage reference $\mathbf{v^{ref}_{C_{xy}}}$ received by the control stage at time k, the objective is to make sure that $\mathbf{v_{C_{xy}}}$ reaches it at time $k+1$. To satisfy this second objective, $\mathbf{D^e_{xy}}$ must therefore be a solution of:

$$\mathbf{v^{ref}_{C_{xy}}}(k) = \mathbf{v_{C_{xy}}}(k) + \frac{T_c}{C} i^*_{xy}(k) L_{xy} \mathbf{D^e_{xy}}(k) + \frac{T_c}{C} i^*_{xy}(k)\mathbf{T_{xy}} \tag{5.3}$$

Taking into account these control objectives, the control $\mathbf{D^e_{xy}}$ should therefore aim to solve the two equations above at each time k. However, the duty cycles are limited by $\mathbf{D^{e^{min}}_{xy}}$ and $\mathbf{D^{e^{max}}_{xy}}$, so the two equations above cannot always be verified, as in the case where the reference v^{ref}_{xy} would be too large. Since the control objectives cannot be continuously satisfied in all the operating conditions of the MMC, a deviation from their satisfaction is introduced in the same way as in Section 4.B.1 of the previous chapter. Building on the approach of the previous chapter, a first deviation $\mathbf{e^{xy}_{LL}}$ representing how much the solution deviates from the first control objective (5.2) is defined as well as a second $\mathbf{e^{xy}_{pLL}}$ measuring the deviation from the secondary objective (5.3).

$$\begin{aligned} \mathbf{e^{xy}_{LL}} &= \sigma(x)\mathbf{v_{C_{xy}}}(k)^T L_{xy} \mathbf{D^e_{xy}}(k) - \left(v^{ref}_{xy}(k) - \sigma(x)\mathbf{T_{xy}}^T \mathbf{v_{C_{xy}}}(k) \right) \\ \mathbf{e^{xy}_{pLL}} &= \tfrac{T_c}{C} i^*_{xy}(k) L_{xy} \mathbf{D^e_{xy}}(k) - \left(\mathbf{v^{ref}_{C_{xy}}}(k) - \mathbf{v_{C_{xy}}}(k) - \tfrac{T_c}{C} i^*_{xy}(k)\mathbf{T_{xy}} \right) \end{aligned} \tag{5.4}$$

The control algorithm will then aim at minimizing these deviations and an optimization will take place in this sense. A cost function is thus defined from the mentioned deviations by bringing a weighting $w_{v_C} \in [0; 1[$ for the secondary control objective:

$$J^{xy}_{l_{LL}} = ||\mathbf{e^{xy}_{LL}}||^l_l + w_{v_C} ||\mathbf{e^{xy}_{pLL}}||^l_l \tag{5.5}$$

with l the norm chosen for the optimization. As proposed in the development carried out in the Section 4.B.2, this criterion can take the form of the norm of a single globalized deviation which combines the two criteria. It is shown that this amounts to directly modifying the allocation equation, which - in the case of low-level control - takes the form below:

$$\begin{bmatrix} \sigma(x)\mathbf{v_{C_{xy}}}(k)^T L_{xy} \\ w_{v_C}{}^{\frac{1}{l}} \frac{T_c}{C} i^*_{xy}(k) L_{xy} \end{bmatrix} \mathbf{D^e_{xy}}(k) = \begin{bmatrix} v^{ref}_{xy}(k) \\ w_{v_C}{}^{\frac{1}{l}} \left(\mathbf{v^{ref}_{C_{xy}}}(k) - \mathbf{v_{C_{xy}}}(k) \right) \end{bmatrix} - \begin{bmatrix} \sigma(x)\mathbf{T_{xy}}{}^T \mathbf{v_{C_{xy}}}(k) \\ w_{v_C}{}^{\frac{1}{l}} \frac{T_c}{C} i^*_{xy}(k) \mathbf{T_{xy}} \end{bmatrix} \tag{5.6}$$

In nominal operation the vector $\mathbf{T_{xy}}$ is zero and the matrix L_{xy} takes a simplified form. Although the complete control allocation problem described by (5.7) will have its resolution programmed in real time, the formulation for the nominal operating case that will be most frequently encountered is given in Appendix J. By (5.6) a formulation of the control objective adapted to the allocation methods has thus been found:

$$LLCAP_{xy}:$$
$$\left\{ \begin{bmatrix} M^{xy}_{LL}(k) \\ w_{v_C}{}^{\frac{1}{l}} M^{\ xy}_{p\,LL}(k) \end{bmatrix} \mathbf{U^{xy}_{LL}}(k) = \begin{bmatrix} \mathbf{a^{xy}_{d\,LL}}(k) \\ w_{v_C}{}^{\frac{1}{l}} \mathbf{a^{xy}_{p\,LL}}(k) \end{bmatrix} \;\middle|\; \mathbf{D^{e\,min}_{xy}} \leq \mathbf{U^{xy}_{LL}}(k) \leq \mathbf{D^{e\,max}_{xy}} \right\} \tag{5.7}$$

This same formulation, dedicated to an arm, will thus have to be solved in real time at each sampling period and for each arm of the MMC. This represents the execution of $2m$ allocation algorithms per sampling step to ensure the low-level control. The notations $\hat{M}^{xy}_{LL}$ and $\mathbf{\hat{a}^{xy}_{d\,LL}}$ are then introduced:

$$LLCAP_{xy}:$$
$$\left\{ \hat{M}^{xy}_{LL}(k) \mathbf{U^{xy}_{LL}}(k) = \mathbf{\hat{a}^{xy}_{d\,LL}}(k) \;\middle|\; \mathbf{D^{e\,min}_{xy}} \leq \mathbf{U^{xy}_{LL}}(k) \leq \mathbf{D^{e\,max}_{xy}} \right\} \tag{5.8}$$

The optimization problem formulation to be solved online is obtained according to the approach of Section 4.B.2:

$$LLCAOP_{xy}: \begin{cases} \min_{\mathbf{D^e_{xy}}, \mathbf{\hat{e}^{xy}_{LL}}} J^{xy}_{l_{LL}} = ||\mathbf{\hat{e}^{xy}_{LL}}||^l_l \\ u.c.: \\ \hat{M}^{xy}_{LL} \mathbf{D^e_{xy}} - \mathbf{\hat{e}^{xy}_{LL}} = \mathbf{\hat{a}^{xy}_{d\,LL}} \\ \mathbf{D^{e\,min}_{xy}} \leq \mathbf{D^e_{xy}} \leq \mathbf{D^{e\,max}_{xy}} \\ -\mathbf{\hat{e}^{xy^{max}}_{LL}} \leq \mathbf{\hat{e}^{xy}_{LL}} \leq \mathbf{\hat{e}^{xy^{max}}_{LL}} \end{cases} \tag{5.9}$$

The size of $\mathcal{A}^{xy}_{LL}$ is an indicator of the complexity of the optimization to solve in real time.

$\mathcal{A}^{xy}_{LL}$	N	$N = 3$ [Ser14]	$N = 400$ [Per+12]
LP	$(N + 1 \times 4N + 2)$	(4×14)	(401×1602)
QP	$(N + 1 \times 3N + 1)$	(4×10)	(401×1201)

Table 5.1: Low-level CAOP for a single arm, equality constraint matrices comparison.

Thus, the complexity of the optimization will be lower when using the QP rather than the LP. The variation in this complexity indicates that as the number of submodules increases, the QP becomes increasingly preferable.

5.B.1.2 Low-level control: from the arm to the entire MMC

Real time solving parallelization

To realize the low-level control for all the arms of the converter from the control allocation dedicated to a single arm, several solutions are possible. The most trivial solution consists in launching in real time the execution in parallel of as many algorithms of control allocation as there are arms in the converter. This first solution is called $2m$ *loops parallel*.

Real time solving in series

The second solution is still done by solving $2m$ different control allocation problems including one by arm using a loop to go through all the arms of the MMC. This solution is called $2m$ *loops series*.

All-in-One

The parallelization solution is the one that takes $2m$ times the computational resources necessary for the optimization of a single arm but, in return, the execution time will be as long as that necessary for the allocation of a single arm. In the dual case of serialization, it is the opposite: the needed resources are the same as for the allocation of a single arm, but the computation time is $2m$ times bigger. The idea of analyzing the third solution which considers a single allocator will solve the control allocation problem of the whole arms in a single allocation equation is to evaluate if - in the current state of the low-level control formulation - such an algorithm would present a trade-off between the first two solutions.

Taking into account all the arms of the MMC in a single control allocation problem is done by concatenating the $2m$ allocation formulations of each of the arms: the main objectives of the LLC are grouped together first, then come the secondary balancing objectives, which gives the formulation detailed in Appendix K. The control allocation problem for the whole converter is then deduced:

$$LLCAP:$$

$$\left\{ \begin{bmatrix} M_{LL}(k) \\ w_{v_C}{}^{\frac{1}{l}} M_{pLL}(k) \end{bmatrix} \mathbf{U_{LL}}(k) = \begin{bmatrix} \mathbf{a_{dLL}}(k) \\ w_{v_C}{}^{\frac{1}{l}} \mathbf{a_{pLL}}(k) \end{bmatrix} \;\middle|\; \mathbf{D^{e^{min}}} \leq \mathbf{U_{LL}}(k) \leq \mathbf{D^{e^{max}}} \right\} \tag{5.10}$$

It is noted that this formulation can also be used for the global control architecture of the MMC. This leads to the formulation of the following optimization problem to be solved online:

$$LLCAOP: \begin{cases} \min_{\mathbf{D^e}, \hat{\mathbf{e}}_{\mathbf{LL}}} J_{l_{LL}} = ||\hat{\mathbf{e}}_{\mathbf{LL}}||_l^l \\ u.c.: \\ \hat{M}_{LL}\mathbf{D^e} - \hat{\mathbf{e}}_{\mathbf{LL}} = \hat{\mathbf{a}}_{\mathbf{dLL}} \\ \mathbf{D^{e^{min}}} \leq \mathbf{D^e} \leq \mathbf{D^{e^{max}}} \\ -\hat{\mathbf{e}}_{\mathbf{LL}}^{\mathbf{max}} \leq \hat{\mathbf{e}}_{\mathbf{LL}} \leq \hat{\mathbf{e}}_{\mathbf{LL}}^{\mathbf{max}} \end{cases} \tag{5.11}$$

In this case, compared to $LLCAOP_{xy}$, the number of rows and columns of the matrix that represents the equality constraints $\mathcal{A}_{LL}$ are multiplied by the number of arms as Table 5.2 reports.

$\mathcal{A}_{LL}$	N	$N = 3$ [Ser14]	$N = 400$ [Per+12]
LP	$(2m(N+1) \times 2m(4N+2))$	(24×84)	(2406×9612)
QP	$(2m(N+1) \times 2m(3N+1))$	(24×60)	(2406×7206)

Table 5.2: Low-level CAOP for the entire MMC, equality constraint matrices comparison.

Low-level control reference model tuned

By the choice made from (5.2) and (5.3) for the development of the control allocation of the converter voltages, the reference model that the capacitors and the voltages across the arms are made to follow in closed-loop is implicitly tuned. For the case of the capacitors, imposing an objective in the form of (5.3) means having to follow $\mathbf{v}_{\mathbf{C_{xy}}}(k+1) = \mathbf{v}^{ref}_{\mathbf{C_{xy}}}(k)$, which is a deadbeat response:

$$\mathbf{Y}^*(k+1) = \mathbb{O}_{n_y}\mathbf{Y}(k) + \mathbb{I}_{n_y}\mathbf{Y}^{ref}(k) \tag{5.12}$$

Let $F^{xy}_{LL,M} = \mathbb{O}_N$ and $G^{xy}_{LL,M} = \mathbb{I}_N$ be the matrices defining the $\mathbf{v}_{\mathbf{C_{xy}}}$ reference model. The reference model tracked by v_{xy} is expressed $v_{xy}(k) = v^{ref}_{xy}(k)$ which is made possible by the feedthrough relation of the open-loop model, i.e. $\mathbf{Y}^*(k) = \mathbf{Y}^{ref}(k)$ in this case.

Low-level control architecture

The different solving procedures for the whole converter $2m$ *loops parallel*, $2m$ *loops series* and 1 *loop all-in-one* are programmed in the perspective of the evaluation of the voltage control performances. The block diagram Figure 5.2 zooms in the low-level control in order to illustrate the various possibilities:

- Performing the low-level control with the arm by arm allocation or with the allocation from whole arms of the MMC in one step.
- The EMOn allocation can be done using LP or QP. The sizes of the equality constraint matrices are specified on the diagram.

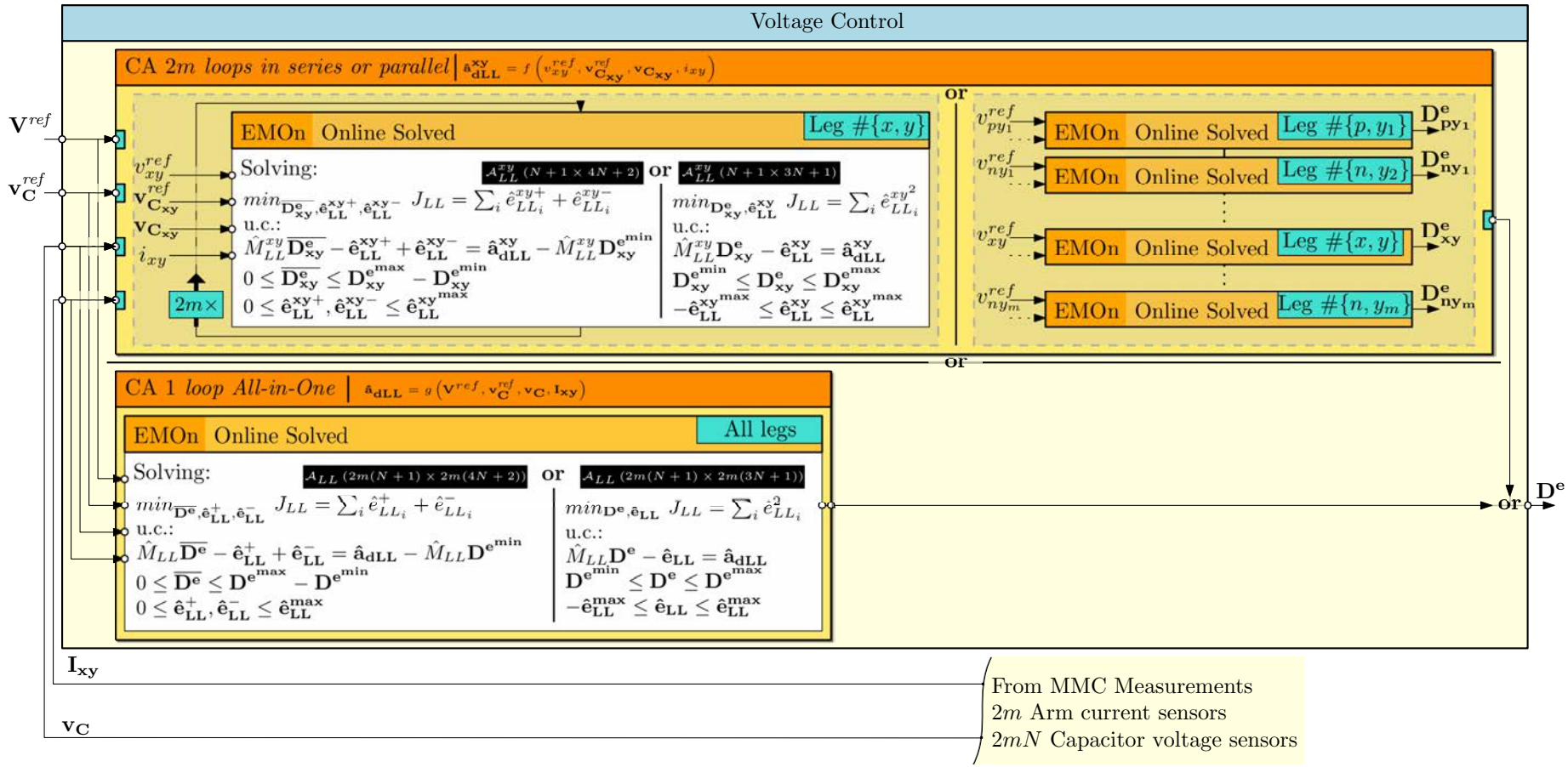

Figure 5.2: Voltage control allocation detailed architecture possibilities.

5.B.2 | High-level control

The high-level models selected for control are the most accurate ones of the models introduced in Chapter 3. According to the simulations of the latter, this corresponds to the GPFOCSSM and the GPFSROBHCCSSM.

In all cases, the current control allocation of the system embodies the scheme described by Figure 1.11 c), which means that the control allocation ensures the role of the *output current control*, that of the *circulating current control*, that of the *DC bus current control* and that of the *common mode current control* simultaneously.

Even though this may seem complex at first, the interest in dealing with coupled control objectives simultaneously is beneficial. Indeed, when focusing on the control of currents, one notices that the four types of currents evolve according to the same quantities which are the arm voltages. Determining these voltages in a unique way by taking into account their saturations to satisfy the tracking objectives of the different currents has the potential to lead to a better closed-loop behavior than considering the control of each current in a decoupled way by taking into account the saturations on these control voltages in a scattered way in different controllers all acting on the same control variables.

5.B.2.1 | High-level control allocation formulation from the GPFOCSSM

The equation representing the influence of the arms voltages on the currents in the natural reference frame according to the GPFOCSSM put in the form (3.68) is recalled:

$$\tilde{C}_{HL}\tilde{G}_{HL}\mathbf{U_{HL}}(k) = \mathbf{Y_{HL}}(k+1) - \tilde{C}_{HL}\tilde{F}_{HL}\tilde{\mathbf{X}}_{\mathbf{HL}}(k) - \tilde{C}_{HL}\tilde{H}_{HL}\tilde{\mathbf{E}}_{\mathbf{HL}}(k) \tag{5.13}$$

It is a controllable and observable representation of the current dynamics adapted for a control law design. By making the terms of this equation explicit from their definition in Chapter 3, and by taking advantage of Section 4.B.1 of the chapter dedicated to the development of allocation methods, (5.13) can be directly adopted as the adequate formulation of the allocation equation in preparation of the control allocation problem:

$$M_{HL}\begin{bmatrix}\mathbf{V_{py}}(k)\\ \mathbf{V_{ny}}(k)\end{bmatrix} = \begin{bmatrix}{I_m}^*(k+1)\\ {I_s}^*(k+1)\\ \tilde{\mathbf{I}}_{\mathbf{c}}{}^*(k+1)\\ \tilde{\mathbf{I}}_{\mathbf{o}}{}^*(k+1)\end{bmatrix} - \left(\tilde{F}_{HL}\tilde{\mathbf{X}}_{\mathbf{HL}}(k) + \tilde{H}_{HL}\tilde{\mathbf{E}}_{\mathbf{HL}}(k)\right) \tag{5.14}$$

where the quantities ${I_m}^*$, ${I_s}^*$, $\tilde{\mathbf{I}}_{\mathbf{c}}{}^*$ and $\tilde{\mathbf{I}}_{\mathbf{o}}{}^*$ represent the reference model of the desired currents in closed-loop. The desired dynamics for these currents is defined by the following reference model:

$$\begin{bmatrix}{I_m}^*(k+1)\\ {I_s}^*(k+1)\\ \tilde{\mathbf{I}}_{\mathbf{c}}{}^*(k+1)\\ \tilde{\mathbf{I}}_{\mathbf{o}}{}^*(k+1)\end{bmatrix} = \mathbf{Y}^*_{\mathbf{HL}}(k+1) = F_{HL,M}\mathbf{Y_{HL}}(k) + G_{HL,M}\mathbf{Y}^{ref}_{\mathbf{HL}}(k) \tag{5.15}$$

The allocation using online optimization aims at cancelling the deviation $\mathbf{e_{HL}}$ between the two terms of (5.14) at each instant by acting on $\mathbf{U_{HL}}$. By the control effectiveness, represented by M_{HL}, a same component of the voltage vector can act on several components of the currents. Thus, in the case where the control bounds do not allow $\mathbf{U_{HL}}$ to cancel all the $\mathbf{e_{HL}}$ components, it is possible to give priority to specific components of the deviation vector, which amounts

to favoring the tracking of the reference model for specific currents. To specify how to favor particular components over others a weighting of the components is introduced. The weights $w_m \in]0;1]$, $w_s \in]0;1]$, $\mathbf{w_c} \in]0;1]^{m-1}$ and $\mathbf{w_o} \in]0;1]^{m-1}$ are then used and the allocation equation becomes:

$$\mathbf{w_I}^{\frac{1}{l}} \circ M_{HL} \begin{bmatrix} \mathbf{V_{py}}(k) \\ \mathbf{V_{ny}}(k) \end{bmatrix} = \begin{bmatrix} w_m{}^{\frac{1}{l}} \\ w_s{}^{\frac{1}{l}} \\ \mathbf{w_c}^{\frac{1}{l}} \\ \mathbf{w_o}^{\frac{1}{l}} \end{bmatrix} \circ \begin{bmatrix} {I_m}^*(k+1) \\ {I_s}^*(k+1) \\ \tilde{\mathbf{I}}_\mathbf{c}{}^*(k+1) \\ \tilde{\mathbf{I}}_\mathbf{o}{}^*(k+1) \end{bmatrix} - \mathbf{w_I}^{\frac{1}{l}} \circ \left(\tilde{F}_{HL} \tilde{\mathbf{X}}_\mathbf{HL}(k) + \tilde{H}_{HL} \tilde{\mathbf{E}}_\mathbf{HL}(k) \right) \tag{5.16}$$

With $\circ$ defined as the HADAMARD product, i.e. the term by term product. The notation l represents the norm which is selected for the optimization. It is then possible to deduce the formulation of the control allocation problem for the high-level control by knowing that the voltages $\mathbf{V_{py}}$, respectively $\mathbf{V_{ny}}$, are bounded between $(1-q)V_{DC}$ and V_{DC}, respectively $-V_{DC}$ and $(q-1)V_{DC}$. $\hat{M}_{HL}$ and $\hat{\mathbf{a}}_\mathbf{dHL}$ are then introduced to account for the weights for each type of current and the allocation problem is then stated:

$$HLCAP_{m-ph} : \left\{ \hat{M}_{HL} \mathbf{U_{HL}}(k) = \hat{\mathbf{a}}_\mathbf{dHL}(k) \mid \mathbf{V_{min}} \leq \mathbf{U_{HL}}(k) \leq \mathbf{V_{max}} \right\} \tag{5.17}$$

Different solutions to solve this control allocation problem are presented here.

Error minimization online control allocation

The adaptation of the approach proposed in Section 4.B.2 makes it possible to establish the high-level control allocation optimization problem from (5.17):

$$HLCAOP_{m-ph} : \begin{cases} \min_{\mathbf{V}, \hat{\mathbf{e}}_\mathbf{HL}} J_{l_{HL}} = ||\hat{\mathbf{e}}_\mathbf{HL}||_l^l \\ u.c. : \\ \hat{M}_{HL} \mathbf{V} - \hat{\mathbf{e}}_\mathbf{HL} = \hat{\mathbf{a}}_\mathbf{dHL} \\ \mathbf{V_{min}} \leq \mathbf{V} \leq \mathbf{V_{max}} \\ -\hat{\mathbf{e}}_\mathbf{HL}^\mathbf{max} \leq \hat{\mathbf{e}}_\mathbf{HL} \leq \hat{\mathbf{e}}_\mathbf{HL}^\mathbf{max} \end{cases} \tag{5.18}$$

Solving this optimization problem is done in real time by EMOn whose equality constraint matrix sizes are given in 5.3.

$\mathcal{A}_{HL}$	N	$m=3$
LP	$(2m \times 6m)$	(6×18)
QP	$(2m \times 4m)$	(6×12)

Table 5.3: High-level CAOP equality constraint matrices comparison.

Model inversion based control allocation

The analysis of $\hat{M}_{HL}$ shows that it is invertible when the gains of $\mathbf{w_I}$ are strictly greater than 0, which is the case by definition, so the control $\mathbf{U_{HL}}$ which guarantees the satisfaction of the allocation equation is expressed:

$$\mathbf{U_{HL}}(k) = \hat{M}_{HL}{}^{-1} \hat{\mathbf{a}}_\mathbf{dHL}(k) \tag{5.19}$$

This solution, which is optimal from the point of view of the allocation equation, is applied to the system only if the control limits are respected. Otherwise, a projection on the admissible set is applied. The MIB being easy to implement, it is therefore programmed for comparison with the EMOn.

High-level reference model tuning

The method of control allocation of the currents implemented here uses a reference model in order to specify the desired closed-loop dynamics of the currents. The current $\mathbf{I_o}$ is the one that represents the energy conversion between the MMC and the AC network, which makes it the current to be ultimately controlled. Its reference has only one fundamental component which is at $f_o = 50$ Hz. The choice is thus made of a pole placement in closed-loop with a bandwidth of 500 Hz, that is to say $p_{CC} = -2\ \pi\ 500 = -1000\ \pi$ rad/s in closed-loop. To keep a harmonious behavior between the different types of currents, the same poles are chosen for all. The reference model embodied by $F_{HL,M}$ and $G_{HL,M}$ is thus defined from these poles and for a unit static gain.

$$F_{HL,M} = e^{p_{CC}\mathbb{I}_{2m}T_c} \qquad G_{HL,M} = \mathbb{I}_{2m} - F_{HL,M} \tag{5.20}$$

5.B.2.2 High-level control allocation formulation from the GPFSROBHCCSSM

In this section, one of the major contributions of this chapter is presented: the formulation for the control allocation of the currents, using the GPFSROBHCCSSM. In order to evaluate the influence of this control-oriented model of reduced order compared to the GPFOCSSM, the dedicated formulation of the control allocation problem is introduced starting from (3.153) which is recalled here:

$$\begin{aligned} &C_{HL}^{dq012} G_{HL}^{dq012} \mathbf{U}_{\mathbf{HL}}^{\mathbf{dq012}}(k) \\ &\quad = \mathbf{Y}_{\mathbf{HL}}^{\mathbf{dq012}}(k+1) - C_{HL}^{dq012} F_{HL}^{dq012} \mathbf{X}_{\mathbf{HL}}^{\mathbf{dq012}}(k) - C_{HL}^{dq012} H_{HL}^{dq012} \mathbf{E}_{\mathbf{HL}}^{\mathbf{dq012}}(k) \end{aligned} \tag{5.21}$$

The current reference model in the Park 12 reference frame is defined:

$$\begin{bmatrix} I_m^{dq012*}(k+1) \\ I_s^{dq012*}(k+1) \\ \tilde{\mathbf{I}}_{\mathbf{c}}^{\mathbf{dq012}*}(k+1) \\ \tilde{\mathbf{I}}_{\mathbf{o}}^{\mathbf{dq012}*}(k+1) \end{bmatrix} = \mathbf{Y}_{\mathbf{HL}}^{\mathbf{dq012}*}(k+1) = F_{HL,M}^{dq012} \mathbf{Y}_{\mathbf{HL}}^{\mathbf{dq012}}(k) + G_{HL,M}^{dq012} \mathbf{Y}_{\mathbf{HL}}^{\mathbf{dq012}^{ref}}(k) \tag{5.22}$$

For the currents to track the reference model (5.22), equation (5.25) represents the allocation equation that the control $\mathbf{U}_{\mathbf{HL}}^{\mathbf{dq012}}$ must satisfy. Equation (5.25) is derived by substituting $\mathbf{Y}_{\mathbf{HL}}^{\mathbf{dq012}}$ for (5.22) in (5.21):

$$M_{HL}^{dq012} \mathbf{U}_{\mathbf{HL}}^{\mathbf{dq012}}(k) = \mathbf{Y}_{\mathbf{HL}}^{\mathbf{dq012}*}(k+1) - \left(F_{HL}^{dq012} \mathbf{X}_{\mathbf{HL}}^{\mathbf{dq012}}(k) + H_{HL}^{dq012} \mathbf{E}_{\mathbf{HL}}^{\mathbf{dq012}}(k) \right) \tag{5.25}$$

With $M_{HL}^{dq012} = C_{HL}^{dq012} G_{HL}^{dq012} = G_{HL}^{dq012}$. The control having limitations, (5.25) will not always admit feasible solutions, a gap may therefore be observed between the two terms of this equation. This gap is then defined according to:

$$\mathbf{e}_{\mathbf{HL}}^{\mathbf{dq012}}(k) = M_{HL}^{dq012} \mathbf{U}_{\mathbf{HL}}^{\mathbf{dq012}}(k) - \left[\mathbf{Y}_{\mathbf{HL}}^{\mathbf{dq012}*}(k+1) - \left(F_{HL}^{dq012} \mathbf{X}_{\mathbf{HL}}^{\mathbf{dq012}}(k) + H_{HL}^{dq012} \mathbf{E}_{\mathbf{HL}}^{\mathbf{dq012}}(k) \right) \right] \tag{5.26}$$

Each component of the vector $\mathbf{e}_{\mathbf{HL}}^{\mathbf{dq012}}$ represents the deviation between the control effectiveness on a given current and the control objective associated with that current. Equation (5.23) in the margin illustrates the distribution of these components in $\mathbf{Y}_{\mathbf{HL}}^{\mathbf{dq012}}$. In order to give the possibility to give more importance to the reference tracking of some currents over the others, weights in the allocation equation are introduced, as in (5.16) previoulsy, in anticipation of the implementation of CAOP for the high-level control. With w_m, w_s, $\mathbf{w_c}$ and $\mathbf{w_o}$[1] the weighting factors specific to

$$\mathbf{Y}_{\mathbf{HL}}^{\mathbf{dq012}} = \begin{bmatrix} I_m \\ I_s \\ I_c^{d_1} \\ I_c^{q_1} \\ I_c^{d_2} \\ I_c^{q_2} \\ I_o^{d_1} \\ I_o^{q_1} \\ I_o^{d_2} \\ I_o^{q_2} \end{bmatrix} \tag{5.23}$$

$$\mathbf{w_I} = \begin{bmatrix} w_m \\ w_s \\ w_c^{d_1} \\ w_c^{q_1} \\ w_c^{d_2} \\ w_c^{q_2} \\ w_o^{d_1} \\ w_o^{q_1} \\ w_o^{d_2} \\ w_o^{q_2} \end{bmatrix} \tag{5.24}$$

[1] It is noted that the weights $\mathbf{w_c}$ and $\mathbf{w_o}$ are then updated to have only four components each as shown by (5.24).

each current type, the deviation error (5.23) is updated:

$$\begin{aligned}\hat{\mathbf{e}}_{\mathbf{HL}}^{\mathbf{dq}012}(k) = \mathbf{w_I}^{\frac{1}{l}}\, M_{HL}^{dq012}\mathbf{U}_{\mathbf{HL}}^{\mathbf{dq}012}(k) \\ -\mathbf{w_I}^{\frac{1}{l}}\,\left[\mathbf{Y}_{\mathbf{HL}}^{\mathbf{dq}012*}(k+1) - \left(F_{HL}^{dq012}\mathbf{X}_{\mathbf{HL}}^{\mathbf{dq}012}(k) + H_{HL}^{dq012}\mathbf{E}_{\mathbf{HL}}^{\mathbf{dq}012}(k)\right)\right]\end{aligned} \tag{5.27}$$

The allocation will therefore minimize this weighted difference in real time:

$$\hat{\mathbf{e}}_{\mathbf{HL}}^{\mathbf{dq}012} = \hat{M}_{HL}^{dq012}\mathbf{U}_{\mathbf{HL}}^{\mathbf{dq}012} - \hat{\mathbf{a}}_{\mathbf{dHL}}^{\mathbf{dq}012} \tag{5.28}$$

The control voltages limits in the rotating frame $\mathbf{U}_{\mathbf{HL}}^{\mathbf{dq}012} = \mathbf{V}^{\mathbf{dq}012}$ are obtained by change of basis of the voltage limits $\mathbf{V_{max}}$ and $\mathbf{V_{min}}$[1]. The allocation problem is then set:

$$HLCAP_{Park\ 12} : \left\{ \hat{M}_{HL}^{dq012}\mathbf{U}_{\mathbf{HL}}^{\mathbf{dq}012}(k) = \hat{\mathbf{a}}_{\mathbf{dHL}}^{\mathbf{dq}012}(k) \;\middle|\; \mathbf{V}_{\mathbf{min}}^{\mathbf{dq}012} \leq \mathbf{U}_{\mathbf{HL}}^{\mathbf{dq}012}(k) \leq \mathbf{V}_{\mathbf{max}}^{\mathbf{dq}012} \right\} \tag{5.29}$$

Error minimization online control allocation

The control allocation problem (5.29) is solved by EMOn and takes the form (5.30) by taking advantage of the development proposed in Section 4.B.2 as it was done previously for the currents in the natural basis

$$HLCAOP_{Park\ 12} : \begin{cases} \min_{\mathbf{V}^{\mathbf{dq}012}, \hat{\mathbf{e}}_{\mathbf{HL}}^{\mathbf{dq}012}} J_{l_{HL}^{dq012}} = ||\hat{\mathbf{e}}_{\mathbf{HL}}^{\mathbf{dq}012}||_l^l \\ u.c. : \\ \hat{M}_{HL}^{dq012}\mathbf{V}^{\mathbf{dq}012} - \hat{\mathbf{e}}_{\mathbf{HL}}^{\mathbf{dq}012} = \hat{\mathbf{a}}_{\mathbf{dHL}}^{\mathbf{dq}012} \\ \mathbf{V}_{\mathbf{min}}^{\mathbf{dq}012} \leq \mathbf{V}^{\mathbf{dq}012} \leq \mathbf{V}_{\mathbf{max}}^{\mathbf{dq}012} \\ -\hat{\mathbf{e}}_{\mathbf{HL}}^{\mathbf{dq}012\mathbf{max}} \leq \hat{\mathbf{e}}_{\mathbf{HL}}^{\mathbf{dq}012} \leq \hat{\mathbf{e}}_{\mathbf{HL}}^{\mathbf{dq}012\mathbf{max}} \end{cases} \tag{5.30}$$

The equality constraint matrix $\mathcal{A}_{HL}^{dq012}$, whose size locks from $m \geq 5$, is then smaller than $\mathcal{A}_{HL}$ as shown Table 5.4.

		m	$m=3$	$m=20$
$\mathcal{A}_{HL}$	LP	$(2m \times 6m)$	(6×18)	(40×120)
	QP	$(2m \times 4m)$	(6×12)	(40×80)
$\mathcal{A}_{HL}^{dq012}$	LP	$(2m' \times 6m')$	(6×18)	(10×30)
	QP	$(2m' \times 4m')$	(6×12)	(10×20)

Table 5.4: High-level CAOP equality constraint matrices comparison. Figure 5.3 recalls the relationship between m' and m.

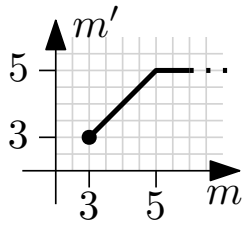

Figure 5.3: Definition of m' as a function of m.

As expected, the CA solved in the PARK 12 reference frame in real time has not only a much lower complexity but also a constant complexity for 5 phases and beyond.

[1] The determination of the limits $\mathbf{V}_{\mathbf{max}}^{\mathbf{dq}012}$ and $\mathbf{V}_{\mathbf{min}}^{\mathbf{dq}012}$ is still a field of investigation here for several reasons. One of them is how it would be possible to better account for the decomposition into several harmonics and how to decouple the limits of these different harmonic components that are all related. Another reason is the fact that even if there were only one harmonic component, the current formulation of the $HLCAP_{Park\ 12}$ does not allow nonlinear constraints on the norm of the rotating vectors in the PARK 12 reference frame.

Model inversion based control allocation

As $\hat{M}_{HL}$ in the previous model, the matrix $\hat{M}_{HL}^{dq012}$ is invertible under the same conditions which are verified, thus:

$$\mathbf{U_{HL}^{dq012}}(k) = \hat{M}_{HL}^{dq012^{-1}}\ \hat{\mathbf{a}}_{\mathbf{d}}\mathbf{_{HL}^{dq012}}(k) \tag{5.31}$$

This solution being able to exceed the control limits, it will be clipped on the latter when going beyond.

High-level PARK 12 reference model tuning

The tuning of the reference model is based on the same performances requirements than the one tuned in the initial stationary reference frame in order to enable the fair comparison between the control performances of the control allocation in the two reference frames. Thus $p_{CC} = 2\,\pi\,500$ rad/s here too. The reference model $F_{HL,M}^{dq012}$, $G_{HL,M}^{dq012}$ is thus tuned for this pole placement and a unit static gain.

$$F_{HL,M}^{dq012} = e^{p_{CC}\mathbb{I}_{2m'}T_c} \qquad G_{HL,M}^{dq012} = \mathbb{I}_{2m'} - F_{HL,M}^{dq012} \tag{5.32}$$

High-level control architecture

Figure 5.4 allows one to have at a glance all the possibilities developed for the high-level control. Several choices are therefore possible:

- Perform the control in the initial stationary reference frame with GPFOCSSM or in the rotating reference frame PARK 12 with GPFSROBHCCSSM.
- Use the EMOn methods or the MIB
- In the case of EMOn methods, real time optimization is possible using LP or QP

In the case of the control in the PARK 12 reference frame, the allocation itself is done from the model GPFSROBHCCSSM, drastically reducing the complexity of the allocation to be carried out as underlined by Table 5.4. However, performing the allocation in this reference frame is only possible if the appropriate change of reference frame for the quantities $\mathbf{I_c}$, $\mathbf{I_o}$, $\mathbf{V_y}$, $\mathbf{I_c^{ref}}$ and $\mathbf{I_o^{ref}}$ has been carried out before. Similarly, the solution of the optimization is given in this same reference frame and an inverse transformation must therefore be applied to the voltages $\mathbf{V_{py}^{dq012}}$ and $\mathbf{V_{ny}^{dq012}}$. In terms of the complexity of the current control algorithm in the PARK 12 reference frame, compared to the one performed in the natural reference frame, consider these 7 changes of bases which are each products with matrices of size $(m' \times m)$, or $(m \times m')$ for the inverse transformation, as well as the computation of the PLL in addition to the complexity - reduced - of the allocation operation itself. Thus, in order to compare the control of the currents in these two reference frames by taking into account all the operations necessary for each one, a study is carried out in this chapter.

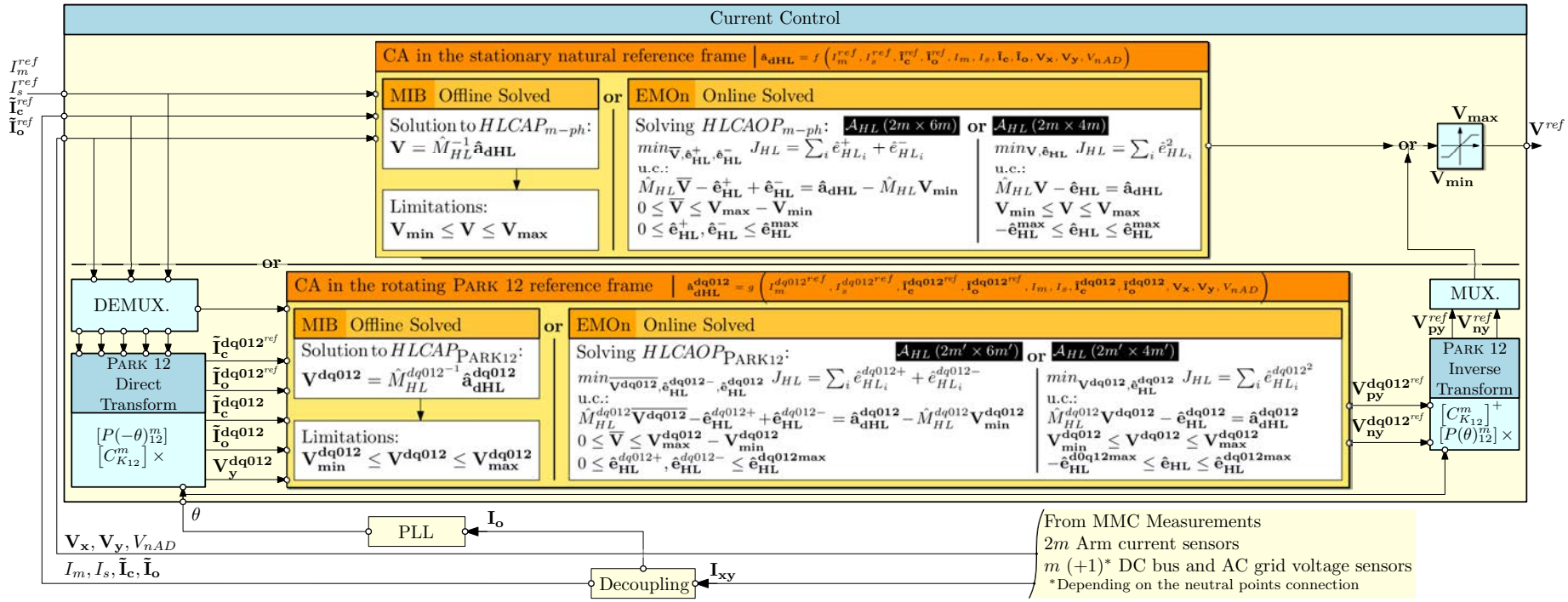

Figure 5.4: Current control allocation detailed architecture possibilities.

It is mentioned that the *Decoupling* operation applied to the measured arm currents is done with the following equations:

$$\begin{cases} i_m = \frac{1}{2m}\sum_{y=y_1}^{y_m} i_{py} + i_{ny} \\ i_s = \frac{1}{2m}\sum_{y=y_1}^{y_m} i_{py} - i_{ny} \end{cases} \quad \forall y \in \{y_1, \ldots, y_m\}, \quad i_{o_y} = \frac{i_{py} + i_{ny}}{2} - i_m \quad \forall y \in \{y_1, \ldots, y_m\}, \quad i_{c_y} = \frac{i_{py} - i_{ny}}{2} - i_m \tag{5.33}$$

5.B.3 | High-level-low-level control: all-in-one

By nesting the current and voltage control loops as proposed so far according to Figure 5.1, each control loop considers its downstream loop as guaranteeing the control objective for which it was designed. In this case, the possible interactions between the different dynamics involved in the MMC are not considered.

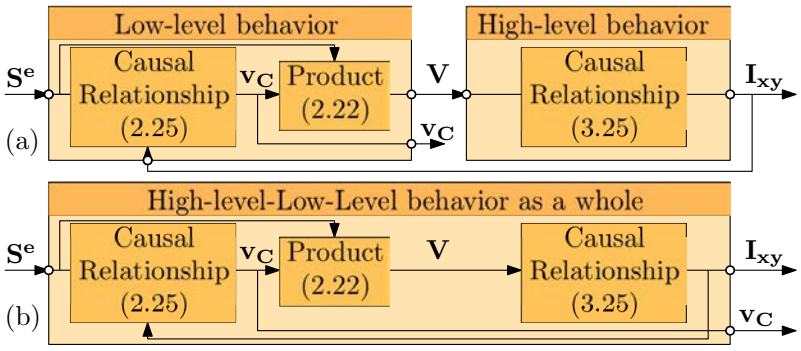

Figure 5.5: Simplified diagram of the global open loop behavior of the MMC. $\mathbf{I_{xy}}$ gathers all the arm currents. (a) Case where high-level and low-level are considered and modeled separately. (b) Case where high-level and low-level are considered together in the objective to derive a high-level-low-level control-oriented model that embraces their interaction.

However, according to the low-level and high-level models, the voltages $\mathbf{v_C}$ directly influences the voltages $\mathbf{V}$, which influence the currents $\mathbf{I_{xy}}$, which in turn influence the voltages $\mathbf{v_C}$, see Figure 5.5 (a). Thus, it could be beneficial to evaluate the influence of taking into account this dynamic coupling, in the control allocation algorithm, on the behavior of the system in closed-loop. Thus, the high-level-low-level model is developed for that purpose as represented on Figure 5.5 (b).

In the case of the high-level-low-level control, the control allocation of the MMC embodies the scheme described by Figure 1.11 d). This means that the control allocation ensures the role of the *output current control*, the *circulating current control*, the *DC bus current control* and the *common mode current control* as well as the *arm voltage control* and the *balancing control algorithm* simultaneously. The first benefit of this approach is to wisely act on the switching states in order to to meet the multiple control objectives as best as possible and in a cooperative manner.

5.B.3.1 | High-level-low-level state-space model

From Chapter 3 and Chapter 2 the idea here is to express the behavior of capacitor voltages and currents from the duty cycles. The low-level functional detailed model full-bridge submodule model which models the voltages v_{xy} and the high-level model which considers them as these input variables will be able to interface through $\mathbf{V}$. The first modelling step is to adapt the (5.1) model to interface with the (5.14) model.

5.B.3.2 The global control-oriented model of the MMC

The derivation of this global model is given in Appendix L. It combines the low-level model (5.1) true for all arms of the converter with the high-level model (3.66), which in the end reads:

$$\begin{cases} \mathbf{X_{MMC}}(k+1) = F_{MMC}\mathbf{X_{MMC}}(k) + G_{MMC}(k)\mathbf{U_{MMC}}(k) + H_{MMC}\mathbf{E_{MMC}}(k) \\ \mathbf{Y_{MMC}}(k) = C_{MMC}\mathbf{X_{MMC}}(k) \end{cases} \tag{5.34}$$

with $\mathbf{Y_{MMC}} = \mathbf{X_{MMC}} = \begin{bmatrix} \mathbf{v_C}^T & I_m & I_s & \tilde{\mathbf{I}}_\mathbf{c}^T & \tilde{\mathbf{I}}_\mathbf{o}^T \end{bmatrix}^T$ and $\mathbf{U_{MMC}} = \mathbf{U_{LL}} = \mathbf{D^e}$. The model obtained represents the dynamics of the all the capacitor voltages and the currents in the MMC and whose two equations can be combined to obtain the form:

$$M_{MMC}(k)\mathbf{U_{LL}}(k) = \mathbf{Y_{MMC}}(k+1) - C_{MMC}\left(F_{MMC}\mathbf{X_{MMC}}(k) + H_{MMC}\mathbf{E_{MMC}}(k)\right) \tag{5.35}$$

5.B.3.3 High-level-low-level control allocation formulation

Let (5.36) be the desired refrence model to impose on the behavior of the voltages and currents in closed-loop:

$$\mathbf{Y^*_{MMC}}(k+1) = \begin{bmatrix} F_{LL,M} & \\ & F_{HL,M} \end{bmatrix} \mathbf{Y_{MMC}}(k) + \begin{bmatrix} G_{LL,M} & \\ & G_{HL,M} \end{bmatrix} \mathbf{Y^{ref}_{MMC}}(k) \tag{5.36}$$

This model is defined from the previous reference models tuned for the low-level control and the high-level control. The approach already adopted from Section 5.B.2.2 is here adapted for (5.35) and (5.36). The vector of weights used here to favor certain control objectives is the combination of the previous ones: $\mathbf{w} = [\mathbf{w_{v_C}}\ w_m\ w_s\ \mathbf{w_c}^T\ \mathbf{w_o}^T]^T$. The control allocation problem is therefore formulated accordingly:

$$HLLLCAP : \left\{ \hat{M}_{MMC}(k)\mathbf{U_{MMC}}(k) = \hat{\mathbf{a}}_{\mathbf{d_{MMC}}}(k) \;\middle|\; \mathbf{D^{e^{min}}} \leq \mathbf{U_{MMC}}(k) \leq \mathbf{D^{e^{max}}} \right\} \tag{5.37}$$

It is noted that $\hat{M}_{MMC}$ is of size $(2m(N+1) \times 4mN)$, so solving the allocation problem by considering the whole MMC in one step represents some complexity compared to solving high-level control and low-level control.

Control allocation optimization problem for the entire MMC

Based on (5.37), the global allocation control formulation of the MMC is formulated:

$$MMCCAOP : \begin{cases} \min_{\mathbf{D^e}, \hat{\mathbf{e}}_\mathbf{MMC}} J_{l_{MMC}} = ||\hat{\mathbf{e}}_\mathbf{MMC}||_l^l \\ u.c. : \\ \hat{M}_{MMC}\mathbf{D^e} - \hat{\mathbf{e}}_\mathbf{MMC} = \hat{\mathbf{a}}_{\mathbf{d_{MMC}}} \\ \mathbf{D^{e^{min}}} \leq \mathbf{D^e} \leq \mathbf{D^{e^{max}}} \\ -\hat{\mathbf{e}}^\mathbf{max}_\mathbf{MMC} \leq \hat{\mathbf{e}}_\mathbf{MMC} \leq \hat{\mathbf{e}}^\mathbf{max}_\mathbf{MMC} \end{cases} \tag{5.38}$$

Solving this optimization problem is done in real time. It is interesting to note that the matrix $\mathcal{A}_{MMC}$ is of the same size as the equality constraint matrix $\mathcal{A}_{LL}$ obtained in the framework of the $LLCAOP$ (5.11). This is understandable because solving the $LLCAOP$ ensures two objectives. First, the v_{xy} reference tracking is ensured, this stands for the reference tracking of the currents in the framework of the low-level control. The second control objective is to ensure the capacitor voltage balancing. Since the role of the $MMCCAOP$ is to ensure the reference tracking of the currents and the capacitor balancing feature as well, $LLCAOP$ and $MMCCAOP$ both have

the same size. The difference between the two is that the $MMCCAOP$ is formulated from a model which takes into account the coupled influence of the capacitor voltages and the currents while $LLCAOP$ does not. A work of comparison of these possibilities of control allocation is thus to be carried out. Figure 5.6 presents the diagram of the control allocation architecture in the case of real time programming of (5.38).

$\mathcal{A}_{MMC}$		$m=3, N=3$	$m=3, N=400$
LP	$(2m(N+1) \times 2m(4N+2))$	(24×84)	(2406×9612)
QP	$(2m(N+1) \times 2m(3N+1))$	(24×60)	(2406×7206)

Table 5.5: $MMC\ CAOP$ equality constraint matrices comparison.

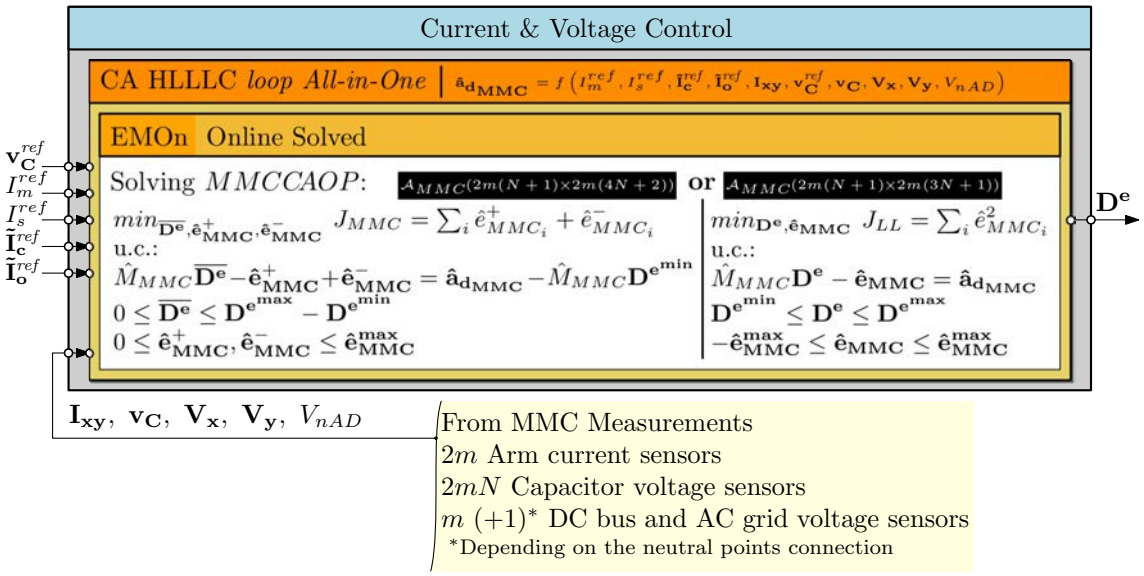

Figure 5.6: High-level low-level control allocation architecture featuring both *Current Control* and *Voltage Control*.

5.B.4 Power-energy control

The power balance of the converter shows conduction losses which involves the square of the current I_s. Determining the reference I_s^{ref} that satisfies the control objective power-energy in the form of a power balance therefore gives two solutions, the objective of power-energy control is to determine the one whose amplitude is the smallest in order to guarantee operation at the point of minimal losses. The work of [BFB19] presents a first approach by model inversion. The approach proposed here builds on these results while adopting a more complete formulation that takes into account a more extensive power balance and is capable of imposing a reference model tracking on the energy. From the Section 3.G.2, the power balance adapted for the allocation is formatted:

$$T_c C_{PE} B_{PE} \mathbf{U_{PE}}(k) + T_c C_{PE} B'_{PE} \mathbf{U_{PE}}(k)^2 = \mathbf{Y_{PE}}(k+1) - C_{PE} X_{PE}(k) - T_c C_{PE} \mathbf{E_{PE}}(k) \tag{5.39}$$

where $\mathbf{U_{PE}} = I_s$, and $\mathbf{Y_{PE}} = E_{MMC}$. The only input variable is the current I_s. The choice is made in closed-loop to tune the dynamics of E_{MMC} from the specification of a reference model defined by the matrices $F_{PE,M} \in \mathbb{R}$ and $G_{PE,M} \in \mathbb{R}$:

$$\mathbf{Y^*_{PE}}(k+1) = F_{PE,M} \mathbf{Y_{PE}}(k) + G_{PE,M} \mathbf{Y^{ref}_{PE}}(k) \tag{5.40}$$

By satisfying (5.39) with $\mathbf{Y}^*_{\mathbf{PE}}(k+1)$ instead of $\mathbf{Y}_{\mathbf{PE}}(k+1)$, I_s will impose on E_{MMC} the dynamics desired by (5.40). By the mentioned substitution, it comes that:

$$M_{PE}(k)\mathbf{U_{PE}}(k)+M'_{PE}\mathbf{U_{PE}}(k)^2=\left[F_{PE,M}\mathbf{Y_{PE}}(k)+G_{PE,M}\mathbf{Y}^{ref}_{\mathbf{PE}}(k)\right]-X_{PE}(k)-T_c\mathbf{E_{PE}}(k) \tag{5.41}$$

where $M_{PE}(k) = T_cC_{PE}B_{PE}(k) = T_cB_{PE}(k)$, $M'_{PE} = T_cC_{PE}B'_{PE} = T_cB'_{PE}$. With $\mathbf{a_{d_{PE}}}$ as the desired action vector, the command $\mathbf{U_{PE}}$ must therefore be a solution of (5.42):

$$M_{PE}(k)\mathbf{U_{PE}}(k) + M'_{PE}\mathbf{U_{PE}}(k)^2 = \mathbf{a_{d_{PE}}}(k) \tag{5.42}$$

With the limits of I_s from the analysis of the zone of operation[1], the control allocation problem is formulated:

$$PECAP : \left\{ M'_{PE}\mathbf{U_{PE}}(k)^2 + M_{PE}(k)\mathbf{U_{PE}}(k) = \mathbf{a_{d_{PE}}}(k) \;\middle|\; \hat{I}_s^{min} \leq \mathbf{U_{PE}}(k) \leq \hat{I}_s^{max} \right\} \tag{5.43}$$

Because of the non-linearity of the control, this control allocation problem has an originality compared to the other allocation problems treated in this study with the LLC and the HLC which are both linear. With a single input, this system therefore does not have the characteristic of being overactuated. The I_s current set point is then simply clipped to its boundaries when exceeded. An optimization CA is therefore of useless here, it is a MIB method which is used to realize the control allocation of the energy. The solution $\mathbf{U_{PE}}$ obtained by model inversion is found by solving the equation (5.42), which amounts to finding the roots of the polynomial P defined by:

$$P(\mathbf{U_{PE}}) = \mathbf{a_{d_{PE}}} - M'_{PE}{\mathbf{U_{PE}}}^2 - M_{PE}\mathbf{U_{PE}} \tag{5.44}$$

By trivial determination of the roots of this second degree polynomial, it follows that:

$$\mathbf{U_{PE}} = \frac{M_{PE} \pm \sqrt{\Delta_{PE}}}{-2M'_{PE}} = \frac{M_{PE} \pm \sqrt{{M_{PE}}^2 + 4M'_{PE}\mathbf{a_{d_{PE}}}}}{-2M'_{PE}} \tag{5.45}$$

The selected root is the one with the smallest absolute value in order to generate the least conduction losses, knowing the sign of M_{PE} and M'_{PE}, $M_{PE}/(-2M'_{PE})$ is positive. Therefore, it follows that:

$${\mathbf{U_{PE}}}^{min\ P_J} = \frac{M_{PE} - \sqrt{\Delta_{PE}}}{-2M'_{PE}} = \frac{M_{PE} - \sqrt{{M_{PE}}^2 + 4M'_{PE}\mathbf{a_{d_{PE}}}}}{-2M'_{PE}} \tag{5.46}$$

Having a negative discriminant means either to ask for an energy setpoint E^{ref}_{MMC} suddenly higher than the energy E_{MMC} contained in the converter at this moment, or to have a power P_o supplied to the output AC network that suddenly increases. In this case, the real current that is closest to the desired control objective is the vertex of the concave parabola, i.e.:

$${\mathbf{U_{PE}}}^{\Delta_{PE}\leq 0} = \frac{M_{PE}}{-2M'_{PE}} \tag{5.47}$$

Consequently, the solution of the allocation by MIB for the level power-energy which will be selected can thus be summarized in the following way:

$$\mathbf{U_{PE}}(k) = \mathfrak{Re}\left(\frac{M_{PE} - \sqrt{{M_{PE}}^2 + 4M'_{PE}\mathbf{a_{d_{PE}}}(k)}}{-2M'_{PE}}\right) \tag{5.48}$$

The power-energy control part of the control architecture will be in charge of performing the energy control from the implementation of (5.48) and its limits $\hat{I}_s^{min} \leq \mathbf{U_{PE}}(k) \leq \hat{I}_s^{max}$.

[1] See Section 3.H.1

Power-energy reference model tuning

The tuning choice for the energy reference model is made from the closed-loop reference model of the currents. It is chosen to set poles one decade slower than those of the currents in closed-loop: $p_{EC} = p_{CC}/10 = 2\,\pi\,50$ rad/s, that is to say, a 50 Hz bandwidth in the closed-loop.

$$F_{PE,M} = e^{p_{EC}T_c} \qquad G_{PE,M} = 1 - F_{PE,M} \tag{5.49}$$

Power-energy control architecture

Figure 5.7 presents the implementation operated in real time for the *Energy Control*. The *Estimator* blocks are made of the simple direct calculation of the necessary quantities from their formula according to the measurable states in the MMC.

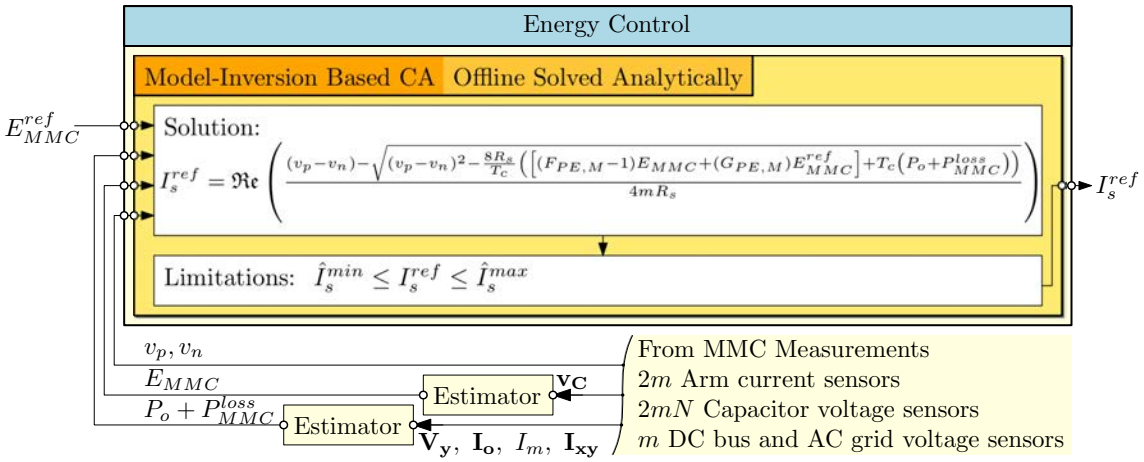

Figure 5.7: Energy control allocation detailed architecture.

5.B.5 The Scalable Control Allocation Architectures of the MMC

This part presents how the different CAOPs formalized so far interact together to build a control allocation architecture of the MMC as a whole.

5.B.5.1 Reference generator

In a causal manner, the first step of the architecture is the specification of the references to be imposed on the currents and voltages that the different allocation algorithms have to track.

Capacitor voltage and Energy reference

The voltage reference sent to all the capacitors is determined in the case of nominal operation without fault[1]. In this case, all the capacitors have the same reference in order to distribute the

[1] Section 5.E provides another determination of the capacitor voltage references in the case of a fault in the sub-modules.

efforts equally on the different capacitors:

$$\mathbf{v_C^{ref}} = \frac{V_{DC}}{N}\mathbb{I}_{2mN,1} \tag{5.50}$$

The energy reference E_{MMC}^{ref} to be sent to the energy controller is directly calculated from (5.51):

$$E_{MMC}^{ref} = \sum_{y=y_1}^{y_m}\sum_{x=n}^{p}\sum_{j=1}^{N} C\frac{{v_{C_{xyj}}}^2}{2} = \frac{mC}{N}{V_{DC}}^2 \tag{5.51}$$

These references are adapted, depending on the fluctuations of the voltage V_{DC} available on the DC bus.

DC source current reference

The reference for the I_s^{ref} current to be drawn from the DC bus is determined from the power balance, knowing the energy reference that must be balanced in the converter. This reference varies according to the operating point required by the other current references, for which more or less current must be drawn from the DC bus in order to maintain the nominal energy amount in the converter.

Common mode current reference

The reference for the common mode current I_m^{ref} is set to zero in order to guarantee the electrical balance of the AC-side network.

AC-side output current reference

The reference $\mathbf{I_o^{ref}}$ is free within the limits imposed by the LOZ. This current reference is a variable which specifies the targeted converter operating point in terms of DC-AC power transfer. It is recalled that the AC-side source voltage is described by:

$$v_y = \hat{V}_{AC}\ \sin(\omega_o t - \varphi_y - \varphi_v) \tag{5.52}$$

Let ${\varphi_P}^{ref}$ specify the desired power factor in the AC-side network, so the phase reference for $\mathbf{I_o^{ref}}$ will be $\varphi_o^{ref} = \varphi_v + {\varphi_P}^{ref}$ In order to form a ${\varphi_P}^{ref}$ phase shift of with the AC network voltage:

$$i_{o_y}^{ref} = \hat{I}_o^{ref}\ \sin\left(\omega_o t - \varphi_y - \varphi_v - {\varphi_P}^{ref}\right) \tag{5.53}$$

In the PARK reference frame with a rotation synchronized on the angle $\omega_o t - \varphi_o^{ref}$, this leads to:

$$\mathbf{\tilde{I}_o^{dq012}}^{ref} = \begin{bmatrix} I_o^{d_1 ref} \\ I_o^{q_1 ref} \\ I_o^{d_2 ref} \\ I_o^{q_2 ref} \end{bmatrix} = \frac{\hat{I}_o^{ref}}{k}\begin{bmatrix} 0 \\ -1 \\ 0 \\ 0 \end{bmatrix} \tag{5.54}$$

Circulating current reference

The presence of circulating current in the converter increases the conduction losses in the arms of the converter especially since these currents are not involved in the energy conversion between

the DC bus and the MMC or between the latter and the AC network. Thus, their reference is zero in most cases, but in order to evaluate the capacity of the control to ensure the tracking of the circulating currents, their reference $\mathbf{I_c^{ref}}$ is sometimes chosen at a non-zero amplitude. In this case, it is defined from an amplitude and a phase. In most cases here, φ_c^{ref} is chosen null.

$$i_c^{ref} = \hat{I}_c^{ref} \sin\left(\omega_c t - 2\varphi_y - 2\varphi_c^{ref}\right) = \hat{I}_c^{ref} \sin\left(2\omega_o t - 2\varphi_y - 2\varphi_c^{ref}\right) \tag{5.55}$$

In the PARK reference frame with a rotation synchronized on the angle $\omega_o t - \varphi_o^{ref}$, this leads to:

$$\tilde{\mathbf{I}}_{\mathbf{c}}^{\mathbf{dq}012\,ref} = \begin{bmatrix} I_c^{d_1\,ref} \\ I_c^{q_1\,ref} \\ I_c^{d_2\,ref} \\ I_c^{q_2\,ref} \end{bmatrix} = \frac{\hat{I}_c^{ref}}{k} \begin{bmatrix} 0 \\ 0 \\ -\sin(2\varphi_c^{ref} - 2\varphi_o^{ref}) \\ -\cos(2\varphi_c^{ref} - 2\varphi_o^{ref}) \end{bmatrix} \tag{5.56}$$

5.B.5.2 Energy Control

The *Energy Control* guarantees the tracking of the global energy balancing objective of the MMC by determining I_s^{ref} to be drawn according to E_{MMC}^{ref} and the powers P_o and P_{MMC}^{loss} that are exchanged through the converter. This reference is computed directly at each sampling period by the analytic formula (5.48) which solves the $PECAP$ (5.43).

5.B.5.3 Current Control

The role of the *Current Control* is to ensure the tracking of the current references by determining the arms voltages. It therefore takes as input the current references I_m^{ref}, I_s^{ref}, $\mathbf{I_c^{ref}}$ and $\mathbf{I_o^{ref}}$ and determines the references $\mathbf{V_{py}^{ref}}$ and $\mathbf{V_{ny}^{ref}}$, i.e. $\mathbf{V}^{ref}$.

To compute the voltage references, the *Current Control* block has several possibilities. The control allocation algorithms are able to solve either the $HLCAOP_{m-ph}$ (5.18) in real time by online optimization EMOn using the LP or the QP, either the $HLCAOP_{Park\ 12}$ (5.30) using one of these same two optimizations. This allocation can also be done using the MIB methods by direct implementation of (5.19) to operate the control in the natural stationary reference frame and (5.31) in the PARK 12 rotating frame.

It is worth noting that the *Current Control* can also be performed commonly with the *Voltage Control* through the resolution by EMOn methods in real time of the $MMCCAOP$ (5.38) in the context of a global control.

5.B.5.4 Voltage Control

To guarantee the *Voltage Control*, the first objective of the associated control stage is to ensure that at each moment the voltages $\mathbf{V_{xy}}$ reach their references $\mathbf{V_{xy}^{ref}}$. However, this control stage also has the important role of managing the active balancing of the capacitors. Indeed, the second objective of the *Voltage Control* is to ensure that the voltages $\mathbf{v_C}$ follow their reference $\mathbf{v_C^{ref}}$. The tracking of these two objectives is made possible by acting on the duty cycles of all the cells of the converter $\mathbf{D^e}$.

All the control allocation laws implemented here are based on an EMOn algorithm using the LP

or the QP. These solving methods are used for different formulations of the low-level CAOP: a first technique is the $2m$ *loops parallel* which executes in parallel one allocation per arm and a second technique $2m$ *loops series* which executes in series all allocations of the arms. These techniques are both based on solving (5.9). A third technique 1 *loop all-in-one*, which differs from the first two by its approach, considering the allocation of the whole arms of the converter in one step is also implemented (5.11).

5.B.5.5 PWM and interface with the MMC

The data exchange between the control architecture and the converter is done through analog-to-digital converters and vice versa. These devices are equiped with a zero-order-hold feature at the sampling period T_c rate. The high frequency computer then generates the switching states from the duty cycles using the selected PWM technique. In the opposite direction, the sensors send back the collected data to the control system through a ZOH which maintains their value during T_c. It is noted that, for the case of the MMC available at the LAPLACE, the sampling period is equal to the switching period of the PWM carrier: $T_c = T_s$. This link between the sampling period and switching period is particularly suitable for lower-power converters. For MMCs with a higher number of SMs that convert higher power levels, a reduction of the switching frequency is necessary to lower the switching losses. In such cases the control sampling period becomes smaller than the switching one $T_c \leq T_s$.

The literature is full of techniques to generate the signals to be sent to the gate drivers of the cells in order to perform the PWM operation with different performances and implementation complexities [HL03]. It is decided here to use the PSPWM method which is both widespread and efficient compared to other more classical methods such as the 3-phase RSPWM [Bow75; Sei88] - equivalent to the SVPWM [Hol92; Jac+01] - or even the SPWM [SS64]. The PSPWM method allows both waveforms to have a lower total harmonic distortion than the RSPWM methods and a wider linear zone than the SPWM method, which makes it an interesting trade-off whose properties have already been proven, see Figure 5.8.

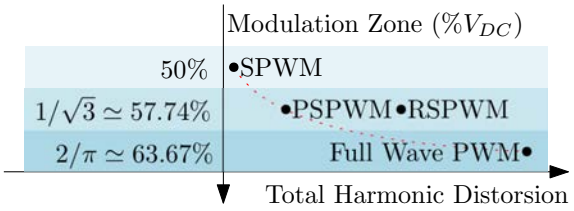

Figure 5.8: Qualitative comparison of popular PWM methods on total harmonic distorsion and modulation zone criteria.

5.B.5.6 Control Architecture

The different control stages are assembled and Figure 5.9 presents the overall control architecture of the MMC, highlighting the different control possibilities and the versatility of the proposed architecture. Here are some key points about what is made possible by the architecture introduced here:

- The three control stages adapt to the number m of phases as well as to the number N of submodules making this control system a scalable architecture. Changing the size of the MMC does not require any modification of the implemented control allocation algorithms or

optimization. It is sufficient to simply specify the size of the converter (m and N) and the whole architecture is updated automatically.

- The *Current Control* as well as *Voltage Control* can use the EMOn control allocation methods with either LP or the QP using the Simplex, the Interior-Point or the Active-Set optimization algorithms au choix. The *Current Control* problem can also be solved using a MIB control allocation method implementing a simple inversion of the state-space model selected.
- About the state-space model selection, the *Current Control* can be computed using the GPFOCSSM or the GPFSROBHCCSSM; while the *Voltage Control* problem can be solved using a $2m$ *loops in series*, a $2m$ *loops parallel* or a 1 *loop all-in-one* model/technique.
- The nature of the architecture is to be chosen also: either a cascaded control where *Current Control* and *Voltage Control* are dealt with as two decoupled control loops or a global control where *Current Control* and *Voltage Control* are ensured by the same control allocation controller that uses the global SSM of the MMC (5.38).

All those features of the control architecture of the MMC make it a **scalable** and **versatile** control system: the Scalable Control Allocation Architecture (SCAA).

Among the whole set of possibilities which are offered by the control architecture, the choice is made to focus only on a subset which is analyzed in greater detail. In particular, the optimization algorithms LP and QP are compared within the framework of the low-level control and an analysis of the internal functioning of these algorithms within the framework of the control allocation is developed. In the case of the high-level control, it is the evaluation of the control allocation methods scalability which is studied in order to compare optimization algorithms and the effectiveness of the $HLCAP$ formulations as the number of phases of the AC network increases. These different analyses are carried out from results obtained in simulation and in HIL with an experimental device allowing to test and develop the algorithms in a safe and efficient way.

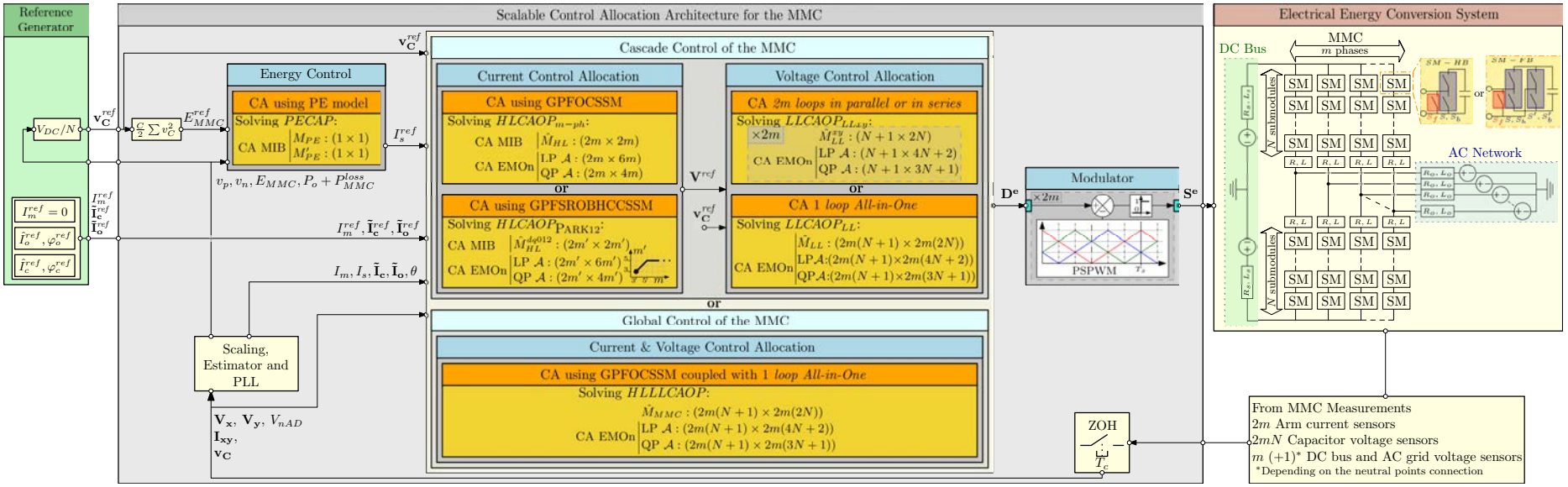

Figure 5.9: Entire scalable control allocation architecture developed for the MMC.

Remark: Whether controlling voltages, currents or both simultaneously, the use of the control allocation allows for a global approach that takes into account the interactions between the different states of the system and the associated coupled control objectives in order to operate the system in a cooperative manner. Therefore, the control of the MMC using the control allocation methods is here done by implementing all possible cutting-edge schemes of Figure 1.11, except the traditional approach shown on Figure 1.11 a).

5.C | Study of the low-level control allocation of the MMC

The main objective of this section is to show the capabilities of the control allocation methods to solve the low-level control problem: to guarantee arm voltages reference tracking as well as the active capacitor balancing feature. In particular, the focus will be on proving that the control allocation methods are valuable candidates for the control of the MMC.

5.C.1 | Low-level control allocation: comparing linear programming with quadratic programming

In the framework of the control allocation, work on the EMOn methods has shown the differences between the use of the LP and the QP for systems mainly belonging to the aeronautics domain as in [FB10]. A first reason to compare the LP with the QP for the case of the MMC is to see how it behaves with a system belonging to a different domain and especially with a system which has a number of inputs that can be much more important. A second reason for this comparison is the desire to better understand the internal behavior of how the optimization algorithms distribute the effort among the control variables when solving the CAP.

5.C.1.1 | Dedicated control allocation optimization formulations

The formulations that are compared here are the formulations (4.24) for LP and (4.26) for the QP in the case of $LLCAOP_{xy}$ recalled here (5.9). The development of detailed CA EMOn formulations that are solved in real time are given in Appendix M.

$$LLCAOP_{xy} : \begin{cases} \min_{\mathbf{D^e_{xy}}, \hat{\mathbf{e}}^{\mathbf{xy}}_{\mathbf{LL}}} J^{xy}_{l_{LL}} = ||\hat{\mathbf{e}}^{\mathbf{xy}}_{\mathbf{LL}}||^l_l \\ u.c. : \\ \hat{M}^{xy}_{LL}\mathbf{D^e_{xy}} - \hat{\mathbf{e}}^{\mathbf{xy}}_{\mathbf{LL}} = \hat{\mathbf{a}}_{\mathbf{d}}{}^{\mathbf{xy}}_{\mathbf{LL}} \\ \mathbf{D^{e^{min}}_{xy}} \leq \mathbf{D^e_{xy}} \leq \mathbf{D^{e^{max}}_{xy}} \\ -\hat{\mathbf{e}}^{\mathbf{xy}^{\mathbf{max}}}_{\mathbf{LL}} \leq \hat{\mathbf{e}}^{\mathbf{xy}}_{\mathbf{LL}} \leq \hat{\mathbf{e}}^{\mathbf{xy}^{\mathbf{max}}}_{\mathbf{LL}} \end{cases} \tag{5.57}$$

5.C.1.2 | Hardware-In-the-Loop testing

The MMC belongs to the family of multicellular capacitor converters. Such a converter represents a large potential energy storage all the more that it is modular: the more submodules it has, the more electric energy it stores[1]. Thus, before implementing a control law on a real MMC, it is preferable to verify its performance in a closed-loop from tests that do not involve electrical power. It is from this point of view that the hardware-in-the-loop test methods are particularly suited.

[1] For example, for the case of the MMC available at the LAPLACE - whose characteristics are recalled in Table 5.7 - with capacitors all balanced at a nominal voltage of 200 V, it contains a nominal energy of 720 J - this is the amount of energy equivalent to a body of 80 kg running at 15.3 km/h (9.5 mph) - which is quite significant. In the case of a grid-scale MMC system, as the one studied by [Per+12], this same energy reaches 30 MJ, that is to say a vehicle of 55 metric tons driving at 120 km/h (75 mph).

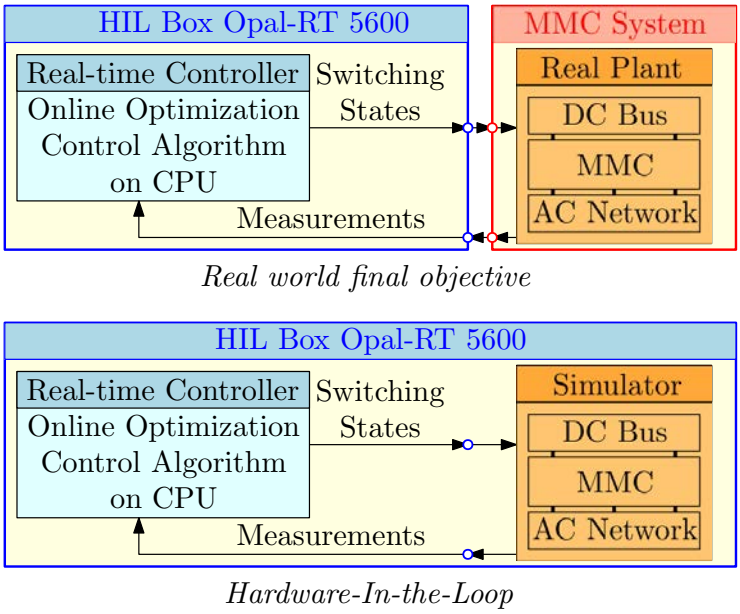

Figure 5.10: Hardware-in-the-loop test principle with comparison to the real world operation.

As expressed in Figure 5.10, in the context of the use of the HIL, the plant is replaced by a *simulator* of the system that aims at reproducing the real operation of the system with enough accuracy to be able to evaluate, analyze and correct the control law that is executed in real time by the *real time controller* which is the real calculator that is used afterwards to drive the real system[1]. With such a test method, it is possible to modify the control algorithm as much as desired in safety without damaging physical hardware or putting personnel at risk. The control is computed with the selected sampling period of 250 µs and the information exchange is done through zero-order hold. The parameters of the HIL box are given in Table 5.6. Figure 5.11 shows the setup of the HIL procedure, with the black box as the OP5600.

Opal-RT HIL Box Parameters	
HIL box	OP5600
CPU Type	Intel Xeon X5690
CPU Clock frequency	3.46 GHz
CPU Cache	12 Mb
CPU RAM	4 Gb

Table 5.6: HIL Hardware Parameters

[1] Rapid control prototyping differs from hardware-in-the-loop in that the control strategy is simulated in real time and the plant, or system under control, is the real one. This is the dual case from hardware-in-the-loop.

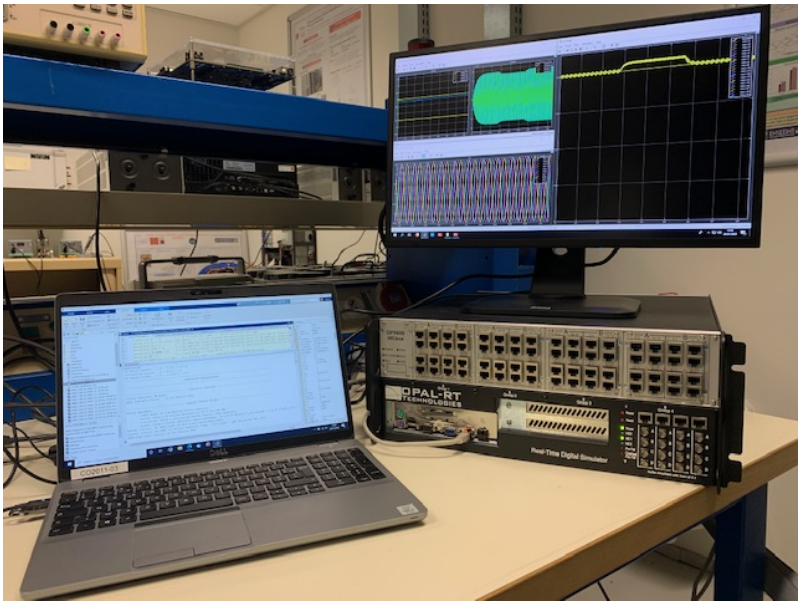

Figure 5.11: Hardware-In-the-Loop test setup with the Opal-RT OP5600 HIL box (under the monitor) at the LAPLACE laboratory. Results displayed on the right monitor are those from the actual test, see Figure 5.17.

Although the tests are carried out in a safe way at first, for the tests *real world* - as represented in Figure 5.10 - the experimental setup located in the LAPLACE is presented. To allow the proof-of-concept of control laws, it is a low-power converter, with respect to its modular capacities, which was designed in the work of [Ser14]. It features a 10 kVA rated power for a 600 V bus.

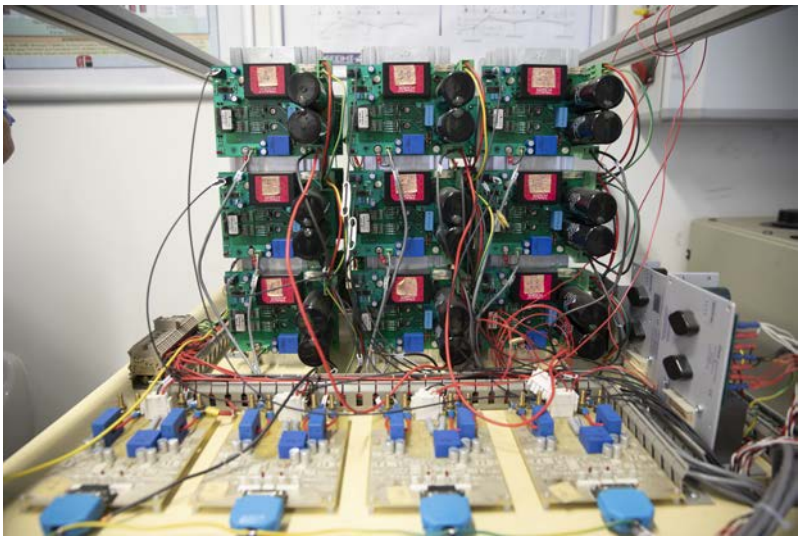

Figure 5.12: LAPLACE-MMC front side where 9 submodules and 4 sensor cards are displayed.

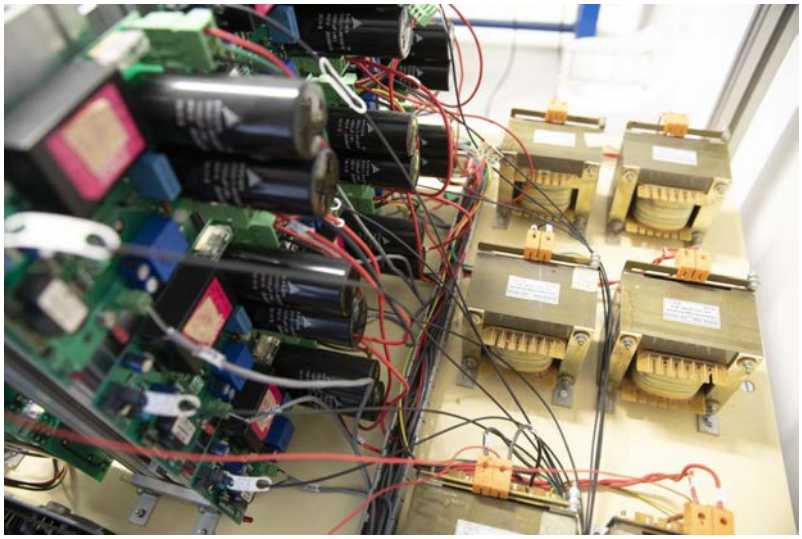

Figure 5.13: LAPLACE-MMC back side with 9 submodules the 2×3 arm inductances. Photo credits: CNRS, LAPLACE, Frédéric Maligne.

Figure 5.12 shows the front side of the setup with half of the submodules. The back side shows the same configuration of cells. The MMC has a total of 18 submodules and the connectors allow it to be put either in a 2-phase configuration with 9 submodule per leg, or in 3-phase with $N = 3$ submodules per arm. As shown in this figure, each submodule contains two capacitors in parallel, each of which is sized for a nominal voltage of 200 V with a capacitance of 1 mF each, i.e. a capacitance of 2 mF in each submodule. In nominal operation, the energy contained in the converter is thus 720 J in average value for the 3-phase configuration. The right side of Figure 5.13 shows the 5 mH inductances that constitute the interconnections between the positive and negative arms of a same leg.

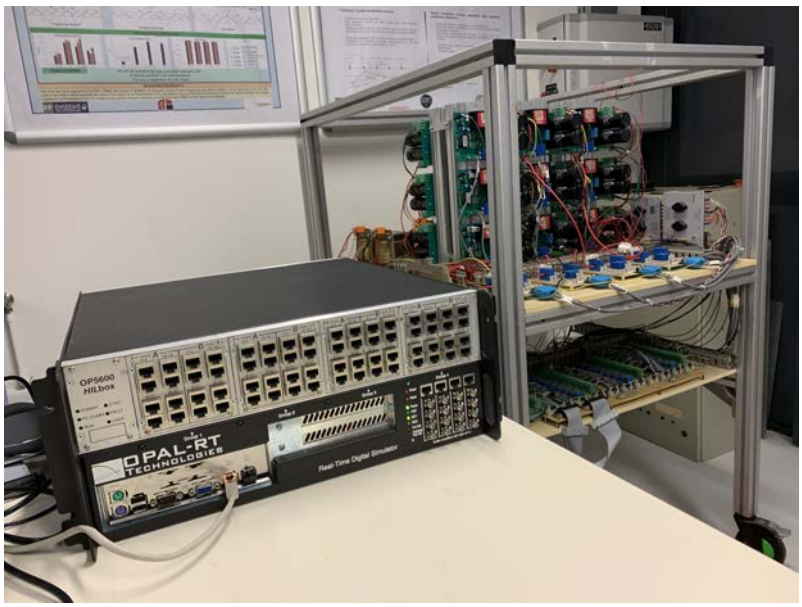

Figure 5.14: LAPLACE-MMC global view with and its connection to the OP5600.

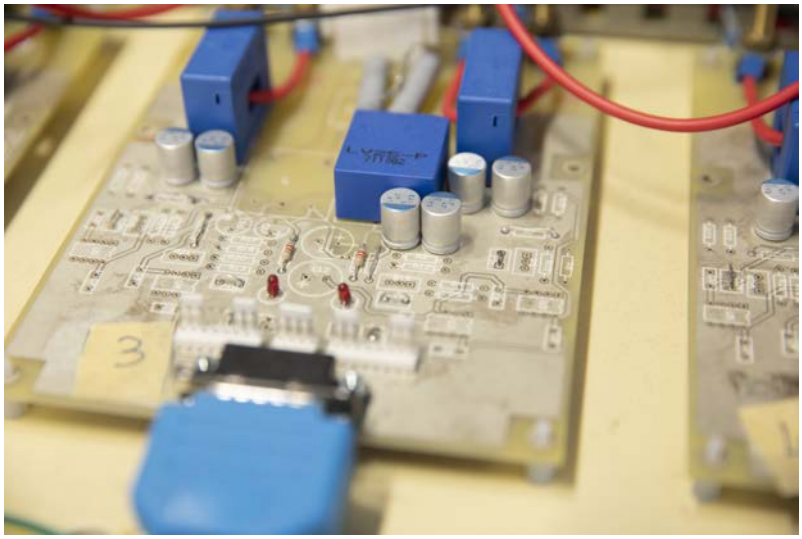

Figure 5.15: LAPLACE-MMC current and voltage sensor card. Photo credits: CNRS, LAPLACE, Frédéric Maligne.

On Figure 5.14, one can see that the MMC interfaces with the Opal-RT OP5600 by means of the gray interconnection cable. This OP5600 executes in real time the control algorithm on a central processing unit before sending the duty cycles to the FPGA card which generates the gate signals with any PWM technique. The gate signals received by the system are then transmitted to the submodules by optical fibres. Each submodule contains a capacitor voltage $v_{C_{xyj}}$ sensor. Figure 5.15 shows one of the four additional measurement cards for the arm currents i_{xy}, the DC bus current I_s, the AC network voltages v_y and the DC bus voltage V_{DC}. The gray cable then return these measurements to the Opal-RT OP5600 in order to close the loop.

5.C.1.3 Test conditions

The purpose of the test here is to compare the linear programming with the quadratic programming solutions for the low-level control. The *Current Control* is therefore not analyzed in detail here[1]. It is only specified that the latter is done by CA EMOn solving the $HLCAOP_{m-ph}$ (5.30) using the Interior-Point algorithm. The *Energy Control* is done by MIB (5.48), the only solution designed here. The *Voltage Control* is a $2m$ *loops in series* implementation technique which is chosen to successively carry out the allocation for each arm of the converter.

The simulations perform the following pattern: the capacitors are first initialized with their nominal voltage V_{DC}/N. At the beginning of the simulation, the power factor reference for the current $\mathbf{I_o}^{ref}$ is set to $\cos({\varphi_P}^{ref}) = 0.95$ and the current amplitude reference is chosen to $\hat{I}_o^{ref} = 20\%\hat{I}_o^{max}$[2]. To evaluate whether the capacitors can be balanced in the presence of circulating current, $\mathbf{I_c}^{ref}$ is chosen such that $\hat{I}_c^{ref} = 0.75$ A. These reference amplitudes for the circulating current and the output current remain constant throughout the simulation. The other currents follow the references described in Section 5.B.5.1. With a simulation starting with capac-

[1] The high-level control analysis is detailed in the next section, see Section 5.D.

[2] This reference amplitude seems small compared to the capabilities of the MMC but the goal here is to verify the capabilities of the *Voltage Control*, tests covering a wider range of the operating zone of the currents are carried out in the part dedicated to the analysis of the *Current Control* in the next section. The latter, necessarily using a *Voltage Control* stage, shows the extension of the capacitor balancing performances in the case where currents of higher amplitude are converted.

itors initialized at their nominal value, the static balancing performance of the control allocation is probed. In order to trigger the dynamic behavior of the capacitors in closed-loop, a $\mathbf{v_C^{ref}}$ set-point step is added to the simulation which is then divided into three time intervals as shown on Figure 5.16. With the HIL, control architecture computations are performed in real time on the same computer as the one used to control the real converter, and in this case the converter is replaced by a *simulator* of its behavior.

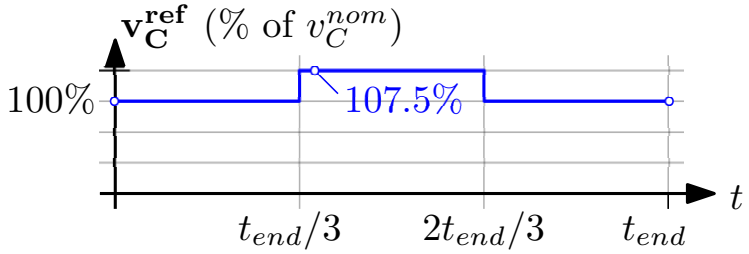

Figure 5.16: $\mathbf{v_C^{ref}}$ pattern over time in the hardware-in-the-loop tests.

Meaning	Symbol	Value
MMC Power System Parameters		
DC bus		
Nominal capacitor voltage	v_C^{nom}	200 V
Submodules per arm	N (several tests)	$3, 7, 20, 50$
DC Bus voltage	$V_{DC} = N v_C^{nom}$	$N \cdot 200$ V
Half-bus voltage	$v_p = -v_n$	$V_{DC}/2 = N \cdot 100$ V
DC Bus impedance	R_s, L_s	50 mΩ, 2 mH
MMC		
Submodules type	q	1 (half-bridge submodule)
Capacitor capacity	C	2 mF
Switching frequency and period	f_s, T_s	4 kHz, 250 µs
Arm resistance and inductance	R, L	10 mΩ, 5 mH
AC network		
Number of phases	m	5
AC active voltage amplitude	$\hat{V}_{AC}$	150 V
AC active voltage phase	φ_v	0 rad
AC grid frequency and period	f_o, T_o	50 Hz, 20 ms
AC grid frequency	ω_o	$2\pi f_o \simeq 314$ rad/s
AC load resistance and inductance	R_o, L_o	40 Ω, 5 mH
Closed-Loop HIL Simulation Parameters		
Simulation time step	T_{step}	$T_s/100 = 2.5$ µs
Simulation end time	t_{end}	$42\ T_o = 840$ ms

Table 5.7: Closed-Loop HIL Simulation & MMC Parameters - low-level control testing

5.C.1.4 Hardware-In-the-Loop test results

Figures 5.17, 5.18, and 5.19 as well as Table 5.9 contain the results of tests performed in HIL for this case where a 5-phase polyphase system is considered. The figures give these results for the case of $N = 7$ while the table gives a summary of the results for the list of $N = \{3, 7, 20, 50\}$.

Hardware-in-the-loop tests for 7 submodules per arm

The observation of the simulation results shows that the control allocation manages to guarantee the balancing not only in steady state but also under transient conditions. This balancing is ensured when using the linear programming as well as in the case of the quadratic programming, although the latter more easily achieves balancing. This shows therefore that it is possible to use CA EMOn methods to meet the performances required for the low-level control of the MMC by having a single control device to ensure both arm voltage reference tracking and capacitor voltage balancing by acting directly on the duty cycles.

Equation (2.27) modelling the dynamic behavior of the voltages in the capacitors show that they depend directly on the product between the current i_{xy} in the arm to which their submodule belongs and the duty cycle of the considered cell. In the modelling approach, it was shown that the current i_{xy} is composed of the four types of currents which cross the MMC during its operation. It is thus composed of alternating components due to the output current $\mathbf{I_o}$ and the circulating current $\mathbf{I_c}$. Although the duty cycles are best adapted by the low-level control allocation to guarantee the active balancing of the capacitors, they still have boundaries that limit the freedom of operation. As a result, the voltages across the capacitors are still subject to fluctuations in the current, which, as shown by Figure 5.19, has as its largest AC component the fundamental component at 50 Hz. This explains the presence of capacitor voltage ripples at this same frequency, which can be found in Figure 5.17.

Although the purpose of this section is not to show the capabilities of the control allocation to guarantee the current reference tracking for the four types of currents in the MMC, it is still interesting to make sure tracking is achieved. As can be seen from Figure 5.18, the i_{py_5} and i_{ny_5} currents are controlled with good reference tracking performance. Section 5.D will focus in more detail on the closed-loop behavior of each of the four current types.

The most obvious observation that appears when looking at Figure 5.18 (a) and (b) is the strong difference between the use of the linear programming and the quadratic programming in solving the CAOP. Indeed, it is visible at first glance that the QP manages to balance the capacitors and the use of duty cycles of the same arm in a significantly more uniform way than the LP. More precisely, during this simulation the LP induces a maximum voltage ripple of 1.2% on the capacitors and the maximum deviation that $\mathbf{v_{C_{py_5}}}$ has from its reference is 3.8%. Comparatively, using the QP its same quantities are respectively worth 0.61% and 1.2%. Moreover the measurement of the extremum gap of the preference difference $\varepsilon_g(\mathbf{e_{pLL}^{py_5}})$ gives 5.7% contrary to 0% for the QP and thus confirms that the latter distributes the variations of the voltages much more equitably within the same arm than the LP. The QP balances the capacitors more harmoniously.

Figure 5.18 (c) provides an interesting information about the computational resources needed by each of the optimization algorithms in real time. The number of iterations displayed per computational step corresponds to the number of iterations required by the selected optimization algorithm to give a solution. The number of iterations thus indicated represents the total number of iterations for the set of $2m = 10$ arms. To have an estimate of the number of iterations that would be taken by the algorithms of control allocation EMOn algorithms for a single arm it is thus advisable to divide the displayed values by 10. The first observation is that, for this simulation with $N = 7$ submodules per arm, the use of the QP requires nearly 18% less iterations than the LP at each sampling step on average over the simulation according to the values found in Table 5.8. It is noticed that for the QP the number of iterations at each step is relatively close to the average although variations are still present, contrary to the LP where the variations are much larger. By observing more in detail these variations for the LP as for the QP, it is noticed

that a certain periodicity in the evolution of this quantity. Every 20 ms the pattern repeats itself, which corresponds to the 50 Hz frequency of the $\mathbf{v_{C_{xy}}}$ voltages ripples. In addition to these variations, when going through the second third of the simulations, this number of iterations per step is modified even more extensively but stabilizes once the operation around the new operating zone, aksed by the step of $\mathbf{v}^{ref}_{\mathbf{C_{xy}}}$, is reached.

Total number of iterations	Linear programming	Quadratic programming
Mean	106.3	77.95
Maximum variation	70	7
Maximum variation around an operating point	40	5

Table 5.8: Low-level control $2m$ *loops in series* LP and QP total number of iterations per step for $N = 7$, $m = 5$.

These variations provide two insights. The first is that the number of iterations per sampling step varies according to the operating point of the converter. This means that, for some operating points, the optimal solution is easier to find than for others. This may correspond to the operating directions naturally favored by the converter. The second lesson is that by using the QP the number of iterations per calculation step is much more stable than in the case of the LP since its variation according to the operating point is smaller, allowing a better predictability of the number of iterations necessary in the case of the QP.

According to the observations made, the quadratic programming works to balance the capacitors in a harmonious way as well as the use of duty cycles, so it would be possible to conclude that the quadratic programming tends to favor a uniform use of the control variables in the case of this system that is the MMC. The question then arises to analyze this observed behavior to evaluate if it would be possible to anticipate this type of behavior on other systems and what would be the "*harmony indicator*" to use in a general way.

Hardware-in-the-loop tests for a range of submodules per arm

Table 5.9 presents the results of several simulations carried out identically to those whose results are presented in Figure 5.17 and Figure 5.18 but testing several cases of different quantities of submodules. To observe an interesting trend of the evolution of the characteristics while keeping reasonable simulation times, it is proposed to perform the simulations for $N \in \{3, 20, 50\}$ in addition to the previous case $N = 5$.

	$(\Delta\mathbf{e}^{\mathbf{xy}}_{\mathbf{pLL}})^{max}$		$(\mathbf{e}^{\mathbf{xy}}_{\mathbf{pLL}})^{max}$		$\varepsilon_g(\mathbf{e}^{\mathbf{xy}}_{\mathbf{pLL}})^{max}$		Mean tot. iter. num.	
N	LP	QP	LP	QP	LP	QP	LP	QP
3	0.82%	0.52%	12.3%	6.28%	9.4%	0%	49.90	86.04
7	1.2%	0.61%	10.3%	5.27%	8.0%	0%	106.3	77.95
20	4.7%	1.97%	8.00%	4.69%	5.7%	0%	272.3	79.91
50	0.9%	0.655%	11.3%	5.18%	8.2%	0%	724.4	76.58

Table 5.9: Low-level control $2m$ *loops in series* LP and QP characteristics evolution with N.

First, it should be noted that for the simulation case with $N = 50$, in which the LP is used, a different operating point was selected due to current operating concerns. This is why the case $N = 50$ cannot be compared to the others in terms of capacitor balancing performance since it was not obtained in the same operating conditions for the LP. However, changing the operating point does not change the size of the optimization problem, and the number of iterations obtained still gives a good indication of the computational resources needed. This explains the different colors in Table 5.9.

Regardless of the table size, the QP outperforms the LP for each criterion and for each quantity of submodules.

The column dedicated to the extremum gap ε_g[1], represents the level at which the vector that embodies the preference gap is uniform. These data first show that - for the tests performed - the LP does not guarantee that $\mathbf{e}_{\mathbf{pLL}}^{\mathbf{xy}}$ is uniform. However, the uniformity character is improved as the number of submodule increases[2]. The QP on the other hand guarantees a uniform $\mathbf{e}_{\mathbf{pLL}}^{\mathbf{xy}}$ in all circumstances obtained in simulations. The table also confirms the fact that the LP requires more iterations than the QP per sampling step and this is also true as the number of submodules increases.

This table shows us that the number of iterations for the QP hardly increases, it will even decrease in the case of the increase from 3 to 7 submodules. This characteristic of the QP observed here is particularly interesting and should be studied more extensively: is it possible to guarantee an almost constant number of iterations for the low-level CA EMOn using QP as N increases to the point of reaching several hundreds as in MMCs designed for high power ?

For the same algorithm, like the QP, if it happened that an increase of N did not lead to any increase of iterations, the algorithm would have to solve a more complex problem with matrices of larger size, the operations would be heavier and the computation time would be longer even if the quantity of iterations remains the same. An interesting phenomenon is observed for the LP: it is possible to approximate the number of iterations by a linear function of N with a good precision. Indeed this number of iterations can be approximated by $14.37\ N + 0.584$, over the range of values of N tested, with a correlation coefficient of $R^2 = 0.9988$. With such a slope and such an accuracy of the linear model - assuming that it can indicate a trend for higher values of N - it seems much more beneficial to use the QP with a much more stable number of iterations both as a function of the operating point of the converter and the number of submodules.

The results that have been obtained here concerning the comparison between the functioning of the linear programming and the quadratic programming are analyzed through the study proposed in the next section.

[1] Definition 10 defines the extremum gap

[2] The uniformity is improved as N increases except for the $N = 50$ case which cannot be compared to the others as explained.

(a)

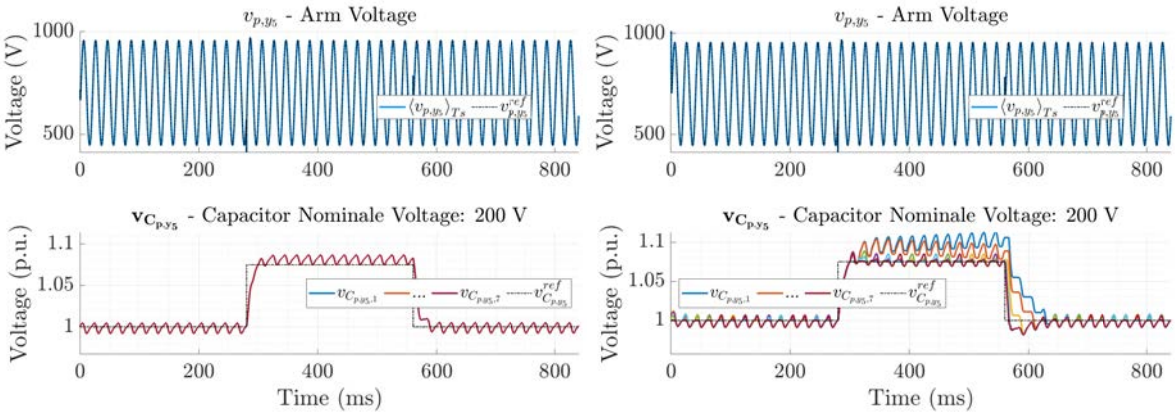

(b)

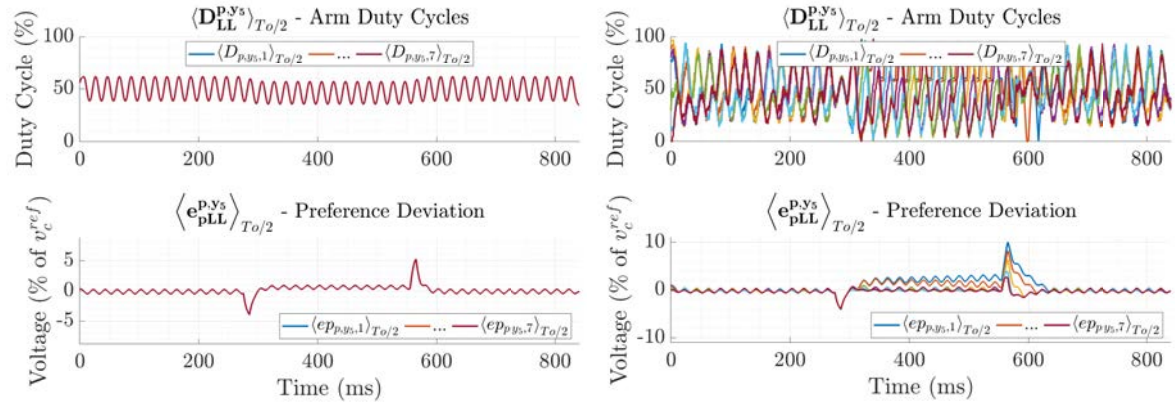

(c)

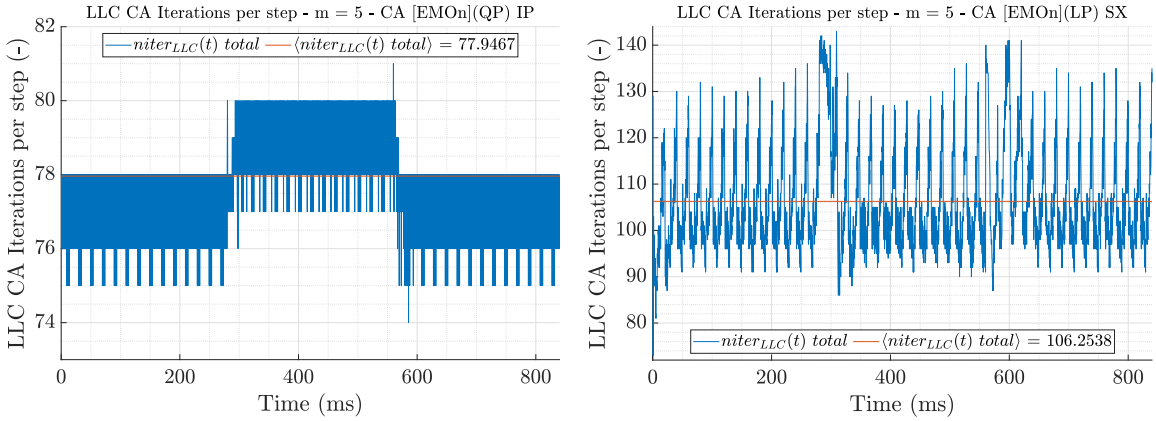

Figure 5.17: Behavior of the voltages in the arm $\#py_5$ as a result of low-level control allocation $2m$ *loops in series* using quadratic programming (left column) and linear programming (right column). (a) Arm voltage and capacitor voltages, (b) Duty cycles and deviation to the low-level preference objective, (c) Total number of iterations of the control allocation method. HIL simulations are done in the 5**-phase** case.

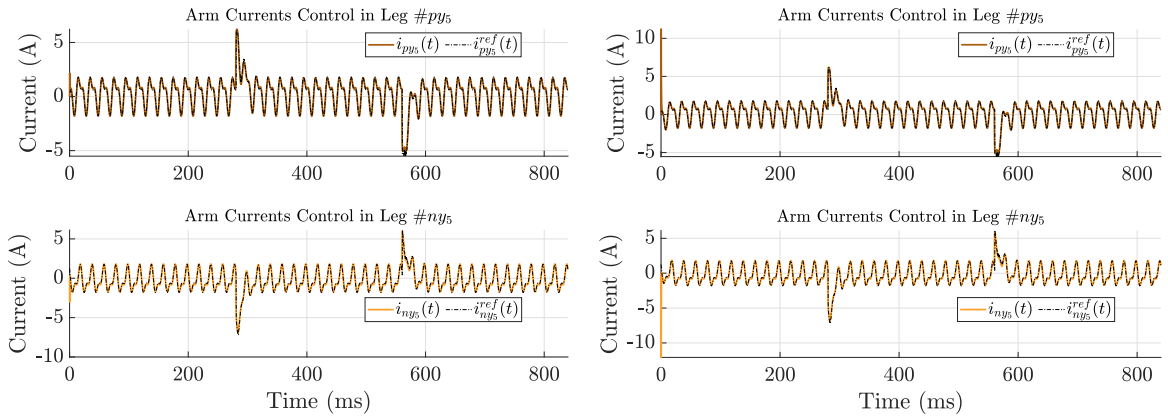

Figure 5.18: Second part of Figure 5.17: MMC leg $\#y_5$ current reference tracking, all phases show a similar result but $2\pi/m$ shifted in time. HIL simulations are done in the 5**-phase** case.

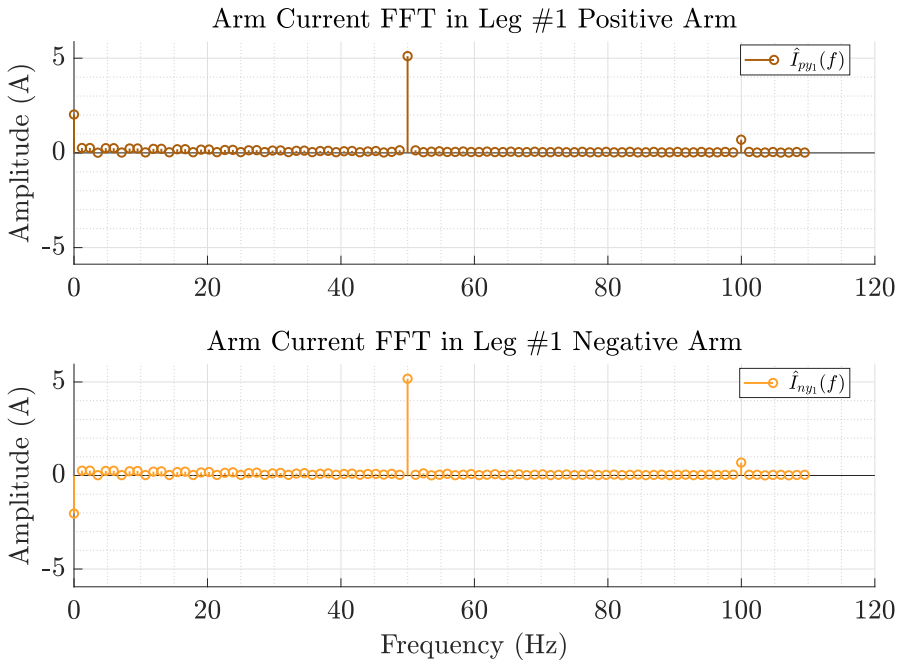

Figure 5.19: Arm currents FFT in leg $\#1$ of the converter, all phases show the same result. For frequencies over 110 Hz amplitudes are lower than 40 mA, which is lower than 0.8% of the fondamental amplitude.

5.C.1.5 Analysis of the LP and QP behaviors

To analyze the behavior of the LP compared to the QP in closed-loop, it is suggested to compare two neighboring solutions to which the two optimization algorithms could converge. This analysis is done in the general case of the EMOn control allocation without assuming that the interest is on a particular physical system.

Let $\mathbf{U}(k)$, the allocated control at time k, such that it ensured an ideal allocation: $\mathbf{e}(k) = 0$. Two neighboring situations U to be applied on the system at time $k+1$ are compared. It is assumed that these neighboring solutions both respect the bounds imposed on the control, so as to compare these two solutions, the indicator that allows us to discriminate them is the cost function of the selected optimization. The question then arises as to which criterion, LP or QP, will prefer the

first and/or the second solution. To be able to evaluate each of the neighboring solutions with respect to the criteria, it is assumed that each one has as for consequence a different deviation $(\mathbf{e}(k)$ to the satisfaction of the allocation equation.

Assume that solutions $\mathbf{U}_1(k+1)$ and $\mathbf{U}_2(k+1)$ exist such $\mathbf{U}_1(k+1)$ gives a deviation

$$\mathbf{e}_1(k+1) = \begin{bmatrix}\delta e & \dots & \delta e & \delta e & \delta e & \delta e & \dots & \delta e\end{bmatrix}^T \in \mathbb{R}^{n_a}, \delta e \in \mathbb{R}, \tag{5.58}$$

and $\mathbf{U}_2(k+1)$ leads to:

$$\mathbf{e}_2(k+1) = \begin{bmatrix}\delta e & \dots & \delta e & (1-\alpha)\delta e & (1+\alpha)\delta e & \delta e & \dots & \delta e\end{bmatrix}^T \in \mathbb{R}^{n_a} \tag{5.59}$$

with $\alpha \in]0;1]$. The closer α is chosen to zero, the more $\mathbf{U}_1(k+1)$ and $\mathbf{U}_2(k+1)$ will be neighboring solutions, which means that α tweaks the size of the neighborhood. In order to characterize the two solutions considered, the following definition is introduced:

Definition 10. *Let $\nu \in \mathbb{R}^n$, the extremum gap of a given vector ν is then expressed as $\varepsilon_g(\nu) = max(\nu) - min(\nu)$. The notion of vector uniformity is then defined as follows: the smaller $\varepsilon_g(\nu)$ is, the more uniform ν is. If $\varepsilon_g(\nu)$ is null, the distribution of the components from ν is said to be uniform. Figure 5.20 shows an example of the extremum gap of a vector.*

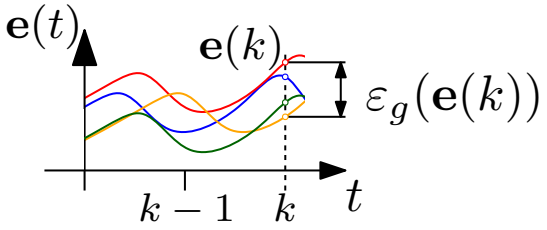

Figure 5.20: Illustrative example of Definition 10 for the vector $\nu = \mathbf{e}(k)$.

According to Definition 10, the extremum gap of each deviation vector can be computed. $\varepsilon_g(\mathbf{e}_1(k+1)) = 0$ confirms that $\mathbf{e}_1(k+1)$ is uniformly distributed whereas $\varepsilon_g(\mathbf{e}_2(k+1)) = 2\,\alpha\,\delta e$ shows that $\mathbf{e}_2(k+1)$ is not.

The two solutions $\mathbf{U}_1(k+1)$ and $\mathbf{U}_2(k+1)$ are then compared with the criteria associated with the two formulations of the online optimization.

Linear programming optimization criterion analysis

In the case of LP, the calculation of the objective function is done directly from (4.24):

$$J_{lLP} = ||\mathbf{e}||_1^1 = |\mathbf{e}| = \sum_i |e_i| \tag{5.60}$$

Thus, the value of the cost associated with $(\mathbf{U}_1(k+1)$ and $(\mathbf{U}_2(k+1)$ is directly deduced:

$$J_{lLP_1} = ||\mathbf{e}_1(k+1)||_1^1 = |\mathbf{e}_1(k+1)| = \sum_i |e_{1_i}| = n_a|\delta e| \tag{5.61}$$

$$J_{lLP_2} = |\mathbf{e}_2(k+1)| = \sum_i |e_{2_i}| = (n_a-2)|\delta e| + (1-\alpha)|\delta e| + (1+\alpha)|\delta e| = n_a|\delta e| \tag{5.62}$$

One can see that $J_{lLP_1} = J_{lLP_2}$, so according to the linear programming criterion, this optimization has no more interest in choosing the solution $\mathbf{U}_1(k+1)$ than the solution $\mathbf{U}_2(k+1)$. The cost of the two solutions being the same, one cannot predict which solution the linear programming will choose in real time, it is more likely that it will choose one of the two solutions according to the one which arrives first during the iterations performed by the optimization algorithm.

Quadratic programming optimization criterion analysis

This same analysis then takes place for the QP. The calculation of the objective function is done directly from (4.27):

$$J_{lQP} = ||\mathbf{e}||_2^2 = \mathbf{e}^2 = \sum_i e_i^2 \tag{5.63}$$

Thus, the value of the cost associated with $(\mathbf{U}_1(k+1)$ and $(\mathbf{U}_2(k+1)$ is directly deduced:

$$J_{lQP_1} = ||\mathbf{e}_1(k+1)||_2^2 = \sum_i e_{1_i}^2 = n_a \delta e^2 \tag{5.64}$$

$$J_{lQP_2} = \sum_i e_{2_i}^2 = (n_a - 2)\delta e^2 + (1-\alpha)^2 \delta e^2 + (1+\alpha)^2 \delta e^2 = (n_a + 2\alpha^2)\delta e^2 \tag{5.65}$$

One can see that $J_{lQP_1} < J_{lQP_2}$ since $0 < \alpha \leq 1$. So, according to the quadratic programming criterion, this optimization has more interest to choose the solution $\mathbf{U}_1(k+1)$ than the solution $\mathbf{U}_2(k+1)$. In real time, between these two solutions which - by assumption - both respect the bounds of the control, the will thus choose $\mathbf{U}_1(k+1)$.

From the comparison of LP and QP to the control allocation behavior analysis

The analysis carried out above can be summarized in the following behavior: two solutions $\mathbf{U}_1$ and $\mathbf{U}_2$ which are extremely close, will not be able to make any difference for the LP. Whereas, contrary to the LP, the QP will favor the choice of a control $\mathbf{U}$ which - through the contribution of each of the u_j to the generation of the desired control objective $\mathbf{a_d}$ - will generate a deviation $\mathbf{e}$ to the allocation equation whose components e_i are balanced as long as the u_j do not saturate. This means that, in the case of QP, all the u_j will be selected according to their weight in the contribution to the generation of $\mathbf{a_d}$, weights which are the terms of M, in order to have balanced e_i gaps. In other words, the weighted contributions of the u_j will be balanced. It is only in some cases of systems where the matrix M has a particular shape that aiming to balance the deviation among all the e_is will result in balancing the use of the u_js. This is in fact the case for the low-level control here as it has been observed with the hardware-in-the-loop simulations.

The generalized study of how the u_j are balanced from their contribution to the creation of $\mathbf{a_d}$ is an appealing perspective that can be done by analyzing $J_l = ||M\mathbf{U} - \mathbf{a_d}||_l^l$ for the two norms ($l = 1$ and $l = 2$).

In the particular case of the low-level control, Figures 5.17-5.18 show that the capacitor voltages are balanced in steady state such that $\forall i, j \in [\![1, N]\!]^2, v_{C_{x,y,i}} \simeq v_{C_{x,y,j}}$, this means that all terms of M_{LL}^{xy} are approximatively the same. Since the voltage reference for all the capacitors is the same, $\forall i, j \in [\![1, N]\!]^2, v_{C_{x,y,i}}^{ref} - v_{C_{x,y,i}} \simeq v_{C_{x,y,j}}^{ref} - v_{C_{x,y,j}}$ in steady state, which means that all terms of $\mathbf{a_{pLL}^{xy}}$ are similar. Moreover, in the second part, M_{pLL}^{xy}, of the matrix $\hat{M}_{LL}^{xy}$, the same factor $T_c i_{xy}^*(k)/C$ weights all the remaining rows of the matrix. Through $\hat{M}_{LL}^{xy}$ (A.184) it is thus found that the converter has control variables that have very close weighting in contributing

to the achievement of the control objective $\hat{\mathbf{a}}_{\mathbf{d}}^{\mathbf{xy}}_{\mathbf{LL}}$. Having approximately the same weighting, these degrees of freedom, which are the duty cycles, will be used in a balanced way by the QP, contrary to the case of resolution by LP, as shown by the hardware-in-the-loop tests in Figures 5.17-5.18.

5.C.1.6 Conclusion of the LP and QP analysis

The analysis carried out in this part on the comparison between the LP and the QP to guarantee the low-level control put forward the fact that the two formulations are able to ensure the balancing of the capacitors as well as the arm voltage reference tracking. However, this study also allowed to highlight the differences between the use of these two optimization algorithms to realize the EMOn control allocation that one can briefly list:

- The use of the QP results in a more uniform balancing of the capacitors and their use compared to the use of LP
- Another advantage to the use of the QP is that in this case the number of iterations necessary for solving the CAOP in real time is more stable and reliable according to the operating point of the MMC
- Moreover, for the QP, this number of iterations varies very little as the complexity of the problem to be treated increases in what could be observed in hardware-in-the-loop simulations.

These results are however to be qualified by the fact that they have been obtained by using two specific algorithmic implementations of the optimization for the linear programming and for the quadratic programming. Some of the conclusions made here could be influenced by the solving algorithm itself such as the number of iterations per sampling step for example. However, the favored balancing behavior of $\mathbf{e}$ in the case of quadratic programming compared to linear programming being explained by the cost function itself, it is highly probable that by changing the optimization algorithm, the result is the same and thus does not depend much or not at all on the optimization algorithm itself.

The use of capacitors and their uniform balancing being a preferred operation for a better and healthy operation of the converter on the long term, the use of the QP for the low-level control will be favored in the tests which are presented in the continuation of the study.

5.D | Study of the high-level control allocation of the MMC

The objective of this part is to study the various algorithms of control allocation to ensure the *Current Control* by highlighting their capacity to adapt to a polyphase electrical system comprising an important number of phases.

After having studied and analyzed in details the behavior of the low-level control for the different real time optimization algorithms used, it is now the turn of the high-level control to be studied. It has been put forward in several ways in Chapter 3 about the dynamic behavior of the currents that the high-level models are scalable to the number of phases of the AC-network. This has been shown by the analytical development of the models themselves but also through simulations in open-loop. In particular, the simulation results presented in Figure 3.21 show a small linear variation of the computation time required for the GPFSROBHCCSSM model as a function of the number of phases, contrary to the GPFOCSSM model whose computation time increases quadratically as a function of m. It would therefore be interesting to see what the influence of such a variation in complexity is when these same models are used in closed-loop to perform the control of the currents. Throughout this study, the focus is on the scalability of the current control methods: to evaluate their control and computational performance as the number of phases increases in the electrical system. This will be the basis of a comparative study of different elements, the models GPFOCSSM and GPFSROBHCCSSM are compared as well as the algorithms of control allocation itself: MIB and EMOn, LP and QP. This comparative study will allow to evaluate how the different possibilities of the *Current Control* architecture differ from each other.

Among all the possibilities of the *Current Control* architecture all the various solutions will be explored in the study carried out in this part. Among the range of possibilities described in Section 5.B.5.6, only the use of the Interior-Point to solve the current control CAOP in LP is not studied here because its adaptation to the high-level control has not been programmed yet.

5.D.1 | High-level control allocation: comparing the algorithms in the objective of scalability

5.D.1.1 | Dedicated control allocation formulations

The aim of the study being to compare the different algorithms of high-level control, their formulations are detailed in Appendix N in order to allow the visualization of the algorithms that are implemented in the different optimizations cases and models of the currents from (A.194) for the GPFOCSSM and (A.197) for the GPFSROBHCCSSM.

5.D.1.2 | Test conditions

For the tests carried out for the high-level control here, the testing approach is the same as the one operated for the low-level control tests: a hardware-in-the-loop procedure is used as presented in Figure 5.10. The same real time computation tool *OP5600* is used here. These parameters are given in Table 5.6.

Regarding the elements of the control architecture of the MMC that are implemented here, it is the EMOn QP control allocation using the optimization algorithm Active-Set which is selected here to ensure the role of the *Voltage Control* for the low-level by solving in real time the

$LLCAOP_{xy}$ (5.11). The role of the *Energy Control* is ensured by MIB, as it was already the case during the previous tests by determining in real time the current reference I_s^{ref} from (5.48). The *Current Control* is the stage which is the subject of the present study, and all the current algorithms represented on Figure 5.4 are mobilized here. In the first test series performed, see Section 5.D.1.3, the determination of the reference voltages across the arms is done by EMOn QP using the Active-Set algorithm from the high-level model in the natural reference frame and with the one in the PARK 12 reference frame. The choice to perform the control in these two reference frames will allow to compare them during a first test which will show the different waveforms of the currents and will do a first verification of control capabilities to meet the requirements. Then, the second test series, allowing to analyze the scalability of the control law, is made possible thanks to the use of all the possibilities of *Current Control* introduced in this document, see Section 5.D.1.4.

During these different tests, a reference will be imposed on the quantities to be controlled. For the case of the capacitor voltages, the reference $\mathbf{v_C^{ref}}$ will be maintained at its nominal level V_{DC}/N for all the capacitors and this throughout the simulations. The references of the common-mode currents I_m^{ref} and the current I_s^{ref} are imposed as described in the Section 5.B.5.1. Concerning the circulating current, as in the case of the tests carried out for the low-level control, a non-zero reference is chosen which is defined from the parameters $\hat{I}_c^{ref} = 0.75$ A and $\varphi_c^{ref} = 0°$. The references of these different electrical quantities will remain the same for all the simulations. However, those of $\mathbf{I_o^{ref}}$ will evolve during the different tests.

I_m has its reference imposed at zero to guarantee a balance of the electrical network; I_s follows the reference imposed on it by the *Energy Control* stage; $\mathbf{I_c}$ has a non-zero reference in order to verify that the high-level control is able to guarantee the existence of a circulating current[1]. The remaining variable is therefore the reference to be chosen for $\mathbf{I_o}$, this variable is finally the one that makes it possible to control the power flow conversion operated by the MMC because the other currents are assigned other roles through the references that are imposed on them. Thus, in order to cover the entire operating region of the converter in terms of converted powers, $\mathbf{I_o^{ref}}$ will be imposed different values during the two test series proposed here. For the first test series, see paragraph 5.D.1.3, $\mathbf{I_o^{ref}}$ follows the sequence represented on Figure 5.21 while for the second test series, see paragraph 5.D.1.4, it is the waveform of Figure 5.22 that will be tracked.

The first pattern of $\mathbf{I_o^{ref}}$ allows us to test the current control laws in both transient and steady state by reaching operating points that sweep the operating zone to a greater and a smaller extent, as shown by Figure 5.21. At the maximum, the reference $\mathbf{I_o^{ref}}$ sees its amplitude reach $\hat{I}_o^{max}$, thus allowing to evaluate the high-level control at the limits of the operating zone of the MMC.

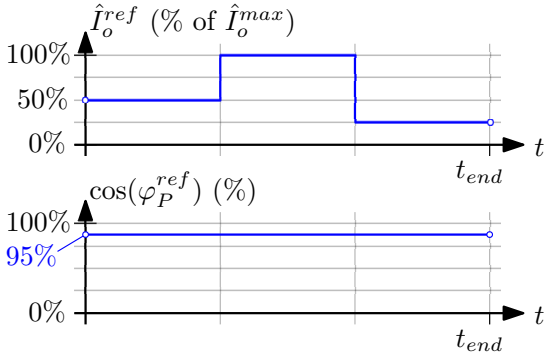

Figure 5.21: $\mathbf{I_o^{ref}}$ pattern over time in the hardware-in-the-loop first test series.

[1]Under certain operating conditions of the MMC, it is possible to show that having a circulating current can contribute to balance the capacitors more easily [Den+20].

The purpose of the second pattern is to sweep the converter operating zone more broadly by describing a circle in the (P_{AC},Q_{AC}) plane in order to verify whether the high-level control allows for operating points in all four quadrants and the quality with which this is made possible. Describing a circle in this (P_{AC},Q_{AC}) plane translates in terms of amplitude and phase for $\mathbf{I_o^{ref}}$ as shown in Figure 5.22. In this operating case, the amplitude is maintained at 1.5 A at the maximum whatever the number of phases in the electrical system. For the simulated MMC parameters, considering the case of $m = 101$ phases only allows a max amplitude $\hat{I}_o^{max}$ of 1.51 A. However, for a lower number of m, $\hat{I}_o^{max}$ is larger as suggested by the analysis of the LOZ[1]. In order to compare on an equivalent basis the behavior of the high-level control for the different m cases, $\hat{I}_o^{ref}$ is chosen at a level that can be reached for all the tested cases of m. This explains the choice of the 1.5 A.

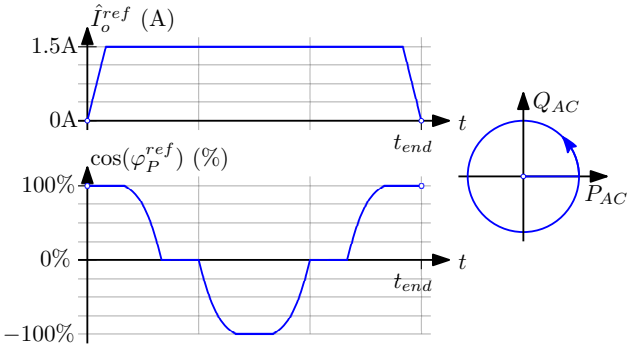

Figure 5.22: $\mathbf{I_o^{ref}}$ pattern over time in the hardware-in-the-loop second test series.

[1] The analysis of the operating zone limits gives $\hat{I}_o^{max}$ of 1.85 A for the 3-phase case and 1.51 A for the 101-phase case. By choosing a maximum reference amplitude of 1.5 A, tests will reach 99.3% of the operating zone in 101-phase and 81.1% in 3-phase. Such a choice of reference will therefore cover a major part of the operating region of the MMC for all the number of phases tested.

Meaning	Symbol	Value
MMC Power System Parameters		
DC bus		
DC Bus voltage	V_{DC}	600 V
Half-bus voltage	$v_p = -v_n$	$V_{DC}/2 = 300$ V
DC Bus impedance	R_s, L_s	50 mΩ, 2 mH
MMC		
Submodules per arm	N	3
Nominal capacitor voltage	v_C^{nom}	200 V
Submodules type	q	1 (half-bridge submodule)
Capacitor capacity	C	2 mF
Switching frequency and period	f_s, T_s	4 kHz, 250 µs
Arm resistance and inductance	R, L	10 mΩ, 5 mH
AC network		
Number of phases	m (several tests)	3 to 101
AC active voltage amplitude	$\hat{V}_{AC}$	150 V
AC active voltage phase	φ_v	0 rad
AC grid frequency and period	f_o, T_o	50 Hz, 20 ms
AC grid frequency	ω_o	$2\pi f_o \simeq 314$ rad/s
AC load resistance and inductance	R_o, L_o	40 Ω, 5 mH
Closed-Loop HIL Simulation Parameters		
Simulation time step	T_{step}	$T_s/10 = 25$ µs
Simulation end time	t_{end}	$7\,T_o = 140$ ms

Table 5.10: Closed-Loop HIL Simulation & MMC Parameters - high-level control testing

5.D.1.3 Hardware-in-the-loop test results for the 7-phase case

Figures 5.23 and 5.24 as well as Table 5.11 show the results of the HIL tests performed for the case where a polyphase system of 7-phase is considered. The high-level control allocation EMOn QP Active-Set is performed in the natural stationary reference frame and is compared to that performed in the Park 12 reference frame.

According to the different figures presented, the first observation made is that the current control allocation developed reached the tracking objectives of the different current references that were targeted. This capacity to ensure such a tracking is then shown for each type of current involved in the MMC. Moreover, these results are quite similar for the two current control architectures. This is a good point because it means that the performing the control in the natural basis as well as in the Park 12 reference frame ensures good performances for the current tracking.

The output polyphase electrical system is well balanced with zero common mode current and the source current follows the setpoint given by the *Energy Control* stage.

From the choice that has been made here for the reference of the circulating current, it is observed that it is not zero and does follow the desired reference. However, although not shown in the present case, the control allocation of the currents is still capable of providing a CCSC function as was shown by [LFB22c] in the 7-phase case. It can be noted that in the case of the latter, the presence of currents of an alternating nature gives the $\mathbf{I_{xy}}$ current its alternating component contributing to the ripples but also to the balancing of the capacitors through the intermediary of the low-level control which can use the ripples of the arm current to its advantage.

It is also noted, as shown in Figure 5.23 (d), that the current $\mathbf{I_o}$ which represents the energy conversion tracks its reference for all the different operating points as confirmed by Figure 5.24 (a) although this last figure shows a static error. This static error evolves for the two control laws according to the operating point to reach 11% of the current amplitude for the case at a quarter of the maximum current and to decrease as one approaches the operating point at maximum current to be around 2%.

To complete the information given by Figure 5.23 (d), Figure 5.24 (a) is given. This figure, unlike the others, shows at the top the norm of the current vector in the first dq_1 part of the 12 PARK reference frame, the $\#2$ rank harmonic components of the current $\mathbf{I_o}$ being zero here. This norm is expressed: $||\mathbf{I_o}^{\mathbf{dq1}}||_2 = \sqrt{I_o^{d1^2} + I_o^{q1^2}}$. The phase which is then represented on the second part of the figure is determined by: $\varphi_o^{dq1} = \arctan(I_o^{q1}/I_o^{d1})$. This Figure 5.24 (a) therefore allows one to observe not only a static error in the amplitude of the currents but also in the phase. The phase reached in the case of GPFSROBHCCSSM is closer to the reference than in the case of GPFOCSSM. However, in both cases, this is equivalent to the case where the current vector reached is neither of the same amplitude, nor in phase with the reference vector in the dq_1 frame. Thus, to better account for the static error as a whole, the determination of a vectorial error is performed. This vectorial error $\varepsilon_{\mathbf{v}}$[1] is determined in the case of the current $\mathbf{I_o}$ from:

$$\varepsilon_{\mathbf{v}o} = \frac{||\mathbf{I_o}^{\mathbf{dq1}^{ref}} - \mathbf{I_o}^{\mathbf{dq1}}||_2}{||\mathbf{I_o}^{\mathbf{dq1}^{ref}}||_2} \tag{5.66}$$

Plotted over time in Figure 5.24 (b), it shows the distinct superiority of the control law performed in the PARK 12 frame compared to the one performed in the natural basis: a better tracking of the reference vector is obtained. On average, the static vector deviation is 21.34% for the GPFOCSSM against 13.96% for the GPFSROBHCCSSM.

Each time the output network calls for power, which corresponds to a reference step for $\mathbf{I_o}^{ref}$, the latter transiently modifies the balance of the power balance of the converter. As can be seen on Figure 5.23 (b), the *Energy Control* instantly adapts the reference of the current I_s to be drawn from the DC bus accordingly so as not to discharge the capacitors during these transients. Figure 5.24 (c) confirms this reactivity of the current control loop by showing that the voltages in the capacitors are maintained around their nominal value, it even appears that the latter are insensitive to the transients of the current calls on the AC side. However, the amplitude of the capacitor voltage ripples are modified on the $\mathbf{I_o}$ plateaus. This can be explained by the fact that this current is involved in the arms current $\mathbf{I_{xy}}$ on which the $\mathbf{v_{C_{xy}}}$ depends directly, as explained previously.

Table 5.11 completes the observations of the current curves by giving the detail of quantified performances in order to be able to compare quantitatively the control made from the GPFOCSSM of that made in GPFSROBHCCSSM. The circulating current having a behavior and a reference whose component is of frequency $2\omega_o$, the error $\langle \varepsilon_{\mathbf{v}c} \rangle_{t_{end}}$ is determined from the components of the circulating current in the second part of the PARK reference frame:

$$\langle \varepsilon_{\mathbf{v}c} \rangle_{t_{end}} = \left\langle \frac{||\mathbf{I_c}^{\mathbf{dq2}^{ref}} - \mathbf{I_c}^{\mathbf{dq2}}||_2}{||\mathbf{I_c}^{\mathbf{dq2}^{ref}}||_2} \right\rangle_{t_{end}} \tag{5.67}$$

[1] The determination of the average value of the vectorial error $\langle \varepsilon_{\mathbf{v}} \rangle_{t_{end}}$ as well as that of the traditional static error $\langle \varepsilon_{\mathbf{s}} \rangle_{t_{end}}$ is done by averaging the error over the steady-state zones and not by taking the whole simulation with the transients, which is consistent with the fact that the errors are meant to be steady-state errors.

HLC		GPFSROBHCCSSM	GPFOCSSM
I_m	$\langle \varepsilon_{\mathbf{s}m} \rangle_{t_{end}}$	< 0.01 A	< 0.01 A
I_s	$\langle \varepsilon_{\mathbf{s}s} \rangle_{t_{end}}$	$< 0.01\%$	$< 0.01\%$
$\mathbf{I_c}$	$\langle \varepsilon_{\mathbf{s}c} \rangle_{t_{end}}$ $\langle \varepsilon_{\mathbf{v}c} \rangle_{t_{end}}$	1.26% 15.39%	2.82% 13.24%
$\mathbf{I_o}$	$\langle \varepsilon_{\mathbf{s}o} \rangle_{t_{end}}$ $\langle \varepsilon_{\mathbf{v}o} \rangle_{t_{end}}$	6.03% 13.96%	5.79% 21.34%
HLC optimization time per sample	Mean Max	94.12 µs 158.7 µs	110.4 µs 496.3 µs
HLC total time per sample	Mean Max	175.9 µs 244.2 µs	186.6 µs 573 µs

Table 5.11: High-level control GPFOCSSM vs. GPFSROBHCCSSM comparative test closed-loop performances for the 7-phase case.

The data in the table confirm that both control architectures evaluated here provide current control with some accuracy. The static error on the output current amplitude alone is smaller in the case of the control using the GPFOCSSM, but it is only 0.24% better on average than that using the GPFSROBHCCSSM. The deviation that matters most here is the vector deviation because it takes into account all the available information: both the deviation on the amplitude but also the phase deviation, and this deviation is much lower with the GPFSROBHCCSSM. Concerning the circulating current, the measured vector deviation shows that the use of the GPFOCSSM is slightly favorable.

The table also gives information about the real time computation time needed for one control step, which is the entire high-level control step. The total computation time as well as the time needed for the optimization algorithm only is given. The computation time values are averaged on the entire simulation and the maximum value over the same duration is also determined. The first observation is that the control using the Park 12 model is faster than the one using the model in the natural basis, which highlights another beneficial feature of the use of such a reduced size model. This difference is explained by the fact that the Park model of the current is of order 10 unlike the natural state-space model which is of order 14. The other observation is that the maximum time required to compute the control is less than 1.5 times the average value for the GPFSROBHCCSSM against more than 3 times for the GPFOCSSM.

Although the realization of the control with the two solutions studied here presents a relatively large vector deviation for the output current on average, the error on reference tracking for the other currents remains much smaller. This allows us to validate, by a first approach, the implementation of CA methods in the framework of the current control for the MMC using real time optimization algorithms in a polyphase system.

From a comparative point of view, of the two control methods evaluated, the one in the Park 12 reference frame is significantly more efficient both in terms of the quality of the control and of the time needed to execute it for this 7-phase case. The question arises as to how this performance evolves as the number of phases in the electrical system increases.

The static error observed when using both methods has a magnitude that also raises the question of the possibility of improving the high-level control allocation with the aim to reduce it.

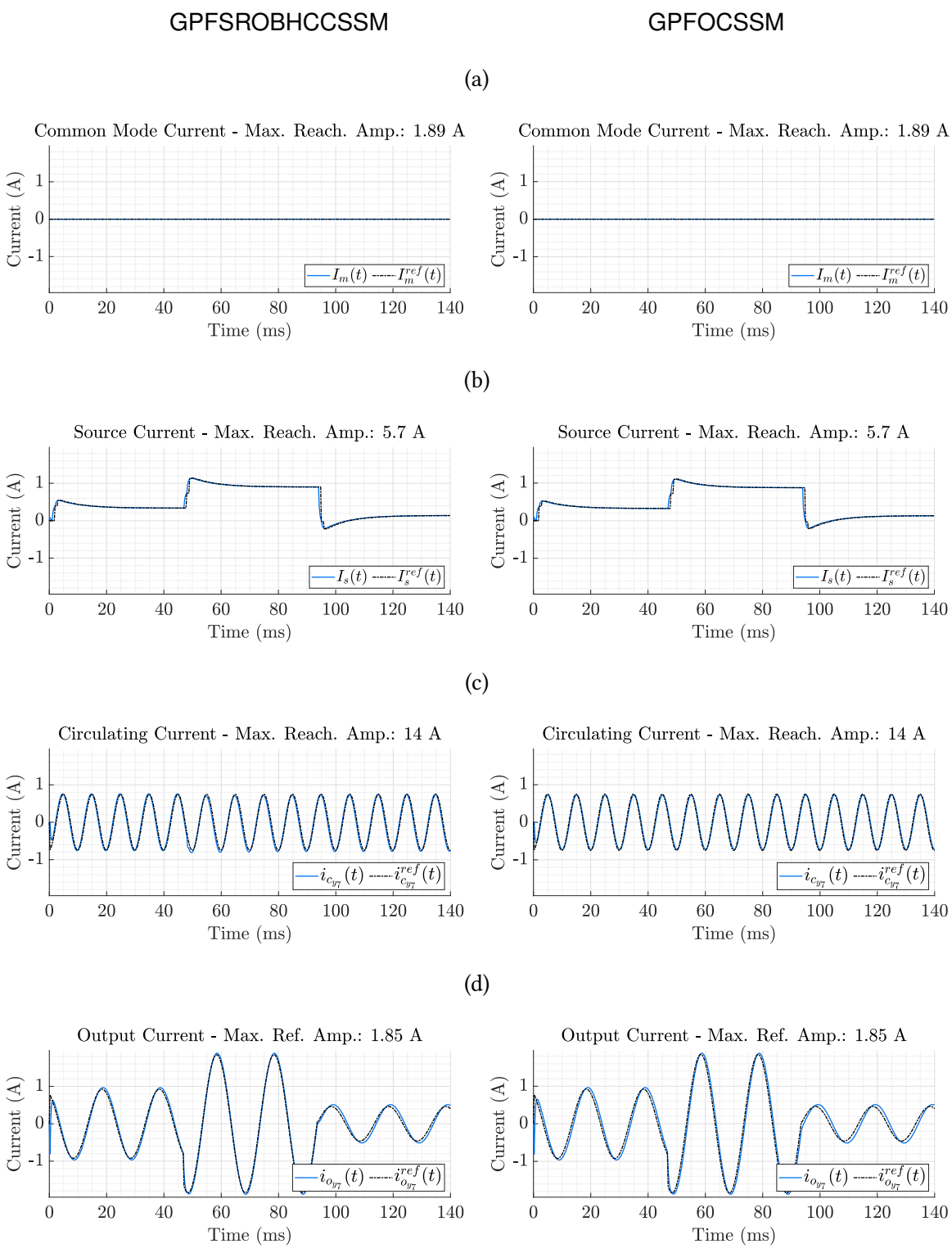

Figure 5.23: Closed-loop behavior of the currents when using the control allocation EMOn QP using GPFSROBHCCSSM (left column) and GPFOCSSM (right column). (a) Common mode current, (b) DC source current, (c) Circulating current, (d) AC-side output current. HIL simulations are done in the 7-**phase** case.

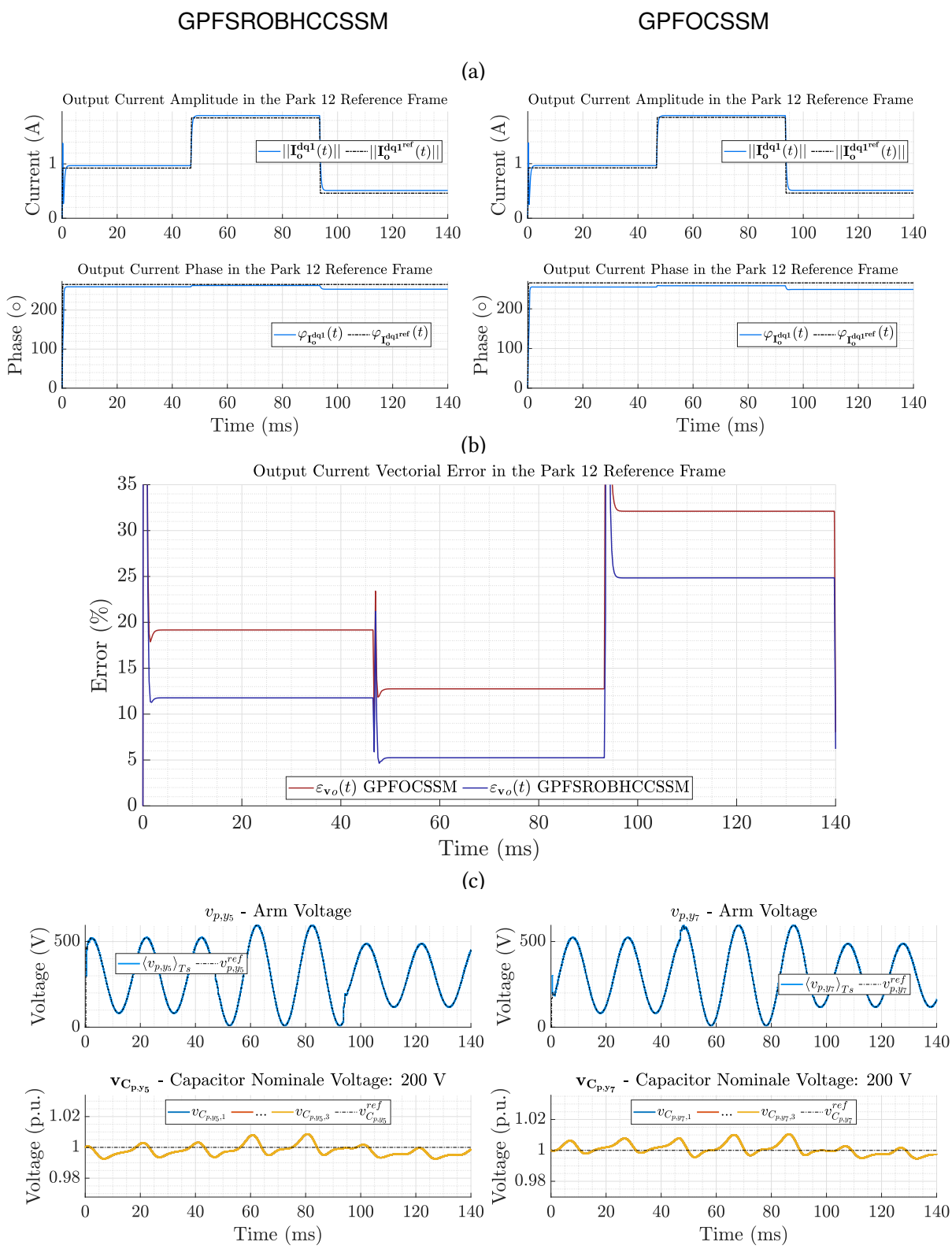

Figure 5.24: Closed-loop behavior of the currents when using the control allocation EMOn QP using GPFSROBHCCSSM (left column) and GPFOCSSM (right column). (a) Output current in the PARK 1 reference frame, (b) Arm voltage and capacitor voltages in a selected arm, (c) Duty cycles and low-level control allocation deviation in a selected arm. HIL simulations are done in the 7**-phase** case.

5.D.1.4 | Hardware-in-the-loop test results from the 3-phase up to the 101-phase case

The previous test has shown that the real time optimization allocation methods can be implemented to perform the control of the currents in the MMC on a given case of system with $m = 7$ phases. The control-oriented models having been developed in a scalability approach, the idea of the tests carried out in this part is thus to evaluate the scalability of the control method for the various possibilities of high-level control developed in this chapter. To do this, the same setpoint profile for the four types of currents and voltages in the capacitors is chosen.

In this second test, the reference pattern of Figure 5.22 is used for the output current. The other currents are given the same references as in the previous tests. As previously mentioned, the output current is the one that makes it possible to control the power conversion, so having shown in the previous tests the ability of the control allocation to ensure the control of each type of current, the focus will be made this time only on this current for the study of scalability.

The current possibilities of the control architecture SCAA open the way to several scalability studies because different allocation algorithms allow to ensure the control by relying on different control models. Thus, in a first step, the scalability of the models will be evaluated for a given type of control, then it will be the turn of the control algorithms to be compared for the same model.

Comparing the high-level models when used for a control purpose

In the set of simulations performed here, the choice is made to control the currents with the real time optimization algorithm QP Active-Set. The proposed comparison is then made between designing the control from the GPFOCSSM model and the control designed with the GPFSROBHCCSSM. Although the different current control methods are functional, the choice of a reduced number of simulation figures was made in order not to overload the material. However, Figure 5.25 shows the entire set of current control allocation approaches and the publications in which these results can be found. For those whose results are displayed here, Figure 5.26 and Table 5.12 present the results obtained in a condensed manner.

For each type of current, Figure 5.26 (a) represents the evolution as a function of the number of phases of the most relevant error. For a given number of phases, a simulation is performed and the average value of each error is determined and represented on this figure.

The error types represented here are the same as a part of the ones listed in Table 5.11 but this time determined for a set of phase numbers. Only the most relevant subset of these errors is shown here. Since the common mode current has a null reference, the choice is made to represent the absolute error $\langle \varepsilon_{\mathbf{s}m} \rangle_{t_{end}}$. For the source current the relative error $\langle \varepsilon_{\mathbf{s}s} \rangle_{t_{end}}$ is selected. For the two types of currents of an alternating nature, $\mathbf{I_c}$ and $\mathbf{I_o}$ it is the relative vector deviation, respectively $\langle \varepsilon_{\mathbf{v}o} \rangle_{t_{end}}$ and $\langle \varepsilon_{\mathbf{v}c} \rangle_{t_{end}}$, respectively, which is used here to indicate the quality of the performed control.

In Figure 5.26 (b), the vectorial error on the output current is displayed in more detail and the evolution of the computation time required for the control algorithms using GPFOCSSM and GPFSROBHCCSSM is shown. A zoom is made on the evolution of the computation time of the law using the model in the PARK 12 reference frame. Two average computation times are indicated each time, one represents the total computation time per sampling step and the second one, necessarily lower, represents the time necessary to the allocation core, which is the Active-Set optimization algorithm here.

The first observation that comes with Figure 5.26 (a) is the fact that the error on all the currents remains constant as the number of phases increases. The error on the common mode current varies however, but it remains of the order of one mA, which is about 1000 times smaller than the other currents converted by the converter. One can therefore validate the control of this current for polyphase systems and concentrate on the other currents whose objective is to follow, here, a non zero reference. It is also noticed on this figure that the control in the PARK reference frame is more efficient than the one in the natural basis for the output current and the DC source current whereas for the circulating current and the common mode current it is the opposite. For both approaches, the difference on the source current is the smallest (0.77% for both models), the one on the output current comes next (from 8.04% to 8.98% depending on the model) and lastly the one on the circulating current (from 12.9% to 16.0% depending on the model).

The strong result here is that for both control-oriented models, the error on the currents I_s, $\mathbf{I_c}$ and $\mathbf{I_o}$ remains constant whatever the number of phases in the electrical system. The steadiness of these deviations shows not only that the proposed control architecture is scalable in itself by its algorithmic structure but that its control performance remains the same as the number of phases increases. This means that it is possible to use this control algorithm to control a polyphase system of any number of phases with the same accuracy.

Figure 5.26 (b) brings a second set of interesting information about the computation time needed by the control allocation algorithm using the QP Active-Set to solve its optimization.

The first observation is that the command using the GPFOCSSM will take a computation time that increases quadratically and strongly as a function of the number of phases, whereas - as shown in the zoom - the command using the GPFSROBHCCSSM sees its computation time increase linearly and weakly as a function of the number of phases. The curve fitting whose results are given in Table 5.12, confirms this observation. The quality of the fitting is sufficient to indicate a trend in the evolution of the calculation times. The one with GPFOCSSM is quadratic while the one with GPFSROBHCCSSM evolves in a linear way with a small slope. From the 3-phase case to the 101-phase case, the GPFOCSSM sees its computation time multiplied by 227 against only 1.73 for the GPFSROBHCCSSM. Below 5 phases, the two control models have the same size, but beyond that the order of the state model in the PARK 12 reference frame no longer varies with the number of phases and remains constant at 10 while that of the model in the natural basis sees its order $2m$ increases linearly with the number of phases. This reason explains the quadratic evolution of the complexity of the control algorithm for GPFOCSSM. Therefore, the model in the PARK reference frame, of constant order, should not see the computation time change as a function of the number of phases, but this is without taking into account the necessary basis changes - as represented in Figure 5.4 - to the control law, which are carried out thanks to matrices of which only one of the dimensions varies linearly with m. This explains the linear evolution of the computation time of the control algorithm using GPFSROBHCCSSM.

The study of the computation time evolution curves leads to the results given in Table 5.12. The choice of the curve fitting is made on the time necessary for the optimization and not on the total time necessary for the order because the time of the optimization is an incompressible duration which the allocation needs whereas the total time depends on the algorithmic implementation made by the user that is wrapped around this optimization algorithm.

Optimization time	GPFSROBHCCSSM			GPFOCSSM		
Curve fitting	$2.33m + 282.9$ µs			$5.47m^2 - 106m + 1053$ µs		
R^2	0.8547			0.9987		
Root mean square error	0.2733			5.003		
m	3	5	101	3	5	101
Proportion in tot. comp. time	50%	65%	85%	20%	35%	40%

Table 5.12: High-level control GPFOCSSM vs. GPFSROBHCCSSM computation time comparison from the 3**-phase** case up to the 101**-phase** case.

It is moreover noted, as indicated by Table 5.12, that in the case of the GPFSROBHCCSSM the time necessary for the optimization rises from 35% of the total time of the control for 5 phases to 40% for 101 phases, against a rise from 65% to 85% in the case of the GPFOCSSM. Thus, the increase in the number of phases is responsible for the major part of the complexity of the control law made in GPFOCSSM while for GPFSROBHCCSSM the proportion of the computation time occupied by the optimization remains stable.

The analysis of the computation time curves of the two solutions show that it is more interesting to perform the optimization in the Park reference frame for $m = 7$ and beyond. Table 5.11 confirms this, although it is for a simulation going through different operating points of the MMC.

From the simulations carried out, it is concluded that by using the GPFSROBHCCSSM to carry out the CA of the currents, it is possible to have a scalable control algorithm while preserving the same control performances and guaranteeing an almost constant computation time whatever the number of phases. This makes it a generic control architecture that can easily be adapted to any polyphase system. However, below a 7-phase network, a compromise will have to be chosen between the GPFSROBHCCSSM and the GPFOCSSM, because one has better control performances for some of the currents while the other needs a lower optimization time.

The beneficial use of the GPFSROBHCCSSM for any number of phases leads to its selection to perform the following control architecture tests.

Comparing the high-level control allocation algorithms

In the previous analysis, for a given control allocation algorithm, the two control models were compared. The dual analysis will be performed here: for the choice of the GPFSROBHCCSSM, all the implemented control allocation are compared. The goal being to compare the performances of control and computation time of the MIB, EMOn LP Simplex, EMOn QP Active-Set and EMOn QP Interior-Point methods. Figure 5.27 presents the results obtained.

The focus on the output current, because of its role in the power exchange, shows that whatever the allocation algorithm used, the error that the output current has with its reference is identical. This means that all the control allocation algorithms have the same performance and the static error criterion does not differentiate them.

The criterion of computation time is therefore the one that separates the algorithms. The first remark is that they all present an evolution similar to the one described above: a linear and very slight increase according to the number of phases. This makes them all generic current control algorithms that can adapt quickly to the number of phases. However, differences in computation time are present between the algorithms. The MIB is the fastest of all, this is explained by

the fact that it is based on a simple matrix inversion performed offline. In real time, a single matrix product is required, while the other algorithms of EMOn type perform several iterations before converging to the optimized solution. The LP Simplex, although known for its speed of convergence in practice for a given class of problems is finally found to be the slowest optimization algorithm is this case, while the QP algorithms, the Active-Set and the Interior-Point, both require a comparable computation time.

In the context of these tests, the swept operating zone reaches between 81.1% and 99.3% of the maximum capabilities, current references going beyond the limits of the operating zone have not been requested and it would therefore be interesting to extend the study to this case in order to see how these different control algorithms behave under these conditions. Moreover the only LP algorithm having been tested for the high-level control is the Simplex, it would thus be interesting to use the same as the one used for the low-level control in order to determine if it would present a comparable execution time to the algorithms of QP.

	GPFOCSSM	GPFSROBHCCSSM
MIB	In 1	In 2
EMOn LP SX	In 1	In 2
EMOn QP IP		In 2
EMOn QP AS	In 1 and 2	In 2

1: [LFB22c]
2: Chapter 5 (Here)

Figure 5.25: Our 2022 literature coverage of the simulation results from the high-level control architecture possibilities presented in this manuscript.

The results presented here on the steadiness of the vector deviation for the output current as a function of the number of phases and as a function of the algorithm used for the control allocation, are related to having a control designed from the GPFSROBHCCSSM. The same results, qualitatively, are obtained for the GPFOCSSM as shown in [LFB22c][1].

Figure 5.25 shows the different possibilities of the current control allocation architecture whose results have been presented here and in the article [LFB22c] for simulations ranging from 3 to 101 phases. Together, they cover almost all the possibilities developed for the high-level control[2].

Depending on the constraints of the real time computing device, it will not necessarily be able to use all the algorithms, but if a computer is capable of executing one of the CA algorithms from GPFSROBHCCSSM for a given number of phases, there is a good chance that the same algorithm can be used on the same device for any other number of phases. This is not the case if the GPFOCSSM is used since the computation time increases quadratically with the number of phases. Thus, if the allocation is chosen to be executed in the natural basis, the computational unit selected to execute one of the allocation algorithms for a given number of phases, will not be able to perform for a system with a much larger number of phases.

[1] The results presented in this paper show a different value of the deviation vector of the output current. This is due to the fact that, in the paper, the setpoint profile tracked is the one shown in Figure 5.21 and the calculation of the vectorial error is different.

[2] The results when using the GPFOCSSM for QP Interior-Point are not present in the article due to the fact that this last algorithm was not fully implemented and functional by the time the paper was written.

5.D.1.5 Conclusion of the high-level control scalability analysis

To summarize this section, all the algorithms proposed for the high-level control based on control allocation methods have a scalable algorithmic architecture to any number of phases that maintains identical control performance as the number of phases is increased and whatever the allocation algorithm. In the case where the control is designed from the Park 12 model, the execution time of the different allocation methods remains almost constant and low while it increases quadratically for the use of the model in the natural basis. Thanks to this work, it is now possible to design a control algorithm using real time optimization of the currents of a MMC having any number of phases while keeping an almost constant execution time. This makes it possible to develop generic algorithms and real time computers for such systems.

In aiming to choose a control allocation algorithm for current control that embodies a good trade-off between current control performance, efficiency in redistributing efforts among control variables, and real time execution time, the QP Active-Set and Interior-Point algorithms are particularly suited. They have a better computation time than the Simplex and are still based on a real time optimization principle, which gives them a better adaptation capacity when the limits of the control are reached than MIB.

An interesting study perspective however is the behavior of these algorithms when the current reference setpoints require to reach values beyond their limits. It would also be interesting, in regard to the absolute and vectorial static errors observed in the different simulations, to aim at reducing them.

(a)

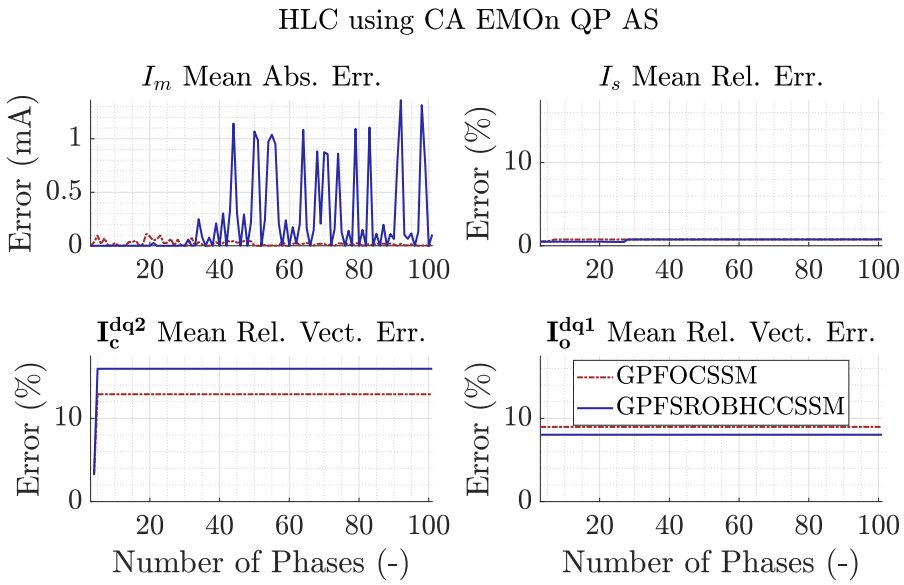

(b)

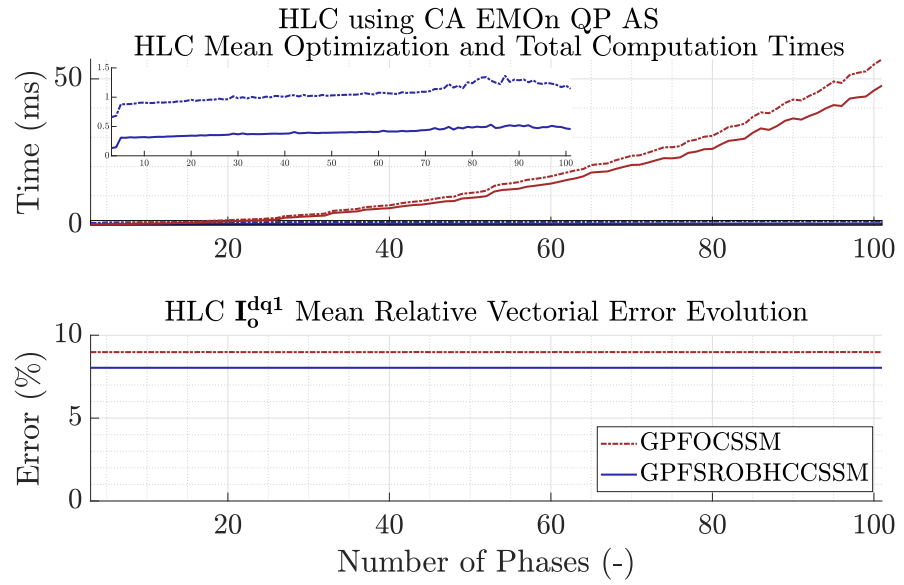

Figure 5.26: Evolution of the high-level control control allocation done with the GPFOCSSM and the GPFSROBHCCSSM from the 3**-phase** up to the 101**-phase** case. (a) Evolution of the four current types most relevant error with m, (b) Focus on the output current vectorial error and the current control algorithm computation time evolution with m.

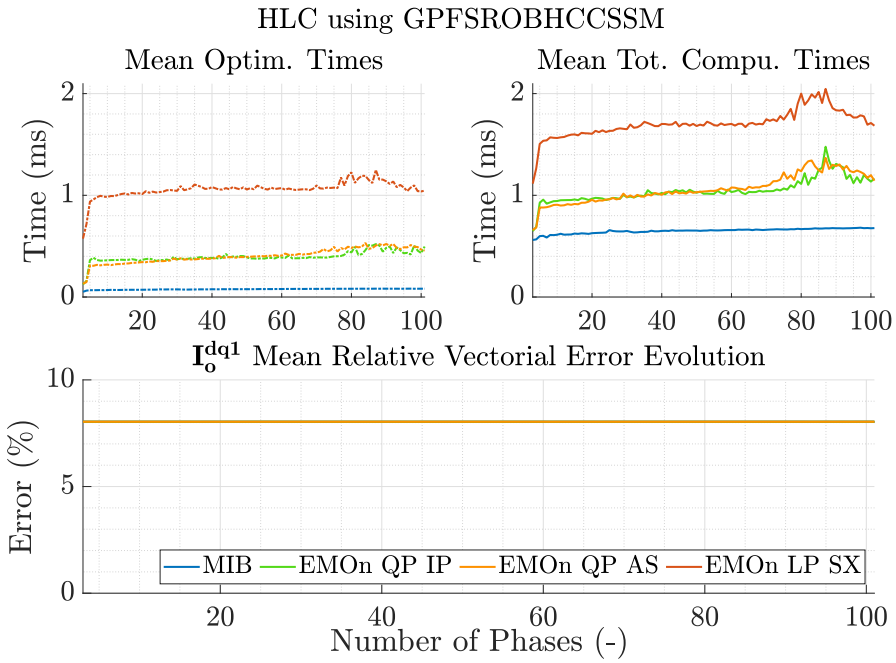

Figure 5.27: Evolution of the high-level control control allocation done with the GPFSROBHCCSSM. Comparing the performances in terms of output current vectorial error and control computation time for all the different implemented control allocation algorithms from the 3-**phase** up to the 101-**phase** case.

5.D.2 High-level control allocation with integrator: studying the influence of the integral action

Starting from the fact that the control allocation methods of the currents for the MMC designed until now were unable to eliminate the static error for the output current $\mathbf{I_o}$, the development of new control allocation architectures including the additional functionality of cancellation of the static error with the will to keep adhering to the classical control allocation formulation was initiated.

It is in this context that the work presented in Chapter 4 was carried out to improve the control allocation of the currents. The control architecture developed in the previous chapter will therefore be adapted here for the high-level control. The model to which this control will be applied is the one identified in the previous section as the one presenting the best trade-off between real time computation speed and control accuracy: the GPFSROBHCCSSM. The objective is to evaluate the influence of the control allocation with integral compensator compared with the control allocation designed from the GPFSROBHCCSSM which has already been studied in the Section 5.D.1.3.

5.D.2.1 Adaptation of the control allocation with integral compensator to the high-level control

Until now, the presented current control in the Park 12 frame solves the $HLCAP_{Park\ 12}$ (5.29):

$$\left\{ \hat{M}_{HL}^{dq012} \mathbf{U}_{\mathbf{HL}}^{\mathbf{dq012}}(k) = \hat{\mathbf{a}}_{\mathbf{dHL}}^{\mathbf{dq012}}(k) = \mathbf{w_I}^{\frac{1}{l}} \circ \mathbf{a}_{\mathbf{dHL}}^{\mathbf{dq012}}(k) \;\middle|\; \mathbf{V}_{\mathbf{min}}^{\mathbf{dq012}} \leq \mathbf{U}_{\mathbf{HL}}^{\mathbf{dq012}}(k) \leq \mathbf{V}_{\mathbf{max}}^{\mathbf{dq012}} \right\} \tag{5.68}$$

With the introduction of the integral action according to Figure 4.4, the desired action vector related to the latter is formulated here for the current control:

$$\mathbf{a_{d_I}}^{\mathbf{dq012}}_{\mathbf{HL}} = \left(\mathbb{I}_{2m'} - Z_{HL,M}^{dq012}\right)\left[(z-1)^{-1}\left(\mathbb{I}_{2m'} - F_{HL,M}^{dq012}\right)\left(\mathbf{Y}^{\mathbf{dq012}^{ref}}_{\mathbf{HL}} - \mathbf{Y}^{\mathbf{dq012}}_{\mathbf{HL}}\right) - \mathbf{Y}^{\mathbf{dq012}}_{\mathbf{HL}}\right] \tag{5.69}$$

The desired action vector is then updated to:

$$\tilde{\mathbf{a}}^{\mathbf{dq012}}_{\mathbf{dHL}} = \mathbf{a}^{\mathbf{dq012}}_{\mathbf{dHL}} + \mathbf{a_{d_I}}^{\mathbf{dq012}}_{\mathbf{HL}} \tag{5.70}$$

$\hat{\mathbf{a}}^{\mathbf{dq012}}_{\mathbf{dHL}}$ is then determined not from $\mathbf{a}^{\mathbf{dq012}}_{\mathbf{dHL}}$ but from $\tilde{\mathbf{a}}^{\mathbf{dq012}}_{\mathbf{dHL}}$. The $HLCAP_{Park\ 12}$ then becomes:

$$\left\{\hat{M}_{HL}^{dq012}\mathbf{U}^{\mathbf{dq012}}_{\mathbf{HL}}(k) = \mathbf{w_I}^{\frac{1}{l}} \circ \left(\mathbf{a}^{\mathbf{dq012}}_{\mathbf{dHL}}(k) + \mathbf{a_{d_I}}^{\mathbf{dq012}}_{\mathbf{HL}}(k)\right) \;\middle|\; \mathbf{V}^{\mathbf{dq012}}_{\mathbf{min}} \leq \mathbf{U}^{\mathbf{dq012}}_{\mathbf{HL}}(k) \leq \mathbf{V}^{\mathbf{dq012}}_{\mathbf{max}}\right\} \tag{5.71}$$

The entire control allocation, MIB, EMOn LP Simplex, QP Interior-Point et Active-Set, using the model GPFSROBHCCSSM is updated accordingly. The high-level control allocation architecture of Figure 5.4 thus shifts from the formulation of Figure 4.1 to that of Figure 4.4. The matrix $F_{HL,M}^{dq012}$ being already tuned (5.32), the only gain that has to be set is $Z_{HL,M}^{dq012}$. The selection of the disturbance rejection poles is left to the user, as long as the stability limit is not exceeded. Usually, for the class of physical systems considered here, the rejection of a disturbance solicits the control in a more moderate way than reaching the steady state, so the pole placement for disturbance rejection can be faster than for reference tracking. In the current study, the disturbance rejection poles are chosen by successive tests such that:

$$Z_{HL,M}^{dq012} = 0.75\ F_{HL,M}^{dq012} \tag{5.72}$$

5.D.2.2 | Test conditions

The test conditions used here are identical to those of the simulation with a number of 7 phases, see Section 5.D.1.3. The capacitor voltage references are set at their nominal value, the common mode current is intended to be cancelled, the source current responds to the reference from the energy control stage, the circulating current is imposed to a non-zero value and the output current follows the reference described by the pattern Figure 5.21. The parameters of the system are those from (5.10).

5.D.2.3 | Hardware-in-the-loop test results for the 7-phase case

The simulations carried out lead to the Figures 5.28 and 5.29 as well as Table 5.13. Half of the results come from Section 5.D.1.3 since the idea here is to evaluate the influence of the control allocation with integral compensator compared to the control allocation in the case where the high-level control is performed in the Park 12 frame. Concerning the choice of the optimization algorithm, the QP Active-Set is used here.

More particularly, from the Figure 5.28 first, it is observed that the switch from control allocation to control allocation with integral compensator improves in a general way the control of the different types of steady state currents. Concerning the currents I_m and I_s the differences are small because the tracking of these currents was already assured with good performances without the addition of the transparent integral compensator. Figure 5.28 (c) shows that this addition has an effect that slightly degrades the transient behavior of the circulating current with respect to its reference but ensures a better convergence in steady state.

Observation of Figure 5.28 (d) shows that the output current tracks its reference with at least as good a performance as in the classical control allocation case. This observation is completed by Figure 5.29 (a), which exacerbates the differences from a vector view of the output current with respect to its reference. One can then see that the static error both on the amplitude of the vector representing $\mathbf{I_o}$ and on its phase is completely cancelled by the switch to CAI-IPII. This figure allows us to evaluate the 5% settling time, which is about 1 ms in both cases, in accordance with the closed-loop pole placement for the currents.

The strong result obtained here embodies the achievement of the control allocation with integral compensator architecture development and allows us to validate the fact that this architecture meets the first objective for which it was designed: improving the static performances of the current $\mathbf{I_o}$ which drives the energy conversion between DC and AC sides of the converter.

Compared to the classical control allocation, Figure 5.29 (b) confirms the steady state cancellation of the vector deviation for the CAI-IPII as opposed to the CA. It is important to note that, by this modification of the control allocation, the active balancing the capacitors is preserved, as shown by Figure 5.29 (c).

The additional information that Table 5.13 provides is that the computation time required for the two architectures are close enough to be considered similar in computation time.

HLC		GPFSROBHCCSSM CA	GPFSROBHCCSSM CAI
I_m	$\langle \varepsilon_{\mathbf{s}m} \rangle_{t_{end}}$	< 0.01 A	< 0.01 A
I_s	$\langle \varepsilon_{\mathbf{s}s} \rangle_{t_{end}}$	$< 0.01\%$	0%
$\mathbf{I_c}$	$\langle \varepsilon_{\mathbf{s}c} \rangle_{t_{end}}$ $\langle \varepsilon_{\mathbf{v}c} \rangle_{t_{end}}$	1.26% 15.39%	0% 0%
$\mathbf{I_o}$	$\langle \varepsilon_{\mathbf{s}o} \rangle_{t_{end}}$ $\langle \varepsilon_{\mathbf{v}o} \rangle_{t_{end}}$	6.03% 13.96%	0% 0%
HLC optimization time per sample	Mean Max	94.12 µs 158.7 µs	86.23 µs 130.9 µs
HLC total time per sample	Mean Max	175.9 µs 244.2 µs	165.5 µs 250.5 µs

Table 5.13: High-level control GPFSROBHCCSSM, classical control allocation vs. control allocation with integral compensator comparative test closed-loop performances for the 7**-phase** case.

5.D.2.4 Conclusion about the benefit of the CAI over the CA for the high-level control

The result obtained here attests to the quality of the control allocation algorithm of the currents that has been developed. Thanks to the control methods that are introduced here, it is now possible not only to guarantee an efficient and optimized use of the control variables, but also to ensure a static error elimination without influencing the dynamics of the previously tuned currents. This modification has been shown to be easily done by immediately updating the CAP into (5.71).

In a more general way, performing control allocation with integral compensator of the currents from the GPFSROBHCCSSM solved in real time by the EMOn QP Active-Set combines all the beneficial features of the different novel elements developed in this chapter:

- Choice of EMOn versus MIB for the ability to optimally distribute the efforts among the

control variables taking into account the limitations *a priori*
- Choice of the QP Active-Set compared to the LP Simplex for the execution time of the optimization which is lower
- Choice of the GPFSROBHCCSSM rather than the GPFOCSSM to develop the control system since it ensures a better tracking quality for the currents and an almost constant computation time whatever the number of phases
- Choice of the CAI instead of CA in order to ensure a static error cancellation with disturbance rejection while keeping the same tracking dynamics in closed-loop

These different elements make it the best trade-off for the role of the high-level control among the variety of architectures developed in this chapter.

However, studies are still to be explored on the topic of the current control comparison between that in the Park 12 frame and the one in the natural basis using the control allocation with integral compensator or the evaluation of the perturbation rejection capabilities.

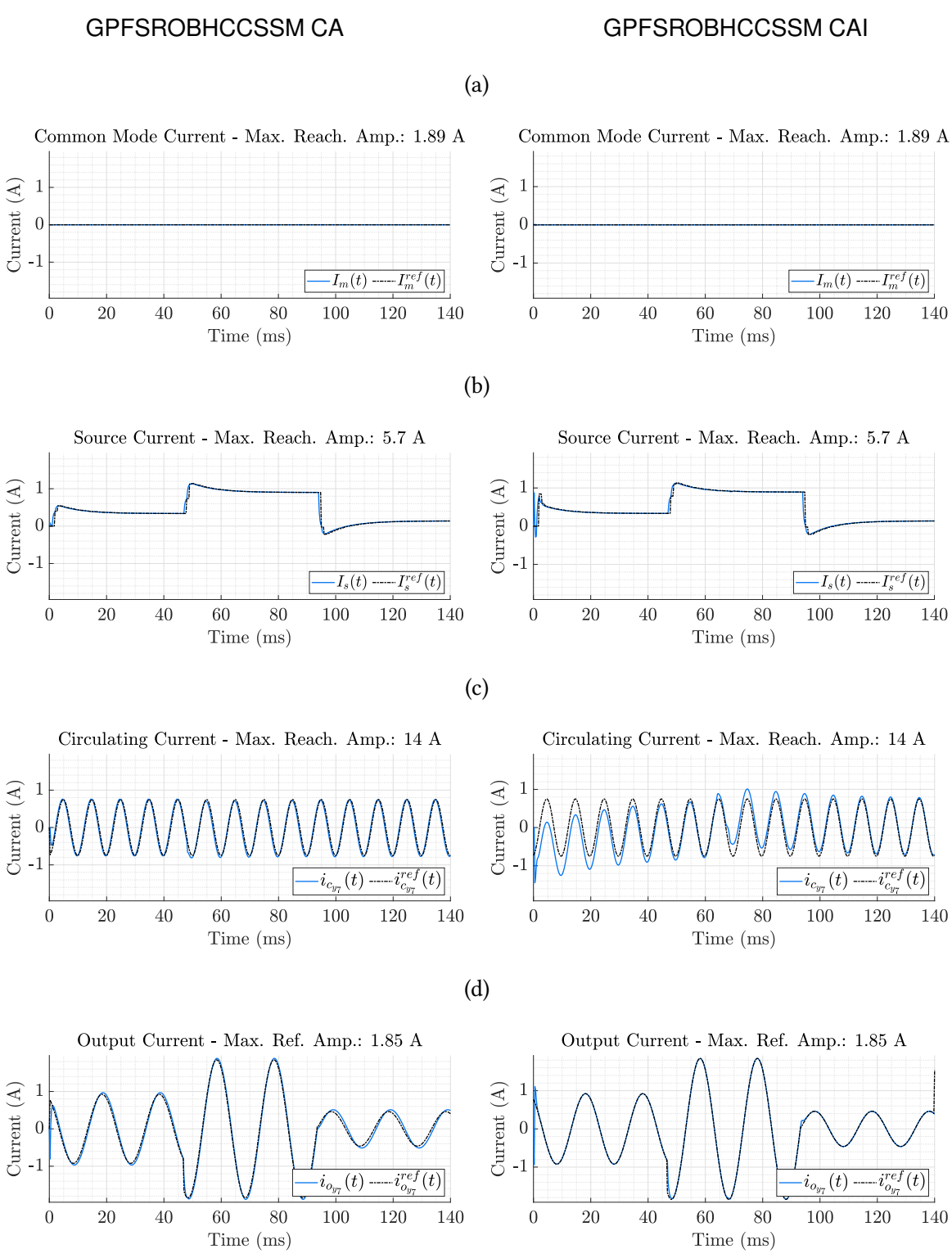

Figure 5.28: Closed-loop behavior of the currents when using the control allocation GPFSROBHCCSSM (left column) and control allocation with integral compensator GPFSROBHCCSSM (right column). (a) Common mode current, (b) DC source current, (c) Circulating current, (d) AC-side output current. HIL simulations are done in the 7-**phase** case.

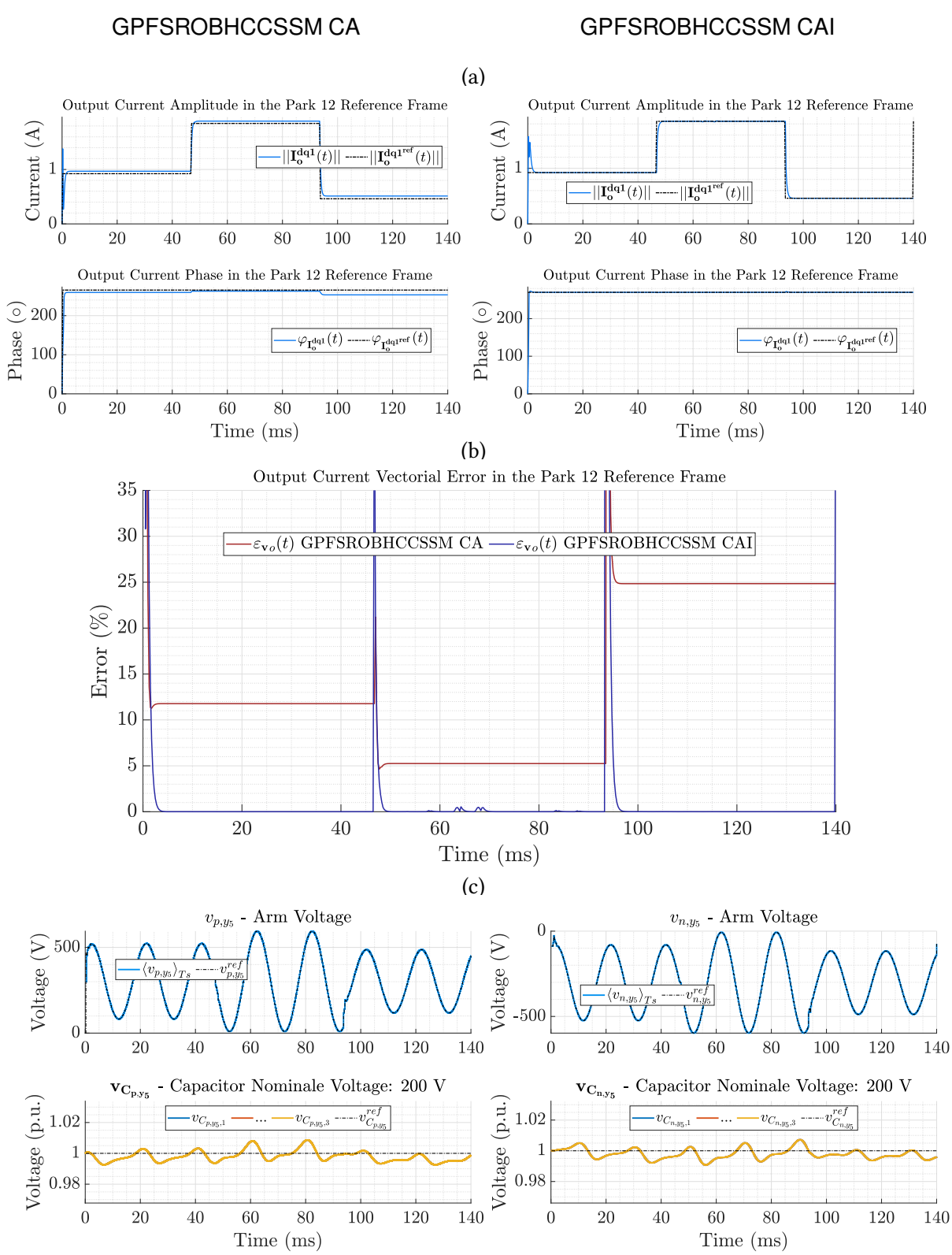

Figure 5.29: Closed-loop behavior of the currents when using the control allocation GPFSROBHCCSSM (left column) and control allocation with integral compensator GPFSROBHCCSSM (right column). (a) Output current in the PARK 1 reference frame, (b) Output current vectorial error evolution over time, (c) Arm voltage and capacitor voltages in a selected arm. HIL simulations are done in the 7**-phase** case.

5.E | Reconfiguration of the MMC under faults with allocation methods

Fault tolerant control of the MMC

With the low-level control using the CA, it has been shown that it is possible to take advantage of the multiplicity of the submodules and their redundancy to optimally ensure reference tracking of the arm voltage. One can then legitimately wonder how the CA-driven system would behave if, out of the large number of submodules that an arm can have, one were to lose one or more. Would allocation methods be able to adapt the operation of the converter in real time and to distribute the control effort optimally among the remaining submodules ?

The work from [LLB13] proposes a wide nomenclature of the set of faults that can occur at the level of a MMC-based power conversion system ranging from faults at the submodule level (e.g., a semiconductor short circuit) to faults at the converter and system level (e.g., DC pole-to-ground).

Submodule faults To counteract faults in the submodules, several FTC techniques have been proposed. A first solution consists in providing the MMC with additional submodules that are mobilized when one of their peers is faulty [Saa+15; SDA11]. The faulty submodule is then shunted by the dedicated fault switch and several scenarios are then possible. To compare the scenarios, an indicator is introduced:

Definition 11. *Let $\mu_H \in [0;1]$ be the healthy submodule occupancy rate or healthy occupancy rate. In the case where the MMC experiences a submodule fault, the healthy submodule occupancy rate represents the proportion of submodules still involved in the energy conversion with respect to the total amount of remaining healthy submodules.*

A first scenario is then to shunt a healthy submodule in each arm to easily ensure the global balance of energy between the arms and legs of the MMC [Hu+14]. This simple solution is still not ideal because it leaves a significant amount of healthy submodules remaining unused. For a single faulty submodule in a N-submodule per arm m-leg MMC, the healthy occupancy rate falls down to $\mu_{H_1} = \frac{2m(N-1)}{2mN-1} < 1$.

Another scenario is to shunt only one healthy submodule, the one that is in the complementary arm of the one that lost a submodule [Wu+19]. This solution is better in terms of the occupancy rate of the submodules, but the energy balancing of the MMC is less obvious to guarantee in the legs. In this case: $\mu_{H_2} = \frac{2mN-2}{2mN-1} < 1$ and $\mu_{H_2} \geq \mu_{H_1}$.

The third scenario is the most difficult to manage in terms of energy balance since it proposes not to shunt any additional submodule, but the major advantage is that the occupancy rate of the healthy submodule remains maximum: $\mu_{H_3} = 1 > \mu_{H_2} \geq \mu_{H_1}$. In this case, it is possible to design FTC algorithms to preserve the energy balance of the converter [Den+16]. The method of interleaved control of the submodules proposed by [Sel+19] is applied on a system without addition of spare submodules, it shows an adaptation of the energy contained in an arm when only the faulty submodule is shunted, the behavior of the converter returns easily to the nominal one when the faulty submodule is replaced and reintroduced in the power conversion.

Converter faults For converter scale faults, the objective is to ensure continuity of operation at the level of the converted power and the global energy balance of the MMC, EC methods at the level of the arms can then be implemented [AÄN09; Ber+12]. In the case of asymmetrical faults, FTC are set up to protect the MMC and aim at decreasing the voltage ripples on the DC bus [Tu+12; Gru+20].

The solution of allocation methods for fault tolerant control of the MMC

Allocation methods have proven their worth by being used in different systems with the objective of managing the control variables in an optimized way, as we were able to show in the study carried out in the previous sections and chapters. However, there is another feature of which the allocation methods have shown to be capable: the reconfiguration under faults of the system operation by the control, which ensures a continuity of service in degraded mode instead of stopping the system. This capability of the allocation methods can indeed be critical in the case of systems that cannot stop immediately and where there is a strong need for continuity of operation. One can think, for example, of the application domain of choice for the control allocation: aeronautics, for which a strong guarantee of operation in case of failure must be ensured.

If the CA is particularly adapted to manage the reconfiguration case, it is because it distributes the effort required by the control objective over all the input variables. Conceptually, it is then sufficient to set up a formalism to indicate to the CA which input variables are still available after the occurrence of the fault and which are no longer available. The distribution of the control effort among all the available variables will then be done automatically for the CA, as if it simply had another CAP to solve.

In order to provide a reconfiguration procedure for the MMC in the event of a fault in the MMC, the first step consists of classifying the various faults that can be encountered in a MMC. Then, based on working assumptions to adopt a first approach, a reconfiguration procedure is proposed and the reformulation of the $LLCAP_{xy}$ (5.10) is introduced. A simulation in one of the possible fault cases - faulty submodule in an arm that becomes shunted - is performed to show the capabilities of the CA to reconfigure the operation of the MMC.

The objective of the reconfiguration that guides the approach proposed here is to guarantee a minimal impact of the semiconductor fault on the global energy conversion function that the converter must ensure. In other words, the impact of the loss of controllability of a semiconductor must have the least possible impact on the output current $\mathbf{I_o}$ ability to reach its maximum operating zone.

5.E.1 | Classification of faults in the arms

The interest here is focused on the most general case of the submodule, the full-bridge submodule whose functional diagram is recalled by Figure 5.30. The faults that can occur in a cell that are considered here are those at the level of the semiconductors. A faulty semiconductor component (here diode or IGBT transistor) is defined as being forced into a single state according to the Assumption 13 that hold for this study.

Assumption 13. *A faulty semiconductor is a semiconductor forced to a unique state. This forced state can either be "open" or "closed".*

Each semiconductor can then be forced into two different states during a fault, the SM-FB being composed of four IGBT-diode associations in antiparallel, that makes a total of eight semiconductors, and thus 256 different fault cases. The analysis of these different defect cases at the semiconductor level shows that they are gathered in two different defect classes at the submodule level.

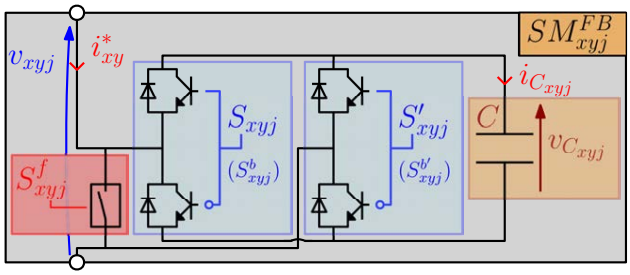

Figure 5.30: Full-bridge submodule functional electrical diagram.

In the first case of a fault, the semiconductors can be in the configuration where the cell capacitor is forced in exclusion from the arm to which the submodule belongs. Figure 5.31 shows an example. The set of configurations in which the capacitor is forced in exclusion constitutes the first possible class of fault. A second case of fault is when the capacitor is forced in inclusion on the arm to which it belongs, it is then as if it was welded to the arm. Figure 5.32 shows a configuration of the semiconductors that lead to it. The capacitor is then in the case where its voltage comes to participate positively to the voltage available in the arm, it is then connected in direct orientation. But there is another possible configuration, see Figure 5.33, where the capacitor is also forced to be included in the arm but in the reverse direction: the capacitor voltage participates negatively in the voltage available in the bus. All of these configurations where the capacitor is forced into inclusion - direct or reverse - makes the second class of fault in which a submodule can be found. It may be noted that in the SM-HB case, the reverse forcing does not exist because the half-bridge does not have the necessary switches to allow it.

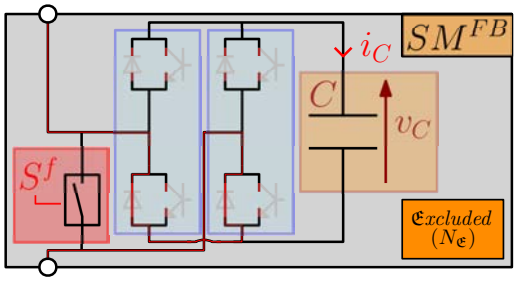

Figure 5.31: Full-bridge submodule diagram under an example of the first fault class: exclusion of the capacitor from the arm.

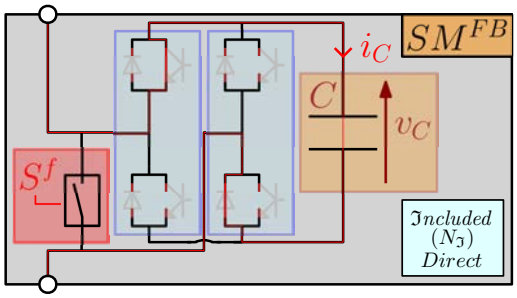

Figure 5.32: Full-bridge submodule diagram under a first example of the second fault class: forced inclusion of the capacitor to the arm.

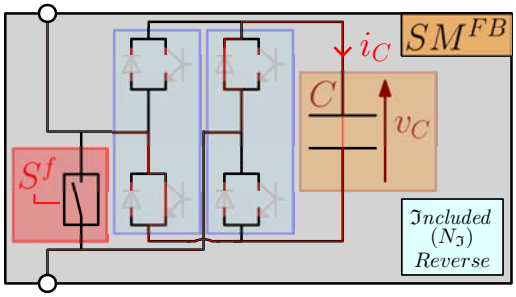

Figure 5.33: Full-bridge submodule diagram under a second example of the second fault class: forced inclusion of the capacitor to the arm.

Figure 5.34 allows one to summarize this classification of the different fault cases of a submodule. From a functional point of view, in order to represent the behavior of a faulty submodule on the arm of the converter, it is interesting to identify how to describe each of these three classes at the level of the LL model:

- A submodule of the *Excluded* class will impose on the arm a behavior equivalent to that submodule for which $S = 0$ and $S' = 0$
- The class *Included* in direct will impose on the arm a behavior equivalent to $S = 1$ and $S' = 0$
- The class *Included* in reverse will impose on the arm a behavior equivalent to $S = 0$ and $S' = 1$

To analyze how the state of a submodule can navigate between the different classes represented, and in order to derive a first approach, assumptions are made:

Assumption 14. *As soon as one of the semiconductors of a submodule is faulty, the whole submodule is considered inoperative, even if one or more of the remaining semiconductors are still operational*

Assumption 15. *As soon as one of the semiconductors of a submodule is faulty, it is assumed that the system controller is able to know which submodule has been affected and in which state its capacitor is forced.*

From these assumptions, it is possible to focus only on our objective here: how to reconfigure the operation of the control system once the fault is detected and known.

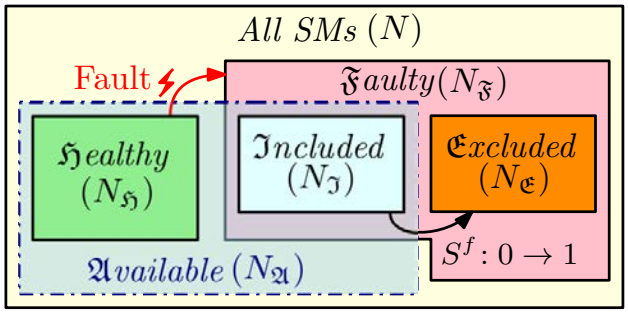

Figure 5.34: Submodule state classification.

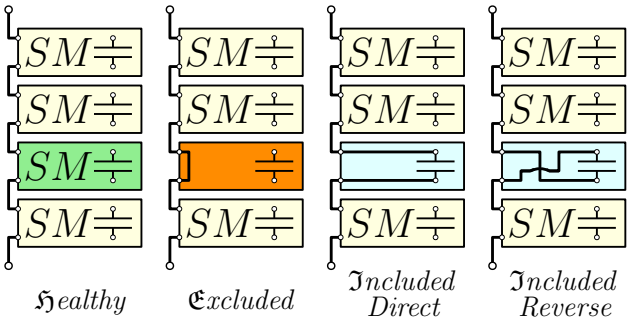

Figure 5.35: Example of the different states from the classification that a submodule from any arm can adopt.

When the submodule is in the *Healthy* state, it is fully controllable and operates nominally. When a fault occurs in one of the semiconductors of this submodule, it changes class to be considered fully *Faulty* under Assumption 14 and is therefore no longer considered controllable. Depending on its fault state, it will be placed in one of the two remaining subclasses. If the submodule forces its capacitor into one of the two states of inclusion in the arm, it will be put into the *Included* class. If its capacitor is forced into exclusion, it is put into the *Excluded* class.

In the case where the submodule belongs either to the *Healthy* class or to the *Included* class, it can make its capacitor voltage participate in the voltage of the arm to which it belongs. In other words, the voltage at the terminals of its capacitor is said to be *Available*.

If there comes a time when the capacitor of a submodule *Included* adopts an undesired behavior, which is possible since it is forced into the arm and there is no more way to directly modulate the current flowing through it, it is always possible to force the switching of the fault switch, whose state is represented by the binary variable S^f, to put it in the *Excluded* state so that it no longer disturbs the arm to which it belongs.

This first approach to the classification of fault states of a submodule is the starting point of the reconfiguration procedure that is introduced here.

5.E.2 | Reconfiguration procedure

Ideally, the desire of the operation reconfiguration under fault conditions is to get as close as possible to the nominal operation of the converter. The objective here is to get the closest possible to the operation that makes it possible to guarantee the rated power conversion for the converter, and thus the continuity of the maximum operating zone of the system. Note that when the rated power cannot be maintained while experiencing faults, degraded operation is an option that is still possible and more desirable than shutting down the system. The possibility of a degraded operation is also taken into account here.

In the will to ensure the continuity of the maximum operating zone of the converter, it is necessary to guarantee the tracking of the same maximum voltage level V_{DC} in each arm of the MMC. It is therefore necessary to ensure that all the capacitor of an arm, which are capable of participating in this energy conversion, add up to V_{DC}. The capacitors concerned are all grouped in the submodules of the *Available* class. This condition on the maximum available voltage in

any $\#xy$ arm is expressed:

$$\sum_{j\in\mathfrak{A}}^{N_{\mathfrak{A}}} v_{C_{xyj}} = V_{DC} \tag{5.73}$$

Capacitor voltage reference reconfiguration

In the class of submodules *Available*, there is that of *Included* and *Healthy*. This equation can therefore be rewritten as follows:

$$\sum_{j\in\mathfrak{H}}^{N_{\mathfrak{H}}} v_{C_{xyj}} + \sum_{j\in\mathfrak{I}}^{N_{\mathfrak{I}}} v_{C_{xyj}} = V_{DC} \tag{5.74}$$

The only capacitors whose voltage is still controllable are those that are *Healthy* and those whose voltage can vary freely are the *Included*. Thus, depending on the voltage value that the *Included* will bring into the arm, the remaining controllable submodules will have to adapt the voltage level of their capacitor to continue to guarantee V_{DC} in total. This means that the voltage reference of the remaining controllable capacitors will have to be adapted. Considering that the goal is to distribute the effort required from the controllable capacitors in a balanced manner, they are all given the same reference $\mathbf{v}^{ref}_{\mathbf{C_{xy}}}$ which therefore verifies the equation

$$N_{\mathfrak{H}}\mathbf{v}^{ref}_{\mathbf{C_{xy}}} + \sum_{j\in\mathfrak{I}}^{N_{\mathfrak{I}}} v_{C_{xyj}} = V_{DC} \tag{5.75}$$

In total, there are N submodules per arm, so the number of *Healthy* submodules $N_{\mathfrak{H}}$ is also $N - N_{\mathfrak{I}} - N_{\mathfrak{E}}$ or $N - N_{\mathfrak{F}}$ according to the classification of Figure 5.34. The reference to be imposed on the still controllable submodules is therefore the following:

$$\mathbf{v}^{ref}_{\mathbf{C_{xy}}} = \frac{V_{DC} - \sum_{j\in\mathfrak{I}}^{N_{\mathfrak{I}}} v_{C_{xyj}}}{N - N_{\mathfrak{F}}} \tag{5.76}$$

Ideally, in order to guarantee the conservation of the LOZ, one would like to be able to adapt the voltage reference according to (5.76) as desired. However, the capacitors have a maximum voltage for which they are designed and therefore cannot exceed it. By noting α_C^{max} the factor defining the overvoltage that the capacitors are able to withstand, the maximum voltage of the latter is expressed:

$$v_C^{max} = (1 + \alpha_C^{max})\, v_C^{nom} \tag{5.77}$$

Thus, the adapted voltage reference $\mathbf{v}^{ref}_{\mathbf{C_{xy}}}$ cannot exceed this upper limit:

$$\frac{V_{DC} - \sum_{j\in\mathfrak{I}}^{N_{\mathfrak{I}}} v_{C_{xyj}}}{N - N_{\mathfrak{F}}} \leq (1 + \alpha_C^{max})\, v_C^{nom} \tag{5.78}$$

Taking the worst case to identify the maximum number of submodules that can be lost, it is considered that the submodule *Included* do not contribute to the effort required, and the previous equation then becomes:

$$N_{\mathfrak{F}} \leq N - \frac{V_{DC}}{(1 + \alpha_C^{max})\, v_C^{nom}} \tag{5.79}$$

Knowing that $v_C^{nom} = V_{DC}/N$, the maximum value of the number of submodules that can be lost before requiring the still controllable capacitors to reach their maximum allowed voltage is expressed as:

$$N_{\mathfrak{F}}^{max} = \left\lfloor N \frac{\alpha_C^{max}}{1 + \alpha_C^{max}} \right\rfloor \tag{5.80}$$

The reference chosen for the remaining *Healthy* capacitors is therefore:

$$\mathbf{v}_{\mathbf{C_{xy}}}^{ref} = \min\left(\frac{V_{DC} - \sum_{j\in\mathfrak{I}}^{N_{\mathfrak{I}}} v_{C_{xyj}}}{N - N_{\mathfrak{F}}}, (1+\alpha_C^{max})\, v_C^{nom}\right) \tag{5.81}$$

As soon as an arm loses one more submodule than $N_{\mathfrak{F}}^{max}$, the converter LOZ is immediately reduced in a permanent way until at least one of them is repaired. In the worst case, the loss of each additional submodule can decrease the LOZ of v_{xy} by $(1+\alpha_C^{max})/N$ p.u..

Low-level control allocation reconfiguration

To continue to ensure service continuity, not only must the voltage reference that the capacitors must follow be adapted, but the low-level control must also be modified to account for the loss of steering capabilities with input variables that are forced to a given state. Several possibilities exist to reconfigure the allocation algorithm in the case of a fault.

Given a system with 3 inputs and 1 output, its allocation equation can then be put in the form:

$$\begin{aligned}&\{M\mathbf{U} = \mathbf{a_d}\,|\mathbf{U}_{min} \leq \mathbf{U} \leq \mathbf{U}_{max}\}\\ &\iff \left\{ \begin{bmatrix} m_1 & m_2 & m_3 \end{bmatrix} \begin{bmatrix} u_1 \\ u_2 \\ u_3 \end{bmatrix} = a_d \in \mathbb{R} \;\middle|\; \begin{bmatrix} u_1^{min} \\ u_2^{min} \\ u_3^{min} \end{bmatrix} \leq \begin{bmatrix} u_1 \\ u_2 \\ u_3 \end{bmatrix} \leq \begin{bmatrix} u_1^{max} \\ u_2^{max} \\ u_3^{max} \end{bmatrix} \right\}\end{aligned} \tag{5.82}$$

Assume then that u_2 is faulty and that its state forces it to take the value u_2^{min}. A first possibility to reconfigure the allocation is to reformulate the allocation by taking into account the influence of u_2 on the desired action vector and by taking u_2 out of the vector containing the control variables to be determined:

$$Reco._{Reformulate-CA}: \left\{ \begin{bmatrix} m_1 & m_3 \end{bmatrix} \begin{bmatrix} u_1 \\ u_3 \end{bmatrix} = a_d - m_2 u_2^{min} \;\middle|\; \begin{bmatrix} u_1^{min} \\ u_3^{min} \end{bmatrix} \leq \begin{bmatrix} u_1 \\ u_3 \end{bmatrix} \leq \begin{bmatrix} u_1^{max} \\ u_3^{max} \end{bmatrix} \right\} \tag{5.83}$$

Another possible solution, which is more direct, is simply to modify the boundary of the faulty input variable to indicate to the allocation that it can only affect it in its forced state. In this case, the reconfiguration takes the form:

$$Reco._{Update-Boundaries}: \left\{ \begin{bmatrix} m_1 & m_2 & m_3 \end{bmatrix} \begin{bmatrix} u_1 \\ u_2 \\ u_3 \end{bmatrix} = a_d \;\middle|\; \begin{bmatrix} u_1^{min} \\ u_2^{min} \\ u_3^{min} \end{bmatrix} \leq \begin{bmatrix} u_1 \\ u_2 \\ u_3 \end{bmatrix} \leq \begin{bmatrix} u_1^{max} \\ u_2^{min} \\ u_3^{max} \end{bmatrix} \right\} \tag{5.84}$$

The first reconfiguration solution has the benefit of reducing the complexity of the allocation to be carried out, since for each faulty input variable, the allocation will have one less decision variable to deal with. However, the algorithmic modification to be made is not immediate because a new allocation must be set up. In contrast, the second solution keeps the same allocation complexity as in the nominal case, but it has the advantage that the algorithmic modification to be performed is minimal.

The idea is to evaluate if the control allocation algorithms developed so far are able to reconfigure - in the current state of the algorithms - the control of the MMC with minimal modifications. It is thus the second solution which is going to be tried in this first approach: simply modify the boundaries of the duty cycles of the faulty submodules, and this according to the type of fault. Based on the presentation of the different submodule fault classes made previously, Table 5.14

indicates how to modify the bounds of the low-level control allocation in the case of a fault and according to the type of submodule considered.

	SM-HB	SM-FB
$\mathfrak{Excluded}$	$0 \leq D_{xyj} \leq 0$	$0 \leq D_{xyj} \leq 0$ $0 \leq D'_{xyj} \leq 0$
$\mathfrak{Included}$ *Direct*	$1 \leq D_{xyj} \leq 1$	$1 \leq D_{xyj} \leq 1$ $0 \leq D'_{xyj} \leq 0$
$\mathfrak{Included}$ *Reverse*	N/A	$0 \leq D_{xyj} \leq 0$ $1 \leq D'_{xyj} \leq 1$

Table 5.14: Low-level control control variables boundaries update for reconfiguration.

The low-level control allocation algorithm programmed so far is then adapted to take into account the modifications to be made to the duty cycles limitations as soon as a fault appears on one of the submodule.

5.E.3 Simulation conditions

In order to verify that the control allocation law designed to reconfigure itself in case of a fault is functional, the realization of a simulation is proposed. In this case, it is a non HIL simulation that is implemented.

To ensure the control of the MMC, the selected architecture is the one composed of the following elements:

- MIB for the *Energy Control*
- EMOn QP Active-Set from the GPFSROBHCCSSM for the *Current Control*
- EMOn QP Active-Set with the reconfiguration upgrade for the *Voltage Control*

The simulation carried out here aims at evaluating the behavior of the system in the case where it loses a submodule in one of its arms which is then imposed in the first possible state: *Excluded*. The choice is made for the simulation to focus then on the first arm of the MMC, the $\#py_1$. The work done by [Sel+19] showed a similar test to prove the quality of its carrier auto-interleaving technique to reconfigure the control of the converter in case of the failure of a submodule then also forced in exclusion state.

At the initial time, the capacitors are all charged to their nominal value V_{DC}/N and all the currents are zero. The voltage reference will remain stable at V_{DC}/N for capacitors belonging to fully *Healthy* arms. The common mode current as well as the current of the DC source are given the same references as in the previous tests. The reference for the circulating current is this time chosen null and that for the output current is a step which keeps the same value, $\hat{I}_o^{max}$, throughout the simulation with a constant power factor reference of 0.95. All the parameters of the converter and of the simulation are given in Table 5.15. Note that this time, unlike the previous tests, the converter is in a three-phase configuration with three submodules per arm and the three-phase load is not active[1]. The simulations are performed in the Matlab®-Simulink® environment this time and not in HIL for hardware availability reasons.

The operation in which the converter is initialized is a nominal operation without faults where

[1] The parameters of the MMC used here are then those of the experimental setup which the LAPLACE has.

the current called by the three-phase network is the maximum current that the converter can deliver and this operating point is requested over the whole duration of the simulation. At time $t = 2\ T_o$, the third submodule of the first arm of the converter is forced in the *Excluded* state.

Paramètres du MMC		
Parameter	Notation	Value
DC Bus		
DC Bus voltage	V_{DC}	600 V
DC link impedance	R_s, L_s	50 mΩ, 2 mH
MMC		
Rated power	S_o^{nom}	10 kVA
Number of submodules	N	3
Type of submodules	q	1 (half-bridge submodule)
Arm impedance	R, L	10 mΩ, 5 mH
AC Network		
Number of phases	m	3
AC active voltage amplitude	$\hat{V}_{AC}$	0 V
AC active voltage phase	φ_v	0 rad
Fondam. freq. and per. of the network	f_o, T_o	50 Hz, 20 ms
Network pulsation	ω_o	$2\pi f_o \simeq 314$ rad/s
AC load impedance	R_o, L_o	40 Ω, 5 mH
Closed-Loop Simulation Parameters		
Simulation time step	T_{step}	$T_s = 250$ µs
Simulation end time	t_{end}	$15\ T_o = 300$ ms

Table 5.15: Parameters of the MMC for the reconfiguration test.

5.E.4 | Simulation results

Figures 5.36 and 5.37 contain the results of tests performed to evaluate the reconfiguration capabilities of the MMC control allocation law.

The first observations are particularly interesting. In fact, from the appearance of the fault, the control architecture implemented is not only capable of ensuring that the voltage available on the faulty device returns to its nominal level, but this property is guaranteed relatively quickly with a time taken to return to the $\pm 5\%$ band around the nominal value of the order of 59 ms, i.e. less than three fundamental periods.

As shown in Figure 5.37 (b), the three submodules available at the start in the arm are all balanced at 200 V, the two remaining submodules operational after the fault occurs are uniformly rebalanced at 300 V in steady state, thus guaranteeing a return to the converter nominal operating zone for the currents to be converted. The evolution obtained for the available arm voltage returns quickly to its nominal value, see Figure 5.37 (c). It is noted that this rebalancing of the capacitors is done in a uniform manner because it is a QP method which is used for the low-level control here. It is noted that a I_s current surge is drawn at the moment the fault occurs in order to overload the capacitors still available in the arm $\#py_1$.

The operating continuity of the converter is confirmed but not that of the the maximum operating zone, as seen on Figure 5.36 (d) which represents the behavior of the output currents. After the time of the fault occurrence, a disturbance in the current behavior is observed. It is due to the

fact that the LOZ is abruptly reduced, but, the current quickly returns to track its reference. The return to normal operation for the current is much faster than the time taken for the voltage available in the arm to return around V_{DC}, and the disturbance on the current is not felt before $t = 48$ ms while the fault appears at $t = 40$ ms. The voltage available is below its nominal level between $t = 40$ ms and $t = 109$ ms, while the current is disturbed between $t = 48$ ms and $t = 56$ ms. This is explained by the comparison between v_{xy} and the sum of the capacitor voltages still available in the arm because it is v_{xy} that controls the currents in the converter.

As shown in Figure 5.37 (b), the arm voltage is forced to be limited by the total voltage available in the capacitors of the arm between $t = 48$ ms and $t = 56$ ms only. At the time when the fault appears, the voltage available in the arm suddenly falls from 600 V to 400 V while at the same time the reference voltage v_{xy}^{ref} is around 150 V, the reference value requested by the current control loop can therefore be reached and the currents are not disturbed. But between $t = 48$ ms and $t = 56$ ms, Figure 5.37 (b) clearly shows that v_{xy} cannot follow the expected sinusoidal shape because it then encounters the total voltage available in the arm which limits it. This is confirmed by Figure 5.37 (a) which shows that the amplitude and phase of $\mathbf{I_o}$ are finally impacted for a very short time between $t = 48$ ms et $t = 56$ ms. The influence of the fault on the energy conversion capabilities of the MMC under this conditions is thus quickly erased by the reconfiguration of the control that the CA developed here allows.

The results obtained allow to validate the reconfiguration capabilities of the control allocation for the MMC in a first simplified approach that considered only the case of the fault where the submodule is imposed in exclusion and the case where the LOZ is not permanently reduced. Other tests are to be carried out using the reconfiguration procedure proposed here in order to cover all the identified fault classes. This study opens an interesting perspective of exploration on the fault tolerant control allocation of the MMC.

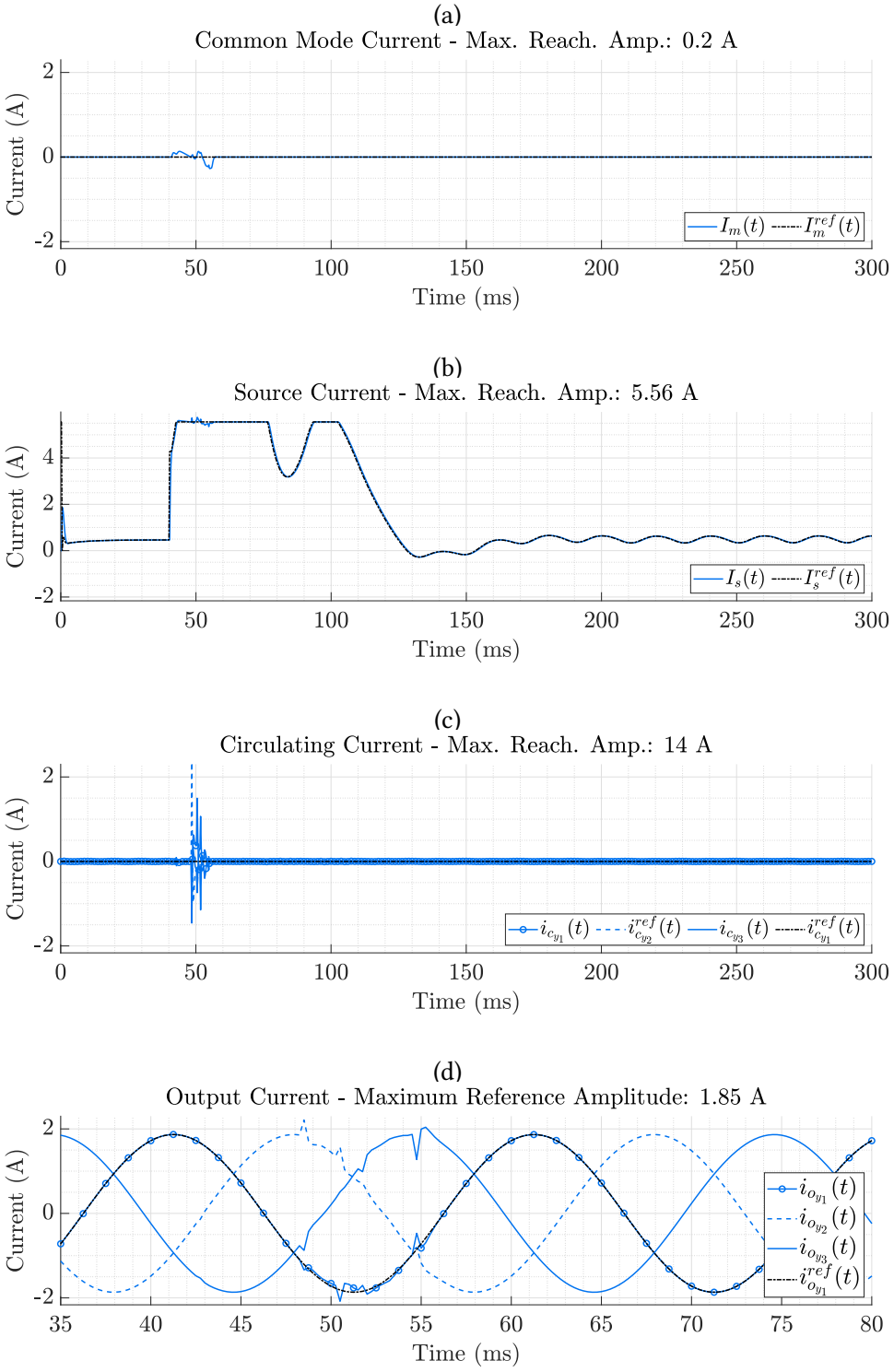

Figure 5.36: Closed-loop behavior of the currents when testing the reconfiguration capabilities of the control allocation for the MMC. (a) Common mode current, (b) DC source current, (c) Circulating current, (d) AC-side output current, zoom around the fault from 35 ms to 80 ms. Simulations are done in the 3-**phase** case.

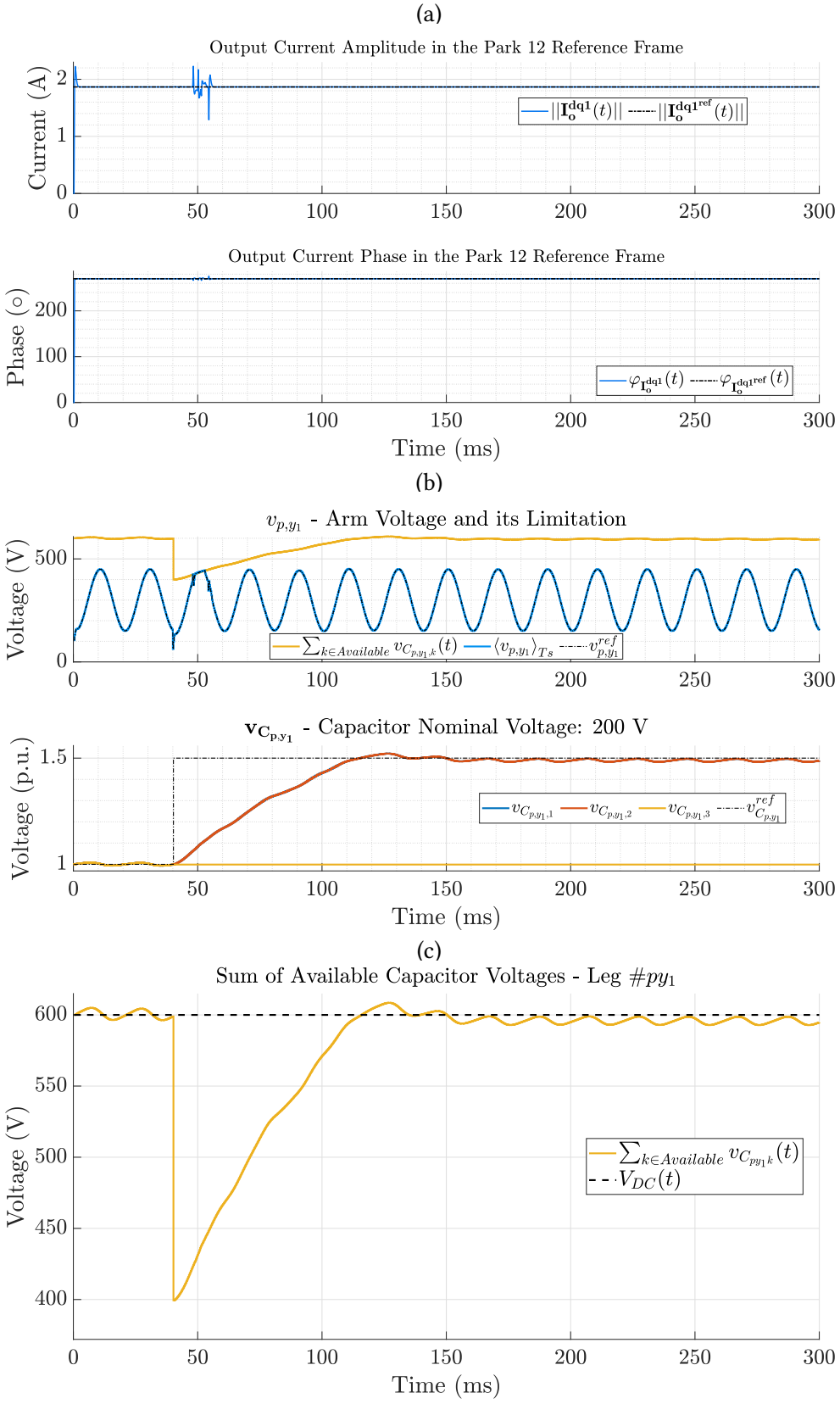

Figure 5.37: Closed-loop behavior of the currents when testing the reconfiguration capabilities of the control allocation for the MMC. (a) Output current in the PARK 1 reference frame, (b) Arm voltage and capacitor voltages in a selected arm, (c) Sum of the $\mathfrak{Available}$ capacitor voltages in a selected arm. HIL simulations are done in the 7-**phase** case.

5.F | Conclusion about the contribution to the development of control allocation methods for the MMC

In this chapter, several control methods have been developed to guarantee the control performance requirements for the proper operation of the MMC. The control architecture of this converter is divided into three large nested loops which are the *Energy Control*, the *Current Control* and the *Voltage Control*. For each of these control loops, allocation algorithms have been designed based on the models developed in Chapter 2 and Chapter 3. The results show overall that this new control method of the MMC made by allocation meets the requirements: the balancing of the capacitors as well as the reference tracking of the currents is ensured and the appropriate energy level in the converter is guaranteed.

This study result in the design of a scalable and versatile control architecture of the MMC, see Figure 5.9. It adapts to any number of phases and submodules, being able to control a large variety of MMC due to the versatility of the introduced models. This SCAA architecture uses real time optimization algorithms to optimally distribute the control efforts among the set of available control variables.

The exploration axis followed for the current control has led to the development of a new control allocation algorithm which is scalable to the number of phases while keeping the same control performance and whose computation time hardly changes with the number of phases. By taking advantage of the new method of control allocation with integral compensator developed in Chapter 4, this current control algorithm was seamlessly upgraded allowing to guarantee better performances in steady-state without modifying the dynamic performances by the addition of the integral compensator which is thus transparent. The fact of having a current control algorithm, whose computation time does not increase with the number of phases, opens the way for the design of generic and versatile controllers for electrical systems that can be easily adapted.

The study carried out in the context of active capacitor balancing has initially led to a variety of voltage control allocation algorithms that give the general architecture its scalability to the number of submodules while guaranteeing the required balancing. Differences between the optimizers have been highlighted in the context of the new application of these algorithms in power electronics. The analysis carried out to better understand the operation of the allocation optimization algorithms has shown that, in general, the methods using a quadratic criterion favor control solutions that balance the deviation from the allocation equation (4.12), as opposed to the use of a linear criterion, which has no particular preference.

The last study of this chapter, about the evaluation of the reconfiguration capabilities of the MMC operation during a fault, showed encouraging results. This was obtained thanks to a minor modification to the control allocation methods developed for the nominal operation case. This validates the reconfiguration capabilities of the allocation approach on given a fault case in simulation. This opens the perspective of fault tolerant control allocation for the MMC and more generally in power electronics.

Overall, as a conclusion of the studies carried out in this chapter, the allocation-based control architecture of the MMC that presents the best trade-off between guaranteed control performance, efficiency in distributing control efforts, real time computation time and transparent scalability is defined as follows:

- Low-level control using the CA EMOn QP (Active-Set ou Interior-Point)
- High-level control using the CAI EMOn QP from the control-oriented model GPFSROB-HCCSSM

- Power-energy control for energy control using the only possibility studied is selected: CA MIB.

The work carried out in this chapter has made it possible to understand and develop new control laws using the principle of real time allocation using optimization for the MMC. However, several investigation perspectives are available such as the comparative study between the implementation of the active balancing of the voltages per arm and that all the arms in one allocation, the analysis of the influence of the current limitations on the various high-level control algorithms when the latter are reached, the behavior of the system when it is under disturbances, the fault tolerant control allocation for the MMC or the allocation-optimal choice of the circulating current references in order to improve the balancing of the capacitors such as the reduction of the ripples for example.

General Conclusion

In general, the propositions that have been made here are part of a global scalability approach both for the models of the modular multilevel converter and for the control methods by real time optimization of the latter.

Control allocation: a relevant approach for the MMC

The interest of using control allocation methods for the modular multilevel converter has been highlighted here. This converter has - by the modularity which characterizes it - a number of input control variables at least as large as the number of submodules. Being, particularly suitable for high-voltage direct current conversion, its use in such networks with a large number of submodules is both growing and represents a significant control challenge. This multiplicity of control degrees of freedom makes it possible to formulate control objectives in the form of an overactuated control problem that control allocation methods are tailored to deal with.

Among the different families of allocation methods, there is one that offers a good trade-off between problem solving efficiency, implementation complexity and real time computation speed: the online optimization allocation methods. Although they are the most demanding of the different families in terms of real time computation resources, the current embedded computer hardware technologies have shown to be able to execute them with a sufficient speed to be used in the context of the control of electrical systems. As a consequence, these allocation methods have been mainly developed here for the modular multilevel converter.

Scalable modelling: more modularity for the MMC

Within the framework of this choice of allocation methods for the modular converter studied, scalable models of the submodules and the arms of the converter were established. This was done with the objective of using them for control purposes and, more particularly, for allocation. This approach was carried out while aiming at unifying in the same model the already existing suitable models as well as the new additions proposed here to represent half-bridge and full-bridge submodules.

The contribution proposed here consists in the derivation of models that represent the influence of all the switches that can be present in a submodule in nominal, blocked or faulty operation through a single variable called submodule state. This approach is extended to take into account a model of conduction losses in the semiconductors in order to provide - for control purposes - an easy-to-handle loss model. The control-oriented model is then extended to the whole set of arms, it is then usable for other control approaches than allocation. A dedicated formulation for allocation is then deduced.

The modular multilevel converter being a modular converter in number of submodules, which makes it possible to widen the voltage that it can convert and thus its power, it is then proposed to give it a modularity in number of phases by developing adapted control models.

The introduced contribution consists of several control-oriented high-level current modelling approaches with varying degrees of complexity and accuracy. First, a general polyphase model of the converter is introduced with a state-space formulation able to accommodate any number of phases. It represents the converter and its interfaces without loss of generality on the possibilities of the DC bus and AC network with the consideration of impedances, voltage sources and different neutral connections. This generality is given to all the proposed high-level models. This first model which is the simplest in terms of derivations is also the most accurate but on the other hand it is the heaviest in terms of computation time. An order reduction approach is then implemented from the design of a polyphase Park transform dedicated to the representation of the dominant harmonic content in the converter.

The state-space model then obtained in the Park reference frame offers a very good trade-off between accuracy and low computation time since beyond five phases it is of constant order. The proposed state-space models can be used in any current control approach, they then adopt here a formulation for the allocation.

Control allocation methods: towards a wider adoption

Online optimization allocation methods show various formalisms that depend on the type of cost function. A unifying approach of these methods is therefore introduced to allow a quick and easy formalization of an optimization-based control allocation for a large class of optimization criteria.

In order to improve the control performance observed when using real time optimization allocation, a novel reference model based control allocation method including a built-in integral compensator was proposed. Its features have been proven theoretically and through simulations. A major feature of the tuning method introduced is that adding the integrator is transparent for the closed-loop response: no supplementary zero or pole appears due to the integrator and the same reference model is followed. Those features are combined with the intrinsic features from the classical control allocation such as the optimal distribution of the control effort among the available control variables. Interestingly, the new method can be readily combined with existing ones for an important performance gain and little change of the control algorithm.

The static and dynamic performances obtained with this upgrade of the allocation methods in terms of reference tracking, static deviation cancellation and perturbation rejection give a new capability to the allocation methods. This ability translates into a high value-added ratio between control performance and implementation complexity. This allows the allocation methods to be considered for the control of a wider class of systems thanks to the transparent integral compensator.

Scalable control allocation: achievements and future perspectives

The major contribution of the work presented here is the development of allocation methods for the modular multilevel converter. This approach has allowed the design of a variety of control architectures by online optimization. This made it possible to take advantage of the numerous switches of the converter to steer the currents, voltages and energy contained in the latter. A part of them have been the topic of an in-depth analysis, highlighting the possibilities and the performances of the control obtained. This shows the interest and relevance of the allocation methods for the control of the modular multilevel converter, which are able to achieve the DC-AC conversion of the desired power, the reference tracking of circulating current while guaranteeing

the balance of the capacitors. For more details on the qualitative comparison of control allocation with classical control approaches of the MMC, see Appendix O.

However, two aspects still need to be worked on in order to put forward these allocation approaches. A quantitative comparison of the control allocation with the classical converter control methods has to be carried out.

Low-level control allocation optimization criteria For the low-level control of the converter more specifically, it has been shown that the allocation methods are capable of guaranteeing the objectives. In particular, compared to traditional control methods where an arm voltage control and a capacitor balancing control algorithm are implemented sequentially, the allocation approach proposed here takes into account the two objectives of arm voltage reference tracking and capacitor balancing at the same time and ensures them in a cooperative manner. This allows for a novel and aggregated approach that takes into account the interactions between the two control objectives.

It has also been shown that the formulation of control problems for power electronics systems, where the effectiveness of the control is similar for all degrees of freedom, is such that quadratic programming leads to a more uniform use of the control input variables than linear programming. This question of the fine understanding of the behavior of optimization algorithms is a perspective of investigation that may be interesting to explore in order to better predict the behavior of optimization algorithms in the allocation framework, and thus allow a more detailed study of the stability of the system in closed-loop when it is controlled using an online optimization allocation.

High-level control allocation optimization criteria Contrary to what has been observed in the literature for several types of systems, when using the linear programming and quadratic programming algorithms, the formulation of the allocation implemented here has shown the interesting result that the quadratic optimization is faster to converge than the linear one, which is even more true as the number of phases increases. It would be interesting to investigate the causes of this and to evaluate if a different formulation of the optimization could modify the complexity of the problem in such a way as to make the performance of linear programming more competitive with that of quadratic programming.

This first comparative adaptation of linear and quadratic programming for control allocation in the case of power electronics gives both a first implementation that achieves the required perfomance but also opens the way to a deeper investigation of the use of quadratic programming for allocation in this field of engineering where a certain variety of losses is expressed as a function of the square of input control variables or state variables.

High-level global current control allocation The method of control allocation of the currents introduced in this study brings a global approach to the control of electrical quantities. Instead of performing the control of currents - as many works do - by focusing on the different currents such as the circulating current or the output current independently with a dedicated controller for each, the allocation implemented allows, from a single algorithm, the control of all types of currents in a cooperative manner. This makes it possible both to act on all the control variables jointly, taking into account the interaction of each of them on the different currents, but also to manage their saturation in a single place with a single algorithm that does it in an optimized way.

This global approach, which is a strength of the allocation algorithm developed here, is a first step that was made possible by a choice of model and allocation formulation. This promising approach

can be further explored by adopting, for example, different broader models of the converter and different optimization criteria in order to obtain a specific and improved operation of the modular multilevel converter for a given purpose, and perhaps even capable of adapting itself in an optimal way in the different cases of its operation.

Scalable and quasi-constant execution time control allocation For current control, scalable modelling approaches have been used to design online optimization allocation algorithms that feature this same scalability property. Moreover, a judicious reduction of the model order has made the complexity almost insensitive to the number of phases.

This makes it possible to design generic real time optimization control algorithms that can be scaled to any number of phases while maintaining a computation time that hardly changes with the number of phases. It is then possible to use the same embedded hardware computer to operate a three-phase system than a hundred-phase system with a very little difference in computation time. Knowing that we are able to design such a control law with quasi-constant execution time and constant performance for a system whatever its number of phases, opens also the possibility to include the number of phases in the design parameters of a modular multilevel converter and potentially of a fault tolerant electrical system. With this change in the status of this parameter, it offers an additional degree of freedom for a global optimization of the design of an electrical system that does not have to worry about whether the control system will be able to control the system with the determined number of phases, nor about the necessary optimization time in real time. This control scalability property can be extended to other power converters starting from the same modelling approach.

MMC fault tolerant control allocation The implementation of the fast reconfiguration strategy of the allocation algorithm highlighted the capabilities of these control methods to ensure reconfiguration of the converter operation when a submodule is in one of the specific classes of possible faults. The allocation has been shown to be able to quickly restore the operation of the converter, allowing for almost continuous operation of the conversion at maximum active power.

The reconfiguration performances achieved were obtained in a single fault case and under specific operating conditions only, which constitutes encouraging results that open the way to the use of allocation methods more generally in power electronics for fault tolerant control. However, there is still work to be done to evaluate the capabilities of the allocation to reconfigure the operation of the MMC on the entire operating region, especially in the worst conditions. More generally, as several fault cases have been identified, another track of investigation that remains to be explored is the evaluation of the capabilities of the allocation to adapt the operation of the modular multilevel converter in other fault cases and how to modify the allocator to improve performance in this case as well as in other cases such as when a submodule is repaired or replaced and made available again for power conversion.

Vision for the future Although allocation has been used here in the context of the modular multilevel converter, which can be seen as featuring some redundancy in the control input variables, as in the case of [Bou17] and [Kre+21] for other overactuated converter topologies, allocation methods are not limited to such systems. The primary capability of allocation methods remains to distribute the control effort optimally and quickly in real time among the control input variables while taking into account their limitations. These methods have additional features, graphically summarized in Figure 1.14, that make them attractive and highly relevent also for the control of non-overactuated systems. Among these key features one finds 1) the ability to determine the control by real time optimization for a given objective, 2) the ability to take into account the constraints *a priori* during the determination of the control, and not *a posteriori* like

a major proportion of the control methods, 3) the ability to easily specify and adjust the desired closed-loop dynamics, and 4) the new ability, brought here by the transparent integral compensator, to guarantee the cancellation of the static error without modifying the closed-loop tracking dynamics. This could allow power electronics to quickly determine in real time and optimally the values of control variables such as voltages, currents or duty cycles by taking into account their limitations *a priori* in the formulation of the control algorithm and not by adding a saturation *a posteriori*. An interesting exploration perspective is then the evaluation of the performances of the control allocation compared to the well known model predictive control in the context of power electronics.

The improvements achieved in this study, for the allocation methods generally and their use for the modular multilevel converter, further emphasize the interest in employing these control methods which have the potential to be beneficially used more widely in electrical engineering for overactuated or non-overactuated systems.

Appendix

A | Exponential matrix discretization of a state-space model

Let a state-space model be defined by:

$$\begin{cases} \dot{\mathbf{X}} = A\mathbf{X} + b(\mathbf{U}) + \mathbf{E} \\ \mathbf{Y} = C\mathbf{X} \end{cases} \tag{A.1}$$

With $b(\mathbf{U})$ standing for the influence of the control on the system, this function can also be linear, case of $b(\mathbf{U}) = B\mathbf{U}$, or nonlinear, case of $b(\mathbf{U}) = B\mathbf{U} + \mathbf{U}^T B'\mathbf{U}$ for example. According to the principle of the zero-order-hold, using a sampling that assumes that during the sampling period T_c, the signals $\mathbf{U}$ and $\mathbf{E}$ do not vary, it is found by solving the differential equation that:

$$\begin{cases} \mathbf{X}_{k+1} = e^{AT_c}\mathbf{X}_k + \int_{kT_c}^{(k+1)T_c} e^{A[(k+1)T_c - t]} \left[b(\mathbf{U}_k) + \mathbf{E}_k\right] dt \\ \mathbf{Y}_k = C\mathbf{X}_k \end{cases} \tag{A.2}$$

As it is considered that $\mathbf{U}_k$ and $\mathbf{E}_k$ are invariant over T_c, they can be removed from the integral, which gives then:

$$\int_{kT_c}^{(k+1)T_c} e^{A[(k+1)T_c - t]} \left[b(\mathbf{U}_k) + \mathbf{E}_k\right] dt = \left(\int_{kT_c}^{(k+1)T_c} e^{A[(k+1)T_c - t]} dt\right) \cdot \left[b(\mathbf{U}_k) + \mathbf{E}_k\right] \tag{A.3}$$

Assuming that A is invertible, the following derivation is trivial:

$$\int_{kT_c}^{(k+1)T_c} e^{A[(k+1)T_c - t]} dt = \left[-A^{-1}e^{A[(k+1)T_c - t]}\right]_{kT_c}^{(k+1)Ts} = A^{-1}(e^{AT_c} - \mathbb{I}_n) \tag{A.4}$$

By substitution, this results into:

$$\int_{kT_c}^{(k+1)T_c} e^{A[(k+1)T_c - t]} \left[b(\mathbf{U}_k) + \mathbf{E}_k\right] dt = A^{-1}(e^{AT_c} - \mathbb{I}_n) \cdot \left[b(\mathbf{U}_k) + \mathbf{E}_k\right] \tag{A.5}$$

The discrete state-space model thus becomes:

$$\begin{cases} \mathbf{X}_{k+1} = e^{AT_c}\mathbf{X}_k + A^{-1}(e^{AT_c} - \mathbb{I}_n) \cdot \left[b(\mathbf{U}_k) + \mathbf{E}_k\right] \\ \mathbf{Y}_k = C\mathbf{X}_k \end{cases} \tag{A.6}$$

Introducing the definitions $F = e^{AT_c}$ and $H = A^{-1}(F - \mathbb{I}_n)$, it comes that:

$$\begin{cases} \mathbf{X}_{k+1} = F\mathbf{X}_k + H\left[b(\mathbf{U}_k) + \mathbf{E}_k\right] \\ \mathbf{Y}_k = C\mathbf{X}_k \end{cases} \tag{A.7}$$

Remarks:

- In the case where $b(\mathbf{U}) = B\mathbf{U}$, The discrete state-space model becomes:

$$\begin{cases} \mathbf{X}_{k+1} = F\mathbf{X}_k + G\mathbf{U}_k + H\mathbf{E}_k \\ \mathbf{Y}_k = C\mathbf{X}_k \end{cases} \tag{A.8}$$

  With $G = A^{-1}(F - \mathbb{I}_n)B = HB$.

- In the case of specific state-space models where the dynamic matrix A is null, the state-space model is defined:

$$\begin{cases} \dot{\mathbf{X}} = b(\mathbf{U}) + \mathbf{E} \\ \mathbf{Y} = C\mathbf{X} \end{cases} \tag{A.9}$$

The discretisation of this model using the matrix exponential transforms the state-space model into:

$$\begin{cases} \mathbf{X}_{k+1} = F\mathbf{X}_k + H\left[b(\mathbf{U}_k) + \mathbf{E}_k\right] \\ \mathbf{Y}_k = C\mathbf{X}_k + g(\mathbf{U}_k) \end{cases} \tag{A.10}$$

where the introduced matrices are defined according to:

$$\begin{cases} F = \mathbb{I} \\ H = T_c \end{cases} \tag{A.11}$$

According to the definitions given in (A.11), the first line of equation (A.10) can also be formulated as:

$$\frac{\mathbf{X}_{k+1} - \mathbf{X}_k}{T_c} = b(\mathbf{U}_k) + \mathbf{E}_k \tag{A.12}$$

Therefore the discretization of a state-space model where the dynamic matrix is null is equivalent to the Euler explicit approximation of (A.9).

B | Control allocation formulation from a state-space model

Let a state-space model be defined by:

$$\begin{cases} \dot{\mathbf{X}} = A\mathbf{X} + b(\mathbf{U}) + \mathbf{E} \\ \mathbf{Y} = C\mathbf{X} \end{cases} \tag{A.13}$$

The discretisation of this model using the matrix exponential transforms the state-space model into:

$$\begin{cases} \mathbf{X}_{k+1} = F\mathbf{X}_k + H\left[b(\mathbf{U}_k) + \mathbf{E}_k\right] \\ \mathbf{Y}_k = C\mathbf{X}_k \end{cases} \tag{A.14}$$

where the introduced matrices are defined, when A is invertible, according to:

$$\begin{cases} F = e^{AT_c} \\ H = A^{-1}\left(F - \mathbb{I}\right) \end{cases} \tag{A.15}$$

with T_c the sampling period of the control. If one combines the two equations of the discrete state-space model, $\mathbf{Y}_{k+1}$ is derived:

$$\mathbf{Y}_{k+1} = CF\mathbf{X}_k + CHb(\mathbf{U}_k) + CH\mathbf{E}_k \tag{A.16}$$

Isolating the control term in the left side of this equation gives:

$$\begin{aligned} CHb(\mathbf{U}_k) = \mathbf{Y}_{k+1} - CF\mathbf{X}_k - CH\mathbf{E}_k \\ \iff \mathcal{M}(\mathbf{U}_k) = \mathbf{a}_k \end{aligned} \tag{A.17}$$

Where $\mathcal{M}(\cdot) = CHf(\cdot)$ is the effectivness function and $\mathbf{a}_k$ is the action vector generated at time $t = kT_c$ by applying $\mathbf{U}_k$ to the system.

Remark:

In the case where the state-space model be defined by:

$$\begin{cases} \dot{\mathbf{X}} = A\mathbf{X} + B\mathbf{U} + \mathbf{E} \\ \mathbf{Y} = C\mathbf{X} \end{cases} \tag{A.18}$$

The function $f(\cdot)$ is updated as $b(\mathbf{U}) = B\mathbf{U}$. Thus, (A.17) becomes:

$$\begin{aligned} CG\mathbf{U}_k = \mathbf{Y}_{k+1} - CF\mathbf{X}_k - CH\mathbf{E}_k \\ \iff M \cdot \mathbf{U}_k = \mathbf{a}_k \end{aligned} \tag{A.19}$$

With $G = HB$ and where M is the effectivness matrix CG.

C | Amplitude of biharmonic waveforms

Let $s_a(t)$ and $s_b(t)$ be two signals defined by:

$$\begin{aligned} s_a(t) &= S_0 + S_1 \ \cos(\omega t - \varphi) \\ s_b(t) &= S_0 + S_1 \ \cos(\omega t - \varphi) + S_2 \ \cos(2\omega t - 2\varphi) \end{aligned} \tag{A.20}$$

The maximum amplitude of $s_a(t)$ is trivial:

$$s_a^{max} = \max_t s_a(t) = S_0 + S_1 \tag{A.21}$$

However, the maximum amplitude reached by $s_b(t)$ is less obvious and needs to be derived properly:

$$\frac{ds_b(t)}{dt} = \omega \ S_1 \ \sin(\omega t - \varphi) + 2 \ \omega \ S_2 \ \sin(2\omega t - 2\varphi) \tag{A.22}$$

In order to find t^* so that $s_b(t)$ is maximum, $\frac{ds_b(t)}{dt} = 0$ must be solved:

$$\frac{ds_b(t)}{dt} = 0 \Longleftarrow S_1 \ \sin(\omega t^* - \varphi) + 2 \ S_2 \ \sin(2\omega t^* - 2\varphi) = 0 \tag{A.23}$$

Let $\theta = \omega t^* - \varphi$, thus the previous equation becomes:

$$S_1 \ \sin(\theta) + 2 \ S_2 \ \sin(2\theta) = 0 \tag{A.24}$$

Since $\sin(2\theta) = 2\sin(\theta)\cos(\theta)$, the previous equation becomes:

$$S_1 \ \sin(\theta) + 4 \ S_2 \ \sin(\theta)\cos(\theta) = 0 \tag{A.25}$$

Depending on the signs from S_1 and S_2, different solutions are found for θ. From those solutions, the solutions t^* can be found thanks to $t^* = (\theta + \varphi)/\omega$. In the case where both S_1 and S_2 are positive values, solving the previous equation gives t_1^*:

$$\theta_1 = \omega t_1^* - \varphi = 0 + 2k\pi, \quad k \in \mathbb{N} \tag{A.26}$$

The substitution of t by t_1^* in $s_b(t)$ shows that:

$$s_b^{max_1} = s_b(t_1^*) = S_0 + S_1 + S_2 \tag{A.27}$$

In the case where $S_1 > 0$ and $S_2 < 0$, solving the same equation gives t_2^*:

$$\theta_2 = \omega t_2^* - \varphi = \arctan\left(\frac{\sqrt{1-\left(\frac{S_1}{4S_2}\right)^2}}{\frac{-S_1}{4S_2}}\right) + 2k\pi, \quad k \in \mathbb{N} \tag{A.28}$$

The substitution of t by t_2^* in $s_b(t)$ shows that:

$$s_b^{max2} = s_b(t_2^*) = S_0 - \frac{S_1^2 + 8S_2^2}{8S_2} \tag{A.29}$$

This means that depending on the signs from S_1 and S_2, different solutions are possible and some are even nonlinear.

Note that (A.29) is valid as long as the magnitude of S_2 is not too small compared to S_1. Therefore, work still needs to be continued to derive a comprehensive formula describing the maximum of $s_b(t)$ in all cases. But the point here was to show that the maximum of $s_b(t)$ does not have a straightforward formula, easily applicable in all cases.

D | Derivation of the low-level analytical detailed model of the half-bridge submodule

From the influence of the variables S_{xyj}, S_{xyj}^b, S_{xyj}^f and the associated switches on the behavior of the submodule, it is possible to derive the evolution of the electrical signals $i_{C_{xyj}}$, $v_{C_{xyj}}$, v_{xyj} and v_{xy} which are directly linked to the considered SM and its state. For that the use of a truth table will make it possible to extract a formula of the state of the cell in the form of logical equation.

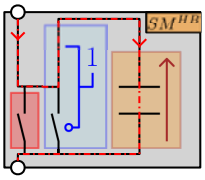

Figure 9: SM-HB in its active state.

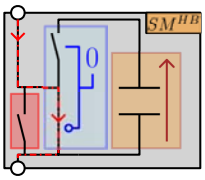

Figure 10: SM-HB in its passive state.

For example, for the state characterized by $S_{xyj} = 1$, $S_{xyj}^b = 0$ and $S_{xyj}^f = 0$ which is shown on the Figure 9, it comes from the KCL that the current flowing through the capacitor will be $i_{C_{xyj}} = i_{xy}^*$ as long as the capacitor is not discharged and from the KVL the voltage across the submodule will be $v_{xyj} = v_{C_{xyj}}$. For the dual state which is represented on the Figure 10 and characterized by $S_{xyj} = 0$, $S_{xyj}^b = 0$ and $S_{xyj}^f = 0$, the current through the capacitor will be zero $i_{C_{xyj}} = 0$ as well as the voltage across the submodule $v_{xyj} = 0$. In normal operation of the submodule, the latter will be in one of those two states. By applying KIRCHHOFF's laws to the half-bridge submodule in the different possible combinations of the variables S_{xyj}, S_{xyj}^b and S_{xyj}^f, all the different states are analyzed. The result of this process is given in the Table 16.

S_{xyj}^f	S_{xyj}^b	S_{xyj}		$i_{C_{xyj}}$	v_{xyj}
0	0	0		0	0
0	0	1		i_{xy}^*	$v_{C_{xyj}}$
0	1	-		$i_{xy}^* \cdot (i_{xy}^* > 0)$	$v_{C_{xyj}} \cdot (i_{xy}^* > 0)$
0	1	-		$i_{xy}^* \cdot (i_{xy}^* > 0)$	$v_{C_{xyj}} \cdot (i_{xy}^* > 0)$
1	-	-		0	0

Table 16: Truth table - Behavior of the SM-HB

Newly introduced notations in the table make it possible to simplify it[1]. From the truth table it

[1] Binary variables standing for of the sign of the current and the voltage are introduced:

$$(i_{xy}^* > 0) = \begin{cases} 1, \text{if } i_{xy}^* > 0 \\ 0, \text{if } i_{xy}^* \leq 0 \end{cases} \implies (i_{xy}^* > 0) = (sign(i_{xy}^*) + 1)\,\frac{sign(i_{xy}^*)}{2} \tag{A.30}$$

is possible to derive the logic equation modelling the behavior of the submodule according to the states of the switches. In order to develop the model with a gradual complexity, a first step without taking into account the variables S^b_{xyj} and S^f_{xyj} is done. To do so, the interest is focused on the first two lines of the Table 16. The current flowing through the capacitor is then expressed:

$$C\,\frac{dv_{C_{xyj}}}{dt} = i_{C_{xyj}} = i^*_{xy}\,S_{xyj} \tag{A.32}$$

The voltage at the terminals of the submodule is obtained in the same way from the table:

$$v_{xyj} = v_{C_{xyj}}\,S_{xyj} \tag{A.33}$$

It is worth noting that the voltage v_{xyj} is then bounded between 0 and $v_{C_{xyj}}$ for the half-bridge submodule case. The model of the half-bridge submodule can then be put in the following form.

$$\begin{cases} i_{C_{xyj}} = C\,\frac{dv_{C_{xyj}}}{dt} = i^*_{xy}\,S_{xyj} \\ v_{xyj} = v_{C_{xyj}}\,S_{xyj} \in \left[0; v_{C_{xyj}}\right] \end{cases} \tag{A.34}$$

The system (A.34) describes the behavior that will be experienced by the half-bridge submodule under normal operation, which is most of the time. Taking into account the remaining binary variables increases the complexity of the model. The principles of logic equation synthesis applied to the truth table as a whole makes it possible to establish more complete behavioral equations for the half-bridge submodule:

$$\begin{cases} i_{C_{xyj}} = C\,\frac{dv_{C_{xyj}}}{dt} = i^*_{xy}\left[S_{xyj}\,\overline{S^b_{xyj}}\,\hat{p}_{xyj}(i^*_{xy}, v_{C_{xyj}}) + (i^*_{xy} > 0)\,S^b_{xyj}\right]\,\overline{S^f_{xyj}} \\ v_{xyj} = v_{C_{xyj}}\left[S_{xyj}\,\overline{S^b_{xyj}}\,\hat{p}_{xyj}(i^*_{xy}, v_{C_{xyj}}) + (i^*_{xy} > 0)\,S^b_{xyj}\right]\,\overline{S^f_{xyj}} \end{cases} \tag{A.35}$$

Which corresponds to the analytical DM from [Zam17] with the notations used here. The notation $\overline{x}$ for a logical variable x stands for its inverse, $\overline{x}$ is also sometimes noted $not(x)$.

E | Derivation of the functional detailed and physical detailed models of the full bridge submodule

E.1 | Functional detailed model of the full bridge submodule

The same reasoning as for the half-bridge submodule is extended to the case of the full-bridge submodule represented with the detail of the switches on the Figure 11.

This change of type of submodule induces the addition of an switching cell associated with its binary variables which are S'_{xyj} and $S^{b'}_{xyj}$. The global state of the SM-FB will then be determined from 5 binary variables which leads to a truth table with $2^5 = 32$ states in total. However, it is mentionned that with the development for the case of the half-bridge submodule, see the Table 2.1, that when the fault variable S^f_{xyj} is activated, all the electric quantities of the submodule are null. For the sake of clarity, these cases where S^f_{xyj} is zero will not be displayed in the truth table dedicated to the full-bridge submodule. The description of the binary variables is the same as for the case of the half-bridge submodule except that S'_{xyj} will also influence the connection of the capacitor to the arm of the MMC and that $S^{b'}_{xyj}$ will deal with the blocking of the second switching cell. The following truth table is then established.

$$(i^*_{xy} < 0) = \begin{cases} 1, \text{if } i^*_{xy} < 0 \\ 0, \text{if } i^*_{xy} \geq 0 \end{cases} \implies (i^*_{xy} < 0) = (sign(i^*_{xy}) - 1)\,\frac{sign(i^*_{xy})}{2} \tag{A.31}$$

The variables $(v_{C_{xyj}} > 0)$ and $(v_{C_{xyj}} < 0)$ are defined analogously.

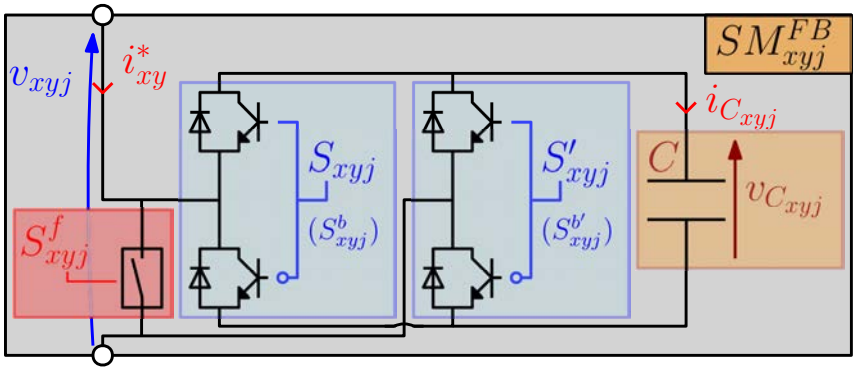

Figure 11: Electrical diagram of the SM-FB with the detail of the switches.

S^f_{xyj}	$S^{b'}_{xyj}$	S^b_{xyj}	S'_{xyj}	S_{xyj}		$i_{C_{xyj}}$	v_{xyj}
0	0	0	0	0		0	0
0	0	0	0	1		$i^*_{xy}\ \hat{p}_{xyj}(i^*_{xy}, v_{C_{xyj}})$	$v_{C_{xyj}}\ \hat{p}_{xyj}(i^*_{xy}, v_{C_{xyj}})$
0	0	0	1	0		$-i^*_{xy}\ \tilde{p}_{xyj}(i^*_{xy}, v_{C_{xyj}})$	$-v_{C_{xyj}}\ \tilde{p}_{xyj}(i^*_{xy}, v_{C_{xyj}})$
0	0	0	1	1		0	0
0	0	1	0	-		$i^*_{xy}\ (i^*_{xy} > 0)$	$v_{C_{xyj}}\ (i^*_{xy} > 0)$
0	0	1	0	-		$i^*_{xy}\ (i^*_{xy} > 0)$	$v_{C_{xyj}}\ (i^*_{xy} > 0)$
0	0	1	1	-		$-i^*_{xy}\ (i^*_{xy} < 0)$	$-v_{C_{xyj}}\ (i^*_{xy} < 0)$
0	0	1	1	-		$-i^*_{xy}\ (i^*_{xy} < 0)$	$-v_{C_{xyj}}\ (i^*_{xy} < 0)$
0	1	0	-	0		$-i^*_{xy}\ (i^*_{xy} < 0)$	$-v_{C_{xyj}}\ (i^*_{xy} < 0)$
0	1	0	-	0		$-i^*_{xy}\ (i^*_{xy} < 0)$	$-v_{C_{xyj}}\ (i^*_{xy} < 0)$
0	1	0	-	1		$i^*_{xy}\ (i^*_{xy} > 0)$	$v_{C_{xyj}}\ (i^*_{xy} > 0)$
0	1	0	-	1		$i^*_{xy}\ (i^*_{xy} > 0)$	$v_{C_{xyj}}\ (i^*_{xy} > 0)$
0	1	1	0	0		$i^*_{xy}\ sign(i^*_{xy})$	$v_{C_{xyj}}\ sign(i^*_{xy})$
0	1	1	0	1		$i^*_{xy}\ sign(i^*_{xy})$	$v_{C_{xyj}}\ sign(i^*_{xy})$
0	1	1	1	0		$i^*_{xy}\ sign(i^*_{xy})$	$v_{C_{xyj}}\ sign(i^*_{xy})$
0	1	1	1	1		$i^*_{xy}\ sign(i^*_{xy})$	$v_{C_{xyj}}\ sign(i^*_{xy})$
1	-	-	-	-		0	0

Table 17: Truth table - Behavior of the SM-FB

In the final objective of having a control model, some behaviors much faster than the sampling period of the control are neglected. As in the case of the half-bridge submodule, in certain configurations where the safety switch is closed, the capacitor will discharge itself, thus generating a strong increase in the current leaving the capacitor during a brief transient. This current spike will result in a sharp rise in the voltage across the submodule during this transient. Once the steady state is reached, the current in the capacitor and the voltage at its terminals will cancel each other out (in the case of the functional model, without taking into account the conduction resistances). The discharge of the capacitor occurs in the case where, when the switch driven by S^f_{xyj} is closed, at least one of the cells can impose its state to 1, the current of the capacitor can then flow through one of the upper transistors of the switching cells and discharge through the resistance of the safety switch. A notation is newly introduced in the truth table to simplify the analytical representations[1].

[1] In order to describe the availability state of the capacitor when the current $-i^*_{xy}$ is assumed to be the one flowing through the capacitor, the binary variable $\tilde{p}_{xyj}(i^*_{xy}, v_{C_{xyj}})$ is used. This variable has an analogous role to $\hat{p}_{xyj}(i^*_{xy}, v_{C_{xyj}})$ but for the opposite current: $-i^*_{xy}$; it representes the availability of the capacitor to be charged or discharged when it is 1. It is defined by $\tilde{p}_{xyj}(i^*_{xy}, v_{C_{xyj}}) \triangleq \left[(i^*_{xy} < 0) + (i^*_{xy} > 0)\ (v_{C_{xyj}} > 0)\right]$.

To establish the model with a gradual complexity, a first step without taking into account S^{b}_{xyj}, $S^{b'}_{xyj}$ and S^{f}_{xyj} is performed:

$$\begin{cases} i_{C_{xyj}} = C\frac{dv_{C_{xyj}}}{dt} = i^{*}_{xy} \cdot \left[S_{xyj}\hat{p}_{xyj}(i^{*}_{xy}, v_{C_{xyj}}) - S'_{xyj}\ \tilde{p}_{xyj}(i^{*}_{xy}, v_{C_{xyj}}) \right] \\ v_{xyj} = v_{C_{xyj}} \cdot \left[S_{xyj}\hat{p}_{xyj}(i^{*}_{xy}, v_{C_{xyj}}) - S'_{xyj}\ \tilde{p}_{xyj}(i^{*}_{xy}, v_{C_{xyj}}) \right] \end{cases} \tag{A.36}$$

It is worth to note that the voltage v_{xyj} is then bounded between $-v_{C_{xyj}}$ and $v_{C_{xyj}}$ for the half-bridge submodule case. The usual model of a DC-DC converter with a full-bridge differential structure is thus obtained, which is consistent with the topology of full-bridge submodule. By extending the model with the influence of S^{b}_{xyj}, $S^{b'}_{xyj}$ and S^{f}_{xyj}, it is possible to extract from the truth table the expression of the electrical signals:

$$\begin{cases} i_{C_{xyj}} = C\frac{dv_{C_{xyj}}}{dt} = i^{*}_{xy}\ S^{FB}_{xyj} \\ v_{xyj} = v_{C_{xyj}}\ S^{FB}_{xyj} \in \left[-v_{C_{xyj}}; v_{C_{xyj}} \right] \end{cases} \tag{A.37}$$

In order to simplify the expressions, the global state of the full-bridge submodule is given a dedicated notation as it is the case for the half-bridge submodule that one finds in the equation (2.4).

$$\begin{aligned} S^{FB}_{xyj} &= S^{FB}_{xyj}\left(S_{xyj}, S^{b}_{xyj}, S'_{xyj}, S^{b'}_{xyj}, S^{f}_{xyj} \right) \\ &\triangleq \Big[\left(S_{xyj}\ \hat{p}_{xyj}(i^{*}_{xy}, v_{C_{xyj}}) - S'_{xyj}\ \tilde{p}_{xyj}(i^{*}_{xy}, v_{C_{xyj}}) \right) \overline{S^{b}_{xyj}}\ \overline{S^{b'}_{xyj}} \\ &\quad + \left((i^{*}_{xy} > 0)\overline{S'_{xyj}} - (i^{*}_{xy} < 0)S'_{xyj} \right) S^{b}_{xyj}\overline{S^{b'}_{xyj}} \\ &\quad + \left((i^{*}_{xy} > 0)S_{xyj} - (i^{*}_{xy} < 0)\overline{S_{xyj}} \right) \overline{S^{b}_{xyj}} S^{b'}_{xyj} \\ &\quad + sign(i^{*}_{xy}) S^{b}_{xyj} S^{b'}_{xyj} \Big]\ \overline{S^{f}_{xyj}} \end{aligned} \tag{A.38}$$

By setting S^{b}_{xyj}, $S^{b'}_{xyj}$ and S^{f}_{xyj} to zero, the model described by (A.36) is obtained, which confirms the consistency of (A.37). The low-level functional detailed model of full-bridge submodule is now fully developed.

FUNCTIONAL DETAILED MODEL OF THE FULL-BRIDGE SUBMODULE

$$\begin{cases} i_{C_{xyj}} = C\ \frac{dv_{C_{xyj}}}{dt} = i^{*}_{xy}\ S^{FB}_{xyj} \\ v_{xyj} = v_{C_{xyj}}\ S^{FB}_{xyj} \in \left[-v_{C_{xyj}}; v_{C_{xyj}} \right] \end{cases} \tag{A.39}$$

with the global state of the full-bridge submodule S^{FB}_{xyj} defined by equation (A.38).

E.2 | Functional physical detailed model of the full bridge submodule

The study for the full-bridge submodule is based on that from the half-bridge submodule. The full-bridge submodule has a total of 8 conductions resistances associated with its semiconductors as shown on the Figure 12.

Having the necessity to consider an additional switching cell, the approach to follow is more complex than for the half-bridge submodule but the same process as used for the half-bridge submodule is derived. The Table 18 presenting the evolution of the resistance as a function of the state of the binary variables is then drawn up. For the sake of readability, this table uses the notation $\cdot//\cdot$[1].

[1] This notation represents the equivalent impedance for an electric circuit composed of two impedances in parallel.

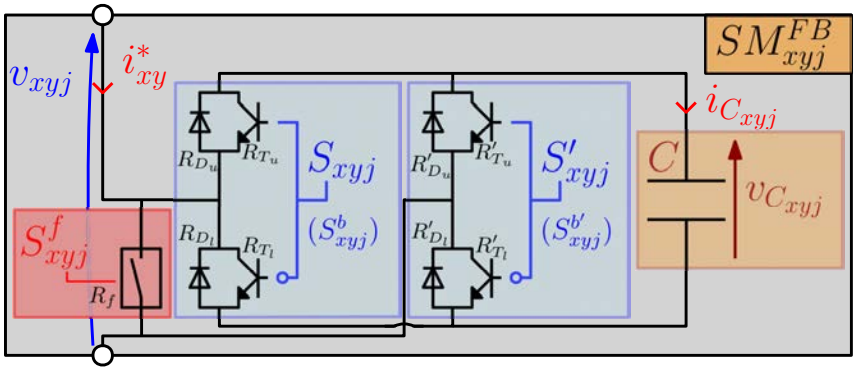

Figure 12: Electrical diagram of the SM-FB with the detail of the conduction resistances of each semiconductor.

A logical function analysis is then applied to the Table 18, leading to the expression of the conduction resistance of the submodule. The logical expression of R^{FB}_{xyj} is thus developed.

$$
\begin{aligned}
R^{FB}_{xyj} = \Big[\Big(\Big[& (R_{T_l} + R'_{D_l})(i^*_{xy} > 0) + (R_{D_l} + R'_{T_l})(i^*_{xy} < 0) \Big] \overline{S_{xyj}}\, \overline{S'_{xyj}} \\
& + \Big[(R_{D_u} + R'_{D_l})(i^*_{xy} > 0) + [R_{T_u}(v_{C_{xyj}} > 0) + R_{D_l}(v_{C_{xyj}} = 0) + R'_{T_l}](i^*_{xy} < 0) \Big] S_{xyj} \overline{S'_{xyj}} \\
& + \Big[[R_{T_l} + R'_{T_u}(v_{C_{xyj}} > 0) + R'_{D_l}(v_{C_{xyj}} = 0)](i^*_{xy} > 0) + (R_{D_l} + R'_{D_u})(i^*_{xy} < 0) \Big] \overline{S_{xyj}} S'_{xyj} \\
& + \Big[(R_{D_u} + R'_{T_u})(i^*_{xy} > 0) + (R_{T_u} + R'_{D_u})(i^*_{xy} < 0) \Big] S_{xyj} S'_{xyj} \Big)\, \overline{S^b_{xyj}}\, \overline{S^{b'}_{xyj}} \\
& + \Big(\Big[(R_{D_u} + R'_{D_l})(i^*_{xy} > 0) + (R_{D_l} + R'_{T_l})(i^*_{xy} < 0) \Big] \overline{S'_{xyj}} \\
& + \Big[(R_{D_u} + R'_{T_u})(i^*_{xy} > 0) + (R_{D_l} + R'_{D_u})(i^*_{xy} < 0) \Big] S'_{xyj} \Big)\, S^b_{xyj} \overline{S^{b'}_{xyj}} \\
& + \Big(\Big[(R_{T_l} + R'_{D_l})(i^*_{xy} > 0) + (R_{D_l} + R'_{D_u})(i^*_{xy} < 0) \Big] \overline{S_{xyj}} \\
& + \Big[(R_{D_u} + R'_{D_l})(i^*_{xy} > 0) + (R_{T_u} + R'_{D_u})(i^*_{xy} < 0) \Big] S_{xyj} \Big)\, \overline{S^b_{xyj}} S^{b'}_{xyj} \\
& + \Big((R_{D_u} + R'_{D_l})(i^*_{xy} > 0) + (R_{D_l} + R'_{D_u})(i^*_{xy} < 0) \Big)\, S^b_{xyj} S^{b'}_{xyj} \Big]\, \overline{S^f_{xyj}} \\
& + \Big[\Big(\Big[R_f // (R_{T_l} + R'_{D_l})(i^*_{xy} > 0) + R_f // (R'_{T_l} + R_{D_l})(i^*_{xy} < 0) \Big] \overline{S_{xyj}}\, \overline{S'_{xyj}} \\
& + \Big[R_f \Big] (S_{xyj} \overline{S'_{xyj}} + \overline{S_{xyj}} S'_{xyj}) \\
& + \Big[R_f // (R_{D_u} + R'_{T_u})(i^*_{xy} > 0) + R_f // (R'_{D_u} + R_{T_u})(i^*_{xy} < 0) \Big] S_{xyj} S'_{xyj} \Big)\, \overline{S^b_{xyj}}\, \overline{S^{b'}_{xyj}} \\
& + \Big(\Big[R_f (i^*_{xy} > 0) + R_f // (R'_{T_l} + R_{D_l})(i^*_{xy} < 0) \Big] \overline{S'_{xyj}} \\
& + \Big[R_f // (R_{D_u} + R'_{T_u})(i^*_{xy} > 0) + R_f (i^*_{xy} < 0) \Big] S'_{xyj} \Big)\, S^b_{xyj} \overline{S^{b'}_{xyj}} \\
& + \Big(\Big[R_f // (R_{T_l} + R'_{D_l})(i^*_{xy} > 0) + R_f (i^*_{xy} < 0) \Big] \overline{S_{xyj}} \\
& + \Big[R_f (i^*_{xy} > 0) + R_f // (R'_{D_u} + R_{T_u})(i^*_{xy} < 0) \Big] S_{xyj} \Big)\, \overline{S^b_{xyj}} S^{b'}_{xyj} \\
& + (R_f)\, S^b_{xyj} S^{b'}_{xyj} \Big]\, S^f_{xyj}
\end{aligned}
\tag{A.41}
$$

In a similar way to the half-bridge submodule, the voltage at the terminals of the submodule is increased by ohmic losses and the associated conduction losses are deduced. The expressions of these two electrical quantities being the same as for the case of the half-bridge submodule, it is possible to derive directly the final model taking into account the resistance of the full-bridge

In the case of two resistors R_a and R_b in parallel, it is defined as follows:

$$\forall \{R_a, R_b\} \in (\mathbb{R}^+ \times \mathbb{R}^{+*}) \cup (\mathbb{R}^{+*} \times \mathbb{R}^+), \quad R_a // R_b = \frac{R_a \times R_b}{R_a + R_b} \tag{A.40}$$

submodule.

FUNCTIONAL PHYSICAL DETAILED MODEL OF THE FULL-BRIDGE SUBMODULE

$$\begin{cases} i_{C_{xyj}} = C\ \frac{dv_{C_{xyj}}}{dt} = i^*_{xy}\ S^{FB}_{xyj} \\ v_{xyj} = v_{C_{xyj}}\ S^{FB}_{xyj} + R^{FB}_{xyj}\ i^*_{xy} \in \left[R^{HB}_{xyj} i^*_{xy} - v_{C_{xyj}}; R^{HB}_{xyj} i^*_{xy} + v_{C_{xyj}}\right] \\ P^{loss}_{xyj} = R^{FB}_{xyj}\ {i^*_{xy}}^2 \end{cases} \tag{A.42}$$

with the global state of the full-bridge submodule S^{FB}_{xyj} defined by equation (A.38) and the resistance of SM is R^{FB}_{xyj}, defined by (A.52).

S^f_{xyj}	$S^{b'}_{xyj}$	S^b_{xyj}	S'_{xyj}	S_{xyj}		R^{FB}_{xyj}
0	0	0	0	0		$(R_{T_l} + R'_{D_l})(i^*_{xy} > 0) + (R_{D_l} + R'_{T_l})(i^*_{xy} < 0)$
0	0	0	0	1		$(R_{D_u} + R'_{D_l})(i^*_{xy} > 0) + [R_{T_u}(v_{C_{xyj}} > 0) + R_{D_l}(v_{C_{xyj}} = 0) + R'_{T_l}](i^*_{xy} < 0)$
0	0	0	1	0		$[R_{T_l} + R'_{T_u}(v_{C_{xyj}} > 0) + R'_{D_l}(v_{C_{xyj}} = 0)](i^*_{xy} > 0) + (R_{D_l} + R'_{D_u})(i^*_{xy} < 0)$
0	0	0	1	1		$(R_{D_u} + R'_{T_u})(i^*_{xy} > 0) + (R_{T_u} + R'_{D_u})(i^*_{xy} < 0)$
0	0	1	0	-		$(R_{D_u} + R'_{D_l})(i^*_{xy} > 0) + (R_{D_l} + R'_{T_l})(i^*_{xy} < 0)$
0	0	1	0	-		$(R_{D_u} + R'_{D_l})(i^*_{xy} > 0) + (R_{D_l} + R'_{T_l})(i^*_{xy} < 0)$
0	0	1	1	-		$(R_{D_u} + R'_{T_u})(i^*_{xy} > 0) + (R_{D_l} + R'_{D_u})(i^*_{xy} < 0)$
0	0	1	1	-		$(R_{D_u} + R'_{T_u})(i^*_{xy} > 0) + (R_{D_l} + R'_{D_u})(i^*_{xy} < 0)$
0	1	0	-	0		$(R_{T_l} + R'_{D_l})(i^*_{xy} > 0) + (R_{D_l} + R'_{D_u})(i^*_{xy} < 0)$
0	1	0	-	0		$(R_{T_l} + R'_{D_l})(i^*_{xy} > 0) + (R_{D_l} + R'_{D_u})(i^*_{xy} < 0)$
0	1	0	-	1		$(R_{D_u} + R'_{D_l})(i^*_{xy} > 0) + (R_{T_u} + R'_{D_u})(i^*_{xy} < 0)$
0	1	0	-	1		$(R_{D_u} + R'_{D_l})(i^*_{xy} > 0) + (R_{T_u} + R'_{D_u})(i^*_{xy} < 0)$
0	1	1	0	0		$(R_{D_u} + R'_{D_l})(i^*_{xy} > 0) + (R_{D_l} + R'_{D_u})(i^*_{xy} < 0)$
0	1	1	0	1		$(R_{D_u} + R'_{D_l})(i^*_{xy} > 0) + (R_{D_l} + R'_{D_u})(i^*_{xy} < 0)$
0	1	1	1	0		$(R_{D_u} + R'_{D_l})(i^*_{xy} > 0) + (R_{D_l} + R'_{D_u})(i^*_{xy} < 0)$
0	1	1	1	1		$(R_{D_u} + R'_{D_l})(i^*_{xy} > 0) + (R_{D_l} + R'_{D_u})(i^*_{xy} < 0)$
1	0	0	0	0		$R_f // (R_{T_l} + R'_{D_l})(i^*_{xy} > 0) + R_f // (R'_{T_l} + R_{D_l})(i^*_{xy} < 0)$
1	0	0	0	1		R_f
1	0	0	1	0		R_f
1	0	0	1	1		$R_f // (R_{D_u} + R'_{T_u})(i^*_{xy} > 0) + R_f // (R'_{D_u} + R_{T_u})(i^*_{xy} < 0)$
1	0	1	0	-		$R_f(i^*_{xy} > 0) + R_f // (R'_{T_l} + R_{D_l})(i^*_{xy} < 0)$
1	0	1	0	-		$R_f(i^*_{xy} > 0) + R_f // (R'_{T_l} + R_{D_l})(i^*_{xy} < 0)$
1	0	1	1	-		$R_f // (R_{D_u} + R'_{T_u})(i^*_{xy} > 0) + R_f(i^*_{xy} < 0)$
1	0	1	1	-		$R_f // (R_{D_u} + R'_{T_u})(i^*_{xy} > 0) + R_f(i^*_{xy} < 0)$
1	1	0	-	0		$R_f // (R_{T_l} + R'_{D_l})(i^*_{xy} > 0) + R_f(i^*_{xy} < 0)$
1	1	0	-	0		$R_f // (R_{T_l} + R'_{D_l})(i^*_{xy} > 0) + R_f(i^*_{xy} < 0)$
1	1	0	-	1		$R_f(i^*_{xy} > 0) + R_f // (R'_{D_u} + R_{T_u})(i^*_{xy} < 0)$
1	1	0	-	1		$R_f(i^*_{xy} > 0) + R_f // (R'_{D_u} + R_{T_u})(i^*_{xy} < 0)$
1	1	1	0	0		R_f
1	1	1	0	1		R_f
1	1	1	1	0		R_f
1	1	1	1	1		R_f

Table 18: Truth table - Resistance of the SM-FB

F | Generalized matrix model for the low-level

F.1 | Generalized matrix model for the global state of the submodule

As indicated by (A.38), the state of the SM depends on five binary variables, only two of which can be controlled by the low-level control of the SM: S_{xyj} and S'_{xyj}. The other control variables S^b_{xyj}, $S^{b'}_{xyj}$ and S^f_{xyj} will be managed by an external supervision algorithm, higher in the control hierarchy, dealing with singular operating cases such as startup procedures and faults. The goal here is to implement a model that brings out the control variables as the allocation methods require. From the functional detailed model (A.38), the variables S_{xyj} and S'_{xyj} are isolated into a single vector.

$$\begin{aligned} S^{FB}_{xyj} \triangleq \Big[\Big(S_{xyj}\, \hat{p}_{xyj}(i^*_{xy}, v_{C_{xyj}}) - S'_{xyj}\, \tilde{p}_{xyj}(i^*_{xy}, v_{C_{xyj}}) \Big) \overline{S^b_{xyj}}\, \overline{S^{b'}_{xyj}} \\ + \Big((i^*_{xy} > 0) \overline{S'_{xyj}} - (i^*_{xy} < 0) S'_{xyj} \Big) S^b_{xyj} \overline{S^{b'}_{xyj}} \\ + \Big((i^*_{xy} > 0) S_{xyj} - (i^*_{xy} < 0) \overline{S_{xyj}} \Big) \overline{S^b_{xyj}} S^{b'}_{xyj} \\ + sign(i^*_{xy}) S^b_{xyj} S^{b'}_{xyj} \Big] \overline{S^f_{xyj}} \end{aligned} \tag{A.43}$$

To simplify the reading of future equation developments, the notations x, y and j are removed. It comes then without loss of generality:

$$\begin{aligned} S^{FB} = \Big[(S\hat{p} - S'\tilde{p}) \overline{S^b}\, \overline{S^{b'}} \\ + \Big((i > 0) \overline{S'} - (i < 0) S' \Big) S^b \overline{S^{b'}} \\ + \Big((i > 0) S - (i < 0) \overline{S} \Big) \overline{S^b} S^{b'} \\ + sign(i) S^b S^{b'} \Big] \overline{S^f} \end{aligned} \tag{A.44}$$

Isolating the control variables of the switching cells, S and S', on the left, it is obtained that:

$$\begin{aligned} S^{FB} = S \Big[\hat{p} \overline{S^b}\, \overline{S^{b'}} + (i > 0) \overline{S^b} S^{b'} \Big] \overline{S^f} + \overline{S} \Big[-(i < 0) \overline{S^b} S^{b'} \Big] \overline{S^f} \\ + S' \Big[-\tilde{p} \overline{S^b}\, \overline{S^{b'}} - (i < 0) S^b \overline{S^{b'}} \Big] \overline{S^f} + \overline{S'} \Big[(i > 0) S^b \overline{S^{b'}} \Big] \overline{S^f} \\ + sign(i) S^b S^{b'} \overline{S^f} \end{aligned} \tag{A.45}$$

In binary logic, the complement of a variable can be expressed as $\overline{S} = 1 - S$ and $\overline{S'} = 1 - S'$. Thus S^{FB} can be expressed as a function of fewer binary variables and thus lighten the expression.

$$\begin{aligned} S^{FB} = S \Big[& \hat{p}\overline{S^b}\,\overline{S^{b'}} + [(i>0) + (i<0)]\overline{S^b}S^{b'} \Big] \overline{S^f} \\ & + S' \Big[-\tilde{p}\overline{S^b}\,\overline{S^{b'}} - [(i<0) + (i>0)]S^b\overline{S^{b'}} \Big] \overline{S^f} \\ & + \Big[-(i<0)\overline{S^b}S^{b'} + (i>0)S^b\overline{S^{b'}} + sign(i)S^bS^{b'} \Big] \overline{S^f} \end{aligned} \tag{A.46}$$

From the definitions of $(i > 0)$ and $(i < 0)$, respectively by (2.1) and (2.2), it is achieved that:

$$(i>0) + (i<0) = \left(\frac{sign(i)+1}{2} + \frac{sign(i)-1}{2} \right) sign(i) = |sign(i)| \tag{A.47}$$

This simplifies the expression of S^{FB} as follows:

$$\begin{aligned} S^{FB} = S \Big[& \hat{p}\overline{S^b}\,\overline{S^{b'}} + |sign(i)|\,\overline{S^b}S^{b'} \Big] \overline{S^f} \\ & + S' \Big[-\tilde{p}\overline{S^b}\,\overline{S^{b'}} - |sign(i)|\,S^b\overline{S^{b'}} \Big] \overline{S^f} \\ & + \Big[-(i<0)\overline{S^b}S^{b'} + (i>0)S^b\overline{S^{b'}} + sign(i)S^bS^{b'} \Big] \overline{S^f} \end{aligned} \tag{A.48}$$

The goal being to derive S^{FB} as a function of the cell states only, the other elements are considered as parameters that are determined externally, so it is decided to encapsulate these sets of parameters in dedicated variables. The variables l, l' and t are then introduced.

$$\begin{aligned} l &= \Big[\hat{p}\overline{S^b}\,\overline{S^{b'}} + |sign(i)|\,\overline{S^b}S^{b'} \Big] \overline{S^f} \\ l' &= \Big[-\tilde{p}\overline{S^b}\,\overline{S^{b'}} - |sign(i)|\,S^b\overline{S^{b'}} \Big] \overline{S^f} \\ \tau &= \Big[-(i<0)\overline{S^b}S^{b'} + (i>0)S^b\overline{S^{b'}} + sign(i)S^bS^{b'} \Big] \overline{S^f} \end{aligned} \tag{A.49}$$

By substitution of parameter sets for the newly introduced dedicated variables, it is shown that

$$S^{FB} = \begin{bmatrix} l & l' \end{bmatrix} \begin{bmatrix} S \\ S' \end{bmatrix} + [\tau] \tag{A.50}$$

Either, by rehabilitating the initial notation:

$$S_{xyj}^{FB} = \begin{bmatrix} l_{xyj} & l'_{xyj} \end{bmatrix} \begin{bmatrix} S_{xyj} \\ S'_{xyj} \end{bmatrix} + \begin{bmatrix} \tau_{xyj} \end{bmatrix} \tag{A.51}$$

The equation (A.51) is thus a matrix model that directly links the control variables from the submodule to its state. However, the submodule resistance also depends on the different binary variables associated with the switches, thus it is also necessary to go through the transformation into a matrix model for the equation defining R_{xyj}^{FB}.

F.2 | Generalized matrix model for the resistance of the submodules

The same approach carried out for the state of submodule will be applied to the resistance R_{xyj}^{FB} with the aim of formulating R_{xyj}^{FB} matrixically as a function of S_{xyj} and S'_{xyj}. This development is based on the derivation previously found for R_{xyj}^{FB} from the equation (A.42). In order to ease the visualization of its expression, colors are added on the sets of resistive parameters that do not depend on the switching states.

$$
\begin{aligned}
R^{FB}_{xyj} = \Big[\Big(\Big[&(R_{T_l} + R'_{D_l})(i^*_{xy} > 0) + (R_{D_l} + R'_{T_l})(i^*_{xy} < 0)\Big]\overline{S_{xyj}}\,\overline{S'_{xyj}} \\
&+ \Big[(R_{D_u} + R'_{D_l})(i^*_{xy} > 0) + [R_{T_u}(v_{C_{xyj}} > 0) + R_{D_l}(v_{C_{xyj}} = 0) + R'_{T_l}](i^*_{xy} < 0)\Big]S_{xyj}\overline{S'_{xyj}} \\
&+ \Big[[R_{T_l} + R'_{T_u}(v_{C_{xyj}} > 0) + R'_{D_l}(v_{C_{xyj}} = 0)](i^*_{xy} > 0) + (R_{D_l} + R'_{D_u})(i^*_{xy} < 0)\Big]\overline{S_{xyj}}S'_{xyj} \\
&+ \Big[(R_{D_u} + R'_{T_u})(i^*_{xy} > 0) + (R_{T_u} + R'_{D_u})(i^*_{xy} < 0)\Big]S_{xyj}S'_{xyj}\Big)\,\overline{S^b_{xyj}}\,\overline{S^{b'}_{xyj}} \\
&+ \Big(\Big[(R_{D_u} + R'_{D_l})(i^*_{xy} > 0) + (R_{D_l} + R'_{T_l})(i^*_{xy} < 0)\Big]\overline{S'_{xyj}} \\
&+ \Big[(R_{D_u} + R'_{T_u})(i^*_{xy} > 0) + (R_{D_l} + R'_{D_u})(i^*_{xy} < 0)\Big]S'_{xyj}\Big)\,S^b_{xyj}\overline{S^{b'}_{xyj}} \\
&+ \Big(\Big[(R_{T_l} + R'_{D_l})(i^*_{xy} > 0) + (R_{D_l} + R'_{D_u})(i^*_{xy} < 0)\Big]\overline{S_{xyj}} \\
&+ \Big[(R_{D_u} + R'_{D_l})(i^*_{xy} > 0) + (R_{T_u} + R'_{D_u})(i^*_{xy} < 0)\Big]S_{xyj}\Big)\,\overline{S^b_{xyj}}S^{b'}_{xyj} \\
&+ \Big(\Big[(R_{D_u} + R'_{D_l})(i^*_{xy} > 0) + (R_{D_l} + R'_{D_u})(i^*_{xy} < 0)\Big]S^b_{xyj}S^{b'}_{xyj}\Big]\,\overline{S^f_{xyj}} \\
&+ \Big[\Big(\Big[R_f//(R_{T_l} + R'_{D_l})(i^*_{xy} > 0) + R_f//(R'_{T_l} + R_{D_l})(i^*_{xy} < 0)\Big]\overline{S_{xyj}}\,\overline{S'_{xyj}} \\
&+ \Big[R_f\Big](S_{xyj}\overline{S'_{xyj}} + \overline{S_{xyj}}S'_{xyj}) \\
&+ \Big[R_f//(R_{D_u} + R'_{T_u})(i^*_{xy} > 0) + R_f//(R'_{D_u} + R_{T_u})(i^*_{xy} < 0)\Big]S_{xyj}S'_{xyj}\Big)\,\overline{S^b_{xyj}}\,\overline{S^{b'}_{xyj}} \\
&+ \Big(\Big[R_f(i^*_{xy} > 0) + R_f//(R'_{T_l} + R_{D_l})(i^*_{xy} < 0)\Big]\overline{S'_{xyj}} \\
&+ \Big[R_f//(R_{D_u} + R'_{T_u})(i^*_{xy} > 0) + R_f(i^*_{xy} < 0)\Big]S'_{xyj}\Big)\,S^b_{xyj}\overline{S^{b'}_{xyj}} \\
&+ \Big(\Big[R_f//(R_{T_l} + R'_{D_l})(i^*_{xy} > 0) + R_f(i^*_{xy} < 0)\Big]\overline{S_{xyj}} \\
&+ \Big[R_f(i^*_{xy} > 0) + R_f//(R'_{D_u} + R_{T_u})(i^*_{xy} < 0)\Big]S_{xyj}\Big)\,\overline{S^b_{xyj}}S^{b'}_{xyj} \\
&+ (R_f)\,S^b_{xyj}S^{b'}_{xyj}\Big]\,S^f_{xyj}
\end{aligned}
\tag{A.52}
$$

So as to simplify the mathematical manipulations, the resistive sets are encapsulated in dedicated variables and the notations x, y and j are removed without loss of generality:

$$\begin{aligned}
R^{FB} = &\Big[\left(R_a \overline{S}\,\overline{S'} + R_b S\overline{S'} + R_c \overline{S} S' + R_d S S'\right)\overline{S^b}\,\overline{S^{b'}} \\
&+\left(R'_\alpha \overline{S'} + R'_\beta S'\right) S^b \overline{S^{b'}} \\
&+\left(R_\alpha \overline{S} + R_\beta S\right)\overline{S^b} S^{b'} \\
&+R_\gamma S^b S^{b'}\Big]\,\overline{S^f} \\
&+\Big[\left(R^f_a \overline{S}\,\overline{S'} + R^f_b (S\overline{S'} + \overline{S} S') + R^f_c S S'\right)\overline{S^b}\,\overline{S^{b'}} \\
&+\left(R'^{\,f}_\alpha \overline{S'} + R'^{\,f}_\beta S'\right) S^b \overline{S^{b'}} \\
&+\left(R^f_\alpha \overline{S} + R^f_\beta S\right)\overline{S^b} S^{b'} \\
&+R^f_\gamma S^b S^{b'}\Big]\, S^f
\end{aligned} \tag{A.53}$$

Using the fact that $\overline{S} = 1 - S$ and $\overline{S'} = 1 - S'$, it is possible to factor some expressions as follows:

$$\begin{aligned}
R^{FB} = &\, S\left[(R_b - R_a)\,\overline{S^b}\,\overline{S^{b'}} + (R_\beta - R_\alpha)\,\overline{S^b}\,S^{b'}\right]\overline{S^f} \\
&+S'\left[(R_c - R_a)\,\overline{S^b}\,\overline{S^{b'}} + \left(R'_\beta - R'_\alpha\right) S^b\,\overline{S^{b'}}\right]\overline{S^f} \\
&+S'S\left[(R_a - R_b - R_c + R_d)\,\overline{S^b}\,\overline{S^{b'}}\right]\overline{S^f} \\
&+\left[R_a \overline{S^b}\,\overline{S^{b'}} + R'_\alpha S^b\,\overline{S^{b'}} + R_\alpha \overline{S^b}\,S^{b'} + R_\gamma S^b\,S^{b'}\right]\overline{S^f} \\
&+S\left[\left(R^f_b - R^f_a\right)\overline{S^b}\,\overline{S^{b'}} + \left(R^f_\beta - R^f_\alpha\right)\overline{S^b}\,S^{b'}\right] S^f \\
&+S'\left[\left(R^f_c - R^f_a\right)\overline{S^b}\,\overline{S^{b'}} + \left(R'^{\,f}_\beta - R'^{\,f}_\alpha\right) S^b\,\overline{S^{b'}}\right] S^f \\
&+S'S\left[\left(R^f_a - 2R^f_b + R^f_c\right)\overline{S^b}\,\overline{S^{b'}}\right] S^f \\
&+\left[R^f_a \overline{S^b}\,\overline{S^{b'}} + R'^{\,f}_\alpha S^b\,\overline{S^{b'}} + R^f_\alpha \overline{S^b}\,S^{b'} + R^f_\gamma S^b\,S^{b'}\right] S^f
\end{aligned} \tag{A.54}$$

It is then observed that a nonlinear term depending on SS' is in the expression of the resistive model. It is then possible to group these nonlinear terms together:

$$\begin{aligned}
R^{FB} = & S\left[(R_b - R_a)\,\overline{S^b}\,\overline{S^{b'}} + (R_\beta - R_\alpha)\,\overline{S^b}\,S^{b'}\right]\overline{S^f} \\
& + S'\left[(R_c - R_a)\,\overline{S^b}\,\overline{S^{b'}} + \left(R'_\beta - R'_\alpha\right)S^b\,\overline{S^{b'}}\right]\overline{S^f} \\
& + \left[R_a\overline{S^b}\,\overline{S^{b'}} + R'_\alpha S^b\,\overline{S^{b'}} + R_\alpha\overline{S^b}\,S^{b'} + R_\gamma S^b\,S^{b'}\right]\overline{S^f} \\
& + S\left[\left(R_b^f - R_a^f\right)\overline{S^b}\,\overline{S^{b'}} + \left(R_\beta^f - R_\alpha^f\right)\overline{S^b}\,S^{b'}\right]S^f \\
& + S'\left[\left(R_c^f - R_a^f\right)\overline{S^b}\,\overline{S^{b'}} + \left({R'}_\beta^f - {R'}_\alpha^f\right)S^b\,\overline{S^{b'}}\right]S^f \\
& + \left[R_a^f\overline{S^b}\,\overline{S^{b'}} + {R'}_\alpha^f S^b\,\overline{S^{b'}} + R_\alpha^f\overline{S^b}\,S^{b'} + R_\gamma^f S^b\,S^{b'}\right]S^f \\
& + SS'\overline{S^b}\,\overline{S^{b'}}\left[\left(R_a^f - 2R_b^f + R_c^f - R_a + R_b + R_c - R_d\right)S^f + (R_a - R_b - R_c + R_d)\right]
\end{aligned} \tag{A.55}$$

The objective being to formulate the resistance as a product of the variables S and S', the expression of R^{FB} is therefore factorized as follows:

$$\begin{aligned}
R^{FB} = & S\left(\left[(R_b - R_a)\,\overline{S^b}\,\overline{S^{b'}} + (R_\beta - R_\alpha)\,\overline{S^b}\,S^{b'}\right]\overline{S^f} + \left[\left(R_b^f - R_a^f\right)\overline{S^b}\,\overline{S^{b'}} + \left(R_\beta^f - R_\alpha^f\right)\overline{S^b}\,S^{b'}\right]S^f\right) \\
& + S'\left(\left[(R_c - R_a)\,\overline{S^b}\,\overline{S^{b'}} + \left(R'_\beta - R'_\alpha\right)S^b\,\overline{S^{b'}}\right]\overline{S^f} + \left[\left(R_c^f - R_a^f\right)\overline{S^b}\,\overline{S^{b'}} + \left({R'}_\beta^f - {R'}_\alpha^f\right)S^b\,\overline{S^{b'}}\right]S^f\right) \\
& + \left[R_a\overline{S^b}\,\overline{S^{b'}} + R'_\alpha S^b\,\overline{S^{b'}} + R_\alpha\overline{S^b}\,S^{b'} + R_\gamma S^b\,S^{b'}\right]\overline{S^f} + \left[R_a^f\overline{S^b}\,\overline{S^{b'}} + {R'}_\alpha^f S^b\,\overline{S^{b'}} + R_\alpha^f\overline{S^b}\,S^{b'} + R_\gamma^f S^b\,S^{b'}\right]S^f \\
& + SS'\overline{S^b}\,\overline{S^{b'}}\left[\left(R_a^f - 2R_b^f + R_c^f - R_a + R_b + R_c - R_d\right)S^f + (R_a - R_b - R_c + R_d)\right]
\end{aligned} \tag{A.56}$$

In order to reduce the size of the equation to the essential, i.e. to an expression in function of the switching states which will be the variables on which the control law will be able to act in real time, the following parameters are introduced:

$$\begin{aligned}
w &= \left(\left[(R_b - R_a)\,\overline{S^b}\,\overline{S^{b'}} + (R_\beta - R_\alpha)\,\overline{S^b}\,S^{b'}\right]\overline{S^f} + \left[\left(R_b^f - R_a^f\right)\overline{S^b}\,\overline{S^{b'}} + \left(R_\beta^f - R_\alpha^f\right)\overline{S^b}\,S^{b'}\right]S^f\right) \\
w' &= \left(\left[(R_c - R_a)\,\overline{S^b}\,\overline{S^{b'}} + \left(R'_\beta - R'_\alpha\right)S^b\,\overline{S^{b'}}\right]\overline{S^f} + \left[\left(R_c^f - R_a^f\right)\overline{S^b}\,\overline{S^{b'}} + \left({R'}_\beta^f - {R'}_\alpha^f\right)S^b\,\overline{S^{b'}}\right]S^f\right) \\
z &= \left[R_a\overline{S^b}\,\overline{S^{b'}} + R'_\alpha S^b\,\overline{S^{b'}} + R_\alpha\overline{S^b}\,S^{b'} + R_\gamma S^b\,S^{b'}\right]\overline{S^f} + \left[R_a^f\overline{S^b}\,\overline{S^{b'}} + {R'}_\alpha^f S^b\,\overline{S^{b'}} + R_\alpha^f\overline{S^b}\,S^{b'} + R_\gamma^f S^b\,S^{b'}\right]S^f \\
\theta &= \overline{S^b}\,\overline{S^{b'}}\left[\left(R_a^f - 2R_b^f + R_c^f - R_a + R_b + R_c - R_d\right)S^f + (R_a - R_b - R_c + R_d)\right]
\end{aligned} \tag{A.57}$$

The definition of these parameters allows one to summarize the affine expression of the resistance of a half-bridge submodule in the following way:

$$R^{FB} = \begin{bmatrix} w & w' \end{bmatrix}\begin{bmatrix} S \\ S' \end{bmatrix} + [\theta]\,SS' + [z] \tag{A.58}$$

And so, with the general notation:

$$R_{xyj}^{FB} = \begin{bmatrix} w_{xyj} & w'_{xyj} \end{bmatrix} \begin{bmatrix} S_{xyj} \\ S'_{xyj} \end{bmatrix} + \begin{bmatrix} \theta_{xyj} \end{bmatrix} S_{xyj} S'_{xyj} + \begin{bmatrix} z_{xyj} \end{bmatrix} \tag{A.59}$$

It is thus obtained a full-bridge submodule resistance model which adopts a non-linear form unlike the case of the global full-bridge submodule state according to the equation (A.51).

F.2.1 | Generalized matrix model of the arms

The two previous paragraphs allowed to establish the matrix model at the scale of the submodule, it is now necessary to move on to the complete arm. The objective is therefore to establish a model linking the control variables of each submodule to the evolution of the electrical signals of the entire arm composed of all these submodules. The developments carried out here, are based on the results represented by the equations (2.18) and (2.19) and (2.17). The latter is recalled below and focuses on describing the behavior of a single submodule:

$$\begin{cases} i_{C_{xyj}} = C\,\frac{dv_{C_{xyj}}}{dt} = i^*_{xy}\,S^{FB}_{xyj} \\ v_{xyj} = v_{C_{xyj}}\,S^{FB}_{xyj} + R^{FB}_{xyj}\,i^*_{xy} \in \left[R^{HB}_{xyj} i^*_{xy} - v_{C_{xyj}}; R^{HB}_{xyj} i^*_{xy} + v_{C_{xyj}}\right] \\ v_{xy} = \sigma(x)\,\sum_{j=1}^{N} v_{xyj} \in \left[\sum_{j=1}^{N} R^{HB}_{xyj} i^*_{xy} + (1-q) v_{C_{xyj}}; \sum_{j=1}^{N} R^{HB}_{xyj} i^*_{xy} + v_{C_{xyj}}\right] \\ P^{loss}_{xyj} = R^{FB}_{xyj}\,{i^*_{xy}}^2 \end{cases} \tag{A.60}$$

Combining equations #2 and #3 of the system (A.60) it is possible to substitute S^{FB}_{xyj} by its expression in that of v_{xy}:

$$v_{xy} = \sigma(x)\sum_{j=1}^{N} v_{xyj} = \sigma(x)\sum_{j=1}^{N}\left(v_{C_{xyj}} S^{FB}_{xyj} + R^{FB}_{xyj} i^*_{xy}\right) \tag{A.61}$$

The equations (A.51) and (A.59) can then be beneficially used to substitute S^{FB}_{xyj} and R^{FB}_{xyj} by their expression in (A.61):

$$\begin{aligned} v_{xy} = \sigma(x)\Bigg[&\textstyle\sum_{j=1}^{N} v_{C_{xyj}}\left(\begin{bmatrix} l_{xyj} & l'_{xyj}\end{bmatrix}\begin{bmatrix} S_{xyj} \\ S'_{xyj}\end{bmatrix} + \begin{bmatrix}\tau_{xyj}\end{bmatrix}\right) \\ &+ i^*_{xy}\textstyle\sum_{j=1}^{N}\left(\begin{bmatrix} w_{xyj} & w'_{xyj}\end{bmatrix}\begin{bmatrix} S_{xyj} \\ S'_{xyj}\end{bmatrix} + \begin{bmatrix}\theta_{xyj}\end{bmatrix} S_{xyj} S'_{xyj} + \begin{bmatrix} z_{xyj}\end{bmatrix}\right)\Bigg] \end{aligned} \tag{A.62}$$

To comply with the objective of having a matrix model for the enitre arm, it is necessary to introduce vectors containing the states of the switches of the set of submodule of a same leg. The following notations are then introduced:

$$\mathbf{S^e_{xy}} \triangleq [S_{x,y,1}, S'_{x,y,1}, S_{x,y,2}, S'_{x,y,2}, \ldots, S_{x,y,N}, S'_{x,y,N}]^T \in \mathbb{R}^{2N} \tag{A.63}$$

$$\mathbf{S^{es}_{xy}} \triangleq [S_{x,y,1}, \ldots, S_{x,y,N}, S'_{x,y,1}, \ldots, S'_{x,y,N}]^T \in \mathbb{R}^{2N} \tag{A.64}$$

$$\mathbf{S_{xy}} \triangleq [S_{x,y,1}, S_{x,y,2}, \ldots, S_{x,y,N}]^T \in \mathbb{R}^{N} \tag{A.65}$$

The introduction of these vectors is associated with new matrices and vectors needed for the model:

$$\mathbf{v_{C_{xy}}} \triangleq [v_{C_{x,y,1}}, v_{C_{x,y,2}}, \ldots, v_{C_{x,y,N}}]^T \in \mathbb{R}^{N} \tag{A.66}$$

$$L_{xy} \triangleq \begin{bmatrix} l_{x,y,1} & l'_{x,y,1} & & & & & \\ & & l_{x,y,2} & l'_{x,y,2} & & & \\ & & & & \ddots & \ddots & \\ & & & & & l_{x,y,N} & l'_{x,y,N} \end{bmatrix} \in \mathcal{M}_{N,2N}(\mathbb{N}) \tag{A.67}$$

$$\mathbf{T_{xy}} \triangleq [\tau_{x,y,1}, \tau_{x,y,2}, \ldots, \tau_{x,y,N}]^T \in \mathbb{R}^{N} \tag{A.68}$$

$$W_{xy} \triangleq \mathbb{J}_{1,N} \begin{bmatrix} w_{x,y,1} & w'_{x,y,1} & & & & & \\ & & w_{x,y,2} & w'_{x,y,2} & & & \\ & & & & \ddots & \ddots & \\ & & & & & w_{x,y,N} & w'_{x,y,N} \end{bmatrix} \in \mathcal{M}_{1,2N}(\mathbb{R}) \tag{A.69}$$

$$\Theta_{xy} \triangleq \begin{bmatrix} \begin{bmatrix} 0 & \theta_{x,y,1} \\ 0 & 0 \end{bmatrix} & & & \\ & \begin{bmatrix} 0 & \theta_{x,y,2} \\ 0 & 0 \end{bmatrix} & & \\ & & \ddots & \\ & & & \begin{bmatrix} 0 & \theta_{x,y,N} \\ 0 & 0 \end{bmatrix} \end{bmatrix} \in \mathcal{M}_{2N}(\mathbb{R}) \tag{A.70}$$

$$\mathbf{Z_{xy}} \triangleq \mathbb{J}_{1,N} \left[z_{x,y,1}, z_{x,y,2}, \ldots, z_{x,y,N} \right]^T \in \mathbb{R} \tag{A.71}$$

With $\mathbb{J}_{a,b}$ the matrix of size $(a \times b)$ filled with 1s. By usual matrix operations, the following relations are found:

$$\left(L_{xy} \mathbf{S^e_{xy}} + \mathbf{T_{xy}} \right) = \begin{bmatrix} S^{FB}_{x,y,1} \\ S^{FB}_{x,y,2} \\ \vdots \\ S^{FB}_{x,y,N} \end{bmatrix} \tag{A.72}$$

$$\mathbf{v_{C_{xy}}}^T \left(L_{xy} \mathbf{S^e_{xy}} + \mathbf{T_{xy}} \right) = \sum_{j=1}^{N} v_{C_{xyj}} \left(\begin{bmatrix} l_{xyj} & l'_{xyj} \end{bmatrix} \begin{bmatrix} S_{xyj} \\ S'_{xyj} \end{bmatrix} + \begin{bmatrix} \tau_{xyj} \end{bmatrix} \right) \tag{A.73}$$

$$\begin{aligned} &\left(W_{xy} \mathbf{S^e_{xy}} + \mathbf{S^e_{xy}}^T \Theta_{xy} \mathbf{S^e_{xy}} + \mathbf{Z_{xy}} \right) \\ &\quad = \sum_{j=1}^{N} \left(\begin{bmatrix} w_{xyj} & w'_{xyj} \end{bmatrix} \begin{bmatrix} S_{xyj} \\ S'_{xyj} \end{bmatrix} + \begin{bmatrix} \theta_{xyj} \end{bmatrix} S_{xyj} S'_{xyj} + \begin{bmatrix} z_{xyj} \end{bmatrix} \right) = \sum_{j=1}^{N} R^{FB}_{xyj} \end{aligned} \tag{A.74}$$

These developments lead to the synthetic expression:

$$v_{xy} = \sigma(x) \left[\mathbf{v_{C_{xy}}}^T \left(L_{xy} \mathbf{S^e_{xy}} + \mathbf{T_{xy}} \right) + i^*_{xy} \left(W_{xy} \mathbf{S^e_{xy}} + \mathbf{S^e_{xy}}^T \Theta_{xy} \mathbf{S^e_{xy}} + \mathbf{Z_{xy}} \right) \right] \tag{A.75}$$

By isolating the control variable which is $\mathbf{S^e_{xy}}$ here, the voltage v_{xy} is expressed:

$$v_{xy} = \sigma(x) \left[\left(\mathbf{v_{C_{xy}}}^T L_{xy} + i^*_{xy} W_{xy} \right) \mathbf{S^e_{xy}} + i^*_{xy} \mathbf{S^e_{xy}}^T \Theta_{xy} \mathbf{S^e_{xy}} + \left(\mathbf{v_{C_{xy}}}^T \mathbf{T_{xy}} + i^*_{xy} \mathbf{Z_{xy}} \right) \right] \tag{A.76}$$

This equation makes it possible to perceive how it is possible to act on the control variables of each submodule to influence the global voltage of the arm in order to reach a given voltage reference.

The vector containing all the currents flowing through each of the capacitors of a single arm can be defined by:

$$\mathbf{i_{C_{xy}}} = \left[i_{C_{x,y,1}}, i_{C_{x,y,2}}, \ldots, i_{C_{x,y,N}} \right]^T \in \mathbb{R}^N \tag{A.77}$$

Since the equation #1 of (A.60) is true for all $j \in [\![1; N]\!]$, it follows that:

$$\mathbf{i_{C_{xy}}} = C \frac{d\mathbf{v_{C_{xy}}}}{dt} = i^*_{xy} \begin{bmatrix} S^{FB}_{x,y,1} \\ S^{FB}_{x,y,2} \\ \vdots \\ S^{FB}_{x,y,N} \end{bmatrix} = i^*_{xy} \left(L_{xy} \mathbf{S^e_{xy}} + \mathbf{T_{xy}} \right) \tag{A.78}$$

Finally, combining the contributions of (A.76), (A.78) and (A.74) the low-level matrix model extended to the full arm is derived. This model will be able to be adapted thereafter to carry out the low-level control.

FUNCTIONAL PHYSICAL DETAILED MODEL OF THE ARM

$$\begin{cases} \mathbf{i_{C_{xy}}} = C\frac{d\mathbf{v_{C_{xy}}}}{dt} = i^*_{xy}\left(L_{xy}\mathbf{S^e_{xy}} + \mathbf{T_{xy}}\right) \\ v_{xy} = \sigma(x)\left[\left(\mathbf{v_{C_{xy}}}^T L_{xy} + i^*_{xy}W_{xy}\right)\mathbf{S^e_{xy}} + i^*_{xy}\mathbf{S^e_{xy}}^T\Theta_{xy}\mathbf{S^e_{xy}} + \left(\mathbf{v_{C_{xy}}}^T\mathbf{T_{xy}} + i^*_{xy}\mathbf{Z_{xy}}\right)\right] \\ v_{xy} \in \left[\sum_{j=1}^{N} R^{HB}_{xyj} i^*_{xy} + (1-q)v_{C_{xyj}}; \sum_{j=1}^{N} R^{HB}_{xyj} i^*_{xy} + v_{C_{xyj}}\right] \\ P^{loss}_{xy} = \left(W_{xy}\mathbf{S^e_{xy}} + \mathbf{S^e_{xy}}^T\Theta_{xy}\mathbf{S^e_{xy}} + \mathbf{Z_{xy}}\right) {i^*_{xy}}^2 \end{cases} \tag{A.79}$$

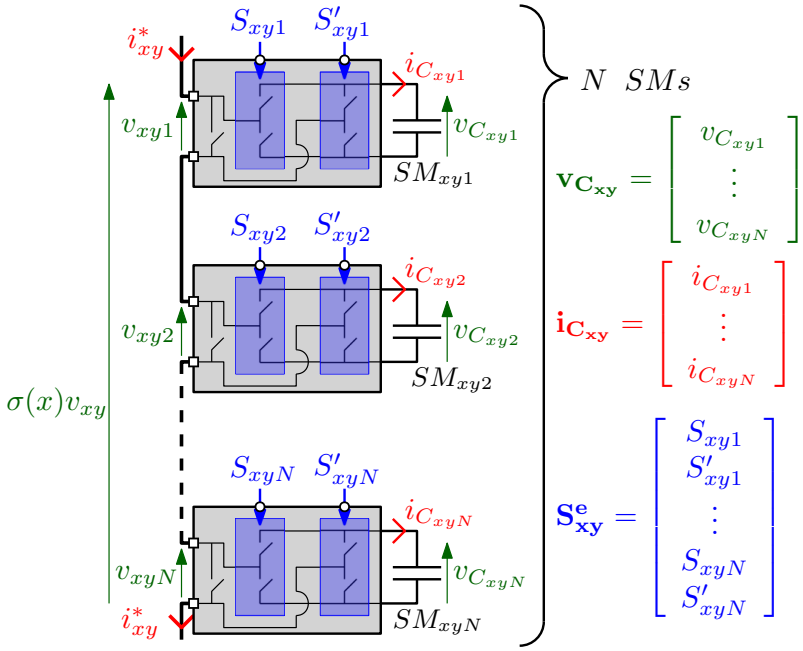

Figure 13: Functional diagram of an arm from the MMC

The Figure 2.13 is provided with (A.79) and (A.80) in order to visualize the quantities involved in the functional physical detailed model of the arm.

In the case one only wants to use the model without taking into account the conduction resistances, it is sufficient to remove the resistive terms W_{xy}, Θ_{xy} and $\mathbf{Z_{xy}}$ from the equation (A.79):

FUNCTIONAL DETAILED MODEL OF THE ARM

$$\begin{cases} \mathbf{i_{C_{xy}}} = C\frac{d\mathbf{v_{C_{xy}}}}{dt} = i^*_{xy}\left(L_{xy}\mathbf{S^e_{xy}} + \mathbf{T_{xy}}\right) \\ v_{xy} = \sigma(x)\left[\left(\mathbf{v_{C_{xy}}}^T L_{xy}\right)\mathbf{S^e_{xy}} + \left(\mathbf{v_{C_{xy}}}^T\mathbf{T_{xy}}\right)\right] \\ v_{xy} \in \left[\sum_{j=1}^{N}(1-q)v_{C_{xyj}}; \sum_{j=1}^{N} v_{C_{xyj}}\right] \end{cases} \tag{A.80}$$

G | Electrical model change of basis: from the stationary reference frame to a given PARK rotating reference frame

Let an electrical model be:

$$R\mathbf{I^m} + Ls\mathbf{I^m} = N_c\mathbf{V^m_{ctrl}} + N_e\mathbf{V^m_{ext}} \tag{A.81}$$

With R some resistance, L some inductance, $\mathbf{V_{ctrl}^{m}} \in \mathbb{R}^m$ the voltage vector considered to be the one that controls the current vector $\mathbf{I^m} \in \mathbb{R}^{n_I}$ and $\mathbf{V_{ext}^{m}} \in \mathbb{R}^{n_e}$ a voltage vector externally enforced. The matrices $N_c \in \mathbb{R}^{n_I \times m}$ and $N_e \in \mathbb{R}^{n_I \times n_e}$ are some voltage vector weightening matrices.

Let the change of basis from the natural stationary reference frame $\{1, \dots, m\}$ to the stationary reference frame $\{\alpha, \beta, 0\}$ be defined by the transformation defined by (3.74):

$$\mathbf{X}^{\alpha\beta 0} = [C_K]\mathbf{X^m} \Longrightarrow \mathbf{X^m} = [C_K]^+\mathbf{X}^{\alpha\beta 0} \tag{A.82}$$

Benefiting from this change of basis, the $\mathbf{X^m}$ quantities can be subsituted by the $\mathbf{X}^{\alpha\beta 0}$ ones. The electrical model then reads:

$$R[C_K]^+\mathbf{I}^{\alpha\beta 0} + Ls[C_K]^+\mathbf{I}^{\alpha\beta 0} = N_c[C_K]^+\mathbf{V_{ctrl}}^{\alpha\beta 0} + N_e[C_K]^+\mathbf{V_{ext}}^{\alpha\beta 0} \tag{A.83}$$

Since $[C_K]^+$ does not depend of the time, the following permutation is allowed: $s[C_K]^+ = [C_K]^+ s$. Moreover, not only the LAPLACE variable s is a scalar but also R and L are, meaning that permutations with $[C_K]^+$ are possible. Thus:

$$[C_K]^+R\mathbf{I}^{\alpha\beta 0} + [C_K]^+Ls\mathbf{I}^{\alpha\beta 0} = N_c[C_K]^+\mathbf{V_{ctrl}}^{\alpha\beta 0} + N_e[C_K]^+\mathbf{V_{ext}}^{\alpha\beta 0} \tag{A.84}$$

Since $[C_K]^+$ is at least the pseudo-inverse from $[C_K]$ and at most its inverse, their multiplication give the identity matrix, see (3.73) and its following equation. Thus, the left multiplication of the model by $[C_K]$ gives:

$$R\mathbf{I}^{\alpha\beta 0} + Ls\mathbf{I}^{\alpha\beta 0} = [C_K]N_c[C_K]^+\mathbf{V_{ctrl}}^{\alpha\beta 0} + [C_K]N_e[C_K]^+\mathbf{V_{ext}}^{\alpha\beta 0} \tag{A.85}$$

The notations $N_c^{\alpha\beta 0} = [C_K]N_c[C_K]^+$ and $N_e^{\alpha\beta 0} = [C_K]N_e[C_K]^+$ are introduced, changing the model into:

$$R\mathbf{I}^{\alpha\beta 0} + Ls\mathbf{I}^{\alpha\beta 0} = N_c^{\alpha\beta 0}\mathbf{V_{ctrl}}^{\alpha\beta 0} + N_e^{\alpha\beta 0}\mathbf{V_{ext}}^{\alpha\beta 0} \tag{A.86}$$

Now, let the change of basis from the stationary reference frame $\{\alpha, \beta, 0\}$ to the stationary reference frame $\{d, q, 0\}$ be defined by the transformation defined by (3.75):

$$\mathbf{X^{dq0}} = [P(-\theta)]\mathbf{X}^{\alpha\beta 0} \Longrightarrow \mathbf{X}^{\alpha\beta 0} = [P(\theta)]\mathbf{X^{dq0}} \tag{A.87}$$

Benefiting from this change of basis in the same way in was done previously, the $\mathbf{X}^{\alpha\beta 0}$ are subsituted by the $\mathbf{X^{dq0}}$ ones. The change of basis is applied to the electrical model:

$$R[P(\theta)]\mathbf{I^{dq0}} + Ls[P(\theta)]\mathbf{I^{dq0}} = N_c[P(\theta)]\mathbf{V_{ctrl}^{dq0}} + N_e[P(\theta)]\mathbf{V_{ext}^{dq0}} \tag{A.88}$$

Since the angle θ changes over time, the $[P(\theta)]$ matrix is a function of time. Thus $s[P(\theta)]\mathbf{I^{dq0}}$ has to be developed:

$$R[P(\theta)]\mathbf{I^{dq0}} + L\left(s[P(\theta)]\right)\mathbf{I^{dq0}} + L[P(\theta)]s\mathbf{I^{dq0}} = N_c[P(\theta)]\mathbf{V_{ctrl}^{dq0}} + N_e[P(\theta)]\mathbf{V_{ext}^{dq0}} \tag{A.89}$$

Since R and L are still scalars, permutations are possible:

$$[P(\theta)]R\mathbf{I^{dq0}} + \left(s[P(\theta)]\right)L\mathbf{I^{dq0}} + [P(\theta)]Ls\mathbf{I^{dq0}} = N_c[P(\theta)]\mathbf{V_{ctrl}^{dq0}} + N_e[P(\theta)]\mathbf{V_{ext}^{dq0}} \tag{A.90}$$

Since $[P(-\theta)]$ is the inverse from $[P(\theta)]$, their multiplication give the identity matrix. Thus, the left multiplication of the model by $[P(-\theta)]$ gives:

$$R\mathbf{I^{dq0}} + [P(-\theta)]\left(s[P(\theta)]\right)L\mathbf{I^{dq0}} + Ls\mathbf{I^{dq0}} = [P(-\theta)]N_c[P(\theta)]\mathbf{V_{ctrl}^{dq0}} + [P(-\theta)]N_e[P(\theta)]\mathbf{V_{ext}^{dq0}} \tag{A.91}$$

The notations $N_c^{dq0} = [P(-\theta)]N_c^{\alpha\beta 0}[P(\theta)]$ and $N_e^{dq0} = [P(-\theta)]N_e^{\alpha\beta 0}[P(\theta)]$ are introduced, thus simplifying he model into:

$$R\mathbf{I^{dq0}} + [P(-\theta)]\,(s[P(\theta)])\,L\mathbf{I^{dq0}} + Ls\mathbf{I^{dq0}} = N_c^{dq0}\mathbf{V_{ctrl}^{dq0}} + N_e^{dq0}\mathbf{V_{ext}^{dq0}} \tag{A.92}$$

For further development of the model, $[P(-\theta)]\,(s[P(\theta)])$ needs to be derived:

$$s[P(\theta)] = \frac{d[P(\theta)]}{dt} = \frac{d\theta}{dt}\frac{d[P(\theta)]}{d\theta} = \omega\begin{bmatrix} -\sin(\theta) & -\cos(\theta) & 0 \\ \cos(\theta) & -\sin(\theta) & 0 \\ 0 & 0 & 0 \end{bmatrix} \tag{A.93}$$

Therefore, left multiplication by $[P(-\theta)]$ gives:

$$[P(-\theta)]\,(s[P(\theta)]) = \omega\begin{bmatrix} 0 & -1 & 0 \\ 1 & 0 & 0 \\ 0 & 0 & 0 \end{bmatrix} \tag{A.94}$$

Finally the electrical model adopts the form:

$$R\mathbf{I^{dq0}} + Ls\mathbf{I^{dq0}} + \omega L\begin{bmatrix} -I^q \\ +I^d \\ 0 \end{bmatrix} = N_c^{dq0}\mathbf{V_{ctrl}^{dq0}} + N_e^{dq0}\mathbf{V_{ext}^{dq0}} \tag{A.95}$$

Where I^d and I^q are the two first components contained in $\mathbf{I^{dq0}}$.

Remark:

The previous derivations perform the change of basis from the initial rotating frame to the PARK synchronously rotating reference frame. Note that for the change of basis from the initial stationary frame to the PARK 12 synchronously rotating reference frame different transformation matrices need to be used.

As described in Sections 3.E.2.2 and 3.E.2.3, one must use $\left[C_{K_{12}}^m\right]$, $\left[C_{K_{12}}^m\right]^+$, $[P(\theta)_{12}^m]$ and $[P(-\theta)_{12}^m]$ rather than $[C_K]$, $[C_K]^+$, $[P(\theta)]$ and $[P(-\theta)]$ respectively. Therefore, the resulting vectors in the $\{\alpha_1, \beta_1, \alpha_2, \beta_2, 0\}$ and $\{d_1, q_1, d_2, q_2, 0\}$ reference frames will feature up to 5 components instead of 3 only in the $\{\alpha, \beta, 0\}$ and $\{d, q, 0\}$ reference frames. Some of those components may always be null. In that case, the corresponding components are erased from the vectors and the model without loss of information. Matrices are adapted accordingly, leading to even lower order models.

H | Biharmonic PARK transformation matrices

H.1 | From the m-phase $(1, 2, \ldots, m)$ stationary frame to the $(\alpha_1, \beta_1, \alpha_2, \beta_2, 0)$ stationary frame

From the list of eigenvectors which are selected - see Table 3.6 - to build the new basis, it is possible to determine the different basis change matrices allowing to keep the desired harmonic components according to the number of phases. For the following, it is decided to use $k_0 = \sqrt{2}$.

Case $m = 1$

In the single-phase case it comes that:

$$\mathbf{x}_0 = \mathbf{x}_1^{\mathbf{c}} = \mathbf{c}_1 = c_1 \sum_{k=1}^{1} \mathbf{x}_{\mathbf{k}}^{\mathbf{m}} = c_1 \mathbf{x}_1^{\mathbf{m}} \tag{A.96}$$

This gives the basis change matrix:

$$[C_{K_{12}}^1] = [c_1] = \sqrt{2} c_1 [1/\sqrt{2}] = K[1/k_0] \tag{A.97}$$

The notation "12" in subscript is added to $[C_K^1]$ to specify the harmonic content represented: the fundamental and second order harmonic component.

Case $m = 2$

For the two-phase case ($\theta_m = \pi$) it comes, by choosing to put the homopolar component at the bottom:

$$\begin{aligned} \mathbf{x}_{0*} &= \mathbf{x}_2^{\mathbf{c}} = c_1 \textstyle\sum_{k=1}^{2} (-1)^{k-1} \mathbf{x}_{\mathbf{k}}^{\mathbf{m}} = c_1 (\mathbf{x}_1^{\mathbf{m}} - \mathbf{x}_2^{\mathbf{m}}) \\ \mathbf{x}_0 &= \mathbf{x}_1^{\mathbf{c}} = \mathbf{c}_1 = c_1 \textstyle\sum_{k=1}^{2} \mathbf{x}_{\mathbf{k}}^{\mathbf{m}} = c_1 (\mathbf{x}_1^{\mathbf{m}} + \mathbf{x}_2^{\mathbf{m}}) \end{aligned} \tag{A.98}$$

Which gives the basis change matrix:

$$[C_{K_{12}}^2] = c_1 \begin{bmatrix} 1 & -1 \\ 1 & 1 \end{bmatrix} = \sqrt{2} c_1 \begin{bmatrix} 1/\sqrt{2} & -1/\sqrt{2} \\ 1/\sqrt{2} & 1/\sqrt{2} \end{bmatrix} = K \begin{bmatrix} 1/k_0 & -1/k_0 \\ 1/k_0 & 1/k_0 \end{bmatrix} \tag{A.99}$$

Case $m = 3$

For the three-phase case it comes, choosing to put the homopolar component at the bottom:

$$\begin{aligned} \mathbf{x}_{\alpha_1} &= \mathbf{x}_2^{\mathbf{c}} = \sqrt{2} c_1 \textstyle\sum_{k=1}^{3} \cos(\theta_m (k-1)) \mathbf{x}_{\mathbf{k}}^{\mathbf{m}} \\ \mathbf{x}_{\beta_1} &= \mathbf{x}_3^{\mathbf{c}} = \sqrt{2} c_1 \textstyle\sum_{k=1}^{3} \sin(\theta_m (k-1)) \mathbf{x}_{\mathbf{k}}^{\mathbf{m}} \\ \mathbf{x}_0 &= \mathbf{x}_1^{\mathbf{c}} = \mathbf{c}_1 = c_1 \textstyle\sum_{k=1}^{3} \mathbf{x}_{\mathbf{k}}^{\mathbf{m}} = c_1 (\mathbf{x}_1^{\mathbf{m}} + \mathbf{x}_2^{\mathbf{m}} + \mathbf{x}_3^{\mathbf{m}}) \end{aligned} \tag{A.100}$$

With $\theta_m = 2\pi/3$. This gives the base change matrix:

$$[C_{K_{12}}^3] = K \begin{bmatrix} 1 & \cos(\theta_m) & \cos(2\theta_m) \\ 0 & \sin(\theta_m) & \sin(2\theta_m) \\ 1/k_0 & 1/k_0 & 1/k_0 \end{bmatrix} \tag{A.101}$$

It can be noted that it is then obtained the usual transformation matrix used in the three-phase case to switch from the $\{1, 2, 3\}$ reference frame to the $\{\alpha, \beta, 0\}$ reference frame.

Case $m = 4$

For the four-phase case it comes, choosing to put the homopolar component at the bottom:

$$\begin{aligned} \mathbf{x}_{\alpha_1} &= \mathbf{x}_2^{\mathbf{c}} = \sqrt{2} c_1 \textstyle\sum_{k=1}^{4} \cos(\theta_m (k-1)) \mathbf{x}_{\mathbf{k}}^{\mathbf{m}} \\ \mathbf{x}_{\beta_1} &= \mathbf{x}_3^{\mathbf{c}} = \sqrt{2} c_1 \textstyle\sum_{k=1}^{4} \sin(\theta_m (k-1)) \mathbf{x}_{\mathbf{k}}^{\mathbf{m}} \\ \mathbf{x}_{0*} &= \mathbf{x}_4^{\mathbf{c}} = c_1 \textstyle\sum_{k=1}^{4} \cos(2\theta_m (k-1)) \mathbf{x}_{\mathbf{k}}^{\mathbf{m}} = c_1 (\mathbf{x}_1^{\mathbf{m}} - \mathbf{x}_2^{\mathbf{m}} + \mathbf{x}_3^{\mathbf{m}} - \mathbf{x}_4^{\mathbf{m}}) \\ \mathbf{x}_0 &= \mathbf{x}_1^{\mathbf{c}} = \mathbf{c}_1 = c_1 \textstyle\sum_{k=1}^{4} \mathbf{x}_{\mathbf{k}}^{\mathbf{m}} = c_1 (\mathbf{x}_1^{\mathbf{m}} + \mathbf{x}_2^{\mathbf{m}} + \mathbf{x}_3^{\mathbf{m}} + \mathbf{x}_4^{\mathbf{m}}) \end{aligned} \tag{A.102}$$

With $\theta_m = \pi/2$. This gives the base change matrix:

$$[C^4_{K_{12}}] = K\begin{bmatrix} 1 & \cos(\theta_m) & \cos(2\theta_m) & \cos(3\theta_m) \\ 0 & \sin(\theta_m) & \sin(2\theta_m) & \sin(3\theta_m) \\ 1/k_0 & -1/k_0 & 1/k_0 & -1/k_0 \\ 1/k_0 & 1/k_0 & 1/k_0 & 1/k_0 \end{bmatrix} = K\begin{bmatrix} 1 & 0 & -1 & 0 \\ 0 & 1 & 0 & -1 \\ 1/k_0 & -1/k_0 & 1/k_0 & -1/k_0 \\ 1/k_0 & 1/k_0 & 1/k_0 & 1/k_0 \end{bmatrix} \tag{A.103}$$

Case $m \geq 5$

For the general case it comes, choosing to put the homopolar component at the bottom:

$$\begin{array}{l} \mathbf{x}_{\alpha_1} = \mathbf{x}^{\mathbf{c}}_2 = \sqrt{2}c_1 \sum_{k=1}^{m} \cos(\theta_m(k-1))\mathbf{x}^{\mathbf{m}}_{\mathbf{k}} \\ \mathbf{x}_{\beta_1} = \mathbf{x}^{\mathbf{c}}_3 = \sqrt{2}c_1 \sum_{k=1}^{m} \sin(\theta_m(k-1))\mathbf{x}^{\mathbf{m}}_{\mathbf{k}} \\ \mathbf{x}_{\alpha_2} = \mathbf{x}^{\mathbf{c}}_4 = \sqrt{2}c_1 \sum_{k=1}^{m} \cos(2\theta_m(k-1))\mathbf{x}^{\mathbf{m}}_{\mathbf{k}} \\ \mathbf{x}_{\beta_2} = \mathbf{x}^{\mathbf{c}}_5 = \sqrt{2}c_1 \sum_{k=1}^{m} \sin(2\theta_m(k-1))\mathbf{x}^{\mathbf{m}}_{\mathbf{k}} \\ \mathbf{x}_0 = \mathbf{x}^{\mathbf{c}}_1 = \mathbf{c}_1 = c_1 \sum_{k=1}^{m} \mathbf{x}^{\mathbf{m}}_{\mathbf{k}} \end{array} \tag{A.104}$$

With $\theta_m = 2\pi/m$. This gives the transformation matrix:

$$[C^{m\geq 5}_{K_{12}}] = K\begin{bmatrix} 1 & \cos(\theta_m) & \cos(2\theta_m) & \cos(3\theta_m) & \cos(4\theta_m) & \dots & \cos((m-1)\theta_m) \\ 0 & \sin(\theta_m) & \sin(2\theta_m) & \sin(3\theta_m) & \sin(4\theta_m) & \dots & \sin((m-1)\theta_m) \\ 1 & \cos(2\theta_m) & \cos(4\theta_m) & \cos(6\theta_m) & \cos(8\theta_m) & \dots & \cos(2(m-1)\theta_m) \\ 0 & \sin(2\theta_m) & \sin(4\theta_m) & \sin(6\theta_m) & \sin(8\theta_m) & \dots & \sin(2(m-1)\theta_m) \\ 1/k_0 & 1/k_0 & 1/k_0 & 1/k_0 & 1/k_0 & \dots & 1/k_0 \end{bmatrix} \tag{A.105}$$

Finally, depending on the number m of phases, there will come a transformation matrix $\left[C^m_{K_{12}}\right]$ having a fixed number of rows only from $m = 5$, below that, $\left[C^m_{K_{12}}\right]$ will be of smaller size. Although the size of $\left[C^m_{K_{12}}\right]$ varies as a function of m, it is still possible to show the following relations knowing that $k_0 = \sqrt{2}$:

$$\left[C^m_{K_{12}}\right] \cdot \left[C^m_{K_{12}}\right]^T = \begin{cases} \frac{K^2 m}{2}\mathbb{I}_m, \text{ for } m \in [\![1;5]\!] \\ \frac{K^2 m}{2}\mathbb{I}_5, \text{ for } m \geq 5 \end{cases} \tag{A.106}$$

Since $\left[C^m_{K_{12}}\right]$ is not always square in function of m, the previous relation allows one to define its pseudo-inverse matrix:

$$\left[C^m_{K_{12}}\right]^+ \triangleq \frac{2}{K^2 m}\left[C^m_{K_{12}}\right]^T \tag{A.107}$$

It is thus with this transformation matrix that the shift from the initial stationary reference frame $(1, 2, \dots, m)$ to the stationary reference frame $(\alpha_1, \beta_1, \alpha_2, \beta_2, 0)$ is going to be operated for $m \geq 5$. For $m < 5$ the destination frame will not be $(\alpha_1, \beta_1, \alpha_2, \beta_2, 0)$ but will depend on the number of phases:

- For $m = 1$: (0)
- For $m = 2$: $(0^*, 0)$
- For $m = 3$: $(\alpha_1, \beta_1, 0)$
- For $m = 4$: $(\alpha_1, \beta_1, 0^*, 0)$

In all cases the change of basis for the vectors will be realized by the following matrix product:

$$\mathbf{X}^{\{\alpha_1,\beta_1,\alpha_2,\beta_2,0\}} = \mathbf{X}^{\alpha\beta012} = \left[C^m_{K_{12}}\right]\mathbf{X}^{\mathbf{m}} \tag{A.108}$$

For the inverse transformation the following relation will be used:

$$\mathbf{X^m} = \left[C^m_{K_{12}}\right]^{+}\mathbf{X}^{\alpha\beta012} = \frac{2}{K^2 m}\left[C^m_{K_{12}}\right]^{T}\mathbf{X}^{\alpha\beta012} \tag{A.109}$$

The determination of the factor K will not be detailed here but in the case of the transformation of CONCORDIA this coefficient is calculated so that the conservation of electric powers by transformation is guaranteed. This is obtained with $K = \sqrt{2/m}$. In the case of the CLARKE transformation this coefficient is calculated to guarantee the conservation of the amplitudes of the waveforms. To do this it is necessary to have $K = 2/m$.

H.2 From the $(\alpha_1, \beta_1, \alpha_2, \beta_2, 0)$ stationary frame to the $(d_1, q_1, d_2, q_2, 0)$ synchronous rotating frame

As for the case of the usual PARK [Par29; Par33] transform for three-phase systems, the shift from the $(\alpha_1, \beta_1, \alpha_2, \beta_2, 0)$ reference frame to the rotating $(d_1, q_1, d_2, q_2, 0)$ reference frame will be done using a change of base using a rotation. To determine the angle of this rotation the information available in Table 3.6 is used.

For example, for the case $m \geq 5$, this table indicates that the fundamental components of the electrical signals will be carried by the axes α_1 and β_1 while the second order harmonics will be carried by α_2 and β_2. By setting $\theta = \omega t$ an angle with ω the fundamental frequency of the alternating component of the electrical signals to which the base change is applied, the axes α_1 and β_1 will be subject to a rotation of θ. And α_2 and β_2, a 2θ rotation in order to make continuous the waveforms of the second order harmonics they carry. This reasoning carried out for the different cases of m will thus bring the required transformation matrices.

Case $m = 1$:

In the single-phase case, all the harmonic components are carried by $\mathbf{x}_0$, so it would be necessary to do no transformation (homopolar component), to rotate at θ (fundamental components) and at 2θ (second order harmonic components). However, in order to perform a rotation one needs to have two vectors in quadrature, one carrying the sinusoidal component and the other carrying the cosinusoidal component, which is not the case here since there is only one vector. The transformation that will be operated will be the identity:

$$\mathbf{x}_0 = \mathbf{x}_0 = [P(-\theta)^1_{12}]\mathbf{x}_0 = 1\ \mathbf{x}_0 \tag{A.110}$$

Case $m = 2$:

In the two-phase case the fundamental components are carried by $\mathbf{x}_0$ while the second order harmonic components are carried by $\mathbf{x}_{0*}$. The rotation should therefore be performed at θ for $\mathbf{x}_0$ and at 2θ for $\mathbf{x}_{0*}$ but in this case also these two vectors each carry a single harmonic component; there are no other vectors in quadrature with the latter which carry these same harmonic components. The transformation that will be operated will be the identity:

$$\begin{matrix}\mathbf{x}_0 = \mathbf{x}_0 \\ \mathbf{x}_{0*} = \mathbf{x}_{0*}\end{matrix} \Longrightarrow \begin{bmatrix}\mathbf{x}_0 \\ \mathbf{x}_{0*}\end{bmatrix} = \begin{bmatrix}1 & 0 \\ 0 & 1\end{bmatrix}\begin{bmatrix}\mathbf{x}_0 \\ \mathbf{x}_{0*}\end{bmatrix} = [P(-\theta)^2_{12}]\begin{bmatrix}\mathbf{x}_0 \\ \mathbf{x}_{0*}\end{bmatrix} \tag{A.111}$$

Case $m = 3$:

In the three-phase case the fundamental and second order harmonic components are carried by the same vectors: $\mathbf{x}_{\alpha_1}$ and $\mathbf{x}_{\beta_1}$. However, these vectors form a pair $\{\mathbf{x_k^c}; \mathbf{x_{k+1}^c}\}$ and are therefore orthogonal: one carries the sinusoidal components and the other the cosinusoidal components. A change of basis by rotation can then be performed. Whatever the choice of the rotation angle, θ or 2θ, the second order harmonics and the fundamental components being carried by the same vectors, the waveforms in the PARK reference frame will necessarily be composed of an alternating component in addition to a continuous component.

By choosing a rotation of angle θ, the signals carried by the axes d_1 and q_1 will feature as continuous component the fundamental component resulting from the natural basis; the alternative component they will showcase will be the second order harmonic component coming from the natural basis. In the opposite case, by choosing a rotation of angle 2θ, the signals carried by the axes d_1 and q_1 will present for continuous component the second order harmonic component resulting from the natural basis; the alternative component which they will present will be the fundamental component resulting from the natural basis.

Arbitrarily the choice is then made to carry out the rotation at the angle θ, which gives:

$$\begin{aligned} \mathbf{x}_{\mathbf{d}_1} &= \cos(\theta)\mathbf{x}_{\alpha_1} + \sin(\theta)\mathbf{x}_{\beta_1} \\ \mathbf{x}_{\mathbf{q}_1} &= -\sin(\theta)\mathbf{x}_{\alpha_1} + \cos(\theta)\mathbf{x}_{\beta_1} \\ \mathbf{x}_0 &= \mathbf{x}_0 \end{aligned} \tag{A.112}$$

Either in matrix form:

$$\begin{bmatrix} \mathbf{x}_{\mathbf{d}_1} \\ \mathbf{x}_{\mathbf{q}_1} \\ \mathbf{x}_0 \end{bmatrix} = \begin{bmatrix} \cos(\theta) & \sin(\theta) & 0 \\ -\sin(\theta) & \cos(\theta) & 0 \\ 0 & 0 & 1 \end{bmatrix} \begin{bmatrix} \mathbf{x}_{\alpha_1} \\ \mathbf{x}_{\beta_1} \\ \mathbf{x}_0 \end{bmatrix} = [P(-\theta)_{12}^3] \begin{bmatrix} \mathbf{x}_{\alpha_1} \\ \mathbf{x}_{\beta_1} \\ \mathbf{x}_0 \end{bmatrix} \tag{A.113}$$

Case $m = 4$:

In the four-phase case the fundamental components are carried by $\mathbf{x}_{\alpha_1}$ and $\mathbf{x}_{\beta_1}$, while the second order harmonic components are carried by $\mathbf{x}_{0*}$. As seen in Case $m = 3$, the vectors $\mathbf{x}_{\alpha_1}$ and $\mathbf{x}_{\beta_1}$ form a pair $\{\mathbf{x_k^c}; \mathbf{x_{k+1}^c}\}$ of orthogonal vectors on which a rotation can be performed. As they carry the fundamental component here, they will be rotated by an angle θ. The second order harmonic components are represented by the unique vector $\mathbf{x}_{0*}$ which has no vector in quadrature which would allow an interesting rotation, $\mathbf{x}_{0*}$ will thus be kept and no rotation will be applied to it. The transformation is therefore done in the following way:

$$\begin{aligned} \mathbf{x}_{\mathbf{d}_1} &= \cos(\theta)\mathbf{x}_{\alpha_1} + \sin(\theta)\mathbf{x}_{\beta_1} \\ \mathbf{x}_{\mathbf{q}_1} &= -\sin(\theta)\mathbf{x}_{\alpha_1} + \cos(\theta)\mathbf{x}_{\beta_1} \\ \mathbf{x}_{0*} &= \mathbf{x}_{0*} \\ \mathbf{x}_0 &= \mathbf{x}_0 \end{aligned} \tag{A.114}$$

Either in matrix form:

$$\begin{bmatrix} \mathbf{x}_{\mathbf{d}_1} \\ \mathbf{x}_{\mathbf{q}_1} \\ \mathbf{x}_{0*} \\ \mathbf{x}_0 \end{bmatrix} = \begin{bmatrix} \cos(\theta) & \sin(\theta) & 0 & 0 \\ -\sin(\theta) & \cos(\theta) & 0 & 0 \\ 0 & 0 & 1 & 0 \\ 0 & 0 & 0 & 1 \end{bmatrix} \begin{bmatrix} \mathbf{x}_{\alpha_1} \\ \mathbf{x}_{\beta_1} \\ \mathbf{x}_{0*} \\ \mathbf{x}_0 \end{bmatrix} = [P(-\theta)_{12}^4] \begin{bmatrix} \mathbf{x}_{\alpha_1} \\ \mathbf{x}_{\beta_1} \\ \mathbf{x}_{0*} \\ \mathbf{x}_0 \end{bmatrix} \tag{A.115}$$

Case $m \geq 5$:

In the case with at least 5 phases, the fundamental components are carried by $\mathbf{x}_{\alpha_1}$ and $\mathbf{x}_{\beta_1}$, while the second order harmonic components are carried by $\mathbf{x}_{\alpha_2}$ and $\mathbf{x}_{\beta_2}$. The vectors $\mathbf{x}_{\alpha_1}$ and $\mathbf{x}_{\beta_1}$ form a pair $\{\mathbf{x}^{\mathbf{c}}_{\mathbf{k}}; \mathbf{x}^{\mathbf{c}}_{\mathbf{k+1}}\}$ of orthogonal vectors on which a rotation can be operated, it is the same for $\mathbf{x}_{\alpha_2}$ and $\mathbf{x}_{\beta_2}$. As $\mathbf{x}_{\alpha_1}$ and $\mathbf{x}_{\beta_1}$ carry the fundamental component here, they will be rotated by an angle θ. The second order harmonic components being carried by $\mathbf{x}_{\alpha_2}$ and $\mathbf{x}_{\beta_2}$, these last ones are applied a 2θ rotation. The transformation is therefore done in the following way:

$$\begin{aligned}
\mathbf{x}_{\mathbf{d}_1} &= \cos(\theta)\mathbf{x}_{\alpha_1} + \sin(\theta)\mathbf{x}_{\beta_1} \\
\mathbf{x}_{\mathbf{q}_1} &= -\sin(\theta)\mathbf{x}_{\alpha_1} + \cos(\theta)\mathbf{x}_{\beta_1} \\
\mathbf{x}_{\mathbf{d}_2} &= \cos(2\theta)\mathbf{x}_{\alpha_2} + \sin(2\theta)\mathbf{x}_{\beta_2} \\
\mathbf{x}_{\mathbf{q}_2} &= -\sin(2\theta)\mathbf{x}_{\alpha_2} + \cos(2\theta)\mathbf{x}_{\beta_2} \\
\mathbf{x}_0 &= \mathbf{x}_0
\end{aligned} \tag{A.116}$$

Either in matrix form:

$$\begin{bmatrix} \mathbf{x}_{\mathbf{d}_1} \\ \mathbf{x}_{\mathbf{q}_1} \\ \mathbf{x}_{\mathbf{d}_2} \\ \mathbf{x}_{\mathbf{q}_2} \\ \mathbf{x}_0 \end{bmatrix} = \begin{bmatrix} \cos(\theta) & \sin(\theta) & 0 & 0 & 0 \\ -\sin(\theta) & \cos(\theta) & 0 & 0 & 0 \\ 0 & 0 & \cos(2\theta) & \sin(2\theta) & 0 \\ 0 & 0 & -\sin(2\theta) & \cos(2\theta) & 0 \\ 0 & 0 & 0 & 0 & 1 \end{bmatrix} \begin{bmatrix} \mathbf{x}_{\alpha_1} \\ \mathbf{x}_{\beta_1} \\ \mathbf{x}_{\alpha_2} \\ \mathbf{x}_{\beta_2} \\ \mathbf{x}_0 \end{bmatrix} = [P(-\theta)^{m\geq 5}_{12}] \begin{bmatrix} \mathbf{x}_{\alpha_1} \\ \mathbf{x}_{\beta_1} \\ \mathbf{x}_{\alpha_2} \\ \mathbf{x}_{\beta_2} \\ \mathbf{x}_0 \end{bmatrix} \tag{A.117}$$

Finally, whatever the number of phases it is possible to verify that the matrix $[P(-\theta)^m_{12}]$ will always be invertible which will allow to operate the transformations in the following way:

$$\mathbf{X}^{\{\mathbf{d}_1,\mathbf{q}_1,\mathbf{d}_2,\mathbf{q}_2,0\}} = \mathbf{X}^{\mathbf{dq}012} = [P(-\theta)^m_{12}]\, \mathbf{X}^{\alpha\beta 012} \tag{A.118}$$

The inverse transformation is then performed by:

$$\alpha\beta 012 = [P(-\theta)^m_{12}]^{-1}\mathbf{X}^{\mathbf{dq}012} = [P(\theta)^m_{12}]\, \mathbf{X}^{\mathbf{dq}012} \tag{A.119}$$

It is noted that as a function of the number m of phases, the size of the transformation matrices will evolve, and the size of the vectors in the PARK reference frame will also evolve accordingly. Noting m' the size of the vectors obtained after the full transformation to this last reference frame, the Figure 14 shows the evolution of this size as a function of the number of phases.

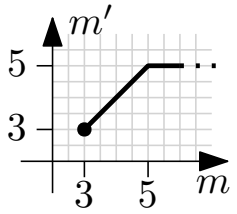

$$m' = \begin{cases} m, \text{ if } m \leq 5 \\ 5, \text{ if } m \geq 5 \end{cases} \tag{A.120}$$

Figure 14: Definition of m' as a function of m.

I Detailed analysis from the limits of the operating zone of the MMC

The objective of this seciton in to derive the limits of the region of operation from the MMC from the point of view of the control first (e.g., duty cycles limitations), but physical limitations

(e.g., maximum current in the semiconductors) can also be taken into account afterwords with no loss of generality.

Taking into account the Assumptions 6 to 9 allows the following simplifications:

$$\begin{array}{l} N_\Sigma(2)\mathbf{V_x} = \frac{v_p+v_n}{2} = 0 \\ N_\Sigma(m)\mathbf{V_y} = \frac{\hat{V}_{AC}}{m}\sum_{y=y_1}^{y_m} sin(\omega_o t - \varphi_y - \varphi_v) = 0 \\ N_\Sigma(1)V_{n_{AD}} = V_{n_{AD}} \\ -N_\Delta(m)\mathbf{V_y} = -\mathbf{V_y} \end{array} \tag{A.121}$$

And:

$$[1\ \ 0] \cdot N_\Delta(2)\mathbf{V_x} = \frac{v_p - v_n}{2} = \frac{V_{DC}}{2} \tag{A.122}$$

By substitution, (3.165) becomes then:

$$\begin{cases} Z_m(t)I_m = V_m - V_{n_{AD}} \\ Z_s(t)I_s = V_s + \frac{V_{DC}}{2} \\ Z_c(t)\mathbf{I_c} = \mathbf{V_c} \\ Z_o(t)\mathbf{I_o} = \mathbf{V_o} - \mathbf{V_y} \end{cases} \tag{A.123}$$

Assuming that the converter operates in steady state, is equivalent to consider that the alternating network is balanced, which implies that the alternating output currents i_{o_y} are balanced in the same way as the circulating currents i_{c_y}. All the alternating output currents i_{o_y} will therefore all have the same amplitude, for the analysis of the zone of operation, the aim of which is to determine the maximum current limits that can be reached, the interest will therefore be focused on i_{o_y} and not on all the alternating output currents contained in the vector $\mathbf{I_o}$. The same reasoning applies for the circulating currents, so the interest is focused on i_{c_y} and not on $\mathbf{I_c}$. Therefore only a subset of the equations contained in the equation (A.123) is considered:

$$\begin{cases} Z_m(t)i_m = v_m - v_{n_{AD}} \\ Z_s(t)i_s = v_s + \frac{V_{DC}}{2} \\ Z_c(t)i_{c_y} = v_{c_y} \\ Z_o(t)i_{o_y} = v_{o_y} - v_y \end{cases} \tag{A.124}$$

It is noted that the terms I_m, $V_{n_{AD}}$ and I_s are scalars, and it is also recalled that $I_m = i_m$, $V_{n_{AD}} = v_{n_{AD}}$ and $I_s = i_s$.

In order to continue simplifying (A.124), it is necessary to look at the values that the control voltages $\mathbf{V_{py}}$ and $\mathbf{V_{ny}}$ will take. In order to have an analysis showing waveforms for the four types of currents, the choice is made to have control voltages which feature a continuous component and a fundamental component in order to conform to the Assumption 9:

$$\forall y \in \{y_1, \ldots, y_m\}, \begin{cases} v_{py} = \frac{V_{DC}}{2}\left[m_p - d_p \cdot \cos(\omega_o t - \varphi_y)\right] = m_{py} \cdot V_{DC} \\ v_{ny} = -\frac{V_{DC}}{2}\left[m_n + d_n \cdot \cos(\omega_o t - \varphi_y)\right] = m_{ny} \cdot V_{DC} \end{cases} \tag{A.125}$$

The Figure 15 represents those arm voltage signals.

Thus, by sum and difference applied to (A.125), it comes that:

$$\forall y \in \{y_1, \ldots, y_m\}, \begin{cases} v_{py} + v_{ny} = \frac{V_{DC}}{2}\left[(m_p - m_n) - (d_p + d_n) \cdot \cos(\omega_o t - \varphi_y)\right] \\ v_{py} - v_{ny} = \frac{V_{DC}}{2}\left[(m_n + m_n) - (d_p - d_n) \cdot \cos(\omega_o t - \varphi_y)\right] \end{cases} \tag{A.126}$$

$$\iff \forall y \in \{y_1, \ldots, y_m\}, \begin{cases} v_{py} + v_{ny} = \frac{V_{DC}}{2}\left[\Delta_m - \Sigma_d \cdot \cos(\omega_o t - \varphi_y)\right] \\ v_{py} - v_{ny} = \frac{V_{DC}}{2}\left[\Sigma_m - \Delta_d \cdot \cos(\omega_o t - \varphi_y)\right] \end{cases} \tag{A.127}$$

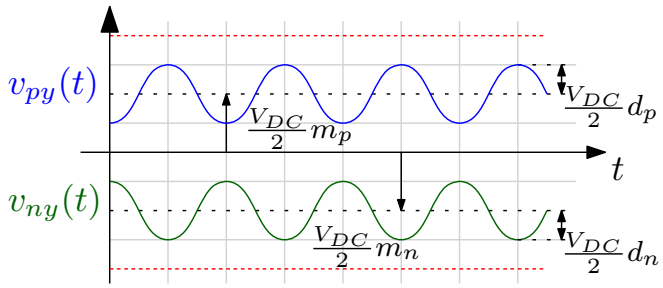

Figure 15: Illustrative waveforms for v_{py} and v_{ny}.

Assuming that $m > 1$, it is shown, by cyclicity of trigonometric functions, that:

$$\begin{cases} \frac{1}{m}\sum_{y=y_1}^{y_m}(v_{py}+v_{ny}) = \frac{V_{DC}}{2}\left[\Delta_m\right] \\ \frac{1}{m}\sum_{y=y_1}^{y_m}(v_{py}-v_{ny}) = \frac{V_{DC}}{2}\left[\Sigma_m\right] \\ \frac{1}{m}\left[(m-1)(v_{py}-v_{ny}) - \sum_{y\neq y_k}^{y_m}(v_{py}-v_{ny})\right] = -\frac{V_{DC}}{2}\left[\Delta_d \cdot \cos(\omega_o t - \varphi_y)\right] \\ \frac{1}{m}\left[(m-1)(v_{py}+v_{ny}) - \sum_{y\neq y_k}^{y_m}(v_{py}+v_{ny})\right] = -\frac{V_{DC}}{2}\left[\Sigma_d \cdot \cos(\omega_o t - \varphi_y)\right] \end{cases} \tag{A.128}$$

By definition of the control voltages of the currents, it is possible to use the expressions developed in the above equation to derive a more detailed form for these voltages:

$$V_m = -\frac{1}{2}N_\Sigma(m)\left(\mathbf{V_{py}}+\mathbf{V_{ny}}\right) = -\frac{1}{2m}\sum_{y=y_1}^{y_m}(v_{py}+v_{ny}) = -\frac{V_{DC}}{4}\Delta_m \tag{A.129}$$

$$V_s = -\frac{1}{2}N_\Sigma(m)\left(\mathbf{V_{py}}-\mathbf{V_{ny}}\right) = -\frac{1}{2m}\sum_{y=y_1}^{y_m}(v_{py}-v_{ny}) = -\frac{V_{DC}}{4}\Sigma_m \tag{A.130}$$

$$\begin{cases} \mathbf{V_c} = -\frac{1}{2}N_\Delta(m)\left(\mathbf{V_{py}}-\mathbf{V_{ny}}\right) = -\frac{1}{2m}\begin{bmatrix} (m-1)(v_{py_1}-v_{ny_1}) - \sum_{y\neq y_1}^{y_m}(v_{py}-v_{ny}) \\ (m-1)(v_{py_2}-v_{ny_2}) - \sum_{y\neq y_2}^{y_m}(v_{py}-v_{ny}) \\ \vdots \\ (m-1)(v_{py_m}-v_{ny_m}) - \sum_{y\neq y_m}^{y_m}(v_{py}-v_{ny}) \end{bmatrix} \\ \mathbf{V_c} = \frac{V_{DC}}{4}\begin{bmatrix} \Delta_d \cdot \cos(\omega_o t - \varphi_{y_1}) \\ \Delta_d \cdot \cos(\omega_o t - \varphi_{y_2}) \\ \vdots \\ \Delta_d \cdot \cos(\omega_o t - \varphi_{y_m}) \end{bmatrix} \end{cases} \tag{A.131}$$

$$\begin{cases} \mathbf{V_o} = -\frac{1}{2}N_\Delta(m)\left(\mathbf{V_{py}}+\mathbf{V_{ny}}\right) = -\frac{1}{2m}\begin{bmatrix} (m-1)(v_{py_1}+v_{ny_1}) - \sum_{y\neq y_1}^{y_m}(v_{py}+v_{ny}) \\ (m-1)(v_{py_2}+v_{ny_2}) - \sum_{y\neq y_2}^{y_m}(v_{py}+v_{ny}) \\ \vdots \\ (m-1)(v_{py_m}+v_{ny_m}) - \sum_{y\neq y_m}^{y_m}(v_{py}+v_{ny}) \end{bmatrix} \\ \mathbf{V_o} = \frac{V_{DC}}{4}\begin{bmatrix} \Sigma_d \cdot \cos(\omega_o t - \varphi_{y_1}) \\ \Sigma_d \cdot \cos(\omega_o t - \varphi_{y_2}) \\ \vdots \\ \Sigma_d \cdot \cos(\omega_o t - \varphi_{y_m}) \end{bmatrix} \end{cases} \tag{A.132}$$

This can be summarized as:

$$\begin{cases} v_m = -\frac{V_{DC}}{4}\Delta_m \\ v_s = -\frac{V_{DC}}{4}\Sigma_m \\ v_{c_y} = \frac{V_{DC}}{4}\Delta_d \cdot \cos(\omega_o t - \varphi_y) \\ v_{o_y} = \frac{V_{DC}}{4}\Sigma_d \cdot \cos(\omega_o t - \varphi_y) \end{cases} \tag{A.133}$$

Thus the equation (A.124) takes the shape:

$$\begin{cases} Z_m(t)i_m = -\frac{V_{DC}}{4}\Delta_m - v_{n_{AD}} \\ Z_s(t)i_s = -\frac{V_{DC}}{4}\Sigma_m + \frac{V_{DC}}{2} \\ Z_c(t)i_{c_y} = \frac{V_{DC}}{4}\left[\Delta_d \cdot \cos(\omega_o t - \varphi_y)\right] \\ Z_o(t)i_{o_y} = \frac{V_{DC}}{4}\left[\Sigma_d \cdot \cos(\omega_o t - \varphi_y)\right] - v_y \end{cases} \tag{A.134}$$

Moreover, by the assumption 8, it is assumed that the output AC network $\mathbf{V_y}$ is balanced. As seen previously, the AC currents $\mathbf{I_c}$ and $\mathbf{I_o}$ are also considered balanced by the assumption 6. Therefore these vectors can be defined from an amplitude and a phase at the origin:

$$\mathbf{V_y} = \hat{V}_{AC}\begin{bmatrix} \cos(\omega_o t - \varphi_{y_1} - \varphi_v) \\ \cos(\omega_o t - \varphi_{y_2} - \varphi_v) \\ \vdots \\ \cos(\omega_o t - \varphi_{y_m} - \varphi_v) \end{bmatrix}$$

$$\mathbf{I_c} = \hat{I}_c\begin{bmatrix} \cos(\omega_o t - \varphi_{y_1} - \varphi_c) \\ \cos(\omega_o t - \varphi_{y_2} - \varphi_c) \\ \vdots \\ \cos(\omega_o t - \varphi_{y_m} - \varphi_c) \end{bmatrix} \tag{A.135}$$

$$\mathbf{I_o} = \hat{I}_o\begin{bmatrix} \cos(\omega_o t - \varphi_{y_1} - \varphi_o) \\ \cos(\omega_o t - \varphi_{y_2} - \varphi_o) \\ \vdots \\ \cos(\omega_o t - \varphi_{y_m} - \varphi_o) \end{bmatrix}$$

With $\hat{V}_{AC}$, $\hat{I}_c$, $\hat{I}_o$ the respective amplitudes of the harmonic components of $\mathbf{V_y}$, $\mathbf{I_c}$, $\mathbf{I_o}$; and φ_v, φ_c, φ_o their phases at the origin. Currents with only one component can be defined from a steady state amplitude:

$$\begin{aligned} I_m &= \hat{I}_m \\ I_s &= \hat{I}_s \end{aligned} \tag{A.136}$$

The purpose of the analysis of the zone of operation is to determine the maximum amplitudes that can be reached by each type of current. It is not necessary to look at each of the components of the vectors representing the AC electrical quantities. The choice is therefore made to focus only on the $\#k$ component of the vectors:

$$\begin{aligned} v_y &= \hat{V}_{AC}\left[\cos(\omega_o t - \varphi_y - \varphi_v)\right] \\ i_{c_y} &= \hat{I}_c\left[\cos(\omega_o t - \varphi_y - \varphi_c)\right] \\ i_{o_y} &= \hat{I}_o\left[\cos(\omega_o t - \varphi_y - \varphi_o)\right] \\ i_m &= \hat{I}_m \\ i_s &= \hat{I}_s \end{aligned} \tag{A.137}$$

By substituting v_y, i_{o_y}, i_{c_y}, i_m and i_s in (A.134), it comes that:

$$\begin{cases} Z_m(t)\hat{I}_m = -\frac{V_{DC}}{4}\Delta_m - v_{n_{AD}} \\ Z_s(t)\hat{I}_s = -\frac{V_{DC}}{4}\Sigma_m + \frac{V_{DC}}{2} \\ Z_c(t)\hat{I}_c\left[\cos(\omega_o t - \varphi_y - \varphi_c)\right] = \frac{V_{DC}}{4}\left[\Delta_d \cdot \cos(\omega_o t - \varphi_y)\right] \\ Z_o(t)\hat{I}_o\left[\cos(\omega_o t - \varphi_y - \varphi_o)\right] = \frac{V_{DC}}{4}\left[\Sigma_d \cdot \cos(\omega_o t - \varphi_y)\right] - \hat{V}_{AC}\left[\cos(\omega_o t - \varphi_y - \varphi_v)\right] \end{cases} \tag{A.138}$$

In electrical steady state, the currents $\mathbf{I_c}$ and $\mathbf{I_o}$ are characterized by a fundamental component while the currents I_m and I_s are continuous. Thus, in steady state, the impedances $Z_m(t)$ and $Z_s(t)$ of the currents I_m and I_s become $Z_m = R_m^{eq}$ and $Z_s = R_m^{eq}$ while those of the currents $\mathbf{I_c}$ and $\mathbf{I_o}$ become $\underline{Z_c} = R_c^{eq} + jL_c^{eq}\omega_c$ et $\underline{Z_o} = R_o^{eq} + jL_o^{eq}\omega_o$. Let ω_c and ω_o be the frequencies associated with the currents $\mathbf{I_c}$ and $\mathbf{I_o}$ in steady state. In the case of the assumption 9 it is important to mention that $\omega_c = \omega_o$. Focusing on the amplitude of the electrical quantities and their evaluation, it is of interest to pass (A.138) in complex form. For this, the phase reference is chosen to be the phase of the control voltages: $cos(\omega_o t - \varphi_y)$. The following notations are thus introduced:

$$\begin{cases} v_y = \hat{V}_{AC}\left[\cos(\omega_o t - \varphi_y - \varphi_v)\right] \\ i_{c_y} = \hat{I}_c\left[\cos(\omega_o t - \varphi_y - \varphi_c)\right] \\ i_{o_y} = \hat{I}_o\left[\cos(\omega_o t - \varphi_y - \varphi_o)\right] \end{cases} \Longrightarrow \begin{cases} \underline{v_y} = \hat{V}_{AC}\cdot e^{-j\varphi_v} = \underline{V_{AC}} \\ \underline{i_{c_y}} = \hat{I}_c\cdot e^{-j\varphi_c} = \underline{I_c} \\ \underline{i_{o_y}} = \hat{I}_o\cdot e^{-j\varphi_o} = \underline{I_o} \end{cases} \tag{A.139}$$

With $\underline{V_{AC}}$, $\underline{I_c}$ and $\underline{I_o}$, notations introduced to represent complex phasors. Using complex formatting, (A.138) thus becomes:

$$\begin{cases} Z_m\,\hat{I}_m = -\frac{V_{DC}}{4}\Delta_m - V_{n_{AD}} \\ Z_s\,\hat{I}_s = -\frac{V_{DC}}{4}\Sigma_m + \frac{V_{DC}}{2} \\ \underline{Z_c}\,\underline{I_c} = \frac{V_{DC}}{4}\Delta_d \\ \underline{Z_o}\,\underline{I_o} = \frac{V_{DC}}{4}\Sigma_d - \underline{V_{AC}} \end{cases} \tag{A.140}$$

Introducing $\hat{V}_m$, $\hat{V}_s$ the amplitude from the control voltages of the common-mode and steady-state source currents, as well as $\underline{V_c}$ and $\underline{V_o}$ the complex variables representing the control voltages of the circulating current and the output current, it comes that:

$$\begin{cases} \hat{V}_m = -\frac{V_{DC}}{4}\Delta_m = Z_m\hat{I}_m + V_{n_{AD}} \\ \hat{V}_s = -\frac{V_{DC}}{4}\Sigma_m = Z_s\hat{I}_s - \frac{V_{DC}}{2} \\ \underline{V_c} = +\frac{V_{DC}}{4}\Delta_d = \underline{Z_c}\,\underline{I_c} \\ \underline{V_o} = +\frac{V_{DC}}{4}\Sigma_d = \underline{Z_o}\,\underline{I_o} + \hat{V}_{AC}\cdot e^{-j\varphi_v} \end{cases} \tag{A.141}$$

The norms of the complex impedances are then defined $Z_c = |\underline{Z_c}|$ and $Z_o = |\underline{Z_o}|$. The quantities $\hat{V}_c$ and $\hat{V}_o$ are the amplitudes of the different control voltages which all have a zero phase at the origin since they represent the reference of the phases in the complex reference frame, thus $\underline{V_c} = \hat{V}_c e^{j0} = \hat{V}_c$ and $\underline{V_o} = \hat{V}_o e^{j0} = \hat{V}_o$. It is then possible to determine the amplitude of the four types of currents depending on the different electrical parameters and the different supply and control voltages:

$$\begin{cases} \hat{I}_m = \frac{1}{Z_m}(\hat{V}_m - V_{n_{AD}}) = \frac{1}{Z_m}\left(-\frac{V_{DC}}{4}\Delta_m - V_{n_{AD}}\right) \\ \hat{I}_s = \frac{1}{Z_s}(\hat{V}_s + \frac{V_{DC}}{2}) = \frac{1}{Z_s}\left(-\frac{V_{DC}}{4}\Sigma_m + \frac{V_{DC}}{2}\right) \\ \hat{I}_c = \frac{1}{Z_c}\hat{V}_c = \frac{1}{Z_c}\frac{V_{DC}}{4}\Delta_d \\ \hat{I}_o = \frac{1}{Z_o}|\hat{V}_o - \hat{V}_{AC}\cdot e^{-j\varphi_v}| = \frac{1}{Z_o}\left|\frac{V_{DC}}{4}\Sigma_d - \hat{V}_{AC}\cdot e^{-j\varphi_v}\right| \end{cases} \tag{A.142}$$

It is from this equation (A.142) that the analysis of the operating zone according to the limits of the control voltages can be carried out. To do this, one must first evaluate the limits of the voltages $\hat{V}_m$, $\hat{V}_s$, $\hat{V}_c$ and $\hat{V}_o$ and thus those of Δ_m, Σ_m, Δ_d and Σ_d which define them respectively.

Current control voltage limits

From the system point of view, the control limits are imposed to the voltages that can be reached at the terminals of the arms, these voltages are $\mathbf{V_{py}}$ and $\mathbf{V_{ny}}$ which are defined from their components v_{py} et v_{ny}. According to (A.127), these components themselves depend on Δ_m, Σ_m, Δ_d and Σ_d. It will therefore be possible to determine the limits of the terms Δ_m, Σ_m, Δ_d and Σ_d by knowing the limits imposed on $\mathbf{V_{py}}$ and $\mathbf{V_{ny}}$. Under the assumption 6 the components of these last two vectors have, in absolute value, the same limits. This is due to the fact that in steady state it is considered that all capacitors are loaded to their nominal value and that this value does not change over time.

The voltage limits that can be reached by $\mathbf{V_{py}}$ and $\mathbf{V_{ny}}$ depend on the choice made for the submodules that make up the converter:

- In the case of the half-bridge submodules made up of a half-bridge, the voltages in the arm will be limited between $0\ V$ and V_{DC} because the capacitors can only be connected directly to the arm to which they belong, thus:

$$\begin{cases} \forall y \in \{y_1, \ldots, y_m\}, 0 \leq v_{py} \leq V_{DC} \\ \forall y \in \{y_1, \ldots, y_m\}, -V_{DC} \leq v_{ny} \leq 0 \end{cases} \quad \text{(A.143)}$$

  Using the relationships $v_{py} = m_{py} V_{DC}$ and $v_{ny} = m_{ny} V_{DC}$, it comes thus:

$$\begin{cases} \forall y \in \{y_1, \ldots, y_m\}, 0 \leq m_{py} \leq 1 \\ \forall y \in \{y_1, \ldots, y_m\}, -1 \leq m_{ny} \leq 0 \end{cases} \quad \text{(A.144)}$$

- In the case of the full-bridge submodules made up of a full-bridge, each conversion cell can connect its capacitor in reverse to the arm, allowing the arm to feature a negative voltage at its terminals. The voltages in the arms will thus be limited between $-V_{DC}$ and V_{DC}:

$$\begin{cases} \forall y \in \{y_1, \ldots, y_m\}, -V_{DC} \leq v_{py} \leq V_{DC} \\ \forall y \in \{y_1, \ldots, y_m\}, -V_{DC} \leq v_{ny} \leq V_{DC} \end{cases} \quad \text{(A.145)}$$

  Thus, by definition of v_{py} and v_{ny}:

$$\begin{cases} \forall y \in \{y_1, \ldots, y_m\}, -1 \leq m_{py} \leq 1 \\ \forall y \in \{y_1, \ldots, y_m\}, -1 \leq m_{ny} \leq 1 \end{cases} \quad \text{(A.146)}$$

It is then decided to introduce the notation q, allowing to take into account the choice of the submodule type, such as:

$$q = \begin{cases} 1, \text{ for the choice of the SM-HB} \\ 2, \text{ for the choice of the SM-FB} \end{cases} \quad \text{(A.147)}$$

The introduction of this variable allows us to summarize the various limitations just mentioned for m_{py} and m_{ny} in the following way:

$$\begin{cases} \forall y \in \{y_1, \ldots, y_m\}, 1 - q \leq m_{py} \leq 1 \\ \forall y \in \{y_1, \ldots, y_m\}, -1 \leq m_{ny} \leq q - 1 \end{cases} \quad \text{(A.148)}$$

Dividing (A.125) by V_{DC}, the definitions of m_{py} and m_{ny} are obtained:

$$\forall y \in \{y_1, \ldots, y_m\}, \begin{cases} m_{py} = \frac{1}{2}\left[m_p - d_p \cdot \cos(\omega_o t - \varphi_y)\right] \\ m_{ny} = -\frac{1}{2}\left[m_n + d_n \cdot \cos(\omega_o t - \varphi_y)\right] \end{cases} \tag{A.149}$$

The equation (A.148) describes the limits that are imposed on m_{py} and m_{ny}. It is from these limits that it is possible to deduce those imposed on m_p, m_n, d_p and d_n. To do so, an analysis of the values reached by m_{py} and m_{ny} is necessary:

$$\begin{cases} \underset{t}{max}(m_{py}) = \frac{1}{2}\left[m_p - \underset{t}{min}\left(d_p \cdot \cos(\omega_o t - \varphi_y)\right)\right] = \frac{1}{2}\left[m_p + |d_p|\right] = \frac{m_p + |d_p|}{2} \\ \underset{t}{min}(m_{py}) = \frac{1}{2}\left[m_p - \underset{t}{max}\left(d_p \cdot \cos(\omega_o t - \varphi_y)\right)\right] = \frac{1}{2}\left[m_p - |d_p|\right] = \frac{m_p - |d_p|}{2} \end{cases} \tag{A.150}$$

$$\begin{cases} \underset{t}{max}(m_{ny}) = -\frac{1}{2}\left[m_n + \underset{t}{min}\left(d_n \cdot \cos(\omega_o t - \varphi_y)\right)\right] = -\frac{1}{2}\left[m_n - |d_n|\right] = \frac{-m_n + |d_n|}{2} \\ \underset{t}{min}(m_{ny}) = -\frac{1}{2}\left[m_n + \underset{t}{max}\left(d_n \cdot \cos(\omega_o t - \varphi_y)\right)\right] = -\frac{1}{2}\left[m_n + |d_n|\right] = \frac{-m_n - |d_n|}{2} \end{cases} \tag{A.151}$$

Combining this result with the equation (A.148), the following constraints are obtained:

$$\begin{cases} \frac{m_p + |d_p|}{2} \leq 1 \\ \frac{m_p - |d_p|}{2} \geq 1 - q \\ \frac{-m_n + |d_n|}{2} \leq q - 1 \\ \frac{-m_n - |d_n|}{2} \geq -1 \end{cases} \iff \begin{cases} m_p + |d_p| \leq 2 \\ m_p - |d_p| \geq 2(1-q) \\ -m_n + |d_n| \leq 2(q-1) \\ -m_n - |d_n| \geq -2 \end{cases} \tag{A.152}$$

It is from these constraints that it will be possible to deduce those on the control voltages of the currents. It is possible to visualize the constraints expressed above in the following way:

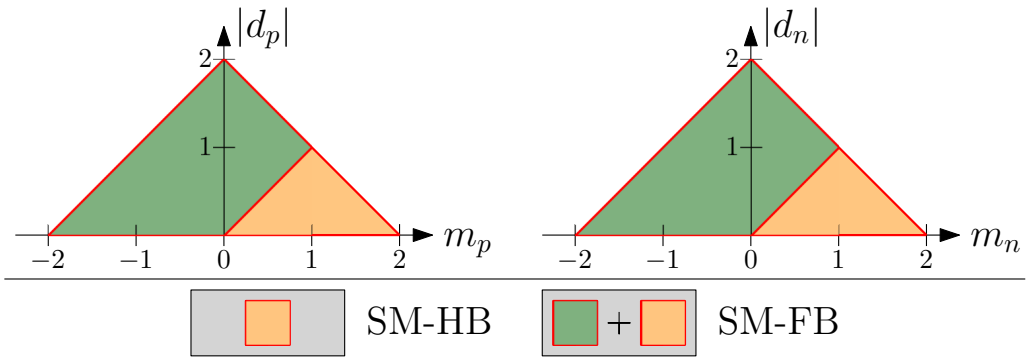

Figure 16: Control-limited operating zone in the maps $(m_p, |d_p|)$ and $(m_n, |d_n|)$

Depending on the choice of submodule, this figure shows the operating zone that can be reached by the system from the point of view of the control; it is interesting to note that the use of full-bridge submodules enables a larger operating zone. This is consitent since in this case it is then possible for the capacitors to impose their voltage in reverse on the terminals of the arm to which they belong: there is then a wider operating freedom.

Taking into account the absolute values, the operating domain becomes that represented by Figure 17.

The next step consists in translating this zone of operation in the maps having for variables Σ_m,

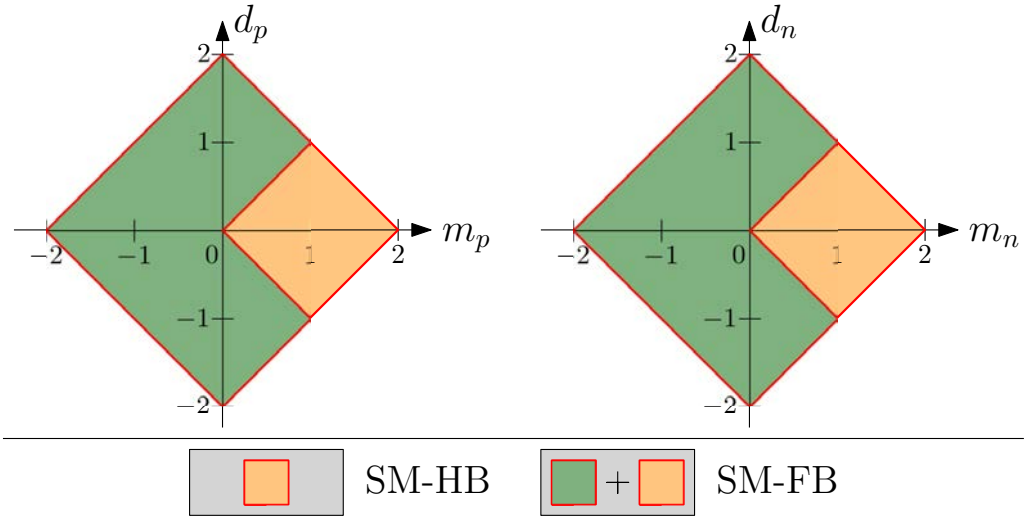

Figure 17: Control-limited operating zone in the maps (m_p, d_p) and (m_n, d_n)

Δ_m, Σ_d and Δ_d. To do so, mathematical operations will be applied to the constraints:

$$\begin{cases} (a): \ m_p + |d_p| \leq 2 \\ (b): \ m_p - |d_p| \geq 2(1-q) \\ (c): \ -m_n + |d_n| \leq 2(q-1) \\ (d): \ -m_n - |d_n| \geq -2 \end{cases} \tag{A.153}$$

By adding constraints:

$$\begin{cases} (a)+(c): \ (m_p - m_n) + (|d_p| + |d_n|) \leq 2q \\ (b)+(d): \ (m_p - m_n) - (|d_p| + |d_n|) \geq -2q \end{cases} \iff \begin{cases} (a)+(c): \ \Delta_m + (|d_p| + |d_n|) \leq 2q \\ (b)+(d): \ \Delta_m - (|d_p| + |d_n|) \geq -2q \end{cases} \tag{A.154}$$

By subtracting constraints:

$$\begin{cases} (b)-(c): \ (m_p + m_n) - (|d_p| + |d_n|) \geq 4(1-q) \\ (a)-(d): \ (m_p + m_n) + (|d_p| + |d_n|) \leq 4 \end{cases} \iff \begin{cases} (b)-(c): \ \Sigma_m - (|d_p| + |d_n|) \geq 4(1-q) \\ (a)-(d): \ \Sigma_m + (|d_p| + |d_n|) \leq 4 \end{cases} \tag{A.155}$$

This opens up the possibility of an analysis of these new constraints in the four possible cases resulting from the four different combinations of: $d_p \geq 0$, $d_n \geq 0$, $d_p \leq 0$ et $d_n \leq 0$. From this analysis the Figure 18 representation of the operation zone is deduced.

Thus are obtained the graphical representations of the limits of Σ_m, Δ_m, Σ_d and Δ_d and the relations between the limits of these variables. It is then recalled that (A.141) describes the relationship between these latter variables, the control voltages of the four types of currents and the

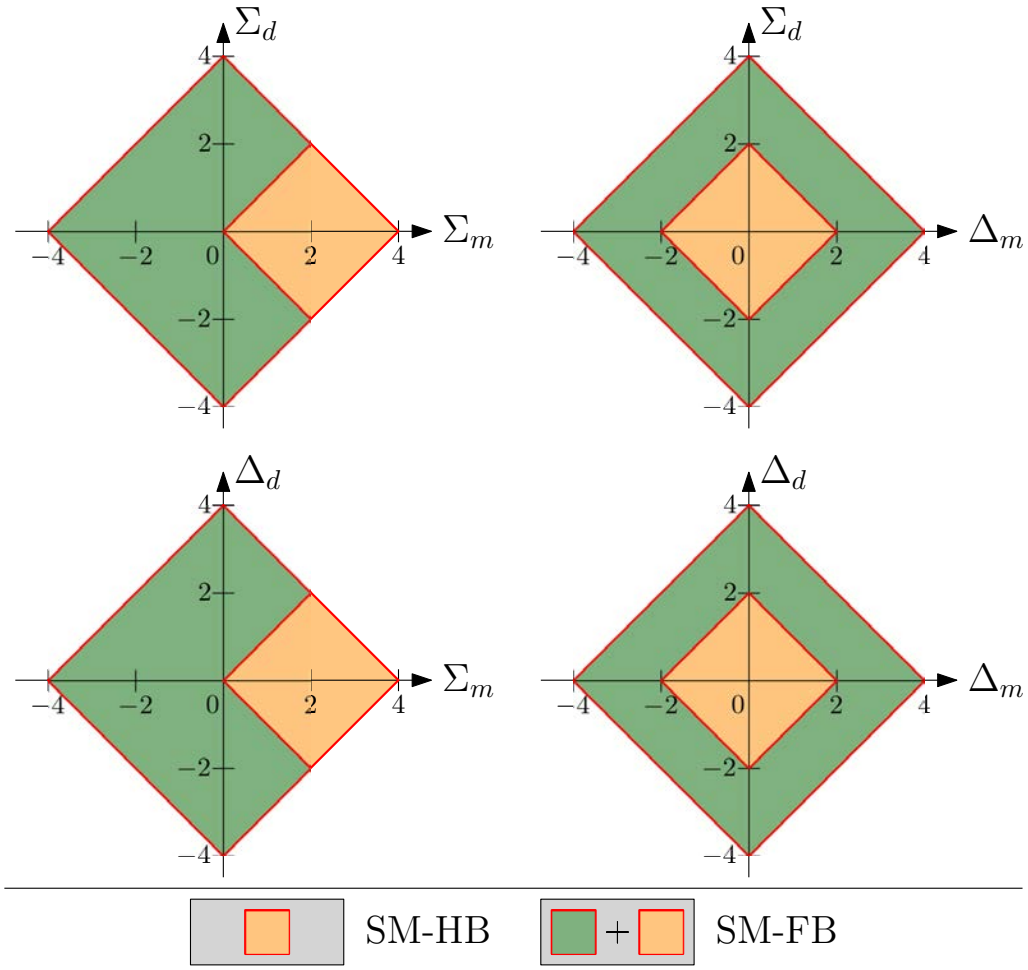

Figure 18: Control-limited operating zone in the maps (Σ_d, Σ_m), (Σ_d, Δ_m), (Δ_d, Σ_m) and (Δ_d, Δ_m)

currents:

$$\begin{cases} \hat{I}_m = \frac{1}{Z_m}(\hat{V}_m - V_{n_{AD}}) = \frac{1}{Z_m}\left(-\frac{V_{DC}}{4}\Delta_m - V_{n_{AD}}\right) \\ \hat{I}_s = \frac{1}{Z_s}(\hat{V}_s + \frac{V_{DC}}{2}) = \frac{1}{Z_s}\left(-\frac{V_{DC}}{4}\Sigma_m + \frac{V_{DC}}{2}\right) \\ \hat{I}_c = \frac{1}{Z_c}\hat{V}_c = \frac{1}{Z_c}\frac{V_{DC}}{4}\Delta_d \\ \hat{I}_o = \frac{1}{Z_o}|\hat{V}_o - \hat{V}_{AC}\cdot e^{-j\varphi_v}| = \frac{1}{Z_o}\left|\frac{V_{DC}}{4}\Sigma_d - \hat{V}_{AC}\cdot e^{-j\varphi_v}\right| \end{cases} \tag{A.156}$$

By the equation (A.156) it is possible to translate the Figure 18 in the maps $(\hat{V}_o, \hat{V}_s)$, $(\hat{V}_o, \hat{V}_m)$, $(\hat{V}_c, \hat{V}_s)$ and $(\hat{V}_c, \hat{V}_m)$. Which gives Figure 19.

The limits of the operating zone are then obtained for the four voltages in charge of driving the four different types of currents. Depending on the choice of type of submodules, the figure shows

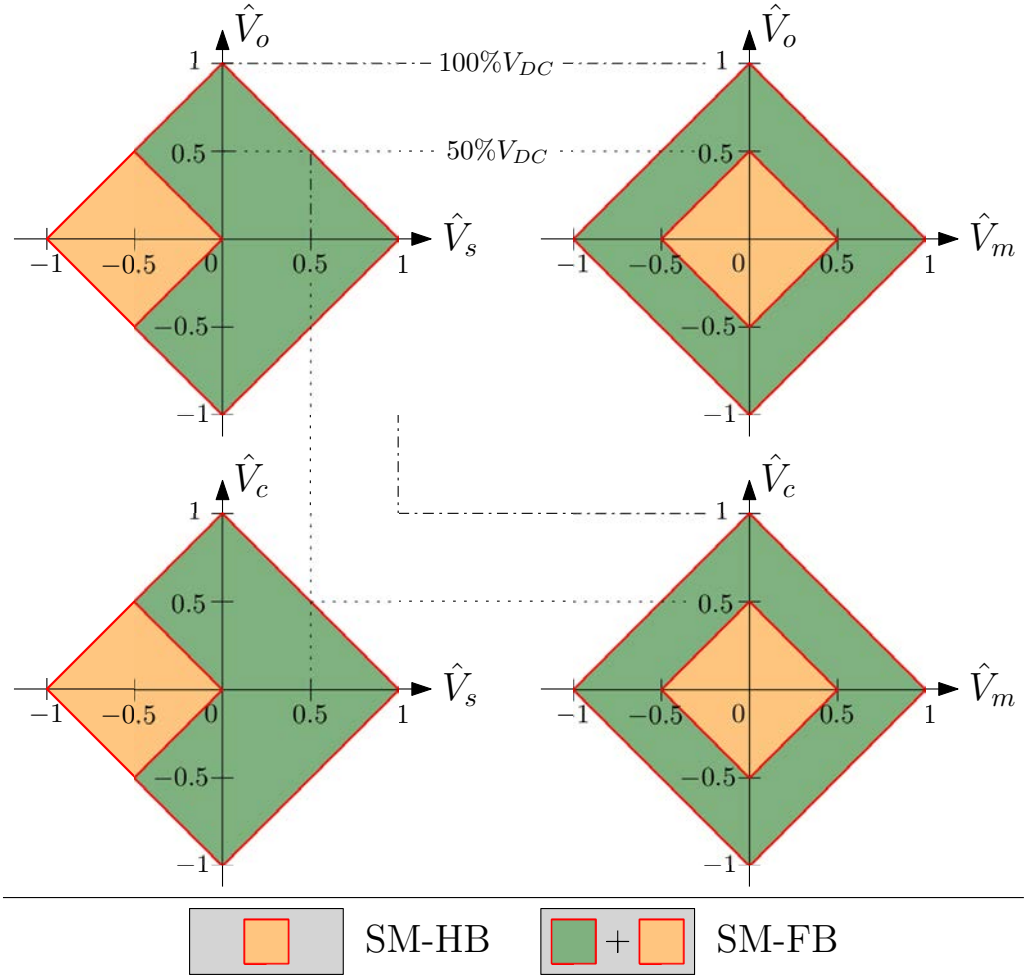

Figure 19: Control-limited operating zone in the maps $(\hat{V}_o, \hat{V}_s)$, $(\hat{V}_o, \hat{V}_m)$, $(\hat{V}_c, \hat{V}_s)$ and $(\hat{V}_c, \hat{V}_m)$

that:

$$\begin{cases} max(\hat{V}_m) = \hat{V}_m^{max} = \frac{q}{2}V_{DC} \\ max(\hat{V}_s) = \hat{V}_s^{max} = (q-1)V_{DC} \\ max(\hat{V}_c) = \hat{V}_c^{max} = \frac{q}{2}V_{DC} \\ max(\hat{V}_o) = \hat{V}_o^{max} = \frac{q}{2}V_{DC} \end{cases} \quad \begin{cases} min(\hat{V}_m) = \hat{V}_m^{min} = -\frac{q}{2}V_{DC} \\ min(\hat{V}_s) = \hat{V}_s^{min} = -V_{DC} \\ min(\hat{V}_c) = \hat{V}_c^{min} = -\frac{q}{2}V_{DC} \\ min(\hat{V}_o) = \hat{V}_o^{min} = -\frac{q}{2}V_{DC} \end{cases} \tag{A.157}$$

The last step will therefore be to move from these limitations in the control voltage map to limitations in the current map.

Limits of the currents by the limitation of their control voltages

The equation (A.156) describing the link between the control voltages of the currents and these currents allows one to translate the limitations in a map linked to the currents. For easier reading, the representation will remain in the form of voltages and not currents:

By combining the equations (A.157) and (A.142), it is possible to determine the maximum currents

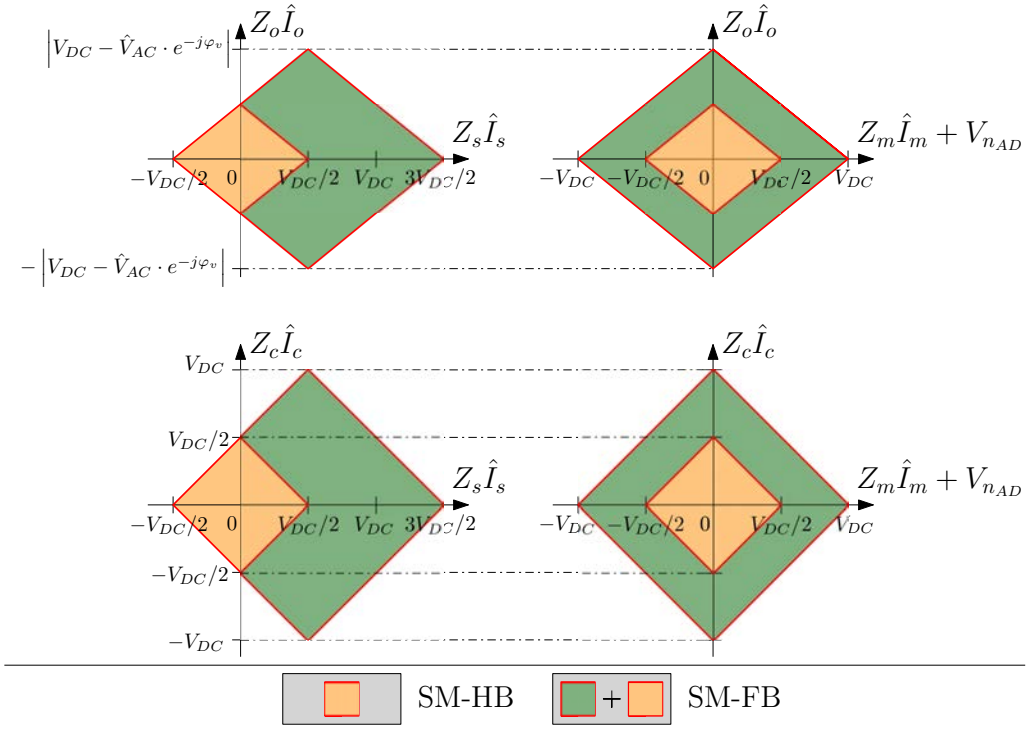

Figure 20: Control-limited operating zone in the voltage maps $(Z_o\hat{I}_o, Z_s\hat{I}_s)$, $(Z_o\hat{I}_o, Z_m\hat{I}_m)$, $(Z_c\hat{I}_c, Z_s\hat{I}_s)$ et $(Z_c\hat{I}_c, Z_m\hat{I}_m)$

magnitudes for control voltages reaching their limits:

$$\begin{cases} \hat{I}_m^{max} = \frac{1}{Z_m}\left(\frac{q}{2}V_{DC} - V_{n_{AD}}\right) \\ \hat{I}_s^{max} = \frac{1}{Z_s}\left(q - \frac{1}{2}\right)V_{DC} \\ \hat{I}_c^{max} = \frac{1}{Z_c}\frac{q}{2}V_{DC} \\ \hat{I}_o^{max} = \frac{1}{Z_o}\left|\frac{q}{2}V_{DC} - \hat{V}_{AC} \cdot e^{-j\varphi_v}\right| \end{cases} \quad \begin{cases} \hat{I}_m^{min} = \frac{1}{Z_m}\left(-\frac{q}{2}V_{DC} - V_{n_{AD}}\right) \\ \hat{I}_s^{min} = -\frac{1}{Z_s}\frac{1}{2}V_{DC} \\ \hat{I}_c^{min} = -\frac{1}{Z_c}\frac{q}{2}V_{DC} \\ \hat{I}_o^{min} = \frac{1}{Z_o}\left|-\frac{q}{2}V_{DC} + \hat{V}_{AC} \cdot e^{-j\varphi_v}\right| \end{cases} \tag{A.158}$$

Remarks:

- It is important to note that these expressions represent the maximum magnitudes of the four types of currents in the case where the voltages driving them reach their own limits. These are current limits obtained from the control point of view and not from the physical point of view. Indeed, additional physical limits, such as the current allowed by the semiconductors or a power limit imposed by the DC bus power, may shrink the operating zone described by the Figure 20 and the equation (A.158).
- Equation (A.158) shows that when the AC and DC neutrals are disconnected, and thus I_m is forced to zero, the potential of the AC neutral point can be moved such that:

$$-\frac{q}{2}V_{DC} \leq V_{n_{AD}} \leq \frac{q}{2}V_{DC} \tag{A.159}$$

De ce fait $\hat{V}_{n_{AD}}^{max} = \frac{q}{2}V_{DC}$ et $\hat{V}_{n_{AD}}^{min} = -\frac{q}{2}V_{DC}$.

Limits of the input and output powers of the converter

An important quantity in the sizing of an inverter is the rated apparent power that it can deliver. It is therefore interesting to evaluate this power, here noted S_o.

The power absorbed by the converter on the DC bus is expressed as $P_s = P_{DC} - P_s^{loss} = V_{DC}I_{DC} - 2R_s{I_{DC}}^2$, that delivered on the active AC network at the output is expressed as an average value $S_{AC} = \frac{m}{2}\left|\underline{V_{AC}} \cdot \underline{I_{AC}}^*\right| = \frac{m}{2}\hat{V}_{AC}\hat{I}_{AC}$ and the one that the converter distributes on the whole output AC network (load and active network) is $S_o = \frac{m}{2}\left|\underline{V'_o} \cdot \underline{I_{AC}}^*\right| = \frac{m}{2}\hat{V}'_o \cdot \hat{I}_{AC}$ avec $\underline{V'_o} = (R_o + j\omega_o L_o)\underline{I_{AC}} + \underline{V_{AC}}$. In a nominal operation where the networks are balanced as well as the capacitors, it comes that:

$$\begin{cases} \hat{I}_s = I_{DC}/m \\ \hat{I}_o = \hat{I}_{AC}/2 \end{cases} \quad \text{(A.160)}$$

Thus, the powers previously introduced can be expressed:

$$\begin{cases} P_s = mV_{DC}\hat{I}_s - 2R_s m^2 {\hat{I}_s}^2 \\ S_{AC} = m\left|\underline{V_{AC}} \cdot \underline{I_o}^*\right| = m\hat{V}_{AC}\hat{I}_o \\ S_o = m\left|\underline{V'_o} \cdot \underline{I_o}^*\right| = m\hat{V}'_o\hat{I}_o \end{cases} \quad \text{(A.161)}$$

By (A.142), it comes that:

$$\begin{cases} \hat{I}_s = \frac{1}{Z_s}\left(\hat{V}_s + \frac{V_{DC}}{2}\right) \\ \hat{I}_o = \frac{1}{Z_o}\left|\hat{V}_o - \hat{V}_{AC} \cdot e^{-j\varphi_v}\right| = \frac{1}{Z_o}\sqrt{{\hat{V}_o}^2 - 2\hat{V}_o\hat{V}_{AC}\cos\varphi_v + {\hat{V}_{AC}}^2} \end{cases} \quad \text{(A.162)}$$

Furthermore:

$$\begin{aligned} &\underline{V'_o} = (R_o + j\omega_o L_o)2\underline{I_o} + \underline{V_{AC}} = (R_o + j\omega_o L_o)2\hat{I}_o\, e^{-j\mathbf{\Phi_o}} + \hat{V}_{AC}\, e^{-j\varphi_v} \\ &\underline{I_o} = \frac{1}{\underline{Z_o}}\left(\hat{V}_o - \hat{V}_{AC} \cdot e^{-j\varphi_v}\right) \end{aligned} \quad \text{(A.163)}$$

By substitution of these current expressions in the power expressions, it is shown that:

$$\begin{cases} P_s = \frac{m}{Z_s}\left(\hat{V}_s + \frac{V_{DC}}{2}\right)V_{DC} - \frac{2R_s m^2}{{Z_s}^2}\left(\hat{V}_s + \frac{V_{DC}}{2}\right)^2 \\ S_{AC} = \frac{m}{Z_o}\hat{V}_{AC}\sqrt{{\hat{V}_o}^2 - 2\hat{V}_o\hat{V}_{AC}\cos\varphi_v + {\hat{V}_{AC}}^2} \\ S_o = m\left|(R_o + j\omega_o L_o)2{\hat{I}_o}^2 + \underline{V_{AC}} \cdot \underline{I_o}^*\right| \end{cases} \quad \text{(A.164)}$$

By substitution of $\hat{I}_o$ and $\underline{I_o}^*$ by their analytical expressions in S_o, it is possible to arrive, after several development steps, at:

$$S_o = m\left|\frac{\left(\hat{V}_{AC}\, e^{-j\varphi_v} + \frac{2(R_o + j\omega_o L_o)\left(\hat{V}_o - \hat{V}_{AC}\, e^{-j\varphi_v}\right)}{(R+2R_o) + j\omega_o(L+2L_o)}\right)\left(\hat{V}_o - \hat{V}_{AC}\, e^{+j\varphi_v}\right)}{(R + 2R_o) + j\omega_o(L + 2L_o)}\right| \quad \text{(A.165)}$$

The above expressions therefore make it possible to evaluate the evolution of the different powers according to variable parameters such as the alternating load (R_o, L_o), the alternating network ($\hat{V}_{AC}$, φ_v), and the output current control voltage ($\hat{V}_o$). It is of interest to analyze the evolution of S_o because it is the apparent power which comes out directly from the converter and during the sizing of the latter, a nominal value of this power is determined. The analysis of S_o must

therefore make it possible to determine the bounds of the variable parameters (R_o, L_o, $\hat{V}_{AC}$, φ_v, $\hat{V}_o$) not to be exceeded so that the apparent power does not exceed the rated power provided. Particular attention must also be paid to the amplitude $\hat{I}_o$ of the output current because a low value of the impedance $R_o + j\omega_o L_o$ could make it possible to reach an amplitude of S_o close to its nominal value while having a too large magnitude for current $\hat{I}_o$, which must be prevented to remain within the physical operating limits.

In the case of the MMC experimental setup used in this study, the parameters $\hat{V}_{AC}$ and φ_v are null, embodying the fact that only a passive load is connected to the output of the converter. The use of the converter in such a configuration therefore makes it possible to simplify the expressions of the powers in the following way:

$$\begin{cases} P_{DC} = \frac{m}{Z_s}\left(\hat{V}_s + \frac{V_{DC}}{2}\right) V_{DC} \\ S_{AC} = 0 \\ S_o = m\hat{V_o}^2 \frac{2|R_o + j\omega_o L_o|}{{Z_o}^2} = 2m\,|R_o + j\omega_o L_o|\,{\hat{I}_o}^2 \end{cases} \tag{A.166}$$

with $\hat{I}_o = \hat{V}_o / Z_o$. The formula of S_o then obtained makes it possible to assert that S_o will reach its maximum when $\hat{V}_o$ has reached its own, i.e. $qV_{DC}/2$, which allows one to express S_o^{max} in terms of V_{DC}:

$$S_o^{max} = m\left(\frac{q}{2}V_{DC}\right)^2 \frac{2\sqrt{{R_o}^2 + {\omega_o}^2{L_o}^2}}{{Z_o}^2} = m\left(\frac{q}{2}V_{DC}\right)^2 \frac{2\sqrt{{R_o}^2 + {\omega_o}^2{L_o}^2}}{(R + 2R_o)^2 + {\omega_o}^2(L + 2L_o)^2} \tag{A.167}$$

Remark: It is interesting to note that the above formula allows the analysis of the evolution of the apparent power that the converter is able to convert at the maximum according to the number of phases of the AC network, the impedance of the arm of the converter, the impedance of the AC network, the voltage available on the DC bus and according to the type of submodules. An interesting property to notice is that switching from half-bridge submodules ($q = 1$) to full-bridge submodules ($q = 2$) makes it possible to multiply by 4 the apparent power that the converter can deliver.

Case study: limits of the MMC experimental setup

The experimental model of the MMC available to the LAPLACE laboratory presents the parameters which are described in the Table 19.

The equations (A.166) and (A.167) allow to know the evolution of S_o and $\hat{I}_o$ according to the control voltage of the output currents $\hat{V}_o$ and variable resistive load R_o. S_o reaching its maximum at the same time as $\hat{V}_o$, the analysis of the evolution of S_o according to R_o at $\hat{V}_o = qV_{DC}/2$ will show the value of R_o to ensure that S_o does not exceed its nominal value in operation. It is then plotted $S_o = f(R_o)$ and $\hat{I}_o = f(R_o)$ for $\hat{V}_o = \hat{V}_o^{max} = qV_{DC}/2$ in Figure 21.

The converter is rated to convert 10 kVA, the load bank to which it is connected will therefore make it possible to cover the entire operating range depending on the resistance selected. To ensure that the nominal power is not exceeded, one must choose $R_o \in [13.16\ \Omega; +\infty\ \Omega[$ to guarantee a current at least less than 22.42 A, operating cas at 100% of the rated apparent power. For example, if it is desired to limit the current $\hat{I}_{AC}^{max}$ to 7.486 A, it will be necessary to set $R_o \geq 40\ \Omega$, the maximum attainable apparent power value will be approximately 33.65% of the rated power, i.e. 3.365 kVA. It is then chosen $R_o = 40\ \Omega$ to limit the current in the load to 7.486 A in order to carry out the first test in a reduced operating zone which will reach at most approximately one third of rated power.

Paramètres du MMC		
Parameter	Notation	Value
DC Bus		
DC Bus voltage	V_{DC}	600 V
DC link impedance	R_s, L_s	50 mΩ, 2 mH
MMC		
Rated power	S_o^{nom}	10 kVA
Type of submodules	q	1 (half-bridge submodule)
Total number of submodules	$2mN$	18
Arm impedance	R, L	10 mΩ, 5 mH
AC Network		
Number of phases	m	3
AC active voltage amplitude	$\hat{V}_{AC}$	0 V
AC active voltage phase	φ_v	0 rad
Fondamental frequency and period of the network	f_o, T_o	50 Hz, 20 ms
Network pulsation	ω_o	$2\pi f_o \simeq 314$ rad/s
AC load impedance	R_o, L_o	Tunable, 40 Ω here, 0 mH

Table 19: Parameters table of the MMC

The application of the equation (A.158) developed here using the data from the Table 19 makes it possible to determine the extrema that can be reached by the various currents which occur during the operation of the converter. These values are entered in the Table 20.

Control-limited current boundaries		
Current	Lower boundary	Upper boundary
$\hat{I}_m$	$\hat{I}_m^{min} = -3.743$ A	$\hat{I}_m^{max} = +3.743$ A
$\hat{I}_s$	$\hat{I}_s^{min} = -1875$ A	$\hat{I}_s^{max} = +1875$ A
$\hat{I}_c$	$\hat{I}_c^{min} = -190.9$ A	$\hat{I}_c^{max} = +190.9$ A
$\hat{I}_o$	$\hat{I}_o^{min} = -3.749$ A	$\hat{I}_o^{max} = +3.749$ A

Table 20: Table of the control-limited current boundaries

It is then found that the circulating current and the source current can reach, when the control voltages reach their extrema, values well above the feasible current values of the semiconductors: 60 A. In addition, the current I_s, whose command limit is 1875 A, exceeds the physical limit imposed on it by the power that the DC bus can deliver. And $\mathbf{I_c}$ exceeds the limit imposed by the sizing of the inductors contained in the converter.

Thus, it is necessary to evaluate the effective operating area by projecting the control-limited operating zone into the feasible space of the maximum powers, voltages and current that the physical system can bear.

The DC bus being limited in power to 10 kW, with a voltage $V_{DC} =$ 600 V, the current I_{DC} will then be limited to 16.7 A i.e. 5.57 A for $\hat{I}_s$. The inductors of the converter arms L are sized for an alternating current with a maximum amplitude of 14 A. As regards the circulating current $\hat{I}_c$, it will therefore be limited to 14 A.

The combination of the control limits and the physical limits which are imposed on the currents leads to the values which are indicated in the Table 21.

The simulations and tests are therefore carried out taking into account all the different limitations

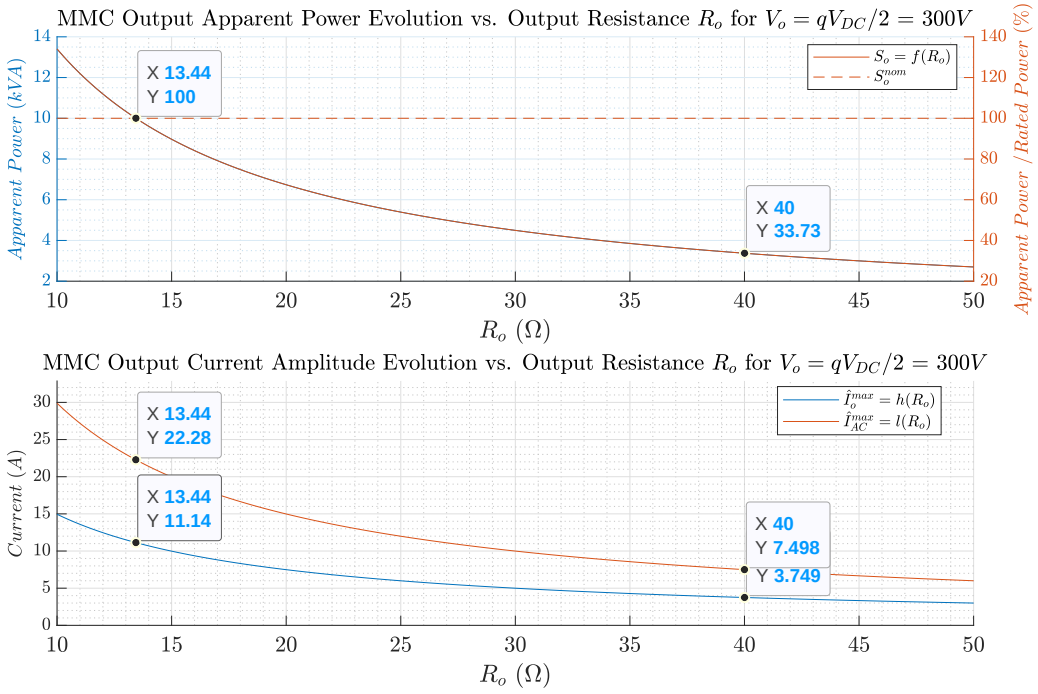

Figure 21: Evolution of the maximum apparent power and the output current as a function of the resistance of the AC network R_o on range $[10\,\Omega; 50\,\Omega]$

Control-limited current boundaries with physical limitations		
Current	Lower boundary	Upper boundary
$\hat{I}_m$	$\hat{I}_m^{min} = -3.743$ A	$\hat{I}_m^{max} = +3.743$ A
$\hat{I}_s$	$\hat{I}_s^{min} = -5.57$ A	$\hat{I}_s^{max} = +5.57$ A
$\hat{I}_c$	$\hat{I}_c^{min} = -14$ A	$\hat{I}_c^{max} = +14$ A
$\hat{I}_o$	$\hat{I}_o^{min} = -3.749$ A	$\hat{I}_o^{max} = +3.749$ A

Table 21: Table of current boudaries by projection into the space of feasible powers, voltages and currents

to which the currents are subject. So the values of Table 21 will be used. The maximum P_{DC} power that the DC bus will be able to supply will therefore be 10 kW and the maximum S_o apparent power that the converter can deliver will be 3.37 kVA .

However during the operation of the converter, in steady state the balance of the powers $P_s - P_{MMC}^{loss} = P_o$ must be guaranteed in order to ensure a quantity of energy E_{MMC} stable in the MMC. The powers $P_s - P_{MMC}^{loss}$ and P_o are plotted as a function of $\hat{I}_s$ and $\hat{I}_o$, for their maximum value ranges, in Figure 22. The power balance, obtained at the intersection of the surfaces representing each of the powers, is embodied by a red line. This figure highlights two elements:

- When operating in steady state, P_o will always be positive. Which is consistent with having a passive load in this case ($\hat{V}_{AC} = 0$): a MMC with these parameters can only operate in inverter mode.
- The maximum power that can be converted by the converter is 3.37 kW, this operating point is reached for $\hat{I}_o = 3.749$ A and $\hat{I}_s = 1.852$ A.

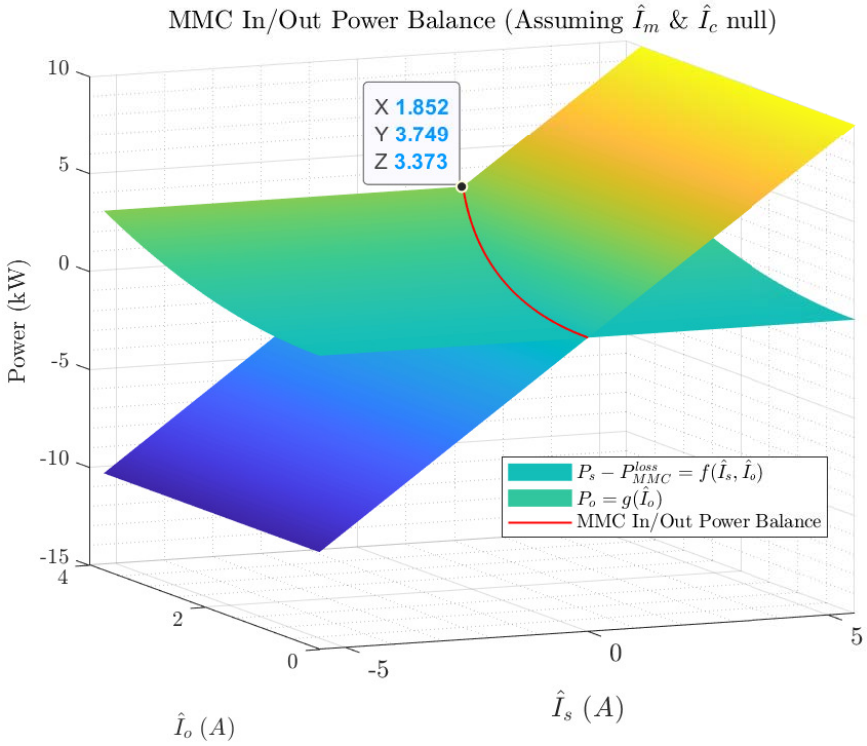

Figure 22: Evolution of the DC-AC power exchange operated by the converter for $R_o = 40\ \Omega$

J | Low-level allocation formulation in nominal operating case

In nominal operation the vector $\mathbf{T_{xy}}$ is zero and the matrix L_{xy} takes a particular simplified form. In this particular case, the matrices embodying the low-level control allocation problem for an arm take the form:

$$
\begin{aligned}
&M_{LL}^{xy}(k) = \sigma(x)\begin{bmatrix} v_{C_{x,y,1}}(k) & -v_{C_{x,y,1}}(k) & v_{C_{x,y,2}}(k) & -v_{C_{x,y,2}}(k) & \dots & v_{C_{x,y,N}}(k) & -v_{C_{x,y,N}}(k)\end{bmatrix}\\
&\mathbf{a_{d_{LL}}^{xy}}(k) = v_{xy}^{ref}(k)\\
&M_{pLL}^{xy}(k) = \frac{T_c}{C}\sigma(x) i_{xy}(k)\begin{bmatrix} 1 & -1 & 0 & 0 & \dots & 0 & 0\\ 0 & 0 & 1 & -1 & \dots & 0 & 0\\ 0 & 0 & 0 & 0 & \ddots & 0 & 0\\ 0 & 0 & 0 & 0 & \dots & 1 & -1\end{bmatrix}\\
&\mathbf{a_{pLL}^{xy}}(k) = \mathbf{v_{C_{xy}}^{ref}}(k) - \mathbf{v_{C_{xy}}}(k)
\end{aligned}
\tag{A.168}
$$

Ce qui donne une équation d'allocation de la forme:

$$
\begin{aligned}
&\begin{bmatrix} \sigma(x)\begin{bmatrix} v_{C_{x,y,1}}(k) & -v_{C_{x,y,1}}(k) & \dots & v_{C_{x,y,N}}(k) & -v_{C_{x,y,N}}(k)\end{bmatrix}\\ w_{v_C}{}^{\frac{1}{l}}\ \frac{T_c}{C}\sigma(x) i_{xy}(k)\begin{bmatrix} 1 & -1 & \dots & 0 & 0\\ 0 & 0 & \ddots & 0 & 0\\ 0 & 0 & \dots & 1 & -1\end{bmatrix}\end{bmatrix}\mathbf{D_{xy}^{e}}(k)\\
&\qquad = \begin{bmatrix} v_{xy}^{ref}(k)\\ w_{v_C}{}^{\frac{1}{l}}\left(v_{C_{x,y,1}}^{ref}(k) - v_{C_{x,y,1}}(k)\right)\\ \dots\\ w_{v_C}{}^{\frac{1}{l}}\left(v_{C_{x,y,N}}^{ref}(k) - v_{C_{x,y,N}}(k)\right)\end{bmatrix}
\end{aligned}
\tag{A.169}
$$

K | Low-level formulation of the entire MMC arms in one allocation

In order to take into account all the arms of the MMC in a single control allocation problem it is necessary to update the formulation made for a single arm (5.7) in order to extend it to the complete converter. One way to do this extension is to group the set of primary objectives of the LLC - namely, reference tracking of voltages across the arms - first, and then to group the secondary objectives of each of the arms. This, from (5.7), thus brings the following form:

$$M_{LL} = \begin{bmatrix} M_{LL}^{py_1} & & & & & & \\ & \ddots & & & & & \\ & & M_{LL}^{py_m} & & & & \\ & & & M_{LL}^{ny_1} & & & \\ & & & & \ddots & & \\ & & & & & M_{LL}^{ny_m} \end{bmatrix} \quad \mathbf{a_{dLL}} = \begin{bmatrix} \mathbf{a}_{\mathbf{d_{LL}}}^{\mathbf{py_1}} \\ \dots \\ \mathbf{a}_{\mathbf{d_{LL}}}^{\mathbf{py_m}} \\ \mathbf{a}_{\mathbf{d_{LL}}}^{\mathbf{ny_1}} \\ \dots \\ \mathbf{a}_{\mathbf{d_{LL}}}^{\mathbf{ny_m}} \end{bmatrix} \tag{A.170}$$

$$M_{pLL} = \begin{bmatrix} M_{pLL}^{py_1} & & & & & & \\ & \ddots & & & & & \\ & & M_{pLL}^{py_m} & & & & \\ & & & M_{pLL}^{ny_1} & & & \\ & & & & \ddots & & \\ & & & & & M_{pLL}^{ny_m} \end{bmatrix} \quad \mathbf{a_{pLL}} = \begin{bmatrix} \mathbf{a}_{\mathbf{p_{LL}}}^{\mathbf{py_1}} \\ \dots \\ \mathbf{a}_{\mathbf{p_{LL}}}^{\mathbf{py_m}} \\ \mathbf{a}_{\mathbf{p_{LL}}}^{\mathbf{ny_1}} \\ \dots \\ \mathbf{a}_{\mathbf{p_{LL}}}^{\mathbf{ny_m}} \end{bmatrix} \tag{A.171}$$

$$\mathbf{D^e} = \begin{bmatrix} \mathbf{D}_{\mathbf{py_1}}^{\mathbf{e}} \\ \vdots \\ \mathbf{D}_{\mathbf{py_m}}^{\mathbf{e}} \\ \mathbf{D}_{\mathbf{ny_1}}^{\mathbf{e}} \\ \vdots \\ \mathbf{D}_{\mathbf{ny_m}}^{\mathbf{e}} \end{bmatrix} \quad \mathbf{D^{e^{max}}} = \begin{bmatrix} \mathbf{D}_{\mathbf{py_1}}^{\mathbf{e^{max}}} \\ \vdots \\ \mathbf{D}_{\mathbf{py_m}}^{\mathbf{e^{max}}} \\ \mathbf{D}_{\mathbf{ny_1}}^{\mathbf{e^{max}}} \\ \vdots \\ \mathbf{D}_{\mathbf{ny_m}}^{\mathbf{e^{max}}} \end{bmatrix} \quad \mathbf{D^{e^{min}}} = \begin{bmatrix} \mathbf{D}_{\mathbf{py_1}}^{\mathbf{e^{min}}} \\ \vdots \\ \mathbf{D}_{\mathbf{py_m}}^{\mathbf{e^{min}}} \\ \mathbf{D}_{\mathbf{ny_1}}^{\mathbf{e^{min}}} \\ \vdots \\ \mathbf{D}_{\mathbf{ny_m}}^{\mathbf{e^{min}}} \end{bmatrix} \tag{A.172}$$

The complete control allocation problem is then deduced which represents the low-level control for the whole converter:

$$LLCAP:$$

$$\left\{ \begin{bmatrix} M_{LL}(k) \\ w_{v_C}{}^{\frac{1}{l}} M_{pLL}(k) \end{bmatrix} \mathbf{U_{LL}}(k) = \begin{bmatrix} \mathbf{a_{dLL}}(k) \\ w_{v_C}{}^{\frac{1}{l}} \mathbf{a_{pLL}}(k) \end{bmatrix} \;\middle|\; \mathbf{D^{e^{min}}} \leq \mathbf{U_{LL}}(k) \leq \mathbf{D^{e^{max}}} \right\} \tag{A.173}$$

L | High-level-low-level global model of the MMC

From the equation (5.1) modelling the low-level behavior an arm of the converter, it is possible to formulate the evolution of $\mathbf{v_{C_{xy}}}$ and v_{xy} in time:

$$\begin{cases} \mathbf{v_{C_{xy}}}(k+1) = \mathbf{v_{C_{xy}}}(k) + \left(\frac{T_c}{C} i_{xy}^*(k) L_{xy}\right) \mathbf{D_{xy}^e}(k) + \frac{T_c}{C} i_{xy}^*(k) \mathbf{T_{xy}} \\ v_{xy}(k) = \sigma(x) \mathbf{v_{C_{xy}}}(k)^T L_{xy} \mathbf{D_{xy}^e}(k) + \sigma(x) \mathbf{T_{xy}}^T \mathbf{v_{C_{xy}}}(k) \end{cases} \tag{A.174}$$

This system of equations being true for any arms of the converter, a matrix model representing all the arms of the converter can be obtained by concatenation:

$$
\begin{cases}
\begin{bmatrix} \mathbf{v_{C_{py_1}}}(k+1) \\ \vdots \\ \mathbf{v_{C_{pym}}}(k+1) \\ \mathbf{v_{C_{ny_1}}}(k+1) \\ \vdots \\ \mathbf{v_{C_{nym}}}(k+1) \end{bmatrix} = \begin{bmatrix} \mathbf{v_{C_{py_1}}}(k) \\ \vdots \\ \mathbf{v_{C_{pym}}}(k) \\ \mathbf{v_{C_{ny_1}}}(k) \\ \vdots \\ \mathbf{v_{C_{nym}}}(k) \end{bmatrix} \\
+ \begin{bmatrix} M_{pLL}^{py_1} & & & & & & \\ & \ddots & & & & & \\ & & M_{pLL}^{py_m} & & & & \\ & & & M_{pLL}^{ny_1} & & & \\ & & & & \ddots & & \\ & & & & & M_{pLL}^{ny_m} \end{bmatrix} \begin{bmatrix} \mathbf{D^e_{py_1}} \\ \vdots \\ \mathbf{D^e_{pym}} \\ \mathbf{D^e_{ny_1}} \\ \vdots \\ \mathbf{D^e_{nym}} \end{bmatrix} \\
+ T_c \begin{bmatrix} \frac{i^*_{py_1}(k)}{C} \mathbf{T_{py_1}} \\ \vdots \\ \frac{i^*_{py_m}(k)}{C} \mathbf{T_{pym}} \\ \frac{i^*_{ny_1}(k)}{C} \mathbf{T_{ny_1}} \\ \vdots \\ \frac{i^*_{ny_m}(k)}{C} \mathbf{T_{nym}} \end{bmatrix} \\
\begin{bmatrix} v_{py_1}(k) \\ \vdots \\ v_{py_m}(k) \\ v_{ny_1}(k) \\ \vdots \\ v_{ny_m}(k) \end{bmatrix} = \begin{bmatrix} \mathbf{T_{py_1}}^T & & & & & \\ & \ddots & & & & \\ & & \mathbf{T_{pym}}^T & & & \\ & & & -\mathbf{T_{ny_1}}^T & & \\ & & & & \ddots & \\ & & & & & -\mathbf{T_{nym}}^T \end{bmatrix} \begin{bmatrix} \mathbf{v_{C_{py_1}}}(k) \\ \vdots \\ \mathbf{v_{C_{pym}}}(k) \\ \mathbf{v_{C_{ny_1}}}(k) \\ \vdots \\ \mathbf{v_{C_{nym}}}(k) \end{bmatrix} \\
+ \begin{bmatrix} \mathbf{v_{C_{py_1}}}(k)^T L_{py_1} & & & & & \\ & \ddots & & & & \\ & & \mathbf{v_{C_{pym}}}(k)^T L_{py_m} & & & \\ & & & -\mathbf{v_{C_{ny_1}}}(k)^T L_{ny_1} & & \\ & & & & \ddots & \\ & & & & & -\mathbf{v_{C_{nym}}}(k)^T L_{ny_m} \end{bmatrix} \begin{bmatrix} \mathbf{D^e_{py_1}} \\ \vdots \\ \mathbf{D^e_{pym}} \\ \mathbf{D^e_{ny_1}} \\ \vdots \\ \mathbf{D^e_{nym}} \end{bmatrix}
\end{cases}
\tag{A.175}
$$

These equations can be seen from the point of view of the state space in which a low-level model can be set by taking advantage of matrices previously defined:

$$
\begin{cases} \mathbf{v_C}(k+1) = \mathbf{v_C}(k) + M_{pLL}(k)\mathbf{D^e}(k) + H_{LL}\mathbf{E_{LL}}(k) \\ \mathbf{V}(k) = C_{LL}\mathbf{v_C}(k) + M_{LL}(k)\mathbf{D^e}(k) \end{cases} \tag{A.176}
$$

Defining the vector of voltages across the set of capacitors as the state vector and the vector of voltages across the arms as the output vector of the low-level model, the formulation comes:

$$
\begin{cases} \mathbf{X_{LL}}(k+1) = F_{LL}\mathbf{X_{LL}}(k) + G_{LL}(k)\mathbf{U_{LL}}(k) + H_{LL}\mathbf{E_{LL}}(k) \\ \mathbf{Y_{LL}}(k) = C_{LL}\mathbf{X_{LL}}(k) + D_{LL}(k)\mathbf{U_{LL}}(k) \end{cases} \tag{A.177}
$$

with $\mathbf{U_{LL}} = \mathbf{D^e}$. It is thus observed that the vector which naturally comes to be considered as the output vector of the low-level model is in fact the input vector for the high-level model (3.66)

which is recalled here:

$$\begin{cases} \tilde{\mathbf{X}}_{\mathbf{HL}}(k+1) = \tilde{F}_{HL}\tilde{\mathbf{X}}_{\mathbf{HL}}(k) + \tilde{G}_{HL}\mathbf{U}_{\mathbf{HL}}(k) + \tilde{H}_{HL}\tilde{\mathbf{E}}_{\mathbf{HL}}(k) \\ \mathbf{Y}_{\mathbf{HL}}(k) = \tilde{C}_{HL}\tilde{\mathbf{X}}_{\mathbf{HL}} \end{cases} \tag{A.178}$$

With $\mathbf{U_{HL}} = \mathbf{Y_{LL}}$ It is then possible to combine these two state space models such that, by substitution of $\mathbf{U_{HL}}$ from (A.178) by $\mathbf{Y_{LL}}$ from (A.177), it comes that:

$$\begin{cases} \tilde{\mathbf{X}}_{\mathbf{HL}}(k+1) = \tilde{F}_{HL}\tilde{\mathbf{X}}_{\mathbf{HL}}(k) + \tilde{G}_{HL}\left(C_{LL}\mathbf{X_{LL}}(k) + M_{LL}(k)\mathbf{U_{LL}}(k)\right) + H_{LL}\mathbf{E_{LL}}(k) \\ \mathbf{X_{LL}}(k+1) = F_{LL}\mathbf{X_{LL}}(k) + G_{LL}(k)\mathbf{U_{LL}}(k) + H_{LL}\mathbf{E_{LL}}(k) \end{cases} \tag{A.179}$$

This two state space equations can be combined into one equation by judiciously organizating the terms:

$$\begin{aligned} \begin{bmatrix} \mathbf{X_{LL}}(k+1) \\ \tilde{\mathbf{X}}_{\mathbf{HL}}(k+1) \end{bmatrix} = \begin{bmatrix} \mathbb{I}_{2mN} & \mathbb{O}_{2mN,2m} \\ \tilde{G}_{HL}C_{LL} & \tilde{F}_{HL} \end{bmatrix} \begin{bmatrix} \mathbf{X_{LL}}(k) \\ \tilde{\mathbf{X}}_{\mathbf{HL}}(k) \end{bmatrix} \\ + \begin{bmatrix} G_{LL}(k) \\ \tilde{G}_{HL}D_{LL}(k) \end{bmatrix} \mathbf{U_{LL}}(k) + \begin{bmatrix} H_{LL}\mathbf{E_{LL}}(k) \\ \tilde{H}_{HL}\tilde{\mathbf{E}}_{\mathbf{HL}}(k) \end{bmatrix} \end{aligned} \tag{A.180}$$

And so the state-space model representing all the dynamics at work in the MMC under the Assumption 1 is defined:

$$\begin{cases} \mathbf{X_{MMC}}(k+1) = F_{MMC}\mathbf{X_{MMC}}(k) + G_{MMC}(k)\mathbf{U_{MMC}}(k) + H_{MMC}\mathbf{E_{MMC}}(k) \\ \mathbf{Y_{MMC}}(k) = C_{MMC}\mathbf{X_{MMC}}(k) \end{cases} \tag{A.181}$$

with $\mathbf{X_{MMC}} = [\mathbf{X_{LL}}^T\ \tilde{\mathbf{X}}_{\mathbf{HL}}{}^T]^T$ and $\mathbf{U_{MMC}} = \mathbf{U_{LL}} = \mathbf{D^e}$. As highlighted by (A.182), the model obtained represents the dynamics of the entire set of capacitor voltages as well as the dynamics of the four types of currents that flow through the MMC during its operation. The combination of the two equations of this state space model can be combined to obtain the form:

$$M_{MMC}(k)\mathbf{U_{LL}}(k) = \mathbf{Y_{MMC}}(k+1) - C_{MMC}\left(F_{MMC}\mathbf{X_{MMC}}(k) + H_{MMC}\mathbf{E_{MMC}}(k)\right) \tag{A.183}$$

The output vector of the state-space model of the MMC is defined:

$$\mathbf{Y_{MMC}} = \begin{bmatrix} \mathbf{v_C} \\ I_m \\ I_s \\ \tilde{\mathbf{I}}_{\mathbf{c}} \\ \tilde{\mathbf{I}}_{\mathbf{o}} \end{bmatrix} \tag{A.182}$$

Remark:

About the model described by (A.180), this global model being intended to be linear, the state-input product between the current i_{xy} and the duty cycle $\mathbf{D^e_{xy}}$ as well as the one between the voltage $\mathbf{v_{C_{xy}}}$ and $\mathbf{D^e_{xy}}$ have been taken into account in the global state model presented here, but without being explicitly represented. The first product with the current is hidden in the matrix $G_{LL}(k)$ which depends on time, the second product with the capacitor voltage is hidden in $D_{LL}(k)$ which also depends on time. Thus, through $G_{MMC}(k)$ which depends on time, the interactions between the low-level and the high-level are taken into account with a first approach. Under the Assumption 1, it is possible to keep this state model by updating its matrices at each control sampling period for use in the allocation algorithm. However, an improvement of this model is an interesting work perspective in order to explicitly represent the nonlinearities of the system in a state-space model of this kind for the control allocation of the MMC.

M | Control allocation optimization formulations for the low-level control

The formulations that are studied here are the formulations (4.24) for the LP and (4.26) for the QP in the case of the $LLCAOP_{xy}$ (5.9):

$$LLCAOP_{xy} : \begin{cases} \min_{\mathbf{D^e_{xy}}, \hat{\mathbf{e}}^{\mathbf{xy}}_{\mathbf{LL}}} J^{xy}_{l_{LL}} = ||\hat{\mathbf{e}}^{\mathbf{xy}}_{\mathbf{LL}}||^l_l \\ u.c. : \\ \hat{M}^{xy}_{LL}\mathbf{D^e_{xy}} - \hat{\mathbf{e}}^{\mathbf{xy}}_{\mathbf{LL}} = \hat{\mathbf{a}}^{\mathbf{xy}}_{\mathbf{dLL}} \\ \mathbf{D^{e^{min}}_{xy}} \leq \mathbf{D^e_{xy}} \leq \mathbf{D^{e^{max}}_{xy}} \\ -\hat{\mathbf{e}}^{\mathbf{xy^{max}}}_{\mathbf{LL}} \leq \hat{\mathbf{e}}^{\mathbf{xy}}_{\mathbf{LL}} \leq \hat{\mathbf{e}}^{\mathbf{xy^{max}}}_{\mathbf{LL}} \end{cases} \tag{A.184}$$

The optimization criteria are put here in the formulation dedicated to the low-level control because they are used in detail for the comparative analysis.

Dedicated linear programming formulation

In the case of linear programming, the optimzation of the following criterion is to be solved:

$$J^{xy}_{l_{LL}} = ||\hat{\mathbf{e}}^{\mathbf{xy}}_{\mathbf{LL}}||_1 = \sum_{i=1}^{N+1} |\hat{\mathbf{e}}^{\mathbf{xy}}_{\mathbf{LL}i}| = \sum_{i=1}^{N+1} \hat{\mathbf{e}}^{\mathbf{xy}\,+}_{\mathbf{LL}i} + \hat{\mathbf{e}}^{\mathbf{xy}\,-}_{\mathbf{LL}i} \tag{A.185}$$

The deviation variable $\hat{\mathbf{e}}^{\mathbf{xy}}_{\mathbf{LL}} = \hat{\mathbf{e}}^{\mathbf{xy}\,+}_{\mathbf{LL}} - \hat{\mathbf{e}}^{\mathbf{xy}\,-}_{\mathbf{LL}}$ is split in two positive vectors $\hat{\mathbf{e}}^{\mathbf{xy}\,+}_{\mathbf{LL}}$ and $\hat{\mathbf{e}}^{\mathbf{xy}\,-}_{\mathbf{LL}}$ since the linear programming algorithm in its standard form only allows 0 as lower boundary. According to the definition of $\hat{\mathbf{e}}^{\mathbf{xy}}_{\mathbf{LL}}$, it comes that:

$$\hat{M}^{xy}_{LL}\mathbf{D^e_{xy}} - \hat{\mathbf{e}}^{\mathbf{xy}\,+}_{\mathbf{LL}} + \hat{\mathbf{e}}^{\mathbf{xy}\,-}_{\mathbf{LL}} = \hat{\mathbf{a}}^{\mathbf{xy}}_{\mathbf{dLL}} \tag{A.186}$$

To take into account the bounds of $\mathbf{D^e_{xy}}$ in the algorithm of the standard linear programming, the change of variable $\mathbf{D^e_{xy}} = \overline{\mathbf{D^e_{xy}}} + \mathbf{D^{e^{min}}_{xy}}$ is implemented, the previous equation is then adapted accordingly by performing a substitution:

$$\hat{M}^{xy}_{LL}\overline{\mathbf{D^e_{xy}}} - \hat{\mathbf{e}}^{\mathbf{xy}\,+}_{\mathbf{LL}} + \hat{\mathbf{e}}^{\mathbf{xy}\,-}_{\mathbf{LL}} = \hat{\mathbf{a}}^{\mathbf{xy}}_{\mathbf{dLL}} - \hat{M}^{xy}_{LL}\mathbf{D^{e^{min}}_{xy}} \tag{A.187}$$

This equation then represents the equality constraints that the LP must satisfy in addition to the constraints on the bounds of the various decision variables: $0 \leq \overline{\mathbf{D^e_{xy}}} \leq \mathbf{D^{e^{max}}_{xy}} - \mathbf{D^{e^{min}}_{xy}}$, $0 \leq \hat{\mathbf{e}}^{\mathbf{xy}\,+}_{\mathbf{LL}} \leq \hat{\mathbf{e}}^{\mathbf{xy^{max}}}_{\mathbf{LL}}$ and $0 \leq \hat{\mathbf{e}}^{\mathbf{xy}\,+}_{\mathbf{LL}} \leq \hat{\mathbf{e}}^{\mathbf{xy^{max}}}_{\mathbf{LL}}$. In the present case $\hat{\mathbf{e}}^{\mathbf{xy^{max}}}_{\mathbf{LL}}$ is chosen with the idea of having a maximum boundary on the deviation from the verification of the allocation equation: $\hat{\mathbf{e}}^{\mathbf{xy^{max}}}_{\mathbf{LL}} = max(abs(\hat{\mathbf{a}}^{\mathbf{xy}}_{\mathbf{dLL}}))$. This is the choice that is implemented here in the online solving algorithm but it could be chosen differently in the case of other systems to give more or less freedom to the allocation by first analyzing the difficulty of finding feasible solutions to the allocation equation. The equation that represents the equality constraints can then be put in matrix form:

$$\begin{bmatrix} M^{xy}_{LL} & -1 & +1 & \\ w_{v_C}\frac{1}{l}M^{xy}_{pLL} & & -\mathbb{I}_N & +\mathbb{I}_N \end{bmatrix} \begin{bmatrix} \overline{\mathbf{D^e_{xy}}} \\ \hat{\mathbf{e}}^{\mathbf{xy}\,+}_{\mathbf{LL}} \\ \hat{\mathbf{e}}^{\mathbf{xy}\,-}_{\mathbf{LL}} \end{bmatrix} = \begin{bmatrix} \mathbf{a}^{\mathbf{xy}}_{\mathbf{dLL}} - M^{xy}_{LL}\mathbf{D^{e^{min}}_{xy}} \\ w_{v_C}\frac{1}{l}\left(\mathbf{a}^{\mathbf{xy}}_{\mathbf{pLL}} - M^{xy}_{pLL}\mathbf{D^{e^{min}}_{xy}}\right) \end{bmatrix} \tag{A.188}$$

The choice of the optimization vector then comes naturally: $\mathbf{x} = \begin{bmatrix} \overline{\mathbf{D^e_{xy}}} & \hat{\mathbf{e}}^{\mathbf{xy}\,+}_{\mathbf{LL}} & \hat{\mathbf{e}}^{\mathbf{xy}}_{\mathbf{LL}} \end{bmatrix}^T$. The optimization criterion therefore takes the form: $J^{xy}_{l_{LL}} = \begin{bmatrix} \mathbb{O}_{1,N} & \mathbb{I}_{1,N+1} & \mathbb{I}_{1,N+1} \end{bmatrix} \mathbf{x}$. The formulation that the linear programming is able to solve is thus obtained, it is defined from the

matrices:

$$
\begin{aligned}
\mathbf{x} &= \begin{bmatrix} \overline{\mathbf{D}^{\mathbf{e}}_{\mathbf{xy}}} & \hat{\mathbf{e}}^{\mathbf{xy}\,+}_{\mathbf{LL}} & \hat{\mathbf{e}}^{\mathbf{xy}\,-}_{\mathbf{LL}} \end{bmatrix}^T \in \mathbb{R}^{3N+2} \\
\mathbf{c}^T &= \begin{bmatrix} \mathbb{O}_{1,N} & \mathbb{I}_{1,N+1} & \mathbb{I}_{1,N+1} \end{bmatrix} \in \mathbb{R}^{3N+2} \\
\mathcal{A} &= \begin{bmatrix} M^{xy}_{LL} & -1 & +1 \\ w_{v_C}{}^{\frac{1}{l}} M^{xy}_{p_{LL}} & -\mathbb{I}_N & +\mathbb{I}_N \end{bmatrix} \in \mathcal{M}_{N+1,3N+2}(\mathbb{R}) \\
\mathbf{b} &= \begin{bmatrix} \mathbf{a}^{\mathbf{xy}}_{\mathbf{dLL}} - M^{xy}_{LL}\mathbf{D}^{\mathbf{e_{min}}}_{\mathbf{xy}} \\ w_{v_C}{}^{\frac{1}{l}} \left(\mathbf{a}^{\mathbf{xy}}_{\mathbf{pLL}} - M^{xy}_{p_{LL}}\mathbf{D}^{\mathbf{e_{min}}}_{\mathbf{xy}} \right) \end{bmatrix} \in \mathbb{R}^{N+1} \\
\mathbf{x}_{max} &= \begin{bmatrix} \mathbf{D}^{\mathbf{e_{max}}}_{\mathbf{xy}} - \mathbf{D}^{\mathbf{e_{min}}}_{\mathbf{xy}} & \hat{\mathbf{e}}^{\mathbf{xy_{max}}}_{\mathbf{LL}} & \hat{\mathbf{e}}^{\mathbf{xy_{max}}}_{\mathbf{LL}} \end{bmatrix} \in \mathbb{R}^{3N+2}
\end{aligned}
\tag{A.189}
$$

Dedicated quadratic programming formulation

In the case of quadratic programming, the optimization is formulated:

$$
J^{xy}_{l_{LL}} = ||\hat{\mathbf{e}}^{\mathbf{xy}}_{\mathbf{LL}}||^2_2 = \sum_{i=1}^{N+1} \hat{\mathbf{e}}^{\mathbf{xy}\,2}_{\mathbf{LL}i} = \frac{1}{2} \hat{\mathbf{e}}^{\mathbf{xy}\,T}_{\mathbf{LL}} \left(2\mathbb{I}_{N+1}\right) \hat{\mathbf{e}}^{\mathbf{xy}}_{\mathbf{LL}} \tag{A.190}
$$

The QP algorithms used here allow to have negative bounds contrary to the standard formulation adopted for the LP, the equation representing the constraints equalities is then preserved in its form without adding supplementary slack variables:

$$
\hat{M^{xy}_{LL}} \mathbf{D}^{\mathbf{e}}_{\mathbf{xy}} - \hat{\mathbf{e}}^{\mathbf{xy}}_{\mathbf{LL}} = \hat{\mathbf{a}}^{\mathbf{xy}}_{\mathbf{dLL}} \tag{A.191}
$$

The variable $\hat{\mathbf{e}}^{\mathbf{xy}}_{\mathbf{LL}}$ is given the same upper bound as for the LP: $\hat{\mathbf{e}}^{\mathbf{xy_{max}}}_{\mathbf{LL}} = max(abs(\hat{\mathbf{a}}^{\mathbf{xy}}_{\mathbf{dLL}}))$. The equation that represents the equality constraints can also be put in matrix form:

$$
\begin{bmatrix} M^{xy}_{LL} & -1 \\ w_{v_C}{}^{\frac{1}{l}} M^{xy}_{p_{LL}} & -\mathbb{I}_N \end{bmatrix} \begin{bmatrix} \mathbf{D}^{\mathbf{e}}_{\mathbf{xy}} \\ \hat{\mathbf{e}}^{\mathbf{xy}}_{\mathbf{LL}} \end{bmatrix} = \begin{bmatrix} \mathbf{a}^{\mathbf{xy}}_{\mathbf{dLL}} \\ w_{v_C}{}^{\frac{1}{l}} \mathbf{a}^{\mathbf{xy}}_{\mathbf{pLL}} \end{bmatrix} \tag{A.192}
$$

The choice of the optimization vector then comes trivially: $\mathbf{x} = \begin{bmatrix} \overline{\mathbf{D}^{\mathbf{e}}_{\mathbf{xy}}} & \hat{\mathbf{e}}^{\mathbf{xy}}_{\mathbf{LL}} \end{bmatrix}^T$. The optimization criterion therefore takes the form: $J^{xy}_{l_{LL}} = \begin{bmatrix} \mathbb{O}_{1,N} & \mathbb{I}_{1,N+1} \end{bmatrix} \mathbf{x}$. The formulation that the

algorithms of Interior-Point and Active-Set are able to solve is thus defined from the matrices:

$$
\begin{aligned}
&\mathbf{x} = \begin{bmatrix} \overline{\mathbf{D^e_{xy}}} & \hat{\mathbf{e}}^{\mathbf{xy}}_{\mathbf{LL}} \end{bmatrix}^T \in \mathbb{R}^{2N+1} \\
&\mathbf{c}^T = \begin{bmatrix} \mathbb{O}_{1,N} & \mathbb{I}_{1,N+1} \end{bmatrix} \in \mathbb{R}^{2N+1} \qquad\qquad f = 0 \in \mathbb{R} \\
&\mathcal{H} = 2 \begin{bmatrix} \mathbb{O}_N & \\ & \mathbb{I}_{N+1} \end{bmatrix} \in \mathcal{M}_{2N+1}(\mathbb{R}) \\
&\mathcal{A} = \begin{bmatrix} M^{xy}_{LL} & -1 & \\ w_{v_C}{}^{\frac{1}{l}} M_{p}{}^{xy}_{LL} & & -\mathbb{I}_N \end{bmatrix} \in \mathcal{M}_{N+1,2N+1}(\mathbb{R}) \\
&\mathbf{b} = \begin{bmatrix} \mathbf{a^{xy}_{dLL}} \\ w_{v_C}{}^{\frac{1}{l}} \mathbf{a}_{\mathbf{pLL}}{}^{\mathbf{xy}} \end{bmatrix} \in \mathbb{R}^{N+1} \\
&\mathbf{x}_{max} = \begin{bmatrix} \mathbf{D^{e_{max}}_{xy}} & \hat{\mathbf{e}}^{\mathbf{xy_{max}}}_{\mathbf{LL}} \end{bmatrix} \in \mathbb{R}^{2N+1} \\
&\mathbf{x}_{min} = \begin{bmatrix} \mathbf{D^{e_{min}}_{xy}} & -\hat{\mathbf{e}}^{\mathbf{xy_{max}}}_{\mathbf{LL}} \end{bmatrix} \in \mathbb{R}^{2N+1}
\end{aligned}
\tag{A.193}
$$

N | Control allocation optimization formulations for the high-level control

The aim of the study being to compare the various algorithms of high-level control, their formulations are given in order to allow the visualization of the optimizations which are set up in the various cases.

Control allocation formulations for the GPFOCSSM

The first formulation used which is based on the GPFOCSSM is directly the MIB control allocation whose equation (5.19) gives the solution by matrix inversion. To save execution time, the computation of the inverse matrix is done off-line because the effectivity matrix does not require any parameter update over time. The computation of $\mathbf{V}^{ref}$ is then done deterministically in real time while ensuring that its bounds are respected.

The formulation of the high-level control for the case of EMOn linear programming is obtained by applying the same development as that performed in section 4.B.3 - from equation (4.21) to equation (4.25) - to the $HLCAOP_{m-ph}$ (5.18):

$$
HLCAOP_{m-ph} : \begin{cases} \min_{\mathbf{V},\hat{\mathbf{e}}_{\mathbf{HL}}} J_{l_{HL}} = ||\hat{\mathbf{e}}_{\mathbf{HL}}||^l_l \\ u.c. : \\ \hat{M}_{HL}\mathbf{V} - \hat{\mathbf{e}}_{\mathbf{HL}} = \hat{\mathbf{a}}_{\mathbf{dHL}} \\ \mathbf{V_{min}} \leq \mathbf{V} \leq \mathbf{V_{max}} \\ -\hat{\mathbf{e}}^{\mathbf{max}}_{\mathbf{HL}} \leq \hat{\mathbf{e}}_{\mathbf{HL}} \leq \hat{\mathbf{e}}^{\mathbf{max}}_{\mathbf{HL}} \end{cases}
\tag{A.194}
$$

This approach leads directly to the matrices to be implemented in real time:

$$\begin{aligned}
&\mathbf{x} = \begin{bmatrix}\overline{\mathbf{V}} & \hat{\mathbf{e}}_{\mathbf{HL}}{}^{+} & \hat{\mathbf{e}}_{\mathbf{HL}}{}^{-}\end{bmatrix}^T \in \mathbb{R}^{6m} \\
&\mathbf{c}^T = \begin{bmatrix}\mathbb{O}_{1,2m} & \mathbb{I}_{1,2m} & \mathbb{I}_{1,2m}\end{bmatrix} \in \mathbb{R}^{6m} \\
&\mathcal{A} = \begin{bmatrix}\hat{M}_{HL} & -\mathbb{I}_{2m} & +\mathbb{I}_{2m}\end{bmatrix} \in \mathcal{M}_{2m,6m}(\mathbb{R}) \\
&\mathbf{b} = \begin{bmatrix}\hat{\mathbf{a}}_{\mathbf{dHL}} - \hat{M}_{HL}\mathbf{V}_{\mathbf{min}}\end{bmatrix} \in \mathbb{R}^{2m} \\
&\mathbf{x}_{max} = \begin{bmatrix}\mathbf{V}_{\mathbf{max}} - \mathbf{V}_{\mathbf{min}} & \hat{\mathbf{e}}_{\mathbf{HL}}^{\mathbf{max}} & \hat{\mathbf{e}}_{\mathbf{HL}}^{\mathbf{max}}\end{bmatrix} \in \mathbb{R}^{6m}
\end{aligned} \tag{A.195}$$

For the formulation of the high-level control for the case of EMOn quadratic programming now, this is obtained by adopting the same approach as in section 4.B.3 - from equation (4.21) to equation (4.28) - to the $HLCAOP_{m-ph}$ (A.194). This development direclty gives:

$$\begin{aligned}
&\mathbf{x} = \begin{bmatrix}\overline{\mathbf{V}} & \hat{\mathbf{e}}_{\mathbf{HL}}\end{bmatrix}^T \in \mathbb{R}^{4m} \\
&\mathbf{c}^T = \begin{bmatrix}\mathbb{O}_{1,2m} & \mathbb{I}_{1,2m}\end{bmatrix} \in \mathbb{R}^{4m} \qquad\qquad f = 0 \in \mathbb{R} \\
&\mathcal{H} = 2\begin{bmatrix}\mathbb{O}_{2m} & \\ & \mathbb{I}_{2m}\end{bmatrix} \in \mathcal{M}_{4m}(\mathbb{R}) \\
&\mathcal{A} = \begin{bmatrix}M_{HL} & -\mathbb{I}_{2m}\end{bmatrix} \in \mathcal{M}_{2m,4m}(\mathbb{R}) \\
&\mathbf{b} = \begin{bmatrix}\mathbf{a}_{\mathbf{dHL}}\end{bmatrix} \in \mathbb{R}^{2m} \\
&\mathbf{x}_{max} = \begin{bmatrix}\mathbf{V}_{\mathbf{max}} & \hat{\mathbf{e}}_{\mathbf{HL}}^{\mathbf{max}}\end{bmatrix} \in \mathbb{R}^{4m} \\
&\mathbf{x}_{min} = \begin{bmatrix}\mathbf{V}_{\mathbf{min}} & -\hat{\mathbf{e}}_{\mathbf{HL}}^{\mathbf{max}}\end{bmatrix} \in \mathbb{R}^{4m}
\end{aligned} \tag{A.196}$$

Control allocation formulations for the GPFSROBHCCSSM

The first formulation based on the GPFSROBHCCSSM is the MIB control allocation. The equation (5.31) provides the solution to be implemented in real time to determine $\mathbf{V}^{\mathbf{dq}012\,ref}$, the inversion of the matrix $\hat{M}_{HL}^{dq012}$ can be precomputed off-line because in the framework of this model also it does not depend on the variation of parameters of the system in time.

The formulation of the high-level control for the case of EMOn linear programming is obtained by applying the same development as that performed in section 4.B.3 - from equation (4.21) to equation (4.25) - to the $HLCAOP_{Park\ 12}$ (5.30):

$$HLCAOP_{Park\ 12}: \begin{cases}
\min_{\mathbf{V}^{\mathbf{dq}012},\hat{\mathbf{e}}_{\mathbf{HL}}^{\mathbf{dq}012}} J_{l_{HL}^{dq012}} = ||\hat{\mathbf{e}}_{\mathbf{HL}}^{\mathbf{dq}012}||_l^l \\
u.c.: \\
\hat{M}_{HL}^{dq012}\mathbf{V}^{\mathbf{dq}012} - \hat{\mathbf{e}}_{\mathbf{HL}}^{\mathbf{dq}012} = \hat{\mathbf{a}}_{\mathbf{dHL}}^{\mathbf{dq}012} \\
\mathbf{V}_{\mathbf{min}}^{\mathbf{dq}012} \leq \mathbf{V}^{\mathbf{dq}012} \leq \mathbf{V}_{\mathbf{max}}^{\mathbf{dq}012} \\
-\hat{\mathbf{e}}_{\mathbf{HL}}^{\mathbf{dq}012\mathbf{max}} \leq \hat{\mathbf{e}}_{\mathbf{HL}}^{\mathbf{dq}012} \leq \hat{\mathbf{e}}_{\mathbf{HL}}^{\mathbf{dq}012\mathbf{max}}
\end{cases} \tag{A.197}$$

This derivation output reads:

$$\begin{aligned}
\mathbf{x} &= \left[\overline{\mathbf{V}^{\mathbf{dq012}}} \quad \hat{\mathbf{e}}_{\mathbf{HL}}^{\mathbf{dq012}+} \quad \hat{\mathbf{e}}_{\mathbf{HL}}^{\mathbf{dq012}-}\right]^T \in \mathbb{R}^{6m'} \\
\mathbf{c}^T &= \left[\mathbb{O}_{1,2m'} \quad \mathbb{I}_{1,2m'} \quad \mathbb{I}_{1,2m'}\right] \in \mathbb{R}^{6m'} \\
\mathcal{A} &= \left[\hat{M}_{HL}^{dq012} \quad -\mathbb{I}_{2m'} \quad +\mathbb{I}_{2m'}\right] \in \mathcal{M}_{2m',6m'}(\mathbb{R}) \\
\mathbf{b} &= \left[\hat{\mathbf{a}}_{\mathbf{dHL}}^{\mathbf{dq012}} - \hat{M}_{HL}^{dq012}\mathbf{V}_{\mathbf{min}}^{\mathbf{dq012}}\right] \in \mathbb{R}^{2m'} \\
\mathbf{x}_{max} &= \left[\mathbf{V}_{\mathbf{max}}^{\mathbf{dq012}} - \mathbf{V}_{\mathbf{min}}^{\mathbf{dq012}} \quad \hat{\mathbf{e}}_{\mathbf{HL}}^{\mathbf{dq012max}} \quad \hat{\mathbf{e}}_{\mathbf{HL}}^{\mathbf{dq012max}}\right] \in \mathbb{R}^{6m'}
\end{aligned} \tag{A.198}$$

The formulation of the high-level control for the case of EMOn quadratic programming is found by adopting the same approach as in section 4.B.3 - from equation (4.21) to the equation (4.28) - to the $HLCAOP_{Park\ 12}$ (A.197). This approach leads to:

$$\begin{aligned}
\mathbf{x} &= \left[\overline{\mathbf{V}^{\mathbf{dq012}}} \quad \hat{\mathbf{e}}_{\mathbf{HL}}^{\mathbf{dq012}}\right]^T \in \mathbb{R}^{4m'} \\
\mathbf{c}^T &= \left[\mathbb{O}_{1,2m'} \quad \mathbb{I}_{1,2m'}\right] \in \mathbb{R}^{4m'} \qquad\qquad f = 0 \in \mathbb{R} \\
\mathcal{H} &= 2\begin{bmatrix}\mathbb{O}_{2m'} & \\ & \mathbb{I}_{2m'}\end{bmatrix} \in \mathcal{M}_{4m'}(\mathbb{R}) \\
\mathcal{A} &= \left[\hat{M}_{HL}^{dq012} \quad -\mathbb{I}_{2m'}\right] \in \mathcal{M}_{2m',4m'}(\mathbb{R}) \\
\mathbf{b} &= \left[\hat{\mathbf{a}}_{\mathbf{dHL}}^{\mathbf{dq012}}\right] \in \mathbb{R}^{2m'} \\
\mathbf{x}_{max} &= \left[\mathbf{V}_{\mathbf{max}}^{\mathbf{dq012}} \quad \hat{\mathbf{e}}_{\mathbf{HL}}^{\mathbf{dq012max}}\right] \in \mathbb{R}^{4m'} \\
\mathbf{x}_{min} &= \left[\mathbf{V}_{\mathbf{min}}^{\mathbf{dq012}} \quad -\hat{\mathbf{e}}_{\mathbf{HL}}^{\mathbf{dq012max}}\right] \in \mathbb{R}^{4m'}
\end{aligned} \tag{A.199}$$

The only step to do after that is to give the matrices of (A.195) for the GPFOCSSM or those of (A.198) for the GPFSROBHCCSSM to the Simplex algorithm by updating them at each sampling step to ensure the control of currents by linear programming. To perform this same control for the quadratic programming case, it is the matrices (A.196) for the GPFOCSSM or those of (A.199) for the GPFSROBHCCSSM that must be provided to the Interior-Point or Active-Set algorithms.

O | Highlights of the control allocation methods compared to classical control approaches for the MMC

This section intends to summarize the key advantages of control allocation methods over other traditional modular multilevel converter control methods.

For low-level control, the two control objectives to be satisfied are the reference tracking for the voltages and the capacitor balancing. Conventional methods deal with these two objectives in a

cascaded manner, while the switching states act directly and simultaneously on both. This leads to an effective operation but is far from optimal.

On the contrary, the control allocation will address the low-level control problem as a whole by aiming to satisfy both control objectives simultaneously from the same control variables. It is a more global control objective that is addressed by taking full advantage of the input variables as their constraints are taken into account by a single algorithm to guarantee both objectives in an optimized way. The decision of the use of each of the submodules is made in an optimized way in order to accurately steer the system and distribute the control effort among all the available submodules. Figure 23 graphically summarizes this. Note that, the reduction of the switching frequency as the number of submodules is increased still needs to be addressed for control allocation methods. However, promising directions have been initiated and solutions based on literature have been outlined.

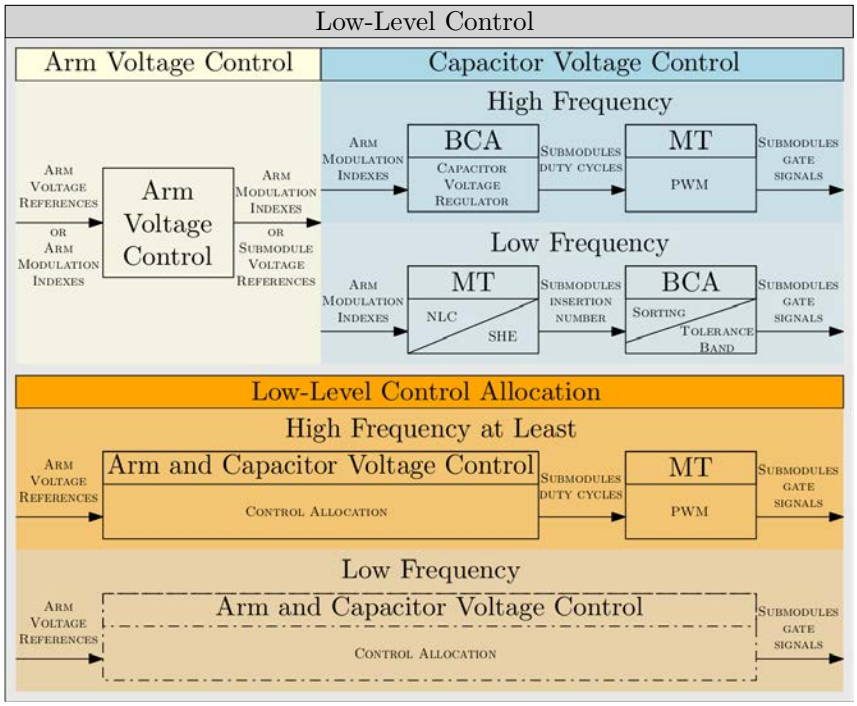

Figure 23: Control architectures: comparing control allocation to classical control approches in the framework of the low-level control of the MMC.

For the high-level control, the control objectives to be satisfied are the reference tracking for each of the four (at least three) current types. The classical methods handle the control of each of these currents independently, each on its side, whereas the same arm voltages act upon all of them, and these voltages must be maintained between their boundaries.

On the other hand, the control allocation offers a more global approach that focuses on the control of the four currents simultaneously from the direct determination of the arm voltages. This determination is done by taking into account the saturations of the voltages *a priori* in a unique algorithm that distributes the control effort among the set of arm in an optimized way. The implemented control allocation also allows one to promptly tune the desired dynamics in closed loop. Figure 24 graphically summarizes this.

By its very principle of cooperative steering of the control objectives via real-time optimization in a unique algorithm, the control allocation approach has the capability to surpass the classical control approaches for both current and voltage control as well as capacitor balancing. In this

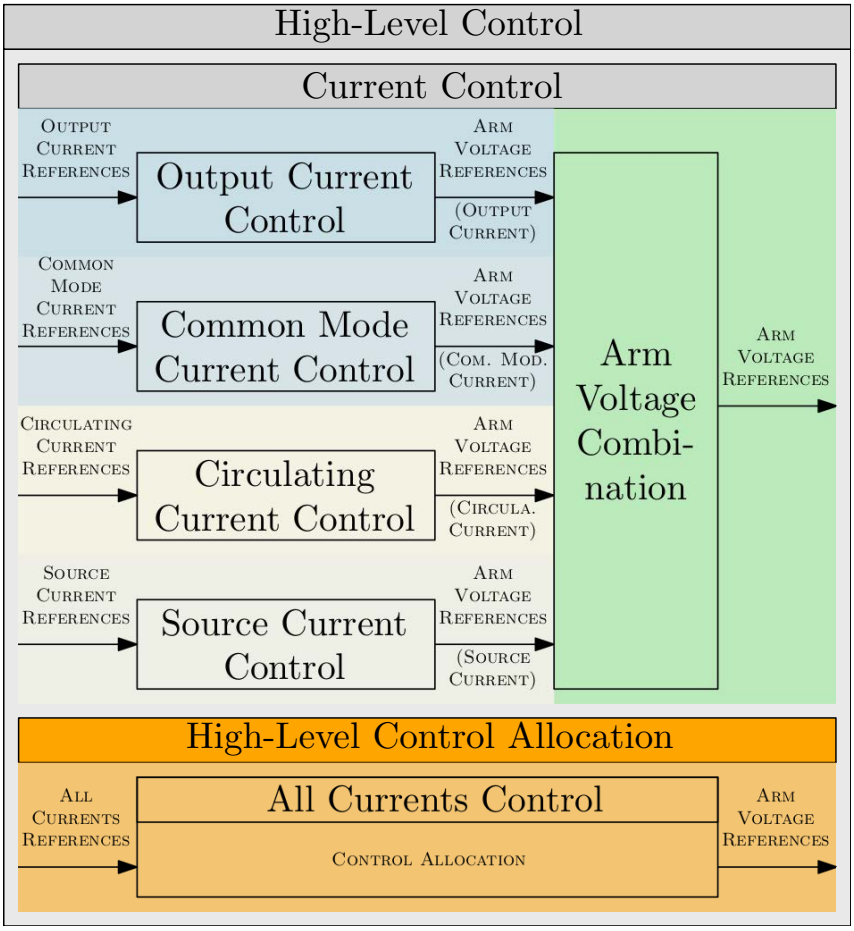

Figure 24: Control architectures: comparing control allocation to classical control approches in the framework of the high-level control of the MMC.

work, control allocation methods have been developed to control the modular multilevel converter, and some qualitative comparisons with classical methods have been identified, it remains now to compare them quantitatively.

Glossary

A | B | C | D | E | F | G | H | I | L | M | N | O | P | Q | R | S | T | W | Z

A

Active-Set
Optimization algorithm designed to solve linear, quadratic and nonlinear programming problems. 41, 48, 49, 148, 199, 215, 216, 218, 223–227, 230–232, 242, 247

adaptive control allocation
An EMOff allocation method. 43

arm
Electrical circuit which is a constitutive part of a converter, it is made of switches and sometimes impedances also, it is either connected to the positive pole of the DC supply or to negative one . . xix, xxi, xxii, xxiv–xxvi, xxx–xxxiii, xxxv, xxxvi, xxxviii, xxxix, xli, xlii, xliv, xlvi, xlix, l, lii–lvi, lviii–lx, lxii, lxv–lxxviii, lxxx, 4, 10–15, 17–32, 49, 51, 53, 54, 59, 61–66, 69, 72–75, 88, 115, 116, 120, 128, 177, 179–183, 185, 190, 192, 196–198, 201, 204, 205, 207, 210, 211, 214, 216, 218, 219, 222, 234–244, 246, 248, III, IV

articifial neural network allocation
An AI-based allocation method. 43

B

Branch-and-Bounds
Optimization algorithm that can be used to solve mixed integer linear programming problems like in the case of [BD04a] for the CA. 42

C

control allocation
Control method that takes advantage of the overactuated property of systems in order to operate optimally the system while taking into account the boundaries of the control variables xxi–xxv, xxvii, xxx, xxxi, xxxiii, xxxvi, xl–xlii, liv, lv, lvii, lviii, lxxvii–lxxix, 4, 8, 33, 34, 36, 39, 41–47, 49, 61, 62, 73, 143, 145, 148–154, 156, 158, 161, 162, 164–167, 172, 176–180, 182, 183, 185–189, 191–195, 197–201, 206, 207, 210, 211, 213–215, 218, 220–231, 233, 234, 236, 241–247, 251, II

control allocation optimization problem
Control optimization is fomulated as:

$$\begin{cases} \min_{\mathbf{U},\mathbf{e}} J_l = ||\mathbf{e}||_l^l \\ u.c.: \\ \mathcal{M}(\mathbf{U}) - \mathbf{e} = \mathbf{a_d} \\ \mathbf{U}_{min} \leq \mathbf{U} \leq \mathbf{U}_{max} \\ -\mathbf{e}_{max} \leq \mathbf{e} \leq \mathbf{e}_{max} \end{cases}$$

. . . . . lxviii, 146–148, 150, 186, 192

control allocation problem
Control problem where the objective is to determine the control vector $\mathbf{U}$ that ensures the control objective $\mathcal{M}(\mathbf{U}) = \mathbf{a_d}$ under the control constraints $\mathbf{U}_{min} \leq \mathbf{U} \leq \mathbf{U}_{max}$. It can be fomulated as:

$$\{\mathcal{M}(\mathbf{U}) = \mathbf{a_d} \mid \mathbf{U}_{min} \leq \mathbf{U} \leq \mathbf{U}_{max}\}$$

.... xxix, lvi, lvii, lxxv, 36, 42, 48, 62, 145–148, 165, 169, 170, 179, 181, 182, 185–188, 192, 194

control allocation with integral compensator
Control method based on the control allocation to which an integral compensator is added internally so as to improve the control performances, as opposed to the control allocation which is the classical method with no integrator. xxiii–xxv, xxvii, xxx, xxxi, xliii, xlv, liv, lv, lx, lxxvii, lxxix, 154–159, 161–164, 166, 170, 172–176, 229–234, 247

D

daisy chaining
A MIB allocation method. 39

detailed model
For a static converter cell, model describing the influence of the switches states on the cell electrical behavior, ability to represent the losses ..... 52, 53, 59, II

dynamic optimization seeking
An EMOff allocation method. 43

dynamic programming
A family of optimal control problem optimization methods, see [Bel56] for more details.. 44

E

exact null-space
A MIB allocation method. 39

F

Fixed-Point Method
Optimization algorithm that was implemented to solve quadratic programming problems in the framework of control allocation, see [Här03] for more details. 41

full-bridge submodule
Type of DC-DC static converter topology available for the SM. This topology was one of the first ones to be used in the MMC after the half-bridge submodule which is the original one.

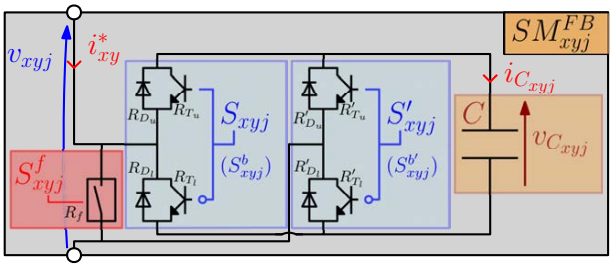

Figure 25: Full-bridge submodule detailed electric diagram.

xxi, xxv, lvi, lxii, lxvi–lxviii, lxxv, lxxx, 11, 20, 21, 26, 55, 56, 59, 61–63, 69, 116, 191, 236–238, II

functional detailed model
Detailed model that describes the power conversion functionalities of the considered submodule. This model has for objective to be used for a control purpose 52, 55, 56, 65, 191

functional physical detailed model
Detailed model that describes the power conversion functionalities of the considered submodule while taking into account the conduction resistance of the semi-conductors, meaning that it make it possible to evaluate the Joules losses in the submodule. This model has for objective to be used for a control purpose 58, 59, 62, 64

G

General Polyphase Fixed-Size Reduced Order BiHarmonic Content Current State-Space Model

See 3.F for more details on the model . . . . . xviii, 71, 107, 109, 111

General Polyphase Fixed-Size Reduced Order Current State-Space Model

See 3.D for more details on the model . . . . . xviii, 71, 88, 89, 91, 93, 95

General Polyphase Full Order Current State-Space Model

See 3.C for more details on the model . . . . . xviii, 71, 84, 85, 87

Gotland HVDC Link

The Gotland HVDC Link was the world's first commercial HVDC transmission link using the first submarine HVDC cable. It was 96 km-long and used 20 MW / 100 kV mercury-arc valves as conversion stations. For more details see the IEEE dedicated webpage. 8

H

half-bridge submodule

Type of DC-DC static converter topology available for the SM. This topology was the first one to be used in the MMC. xxi, lxii, lxvi, 11, 19, 20, 26, 53–59, 61–63, 69, 116, 121, 206, 218, 243, II, III

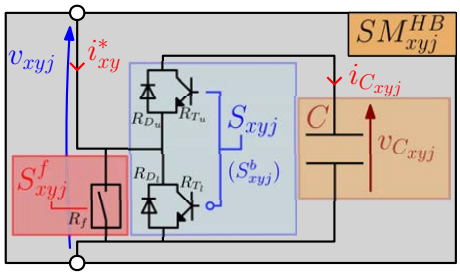

Figure 26: Half-bridge submodule detailed electric diagram.

hardware-in-the-loop

Control loop testing procedure where only a part of the hardware - the control system - is the real hardware and the other part - the plant with power - is simulated by a dedicated computer . . . . . xxiii, xxiv, 4, 201, 202, 206–208, 213–218, 223, 230

high-level

For the considered converter, the high-level refers to the legs' level. . . . . xxii, xxiii, xxvi, xxx–xxxvii, xxxix–xliii, xlvi, xlvii, liv, lvii, lx, lxviii, lxxvi–lxxix, 17, 21–23, 26, 51, 72–75, 81, 84, 87, 88, 96, 97, 115, 120, 121, 123, 125, 126, 128, 130, 132–137, 140, 141, 144, 185–189, 191–193, 215, 216, 218, 220, 223, 225, 230

high-level control

For the considered converter, the high-level control has for objective to ensure the current reference tracking for the four different types of current flowing trough the system. . . . . xxiii, xxiv, xxvi, xxvii, xxxvi, lxxiv, lxxv, 22, 27–30, 157, 178, 179, 186, 187, 189, 192, 199, 205, 215–218, 220, 223, 225–232, 247, 248, IV

high-level-low-level

For the considered converter, the high-level-low-level refers to the association of the high-level (the currents flowing within the arms of the MMC) with the low-level (the one from the capacitor voltages). When adressing the topic of high-level-low-level modelling (or control), the converter currents and capacitor voltage dynamics are considered all together, see Figure 5.5 for illustrative details. . xxiii, xxx, xxxvi, xl, xliii, xlv, xlvi, liv, lvii, lxviii, lxxvi, lxxvii, 191, 192

high-level-low-level control
For the considered converter, the high-level-low-level control has for objective to ensure the low-level control as well as the high-level control together as a whole: the current reference tracking for the four different types of current flowing trough the system and the capacitor voltage balancing at the same time in the same control algorithm. . . . . xxxvi, lxxiv, 191

I

INELFE
The France-Spain Electrical Interconnexion (*Interconnexion Électrique France–Espagne - INELFE*) is a HVDC connexion using the MMC technology between France and Spain. This connexion is done in the South of Perpignan. Its rated power is 2×1 GW in ± 320 kV DC. For more details see INELFE website. 9, 73

Interior-Point
Optimization algorithm designed to solve linear, quadratic and nonlinear programming problems. 41, 49, 148, 149, 166, 199, 205, 215, 225–227, 230, 247

L

leg
Electrical circuit which is a constitutive part of a converter, it is made of two arms, the one connected to the positive pole of the DC supply and the one connected to the negative pole xxi, xxii, xxiv, xlvii–l, lii–liv, lxix, lxxii, lxxiii, lxxvii, 11, 13–15, 22, 26, 27, 31, 32, 73–75, 79, 88, 204, 211, 235, III

linear programming
A family of optimization problems and solving algorithms, where the cost function as well as the constraints are linear. . . . . xxiv, 41, 205, 207–210, 212–214

low-level
For the considered converter, the low-level refers to the arm and submodule level. . . . . xxiii, xxiv, xxvi, xxx–xxxiii, xxxv, xxxviii, xxxix, xli, xlii, xliv, xlvi, lv, lvii, lviii, lxii–lxv, lxviii, lxxvii, lxxviii, 21, 22, 51, 52, 55, 60, 65, 66, 69, 72, 74, 115, 144, 181, 183, 191–193, 198, 207, 209, 210, 215, 222, 241, 242

low-level control
For the considered converter, the low-level control has for objective to ensure the arm voltage reference tracking as well as the capacitor voltage balancing. . . . . xxi, xxiii, xxvi, xxvii, xxxv, xxxvi, lxxv, 22, 27, 28, 30, 33, 51, 52, 54, 63, 65, 66, 69, 178–183, 192, 199, 201, 205–208, 213–216, 218, 226, 235, 241–243, 247, IV

M

mixed integer linear programming
A family of optimization problems and solving algorithms, where the cost function and the constraints are linear. The decision variables are a mix of discrete and continuous quantities. 42

modular multilevel converter
A specific topology of DC-AC static converter that is modular due to the stackability property of its elementary bricks that are called the submodules. xxxvi

N

nonlinear programming
A family of optimization problems and solving algorithms, where the cost function and/or the constraints are nonlinear. 41

O

Operator Splitting Quadratic Programming
Optimization algorithm designed to solve quadratic programming problems, see [Ste+20] for more details. . . . 41

P

polyphase system
AC electrical system having more than three phases . . . 73

power-energy
For the considered converter, the power-energy level refers to the MMC power balance. . . . xviii, xxxi, xxxii, xxxv, xxxvi, xxxviii, xxxix, xlii, xlv, xlvi, lviii, lxi, lxii, lxix, lxxvii–lxxix, 71, 112–115, 193–195

power-energy control
For the considered converter, the power-energy control level refers to the control ensuring that the MMC power balance satisfies the performances requirements at all time. . . . xxxvi, 193–195, 248

pulse width modulation
A modulation technique that generates variable-width pulses to represent the amplitude of an analog input signal . . . xlv, lxvii

Q

quadratic programming
A family of optimization problems and solving algorithms, where the cost function is quadratic and the constraints are linear. . . . xxiv, 38, 41, 205, 207–210, 213, 214

R

rapid control prototyping
Control loop testing procedure where only a part of the hardware - the plant with power - is the real hardware and the other part - the control system - is simulated by a dedicated computer . . . 202

redistributed pseudo-inverse
A MIB allocation method. . . . 39

reinforcement learning
Branch of research in artificial intelligence that is at the crossroads of automatic control. These methods can be used to design a control system: online, or offline, these methods use two complementary neural networks that constitute the Actor-Critic scheme. A first neural network aims at identifying the system behavior (Critic) and the second one (Actor) at deciding the control to apply to the system in order to maximize a Reward Function from knowledge about the system provided by the Critic. . . . 43

reinforcement learning allocation
An AI-based allocation method. . . . 43

S

scalable control allocation architecture
A scalable control system architecture based on control allocation methods. . . . xxiii, 200

Simplex
Optimization algorithm designed to solve linear programming problems. 41, 48, 49, 148, 149, 199, 225–227, 230, 232

stationary reference frame
In an m-phase electrical system having m alternating currents, the stationary reference frame - also called Stationary Frame - is the natural basis reference frame. In this reference frame, all the electrical signals are represented thanks to the application of the KVL and KCL to the real electrical circuit. . . . 91, 92, 97, 107

submodule
DC-DC static converter that embodies the elementary brick constitutive of the MMC. This converter can be of various topologies but must common ones are SM-HB and SM-FB xxi, xxii, xxiv, xxv, xxxii, xxxv, xxxviii, xxxix, xlii, xlix, lvi, lix, lx, lxii, lxv, lxvii–lxx, lxxv, lxxvii, lxxx, 4, 9–14, 17–22, 26–30, 32, 33, 49, 51–56, 59, 61–64, 68, 69, 73–75, 87, 96, 116, 121, 135, 136, 178–181, 195, 198, 201, 203–209, 218, 235–244, 247, II, IV

synchronous rotating reference frame
In an m-phase electrical system having m alternating currents, the synchronous rotating reference frame - also called Synchronous Rotating Frame, or Park reference frame - is the reference frame that rotates at the frequency of the alternating currents. In this reference frame, all the electrical signals are represented thanks to the application of the KVL and KCL to an equivalent electrical circuit of the real circuit. 90, 92

T

Trans Bay Cable
The Trans Bay Cable is a HVDC underwater cable interconnection between San Francisco, California and Pittsburg, California. It is 85 km-long for a 400 MW power rating and a $\pm$200 kV DC bus. For more details see Trans Bay Cable website. 9

W

weighted pseudo-inverse
A MIB allocation method. 38

Z

zero-order hold
The zero-order hold is a mathematical model of the practical signal reconstruction done by a digital-to-analog converter. That is, it describes the effect of converting a continuous-time signal to a discrete-time signal by holding each sample value for one sample interval. . . 202

List of Acronyms

A | B | C | D | E | F | G | H | I | K | L | M | N | O | P | Q | R | S | U | V | W | Z

A

AC Alternating Current . . . . . xxiv, xxv, xxxviii, xliv, xlvii, xlix–lii, liv, lvi, lix–lxii, lxv, lxvii, lxix–lxxii, lxxiv, 8, 10, 13, 15, 17, 18, 22, 24, 26, 29, 31, 32, 73–75, 77, 81, 87, 88, 92, 96, 111–114, 116, 119, 121, 124, 128, 131, 134–137, 140, 141, 179, 187, 194, 196, 197, 199, 205, 207, 215, 219, 221, 231, 233, 245, IV, V

ACA Adaptive Control Allocation 48

AI Artificial Intelligence . . . . . 43, 48, I, V

ANNA Artificial Neural Network Allocation 43

AS Active-Set . . . . . *see also* Active-Set

AVM Average Model . . . . xxi, 18, 20–26, 28, 31, 59, 60, 66, 74, *see also* average model

B

BCA Balancing Control Algorithm 28–32

C

CA Control Allocation . . . . . 4, 8, 31, 36, 37, 39–45, 48, 52, 74, 114, 166–168, 171, 188, 194, 201, 205, 207, 209, 220, 225, 226, 231–236, 241, 244, 247, 248, I, *see also* control allocation

CAI Control Allocation with Integral Compensator . . . 231–234, 247, *see also* control allocation with integral compensator

CAI-II Control Allocation with Integral Compensator - Indirect Injection 154–159, 161, 162

CAI-IPII Control Allocation with Integral Compensator - Integral Proprotionnal Indirect Injection . . . . . xxiii, 154, 158–162, 166–175, 231

CAI-TII Control Allocation with Integral Compensator - Transparent Indirect Injection . . . . . xix, xxiii, 143, 161, 162, 170, 172–175

CAOP Control Allocation Optimization Problem . xxvi, 181, 183, 186–188, 193, 195, 198, 207, 214, 215, *see also* control allocation optimization problem

CAP Control Allocation Problem 34, 35, 37, 47, 48, 199, 201, 231, 236, *see also* control allocation problem

CC Current Control 31, 32

CCI Circulating Current Injection . . . . . 31, 32, *see also* ??

CCSC Circulating Current Supression Control . 31, 32, 218, *see also* circulating current supression control

CNRS Centre National de la Recherche Scientifique (French National Center for Scientific Research) . . . . . xxiv, 204, 205

CSC Current Source Converter 9

D

DA Direct Allocation 40
DBC Deadbeat Control 31
DC Direct Current . . . . . xxi, xxiv, xxv, xlvii, xlix, l, lii, liii, lvi, lvii, lix–lxi, lxv, lxx–lxxiii, lxxvi, 8–15, 17–19, 22, 24–26, 31, 33, 39, 48, 62, 74–76, 81, 82, 87, 88, 91, 92, 112–114, 116, 117, 119, 121, 128, 134–137, 140, 141, 163, 179, 196, 197, 205, 219, 221, 224, 231, 233, 235, 242, 245, I–IV, VI
DM Detailed Model . . . . . 17–21, 60, *see also* detailed model
DP Dynamic Programming . . . . . *see also* dynamic programming

E

EC Energy Control 28, 32, 235
EM Equivalent Model . . . . . 18, 21, 60, *see also* equivalent model
EMOff Error Minimization Offline . . . . . 42, 48, 148, 151, I, II
EMOn Error Minimization Online . . . . . xxiv, 37, 41, 43, 45–49, 148, 150, 151, 178, 183, 186, 188, 189, 197, 199, 201, 205, 207, 209, 211, 214–216, 218, 221, 222, 225, 226, 230, 231, 242, 247

F

FDM Functionnal Detailed Model . . . . . 60, *see also* ??
FFT Fast Fourier Transform . . . . . xxiv, 211
FPDM Functionnal Physical Detailed Model . . . . . 60, 62, *see also* ??
FPGA Field Programmable Gate Array 48, 205
FPM Fixed-Point Method . . . . . *see also* Fixed-Point Method
FTC Fault-Tolerant Control 46, 178, 235

G

GPFOCSSM General Polyphase Full Order Current State-Space Model . . . . . xviii, xxii, xxiv, xxvii, 71, 84, 86, 87, 90, 94, 96, 107, 111, 115, 120, 121, 123, 124, 127, 130–135, 138–140, 185, 187, 189, 199, 215, 219–226, 228, 232, *see also* General Polyphase Full Order Current State-Space Model
GPFSROBHCCSSM General Polyphase Fixed-Size Reduced Order BiHarmonic Content Current State-Space Model . . . . . xviii, xxii, xxiv, xxv, xxvii, 71, 109, 111, 122, 125–127, 130–135, 137–140, 185, 187, 189, 199, 215, 219–226, 228–234, 242, 247, *see also* General Polyphase Fixed-Size Reduced Order BiHarmonic Content Current State-Space Model
GPFSROCSSM General Polyphase Fixed-Size Reduced Order Current State-Space Model xviii, xxii, 71, 88, 96, 111, 122–128, 130–135, 138–140, *see also* General Polyphase Fixed-Size Reduced Order Current State-Space Model
GPI Generalized Pseudo-Inverse 38, 40, 43
GTO Gate Turn-Off Thyristor 9

H

HIL Hardware-In-the-Loop . . . xxiv–xxvi, 4, 153, 178, 199, 202, 203, 206, 210, 211, 218, 221, 222, 233, 234, 242, 246, *see also* hardware-in-the-loop
HL High-Level . . . . . 199, *see also* high-level
HLC High-Level Control . . . . . 194, 220, 231, *see also* high-level control
HLLL High-Level-Low-Level . . . . . *see also* high-level-low-level

HLLLC High-Level-Low-Level Control .... *see also* high-level-low-level control
HVAC High-Voltage Alternating Current 8
HVDC High-Voltage Direct Current ..... 7–9, III, IV, VI

I

IGBT Insulated-Gate Bipolar Transistor 8, 9, 17
IMC Internal Model Control 31
INELFE Interconnexion Électrique France–Espagne ..... *see also* INELFE
IP Interior-Point ..... *see also* Interior-Point
ITER International Thermonuclear Experimental Reactor 48

K

KCL Kirchhoff Current Law ..... 15, 54, 75, 77, 78, V, VI
KKT Karush Khun Tucker ..... 42, *see also* ??
KVL Kirchhoff Voltage Law ..... 22, 54, V, VI

L

LAPLACE Laboratory for Plasma and Conversion of Energy (in French: Laboratoire Plasma et Conversion d'Energie) ..... xxiv, 12, 69, 117, 128, 198, 201, 203–205, 242
LL Low-Level ..... 238, *see also* low-level
LLC Low-Level Control ..... 182, 194, *see also* low-level control
LOZ Limits of the Operating Zone .. 26, 115, 116, 134, 141, 196, 217, 240, 241, 244
LP Linear Programming ..... xxvi, xxxiii, xxxv, xxxviii, lxxvii, 37, 40–42, 48, 49, 148–151, 176, 181, 183, 186, 188, 189, 193, 197, 199, 201, 207–209, 211–215, 225, 226, 230, 232, *see also* linear programming
LQR Linear-Quadratic Regulator 31

M

Matlab® Matrix Laboratory 118, 167, 242
MIB Model Inversion Based 37, 49, 112, 148, 151, 186, 189, 194, 197, 199, 205, 215, 216, 225, 227, 230, 231, 242, 248, II, V, VI
MILP Mixed-Integer Linear Programming ... 42, *see also* mixed integer linear programming
MIMO Multi-Input Multi-Ouput 22
MISO Multi-Input Single-Ouput ..... xix, 143, 162
MMC Modular Multilevel Converter ..... xxi–xxvii, xxx, xxxi, xxxiii, xxxv, xxxvi, xxxviii–lv, lvii–lxii, lxvi–lxx, lxxiii, lxxvi, lxxvii, 7–33, 48, 49, 51–53, 59, 61, 62, 64, 65, 67, 69, 72–76, 79, 80, 87, 88, 92, 95–97, 104, 110–115, 117, 118, 121, 128, 132, 134–137, 140, 141, 143, 148, 153, 154, 158, 176–183, 187, 191–193, 195, 197–201, 203–209, 211, 214–218, 220, 223, 225, 227, 229, 235, 236, 239, 241–248, 251, 252, II–VI
MPC Model Predictive Control ..... 31, 45, *see also* model predictive control
MPCA Model Predictive Control Allocation 45
MT Modulation Technique 28, 29
MTDC Multi-Terminal Direct Current 9, 10

N

NLC Nearest Level Control 29, 30
NLP Nonlinear Programming . . . . . 41, 43, *see also* nonlinear programming

O

OSQP Operator Splitting Quadratic Programming . *see also* Operator Splitting Quadratic Programming

P

PE Power-Energy . . . . . xxii, 114, *see also* power-energy
PEC Power-Energy Control . . . . . *see also* power-energy control
PI Proportional-Integral 29, 31, 37, 40, 47
PLECS® Piecewise Linear Electrical Circuit Simulation . . . . . xxii, 73, 118–121, 123–127, 129–132, 134, 141, *see also* Piecewise Linear Electrical Circuit Simulation
PLL Phase-Locked Loop 189
PM Physics Model . . . . . 17, 18, *see also* physics model
PR Proportional-Resonant 31
PSPWM Phase Shift Pulse Width Modulation 29, 198
PWM Pulse Width Modulation . . . . . xxiii, 29, 36, 48, 65, 163, 198, 205

Q

QP Quadratic Programming xxiv, xxvi, xxxiii, xxxv, xxxviii, xlv, xlvii, lxxvii, 37, 41–43, 45–49, 148–151, 166, 176, 181, 183, 186, 188, 189, 193, 197–199, 201, 207–209, 211, 213–216, 218, 221–227, 230–232, 242, 243, 247, *see also* quadratic programming

R

RCP Rapid Control Prototyping . . . . . *see also* rapid control prototyping
RL Reinforcement Learning . . . . . *see also* reinforcement learning
RLA Reinforcement Learning Allocation 44
RPI Redistributed Pseudo-Inverse 39, 46, 47
RSPWM Regular Symmetric Pulse Width Modulation 198

S

SCAA Scalable Control Allocation Architecture 199, 223, 247, *see also* scalable control allocation architecture
SHE Selective Harmonic Elimination 29, 30
Simulink® Simulink 118, 167, 242
SM Submodule xxi, xxxix, xlix, liii, lxi, lxii, lxiv–lxvi, lxxii, lxxiii, 10–15, 19, 20, 52–54, 56, 58–60, 62, 63, 73, 198, II, III, *see also* submodule
SMC Sliding-Mode Control 31
SM-FB Full-Bridge Submodule . xxi, lxiv–lxvi, 11, 20, 21, 52, 60, 62, 236, 242, VI, *see also* full-bridge submodule
SM-HB Half-Bridge Submodule . xxi, xxvi, lxv, lxvi, 11, 14, 19, 20, 52–54, 56–58, 60, 62, 237, 242, VI, *see also* half-bridge submodule
SPWM Sinusoidal Pulse Width Modulation 198
SRF Stationary Reference Frame . . 88, 138, 139, *see also* stationary reference frame

SRRF Synchronous Rotating Reference Frame . 23, 24, 26, 88, 138, 139, *see also* synchronous rotating reference frame

SSM State-Space Model . . . . . xxxi–xxxix, xli–xliii, xlvi, xlvii, lx, lxviii, lxix, lxxvi–lxxix, 23, 65–67, 199

SSTI Steady-State Time Invariant 23, 24

SVPWM Space Vector Pulse Width Modulation 198

SX Simplex . . . . . *see also* Simplex

U

u.c. Under the constraints 40, 41, 146, 148–150, 181, 182, 186, 188, 192, 201, I

V

VSC Voltage Source Converter . . . . . xxi, 9, 14, 15, 29, 179

W

WPI Weighted Pseudo-Inverse 38–40, 46, 47

Z

ZOH Zero-Order Hold . . . . . 198, *see also* zero-order hold

References

[83] "Looking back [birth of the transistor]". *IEEE Potentials*. 1983, ISSN: 0278-6648. DOI: 10.1109/MP.1983.6499561.

[AÄN09] A. Antonopoulos, L. Ängquist, and H.-P. Nee. "On dynamics and voltage control of the Modular Multilevel Converter". Journal Abbreviation: 13TH European Conference on Power Electronics and Applications Pages: 10 Publication Title: 13TH European Conference on Power Electronics and Applications. 2009.

[Ada+92] R. J. Adams, J. M. Buffington, A. G. Sparks, and S. S. Banda. "An Introduction to Multivariable Flight Control System Design". en. Tech. rep. Section: Technical Reports. WRIGHT LAB WRIGHT-PATTERSON AFB OH, 1992.

[Adi+21] W. A. Adil, J. S. Mayer, A. Greifelt, and D. Gerling. "Novel Inherently Fault Tolerant Permanent Magnet Synchronous Machine (PMSM) With Multiphase Windings". *2021 24th International Conference on Electrical Machines and Systems (ICEMS)*. ISSN: 2642-5513. 2021, DOI: 10.23919/ICEMS52562.2021.9634547.

[AE08] H. Alwi and C. Edwards. "Fault tolerant control using sliding modes with on-line control allocation". en. *Automatica*. 2008, ISSN: 0005-1098. DOI: 10.1016/j.automatica.2007.10.034.

[ALW07] J. Arrillaga, Y. Liu, and N. Watson. "Flexible Power Transmission: The HVDC Options". *Flexible Power Transmission: The HVDC Options*. 2007, DOI: 10.1002/9780470511862.

[Ang+11] L. Angquist, A. Antonopoulos, D. Siemaszko, K. Ilves, M. Vasiladiotis, and H.-P. Nee. "Open-Loop Control of Modular Multilevel Converters Using Estimation of Stored Energy". *IEEE Transactions on Industry Applications*. 2011. Conference Name: IEEE Transactions on Industry Applications, ISSN: 1939-9367. DOI: 10.1109/TIA.2011.2168593.

[Ant+14] A. Antonopoulos, L. Ängquist, L. Harnefors, K. Ilves, and H.-P. Nee. "Global Asymptotic Stability of Modular Multilevel Converters". *IEEE Transactions on Industrial Electronics*. 2014. Conference Name: IEEE Transactions on Industrial Electronics, ISSN: 1557-9948. DOI: 10.1109/TIE.2013.2254100.

[ASC19] A. Argha, S. W. Su, and B. G. Celler. "Control allocation-based fault tolerant control". *Automatica*. 2019, ISSN: 0005-1098. DOI: 10.1016/j.automatica.2019.02.014.

[Asl+11] B. Aslan, E. Semail, J. Korecki, and J. Legranger. "Slot/pole combinations choice for concentrated multiphase machines dedicated to mild-hybrid applications". *IECON 2011 - 37th Annual Conference of the IEEE Industrial Electronics Society*. ISSN: 1553-572X. 2011, DOI: 10.1109/IECON.2011.6119910.

[Bac+15] F. Bachheibl, G. Dajaku, A. Patzak, and D. Gerling. "Control Strategies and Functional Safety for the Intelligent Stator Cage Drive (ISCAD)". en. *World Electric Vehicle Journal*. 2015. Number: 2 Publisher: Multidisciplinary Digital Publishing Institute, ISSN: 2032-6653. DOI: 10.3390/wevj7020211.

[BBF18] A. Bouarfa, M. Bodson, and M. Fadel. "An optimization formulation of converter control and its general solution for the four-Leg two-Level inverter". *IEEE Transactions on Control Systems Technology*. 2018, ISSN: 1063-6536.

[BBM10] M. Barcaro, N. Bianchi, and F. Magnussen. "Analysis and Tests of a Dual Three-Phase 12-Slot 10-Pole Permanent-Magnet Motor". *IEEE Transactions on Industry Applications*. 2010. Conference Name: IEEE Transactions on Industry Applications, ISSN: 1939-9367. DOI: 10.1109/TIA.2010.2070784.

[BD04a] M. A. Bolender and D. B. Doman. "Method for Determination of Nonlinear Attainable Moment Sets". *Journal of Guidance, Control, and Dynamics*. 2004. Publisher: American Institute of Aeronautics and Astronautics _eprint: https://doi.org/10.2514/1.9548, ISSN: 0731-5090. DOI: 10.2514/1.9548.

[BD04b] M. A. Bolender and D. B. Doman. "Nonlinear Control Allocation Using Piecewise Linear Functions". *Journal of Guidance, Control, and Dynamics*. 2004. Publisher: American Institute of Aeronautics and Astronautics _eprint: https://doi.org/10.2514/1.9546, ISSN: 0731-5090. DOI: 10.2514/1.9546.

[BD95a] K. Bordignon and W. Durham. "Null-space augmented solutions to constrained control allocation problems". *Guidance, Navigation, and Control Conference*. American Institute of Aeronautics and Astronautics, 1995.

[BD95b] K. A. Bordignon and W. C. Durham. "Closed-form solutions to constrained control allocation problem". *Journal of Guidance, Control, and Dynamics*. 1995. Publisher: American Institute of Aeronautics and Astronautics _eprint: https://doi.org/10.2514/3.21497, ISSN: 0731-5090. DOI: 10.2514/3.21497.

[BDS16] B. Bahrani, S. Debnath, and M. Saeedifard. "Circulating Current Suppression of the Modular Multilevel Converter in a Double-Frequency Rotating Reference Frame". *IEEE Transactions on Power Electronics*. 2016. Conference Name: IEEE Transactions on Power Electronics, ISSN: 1941-0107. DOI: 10.1109/TPEL.2015.2405062.

[BE92] D. J. Bugajski and D. F. Enns. "Nonlinear control law with application to high angle-of-attack flight". *Journal of Guidance, Control, and Dynamics*. 1992. Publisher: American Institute of Aeronautics and Astronautics _eprint: https://doi.org/10.2514/3.20902, ISSN: 0731-5090. DOI: 10.2514/3.20902.

[BE96] J. M. Buffington and D. F. Enns. "Lyapunov stability analysis of daisy chain control allocation". *Journal of Guidance, Control, and Dynamics*. 1996. Publisher: American Institute of Aeronautics and Astronautics _eprint: https://doi.org/10.2514/3.21776, ISSN: 0731-5090. DOI: 10.2514/3.21776.

[Bel56] R. Bellman. "Dynamic programming and lagrange multipliers". *Proceedings of the National Academy of Sciences*. 1956. Publisher: Proceedings of the National Academy of Sciences, DOI: 10.1073/pnas.42.10.767.

[Ben+09] M. Benosman, F. Liao, K.-Y. Lum, and J. L. Wang. "Nonlinear Control Allocation for Non-Minimum Phase Systems". *IEEE Transactions on Control Systems Technology*. 2009. Conference Name: IEEE Transactions on Control Systems Technology, ISSN: 1558-0865. DOI: 10.1109/TCST.2008.924568.

[Ber+12] G. Bergna, J. C. Vannier, P. Lefranc, A. Arzandé, E. Berne, P. Égrot, and M. Molinas. "Modular Multilevel Converter leg-energy controller in rotating reference frame for voltage oscillations reduction". *2012 3rd IEEE International Symposium on Power Electronics for Distributed Generation Systems (PEDG)*. ISSN: 2329-5767. 2012, DOI: 10.1109/PEDG.2012.6254078.

[Ber+18] G. Bergna-Diaz, J. Freytes, X. Guillaud, S. D'Arco, and J. A. Suul. "Generalized voltage-based state-space modeling of modular multilevel converters with constant equilibrium in steady state". *IEEE Journal of Emerging and Selected Topics in Power Electronics*. 2018, ISSN: 2168-6785. DOI: 10.1109/JESTPE.2018.2793159.

[Ber+19] G. Bergna-Diaz, A. Formentini, P. Zanchetta, and E. Tedeschi. "Particle Swarm Optimization Tuning of Modular Multilevel Converters in a Time-Invariant Framework". *2019 IEEE 13th International Conference on Power Electronics and Drive Systems (PEDS)*. ISSN: 2164-5264. 2019, DOI: 10.1109/PEDS44367.2019.8998775.

[Ber15] G. Bergna-Diaz. "Modular Multilevel Converter Control for HVDC Operation: Optimal Shaping of the Circulating Current Signal for Internal Energy Regulation". en. 2015,

[BF11] M. Bodson and S. Frost. "Control Allocation with Load Balancing". *AIAA Guidance, Navigation, and Control Conference*. _eprint: https://arc.aiaa.org/doi/pdf/10.2514/6.2009-6270. American Institute of Aeronautics and Astronautics, 2011. DOI: 10.2514/6.2009-6270.

[BFB16] A. Bouarfa, M. Fadel, and M. Bodson. "A new PWM method for a 3-phase 4-leg inverter based on the injection of the opposite median reference voltage". *2016 International Symposium on Power Electronics, Electrical Drives, Automation and Motion (SPEEDAM)*. 2016, DOI: 10.1109/SPEEDAM.2016.7525959.

[BFB19] A. Bouarfa, M. Fadel, and M. Bodson. "Optimization method based on simplex algorithm for current control of modular multilevel converters". *2019 IEEE International Conference on Industrial Technology (ICIT)*. 2019,

[BM02] J. Boskovic and R. Mehra. "Control allocation in overactuated aircraft under position and rate limiting". *Proceedings of the 2002 American Control Conference*. 2002,

[BMB14] S. Bacha, I. Munteanu, and A. I. Bratcu. "Power Electronic Converters Modeling and Control: with Case Studies". en. London: Springer-Verlag, 2014. ISBN: 978-1-4471-5477-8.

[Boa+10] J. Boada, C. Prieur, S. Tarbouriech, C. Pittet, and C. Charbonnel. "Multi-saturation anti-windup structure for satellite control". *Proceedings of the 2010 American Control Conference*. ISSN: 2378-5861. 2010, DOI: 10.1109/ACC.2010.5531254.

[Bod02] M. Bodson. "Evaluation of optimization methods for control allocation". *Journal of Guidance, Control, and Dynamics*. 2002,

[Bod20] M. Bodson. "Speed Control for Doubly Fed Induction Motors With and Without Current Feedback". *IEEE Transactions on Control Systems Technology*. 2020. Conference Name: IEEE Transactions on Control Systems Technology, ISSN: 1558-0865. DOI: 10.1109/TCST.2019.2898372.

[Bor+05] F. Borrelli, P. Falcone, T. Keviczky, J. Asgari, and. "MPC-based approach to active steering for autonomous vehicle systems". *International Journal of Vehicle Autonomous Systems*. 2005. Publisher: Inderscience Publishers, ISSN: 1471-0226. DOI: 10.1504/IJVAS.2005.008237.

[Bou+15] A. Bouarfa, M. Fadel, M. Bodson, and J. Lin. "A new control allocation method for power converters and its application to the four-leg two-level inverter". *2015 23rd Mediterranean Conference on Control and Automation (MED)*. 2015,

[Bou17] A. Bouarfa. "Méthodes de commande par allocation de convertisseurs statiques polyphasés, multi-niveaux : de la modélisation à la mise en oeuvre temps-réel". fr. Ph.D. Thesis. Université Toulouse III - Paul-Sabatier, 2017.

[Bow75] S. R. Bowes. "New sinusoidal pulsewidth-modulated invertor". *Proceedings of the Institution of Electrical Engineers*. 1975, ISSN: 0020-3270. DOI: 10.1049/piee.1975.0312.

[Bro85] W. L. Brogan. "Modern Control Theory, 2nd Edition". English. 2nd edition. Englewood Cliffs, N.J: Prentice Hall, 1985. ISBN: 978-0-13-590316-2.

[BSD15] G. Bergna Diaz, J. A. Suul, and S. D'Arco. "Small-signal state-space modeling of modular multilevel converters for system stability analysis". *2015 IEEE Energy Conversion Congress and Exposition (ECCE)*. ISSN: 2329-3748. 2015, DOI: 10.1109/ECCE.2015.7310477.

[BSD16] G. Bergna-Diaz, J. A. Suul, and S. D'Arco. "State-space modelling of modular multilevel converters for constant variables in steady-state". *2016 IEEE 17th Workshop on Control and Modeling for Power Electronics (COMPEL)*. 2016, DOI: 10.1109/COMPEL.2016.7556695.

[Buf97] J. Buffington. "Tailless aircraft control allocation". *Guidance, Navigation, and Control Conference*. American Institute of Aeronautics and Astronautics, 1997.

[Bur+01] J. J. Burken, P. Lu, Z. Wu, and C. Bahm. "Two Reconfigurable Flight-Control Design Methods: Robust Servomechanism and Control Allocation". *Journal of Guidance, Control, and Dynamics*. 2001. Publisher: American Institute of Aeronautics and Astronautics _eprint: https://doi.org/10.2514/2.4769, ISSN: 0731-5090. DOI: 10.2514/2.4769.

[CB19] R. de Castro and J. Brembeck. "Lyapunov-based Control Allocation for Over-actuated Nonlinear Systems". *2019 American Control Conference (ACC)*. ISSN: 2378-5861. 2019, DOI: 10.23919/ACC.2019.8814326.

[CB21] R. de Castro and J. Brembeck. "Lyapunov-based fault tolerant control allocation". *Vehicle System Dynamics*. 2021. Publisher: Taylor & Francis _eprint: https://doi.org/10.1080/00423114.2021.1971265, ISSN: 0042-3114. DOI: 10.1080/00423114.2021.1971265.

[CD15] A. Christe and D. Dujić. "State-space modeling of modular multilevel converters including line frequency transformer". *2015 17th European Conference on Power Electronics and Applications (EPE'15 ECCE-Europe)*. 2015, DOI: 10.1109/EPE.2015.7309055.

[Cid+11] A. Cid-Pastor, R. Giral, J. Calvente, V. I. Utkin, and L. Martinez-Salamero. "Interleaved Converters Based on Sliding-Mode Control in a Ring Configuration". *IEEE Transactions on Circuits and Systems I: Regular Papers*. 2011. Conference Name: IEEE Transactions on Circuits and Systems I: Regular Papers, ISSN: 1558-0806. DOI: 10.1109/TCSI.2011.2131310.

[Cif+21] B. Ciftci, L. Harnefors, X. Wang, J. Gross, and S. Norrga. "Wireless control of modular multilevel converter autonomous submodules". 2021.

[CJ14] A. Cristofaro and T. A. Johansen. "Fault-tolerant control allocation with actuator dynamics: Finite-time control reconfiguration". en. *53rd IEEE Conference on Decision and Control*. Los Angeles, CA, USA: IEEE, 2014, ISBN: 978-1-4673-6090-6 978-1-4799-7746-8 978-1-4799-7745-1. DOI: 10.1109/CDC.2014.7040165.

[Cla43] E. Clarke. "Circuit analysis of AC power systems; symmetrical and related components". en. Wiley, 1943.

[Con51] C. Concordia. "Synchronous machines: theory and performance". en. Wiley, 1951.

[CPJ18] A. Cristofaro, M. M. Polycarpou, and T. A. Johansen. "Fault-Tolerant Control Allocation for Overactuated Nonlinear Systems: Fault-tolerant Control Allocation for Overactuated Nonlinear Systems". en. *Asian Journal of Control*. 2018, ISSN: 15618625. DOI: 10.1002/asjc.1619.

[Cun83] T. B. Cunningham. "Robust reconfiguration for high reliability and survivability for advanced aircraft". *Restructurable Controls*. Nasa Conference Publication 2277. 1983,

[CVR12] N. Cherix, M. Vasiladiotis, and A. Rufer. "Functional modeling and Energetic Macroscopic Representation of Modular Multilevel Converters". *2012 15th International Power Electronics and Motion Control Conference (EPE/PEMC)*. 2012, DOI: 10.1109/EPEPEMC.2012.6397382.

[CW12] Y. Chen and J. Wang. "Fast and Global Optimal Energy-Efficient Control Allocation With Applications to Over-Actuated Electric Ground Vehicles". *IEEE Transactions on Control Systems Technology*. 2012. Conference Name: IEEE Transactions on Control Systems Technology, ISSN: 1558-0865. DOI: 10.1109/TCST.2011.2161989.

[Dan51] G. B. Dantzig. "Maximization of a Linear Function of Variables Subject to LinearInequalities, in Activity Analysis of Production and Allocation". Wiley, 1951.

[Den+15] S. Dennetière, H. Saad, B. Clerc, E. Ghahremani, W. Li, and J. Bélanger. "Validation of a MMC model in a real-time simulation platform for industrial HIL tests". *2015 IEEE Power & Energy Society General Meeting*. ISSN: 1932-5517. 2015, DOI: 10.1109/PESGM.2015.7286153.

[Den+16] F. Deng, Y. Tian, R. Zhu, and Z. Chen. "Fault-Tolerant Approach for Modular Multilevel Converters Under Submodule Faults". *IEEE Transactions on Industrial Electronics*. 2016. Conference Name: IEEE Transactions on Industrial Electronics, ISSN: 1557-9948. DOI: 10.1109/TIE.2016.2538201.

[Den+20] F. Deng, Y. Lu, C. Liu, Q. Heng, Q. Yu, and J. Zhao. "Overview on submodule topologies, modeling, modulation, control schemes, fault diagnosis, and tolerant control strategies of modular multilevel converters". *Chinese Journal of Electrical Engineering*. 2020, DOI: 10.23919/CJEE.2020.000001.

[DG18] G. Dajaku and D. Gerling. "Opportunities of Advanced Multi-phase Concentrated Windings". *2018 XIII International Conference on Electrical Machines (ICEM)*. ISSN: 2381-4802. 2018, DOI: 10.1109/ICELMACH.2018.8506932.

[DGM14] G. Darivianakis, T. Geyer, and W. van der Merwe. "Model predictive current control of modular multilevel converters". *2014 IEEE Energy Conversion Congress and Exposition (ECCE)*. ISSN: 2329-3748. 2014, DOI: 10.1109/ECCE.2014.6954089.

[DGN09] D. B. Doman, B. J. Gamble, and A. D. Ngo. "Quantized Control Allocation of Reaction Control Jets and Aerodynamic Control Surfaces". *Journal of Guidance, Control, and Dynamics*. 2009,

[Din+08] G. Ding, G. Tang, Z. He, and M. Ding. "New technologies of voltage source converter (VSC) for HVDC transmission system based on VSC". *2008 IEEE Power and Energy Society General Meeting - Conversion and Delivery of Electrical Energy in the 21st Century*. ISSN: 1932-5517. 2008, DOI: 10.1109/PES.2008.4596399.

[DKM17] C. Dahmen, F. Kapaun, and R. Marquardt. "Analytical investigation of efficiency and operating range of different Modular Multilevel Converters". *2017 IEEE 12th International Conference on Power Electronics and Drive Systems (PEDS)*. ISSN: 2164-5264. 2017, DOI: 10.1109/PEDS.2017.8289151.

[DLB01] J. B. Davidson, F. J. Lallman, and W. T. Bundick. "Real-Time Adaptive Control Allocation Applied to a High Performance Aircraft". NTRS Author Affiliations: NASA Langley Research Center NTRS Document ID: 20040086083 NTRS Research Center: Langley Research Center (LaRC). 2001.

[DQV19] B. Džonlaga, L. Quéval, and J.-C. Vannier. "Impact of the arm resistance and inductance on the PQ diagram of a modular multilevel converter". *2019 20th International Symposium on Power Electronics (Ee)*. 2019, DOI: 10.1109/PEE.2019.8923290.

[DS02] D. Doman and A. Sparks. "Concepts for constrained control allocation of mixed quadratic and linear effectors". *Proceedings of the 2002 American Control Conference (IEEE Cat. No.CH37301)*. ISSN: 0743-1619. 2002, DOI: 10.1109/ACC.2002.1024507.

[Dur93] W. C. Durham. "Constrained control allocation". *Journal of Guidance, Control, and Dynamics*. 1993,

[Dur94a] W. C. Durham. "Attainable moments for the constrained control allocation problem". *Journal of Guidance, Control, and Dynamics*. 1994. Publisher: American Institute of Aeronautics and Astronautics _eprint: https://doi.org/10.2514/3.21360, ISSN: 0731-5090. DOI: 10.2514/3.21360.

[Dur94b] W. C. Durham. "Constrained control allocation - Three-moment problem". *Journal of Guidance, Control, and Dynamics*. 1994. Publisher: American Institute of Aeronautics and Astronautics _eprint: https://doi.org/10.2514/3.21201, ISSN: 0731-5090. DOI: 10.2514/3.21201.

[Dur99] W. C. Durham. "Efficient, Near-Optimal Control Allocation". *Journal of Guidance, Control, and Dynamics*. 1999. Publisher: American Institute of Aeronautics and Astronautics _eprint: https://doi.org/10.2514/2.4390, ISSN: 0731-5090. DOI: 10.2514/2.4390.

[Els+20] A. I. Elsanabary, G. Konstantinou, S. Mekhilef, C. D. Townsend, M. Seyedmahmoudian, and A. Stojcevski. "Medium Voltage Large-Scale Grid-Connected Photovoltaic Systems Using Cascaded H-Bridge and Modular Multilevel Converters: A Review". *IEEE Access*. 2020, ISSN: 2169-3536. DOI: 10.1109/ACCESS.2020.3044882.

[Enn98] D. Enns. "Control allocation approaches". *Guidance, Navigation, and Control Conference and Exhibit*. _eprint: https://arc.aiaa.org/doi/pdf/10.2514/6.1998-4109. American Institute of Aeronautics and Astronautics, 1998. DOI: 10.2514/6.1998-4109.

[FAD09] N. Flourentzou, V. G. Agelidis, and G. D. Demetriades. "VSC-Based HVDC Power Transmission Systems: An Overview". *IEEE Transactions on Power Electronics*. 2009. Conference Name: IEEE Transactions on Power Electronics, ISSN: 1941-0107. DOI: 10.1109/TPEL.2008.2008441.

[Fat+01] H. Fathy, J. Reyer, P. Papalambros, and A. Ulsov. "On the coupling between the plant and controller optimization problems". *Proceedings of the 2001 American Control Conference. (Cat. No.01CH37148)*. ISSN: 0743-1619. 2001, DOI: 10.1109/ACC.2001.946008.

[FB10] S. A. Frost and M. Bodson. "Resource balancing control allocation". *Proceedings of the 2010 American Control Conference*. 2010,

[FBA09] S. Frost, M. Bodson, and D. Acosta. "Sensitivity Analysis of Linear Programming and Quadratic Programming Algorithms for Control Allocation". en. *AIAA Infotech@Aerospace Conference*. Seattle, Washington: American Institute of Aeronautics and Astronautics, 2009. ISBN: 978-1-60086-979-2. DOI: 10.2514/6.2009-1936.

[Fen+10] L. Feng, Z. Wu, Y. Li, and J. Sun. "Research on traction force allocation for omni-directional mobile robots". *2010 2nd International Conference on Mechanical and Electronics Engineering*. 2010, DOI: 10.1109/ICMEE.2010.5558393.

[FG19] H. Fehr and A. Gensior. "Model-Based Circulating Current References for MMC Cell Voltage Ripple Reduction and Loss-Equivalent Arm Current Assessment". *2019 21st European Conference on Power Electronics and Applications (EPE '19 ECCE Europe)*. 2019, DOI: 10.23919/EPE.2019.8914767.

[FJ15] A. a. J. Far and D. Jovcic. "Circulating current suppression control dynamics and impact on MMC converter dynamics". *2015 IEEE Eindhoven PowerTech*. 2015, DOI: 10.1109/PTC.2015.7232762.

[FJB19] S. Fuchs, M. Jeong, and J. Biela. "Long Horizon, Quadratic Programming Based Model Predictive Control (MPC) for Grid Connected Modular Multilevel Converters (MMC)". *IECON 2019 - 45th Annual Conference of the IEEE Industrial Electronics Society*. ISSN: 1553-572X. 2019, DOI: 10.1109/IECON.2019.8927493.

[Fre+16a] J. Freytes, S. Akkari, J. Dai, F. Gruson, P. Rault, and X. Guillaud. "Small-signal state-space modeling of an HVDC link with modular multilevel converters". en. *2016 IEEE 17th Workshop on Control and Modeling for Power Electronics (COMPEL)*. Trondheim, Norway: IEEE, 2016, ISBN: 978-1-5090-1815-4. DOI: 10.1109/COMPEL.2016.7556693.

[Fre+16b] J. Freytes, L. Papangelis, H. Saad, P. Rault, T. Van Cutsem, and X. Guillaud. "On the modeling of MMC for use in large scale dynamic simulations". en. *2016 Power Systems Computation Conference (PSCC)*. Genoa, Italy: IEEE, 2016, ISBN: 978-88-941051-2-4. DOI: 10.1109/PSCC.2016.7540938.

[Fre+18] J. Freytes, G. Bergna, J. A. Suul, S. D'Arco, F. Gruson, F. Colas, H. Saad, et al. "Improving Small-Signal Stability of an MMC With CCSC by Control of the Internally Stored Energy". *IEEE Transactions on Power Delivery*. 2018. Conference Name: IEEE Transactions on Power Delivery, ISSN: 1937-4208. DOI: 10.1109/TPWRD.2017.2725579.

[FS91] T. I. Fossen and S. I. Sagatun. "Adaptive control of nonlinear systems: A case study of underwater robotic systems". en. *Journal of Robotic Systems*. 1991. _eprint: https://onlinelibrary.wiley.com/doi/pdf/10.1002/rob.4620080307, ISSN: 1097-4563. DOI: 10.1002/rob.4620080307.

[Gao+11] C. Gao, J. Jiang, X. Yang, L. Xie, and K. Cao. "A novel topology and control strategy of modular multilevel converter (MMC)". *2011 International Conference on Electrical and Control Engineering*. 2011, DOI: 10.1109/ICECENG.2011.6057270.

[Gar19] M. Garcia-Sanz. "Control Co-Design: An engineering game changer". en. *Advanced Control for Applications*. 2019. _eprint: https://onlinelibrary.wiley.com/doi/pdf/10.1002/adc2.18, ISSN: 2578-0727. DOI: 10.1002/adc2.18.

[Gat00] S. Gataric. "A polyphase cartesian vector approach to control of polyphase AC machines". *2000 IEEE Industry Applications Conference. Thirty-Fifth IAS Annual Meeting*. 2000, DOI: 10.1109/IAS.2000.882102.

[Gey+18] T. Geyer, W. VAN-DER-MERWE, V. Spudic, and G. Darivianakis. "Model predictive control of a modular multilevel converter". en. 2018.

[Gey16] T. Geyer. "Model Predictive Control of a Modular Multilevel Converter". en. *Model Predictive Control of High Power Convertersand Industrial Drives*. Section: 14 _eprint: https://onlinelibrary.wiley.com/doi/pdf/10.1002/9781119010883.ch14. John Wiley & Sons, Ltd, 2016, ISBN: 978-1-119-01088-3. DOI: 10.1002/9781119010883.ch14.

[GGJ11] U. N. Gnanarathna, A. M. Gole, and R. P. Jayasinghe. "Efficient Modeling of Modular Multilevel HVDC Converters (MMC) on Electromagnetic Transient Simulation Programs". *IEEE Transactions on Power Delivery*. 2011. Conference Name: IEEE Transactions on Power Delivery, ISSN: 1937-4208. DOI: 10.1109/TPWRD.2010.2060737.

[GPM89] C. E. García, D. M. Prett, and M. Morari. "Model predictive control: Theory and practice—A survey". en. *Automatica*. 1989, ISSN: 0005-1098. DOI: 10.1016/0005-1098(89)90002-2.

[Gro] N. Group. "Naval Group AREVA Jeumont 13-phase PM motor".

[Gro94] R. L. Grogan. "On the Application of Neural Network Computing to the Constrained Control Allocation Problem". Virginia Polytechnic Institute & State University. Masters' Thesis. Virginia Polytechnic Institute & State University, 1994.

[Gru+20] F. Gruson, A. Tlemcani, Y. Li, P. Delarue, P. Le Moigne, and X. Guillaud. "Model and control of the DC–DC modular multilevel converter with DC fault tolerance". *EPE Journal*. 2020. Publisher: Taylor & Francis _eprint: https://doi.org/10.1080/09398368.2020.1750847, ISSN: 0939-8368. DOI: 10.1080/09398368.2020.1750847.

[GS21] V. Graber and E. Schuster. "Nonlinear burn control in ITER using adaptive allocation of actuators with uncertain dynamics". en. *Nuclear Fusion*. 2021. ISSN: 0029-5515, 1741-4326. DOI: 10.1088/1741-4326/ac3cd8.

[Gue+11] J. M. Guerrero, J. C. Vasquez, J. Matas, L. G. de Vicuna, and M. Castilla. "Hierarchical Control of Droop-Controlled AC and DC Microgrids—A General Approach Toward Standardization". *IEEE Transactions on Industrial Electronics*. 2011. Conference Name: IEEE Transactions on Industrial Electronics, ISSN: 1557-9948. DOI: 10.1109/TIE.2010.2066534.

[HA09] M. Hagiwara and H. Akagi. "Control and Experiment of Pulsewidth-Modulated Modular Multilevel Converters". *IEEE Transactions on Power Electronics*. 2009, ISSN: 1941-0107. DOI: 10.1109/TPEL.2009.2014236.

[Han+11] M. Hanger, T. A. Johansen, G. K. Mykland, and A. Skullestad. "Dynamic model predictive control allocation using CVXGEN". *2011 9th IEEE International Conference on Control and Automation (ICCA)*. ISSN: 1948-3457. 2011, DOI: 10.1109/ICCA.2011.6137940.

[Här] O. Härkegård. "QCAT - File Exchange - MATLAB Central". en. https://www.mathworks.com/matlabcentral/fileexchange/4609.

[Har+13] L. Harnefors, A. Antonopoulos, S. Norrga, L. Angquist, and H.-P. Nee. "Dynamic Analysis of Modular Multilevel Converters". *IEEE Transactions on Industrial Electronics*. 2013. Conference Name: IEEE Transactions on Industrial Electronics, ISSN: 1557-9948. DOI: 10.1109/TIE.2012.2194974.

[Har+15] L. Harnefors, A. Antonopoulos, K. Ilves, and H.-P. Nee. "Global Asymptotic Stability of Current-Controlled Modular Multilevel Converters". *IEEE Transactions on Power Electronics*. 2015. Conference Name: IEEE Transactions on Power Electronics, ISSN: 1941-0107. DOI: 10.1109/TPEL.2014.2298560.

[Här02a] O. Härkegård. "Efficient active set algorithms for solving constrained least squares problems in aircraft control allocation". *Proceedings of the 41st IEEE Conference on Decision and Control, 2002.* 2002, DOI: 10.1109/CDC.2002.1184694.

[Här02b] O. Härkegård. "Dynamic Control Allocation Using Constrained Quadratic Programming". en. 2002,

[Här03] O. Härkegård. "Backstepping and control allocation with applications to flight control". en. Linköping: Univ, 2003. ISBN: 978-91-7373-647-3.

[Has+15] A. Hassanpoor, L. Ängquist, S. Norrga, K. Ilves, and H.-P. Nee. "Tolerance Band Modulation Methods for Modular Multilevel Converters". *IEEE Transactions on Power Electronics*. 2015. Conference Name: IEEE Transactions on Power Electronics, ISSN: 1941-0107. DOI: 10.1109/TPEL.2014.2305114.

[Has+16] A. Hassanpoor, A. Roostaei, S. Norrga, and M. Lindgren. "Optimization-Based Cell Selection Method for Grid-Connected Modular Multilevel Converters". *IEEE Transactions on Power Electronics*. 2016. Conference Name: IEEE Transactions on Power Electronics, ISSN: 1941-0107. DOI: 10.1109/TPEL.2015.2448573.

[HG84] J. A. Houldsworth and D. A. Grant. "The Use of Harmonic Distortion to Increase the Output Voltage of a Three-Phase PWM Inverter". *IEEE Transactions on Industry Applications*. 1984. Conference Name: IEEE Transactions on Industry Applications, ISSN: 1939-9367. DOI: 10.1109/TIA.1984.4504587.

[HL03] D. G. Holmes and T. A. Lipo. "Pulse Width Modulation for Power Converters: Principles and Practice". en. Google-Books-ID: ckETEAAAQBAJ. John Wiley & Sons, 2003. ISBN: 978-0-471-20814-3.

[Hol92] D. G. Holmes. "The general relationship between regular-sampled pulse-width-modulation and space vector modulation for hard switched converters". *Conference Record of the 1992 IEEE Industry Applications Society Annual Meeting*. 1992, DOI: 10.1109/IAS.1992.244437.

[HT07] Y. Huang and C. K. Tse. "Circuit Theoretic Classification of Parallel Connected DC–DC Converters". *IEEE Transactions on Circuits and Systems I: Regular Papers*. 2007. Conference Name: IEEE Transactions on Circuits and Systems I: Regular Papers, ISSN: 1558-0806. DOI: 10.1109/TCSI.2007.890631.

[Hu+14] P. Hu, D. Jiang, Y. Zhou, Y. Liang, J. Guo, and Z. Lin. "Energy-balancing Control Strategy for Modular Multilevel Converters Under Submodule Fault Conditions". *IEEE Transactions on Power Electronics*. 2014. Conference Name: IEEE Transactions on Power Electronics, ISSN: 1941-0107. DOI: 10.1109/TPEL.2013.2284919.

[Hua+18] H. Huan, W. Wan, C. We, and Y. He. "Constrained Nonlinear Control Allocation based on Deep Auto-Encoder Neural Networks". *2018 European Control Conference (ECC)*. 2018, DOI: 10.23919/ECC.2018.8550445.

[Ilv+11] K. Ilves, A. Antonopoulos, L. Harnefors, S. Norrga, L. Ängquist, and H.-P. Nee. "Capacitor voltage ripple shaping in modular multilevel converters allowing for operating region extension". *IECON 2011 - 37th Annual Conference of the IEEE Industrial Electronics Society*. ISSN: 1553-572X. 2011, DOI: 10.1109/IECON.2011.6120033.

[Ilv+12] K. Ilves, A. Antonopoulos, S. Norrga, and H.-P. Nee. "Steady-state analysis of interaction between harmonic components of arm and line quantities of modular multilevel converters". *IEEE Transactions on Power Electronics*. 2012, ISSN: 1941-0107. DOI: 10.1109/TPEL.2011.2159809.

[Ilv+15a] K. Ilves, L. Bessegato, L. Harnefors, S. Norrga, and H.-P. Nee. "Semi-full-bridge submodule for modular multilevel converters". *2015 9th International Conference on Power Electronics and ECCE Asia (ICPE-ECCE Asia)*. ISSN: 2150-6086. 2015, DOI: 10.1109/ICPE.2015.7167913.

[Ilv+15b] K. Ilves, L. Harnefors, S. Norrga, and H.-P. Nee. "Analysis and Operation of Modular Multilevel Converters With Phase-Shifted Carrier PWM". *IEEE Transactions on Power Electronics*. 2015. Conference Name: IEEE Transactions on Power Electronics, ISSN: 1941-0107. DOI: 10.1109/TPEL.2014.2321049.

[Ilv+15c] K. Ilves, L. Harnefors, S. Norrga, and H.-P. Nee. "Predictive Sorting Algorithm for Modular Multilevel Converters Minimizing the Spread in the Submodule Capacitor Voltages". *IEEE Transactions on Power Electronics*. 2015. Conference Name: IEEE Transactions on Power Electronics, ISSN: 1941-0107. DOI: 10.1109/TPEL.2014.2308018.

[IP06] G. Indiveri and G. Parlangeli. "On thruster allocation, fault detection and accommodation issues for underwater robotic vehicles." en. 2006,

[IP22] G. Indiveri and G. Parlangeli. "On thruster allocation, fault detection and accommodation issues for underwater robotic vehicles.". 2022.

[Jac+01] C. Jacobina, A. Nogueira Lima, E. da Silva, R. Alves, and P. Seixas. "Digital scalar pulse-width modulation: a simple approach to introduce nonsinusoidal modulating waveforms". *IEEE Transactions on Power Electronics*. 2001. Conference Name: IEEE Transactions on Power Electronics, ISSN: 1941-0107. DOI: 10.1109/63.923767.

[JBL08] D. Joosten, T. Boom, and T. Lombaerts. "Computationally Efficient Use of MPC and Dynamic Inversion for Reconfigurable Flight Control". *AIAA Guidance, Navigation and Control Conference and Exhibit*. _eprint: https://arc.aiaa.org/doi/pdf/10.2514/6.2008-7431. American Institute of Aeronautics and Astronautics, 2008. DOI: 10.2514/6.2008-7431.

[JF13] T. A. Johansen and T. I. Fossen. "Control allocation—A survey". *Automatica*. 2013, ISSN: 0005-1098.

[JFB04] T. Johansen, T. Fossen, and S. Berge. "Constrained nonlinear control allocation with singularity avoidance using sequential quadratic programming". *IEEE Transactions on Control Systems Technology*. 2004. Conference Name: IEEE Transactions on Control Systems Technology, ISSN: 1558-0865. DOI: 10.1109/TCST.2003.821952.

[Jin+06] J. Jin, B. Park, Y. Park, and M.-J. Tahk. "Attitude control of a satellite with redundant thrusters". en. *Aerospace Science and Technology*. 2006, ISSN: 1270-9638. DOI: 10.1016/j.ast.2006.04.005.

[Jin+21] Y. Jin, Q. Xiao, H. Jia, Y. Mu, Y. Ji, T. Dragičević, R. Teodorescu, et al. "A Novel Sliding-Discrete-Control-Set Modulated Model Predictive Control for Modular Multilevel Converter". *IEEE Access*. 2021. Conference Name: IEEE Access, ISSN: 2169-3536. DOI: 10.1109/ACCESS.2021.3050340.

[JJ16] A. Jamshidi Far and D. Jovcic. "Small-Signal Dynamic DQ Model of Modular Multilevel Converter for System Studies". *IEEE Transactions on Power Delivery*. 2016. Conference Name: IEEE Transactions on Power Delivery, ISSN: 1937-4208. DOI: 10.1109/TPWRD.2015.2478489.

[Joh+03] T. A. Johansen, T. P. Fuglseth, P. Tøndel, and T. I. Fossen. "Optimal constrained control allocation in marine surface vessels with rudders". en. *IFAC Proceedings Volumes*. 6th IFAC Conference on Manoeuvring and Control of Marine Craft (MCMC 2003), Girona, Spain, 17-19 September, 1997. 2003, ISSN: 1474-6670. DOI: 10.1016/S1474-6670(17)37804-7.

[Joh+08] T. A. Johansen, T. P. Fuglseth, P. Tøndel, and T. I. Fossen. "Optimal constrained control allocation in marine surface vessels with rudders". en. *Control Engineering Practice*. Special Section on Manoeuvering and Control of Marine Craft. 2008, ISSN: 0967-0661. DOI: 10.1016/j.conengprac.2007.01.012.

[Joh04] T. Johansen. "Optimizing nonlinear control allocation". *2004 43rd IEEE Conference on Decision and Control (CDC) (IEEE Cat. No.04CH37601)*. ISSN: 0191-2216. 2004, DOI: 10.1109/CDC.2004.1429240.

[Kar39] W. Karush. "Minima of functions of several variables with inequalities as side conditions". OCLC: 43268508. PhD thesis. 1939.

[Kes03] X. Kestelyn. "Modélisation vectorielle multimachines pour la commande des ensembles convertisseurs-machines polyphasés". Ph.D. Thesis. Université Lille 1, 2003.

[KH83] C. A. Klein and C.-H. Huang. "Review of pseudoinverse control for use with kinematically redundant manipulators". *IEEE Transactions on Systems, Man, and Cybernetics*. 1983. Conference Name: IEEE Transactions on Systems, Man, and Cybernetics, ISSN: 2168-2909. DOI: 10.1109/TSMC.1983.6313123.

[Kha+20] I. Khayour, S. Durand, L. Cuvillon, and J. Gangloff. "Active Damping of Parallel Robots Driven by Elastic Cables using On-Off Actuators through Model Predictive Control Allocation". en. *IFAC-PapersOnLine*. 21st IFAC World Congress. 2020, ISSN: 2405-8963. DOI: 10.1016/j.ifacol.2020.12.2167.

[Kha+22] H. Z. I. Khan, S. Mobeen, J. Rajput, and J. Riaz. "Nonlinear Control Allocation: A Learning Based Approach". en. *arXiv:2201.06180 [cs, eess, math]*. 2022. arXiv: 2201.06180.

[Kis+19] M. Kissai, B. Monsuez, X. Mouton, D. Martinez, and A. Tapus. "Model Predictive Control Allocation of Systems with Different Dynamics". *2019 IEEE Intelligent Transportation Systems Conference (ITSC)*. 2019, DOI: 10.1109/ITSC.2019.8917438.

[KLL20] P. Kolaric, V. G. Lopez, and F. L. Lewis. "Optimal dynamic control allocation with guaranteed constraints and online reinforcement learning". en. *Automatica*. 2020. ISSN: 0005-1098.

[KM18] D. Karwatzki and A. Mertens. "Generalized control approach for a class of modular multilevel converter topologies". *IEEE Transactions on Power Electronics*. 2018, ISSN: 1941-0107. DOI: 10.1109/TPEL.2017.2703917.

[Kre+21] J. Kreiss, M. Bodson, R. Delpoux, J.-Y. Gauthier, J.-F. Trégouët, and X. Lin-Shi. "Optimal control allocation for the parallel interconnection of buck converters". en. *Control Engineering Practice*. 2021. ISSN: 0967-0661.

[Kre19] J. Kreiss. "Allocation de commande pour l'électrotechnique et l'électronique de puissance". fr. 2019,

[KS11] X. Kestelyn and E. Semail. "A Vectorial Approach for Generation of Optimal Current References for Multiphase Permanent-Magnet Synchronous Machines in Real Time". *IEEE Transactions on Industrial Electronics*. 2011. Conference Name: IEEE Transactions on Industrial Electronics, ISSN: 1557-9948. DOI: 10.1109/TIE.2011.2119454.

[KT51] H. W. Kuhn and A. W. Tucker. "Nonlinear Programming". *Proceedings of the Second Berkeley Symposium on Mathematical Statistics and Probability*. 1951. Publisher: University of California Press,

[KW21] H. J. Karssies and C. D. Wagter. “XINCA: Extended Incremental Non-linear Control Allocation on a Quadplane”. en. 2021,

[Lad+12] P. Ladoux, P. Marino, G. Raimondo, and N. Serbia. “Comparison of high voltage modular AC/DC converters”. Pages: 848. 2012. ISBN: 978-1-4673-1299-8. DOI: 10.1109/SPEEDAM.2012.6264569.

[Lal85] F. J. Lallman. “Relative control effectiveness technique with application to airplane control coordination”. NTRS Author Affiliations: NASA Langley Research Center NTRS Report/Patent Number: NAS 1.60:2416 NTRS Document ID: 19850015442 NTRS Research Center: Legacy CDMS (CDMS). 1985.

[LB16] W. Li and J. Bélanger. “An Equivalent Circuit Method for Modelling and Simulation of Modular Multilevel Converters in Real-Time HIL Test Bench”. *IEEE Transactions on Power Delivery*. 2016. Conference Name: IEEE Transactions on Power Delivery, ISSN: 1937-4208. DOI: 10.1109/TPWRD.2016.2541461.

[LBF22] G. Le Goff, M. Bodson, and M. Fadel. “Model Reference Control of Constrained Overactuated Systems with Integral Compensation”. *2022 IEEE 61st Conference on Decision and Control (CDC)*. ISSN: 2576-2370. 2022, DOI: 10.1109/CDC51059.2022.9992648.

[Le +18] H. T. Le Luong, F. Messine, C. Hénaux, G. Bueno Mariani, N. Voyer, and S. Mollov. “3D Electromagnetic and Thermal Analysis for an Optimized Wound Rotor Synchronous Machine”. *2018 XIII International Conference on Electrical Machines (ICEM)*. ISSN: 2381-4802. 2018, DOI: 10.1109/ICELMACH.2018.8507020.

[Let+19] A. Letellier, M. Dubois, J. P. Trovao, and H. Maher. “Calculation of PCB Power Loop Stray Inductance in GaN or High di/dt Applications”. *IEEE Transactions on Power Electronics*. 2019, DOI: 10.1109/TPEL.2018.2826920.

[Lev08] E. Levi. “Multiphase Electric Machines for Variable-Speed Applications”. *IEEE Transactions on Industrial Electronics*. 2008. Conference Name: IEEE Transactions on Industrial Electronics, ISSN: 1557-9948. DOI: 10.1109/TIE.2008.918488.

[Lev17] W. S. Levine, ed. “The Control Handbook: Control System Applications, Second Edition”. 2nd ed. Boca Raton: CRC Press, 2017. ISBN: 978-1-315-21872-4. DOI: 10.1201/b10382.

[LFB21a] G. Le Goff, M. Fadel, and M. Bodson. “Modélisation Analytique Modulaire du Convertisseur Modulaire Multiniveaux (MMC)”. *Symposium de Génie Electrique 2020 (SGE)*. Nantes, France: IREENA, 2021.

[LFB21b] G. Le Goff, M. Fadel, and M. Bodson. “Modular polyphased full order current state-space model of the modular multilevel converter”. *2021 IEEE 19th International Power Electronics and Motion Control Conference (PEMC)*. 2021, DOI: 10.1109/PEMC48073.2021.9432502.

[LFB22a] G. Le Goff, M. Fadel, and M. Bodson. “-Scalable Optimal Control Allocation: Linear and Quadratic Programming Methods Applied to Active Capacitor Balancing in Modular Multilevel Converters”. en. *IFAC-PapersOnLine*. 18th IFAC Workshop on Control Applications of Optimization CAO 2022. 2022, ISSN: 2405-8963. DOI: 10.1016/j.ifacol.2022.09.004.

[LFB22b] G. Le Goff, M. Fadel, and M. Bodson. “_Scalable Control-Oriented Model of the Modular Multilevel Converter for Polyphase Systems”. *IEEE Transactions on Industry Applications (TIA)*. 2022. Conference Name: IEEE Transactions on Industry Applications, ISSN: 1939-9367. DOI: 10.1109/TIA.2022.3152470.

[LFB22c] G. Le Goff, M. Fadel, and M. Bodson. “Scalable Control Allocation: Real-time Optimized Current Control in the Modular Multilevel Converter for Polyphase Systems”. *2022 International Symposium on Power Electronics, Electrical Drives, Automation and Motion (SPEEDAM)*. Sorrento, Italy, 2022, DOI: 10.1109/SPEEDAM53979.2022.9842095.

[LGZ16] T. Li, A. M. Gole, and C. Zhao. “Harmonic Instability in MMC-HVDC Converters Resulting From Internal Dynamics”. *IEEE Transactions on Power Delivery*. 2016. Conference Name: IEEE Transactions on Power Delivery, ISSN: 1937-4208. DOI: 10.1109/TPWRD.2016.2542188.

[Li+14] F. Li, W. Hua, M. Cheng, and G. Zhang. “Analysis of Fault Tolerant Control for a Nine-Phase Flux-Switching Permanent Magnet Machine”. *IEEE Transactions on Magnetics*. 2014. Conference Name: IEEE Transactions on Magnetics, ISSN: 1941-0069. DOI: 10.1109/TMAG.2014.2325060.

[Li+17] Y. Li, J. Han, Y. Cao, Y. Li, J. Xiong, D. Sidorov, and D. Panasetsky. "A modular multilevel converter type solid state transformer with internal model control method". en. *International Journal of Electrical Power & Energy Systems*. 2017, ISSN: 0142-0615. DOI: 10.1016/j.ijepes.2016.09.001.

[Lia+07] F. Liao, K. Lum, J. L. Wang, and M. Benosman. "Constrained nonlinear finite-time control allocation". *2007 American Control Conference*. 2007,

[Lia+09] F. Liao, K.-Y. Lum, J. L. Wang, and M. Benosman. "Adaptive nonlinear control allocation of non-minimum phase uncertain systems". *2009 American Control Conference*. ISSN: 2378-5861. 2009, DOI: 10.1109/ACC.2009.5159887.

[Lim+21a] T. A. Lima, S. Tarbouriech, B. C. Torrico, and F. G. Nogueira. "Energy-based design of dynamic allocation in the presence of saturating actuators". *24th International Symposium on Mathematical Theory of Networks and Systems MTNS 2020*. Cambridge, United Kingdom, 2021. DOI: 10.1016/j.ifacol.2021.06.087.

[Lim+21b] T. A. Lima, S. Tarbouriech, F. G. Nogueira, and B. C. Torrico. "Co-Design of Dynamic Allocation Functions and Anti-Windup". *IEEE Control Systems Letters*. 2021. Conference Name: IEEE Control Systems Letters, ISSN: 2475-1456. DOI: 10.1109/LCSYS.2020.3047361.

[Liu+14] S. Liu, Z. Xu, W. Hua, G. Tang, and Y. Xue. "Electromechanical Transient Modeling of Modular Multilevel Converter Based Multi-Terminal HVDC Systems". en. *IEEE Transactions on Power Systems*. 2014, ISSN: 0885-8950, 1558-0679. DOI: 10.1109/TPWRS.2013.2278402.

[Liu+16] G. Liu, L. Qu, W. Zhao, Q. Chen, and Y. Xie. "Comparison of Two SVPWM Control Strategies of Five-Phase Fault-Tolerant Permanent-Magnet Motor". *IEEE Transactions on Power Electronics*. 2016. Conference Name: IEEE Transactions on Power Electronics, ISSN: 1941-0107. DOI: 10.1109/TPEL.2015.2499211.

[Liu+17] X. Liu, X. Wang, K. Zheng, and J. Wen. "IMC based circulating current controller for MMC-HVDC". *2017 36th Chinese Control Conference (CCC)*. ISSN: 1934-1768. 2017, DOI: 10.23919/ChiCC.2017.8029047.

[Liu+21] X. Liu, Z. Hu, Z. Yang, and W. Zhang. "Real-Time Control Allocation for Autonomous Surface Vehicle Using Constrained Quadratic Programming". *Guidance, Navigation and Control*. 2021. Publisher: World Scientific Publishing Co., ISSN: 2737-4807. DOI: 10.1142/S2737480721400070.

[Liz+15] R. Lizana, M. A. Perez, D. Arancibia, J. R. Espinoza, and J. Rodriguez. "Decoupled current model and control of modular multilevel converters". *IEEE Transactions on Industrial Electronics*. 2015,

[LLB13] H. Liu, P. C. Loh, and F. Blaabjerg. "Review of fault diagnosis and fault-tolerant control for modular multilevel converter of HVDC". *IECON 2013 - 39th Annual Conference of the IEEE Industrial Electronics Society*. ISSN: 1553-572X. 2013, DOI: 10.1109/IECON.2013.6699310.

[LM03] A. Lesnicar and R. Marquardt. "An innovative modular multilevel converter topology suitable for a wide power range". en. *2003 IEEE Bologna Power Tech Conference Proceedings*. 2003. DOI: 10.1109/PTC.2003.1304403.

[Loc+06] F. Locment, E. Semail, X. Kestelyn, and A. Bouscayrol. "Control of a Seven-phase Axial Flux Machine Designed for Fault Operation". *IECON 2006 - 32nd Annual Conference on IEEE Industrial Electronics*. ISSN: 1553-572X. 2006, DOI: 10.1109/IECON.2006.347611.

[LRV10] D. C. Ludois, J. K. Reed, and G. Venkataramanan. "Hierarchical Control of Bridge-of-Bridge Multilevel Power Converters". *IEEE Transactions on Industrial Electronics*. 2010. Conference Name: IEEE Transactions on Industrial Electronics, ISSN: 1557-9948. DOI: 10.1109/TIE.2009.2030205.

[Luo+04] Y. Luo, A. Serrani, S. Yurkovich, D. Doman, and M. Oppenheimer. "Model predictive dynamic control allocation with actuator dynamics". *Proceedings of the 2004 American Control Conference*. ISSN: 0743-1619. 2004, DOI: 10.23919/ACC.2004.1386823.

[Luo+05] Y. Luo, A. Serrani, S. Yurkovich, D. Doman, and M. Oppenheimer. "Dynamic control allocation with asymptotic tracking of time-varying control input commands". *Proceedings of the 2005, American Control Conference, 2005.* ISSN: 2378-5861. 2005, DOI: 10.1109/ACC.2005.1470280.

[Luo+07] Y. Luo, A. Serrani, S. Yurkovich, M. W. Oppenheimer, and D. B. Doman. "Model-Predictive Dynamic Control Allocation Scheme for Reentry Vehicles". *Journal of Guidance, Control, and Dynamics*. 2007. Publisher: American Institute of Aeronautics and Astronautics _eprint: https://doi.org/10.2514/1.25473, ISSN: 0731-5090. DOI: 10.2514/1.25473.

[LV14] D. C. Ludois and G. Venkataramanan. "Simplified Terminal Behavioral Model for a Modular Multilevel Converter". *IEEE Transactions on Power Electronics*. 2014. Conference Name: IEEE Transactions on Power Electronics, ISSN: 1941-0107. DOI: 10.1109/TPEL.2013.2268856.

[Lyu+18] J. Lyu, X. Cai, X. Zhang, and M. Molinas. "Harmonic state space modeling and analysis of modular multilevel converter". *2018 IEEE International Power Electronics and Application Conference and Exposition (PEAC)*. 2018, DOI: 10.1109/PEAC.2018.8590305.

[LZS21] S. Lang, F. Zhang, and Z. Sun. "Fault Tolerant Control for a Hexacopter Based on Optimal Adaptive Control Allocation". *2021 40th Chinese Control Conference (CCC)*. ISSN: 1934-1768. 2021, DOI: 10.23919/CCC52363.2021.9549750.

[Ma+08] J. Ma, W. Li, Z. Zheng, and D. Hu. "Constrained control allocation based on nonlinear compensation with application to flight control". *2008 2nd International Symposium on Systems and Control in Aerospace and Astronautics*. 2008, DOI: 10.1109/ISSCAA.2008.4776360.

[Ma+19] Y. Ma, H. Lin, Z. Wang, and Z. Ze. "Stability analysis of modular multilevel converter based on harmonic state-space theory". en. *IET Power Electronics*. 2019. _eprint: https://onlinelibrary.wiley.com/doi/pdf/10.1049/iet-pel.2019.0613, ISSN: 1755-4543. DOI: 10.1049/iet-pel.2019.0613.

[Mab+22] J. Mabboux, S. Delbecq, V. Pommier-Budinger, J. Bordeneuve-Guibe, A. Truc-Hermel, and J.-M. Kai. "A bi-level co-design approach for multicopters". *ICAS 2022 Proceedings*. arXiv:2301.12905 [cs, eess]. arXiv, 2022. DOI: 10.48550/arXiv.2301.12905.

[MAC04] A. Mitcham, G. Antonopoulos, and J. Cullen. "Favourable slot and pole number combinations for fault-tolerant PM machines". *Electric Power Applications, IEE Proceedings* -. 2004, DOI: 10.1049/ip-epa:20040584.

[Mar02] R. Marquardt. "Current rectification circuit for voltage source inverters with separate energy stores replaces phase blocks with energy storing capacitors". en. 2002.

[Mar10] R. Marquardt. "Modular Multilevel Converter: An universal concept for HVDC-Networks and extended DC-Bus-applications". *The 2010 International Power Electronics Conference - ECCE ASIA* -. ISSN: null. 2010, DOI: 10.1109/IPEC.2010.5544594.

[Mar11] R. Marquardt. "Modular Multilevel Converter topologies with DC-Short circuit current limitation". Pages: 1431. 2011. DOI: 10.1109/ICPE.2011.5944451.

[Mar18] R. Marquardt. "Modular multilevel converters: state of the art and future progress". *IEEE Power Electronics Magazine*. 2018, ISSN: 2329-9215.

[MAR19] M. Majstorović, M. E. R. Abarca, and L. Ristic. "Review of MPC Techniques for MMCs". *2019 20th International Symposium on Power Electronics (Ee)*. 2019, DOI: 10.1109/PEE.2019.8923191.

[Max65] J. C. Maxwell. "VIII. A dynamical theory of the electromagnetic field". *Philosophical Transactions of the Royal Society of London*. 1865. Publisher: Royal Society, DOI: 10.1098/rstl.1865.0008.

[Max68] J. C. Maxwell. "On governors". *Proceedings of the Royal Society of London*. 1868, DOI: 10.1098/rspl.1867.0055.

[MBB11] D. J. Machowski, D. J. W. Bialek, and D. J. Bumby. "Power System Dynamics: Stability and Control". en. Google-Books-ID: wZv92UdKxi4C. John Wiley & Sons, 2011. ISBN: 978-1-119-96505-3.

[MC76] R. Middlebrook and S. Cuk. "A general unified approach to modelling switching-converter power stages". Cleveland, 1976.

[MGB89] D. Mattern, S. Garg, and R. Bullard. "Integrated flight/propulsion control system design based on a decentralized, hierarchical approach". *Guidance, Navigation and Control Conference*. Guidance, Navigation, and Control and Co-located Conferences. American Institute of Aeronautics and Astronautics, 1989. DOI: 10.2514/6.1989-3519.

[MLE10] P. Münch, S. Liu, and G. Ebner. "Multivariable current control of Modular Multilevel Converters with disturbance rejection and harmonics compensation". *2010 IEEE International Conference on Control Applications*. ISSN: 1085-1992. 2010, DOI: 10.1109/CCA.2010.5611205.

[MLY20] C. Ma, C. Liu, and J. Yao. "Fault tolerant control using integral sliding modes with control allocation along the null-space". en. *Transactions of the Institute of Measurement and Control*. 2020. Publisher: SAGE Publications Ltd STM, ISSN: 0142-3312. DOI: 10.1177/0142331220904570.

[MU07] K. Meah and S. Ula. "Comparative Evaluation of HVDC and HVAC Transmission Systems". *2007 IEEE Power Engineering Society General Meeting*. ISSN: 1932-5517. 2007, DOI: 10.1109/PES.2007.385993.

[Mün+10] P. Münch, D. Görges, M. Izák, and S. Liu. "Integrated current control, energy control and energy balancing of Modular Multilevel Converters". *IECON 2010 - 36th Annual Conference on IEEE Industrial Electronics Society*. ISSN: 1553-572X. 2010, DOI: 10.1109/IECON.2010.5675185.

[NÄJ12] S. Norrga, L. Ängquist, and K. Jlves. "Operating region extension for multilevel converters in HVDC applications by optimisation methods". en. 2012. Publisher: IET Digital Library, DOI: 10.1049/cp.2012.1987.

[NW99] J. Nocedal and S. J. Wright. "Numerical optimization". en. Springer series in operations research. New York: Springer, 1999. ISBN: 978-0-387-98793-4.

[Par29] R. H. Park. "Two-reaction theory of synchronous machines generalized method of analysis-part I". *Transactions of the American Institute of Electrical Engineers*. 1929, ISSN: 2330-9431. DOI: 10.1109/T-AIEE.1929.5055275.

[Par33] R. H. Park. "Two-reaction theory of synchronous machines-II". *Transactions of the American Institute of Electrical Engineers*. 1933, ISSN: 2330-9431. DOI: 10.1109/T-AIEE.1933.5056309.

[Par89] J. Paradiso. "A highly adaptable method of managing jets and aerosurfaces for control of aerospace vehicles". en. *Guidance, Navigation and Control Conference*. Boston,MA,U.S.A.: American Institute of Aeronautics and Astronautics, 1989. DOI: 10.2514/6.1989-3429.

[Pat+16] A. Patzak, F. Bachheibl, A. Baumgardt, G. Dajaku, O. Moros, and D. Gerling. "ISCAD - Electric High Performance Drive for Individual Mobility at Extra-Low Voltages". *SAE International Journal of Alternative Powertrains*. 2016. Publisher: SAE International, ISSN: 2167-4191.

[PB05] J. A. Petersen and M. Bodson. "Interior-Point Algorithms for Control Allocation". en. *Journal of Guidance, Control, and Dynamics*. 2005, ISSN: 0731-5090, 1533-3884.

[PB06] J. A. M. Petersen and M. Bodson. "Constrained quadratic programming techniques for control allocation". *IEEE Transactions on Control Systems Technology*. 2006,

[PBW22] M. B. Peterson, R. W. Beard, and J. B. Willis. "Nonlinear, Low-Energy-Actuator-Prioritizing Control Allocation for Winged eVTOL UAVs". *2022 Intermountain Engineering, Technology and Computing (IETC)*. 2022, DOI: 10.1109/IETC54973.2022.9796842.

[Pea10] O. Peake. "The History of High Voltage Direct Current Transmission". en. *Australian Journal of Multi-Disciplinary Engineering*. 2010, ISSN: 1448-8388, 2204-2180. DOI: 10.1080/14488388.2010.11464824.

[Per+12] J. Peralta, H. Saad, S. Dennetiere, J. Mahseredjian, and S. Nguefeu. "Detailed and Averaged Models for a 401-Level MMC–HVDC System". *IEEE Transactions on Power Delivery*. 2012,

[Per+15] M. A. Perez, S. Bernet, J. Rodriguez, S. Kouro, and R. Lizana. "Circuit Topologies, Modeling, Control Schemes, and Applications of Modular Multilevel Converters". *IEEE Transactions on Power Electronics*. 2015, ISSN: 1941-0107. DOI: 10.1109/TPEL.2014.2310127.

[Per13] J. Peralta Rodriguez. "Dynamic averaged models of VSC-based HVDC systems for electromagnetic transient programs". fr. PhD thesis. Ecole Polytechnique de Montréal, 2013.

[PG14] A. Patzak and D. Gerling. "Design of a multi-phase inverter for low voltage high power electric vehicles". *2014 IEEE International Electric Vehicle Conference (IEVC)*. 2014, DOI: 10.1109/IEVC.2014.7056143.

[PK06] L. Parsa and T. Kim. "Reducing Torque Pulsation of Multi-Phase Interior Permanent Magnet Machines". *Conference Record of the 2006 IEEE Industry Applications Conference Forty-First IAS Annual Meeting*. ISSN: 0197-2618. 2006, DOI: 10.1109/IAS.2006.256806.

[Poo+04] V. L. Poonamallee, S. Yurkovich, A. Serrani, and D. B. Doman. "A nonlinear programming approach for control allocation". *Proceedings of the 2004 American Control Conference*. ISSN: 0743-1619. 2004, DOI: 10.23919/ACC.2004.1386822.

[Pou+15] J. Pou, S. Ceballos, G. Konstantinou, V. G. Agelidis, R. Picas, and J. Zaragoza. "Circulating Current Injection Methods Based on Instantaneous Information for the Modular Multilevel Converter". *IEEE Transactions on Industrial Electronics*. 2015. Conference Name: IEEE Transactions on Industrial Electronics, ISSN: 1557-9948. DOI: 10.1109/TIE.2014.2336608.

[PR11] M. A. Perez and J. Rodriguez. "Generalized modeling and simulation of a modular multilevel converter". en. *2011 IEEE International Symposium on Industrial Electronics*. Gdansk, Poland: IEEE, 2011, ISBN: 978-1-4244-9310-4. DOI: 10.1109/ISIE.2011.5984441.

[PRB14] M. A. Perez, J. Rodriguez, and S. Bernet. "Decoupled capacitor voltage control of modular multilevel converters". *2014 IEEE Energy Conversion Congress and Exposition (ECCE)*. 2014, DOI: 10.1109/ECCE.2014.6954079.

[Rak+13] E. Rakhshani, A. M. Cantarellas, D. Remon, P. Rodriguez, and I. Candela. "Modeling and control of multi modular converters using optimal LQR controller with integral action". *2013 IEEE Energy Conversion Congress and Exposition*. ISSN: 2329-3748. 2013, DOI: 10.1109/ECCE.2013.6647226.

[Rak+20] E. Rakhshani, K. Rouzbehi, J. M. Escaño, and J. Rueda Torres. "Optimal Linear Control of Modular Multi-Level Converters with a Prescribed Degree of Stability". *Electric Power Components and Systems*. 2020, ISSN: 1532-5008. DOI: 10.1080/15325008.2020.1732502.

[Ras+09] A. Rasic, U. Krebs, H. Leu, and G. Herold. "Optimization of the modular multilevel converters performance using the second harmonic of the module current". *2009 13th European Conference on Power Electronics and Applications*. 2009,

[RGM15] B. S. Riar, T. Geyer, and U. K. Madawala. "Model Predictive Direct Current Control of Modular Multilevel Converters: Modeling, Analysis, and Experimental Evaluation". *IEEE Transactions on Power Electronics*. 2015, ISSN: 1941-0107. DOI: 10.1109/TPEL.2014.2301438.

[Ric+78] J. Richalet, A. Rault, J. L. Testud, and J. Papon. "Model predictive heuristic control: Applications to industrial processes". en. *Automatica*. 1978, ISSN: 0005-1098. DOI: 10.1016/0005-1098(78)90001-8.

[Ros70] H. H. Rosenbrock. "State-space and multivariable theory". eng. Open Library ID: OL5220438M. New York: Wiley Interscience Division, 1970.

[RP02] J. A. Reyer and P. Y. Papalambros. "Combined Optimal Design and Control With Application to an Electric DC Motor". *Journal of Mechanical Design*. 2002, ISSN: 1050-0472. DOI: 10.1115/1.1460904.

[RS09] E. Ruth and A. J. Sørensen. "A solution to the nonconvex linearly constrained quadrating thrust allocaton". en. *IFAC Proceedings Volumes*. 8th IFAC Conference on Manoeuvring and Control of Marine Craft. 2009, ISSN: 1474-6670. DOI: 10.3182/20090916-3-BR-3001.0002.

[RWB11] S. Rohner, J. Weber, and S. Bernet. "Continuous model of Modular Multilevel Converter with experimental verification". *2011 IEEE Energy Conversion Congress and Exposition*. ISSN: 2329-3748. 2011, DOI: 10.1109/ECCE.2011.6064316.

[Ryn83] E. G. Rynaski. "Experimental experience at Calspan". *Restructurable Controls*. Nasa Conference Publication 2277. 1983,

[Saa+13a] H. Saad, C. Dufour, J. Mahseredjian, S. Dennetière, and S. Nguefeu. "Real Time simulation of MMCs using the State- Space Nodal Approach". en. Vancouver, Canada, 2013,

[Saa+13b] H. Saad, J. Peralta, S. Dennetière, J. Mahseredjian, J. Jatskevich, J. A. Martinez, A. Davoudi, et al. "Dynamic Averaged and Simplified Models for MMC-Based HVDC Transmission Systems". *IEEE Transactions on Power Delivery*. 2013. Conference Name: IEEE Transactions on Power Delivery, ISSN: 1937-4208. DOI: 10.1109/TPWRD.2013.2251912.

[Saa+14] H. Saad, S. Dennetière, J. Mahseredjian, P. Delarue, X. Guillaud, J. Peralta, and S. Nguefeu. "Modular Multilevel Converter Models for Electromagnetic Transients". *IEEE Transactions on Power Delivery*. 2014, ISSN: 1937-4208. DOI: 10.1109/TPWRD.2013.2285633.

[Saa+15] H. Saad, X. Guillaud, J. Mahseredjian, S. Dennetiere, and S. Nguefeu. "MMC Capacitor Voltage Decoupling and Balancing Controls". en. *IEEE Transactions on Power Delivery*. 2015, ISSN: 0885-8977, 1937-4208. DOI: 10.1109/TPWRD.2014.2338861.

[Saa+16] H. Saad, K. Jacobs, W. Lin, and D. Jovcic. "Modelling of MMC including half-bridge and Full-bridge submodules for EMT study". *2016 Power Systems Computation Conference (PSCC)*. ISSN: null. 2016, DOI: 10.1109/PSCC.2016.7541008.

[Saa15] H. A. Saad. "Modélisation et simulation d'une liaison HVDC de type VSC-MMC". fr. PhD thesis. Ecole Polytechnique de Montréal, 2015.

[San+21] M. F. Santos, L. M. Honório, A. P. G. M. Moreira, M. F. Silva, and V. F. Vidal. "Fast Real-Time Control Allocation Applied to Over-Actuated Quadrotor Tilt-Rotor". en. *Journal of Intelligent & Robotic Systems*. 2021, ISSN: 1573-0409. DOI: 10.1007/s10846-021-01411-4.

[SB18] R. S. Sutton and A. G. Barto. "Reinforcement Learning, second edition: An Introduction". en. Google-Books-ID: uWV0DwAAQBAJ. MIT Press, 2018. ISBN: 978-0-262-35270-3.

[SB20] Ö. C. Sakinci and J. Beerten. "Equivalent Multiple dq-Frame Model of the MMC Using Dynamic Phasor Theory in the $\alpha \beta z$-Frame". *IEEE Transactions on Power Delivery*. 2020. Conference Name: IEEE Transactions on Power Delivery, ISSN: 1937-4208. DOI: 10.1109/TPWRD.2020.3025388.

[SBH03] E. Semail, A. Bouscayrol, and J.-P. Hautier. "Vectorial formalism for analysis and design of polyphase synchronous machines". *European Physical Journal: Applied Physics*. 2003, DOI: 10.1051/epjap:2003034.

[SC98] H. Selhi and C. Christopoulos. "Generalised TLM switch model for power electronics applications". en. *IEE Proceedings - Science, Measurement and Technology*. 1998. Publisher: IET Digital Library, ISSN: 1359-7094. DOI: 10.1049/ip-smt:19981896.

[SCF15] D. Siemaszko, M. Carpita, and P. Favre-Perrod. "Conception of a modular multilevel converter in a multi-terminal DC/AC transmission network". *2015 17th European Conference on Power Electronics and Applications (EPE'15 ECCE-Europe)*. 2015, DOI: 10.1109/EPE.2015.7309452.

[Sch+04] J. D. Schierman, D. G. Ward, J. R. Hull, N. Gandhi, M. Oppenheimer, and D. B. Doman. "Integrated Adaptive Guidance and Control for Re-Entry Vehicles with Flight Test Results". *Journal of Guidance, Control, and Dynamics*. 2004. Publisher: American Institute of Aeronautics and Astronautics _eprint: https://doi.org/10.2514/1.10344, ISSN: 0731-5090. DOI: 10.2514/1.10344.

[SDA11] S. Sedghi, A. Dastfan, and A. Ahmadyfard. "Fault detection of a seven level modular multilevel inverter via voltage histogram and Neural Network". *8th International Conference on Power Electronics - ECCE Asia*. ISSN: 2150-6086. 2011, DOI: 10.1109/ICPE.2011.5944674.

[Sei88] P. F. Seixas. "Commande numérique d'une machine synchrone autopilotée : méthode algébrique de modulation de largeur d'impulsion : algorithmes de contrôle et de régulation des courants". These de doctorat. Toulouse, INPT, 1988.

[Sel+19] S. I. Seleme, L.-A. Grégoire, M. Cousineau, and P. Ladoux. "Modular control with carrier auto-interleaving and capacitor-voltage balancing for MMCs". *IET Power Electronics*. 2019. Conference Name: IET Power Electronics, ISSN: 1755-4535. DOI: 10.1049/iet-pel.2018.5096.

[Ser14] N. Serbia. "Modular multilevel converters for HVDC power stations". en. Ph.D. Thesis. Institut National Polytechnique de Toulouse, 2014.

[SGE90] S. Snell, J. Garrard William, and D. Enns. "Nonlinear inversion flight control for a supermaneuverable aircraft". *Guidance, Navigation and Control Conference*. Guidance, Navigation, and Control and Co-located Conferences. American Institute of Aeronautics and Astronautics, 1990. DOI: 10.2514/6.1990-3406.

[Sha+16a] K. Sharifabadi, L. Harnefors, H.-P. Nee, S. Norrga, and R. Teodorescu. "Design, Control, and Application of Modular Multilevel Converters for HVDC Transmission Systems". en. Google-Books-ID: d57LDAAAQBAJ. John Wiley & Sons, 2016. ISBN: 978-1-118-85156-2.

[Sha+16b] K. Sharifabadi, L. Harnefors, H.-P. Nee, S. Norrga, and R. Teodorescu. "Dynamics and control". *Design, control, and application of modular multilevel converters for HVDC transmission systems*. IEEE, 2016, ISBN: 978-1-118-85152-4.

[Sha+16c] K. Sharifabadi, L. Harnefors, H.-P. Nee, S. Norrga, and R. Teodorescu. "Introduction to modular multilevel converters". *Design, control, and application of modular multilevel converters for HVDC transmission systems*. IEEE, 2016, ISBN: 978-1-118-85156-2. DOI: 10.1002/9781118851555.ch1.

[Shi+10] J. Shi, W. Zhang, G. Li, and X. Liu. "Research on allocation efficiency of the redistributed pseudo inverse algorithm". en. *Science China Information Sciences*. 2010, ISSN: 1862-2836. DOI: 10.1007/s11432-010-0032-x.

[Shi+12] Z. Shi, B. Li, Q. Hu, and Q. Gao. "Dynamic control allocation based-on robust adaptive backstepping control for attitude maneuver of spacecraft with redundant reaction wheels". *2012 24th Chinese Control and Decision Conference (CCDC)*. 2012, DOI: 10.1109/CCDC.2012.6243002.

[Sie] Siemens. "SINAVY DC-Prop and SINAVY PERMASYN, Integrated Propulsion Solutions for Submarines".

[SK10] E. Semail and X. Kestelyn. "Modélisation vectorielle et commande de machines polyphasées à pôles lisses alimentées par onduleur de tension". *Commandes d'actionneurs électriques synchrones et spéciaux*. Hermes, Lavoisier, 2010,

[SKB04] E. Semail, X. Kestelyn, and A. Bouscayrol. "Right harmonic spectrum for the back-electromotive force of an n-phase synchronous motor". *Conference Record of the 2004 IEEE Industry Applications Conference, 2004. 39th IAS Annual Meeting*. 2004, DOI: 10.1109/IAS.2004.1348390.

[Sku+18] R. Skulstad, G. Li, H. Zhang, and T. I. Fossen. "A Neural Network Approach to Control Allocation of Ships for Dynamic Positioning". en. *IFAC-PapersOnLine*. 11th IFAC Conference on Control Applications in Marine Systems, Robotics, and Vehicles CAMS 2018. 2018, ISSN: 2405-8963. DOI: 10.1016/j.ifacol.2018.09.481.

[Sku21] R. Skulstad. "Data-Based Modelling of Ships for Motion Prediction and Control Allocation". eng. Accepted: 2021-12-02T09:55:42Z ISSN: 2703-8084. NTNU, 2021. ISBN: 978-82-326-6605-8.

[Sør11] A. J. Sørensen. "A survey of dynamic positioning control systems". en. *Annual Reviews in Control*. 2011, ISSN: 1367-5788. DOI: 10.1016/j.arcontrol.2011.03.008.

[Sør97] O. J. Sørdalen. "Optimal thrust allocation for marine vessels". en. *Control Engineering Practice*. 1997, ISSN: 0967-0661. DOI: 10.1016/S0967-0661(97)84361-4.

[SPA02] N. Sarkar, T. Podder, and G. Antonelli. "Fault-accommodating thruster force allocation of an AUV considering thruster redundancy and saturation". *IEEE Transactions on Robotics and Automation*. 2002. Conference Name: IEEE Transactions on Robotics and Automation, ISSN: 2374-958X. DOI: 10.1109/TRA.2002.999650.

[SS64] A. Schonung and H. Stemmler. "Static Frequency Changers with Subharmonic Control in Conjunction with Reversible Variable-Speed AC Drives". *Brown Boveri Review*. 1964.

[Ste+20] B. Stellato, G. Banjac, P. Goulart, A. Bemporad, and S. Boyd. "OSQP: An Operator Splitting Solver for Quadratic Programs". en. *Mathematical Programming Computation*. 2020. arXiv: 1711.08013, ISSN: 1867-2949, 1867-2957. DOI: 10.1007/s12532-020-00179-2.

[Ste+21] A. Stepanov, J. Mahseredjian, U. Karaagac, and H. Saad. "Adaptive Modular Multilevel Converter Model for Electromagnetic Transient Simulations". *IEEE Transactions on Power Delivery*. 2021. Conference Name: IEEE Transactions on Power Delivery, ISSN: 1937-4208. DOI: 10.1109/TPWRD.2020.2993502.

[Str97] A. Strollo. "A new IGBT circuit model for SPICE simulation". *PESC97. Record 28th Annual IEEE Power Electronics Specialists Conference. Formerly Power Conditioning Specialists Conference 1970-71. Power Processing and Electronic Specialists Conference 1972*. ISSN: 0275-9306. 1997, DOI: 10.1109/PESC.1997.616704.

[Sun+18] Y. Sun, C. A. Teixeira, D. G. Holmes, B. P. McGrath, and J. Zhao. "Low-Order Circulating Current Suppression of PWM-Based Modular Multilevel Converters Using DC-Link Voltage Compensation". *IEEE Transactions on Power Electronics*. 2018. Conference Name: IEEE Transactions on Power Electronics, ISSN: 1941-0107. DOI: 10.1109/TPEL.2017.2670369.

[Tag+09] K. Tagesson, P. Sundstrom, L. Laine, and N. Dela. "Real-time performance of control allocation for actuator coordination in heavy vehicles". *2009 IEEE Intelligent Vehicles Symposium*. ISSN: 1931-0587. 2009, DOI: 10.1109/IVS.2009.5164359.

[Tal+17] E. Talon, D. Siemaszko, S. Gavin, D. Leu, P. Favre-Perrod, and M. Carpita. "Use of Modular Multilevel Converter in Multi-Terminal DC Transmission Network: Reduced Scale Set-up and Experimental Results". 2017. DOI: 10.23919/EPE17ECCEEurope.2017.8099291.

[Tal+18] E. Talon, S. Gavin, D. Siemaszko, B. Frederick, B. Essimbi, M. Marchesoni, and M. Carpita. "Small-Scale Modular Multilevel Converter for Multi-Terminal DC Networks Applications: System Control Validation". *Energies*. 2018. DOI: 10.3390/en11071690.

[Teo+06] R. Teodorescu, F. Blaabjerg, M. Liserre, and P. C. Loh. "Proportional-resonant controllers and filters for grid-connected voltage-source converters". en. *IEE Proceedings - Electric Power Applications*. 2006. Publisher: IET Digital Library, ISSN: 1359-7043. DOI: 10.1049/ip-epa:20060008.

[Tia+17] B. Tian, Q.-T. An, J.-D. Duan, D. Semenov, D.-Y. Sun, and L. Sun. "Cancellation of Torque Ripples With FOC Strategy Under Two-Phase Failures of the Five-Phase PM Motor". *IEEE Transactions on Power Electronics*. 2017. Conference Name: IEEE Transactions on Power Electronics, ISSN: 1941-0107. DOI: 10.1109/TPEL.2016.2598778.

[TJ05a] J. Tjønnås and T. A. Johansen. "Optimizing nonlinear adaptive control allocation". en. *IFAC Proceedings Volumes*. 16th IFAC World Congress. 2005, ISSN: 1474-6670. DOI: 10.3182/20050703-6-CZ-1902.00850.

[TJ05b] P. Tondel and T. Johansen. "Control allocation for yaw stabilization in automotive vehicles using multiparametric nonlinear programming". *Proceedings of the 2005, American Control Conference, 2005*. ISSN: 2378-5861. 2005, DOI: 10.1109/ACC.2005.1469977.

[TJ07] J. Tjonnas and T. A. Johansen. "Optimizing adaptive control allocation with actuator dynamics". *2007 46th IEEE Conference on Decision and Control*. ISSN: 0191-2216. 2007, DOI: 10.1109/CDC.2007.4434782.

[TJ08] J. Tjønnås and T. A. Johansen. "Adaptive control allocation". en. *Automatica*. 2008, ISSN: 0005-1098. DOI: 10.1016/j.automatica.2008.03.031.

[TJ10] J. Tjonnas and T. A. Johansen. "Stabilization of Automotive Vehicles Using Active Steering and Adaptive Brake Control Allocation". *IEEE Transactions on Control Systems Technology*. 2010. Conference Name: IEEE Transactions on Control Systems Technology, ISSN: 1558-0865. DOI: 10.1109/TCST.2009.2023981.

[TN11] A. Tavasoli and M. Naraghi. "Comparison of Static and Dynamic Control Allocation Techniques for Integrated Vehicle Control". en. *IFAC Proceedings Volumes*. 18th IFAC World Congress. 2011, ISSN: 1474-6670. DOI: 10.3182/20110828-6-IT-1002.00398.

[Tri+16] N.-T. Trinh, M. Zeller, K. Wuerflinger, and I. Erlich. "Generic Model of MMC-VSC-HVDC for Interaction Study With AC Power System". *IEEE Transactions on Power Systems*. 2016. Conference Name: IEEE Transactions on Power Systems, ISSN: 1558-0679. DOI: 10.1109/TPWRS.2015.2390416.

[TSN04] F. Terrien, S. Siala, and P. Noy. "Multiphase induction motor sensorless control for electric ship propulsion". *Second International Conference on Power Electronics, Machines and Drives (PEMD 2004)*. ISSN: 0537-9989. 2004, DOI: 10.1049/cp:20040348.

[Tu+12] Q. Tu, Z. Xu, Y. Chang, and L. Guan. "Suppressing DC Voltage Ripples of MMC-HVDC Under Unbalanced Grid Conditions". *IEEE Transactions on Power Delivery*. 2012. Conference Name: IEEE Transactions on Power Delivery, ISSN: 1937-4208. DOI: 10.1109/TPWRD.2012.2196804.

[TV97] V. Thottuvelil and G. Verghese. "Analysis and control design of paralleled DC/DC converters with current sharing". *Proceedings of APEC 97 - Applied Power Electronics Conference*. 1997, DOI: 10.1109/APEC.1997.575646.

[TWL98] H. Toliyat, S. Waikar, and T. Lipo. "Analysis and simulation of five-phase synchronous reluctance machines including third harmonic of airgap MMF". *IEEE Transactions on Industry Applications*. 1998. Conference Name: IEEE Transactions on Industry Applications, ISSN: 1939-9367. DOI: 10.1109/28.663476.

[TX11] Q. Tu and Z. Xu. "Impact of Sampling Frequency on Harmonic Distortion for Modular Multilevel Converter". *IEEE Transactions on Power Delivery*. 2011. Conference Name: IEEE Transactions on Power Delivery, ISSN: 1937-4208. DOI: 10.1109/TPWRD.2010.2078837.

[TXX11] Q. Tu, Z. Xu, and L. Xu. "Reduced Switching-Frequency Modulation and Circulating Current Suppression for Modular Multilevel Converters". *Power Delivery, IEEE Transactions on*. 2011, DOI: 10.1109/TPWRD.2011.2115258.

[TY21] S. S. Tohidi and Y. Yildiz. "Discrete Adaptive Control Allocation". *arXiv:2101.10675 [cs, eess]*. 2021. arXiv: 2101.10675.

[TYK17] S. S. Tohidi, Y. Yildiz, and I. Kolmanovsky. "Adaptive control allocation for over-actuated systems with actuator saturation". en. *IFAC-PapersOnLine*. 20th IFAC World Congress. 2017, ISSN: 2405-8963.

[VB94] J. Virnig and D. Bodden. "Multivariable control allocation and control law conditioning when control effectors limit". en. *Guidance, Navigation, and Control Conference*. Scottsdale, AZ, U.S.A.: American Institute of Aeronautics and Astronautics, 1994. ISBN: 978-1-62410-546-3. DOI: 10.2514/6.1994-3609.

[VD01] R. Venkataraman and D. Doman. "Control allocation and compensation for over-actuated systems with non-linear effectors". *Proceedings of the 2001 American Control Conference. (Cat. No.01CH37148)*. ISSN: 0743-1619. 2001, DOI: 10.1109/ACC.2001.945998.

[VHS15] M. Vatani, M. Hovd, and M. Saeedifard. "Control of the Modular Multilevel Converter Based on a Discrete-Time Bilinear Model Using the Sum of Squares Decomposition Method". *IEEE Transactions on Power Delivery*. 2015. Conference Name: IEEE Transactions on Power Delivery, ISSN: 1937-4208. DOI: 10.1109/TPWRD.2015.2412151.

[VK19] P. S. d. Vries and E.-J. V. Kampen. "Reinforcement Learning-based Control Allocation for the Innovative Control Effectors Aircraft". *AIAA Scitech 2019 Forum*. _eprint: https://arc.aiaa.org/doi/pdf/10.2514/6.2019-0144. American Institute of Aeronautics and Astronautics, 2019. DOI: 10.2514/6.2019-0144.

[Wan+21] J. Wang, Y. Tang, Y. Qi, P. Lin, and Z. Zhang. "A Unified Startup Strategy for Modular Multilevel Converters With Deadbeat Predictive Current Control". *IEEE Transactions on Industrial Electronics*. 2021. Conference Name: IEEE Transactions on Industrial Electronics, ISSN: 1557-9948. DOI: 10.1109/TIE.2020.3007080.

[WBB14] J. Wang, R. Burgos, and D. Boroyevich. "Switching-Cycle State-Space Modeling and Control of the Modular Multilevel Converter". *IEEE Journal of Emerging and Selected Topics in Power Electronics*. 2014. Conference Name: IEEE Journal of Emerging and Selected Topics in Power Electronics, ISSN: 2168-6785. DOI: 10.1109/JESTPE.2014.2354393.

[Wei+21] C. Wei, M. Wang, B. Lu, and J. Pu. "Accelerated Landweber iteration based control allocation for fault tolerant control of reusable launch vehicle". en. *Chinese Journal of Aeronautics*. 2021. ISSN: 1000-9361. DOI: 10.1016/j.cja.2021.03.017.

[Wei+22] H. Wei, L. Fan, Q. Ai, W. Zhao, T. Huang, and Y. Zhang. "Optimal energy allocation strategy for electric vehicles based on the real-time model predictive control technology". en. *Sustainable Energy Technologies and Assessments*. 2022. ISSN: 2213-1388.

[WH00] K. J. Waldron and C. J. Hubert. "Control of contact forces in wheeled and legged off-road vehicles". en. *Experimental Robotics VI*. Ed. by P. Corke and J. Trevelyan. Lecture Notes in Control and Information Sciences. London: Springer, 2000, ISBN: 978-1-84628-541-7. DOI: 10.1007/BFb0119399.

[WLK21] M. Wu, Y. W. Li, and G. Konstantinou. "A Comprehensive Review of Capacitor Voltage Balancing Strategies for Multilevel Converters Under Selective Harmonic Elimination PWM". *IEEE Transactions on Power Electronics*. 2021. Conference Name: IEEE Transactions on Power Electronics, ISSN: 1941-0107. DOI: 10.1109/TPEL.2020.3012915.

[WM73] G. Wester and R. Middlebrook. "Low-Frequency Characterization of Switched dc-dc Converters". *IEEE Transactions on Aerospace and Electronic Systems*. 1973. Conference Name: IEEE Transactions on Aerospace and Electronic Systems, ISSN: 1557-9603. DOI: 10.1109/TAES.1973.309723.

[WSH04] S. Williamson, S. Smith, and C. Hodge. "Fault tolerance in multiphase propulsion motors". *Proceedings of IMarEST - Part A - Journal of Marine Engineering and Technology*. 2004, DOI: 10.1080/20464177.2004.11020174.

[Wu+14] F. Wu, P. Zheng, Y. Sui, B. Yu, and P. Wang. "Design and Experimental Verification of a Short-Circuit Proof Six-Phase Permanent Magnet Machine for Safety Critical Applications". *IEEE Transactions on Magnetics*. 2014. Conference Name: IEEE Transactions on Magnetics, ISSN: 1941-0069. DOI: 10.1109/TMAG.2014.2320902.

[Wu+19] L. Wu, T. Wei, C. Shi, and J. Yin. "Fault-Tolerant Control Strategy for Sub-Module Faults of Modular Multilevel Converters". *2019 IEEE 12th International Symposium on Diagnostics for Electrical Machines, Power Electronics and Drives (SDEMPED)*. 2019, DOI: 10.1109/DEMPED.2019.8864867.

[Wu+22] W. Wu, L. Qiu, J. Rodriguez, X. Liu, J. Ma, and Y. Fang. "Data-Driven Finite Control-Set Model Predictive Control for Modular Multilevel Converter". *IEEE Journal of Emerging and Selected Topics in Power Electronics*. 2022. Conference Name: IEEE Journal of Emerging and Selected Topics in Power Electronics, ISSN: 2168-6785. DOI: 10.1109/JESTPE.2022.3207454.

[WY22] Z. Wang and L. Yao. "Control allocation technology based on fault diagnosis for the unmanned aerial vehicle system subject to physical constraints and fault reconfiguration mismatch". en. *Asian Journal of Control*. 2022. _eprint: https://onlinelibrary.wiley.com/doi/pdf/10.1002/asjc.2896. ISSN: 1934-6093. DOI: 10.1002/asjc.2896.

[Yan+19] J. Yang, X. Xiao, S. Gao, X. Jiang, X. Zhan, J. Wang, and Z. Wu. "Average model of MMC with full-bridge sub-modules for blocking situation". en. 2019. Publisher: IET Digital Library, DOI: 10.1049/cp.2019.0669.

[Yan+22] J. Yang, C. Yang, J. Na, Y. Li, and Y. Xing. "An Adaptive Integral Sliding Mode Control with Allocation Scheme for Reconfigurable Flight Array". *2022 IEEE 11th Data Driven Control and Learning Systems Conference (DDCLS)*. ISSN: 2767-9861. 2022, DOI: 10.1109/DDCLS55054.2022.9858401.

[YCC16] F. Yu, M. Cheng, and K. T. Chau. "Controllability and Performance of a Nine-Phase FSPM Motor Under Severe Five Open-Phase Fault Conditions". *IEEE Transactions on Energy Conversion*. 2016. Conference Name: IEEE Transactions on Energy Conversion, ISSN: 1558-0059. DOI: 10.1109/TEC.2015.2486521.

[Yin+20] J. Yin, J. Leon, M. Perez, L. Franquelo, A. Marquez, and S. Vazquez. "Model Predictive Control of Modular Multilevel Converters Using Quadratic Programming". *IEEE Transactions on Power Electronics*. 2020, DOI: 10.1109/TPEL.2020.3034294.

[YSD17] A. Yadav, S. N. Singh, and S. P. Das. "Modular multi-level converter topologies: Present status and key challenges". *2017 4th IEEE Uttar Pradesh Section International Conference on Electrical, Computer and Electronics (UPCON)*. ISSN: null. 2017, DOI: 10.1109/UPCON.2017.8251061.

[YSP19] Q. Yang, M. Saeedifard, and M. A. Perez. "Sliding Mode Control of the Modular Multilevel Converter". *IEEE Transactions on Industrial Electronics*. 2019. Conference Name: IEEE Transactions on Industrial Electronics, ISSN: 1557-9948. DOI: 10.1109/TIE.2018.2818657.

[YSX16] Z. Yuwei, W. Shaoping, and W. Xingjian. "Control allocation based on adaptive nonlinear dynamic inverse and adaptive pseudo-inverse". *2016 IEEE International Conference on Aircraft Utility Systems (AUS)*. 2016,

[Zac09] L. Zaccarian. "Dynamic allocation for input redundant control systems". en. *Automatica*. 2009, ISSN: 0005-1098. DOI: 10.1016/j.automatica.2009.01.013.

[Zam+16a] A. Zama, S. Bacha, A. Benchaib, D. Frey, and S. Silvant. "A Novel Modular Multilevel Converter Modelling Technique Based on Semi-Analytical Models". *international Conference on Renewable Energy: Generation and Applications*. Belfort, France, 2016.

[Zam+16b] A. I. Zama, D. Frey, A. Benchaib, S. Bacha, B. Luscan, and S. Silvant. "Optimisation des Pertes par Commutation dans un Convertisseur Modulaire Multiniveaux (MMC)". *Symposium de Genie Electrique*. Grenoble, France, 2016.

[Zam17] M. Zama. "Modeling and control of modular multilevel converters (MMCs) for HVDC applications". en. Ph.D. Thesis. Communauté Université Grenoble Alpes, 2017.

[Zha+16] H. Zhang, D. Jovcic, W. Lin, and A. J. Far. "Average value MMC model with accurate blocked state and cell charging/discharging dynamics". *2016 4th International Symposium on Environmental Friendly Energies and Applications (EFEA)*. 2016, DOI: 10.1109/EFEA.2016.7748768.

[Zha+21] H. Zhang, M. M. Belhaouane, F. Colas, R. Kadri, F. Gruson, and X. Guillaud. "On Comprehensive Description and Analysis of MMC Control Design: Simulation and Experimental Study". *IEEE Transactions on Power Delivery*. 2021. Conference Name: IEEE Transactions on Power Delivery, ISSN: 1937-4208. DOI: 10.1109/TPWRD.2020.2977470.

[Zhe+12] P. Zheng, F. Wu, Y. Sui, P. Wang, Y. Lei, and H. Wang. "Harmonic Analysis and Fault-Tolerant Capability of a Semi-12-Phase Permanent-Magnet Synchronous Machine Used for EVs". en. *Energies*. 2012. Number: 9 Publisher: Molecular Diversity Preservation International, ISSN: 1996-1073. DOI: 10.3390/en5093586.

[Zho+17] H. Zhou, W. Zhao, G. Liu, R. Cheng, and Y. Xie. "Remedial Field-Oriented Control of Five-Phase Fault-Tolerant Permanent-Magnet Motor by Using Reduced-Order Transformation Matrices". *IEEE Transactions on Industrial Electronics*. 2017. Conference Name: IEEE Transactions on Industrial Electronics, ISSN: 1557-9948. DOI: 10.1109/TIE.2016.2599501.

????